Novel Molecular Triggers of T-cell Activation and Fibrosis in Cardiac Stress and Cancer

A thesis submitted by

Abraham Louis Bayer

in partial fulfillment of the requirements for the degree of

PhD

in

Immunology

Tufts University

Graduate School of Biomedical Sciences

March 2025

Advisor: Pilar Alcaide, PhD

Abstract:

Cardiovascular disease (CVD) and cancer are the two most common causes of death around the world. Many patients suffer from both diseases, as they share risk factors and elements of their pathogenesis. Patients with both CVD and cancer exhibit chronic inflammation, including T-lymphocytes, which are critical in responding to both cardiac and tumor derived antigens to cause cardiac damage or fight tumor progression, respectively. While immune modulating therapies have been utilized in both cardiology and oncology, their widespread efficacy is limited, and can have significant side effects, requiring greater mechanistic studies of inflammation in the context of cancer and CVD. The goal of this dissertation is investigate mechanisms that regulate T-cell activity in the inflamed heart, tumors, and during cancer treatment to better understand and mitigate cardiovascular risks, and inform cancer immunotherapy.

In response to cardiac damage, the heart undergoes remodeling including cardiac myocyte dysfunction, increased deposition of collagen (fibrosis), and chronic inflammation, which together lead to heart failure (HF). In the inflammatory environment of the heart, or similarly a tumor, damaged cells release damage associated molecular patterns (DAMPs) which trigger an innate immune response. Targeting DAMPs alone, such as IL-1β, has not been effective in treating CVD, warranting deeper study of cellular mechanisms. DAMP receptors commonly signal through MyD88 – an adaptor protein that is a critical regulator of pro-inflammatory immune signaling. Activated T-cells can express MyD88 and DAMP receptors, and while their role in innate cells is well established, there is evidence of broader roles in other cell types. I hypothesized that MyD88 plays an anti-inflammatory role in limiting T-cell over-activation and modulates pro-fibrotic transformation in fibroblasts. I used a mouse model of HF and *in vitro* approaches to show that activated T-cells upregulate MyD88, and that deletion of MyD88 worsens HF and cardiac fibrosis through increased T-cell function and survival (Chapter 2). I then applied this to models of cancer, in which deletion of T-cell MyD88 improved anti-tumor

immunity (Chapter 4). Mechanistically, I showed that MyD88 sequesters BCAP, a pro-inflammatory signaling molecule downstream of the T-cell receptor to limit T-cell function and survival (Chapter 5). I further showed that activated cardiac fibroblasts degrade MyD88, and fibroblast MyD88 deletion worsened fibrosis and HF (Chapter 3). This work outlines novel, cell-specific, mechanistic roles for MyD88 outside of innate immunity that can be modulated in both HF and cancer treatment.

Other cancer therapies, such as the anthracycline Doxorubicin, have established cardio-toxicity but do not overtly modulate the immune system. Patients treated with Doxorubicin exhibit dose dependent cardio-toxicity, cardiac cell death, and increased systemic inflammatory markers, however the direct contributions of inflammation to cardiotoxicity remain unknown. I hypothesized that Doxorubicin induced a cardiac T-cell response secondary to cardiac damage. I used mouse models alongside human and canine patient data to show Doxorubicin induces a $CD8^+$ T-cell response that promotes fibrosis and cardiac dysfunction (Chapter 6). I also found mechanistically that Doxorubicin induces T-cell chemoattractants secondary to the DNA damage response protein STING, which are both pathogenic and potential biomarkers (Chapter 7). Overall this characterized new immunologic contributions to anthracycline cardiotoxicity with therapeutic implications.

Dedication:

To the countless friends, mentors, and family who have helped and inspired me along the way, I am endlessly grateful.

To my husband, Gavin, I couldn't be happier to do this together. I love you.

Acknowledgements:

I first and foremost would like to thank the Alcaide lab for being the perfect place to do a PhD and learn how to be a scientist. Over the last 5 years, I have been challenged, inspired, and learned from each and every member. This group of people makes coming to work not just a place to do experiments, but an absolute blast every day. I will cherish all of my memories of early harvest days, lab meetings that always start with fun photos, and various celebrations over the years. I have felt so supported both professionally and personally in an incredibly unique way. Thank you for putting up with me being “one of the loud lab members” and running around like a crazy person doing 15 things at once. I would like to give a special thank you to Sasha Smolgovsky, now one of my best friends. From teaching me how to isolate T-cells to traveling the world, I think we’ve shown more than enough people that we might actually be married after all. I love you dearly and am excited to continue our professional lives and a lifelong friendship.

I cannot thank my mentor, Pilar Alcaide, enough. I have never experienced such dedication to mentorship and excitement about working towards our shared successes. You have taught me critical thinking, how to communicate my science, how to be an effective mentor, and numerous skills that will be the foundation of my future career as a physician scientist. There is nothing more fun than going over a new piece of data with you or debating how to shape a story, and I have such respect for you as a scientist an am appreciative for how close we’ve grown. I would like to thank the additional mentors I have gained over the years both before and after my PhD – Dr. Rebecca Scheck, Dr. Jodie Babitt, Dr, Phil Hinds, Dr. Aarti Asnani, and more – you all have taught me so much and I look forward to continuing our relationships. I would also like to thank my thesis committee, Dr. Cheryl London, Dr. Iris Jaffe, and Dr. Phil Hinds for your continuous support and feedback over these years.

I am very grateful to the immunology program at Tufts for inspiring a love of immunology and helping train me to become the scientist I am today. I have learned so much from the faculty and the students and am lucky to be part of a collaborative, intelligent, and fun group. I am also

lucky to have made such incredible friends in this program who I know will be lifelong. Similarly, the MD-PhD program has been a core foundation in both my training and my happiness during this time. Whether we are debating a case at CIBR or going to karaoke, I am proud to be part of this group as well. Additional thank you to the dedicated coordinators and staff who have worked so hard to ensure the success of both programs. I also would like to thank the many core facilities and staff at Tufts who have helped significantly on all of my projects. The flow cytometry core, sequencing core, histology core and microscopy core, all of you have helped teach me valuable skills and contributed to my work. I would like to give a special acknowledgement to Mark Aronovitz, who made all of the mouse work involving surgeries possible and has become a good friend over the years as well.

There are many people outside of Tufts who have supported me during my PhD as well. To my incredible friends from home, from college, USY, medical school, GSBS, and more, you make my life infinitely better and I love you all. I would like to thank my family, especially my siblings Rose and Philip for being an inspiration and two of the closest people in my life, and my parents for having spent my whole life working towards and celebrating my success. I want to thank my “new” family members, the Piesters, for supporting me and having always made me feel like a part of the family. Finally, I want to thank my husband Gavin. You listen to me rave about experiments, love and support me in every way possible, and make life more fun. I love you forever.

Table of Contents

Title Page ..... ***i***

Abstract: ..... ***ii***

Dedication: ..... ***iv***

Acknowledgements: ..... ***v***

Table of Contents ..... ***vii***

List of Figures: ..... ***xv***

List of Tables: ..... ***xix***

List of Copyrighted Materials Used: ..... ***xx***

List of Abbreviations Used: ..... ***xxi***

Chapter 1 Introduction: ***1***

1.1 Connections Between Heart Failure and Cancer: **1**
1.1.1 Prevalence of Cardiovascular Disease and Cancer: 1
1.1.2 Classification of HF: 2
1.1.3 Clinical Assessment of HF: 3
1.1.4 Cardio-oncology: Connecting Cardiovascular Disease and Cancer 4
1.1.5 Overview Of Inflammation in Cardiovascular Disease and Cancer 6
1.2 Overview of the Immune System: **9**
1.2.1 Cells of the Innate and Adaptive Immune Systems 9
1.2.2 PRR signaling and MyD88 11
1.2.3 Intracellular DNA Sensing 13
1.2.4 TCR signaling and T-cell Activation 15
1.2.5 T-cells Subtypes and Effector Functions 16
1.2.6 T-cell Recruitment and Vascular Activation 18
1.2.7 Immune Cell Death 19
1.3 Cardiac Remodeling and Inflammation **21**
1.3.1 Cardiac Anatomy and Physiology 21
1.3.2 Pathologic Hallmarks of Heart Failure 23
1.3.3 Pre-clinical Models of HF in Rodents: 25
1.3.4 Cardiac Inflammation in non-ischemic heart failure 26
1.3.5 Cardiac Fibroblast State and Function 27
1.3.6 TGFβ Signaling in Fibroblasts 30
1.3.7 Cardiac Fibroblast Inflammatory Function 31
1.4 Cancer Immunotherapy and Cardiotoxicities **31**
1.4.1 Inflammation in Cancer 31
1.4.2 Subtypes of Cancer and Immunologic Status 33
1.4.3 Anthracycline Treatment and Cardiotoxicity 35
1.4.4 Adoptive Cell Therapies 36

1.4.5 Immune checkpoint inhibitors 38
1.5 Summary and Hypothesis 39

Chapter 2 T-cell MyD88 is Novel Regulator of Cardiac Fibrosis Through Modulation of T-cell Activation and Effector Function[220] 41

2.1 Introduction 42
2.2 Methods 43
2.2.1 Animals 43
2.2.2 *In Vivo* Echocardiography: 43
2.2.3 Transverse Aortic Constriction Model: 44
2.2.4 Generation and Culture of Th1 cells: 45
2.2.5 Histologic Analysis and Immunohistochemistry: 45
2.2.6 Bulk RNA-Sequencing: 46
2.2.7 Analysis of Single-Cell RNA Sequencing Data: 46
2.2.8 Analysis of CITE-seq Data: 47
2.2.9 Immunoblotting: 47
2.2.10 RT-qPCR: 48
2.2.11 Flow Cytometry: 49
2.2.12 Isolation of Cardiac Fibroblasts and Co-culture: 50
2.2.13 T-cell Adhesion and Migration Studies Under Shear Flow Conditions: 50
2.2.14 T-cell Chemotaxis: 51
2.2.15 ELISA: 51
2.2.16 T-cell Viability Assays: 51
2.2.17 T-cell Proliferation: 52
2.2.18 T-cell Activation Assay: 52
2.2.19 Immunofluorescence: 52
2.2.20 Genomic DNA Isolation and PCR: 53
2.2.21 Statistical Analysis 53
2.2.22 Data Availability 54
2.3 Results 55
2.3.1 Adoptive Transfer of Myd88$^{-/-}$ Th1 cells into Tcra$^{-/-}$ Mice Induces Greater Cardiac Fibrosis and Systolic Dysfunction than WT Th1 Cells In Response to TAC 55
2.3.2 Deletion of MyD88 in T-Cells Results in Enhanced Pro-Inflammatory Function 56
2.3.3 Mouse and Human T-cells Express MyD88 in the Cardiac Inflammatory Environment 59
2.3.4 T-cell MyD88 Deletion Results in Increased Adhesion to ICAM-1 and VCAM-1 and Primary Cardiac Endothelial Cells 61
2.3.5 T-cell MyD88 Deletion Results in Enhanced Th1 Cell Adhesion to Cardiac Fibroblast and Cardiac Fibroblast Transformation 63
2.3.6 MyD88 Modulates T-Cell Activation through TCR Signaling 65
2.3.7 MyD88 Deletion Enhances T-Cell Survival: 69
2.3.8 T-cell specific MyD88$^{-/-}$ mice develop more cardiac fibrosis and cardiac fibroblast activation 71

2.3.9 T-cell specific MyD88$^{-/-}$ mice have increased T-cell cardiac infiltration, TCR activation, and decreased survival to TAC 74
2.4 Discussion 78
2.5 Author contributions 83
2.6 Acknowledgements 83

Chapter 3 Cardiac Fibroblast MyD88 Regulates TGFβ-Induced Myofibroblast Transformation 85

3.1 Introduction 86
3.2 Methods 88
3.2.1 Animals, PE-ANGII, and TAC Models: 88
3.2.2 Flow Cytometry: 88
3.2.3 Echocardiography: 89
3.2.4 Histologic Analysis: 90
3.2.5 Analysis of scRNA-seq: 90
3.2.6 Culture of Primary Cardiac Fibroblasts: 90
3.2.7 siRNA Knockdown: 91
3.2.8 Immunoblotting: 91
3.2.9 Immunoprecipitation: 92
3.2.10 RT-qPCR: 92
3.2.11 Gel Contraction: 93
3.2.12 MyD88 Overexpression: 93
3.2.13 Immunofluorescence: 93
3.2.14 Statistical Analysis: 94
3.2.15 Data Availability; 94
3.3 Results 95
3.3.1 PE-ANGII Infusion Induces Partially T-cell Independent Fibrosis: 95
3.3.2 Cardiac Fibroblasts Downregulate Inflammatory MyD88 Signaling in Response to PE-ANGII: 96
3.3.3 MyD88$^{-/-}$ CFB Exhibit Increased Transformation and Contractile Function at Baseline and in Response to TGFβ: 98
3.3.4 TGFβ Induced Myofibroblast Transformation Decreases MyD88 Levels: 100
3.3.5 TGFβ Induces Proteasomal Degradation of MyD88 Through SMURF2: 102
3.3.6 MyD88 Binds to Smad4 to Impair Nuclear Translocation in Response to TGFβ 105
3.3.7 Fibroblast Specific Ablation of MyD88 Increases the Fibrotic Response to PE/ANGII: 107
3.3.8 Fibroblast MyD88 Regulates Cardiac Fibrosis in Transverse Aortic Constriction 109
3.3.9 Aged MyD88$^{-/-}$ Mice Have Mildly Increased Interstitial Fibrosis and Myofibroblast Number: 112
3.3.10 Overexpression of MyD88 Prevents Myofibroblast Transformation: 112
3.3.11 MyD88 Regulates Human Fibroblast Transformation: 115
3.4 Discussion 118
3.5 Author Contributions 121

3.6 Acknowledgements 122

Chapter 4 Deletion of T-cell MyD88 Improves Anti-Tumor Immunity in Melanoma[400] ... 123

4.1 Introduction: 124
4.2 Methods: 126
4.2.1 Animals: 126
4.2.2 Cell Culture: 126
4.2.3 Generation of Tc1 Cells: 126
4.2.4 Melanoma Models and Adoptive Transfer: 127
4.2.5 Tumor Digestion and Flow Cytometry: 127
4.2.6 Immunofluorescence: 128
4.2.7 Immunoblotting: 129
4.2.8 Real Time Cell Imaging: 129
4.2.9 In Vitro Killing: 130
4.2.10 RT-qPCR: 130
4.2.11 T-cell Degranulation Assay: 130
4.2.12 Statistical Analysis: 131
4.2.13 Data Availability: 131
4.3 Results: 132
4.3.1 Adoptive Transfer of MyD88$^{-/-}$ Tc1 Cells into Melanoma Bearing Mice Slows Tumor Growth Compared to WT Tc1 Cells. 132
4.3.2 MyD88 Deletion in OTI Tc1 Cells Improves Antigen Specific Anti-Tumor Immunity. 134
4.3.3 MyD88 Limits CD8^{+} T-cell Activation Status and Survival. 136
4.3.4 Deletion of MyD88 Affords Tc1 Cells Enhanced Anti-Melanoma Cytotoxic Activity. 139
4.3.5 MyD88$^{-/-}$ Tc1 Cells Exhibit Increased Degranulation and ERK Signaling: 140
4.3.6 Genetic Deletion of MyD88 in T-cells Delays Melanoma Growth by Increased T-cell Activation, Tumor Infiltration, and Cytotoxicity. 142
4.4 Discussion: 145
4.5 Author Contributions: 149
4.6 Acknowledgements: 149

Chapter 5 MyD88 Determines T-cell Fate Through BCAP-PI3K Signaling 150

5.1 Introduction 151
5.2 Methods 153
5.2.1 Generation and Culture of Primary Mouse T-cells: 153
5.2.2 Generation and Culture of Primary Mouse Bone Marrow Derived Macrophages: 153
5.2.3 Flow Cytometry: 154
5.2.4 Cellular Viability Imaging: 154
5.2.5 Immunoblotting: 154
5.2.6 In Vivo Induction of Apoptosis by FasL: 155
5.2.7 Immunoprecipitation: 156
5.2.8 Immunofluorescence: 156

5.2.9 Lentiviral Transduction of T-cells with αBCAP shRNA: 157
5.2.10 Statistical Analysis:..... 157
5.2.11 Data Availability:..... 158
5.3 Results 159
5.3.1 MyD88 Deletion Confers a Survival Advantage to CD4+ T-cells Dependent on T-cell Receptor Activation:..... 159
5.3.2 MyD88 Regulates Starvation Induced Apoptosis in Activated $CD4^+$ T-cells:..... 160
5.3.3 Activated $MyD88^{-/-}$ T-cells Undergo Similar Necroptotic Cell Death to WT and No Pyroptotic Cell Death: 162
5.3.4 Loss of T-cell MyD88 Impairs CD4+ T-cell Death In Response to FasL *In vivo* and *In vitro:*..... 163
5.3.5 The Pro-Survival Effect of MyD88 Deletion is Dependent on PI3K-AKT Signaling: 165
5.3.6 T-cell Receptor and Toll-like Receptor Stimulation Differentially Regulate MyD88-BCAP-PI3K Binding 166
5.3.7 BCAP Knockdown Inhibits the Modulation of Cell Death and T-cell Activation by MyD88: 169
5.4 Discussion 172
5.5 Author Contributions 175
5.6 Acknowledgements 176

Chapter 6 Cytotoxic T-cells Drive Doxorubicin Induced Cardiac Fibrosis and Systolic Dysfunction 177

6.1 Introduction 178
6.2 Methods 178
6.2.1 Animals and Doxorubicin Model:..... 178
6.2.2 *In Vivo* Echocardiography: 179
6.2.3 Flow Cytometry: 180
6.2.4 Histologic Analysis: 181
6.2.5 Immunohistochemistry: 182
6.2.6 ELISA:..... 182
6.2.7 Generation and Culture of Activated T-cells and Tc1 Cells: 182
6.2.8 RT-qPCR:..... 183
6.2.9 Isolation of Cardiac Fibroblasts and Co-culture: 183
6.2.10 Immunofluorescence:..... 184
6.2.11 Cytokine Array:..... 184
6.2.12 Western Blotting:..... 184
6.2.13 Canine Patient Samples:..... 185
6.2.14 Human Patient Samples: 186
6.2.15 Statistical Analysis:..... 187
6.2.16 Data Availability:..... 187
6.3 Results 187
6.3.1 Doxorubicin Increases Cardiac and Systemic Cytotoxic T-cells 187
6.3.2 DR Induces a Type-1 $CD8^+$ T-cell Response: 192
6.3.3 DR Induces $CD8^+$ T-cell IFNγ Expression and Degranulation 195

6.3.4 CD8$^+$ T-cells Drive DR Cardiotoxicity and Cardiac Fibrosis 198
6.3.5 DR Induces An Antigen Specific CD8$^+$ T-cell Response 201
6.3.6 *Tcra*$^{-/-}$ Mice are Partially Protected from DR Cardiotoxicity: 203
6.3.7 Adoptive Transfer of Tc1 Cells Restores DR Cardiotoxicity: 208
6.3.8 DR Induces Cardiac Fibroblast/CD8 T-cell Crosstalk 208
6.3.9 DR Induces a CD8$^+$ T-cell Response Across 3 Species: 212
6.4 Discussion 217
6.5 Author Contributions 223
6.6 Acknowledgements 223

Chapter 7 Cell Specific STING Activity Differentially Modulates Cardiac Inflammation and Fibrosis in Doxorubicin Cardiotoxicity 225

7.1 Introduction 226
7.2 Methods 228
7.2.1 Animals and Doxorubicin Model: 228
7.2.2 In Vivo Echocardiography: 228
7.2.3 Flow Cytometry: 229
7.2.4 Histologic Analysis: 230
7.2.5 Immunoblotting: 231
7.2.6 RT-qPCR: 231
7.2.7 ELISA: 232
7.2.8 Generation and Culture of Primary Cardiac Fibroblasts and Co-culture: 232
7.2.9 Generation and Culture of Primary Cardiac Endothelial Cells: 233
7.2.10 Culture of Human Umbilical Vein Endothelial Cell: 233
7.2.11 Generation and Culture of Primary Mouse Tc1 cells: 233
7.2.12 Generation and Culture of Primary Mouse Macrophages: 234
7.2.13 Generation of Thp1 Derived Macrophages: 234
7.2.14 Transwell Migration Assay: 234
7.2.15 Statistical Analysis: 235
7.2.16 Data Availability: 235
7.3 Results 236
7.3.1 Doxorubicin Induces STING Dependent CXCR3+CD8+ Cardiac Inflammation alongside Cardiotoxicity: 236
7.3.2 STING Knockout Mice Have Decreased Cardiac Toxicity and Fibrotic Responses to DR: 238
7.3.3 STING Knockout T-cells Exhibit Decreased Activation in Response to DR *In Vivo* But Similar Activation *In vitro* 240
7.3.4 STING is Activated in Immune, Vascular, and Stromal Cells in Doxorubicin Injured Hearts: 242
7.3.5 Cell Specific Deletion of STING Protects Against DR Cardiotoxicity and CXCL9/10 Driven CD8 Cardiotropism: 245
7.3.6 Doxorubicin Induces STING Dependent Chemotaxis Through CXCR3 towards Endothelial Cells and Macrophages 249
7.3.7 Doxorubicin Induces STING Dependent Transendothelial Migration: 250

7.3.8 STING Knockout Cardiac Fibroblasts Exhibit Impaired Transformation in Response to DR but not TGFβ:..... 252
7.3.9 Doxorubicin Activates STING in Human Cells: 254
7.4 Discussion..... 256
7.5 Author Contributions 260
7.6 Acknowledgements 260

Chapter 8 Discussion 261

8.1 MyD88 Plays Different Roles in Different Cell Types: 261
8.1.1 Introduction to Diverse MyD88 Functionality..... 261
8.1.2 T-cell MyD88 Function is Dependent on Inflammatory Context: 261
8.1.3 T-cell MyD88 Acts through BCAP and is Modulated by TLR Signaling 263
8.1.4 MyD88 Shapes the Humoral Immune Response:..... 264
8.1.5 MyD88 Plays Diverse Roles in Cardiac and Tumor Cells 265
8.2 Factors that Determine the Function of MyD88 267
8.2.1 Expression of Receptors: 267
8.2.2 Spatial Localization of MyD88..... 267
8.2.3 MyD88 Binding Partners and Domains 268
8.2.4 Post-Translational Modification of MyD88 and Regulation of Expression 271
8.3 The Translatability of MyD88 Modulation 273
8.4 Fibroblast States and Function 276
8.4.1 Comparison of Fibroblast Activation Across Models 276
8.4.2 T-cell Fibroblast Cross-talk..... 277
8.4.3 Inflammatory Fibroblast States and Fibroblast Heterogeneity 278
8.4.4 MyD88 Regulation of Fibroblast State: 280
8.5 Remaining Questions on the T-cell Response in Anthracycline Cardiomyopathy..... 282
8.5.1 Potential Antigens in Anthracycline Cardiotoxicity..... 282
8.5.2 Mechanisms of T-cell Activation and Adaptive Immunity in Doxorubicin Cardiotoxicity..... 284
8.5.3 The Role of $CD4^+$ T-cells..... 285
8.5.4 Age and Temporal Regulation of the T-cell Response 287
8.5.5 T-cell Cross-talk with Cardiac Cells..... 290
8.5.6 DNA Damage and the T-cell Response 292
8.6 T-cell Therapies in Doxorubicin Cardiomyopathy 295
8.6.1 Anthracycline Induced Cardiac vs. Tumor T-cell Responses: 295
8.6.2 The Role for T-cells in Doxorubicin's Anti-Tumor Function 297
8.6.3 Chemokine Therapies and Biomarkers..... 299
8.6.4 Anthracycline Immune Checkpoint Inhibitor Cross-talk..... 300
8.7 Conclusion: 302

Chapter 9 Appendices and Supplemental Data 304

9.1 MyD88 Regulates the IFNγ Response and Inflammatory Functions in Cardiac Fibroblasts 304

9.2 Doxorubicin Impacts the Anti-Tumor and Cardiotoxic Effects of Immune Checkpoint Inhibitors 306
9.3 T-cell MyD88 Modulates Doxorubicin Cardiotoxicity 313
9.4 Mechanisms of Doxorubicin and $CD8^+$ T-cell Induced Fibroblast Transformation 315
..... 316
9.5 T-cell Deficient Mice Protected from PE/ANGII Induced Diastolic Dysfunction 317
9.6 Anthracycline Treatment Causes Induces a Pro-Fibrotic State in $CD8^+$ T-cells 318
9.7 Deletion of T-cell TLR4 Does Not Alter Pressure Overload Induced Heart Failure in Mice 324
9.8 DAMP Treatment of T-cells and Cardiac Fibroblasts 326
..... 327
9.9 Additional Characterization of Systemic T-cell Inflammation in Doxorubicin Treated Mice 329
9.10 Primers and siRNAs Used 331

Chapter 10 Bibliography: 336

List of Figures:

Figure 1-1 Classifications of Heart Failure 2
Figure 1-2 Connections Between Cancer and Cardiovascular Disease 4
Figure 1-3 Cells of the Immune System 10
Figure 1-4 The Myd88 Signaling Network and Cell Specific Functions 12
Figure 1-5 STING Signaling in Cardiac or Tumoral Inflammation 15
Figure 1-6 Overview of T-cell Activation and Differentiation 17
Figure 1-7 Mechanisms of T-cell Death 20
Figure 1-8 Pathologic Hallmarks of Heart Failure 24
Figure 1-9 Overview of Cardiac Fibroblast States, Inflammatory Functions, and TGFβ Signaling 29
Figure 1-10 Inflammation and Immune Escape in Cancer 33
Figure 1-11 Cancer Treatment Balances Beneficial Anti-Tumor Effects and Cardiac Toxicities Through Inflammation 39
Figure 2-1 Tcra-/- Mice given Myd88-/- Th1 cells in the onset of TAC develop more cardiac fibrosis and systolic dysfunction 56
Figure 2-2 Reconstitution of TCRα Mice by Adoptive Transfer: 57
Figure 2-3 MyD88 Regulates T-cell Signaling In vitro and In the Heart 58
Figure 2-4 Gating Strategy for In vitro T-cell Experiments and Characterization of Myd88-/- Th1 cells 59
Figure 2-5 Cardiac MyD88+ T-cells Are Found at 1 week Post TAC. 60
Figure 2-6 MyD88 Deletion Increases Th1 Adhesion Ability Without Impairment of Transendothelial Migration 62
Figure 2-7 Myd88-/- Th1 cells Exhibit Similar Chemotaxis to CXCL10 63
Figure 2-8 MyD88-/- Th1 Cells Exhibit Increased Binding to and Activation of Fibroblasts 64
Figure 2-9 Myd88-/- and WT Th1 cells Exhibit Dose Dependent CFB Activation. 65
Figure 2-10 Characterization of Cardiac DAMPs and T-cell DAMP sensing 66
Figure 2-11 MyD88 Acts as a Break During T-cell Activation through TCR but not TLR signaling 68
Figure 2-12 MyD88 Inhibition Increases Th1 Activation Status 69
Figure 2-13 Analysis of MyD88 Expression in T-cells by confocal microscopy 69
Figure 2-14 MyD88 Knockout Enhances Survival but Not Proliferation in Th1 Cells 70
Figure 2-15 T-MyD88-/- Mice Exhibit Similar Hypertrophy and Little Cardiac Cell Death After TAC 73
Figure 2-16 T-Cell Specific MyD88 Knockout Mice Show Increased Cardiac Fibrosis with Increased Cardiac Fibroblast Activation and Proliferation 73
Figure 2-17 T-Cell Specific MyD88 Knockout Mice Show Increased T-cell Activation, Cardiotropism, Systolic Decline, and Survival 75
Figure 2-18 Flow Cytometric Analysis of Cardiac Inflammation in $Myd88^{fl/fl}CD4^{Cre}$ mice 76
Figure 2-19 Continued Flow Cytometric Analysis of Cardiac Inflammation in $Myd88^{fl/fl}CD4^{Cre}$ mice 77
Figure 3-1 MyD88-/- CFB Exhibit Increased Transformation and Contractile Function at Baseline and In Response to TGFβ 99
Figure 3-2 TGFβ-Induced Myofibroblast Transformation Decreases MyD88 Levels 101
Figure 3-3 Fibroblast sorting Gating Strategy 102
Figure 3-4 TGFβ Decreases MyD88 at the transcriptional level 102
Figure 3-5 TGFβ Induces Proteasomal Degradation of MyD88 through Smurf2 104
Figure 3-6 Smurf2 Knockdown Decreases Fibroblast Transformation 105
Figure 3-7 MyD88 Binds SMAD4 to Impair Complex Nuclear Translocation In Response to TGFβ 106

Figure 3-8 Fibroblast Specific Ablation of MyD88 Increases the Fibrotic Response to PE/ANGII 108
Figure 3-9 CFB-MyD88 Mice Have Increased Hypertrophy Compared to WT 109
Figure 3-10 PE AngII Induces Lymphoid CD4+ T-cell activation but not cardiotropism in WT Mice 110
Figure 3-11 Fibroblast MyD88 Regulates Fibrosis in Transverse Aortic Constriction 111
Figure 3-12 Aged MyD88-/- Mice Have Mildly Increased Interstitial Fibrosis and Myofibroblast Number 113
Figure 3-13 Overexpression of MyD88 Prevents Myofibroblast Transformation 114
Figure 3-14 MyD88 Regulates Human Fibroblast Transformation..... 116
Figure 4-1 Adoptive Transfer of MyD88-/- Tc1 Cells into Melanoma Bearing Mice Slows Tumor Growth Compared to WT Tc1 Cells. 133
Figure 4-2 Gating for Adoptive Transfer and Tumor Myeloid Populations. 134
Figure 4-3 MyD88 Deletion in OTI Tc1 Cells Improves Antigen Specific Anti-Tumor Immunity in Melanoma 135
Figure 4-4 MyD88 Limits CD8+ T-cell Activation Status and Survival..... 137
Figure 4-5 MyD88 Mediates TLR Signaling in Tc1 Cells but does not contribute to Tc1 Polarization 138
Figure 4-6 Deletion of MyD88 Affords Tc1 Cells Enhanced Anti-Melanoma Cytotoxic Activity 140
Figure 4-7 MyD88-/- Tc1 Cells Exhibit Increased Degranulation and ERK Signaling. 142
Figure 4-8 Genetic Deletion of MyD88 in T-cells Delays Melanoma Growth by Increased T-cell Activation, Tumor Infiltration, and Cytotoxicity 143
Figure 4-9 Gating for T-MyD88-/- B16 Tumors and Myeloid Cell Populations 144
Figure 5-1 MyD88 Deletion Confers a Survival Advantage to CD4+ T-cells Dependent on T-cell Receptor Activation:..... 159
Figure 5-2 MyD88-/- Macrophages Have Similar Survival As WT at baseline and after FcgR activation 160
Figure 5-3 MyD88 Controls Starvation Induced Apoptosis in Activated CD4+ T-cells: 161
Figure 5-4 Loss of T-cell MyD88 Impairs CD4+ T-cell Death In Response to FasL In vivo and In vitro: 164
Figure 5-5 The Pro-Survival Role of MyD88 Deletion is Dependent on PI3K-AKT Signaling 165
Figure 5-6 T-Cell Receptor Stimulation Induces A MyD88-BCAP-PI3K complex at the TCR 167
Figure 5-7 T-cell Receptor and Toll-like Receptor Stimulation Differentially Regulate MyD88-BCAP-PI3K Binding and Cell Death 168
Figure 5-8 BCAP Knockdown Inhibits the Modulation of Cell Death and T-cell Activation by MyD88..... 170
Figure 6-1 CD8 T-Cells Infiltrate the Heart Concurrently with Doxorubicin Induced Cardiac Pathology and Systemic Inflammation..... 189
Figure 6-2 Doxorubicin Effects on Cardiac and Circulating Myeloid Populations 190
Figure 6-3 Doxorubicin Induces Systemic Inflammation..... 191
Figure 6-4 Female Mice Treated with Doxorubicin Exhibit Cardiotoxicity and Cardiac CD8+ T-cell Infiltration..... 192
Figure 6-5 Gating Strategies for Lymphoid Organ Effector Populations 193
Figure 6-6 Lymphoid T-cells Do Not Increase Exhaustion Markers in Response to Doxorubicin 194
Figure 6-7 Doxorubicin Increases Multiple Helper T-cell Subtypes in Lymphoid Organs ... 195
Figure 6-8 Doxorubicin Does Not Increase T-cell Activation Markers In Vitro..... 196

Figure 6-9 Doxorubicin Directly Increases Cytokine Secretion and CD8 T-cell Degranulation 197
Figure 6-10 CD8 but not CD4 T-cells Drive Cardiac Fibrosis and Systolic Dysfunction in Response to Doxorubicin 199
Figure 6-11 Analysis of Doxorubicin Treatment in Antibody Depleted Mice 200
Figure 6-12 Analysis of Doxorubicin Treatment in Antibody Depleted Mice Cont 201
Figure 6-13 Doxorubicin Induces Antigen Specific CD8+ T-cell Activation Required for Cardiac Fibrosis and Systolic Dysfunction: 203
Figure 6-14 T-Cell Deficient Mice are Partially Protected from Doxorubicin Cardiomyopathy and Develop Less Fibrosis than WT 205
Figure 6-15 TCRa mice Are Partially Protected from Doxorubicin Cardiomyopathy 206
Figure 6-16 Tcra-/- mice Are Partially Protected from Cardiac Fibrosis 207
Figure 6-17 Adoptive Transfer of Tc1 Cells Restores Doxorubicin Cardiotoxicity 209
Figure 6-18 Doxorubicin Induces Cardiac Fibroblast ICAM-1 Increasing CD8 T-cell Adhesion and Contact Dependent Degranulation 211
Figure 6-19 Canine and Human Patients Treated with Anthracyclines Develop a Progressive CD8+ T-cell Response 213
Figure 7-1 Doxorubicin Induces STING Dependent CXCR3+CD8+ Cardiac Inflammation alongside Cardiotoxicity 237
Figure 7-2 STING Knockout Decreases DR Induced Cardiac Myeloid Infiltration but not Cardiac or lymphoid Dendritic Cells 238
Figure 7-3 Flow Cytometry Analysis of Blood T-cells and Gating Strategy 239
Figure 7-4: STING Knockout mice have decreased cardiac toxicity and fibrotic responses to Doxorubicin 240
Figure 7-5 STING Knockout T-cells Exhibit Decreased Activation in Response to DR In Vivo But Similar Activation In vitro 241
Figure 7-6 Doxorubicin activates STING in immune and stromal cells in Doxorubicin injured hearts 243
Figure 7-7 Additional Characterization of STING Activation in the heart at 4 weeks and 8 weeks 244
Figure 7-8 Gating Strategy for pIRF3 245
Figure 7-9 Cell Specific Deletion of STING Protects Against DR Cardiomyopathy and CXCL9/10 Driven CD8 Cardiotropism 246
Figure 7-10 Characterization of STING-Tcf21 Mice and Cardiac Phenotyping of Cell Specific STING KO Mice 247
Figure 7-11 Doxorubicin Induces STING and CXCR3 Dependent Chemotaxis towards Endothelial Cells and Macrophages 250
Figure 7-12 Doxorubicin induces STING dependent transendothelial migration 251
Figure 7-13 STING-/- Cardiac Fibroblasts Exhibit Impaired Transformation in Response to Doxorubicin 253
Figure 7-14 Doxorubicin Activates STING and Induces Chemokine Expression and Fibroblast Transformation in human cells 255
Figure 8-1 Cell Specific Functions of MyD88 262
Figure 8-2 MyD88 Domains, Binding Partners, and Modifications 269
Figure 8-3 Potential Therapeutic Approaches in Heart Failure and Cancer Involving MyD88 274
Figure 8-4 Summary of Mechanisms Regulating Fibroblast State Studied in This Dissertation. 277
Figure 8-5 Potential Antigens and Mechanisms of T-cell Activation in Doxorubicin Cardiotoxicity 283
Figure 8-6 Temporal Regulation of the T-cell Response to Doxorubicin 288

Figure 8-7 Established and Suggested Functions of STING in Selected Cell Types 293
Figure 8-8 Opportunities for T-cell Anti-Inflammatory Therapy in Anthracycline Cardiotoxicity 297
Figure 9-1 MyD88 Deletion or TLR4 Stimulation Decrease IFNγ Responsiveness Without Altering Antigen Processing 304
Figure 9-2 MyD88 and TLR4 Stimulation Do Not Alter IFNγR or JAK expression, but Decrease STAT1 phosphorylation 305
Figure 9-3 Doxorubicin Treatment of Breast Cancer Induces Cardiotoxicity, Cardiac Inflammation, and Intratumoral T-cell Exhaustion 306
Figure 9-4 Doxorubicin Synergizes with PD-1 Inhibition for Anti-Tumor Activity 307
Figure 9-5 Doxorubicin Synergizes with PD-L1 Inhibition for Cardiotoxicity 309
Figure 9-6 Gating Strategies for Heart and Tumor, and Myeloid Cell Quantification 309
Figure 9-7 Doxorubicin Causes Cardiotoxicity and Cardiac Inflammation in Melanoma Bearing Mice 310
Figure 9-8 Gating Strategy for Lymphoid Tissues and Effector T-cell Quantification 310
Figure 9-9 Doxorubicin Induced Cardiac Fibroblast PD-L1 Limits T-cell Degranulation and Fibroblast Transformation 311
Figure 9-10 Graphical Abstract of Doxorubicin and Immune Checkpoint Inhibitor Effects . 312
Figure 9-11 Cardiac T-cells Increase MyD88 Signaling Alongside T-cell Activation Markers in the Doxorubicin Treated Heart 313
Figure 9-12 T-cell Deletion of MyD88 Worsens Doxorubicin Cardiotoxicity 314
Figure 9-13 Doxorubicin Induces TGFβ Independent Myofibroblast Transformation and Activates Several Signaling Pathways 315
Figure 9-14 Tc1 cells Induce TGFβ Dependent But IFNγ Independent Myofibroblast Transformation of Doxorubicin Primed Fibroblasts 316
Figure 9-15 T-cell Deficient Mice are Protected from PE/ANGII Induced Diastolic Dysfunction 317
Figure 9-16 Patient Derived Cytotoxic T-cells Express a Pro-Fibrotic Transcriptome After Anthracycline Treatment 318
Figure 9-17 Treatment of Mouse $CD8^+$ T-cells with Doxorubicin Induces Profibrotic Gene Expression and LOX-Dependent Matrix Stiffening Ability 319
Figure 9-18 Mice Treated with Doxorubicin Increase $CD8^+$ T-cell LOX Expression In Vivo 320
Figure 9-19 Doxorubicin Treatment of $CD8^+$ T-cells Induces TGFβ Signaling 321
Figure 9-20 Doxorubicin Treatment Induces HIF1α-p53 Signaling That Contributes to Matrix Stiffening 322
Figure 9-21 Schematic of Mechanism for DR-Induction of $CD8^+$ T-cell Matrix Stiffening ... 323
Figure 9-22 Adoptive Transfer of $TLR4^{-/-}$ Th1 Cells in the Onset of TAC Results in Similar Pathology As Transfer of WT Cells 324
Figure 9-23 $TLR4^{-/-}$ Th1 cells Show Minor Changes in Differentiation and Worse Survival In vitro 325
Figure 9-24 DAMP Treatment of T-cells Can Alter Cytokine Expression 326
Figure 9-25 DAMPs in TAC Lysate Decrease CD25 in the Absence of Co-stimulation 327
Figure 9-26 MyD88 Stimulation Regulates Fibroblast Transformation and Cytokine Expression in a Temporal Manner 328
Figure 9-27 Doxorubicin Treatment of Nur77-GFP Mice 329
Figure 9-28 Systemic Effector T-cells in Doxorubicin Treated Mice 330

List of Tables:

Table 1-1 Major Anti-Inflammatory Clinical Trials in HF 7
Table 1-2 Selected Cancer Immunotherapy Clinical Trials ..... **Error! Bookmark not defined.**
Table 5-1 shRNA sequences 157
Table 6-1 Canine Patient Characteristics 215
Table 6-2 Human Patient Characteristics 216
Table 9-1 Primers and siRNAs Used 333

List of Copyrighted Materials Used:

Bayer, A.L. & Alcaide, P. MyD88: At the heart of inflammatory signaling and cardiovascular disease. *Journal of Molecular and Cellular Cardiology* 161, 75–85 (2021).

Bayer, A.L., Smolgovsky, S., Ngwenyama, N., Hernández-Martínez, A., Kaur, K., Sulka, K., Amrute, J., Aronovitz, M., Lavine, K., Sharma, S., Alcaide, P., 2023. T-cell MyD88 is a Novel Regulator of Cardiac Fibrosis Through Modulation of T-cell Activation. *Circulation Research.* 133:5(412-419)

Bayer, A.L., Padilla-Rolon, D., Smolgovsky, S., Hinds, P. W. & Alcaide, P. Deletion of MyD88 in T Cells Improves Antitumor Activity in Melanoma. *The American Journal of Pathology* 194, 1007–1019 (2024).

Bayer A.L., Zambrano MA, Smolgovsky S, Robbe ZL, Ariza A, Kaur K, Sawden M, Avery A, London C, Asnani A, et al. Cytotoxic T cells drive doxorubicin-induced cardiac fibrosis and systolic dysfunction. *Nat Cardiovasc Res*. 2024;3:970–986.

Bayer, A.L., Magri, Z., Muendein, H., Poltorak, A., Alcaide, P. MyD88 Determines T-cell Fate Through BCAP-PI3K Signaling. *Journal of Immunology. In press.* (2025)

List of Abbreviations Used:

AAV = Adeno-associated virus
ACC = American College of Cardiology
ACE = Angiotensin converting enzyme
ACT = Adoptive cell therapy
AKT = Protein kinase B
ANOVA = Analysis of variance
ANP = Atrial natriuretic peptide
APC = Antigen presenting cell
ATII = Angiotensin II
αSMA = Alpha smooth muscle actin
BAD = Bcl2 associated death promoter
BAX = Bcl2 associated X protein
BCAP = B-cell adaptor protein
BCL2 = B-cell lymphoma 2
BCL6 = B-cell lymphoma 6
BIDMC = Beth Israel Deaconess Medical Center
BMDM = Bone marrow derived macrophage
BNP = Brain natriuretic peptide
BSA = Bovine serum albumin
BTK = Bruton's tyrosine kinase
BTZ = Bortezomib
CAR-T = Chimeric antigen receptor T-cell
CCR = CC chemokine receptor
CD = Cluster of differentiation
CFB = Cardiac fibroblast
CFSE = carboxyfluorescein diacetate succinimidyl ester
CITE-seq = Cellular indexing of transcriptomes and epitopes by sequencing
cGAS = cyclic GMP-AMP synthase
cGAMP = 2,3-cyclic-GMP-AMP
CM = Cardiomyocyte
CMV = Cytomegalovirus
Col = Collagen
CRP = C-reactive protein
CST = Cell signaling technologies
CTLA-4 = Cytotoxic T-Lymphocyte-Associated 4
CVD = Cardiovascular disease
CXCL = C-X-C chemokine motif ligand
CXCR = C-X-C chemokine motif receptor
DAMP = Damage associated molecular pattern
DC = Dendritic cell
DD = death domain
DDR2 = Discoidin domain containing receptor 2
DLBCL = Diffuse large B-cell lymphoma
DMEM = Dulbecco's modified eagle medium
DNA = Deoxyribonucleic acid
DR = Doxorubicin
EC = Endothelial cell
ECL = Electrochemiluminescence
ECM = Extracellular matrix
EDTA = Ethylenediaminetetracetic acid

EF = Ejection fraction
EKG = Electrocardiogram
ELISA = Enzyme-linked immunosorbent assay
EMT = Endothelial to mesenchymal transformation
ERK = Extracellular signal related kinase
FAP = Fibroblast activation protein
FasL = Fas ligand
FBS = Fetal bovine serum
FCS = Fetal calf serum
FOXO = Forkhead box
FOXP3 = Forkhead box protein 3
Fl = Flox
FS = Fractional shortening
GAPDH = Glyceraldehyde-3-phosphate dehydrogenase
GATA3 = Gata-binding protein 3
GFP = Green fluorescence protein
GSEA = Gene set enrichment analysis
H&E = Hematoxylin and eosin
HEPES = 4-(2-hydroxyethyl)piperazine-1-ethane-sulfonic acid
HER2 = Human epidermal growth factor receptor 2
HF = Heart failure
HFmrEF = Heart failure with moderately reduced ejection fraction
HFpEF = Heart failure with preserved ejection fraction
HFrEF = Heart failure with reduced ejection fraction
HMGB1 = High mobility group box 1
HPF = high powered field
HUVEC = Human umbilical vein endothelial cell
ICAM1 = Intracellular adhesion molecule 1
ICI = Immune checkpoint inhibitor
IF = Immunofluorescence
IFN = Interferon
IGF = Insulin-like growth factor
IL = Interleukin
ILC = Innate lymphoid cell
INT = Intermediate domain
IP = Immunoprecipitation
IRAK = IL-1 receptor associated kinase
IRAE = Immune related adverse event
IRF = Interferon regulatory factor
ISG = Interferon stimulated gene
IsoLG = Isolevuglandin
JAK = Janus associated kinase
LAG3 = Lymphocyte activation gene 3
LFA-1 = Lymphocyte function-associated antigen 1
LPS = Lipopolysaccharide
LRR = Leucine rich repeat
LV = Left ventricle
LVAD = Left ventricular assist device
MACS = Magnetic assisted cell sorting
MAPK = Mitogen-activated protein kinase
MDSC = Myeloid derived suppressor cell

MEFSK4 = Mouse embryonic factor clone SK4
MHC = Major histocompatibility complex
MI = Myocardial infarction
MLKL = Mixed lineage kinase domain like
mLN = Mediastinal lymph nodes
MyD88 = Myeloid differentiation primary response 88
MYH = Myosin heavy chain
NFAT = Nuclear factor of activated T-cells
NF-kB = Nuclear factor kappa-B
NK cell = Natural killer cell
NLR = Nod-like receptor
NTD = N-terminal domain
NYHAC = New York Heart Association Classification
OE = Overexpression
OVA = Ovalbumin
PAGE = polyacrylamide gel electrophoresis
PAMP = Pathogen associated molecular pattern
PBS = Phosphate buffered saline
PCR = Polymerase chain reaction
PD-1 = Programmed cell death protein 1
PDGFrα = Platelet derived growth factor receptor alpha
PE = Phenylephrine
PECAM-1 = Platelet endothelial cell adhesion molecule 1
PFA = Paraformaldehyde
PI = Propidium iodide
PI3K = Phosphoinositide 3-kinase
PMA = Phorbol 12-myristate 13-acetate
PRR = Pattern recognition receptor
PSR = Picrosirius red
PVDF = Polyvinylidene fluoride
RCF = Relative centrifugal force
RIPA = Radioimmunoprecipitation assay
RIP1K = Receptor interacting serine/threonine protein kinase 1
POSTN = Periostin
RBC = Red blood cell
RNA = Ribonucleic acid
Rorγt = Retinoic acid-related orphan receptor gamma-t
ROS = reactive oxygen species
RPMI = Roswell park memorial institute medium
RLR = Retinoic acid inducible gene-I-like receptor
RT-qPCR = Reverse transcriptase quantitative polymerase chain reaction
scRNA-seq = Single cell RNA sequencing
SDS = sodium dodecyl sulfate
SEM = standard error of the mean
SERCA = Sarco/endoplasmic reticulum calcium ATPase
shRNA = short hairpin RNA
siRNA = short interfering RNA
SMAD = Suppressor of mother against decapentaplegic
SMURF = Smad-specific ubiquitin E3 ligase
STAT = Signal transducer and activator of transcription
STING = Stimulator of interferon genes

TCF21 = Transcription factor 21
TBK1 = TANK-binding kinase 1
TBX21 = T-box transcription factor 21
TAC = Transverse aortic constriction
TCR = T-cell receptor
Tc = T-cytotoxic cell
TEM = Transendothelial migration
TIR domain = Toll-interleukin-1 receptor domain
TIRAP = TIR domain containing adaptor protein
Th = T-helper cell
TGFβ = Transforming growth factor beta
TLR = Toll-like receptor
TNBC = Triple negative breast cancer
TNFα = Tumor necrosis factor alpha
TRAF = TNF receptor associated factor
T-reg = Regulatory T-cell
TRIF = TIR-domain containing adaptor inducing interferon-β
TRIS = Tris(hydroxymethyl)aminomethane
TUNEL = Terminal deoxynucleotidyl transferase dUTP nick-end labeling
Ub = Ubiquitin
UPS = Ubiquitin proteasome system
US = United States
VCAM1 = Vascular cell adhesion molecule 1
VLA-4 = Very late antigen 4
WGA = Wheat-germ agglutinin
WT = Wildtype
ZAP70 = Zeta-chain associated protein kinase 70

Chapter 1 Introduction:

1.1 Connections Between Heart Failure and Cancer:

1.1.1 Prevalence of Cardiovascular Disease and Cancer:

The leading two causes of death in the United States are cardiovascular disease (CVD) and cancer, while globally CVD ranks number one. In the United States (US), nearly 50% of adults have some form of CVD, which causes nearly 1 million deaths per year. These numbers include patients with myocardial infarctions, hypertension, stroke, and others. Many of these patients suffering from chronic CVD develop some heart failure (HF), in which due to the previously listed etiologies and more, the heart is unable to provide blood to the body adequately.[1] Second after CVD, there are currently 2 million estimated new cancer cases per year and over 600,000 deaths in the United States, with the most common being breast cancer, colon cancer, and melanoma of the skin.[2] While significant strides have been made in the care and overall mortality of both diseases, globally, CVD kills 18 million people per year, while cancer has an estimated 10 million deaths per year.[1,3] Further, studies have increasingly shown a significant overlap between patients who are diagnosed with CVD and cancer. This has led to work showing not just concurrent diagnoses, but that each disease significantly increases the risk for the other. [4–7] One study showed that of 27 million people, a diagnosis of CVD increased cancer risk by 13%, and vice versa. Another study revealed that among 7.5 million cancer patients studied, the risk of death from CVD was over twice as high compared to matched non-cancer patients.[5,7] As not just two leading causes of mortality, but increasingly intertwined diseases, significant effort is required to understand the shared molecular mechanisms and initiating factors of disease, such as chronic inflammation, the major goal of this dissertation. This work will improve outcomes in this widespread patient population by uncovering novel therapeutic targets, risk factor stratification, and preventative strategies.

1.1.2 Classification of HF:

Heart failure (HF) is defined as a complex clinical syndrome in which there is compromised blood supply to the body, either due to the impairment of the ventricles to contract and eject blood, or relax and fill with blood.[8,9] HF can be classified in many different ways, which is used in both the management and risk assessment for patients (Figure 1-1). The left ventricular ejection fraction (EF), defined as the percent of blood that leaves the left ventricle with each contraction, can classify HF into 3 broad categories: HF with reduced ejection fraction (EF < 40%), HF with mildly reduced ejection fraction (EF 41-49%), or HF with preserved ejection fraction (EF> 50%).[9] Patients can further be classified from I to IV based on the progression of their symptoms, most commonly using the New York Heart Association Classification (NYHAC), which was historically used to predict the benefit of treatment, but due to the diversity of HF patients has become less useful clinically.[10,11] The American College of Cardiology (ACC) has further released a newer 4-tiered class system from Class A to Class D based on both risk factors and existing symptoms which is currently used in part to guide management of these patients.[12]

Classifying HF patients by their etiology has also become commonplace. Those classified with HF with preserved ejection fraction (HFpEF) are often a result of external or

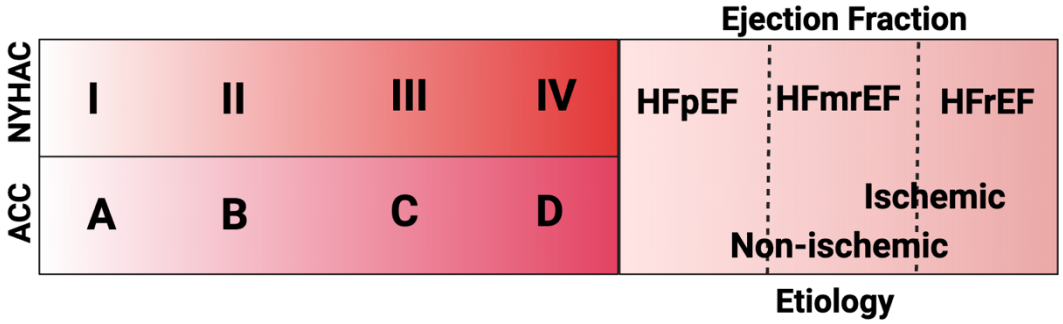


Figure 1-1 Classifications of Heart Failure
NYHAC = New York heart association, ACC = American college of cardiology, HFpEF = heart failure with preserved ejection fraction, HFmrEF = heart failure with moderately reduced ejection fraction, HFrEF = heart failure with reduced ejection fraction.

systemic risk factors including hypertension, atrial fibrillation, aging, diabetes, obesity, kidney disease, and more. These combined risk factors impact the ability of the heart to fill properly,

and have been shown to effect pathophysiology and patient outcomes. [9,13] On the other hand, those diagnosed with HF with reduced ejection fraction (HFrEF) have a very wide set of etiologies. A significant number of HFrEF patients have ischemic heart disease or myocardial infarction, in which blood supply to the heart is compromised acutely or chronically. Non-ischemic HFrEF has many causes, including long standing pressure overload, valvular disease, infection, genetic mutations, endocrinologic or autoimmune diseases, and congenital diseases.[9,14] Importantly, cancer patients have a higher risk for most classifications of HF through shared risk factors. Additionally, cancer therapies have a wide variety of cardiotoxic effects, an additional risk for HF in this patient population. Together, this provides evidence that these patients should be considered as having a separate etiology of HF due to their underlying malignancy.[15,16]

1.1.3 Clinical Assessment of HF:

Pre-existing risk factors for CVD can lead to HF, as such, a full medical history can aid with the diagnosis of HF. This includes family history of CVD to determine genetic risk, behavioral factors including smoking history and diet, as well as elements of the prior medical history which increases risk, such as diabetes, obesity, hypertension, or past cancer diagnosis and treatment.[17,18] HF patients often present with a set of common symptoms that can help with diagnosis, including shortness of breath, orthopnea, fatigue, and occasionally chest pain.[19] Upon exam, patients can show pulmonary rales, altered cardiac auscultation, tachycardia, jugular venous distension, edema, abdominal distension, and others.[19,20] These patients undergo additional workup, such as a chest X-ray to visualize the heart, EKG which can rule out acute MI, and echocardiography to further evaluate cardiac morphologic changes, determine EF, and measure signs of diastolic dysfunction. Blood work for potential biomarkers is often utilized in the diagnosis, although the specificity and sensitivity of these is debatable. HF patients can show elevated natriuretic peptides (ANP/BNP), elevated

troponins with more severe cardiac injury, and elevated inflammatory markers such as CRP.[20,21] While broad inflammatory markers have been commonly seen in HF patients, more specific markers are needed to delineate both sub-classifications of HF and guide both progression and management.

1.1.4 Cardio-oncology: Connecting Cardiovascular Disease and Cancer

With a growing population of patients who are at risk for, diagnosed with, or survivors of both cancer and CVD, the field of cardio-oncology has emerged (Figure 1-2). Cardio-oncology includes the cardiovascular care of patients with cancer before, during, and after their cancer treatment.[22] The largest area in cardio-oncological work is managing the cardiac effects of cancer treatment. Many cancer treatments can have significant, diverse cardiovascular effects, seen broadly across radiation therapy, most chemotherapies, targeted therapies, and newer immunologic treatments.[23,24] Beyond this, the two diseases share many risk factors, including but not limited to hypertension,[25] diabetes,[26] and systemic inflammation.[17] Many lifestyle choices such as diet, smoking, and alcohol use can further increase the risk for both cancer and CVD.[17] Studies have even found common genetic risk

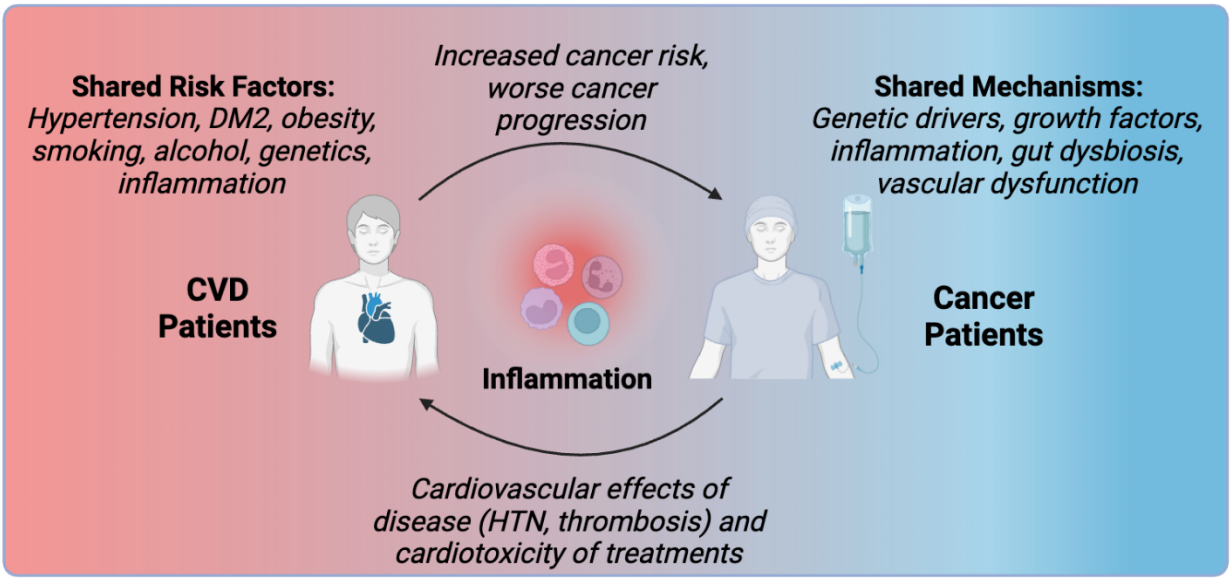


Figure 1-2 Connections Between Cancer and Cardiovascular Disease
CVD patients and cancer patients share common risk factors and mechanisms in their pathobiology, and as such each disease can significantly impact the other. CVD = cardiovascular disease, DM2 = Diabetes mellitus type II, HTN = hypertension.

factors for both cancer and CVD, examples of which include the Wnt signaling pathway, which when mutated can lead to both coronary artery disease and lymphoma[27,28] or clonal hematopoietic changes that can elevate shared risks as well.[29,30]

While shared risk factors have resulted in overlapping patient populations in the oncologic and cardiovascular fields, each disease has been shown to influence the pathobiology of the other (Figure 1-2). Cancer patients have long since been known to have increased incidence of both hypertension[31] and hypercoagulability,[32] both significant risk factors for CVD and HF. The mechanistic connections between CVD on cancer pathogenesis are less clear, however numerous studies have shown elevated cancer diagnoses and worse outcomes in patients with hypertension, atherosclerosis, or prior stroke.[33–35] Chronic inflammation connects both HF and cancer as well, as common inflammatory signatures such as the pro-inflammatory cytokines IL-1β or IL-6, or acute phase inflammatory reactants such as CRP, are found as both biomarkers and contributors to disease in patients with cancer and CVD.[36–38] These phenomena has been further studied using pre-clinical rodent models. Mice subjected to myocardial infarction had worsened development and progression of colorectal, breast, and lung cancer across several studies.[39–42] All three of these malignancies grew significantly faster with the inclusion of a model of pressure overload induced heart failure in mice.[43,44] A variety of mechanisms have been proposed for tumor-cardiac crosstalk in such studies – gut dysbiosis[39], extracellular vesicles,[41] circulating factors,[44] but the most commonly found mechanistic link found between cancer and HF is inflammation.[39,40,42] This positions inflammation as a major target in the improvement of cardio-oncologic outcomes, necessitating further study, including work in chapters 6 and 7 of this dissertation.

1.1.5 Overview Of Inflammation in Cardiovascular Disease and Cancer

Some of the earliest studies of patients with HF showed signs of systemic inflammation, notably the finding that broad inflammatory marker C-reactive protein was elevated in the plasma of these patients.[45] Several pro-inflammatory cytokines and chemokines have been found to be increased in circulation of patients with CVD, which indicate not only systemic inflammation but have been shown to correlate with systolic dysfunction.[46–49] Many of these markers have defined functional roles using animal models[50–52], leading to pursuit of anti-inflammatory therapies that directly inhibit cytokines in patients. Thus far, clinical trials have been conducted using inhibitors or blockade of TNFα and IL-1β, which are well tolerated by patients.[53–55] However, in 2 clinical trials, anti-TNF therapy did not show efficacy in HF patients and in fact might worsen cardiovascular outcomes (Table 1-1). [56,57] Similarly while IL-1β blockade had some positive effects on CV events and hospitalizations, it has yet to improve patient mortality and long term outcomes.[55,58,59] Similarly, broad anti-inflammatory treatment using prednisone or other immunosuppressive agents did not show broad efficacy in improving CV outcomes.[60–62] These trials suggest that targeting inflammation in HF requires more precise mechanistic understanding than broad immunosuppression or inhibition of one cytokine.

Similarly, thus far the use of inflammatory biomarkers in cancer has been limited to correlative studies in which there is some evidence of cytokines predicting therapeutic response. Similar cytokines implicated in HF such as IL-6 and IL-1β are correlated with worse outcomes, whereas cytokines such as IFNγ correlate with better outcomes.[63–65] However, in contrast to HF, cytokine therapies have shown efficacy in treating various malignancies (Table 1-2). Systemic IL-2 therapy has been approved for the treatment of melanoma and renal cell carcinoma, and several other cytokine therapies such as IL-12 or IL-15 have ongoing clinical trials for efficacy against several malignancies.[66–69]

Trial:	Year	Indication:	Target:	Outcome:	Source
Prednisone for Idiopathic CM	1989	Patients with CHF and Suspected DCM	Prednisone	Early Improved EF in some patients, trend towards worse outcomes overall	60
ATTACH	2003	NYHA HF Class III-IV, LVEF < 35%	Infliximab (αTNFa)	Worsened Clinical Status, Increased HF and Death, Decreased CRP	56
RENEWAL	2004	NYHA HF Class II-IV, LVEF < 30%	Etanercept (αTNFa)	No Clinical Benefit	57
ACCLAIM	2006	NYHA HF Class II-IV, LVEF < 30%	Non-specific Immune modulation therapy (NIMT)	No overall clinical benefit, subgroup analysis showed decreased hospitalizations/death	62
TIMIC	2009	Myocarditis with no cardiac viral positivity	Prednisone/Azathioprine	Improved EF and cardiac parameters	61
CANTOS	2017	Patients with Previous MI, CRP > 2	Canakinumab (αIL-1β)	Decreased CV events and hospitalizations, no change in mortality, decreased CRP, increased infections	55
DHART-2	2018	HFpEF, CRP > 2	Anakinra (αIL-1β)	Decreased CRP/BNP, no clinical benefit	59
VCU-ART3	2020	ST-Elevation MI	Anakinra (αIL-1β)	Decreased Acute Hospitalizations/Death, Decreased CRP, Increased infections	58
LoDoCo2	2020	Evidence of Coronary Disease	Colchicine	Lowered Cardiovascular Death	71
COLICA	2024	Acute HF (Clinical Assessment, Furosemide >40 mg, BNP > 900)	Colchicine	Lowered IL-6/CRP, No clinical benefit	72

Table 1-1 Major Anti-Inflammatory Clinical Trials in HF

In addition to soluble inflammatory mediators, various immune cell subsets have been well characterized in both cardiac and tumoral inflammation. Across models of heart failure, both ischemic and non-ischemic, immune cells infiltrate the heart and can promote cardiac dysfunction. Innate immune cells such as monocytes and neutrophils infiltrate early after

cardiac insult, and adaptive immune cells follow suit in a chronic cardiac inflammatory response.[50,70] Specifically, T-cells have been shown to play a central role in most etiologies of HF, and are able to interact with cardiomyocytes, fibroblasts, and other immune cells to induce cardiac damage.[73–77] While cytokine therapies have not yet shown significant efficacy against HF, colchicine, which is able to impair immune cell migration and function, has been approved for patients with chronic coronary disease,[71,78] suggesting medications directly targeting immune cells might be more promising (Table 1-1). This approach has been translated into the cancer field as well, in which the immune cells of the tumor microenvironment play a powerful role in determining tumor progression. The tumor

Trial:	Year	Therapy	Indication	Outcome:	Source:
Aldesleukin Select Trial	1995	Recombinant IL-2	Renal Cell Carcinoma	14% response rate	67
rhIL-12 Phase II Trial	2004	Recombinant IL-12	Lymphoma	21% response rate	68
MDX-10	2010	Anti-CTLA-4	Unresectable Melanoma	10.9% response rate	86
rh IL-15 Phase I Trial	2014	Recombinant IL-15	Melanoma or Renal Cell Carcinoma	Increase in circulating immune cells, no tumor efficacy	69
ELIANA Trial	2019	CD19 Targeted CAR-T	B-cell ALL	81% Remission	84
Lifileucel Phase II Trial	2021	Expanded TILs + IL-2	Melanoma Resistant to Chemotherapy and ICIs	36% response rate	85
Relativity 047	2022	Anti PD-1 + Anti-LAG3	Unresectable Melanoma	Increased progression free survival	87
CheckMate 067	2024	Anti PD-1 + Anti-CTLA-4	Advanced Melanoma	58% response rate	88

Table 1-2 Major Clinical Trials of Immunotherapy for Cancer

microenvironment contains many immune cells, however T-cells are also one of the most critical anti-tumor cell types.[79,80] This has led to the development of T-cell based therapies including adoptive cell transfer and chimeric-antigen receptor (CAR-T) therapies, which are

now commonly used treatments.[81–85] Even more promising, therapies aimed at enhancing T-cell function *in vivo,* called immune checkpoint inhibitors, have revolutionized cancer immunotherapy (Table 1-2).[86–88] In summary, inflammation is a critical hallmark of both cancer and CVD that shares several mechanisms and cell types, including T-cells. While immunotherapies have been approved for both cancer and HF, significant mechanistic work remains to understand and improve these therapeutic approaches, as well as delineate the full relationship between cardiac and tumoral inflammation.

1.2 Overview of the Immune System:

1.2.1 Cells of the Innate and Adaptive Immune Systems

The immune system can be split into two broad subclasses – the innate immune system, which consists of non-cellular protective mechanisms and rapidly responding immune cells, and the adaptative immune system which includes immune cells able to target specific pathogens (Figure 1-3).[89–91] Innate immune cells include granulocytes such as neutrophils, basophils, and eosinophils which contain machinery to fight a wide variety pathogens as well as contribute to sterile inflammation. Other innate immune cells such as natural killer cells (NK) or innate lymphoid cells (ILCs) play specialized roles in both tissue homeostasis and pathogenic inflammatory responses.[92] The innate system also bridges the gap between innate and adaptive immunity through specialized cells known as antigen presenting cells (APCs). APCs most commonly include macrophages and dendritic cells, which after activation endocytose proteins and break them into small peptide antigens that may be presented to T-lymphocytes, one adaptive immune cell. Antigenic peptides are presented on major histocompatibility complex molecules (MHC), which can be recognized by T-cells that mount a specific response to said antigen.[93] T-cells come in two main subtypes: $CD4^+$ T-

cells, that include helper T-cells and regulatory T-cells, and recognize peptide on MHC class II, and $CD8^+$ T-cells, or cytotoxic T-cells, which recognize peptide on MHC class I. Helper T-cells primarily produce a variety of cytokines to aid other immune cells including innate cells or cytotoxic T-cells, while cytotoxic T-cells are able to directly kill infected cells or cancer cells.[91,94] T-cells can also help B-lymphocytes, adaptive immune cells that produce circulating antibodies against antigens. B-cells recognize antigen through surface bound antibody receptors and then can differentiate into sub-classes of B-cells that produce different isotypes of antibody, as well as long lived plasma cells that secrete significant antibody over time. Both B and T-cells are unique in that they are able to form long-lived

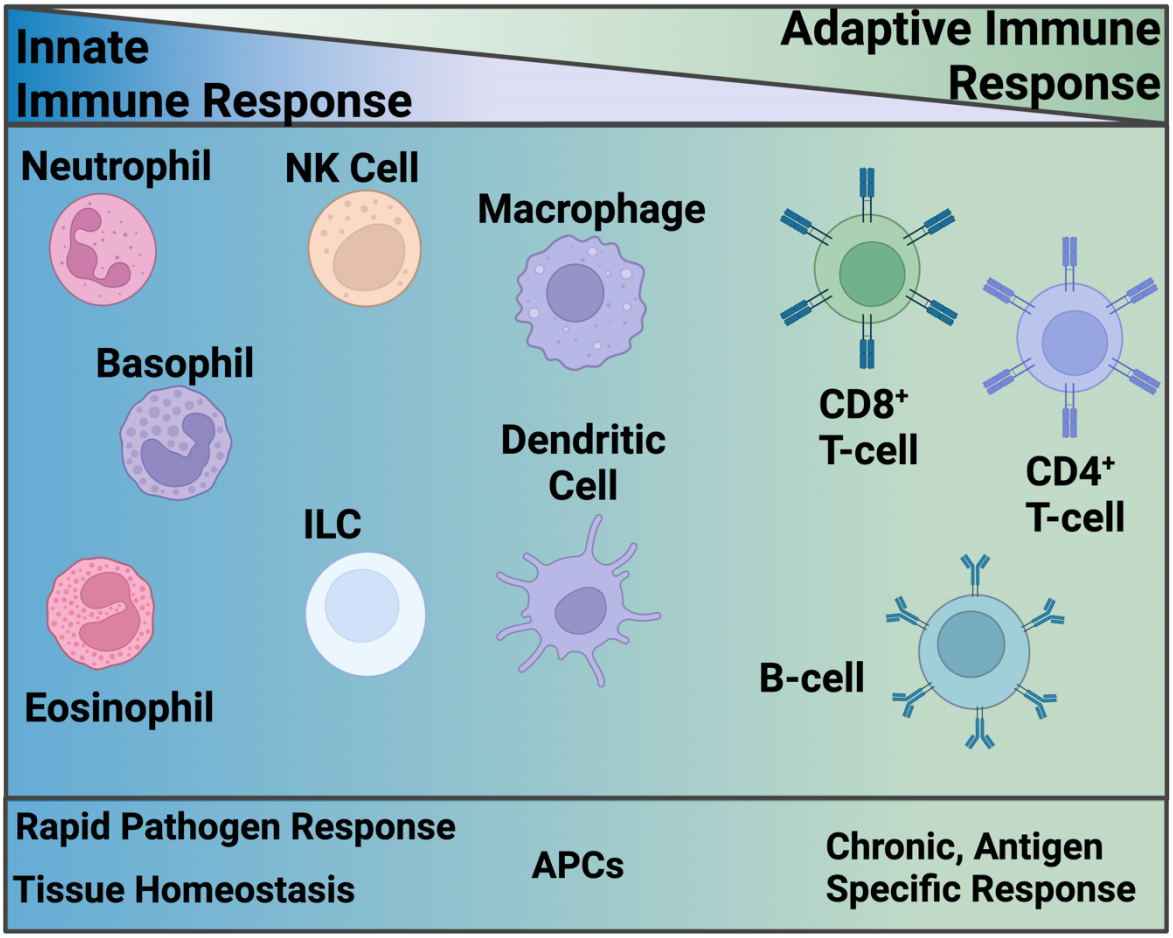


Figure 1-3 Cells of the Immune System
Overview of innate and adaptive cells of the immune system, with broad associated functions. NK = natural killer, ILC – innate lymphoid cell, APC = antigen presenting cell. Figure created with Biorender.

memory cells, which persist in lymphoid organs and tissues and are able to mount a rapid response to repeat antigens.[91,95]

1.2.2 Pattern Recognition Receptor Signaling and MyD88

Innate immune cells are the first to recognize pathogens or sterile inflammation, often in the form of pathogen associated molecular patterns (PAMPs) or damage associated molecular patterns (DAMPs – known as alarmins), released by stressed or dying cells.[96,97] These signals are sensed by a broad class of receptors known as pattern recognition receptors (PRRs) that activate a rapid immune response through production of pro-inflammatory cytokines as well increased antigen presentation by APCs. The most widely expressed family of PRRs are toll-like receptors (TLRs). Ten TLRs have been discovered in humans: TLR1-TLR10, and twelve in mice: TLR1-TLR9, TLR11-TLR13[98]. Almost all TLRs associate with myeloid differentiation primary response factor 88 (MyD88), an intracellular adapter protein that coordinates downstream pro-inflammatory signaling cascades.[98,99] Additionally, the IL-1 receptor family members (IL-1R, IL-18R, and IL-33R) signal through MyD88. TLRs can be further divided into cell surface TLRs: TLR1, TLR2, TLR4, TLR5, TLR6, and TLR10 and intracellular vesicle TLRs: TLR3, TLR7, TLR8, TLR9, TLR11, TLR12, and TLR13.[98,99] Some TLRs recognize specific PAMPs (flagellin, LPS) while others can also recognize alarmins involved in sterile inflammation, such as high mobility group box 1 (HMGB1), S100 proteins, and heat shock proteins. TLR4 serves as the receptor for many alarmins, and is unique in that it can signal through MyD88-dependent and independent pathways both from the membrane and endocytosed vesicles.[100–103] The Toll-IL1R (TIR) domain of MyD88 allows it to associate with TLRs and the IL-1R family. Upon ligand binding, MyD88 dimerizes and recruits IL-1R associated kinases (IRAKs).[98,99] Recruitment of IRAK4 results in autophosphorylation and activation of IRAK1/2, forming a large oligomultimeric complex termed the “Myddosome,” consisting of 6 MyD88s, 4 IRAK4s, and 4 IRAK1/2s.

Binding domains on IRAK1/2 in the Myddosome subsequently recruit TNF receptor associated factor 6 (TRAF6), an E3 ubiquitin ligase which builds polyubiquitin chains on multiple targets to activate downstream signaling cascades.[98,99,101] MyD88-dependent activity leads to the activation of many signaling pathways, including the MAP kinase cascade, NF-κB, and interferon regulatory factor (IRF) 5/7, resulting in the transcription of pro-inflammatory cytokines and type I interferons. These pathways have been mainly characterized in macrophages to induce inflammation for pathogen clearance, but can as well propagate inflammation that contributes to CVD or cancer (Figure 1-4).[98,101]

A parallel MyD88-independent pathway exists, used by TLR3 and TLR4, that involves recruitment of an alternate adaptor protein, TIR-domain containing adaptor inducing interferon-β (TRIF), which is recruited to the TIR domain of TLR3/TLR4. This sequentially activates TRAF3, IRF3, and type I interferon production. TRIF can also activate TRAF6

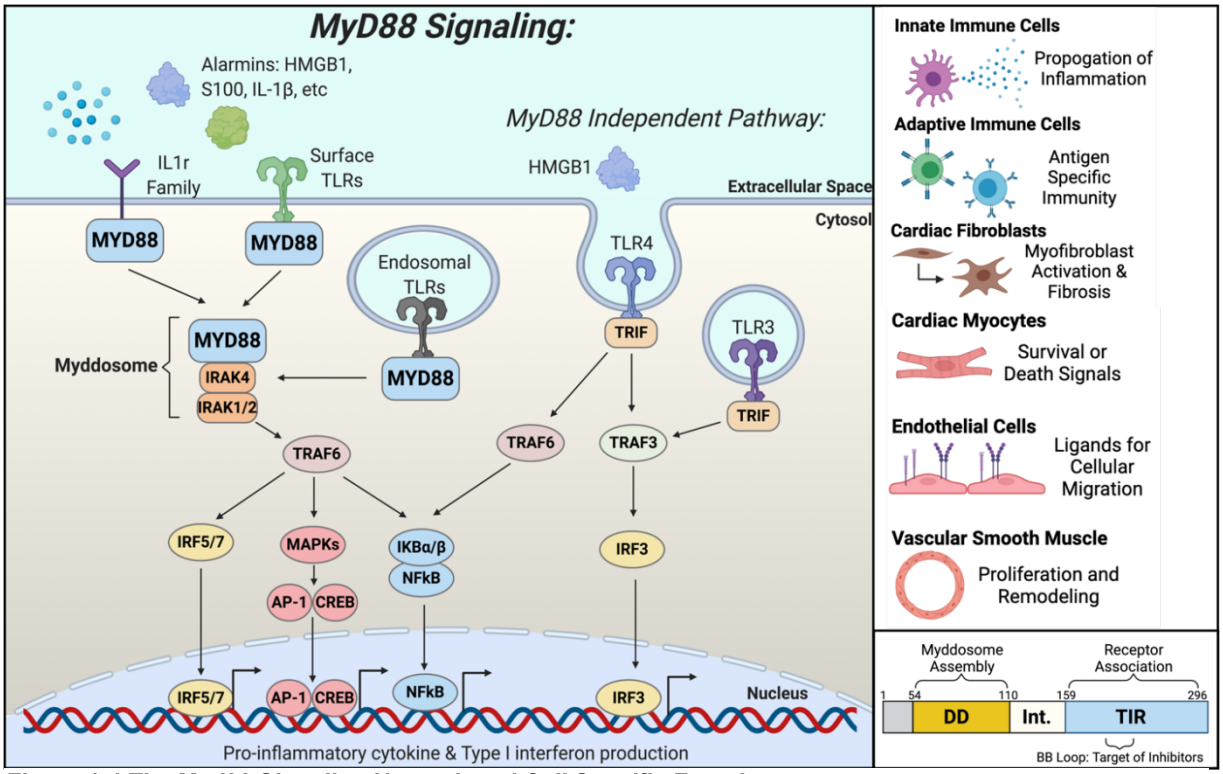


Figure 1-4 The Myd88 Signaling Network and Cell Specific Functions
Alarmins are recognized by TLRs and cytokine receptors, leading to activation of MyD88 and a subsequent immune response, along with cell specific functions (right panel). The MyD88 independent pathway contributes in parallel. The gene structure and domains of MyD88 are shown in the lower right panel. Figure made with Biorender.

through a non-canonical pathway, leading to NF-κB induction and cytokine release that contributes to cardiovascular inflammation.[99,101]. These cascades, while somewhat redundant, allow for the careful and widespread control of inflammatory mediators in response to TLR stimulation, with MyD88 sitting at the epicenter (Figure 1-4).

MyD88 is required for full function of the innate immune response. As a result, patients with a loss of function mutation in *Myd88* have recurrent, pyogenic infections.[104] While this pathway was widely characterized in innate cells, MyD88 and TLRs are also expressed in adaptive immune cells.[105] Interestingly, MyD88 knockout B and T cells have shown impaired antibody and cytokine production, and similarly, TLR agonists that signal through MyD88 can enhance T-cell activation and cytokine production.[105–108] As such, global MyD88 deficient mice are protected in multiple autoimmune disease models, including cardiac myocarditis.[109–111] However, TLR/MyD88 signaling extends beyond immune cells, and most of the work in preclinical models have used globally deficient mice limiting our understanding of cell specific MyD88 functions. MyD88 expression at the transcript and protein level was discovered not only in lymphoid tissues, but in multiple organs including the heart.[112,113] Profiling of TLR components uncovered mRNA expression of every TLR and all downstream signaling molecules in human cardiac tissue.[114] Further, MyD88 expression in tumors has been correlated with worse cancer outcomes in multiple malignancies.[115–117] Targeting of MyD88 genetically or with small molecular inhibitors in animal models or *in vitro* has also been shown to reduce cancer progression and invasiveness[115,116,118]. However, the exact function of MyD88/TLR signaling outside of innate immunity is still not well understood, something explored in T-cells and cardiac fibroblasts in chapters 2-5 of this dissertation.

1.2.3 Intracellular DNA Sensing

A variety of stressors to cells including cardiac injury and cancer treatment can induce DNA damage and subsequent mutations, as such, most cells have several mechanisms to

repair damaged DNA.[119] However, failure of these mechanisms can result in leakage of double stranded DNA from either the nucleus or the mitochondria into the cytosol. This triggers one or multiple anti-viral inflammatory pathways, as double stranded DNA in the cytosol has evolved to be a PAMP indicative of intracellular viral infection.[120,121] Cytosolic DNA can be recognized by one of several DNA sensing proteins: AIM2, ZBP1, IFI16, or cGAS, whereas if the DNA becomes endosomal, TLR9 is triggered. All of these can lead to shared downstream signaling cascades that promote anti-viral inflammation.[120,121] Importantly, DNA damage and the activation of DNA sensing pathways has been associated with poor outcomes across all etiologies of heart failure, and has been mechanistically linked to cardiomyocyte dysfunction.[122–124]

One of the most well characterized DNA sensing pathways is the cGAS-STING pathway, which is highly conserved evolutionarily (Figure 1-5).[125] cGAS recognizes cytosolic double stranded DNA, then produces the small molecular intermediate 2,3-cyclic-GMP-AMP (cGAMP). This is subsequently recognized by STING, which dimerizes, translocates from the endoplasmic reticulum (ER) to the Golgi, then induces downstream phosphorylation of TBK1, IRF3, and NF-kB. This primarily results in type I interferon transcription (IFNα/β), which stimulate a large host of interferon stimulated genes (ISGs) including T-cell chemoattractants such as CXCL9/10 for antiviral immunity.[125–127] STING can also be activated independent of cGAS from mitochondrial stress, DNA damage, or the unfolded protein response, all of which can be explored as potential mechanistic avenues in each cell type.[128,129] Targeting of cGAS or STING has been shown to be protective across several etiologies of HF in animal models, including myocardial infarction,[130] pressure overload,[131,132] anthracycline toxicity,[133] and diabetic cardiomyopathy.[134] In anti-tumor immunity cGAS-STING functionality is more complicated, as STING has been shown to contribute to tumor progression and some tumors downregulate STING to impair anti-tumor immunity.[135,136]

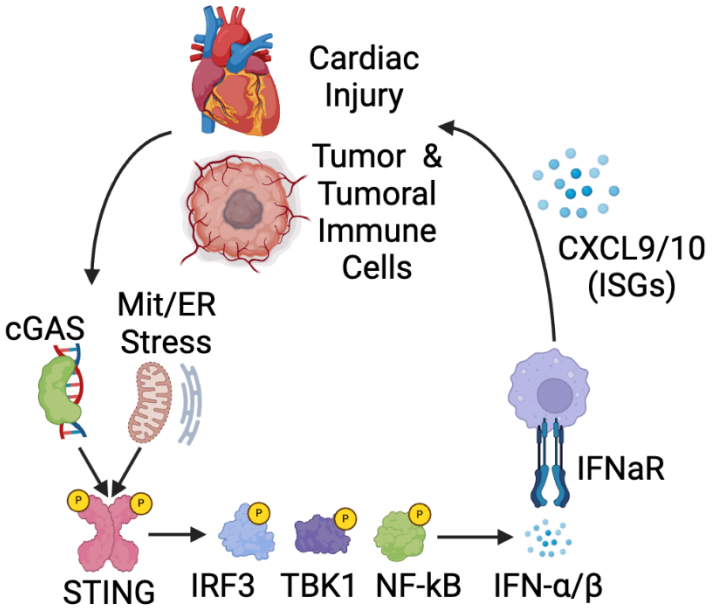


Figure 1-5 STING Signaling in Cardiac or Tumoral Inflammation
Various cardiovascular disease as well as cancers can activate STING with or without cGAS, leading to the activation of several signaling pathways, type I interferon release, and subsequent interferon stimulated gene expression such as CXCL9/10, propagating inflammation. Figure made with Biorender.

However, activating APCs by inducing type I interferon can promote anti-tumor immunity, as such, both STING activation and STING inhibition have been attempted as anti-tumor therapies,[137–139] which leads us to believe that the precise cellular mechanisms and how they can be utilized in either cancer and HF is not fully understood, which I investigate as part of chemotherapeutic cardiotoxicity in chapter 7 of this thesis.

1.2.4 TCR signaling and T-cell Activation

As T-cells are one of the most critical immune cells for cardiac remodeling and anti-tumor immunity, their proper development and function is essential. Naïve T-cells develop in the thymus, then migrate to lymphoid organs until they engage with an APC presenting antigen and become activated. T-cells recognize antigen through their T-cell receptor (TCR), which is specific for the peptide of only one antigen. The TCR binds to a peptide antigen presented on MHC by the APC, with $CD4^+$ T-cells being able to recognize peptide-MHC class II (MHCII) while $CD8^+$ T-cells recognize peptide-MHC class I (MHCI).[93,140] In addition to signaling through the TCR, T-cells require co-stimulation through CD28 in order to become fully activated. T-cell CD28 binds to B7 family proteins such as CD80 and CD86 on APCs, which further enhances TCR signaling.[93,140] Once these two signals begin, a complex signaling cascade in the T-cell begins which allows T-cells to activate fully into effector T-cells (Figure 1-6). This signaling is characterized by the phosphorylation of ZAP-70 and the

subsequent recruitment of scaffold proteins that simultaneously activate many downstream pro-inflammatory pathways: NF-kB, MAPK, NFAT, PI3K-AKT, JUN, and more. Together this combination of signals increase T-cell proliferation and growth, cytokine production – especially that of IL-2, and the expression of several surface activation markers.[141,142] Activated T-cells transiently upregulate CD69, which causes retention in the lymph node for several days to allow for longer T-cell/APC engagement. They also chronically upregulate CD25, a subunit of the IL-2 receptor, leading to T-cell recognition of IL-2 that promotes cell survival and proliferation.[143] T-cells also express several receptors termed “immune checkpoints” to inhibit potential over-activation. Activated T-cells upregulate molecules including PD-1, CTLA-4, and LAG3 among other receptors, all of which bind to ligands that can decrease their activation and in some cases induce T-cell death.[144,145] Importantly, blocking these immune checkpoints therapeutically has been harnessed as a anti-tumor strategy, showing significant efficacy in many malignancies by increasing T-cell activation and killing ability.[146] Finally, the inflammatory environment in which a T-cell is activated can influence its identity and function, shaped by specific cytokines and signals from APCs or other cell-cell communications.[147] One such example is TLR stimulation through MyD88. Numerous studies have shown that TLR stimulation can enhance co-stimulation and increase T-cell activation, although the mechanism for this remains not fully elucidated, which I address in chapter 5 of this dissertation (Figure 1-6).[148,149]

1.2.5 T-cells Subtypes and Effector Functions

When T-cells become activated they can differentiate into many different subtypes, all of which adopt specialized features to exhibit specific functions in the inflammatory response (Figure 1-6). T-cell subtypes can be identified using several key features: the cytokines which induce their differentiation, the transcription factors that they express, and the cytokines that they secrete after differentiation.[147,150] There are a few subtypes of $CD4^+$

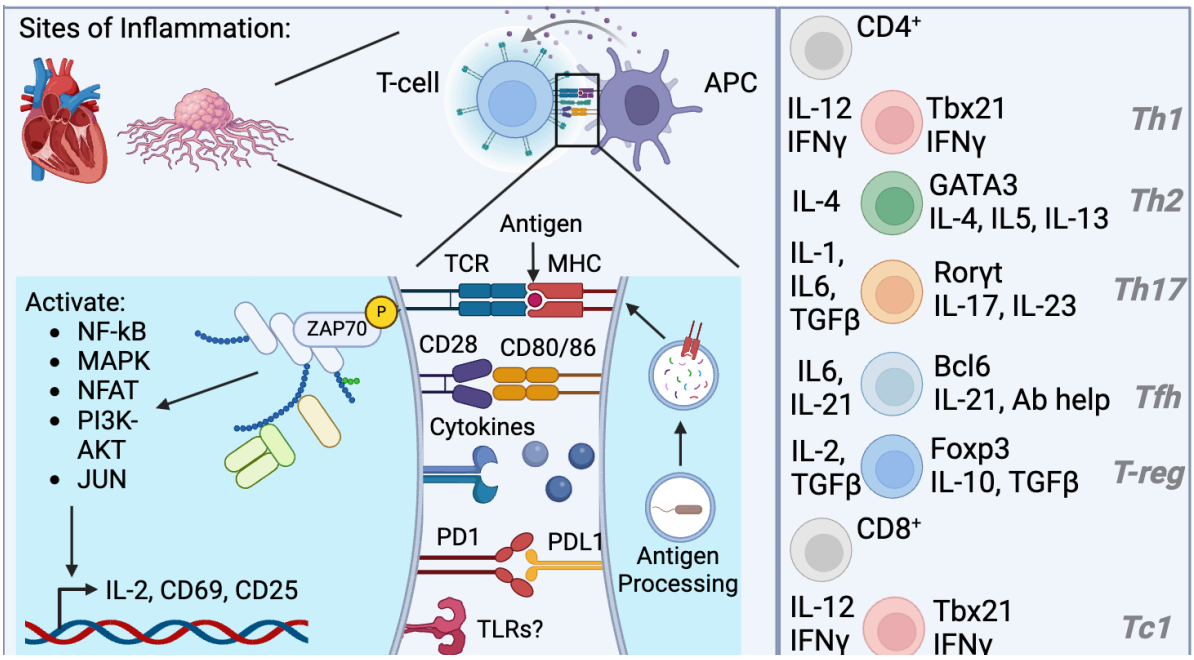


Figure 1-6 Overview of T-cell Activation and Differentiation
T-cells become activated when antigen presenting cells (APC) present antigen through MHC (major histocompatibility complex) to the T-cell receptor (TCR), which requires multiple signals and can be modulated through receptors and cytokines. This results in a complex signaling cascade and the activation of many pro-inflammatory signaling pathways, as well as activation marker expression. When activated, T-cells receive specific cytokine signals that induce differentiation into subtypes characterized by additional cytokine expression and classical transcription factors. Figure made with Biorender.

helper T-cells that are most common. Th1 cells are induced by IL-12 and IFNγ, express the transcription factor Tbx21 or Tbet, and secrete IFNγ to combat intracellular pathogens and participate in autoimmune diseases.[147,150,151] Th2 cells recognize IL-4, express GATA3, IL-4, IL-5, and IL-13 and attack some extracellular parasites as well as play a role in allergy and asthma related inflammation. [147,150,151] Finally, Th17 cells are induced by IL-1, IL-6, and TGFβ, express Rorγt, IL-17, and IL-23, and are used in anti-bacterial/anti-fungal responses and some autoimmune diseases.[147,150,151] $CD4^+$ cells can also become $Bcl6^+$ follicular helper (Tfh) cells in the presence of IL-6 and IL-21, which aid in B-cell differentiation and antibody secretion. [147,150,151] Some helper T-cells differentiate into $Foxp3^+$ T-regulatory cells, which are anti-inflammatory cells. They secrete anti-inflammatory cytokines such as IL-10 and TGFβ, and directly interfere with APC function to halt immune responses.[147,152] On the other hand, $CD8^+$ T-cells most commonly express Tbx21 and differentiate similarly to Th1 cells (known as Tc1 cells), and are characterized by high IFNγ expression. Tc1 cells are able to

directly kill virally infected cells or cancer cells through the release of cytotoxic molecules such as Perforins or Granzymes from small granules that fuse with the membrane upon recognition of antigen through the TCR.[153] Th1, Th17, and Tc1 cells have been implicated in several different types of CVD including chronic HF,[50,73–77] whereas Tc1 cells are the most common class of anti-tumor T-cells.[154] T-regs also play a role in limiting cardiac inflammation, and can significantly blunt the anti-tumor T-cell response.[155–157] T-cell subtypes exhibit some degree of plasticity, and as mentioned in the previous section, the environment a T-cell experiences can shape its' identity and subsequent effector function.[158]

1.2.6 T-cell Recruitment and Vascular Activation

In order for T-cells to infiltrate a tissue into a site of inflammation, they must cross the vascular endothelium in a carefully controlled set of steps. Endothelial cells make up the walls of blood vessels and are the key cell type in regulating immune cell migration into tissues. To help ensure T-cell migration only occurs when needed, endothelial cells become activated and able to recruit T-cells only in response to specific stimuli. Pro-inflammatory cytokines such as TNFα or IL-1β induce endothelial cell activation, PAMP and DAMP signals through TLRs can provide similar signals, and even the environmental cues such as pH or mechanical stimuli can activate endothelial cells.[159,160] Additionally, the secretion of chemokines by immune and stromal cells to attract T-cells only to specific sites of inflammation helps regulate immune cell spatially.[161] Upon activation, endothelial cells begin expressing several factors to help interact with T-cells. First, selectins (p-selectin, e-selectin) are expressed on the luminal surface that are able to interact with selectin-ligands on T-cells, together facilitating the initial capture and rolling of T-cells along the endothelium. Then, firm adhesion factors including ICAM-1 and VCAM-1 bind to integrin complexes on T-cells (LFA-1 and VLA-4, respectively) which results in firm adhesion to the endothelium. After adhesion, T-cells spread out and crawl to search for areas for transmigration, which is

internally facilitated by several signaling cascades such as PI3K, SRC, and VAV kinases. Finally, they migrate across the endothelium into tissue with help from proteins including PECAM1 and CD99.[159,160,162] Modulating immune cell recruitment into tissues has become a strongly desired therapeutic approach. As previously discussed, the approval of colchicine for ischemic heart disease represents one such strategy by blocking neutrophil migration,[71,78] however no such therapies exist for inhibition of T-cell migration into cardiac tissue despite the identification of potentially targetable chemokine axes.[163,164] In cancer treatment, T-cell based therapies that overexpress specific chemokine receptors has been utilized to improve tumor penetration, however the complicated nature of co-recruitment of suppressive immune cells to the tumor microenvironment and redundancy of chemokine signals makes translating these therapeutically challenging.[161,165,166]

1.2.7 Immune Cell Death

For a T-cell to function in an inflammatory response, it must stay alive through a diverse set of cellular triggers, then after inflammation resolves it must die (Figure 1-7).[167,168] Upon T-cell activation in response to an antigen, signaling downstream of the TCR leads to up-regulation of pro-survival factors, which includes NF-kB and AKT signaling upregulating the BCL-2 family of proteins which allow for T-cell survival.[168,169] T-cells require ongoing signal through their TCR, or from pro-survival cytokines such as IL-2, IL-7, and IL-15, otherwise they undergo cell death as part of the resolution of a T-cell inflammatory response, which can be termed “neglect induced cell death.”[167,168] The main mechanism for this cell death is apoptosis, a programmed form of cell death considered to be immunologically silent – necessary for resolving inflammation without off-target damage. In cell-intrinsic apoptosis, the BCL-2 family of proteins sequester pro-apoptotic proteins such as BAX and BAD, which act at the mitochondria to release Cytochrome C and cleave Caspase 9 to it’s functional form. Caspase 9 cleaves Caspase 3 and 7, which initiate widespread protein cleavage

forcing the cell to undergo death. Apoptosis can also occur due to extrinsic signals, such as TNFα or FasL binding. This activates Caspase 8 as part of a large multimeric complex which can also lead to Caspase 3/7 cleavage and cell death.[167,168,170] Interestingly, over-stimulation of the TCR can also lead to "activation induced cell death" which can help prevent auto-reactive T-cell formation and chronic inflammation.[171] Further, during the process of T-cell development, auto-reactive T-cells undergo apoptosis during selection in the thymus, together making the regulation of T-cell death vital for functional adaptive immunity (Figure 1-7).[172]

T-cells can also die by necroptosis – triggered through ligation of various cell death receptors such as TNFα and PRRs including TLR3/4. Necroptosis is regulated through a similar Caspase 8-containing complex as extrinsic apoptosis which includes the sister

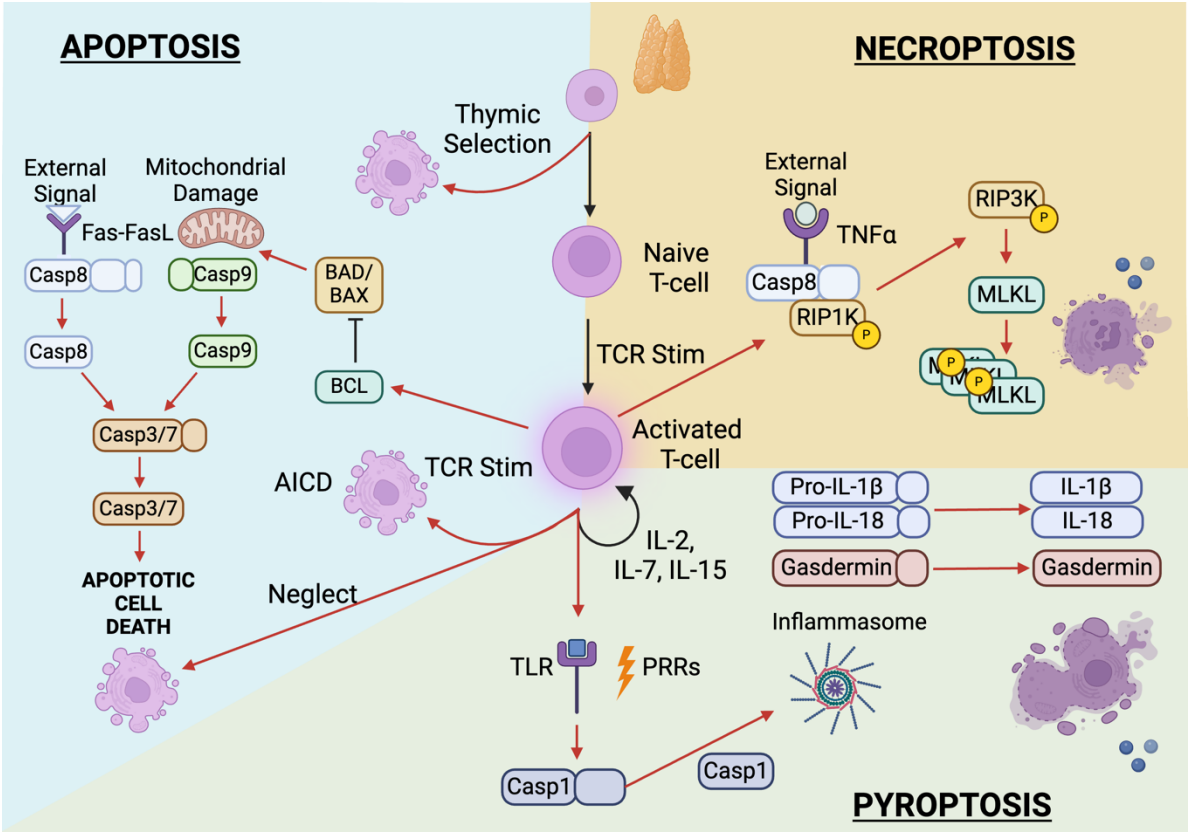


Figure 1-7 Mechanisms of T-cell Death
Schematic of different pathways of cell death undergone across a T-cell lifecycle. T-cells undergo apoptosis as part of thymic selection, external signals, internal damage, activation induced cell death, or death by neglect. In response to specific triggers T-cells can also undergo necroptosis or pyroptosis. TCR = T-cell receptor, AICD = activation induced cell death, TLR = toll-like receptor, PRR = pattern recognition receptor. Figure made with Biorender.

adapter protein to MyD88, TRIF, however in this form of death the phosphorylation of RIP1K and RIP3K leads to phospho-MLKL forming pores in the membrane. This causes cell lysis and the release of intracellular DAMPs, making necroptosis a potent trigger of inflammation (Figure 1-7).[167,173] Additional inflammatory signals through PRRs, cytokine receptors, and a diverse set of cellular stressors including ion efflux, toxins, or crystalline substances can trigger pyroptotic cell death. Pyroptosis results from activation of the inflammasome, a polymeric complex that contains any number of PRRs and cleaved Caspase 1 or 11. This complex is able to rapidly cleave pro-IL-1β and IL-18 to their active forms alongside the pore protein Gasdermin D, which forms pores in the membrane to lyse the cell and release mature IL-1β and IL-18 (Figure 1-7).[167,174] Both necroptosis and pyroptosis have been described in T-cells[175,176] but less is known about their role in canonical T-cell function.

1.3 Cardiac Remodeling and Inflammation

1.3.1 Cardiac Anatomy and Physiology

The heart is tasked with circulating blood, oxygen, and nutrients throughout the whole body for the duration of life, and as such is an incredibly efficient muscular pump. Cardiac function is dependent on proper anatomy of the heart, both at the gross organ level and the cellular level. The heart contains 4 chambers – blood enters into the right atrium from the periphery, passes into the right ventricle, is oxygenated in the lungs, is received by the left atrium, then goes into the left ventricle which is the largest chamber of the heart and responsible for pumping blood into the aorta and to the rest of the body. The walls of the heart have carefully layered sheets of myocardial muscle that allow for efficient contraction and relaxation, each chamber additionally contains valves that prevent backflow of blood, and the entire heart is wrapped in a fibrous sac called the pericardium.[177,178] One cardiac cycle, or heart beat, contains two phases, systole, in which the atria and then ventricles contract to move blood, and diastole, in which the chambers relax and refill with blood.[177,178]

This cycle is carefully regulated by a complex cyclic electrical patterning of the heart. Cardiac rhythm is set by specific pacemaker cardiomyocytes that fire electrical impulses spontaneously. These impulses travel throughout the myocardium causing progressive and widespread depolarization of cardiomyocytes in which sodium and calcium influx into the cells resulting in contraction, or systole, followed by a repolarization period, diastole.[178,179] Cardiovascular disease of different etiologies can affect every part of this anatomy and physiology – systole or diastole, valvular function, myocardial cells, electrophysiology, and more.

Cardiomyocytes, or cardiac muscle cells, make up nearly three fourths of the mass of the heart.[178] Cardiomyocytes are filled with structures termed “sarcomeres” that contain repeating actin and myosin proteins which are responsible for contraction of the cell itself in response to calcium. They also have a widespread system for calcium influx and efflux to control the cardiac cycle, made up of calcium storage in the sarcoplasmic reticulum and T-tubules to efficiently distribute calcium across sarcomeres.[180,181] Importantly, cardiomyocytes are generated in the neonatal period and in humans once fully differentiated are unable to divide.[182] The next most common cardiac cells are endothelial cells that line the cardiac vasculature, as well as smooth muscle cells and pericytes in larger vessels. Cardiac fibroblasts are responsible for maintaining the structure of the heart and play both homeostatic and pathogenic roles. There are a small population of adipocytes in the heart, and neurons to help control cardiac rate and rhythm.[183] Finally, immune cells make up 5-10% of cells in the heart, with most immune cell subsets being represented in the healthy myocardium, however macrophages are the most frequent and participate in homeostasis, electrical conduction, and disease.[183–185] The heart also contains a significant lymphatic system for efficient immune monitoring of cardiac insult, which drains into several sets of mediastinal and pericardial lymph nodes.[186]

1.3.2 Pathologic Hallmarks of Heart Failure

In most etiologies of HF, cardiomyocytes remodel in different fashions in an attempt to preserve cardiac function (Figure 1-8). Cardiac hypertrophy, or enlargement of the cardiac muscle, occurs in the majority of HF. During this process, hypertrophy can be physiologic, in which the contractile function of the heart is maintained, however this can become pathologic in which either contraction or relaxation of the heart is impaired. In hypertrophic hearts, cardiomyocytes can increase in both width and length, leading to eccentric hypertrophy in which the chambers enlarge and contractile function is lost. Alternatively, cardiomyocytes can increase more in width, leading to concentric hypertrophy in which ventricular wall thickness increases significantly and relaxation in diastole is impaired.[187,188] Cardiomyocytes also undergo molecular changes during hypertrophy, such as increases fetal myosin heavy chain (MYH7) and the expression of natriuretic peptides (ANP/BNP)[187,188] which can be used as biomarkers for HF.[21] Cardiac hypertrophy can be triggered by many signals, including but not limited to sympathetic nervous signaling, mechanical forces, hypertensive molecules such as angiotensin II, growth factors, natriuretic peptides, and cytokines.[187,188] Finally, in certain circumstances such as cardiotoxic chemotherapeutic damage, cardiomyocytes can become atrophic and decrease in size, leading to impaired contractility alongside similar molecular changes.[189,190]

Another hallmark of HF is the deposition of extracellular matrix (ECM), or cardiac fibrosis, which can impede both systolic and diastolic function (Figure 1-8). This can occur in the form of a scar to replace dead cardiomyocytes after myocardial infarction, or more diffusely throughout the heart in response to non-ischemic cardiac stressors.[191] At baseline, the heart contains significant ECM including type I and type III collagens, alongside a wide range of other glycoproteins. During pathologic fibrosis, the overall quantity of existing ECM proteins can increase, such as increased collagen I/III.[192] In addition, the content and quality of the ECM can change, including increases in more sparse ECM proteins (collagen V/VI

and fibronectin) as well as alterations in the molecular structure of the ECM, an example of which being increased collagen cross-linking and subsequent tissue stiffness.[192,193] Cardiac fibroblasts are the main cell type that produce ECM in fibrotic hearts in response to mechanical, neural, endocrine, and inflammatory signals.[191,194]

Endothelial dysfunction has been long since associated with heart failure.[195] In the failing heart, capillary density decreases, leading to overall poor perfusion of cardiac muscle. However, capillary function itself is also impaired contributing to cardiomyocyte

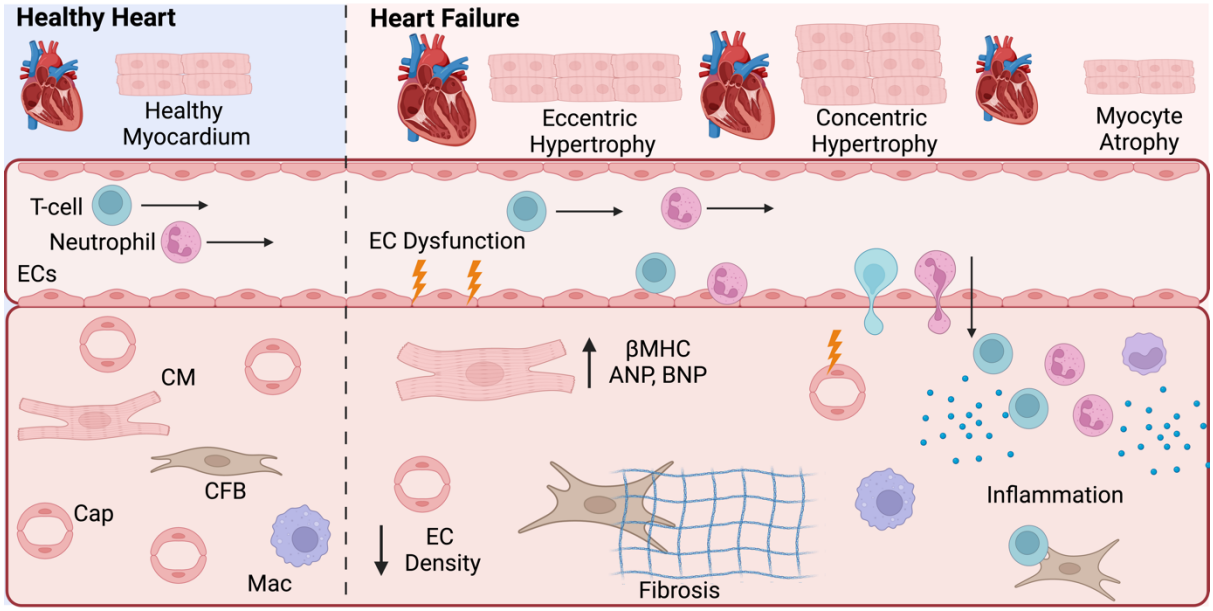


Figure 1-8 Pathologic Hallmarks of Heart Failure
Overview of the cell types and structures of healthy vs. failing hearts, including cardiomyocyte remodeling, endothelial rarefaction, fibrosis, and inflammation. EC = endothelial cell, CM = cardiomyocyte, cap = capillary, mac = macrophage. Figure made with Biorender.

dysfunction.[196,197] Endothelial cells have been shown to have altered production of vasoconstricting and vasodilating stimuli, reduced anti-coagulant secretion, and increased adhesion molecules, cytokines, and chemokines, together leading to dysfunctional and inflamed vasculature.[160,197]

Finally, cardiac inflammation has been highlighted as a critical hallmark of HF. While immune cells play homeostatic roles in the heart, the recruitment of various immune cell subsets to the injured heart can coordinate pathologic cardiac remodeling, however, the nature of cardiac inflammation varies depending on the etiology.[70,198] Following myocardial

infarction, neutrophils are rapidly recruited to remove necrotic cardiomyocytes, followed by monocytes and T-cells which initiate cardiac repair. However, the chronic presence of T-cells and pathogenic macrophages can contribute to long term cardiac fibrosis and systolic dysfunction.[199,200] In other etiologies of HF such as myocarditis or pressure overload, the early recruitment of myeloid cells can increase cardiac T-cell recruitment. T-cells have been shown to play a central role in most etiologies of HF, and can contribute directly to cardiomyocyte hypertrophy and cardiac fibrosis.[201–203]

1.3.3 Pre-clinical Models of HF in Rodents:

A variety of animal models for each etiology of HF have been utilized to further our mechanistic understanding of the disease and test potential therapeutic interventions. While no animal model perfectly recapitulates all elements of human disease, several models show consistent shared elements of human pathobiology used in this dissertation. To model non-ischemic HF, increases in pressure to the LV are often utilized in rodents. This can be accomplished by surgical constriction of the thoracic aorta (TAC),[204] or chronic administration of hypertensive agents such as Angiotensin II with or without phenylephrine usually by subcutaneous osmotic minipump implantation.[205] These models all consistently induce cardiac hypertrophy, cardiac fibrosis, and systolic dysfunction, as seen in patients. To model cancer patient cardiotoxicity, direct dosing of cardiotoxic chemotherapeutic agents such as Doxorubicin is used in mice,[206] although translatability of these models is limited as they are often administered in healthy, non-tumor bearing mice. Additionally, mice can be administered newer immunotherapies such as immune checkpoint inhibitors, which show efficacy in reducing tumor growth, but on their own do not cause cardiac side effects, necessitating genetic models, one significant pre-clinical limitation in the field of cardio-oncology.[207,208]

1.3.4 Cardiac Inflammation in non-ischemic heart failure

As previously discussed in section 1.1.5, human HF patients have chronic inflammation, such as increased circulating and cardiac cytokines, as well as increased PRR expression in the heart.[45–49,209] Further, the frequency of both circulating neutrophils and inflammatory effector T-cells has been correlated with the progression of HF.[210,211] Biopsy samples from failing hearts have also shown elevated $CXCR3^{+}CD4^{+}$ T-cells.[73,163] More recent multi-omics studies on patient samples have implicated specific subsets of pro-fibrotic macrophages across etiologies of HF, which interestingly produce IL-1β, necessitating further study on more targeted anti-IL-1β therapies.[52,212] Additionally, numerous studies characterize auto-antibodies directed against cardiac antigen in human HF patients, making study of the humoral immune response an additional avenue for therapeutic intervention.[213–216]

Mouse models of non-ischemic HF have further elucidated several immunologic mechanisms and contributors to pathophysiology. Pressure overload through TAC can induce the expression and release of DAMPS such as IL-1β, IL-33, and HMGB1 which activate innate immune cells.[217–220] TAC also results in the cardiac expansion of both resident and infiltrating $CCR2^{+}$ monocytes and macrophages, the former of which can be protective while the latter are most frequently pathogenic.[164,221–223] Other innate immune cell types have been implicated through depletion studies, such as neutrophils[224] and NK cells.[225] Importantly, pressure overload can activate and expand DCs,[223,226] leading to a chronic adaptive immune response. Multiple studies have shown that $CD4^{+}$ helper T-cells increase in the heart and are required for the development of pressure-overload induced HF in mice,[73,227] while $CD8^{+}$ T-cells are mostly dispensible.[227,228] Further characterization has shown these pathogenic T-cells are a majority Th1 $IFN\gamma^{+}$ cells, express CXCR3, matching what has been found in patients, and are recruited in response to myeloid derived CXCL9/10 after binding to endothelial ICAM-1. In TAC, Th1 cells are expanded against

oxidative-stress induced cardiac neoantigens, leading to clonal expansion and subsequent cardiotropism.[163,226,229,230] Once in the heart, these T-cells can induce cardiac fibrosis through direct interactions with cardiac fibroblasts and hypertrophy through not-well understood mechanisms, as such T-cell deficient mice are protected from these elements of pathology.[73,229,231]

T-cells have been further implicated in several other models of non-ischemic HF. Using angiotensin II infusion, both $CD4^+$ and $CD8^+$ T-cells, but not B-cells, have been shown to contribute to the development of hypertension and subsequent cardiac remodeling.[232–234] However, whether this is exclusively due to the lack of hypertension or instead due to similar T-cell functions in the cardiac inflammatory environment remains not well understood. Cardiac macrophages, DCs, and γδ T-cells also increase in response to angiotensin II and contribute to pathogenesis, however their exact mechanistic roles remain unclear.[235–237] Even fewer studies have looked at T-cell inflammation in the more commonly used combined angiotensin II/phenylephrine model. Very little is known about inflammation in HFpEF, however one study has defined $CD4^+$ T-cell subsets to be required for the development of diastolic dysfunction and cardiac hypertrophy in mice, through an antigen-nonspecific reprogramming of T-cells which impairs cardiomyocyte relaxation.[74] Overall, much has been learned about the cardiac immune response in HF, however with the dearth of immunotherapies that have been successful in clinical trials, greater mechanistic study remains a necessity.

1.3.5 Cardiac Fibroblast State and Function

Cardiac fibroblasts make up over 25% of the cells in the heart, as identified using canonical markers such as PDGFrα, Tcf21, or DDR2,[238,239] and are required for a diverse set of homeostatic and disease-associated roles (Figure 1-9). Homeostatic, resident fibroblasts secrete common extracellular matrix proteins such as collagen I and III, less abundant

collagens IV-VI, and other matrix proteins such as fibronectin and elastin, all of which contribute to the structural integrity of the heart.[240] Cardiac fibroblasts also promote proper electrical conduction of the heart through expression of gap junctions and voltage gated signaling channels.[241,242]

Fibroblasts can be become activated by a wide variety of signals from within heart. The most common of these are pro-fibrotic cytokines such as TGFβ, IL-1, IL-4, IL-5, or IL-13.[194,243] Importantly, T-cell contact with fibroblasts can induce TGFβ expression and fibroblast activation.[220,244] Fibroblasts also respond to neuro-hormonal signals such as angiotensin II and sympathetic nervous activation and mechanical stressors through mechano-sensors or integrins.[238,245] The initial activation of fibroblasts is often characterized by increased cellular proliferation and increases in contractile or activation markers, including periostin and α-smooth muscle actin (αSMA). These cells can progress to a less proliferative myofibroblast state, the most canonical matrix secreting fibroblast subtype, which express many ECM proteins, periostin, and αSMA. Interestingly, there is some evidence of other cell types (endothelial cells, pericytes, or even immune cells) differentiating into myofibroblasts.[238,245,246] Myofibroblasts increase secretion of full length collagens and other enzymes necessary for collagen maturation. This includes Lysyl-oxidase enzymes to cross-link fibrillar collagen, proline hydroxylases, matrix metalloproteinases and then use the contractile function of αSMA for further collagen remodeling.[247] Myofibroblasts also increase production of many other disease associated ECM proteins, such as fibronectin, elastin, laminin, and more.[240,248] Recent studies have identified a more mature fibroblast state termed the “matrifibrocyte” in which collagens and αSMA have decreased, while increased osteogenic and cartilage markers increase (*Comp, Chad, Clip2*), contributing to long term scar maintenance (Figure 1-9).[246,248]

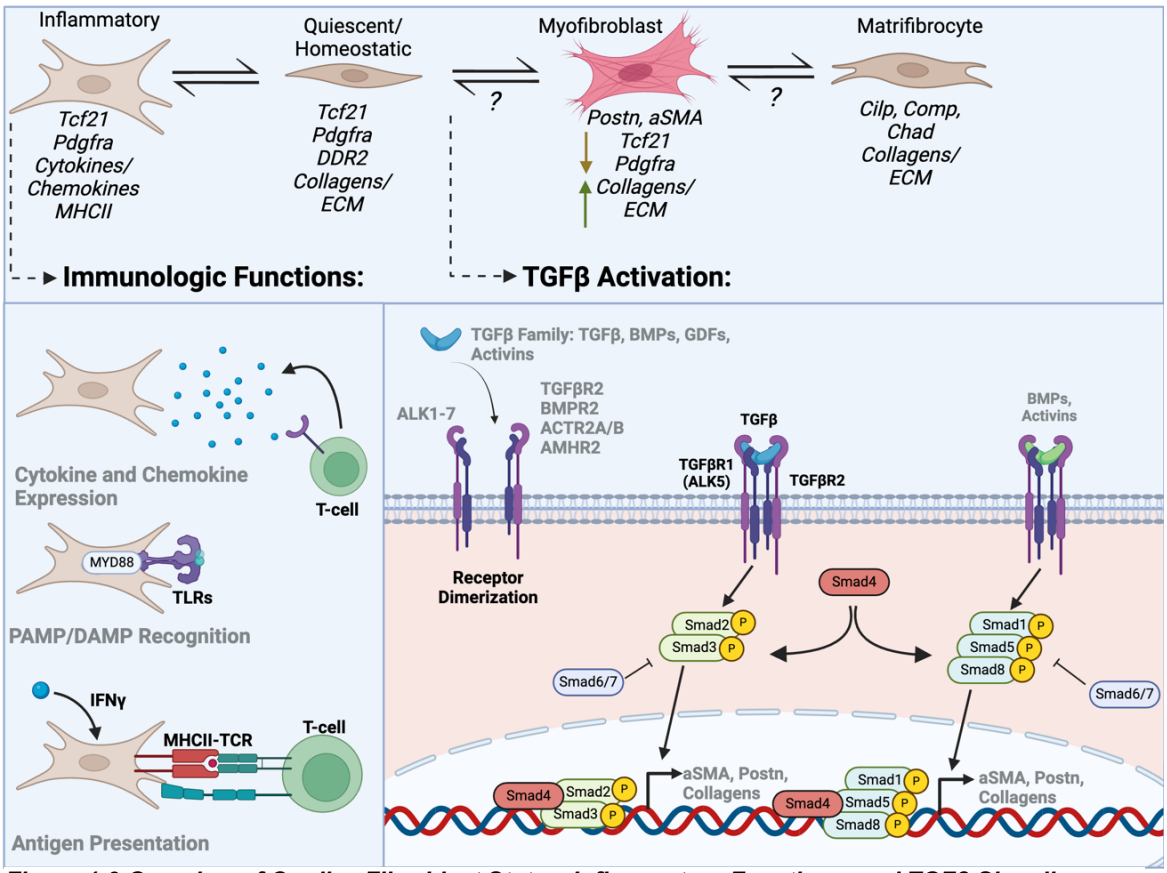


Figure 1-9 Overview of Cardiac Fibroblast States, Inflammatory Functions, and TGFβ Signaling
Fibroblast can change states between homeostatic, myofibroblast, matrifibrocyte, and inflammatory for specific functions, with commonly used markers listed for each state. Schematics of immunologic functions are shown on the left. TGFβ, the most common trigger for myofibroblast differentiation, induces specific signaling cascades shown on the right. Figure made with Biorender.

Cardiac fibroblasts play several other roles that are less defined by exact state. Both *in vitro* and *in vivo,* secreted factors from fibroblasts are able to stimulate angiogenesis of endothelial cells.[249,250] Additionally, fibroblasts contribute to the coordination of cardiac hypertrophy through cross-talk to cardiomyocytes by signaling through growth factors, TGFβ, Notch signaling, and others.[251,252] Importantly, cardiac fibroblasts have been increasingly shown to be immunologically active cells, which will be discussed in depth in the following section. A combination of *in vitro* approaches, lineage tracing, single cell sequencing, and trajectory modeling has uncovered a wide variety of fibroblast states and plasticity beyond what has been discussed thus far, making the exact definition of fibroblast subtypes complicated.[245,248,253]

1.3.6 TGFβ Signaling in Fibroblasts

One of the most potent triggers of myofibroblast activation is the cytokine TGFβ, secreted by a wide variety of stromal and immune cells, and readily recognized by cardiac fibroblasts (Figure 1-9). TGFβ has 3 isoforms and exists in a large superfamily of proteins including activins, growth factors, and bone-morphogenic proteins, all of which share both receptor subunits and downstream signaling cascades.[254,255] TGFβ is first expressed in a pro-complex with the protein LAP and other TGFβ binding proteins (LTPBs) on the surface of a cell, then must be cleaved enzymatically or released by signals such as integrin binding. Free TGFβ can then bind to TGFBR1/2, causing dimerization and phosphorylation of several SMAD proteins, the intracellular signaling partners of the TGFBR. In canonical TGFβ signaling, SMAD2 and SMAD3 become phosphorylated, associate with each other, then bind to the co-factor SMAD4, necessary for nuclear translocation and transcription factor activity. Other TGFβ family members activate a parallel pathway consisting of pSMAD1/5/8, which also uses the SMAD4 cofactor. Inhibitor SMADs 6/7 also exist, which can antagonize multiple points in the TGFβ signaling pathway.[254–256] TGFβ can activate several other pathways in fibroblasts, including ERK, PI3K, JAK-STAT, and p38 pathways,[254] the ladder of which has been shown to be a critical signaling hub in the development of cardiac fibrosis.[257,258] Overall, TGFβ induced fibrosis has been implicated in myocardial infarction, pressure overload by TAC, PE/ANGII, and even arrhythmogenic cardiomyopathy.[244,259–262] Further, direct inhibition of TGFβ or it's receptors has shown efficacy in animal models of pressure overload in reducing cardiac fibrosis.[263–265] Despite this, only one drug directly targeting TGFβ, pirfenidone, has been approved in patients with idiopathic pulmonary fibrosis.[266] Further analysis of the patients from these trials has shown potential minor alterations to cardiac parameters, although cardiac fibrosis was not explicitly measured.[267,268] Ongoing trials[269] and continued mechanistic work aim to translate

Pirfenidone among other anti-TGFβ therapies to prevent cardiac fibrosis in HF. In Chapter 3 of this thesis my data outline a new inflammatory mechanism in TGFβ signaling with a potential therapeutic target.

1.3.7 Cardiac Fibroblast Inflammatory Function

As cardiac fibrosis and inflammation are intertwined processes, cardiac fibroblasts have been shown to play a diverse set of immunologic roles (Figure 1-9). Most fibroblasts express varying PRRs including Toll-like receptors, the IL-1R, and MyD88 which make them immunologically active in response to DAMPs and PAMPs.[270,271] As such, cardiac fibroblasts can directly secrete pro-inflammatory cytokines including IL-1β, IL-6, IL-8, and more to propagate the cardiac immune response.[52,194,272,273] In fact, fibroblast inflammasome activation for IL-1β release has become a potential target for anti-inflammatory therapies in fibrosis.[274,275] Additionally, cardiac fibroblasts are able to secrete chemokines to recruit other immune cells to the heart, such as increases in CXCL9/10 expression to attract $CXCR3^{+}CD4^{+}$ T-cells to the heart in TAC.[163,272,273,276,277] Cardiac fibroblasts are even able to act as non-professional antigen presenting cells. In response to IFNγ, fibroblasts can express MHCII, process, and present antigens to $CD4^{+}$ T-cells resulting in their activation and proliferation. This phenomenon has been shown *in vitro*, *in vivo* using the TAC model, and in single cell transcriptomics data sets from human patients with HF.[231,278] My work in Chapter 3 and appendix 9.1 further outlines new inflammatory functions for cardiac fibroblasts.

1.4 Cancer Immunotherapy and Cardiotoxicities

1.4.1 Inflammation in Cancer

The tumor microenvironment contains a wide variety of immune cells in addition to tumor cells themselves, which play a critical role in modulating the progression of a tumor. Various immune cell types balance anti-tumor activity with anti-inflammatory properties, together

governing whether tumors are rejected or progress (Figure 1-10).[79,279] Cytotoxic $CD8^+$ T-cells are the main anti-tumor cell type,[154,279] and have been shown to be predictive of better prognosis in many malignancies.[280–283] $CD4^+$ T-cells have can also promote anti-tumor immunity through helping $CD8^+$ T-cells, direct killing (cytotoxic $CD4^+$ cells), or release of anti-tumor cytokines (IFNγ), however $CD4^+$ T-regs can significantly impair anti-tumor T-cell activity.[284,285] Classical dendritic cells and pro-inflammatory macrophages can aid in T-cell activation and presentation of tumor-associated antigens, however anti-inflammatory subsets of both cell types can impair T-cell anti-tumor activity.[286] NK cells are another cell type able to directly kill tumor cells, especially in the absence of functional T-cell immunity.[287] Interestingly, neutrophils can be polarized in the context of anti-tumor immunity. In some cases, neutrophils can contribute to tumor cell killing and antigen presentation[288,289], however neutrophils can also promote tumor progression and metastasis.[290,291] Finally, myeloid cells can differentiate into “Myeloid derived suppressor cells” (MDSCs), a diverse group of anti-inflammatory immune cells that prevent anti-tumor immunity.[292]

As many cell types play dual roles in promoting or preventing tumor growth, the tumor microenvironment itself can shift this balance to escape anti-tumor immunity. Tumor cells can secrete anti-inflammatory cytokines, recruit anti-inflammatory immune cells, and directly induce immune cell dysfunction.[79,279] Inflammatory and metabolic cues from the tumor microenvironment can cause T-cell exhaustion, a dysfunctional state for T-cells characterized by high immune checkpoint expression and low cytokine secretion and killing ability.[293,294] These same cues can also promote T-reg differentiation, MDSC differentiation, and anti-inflammatory macrophage phenotypes.[79,293] The most well-known of these is PD-L1 and its associated family members, which can directly induce immune cell dysfunction and death.[146] Further, tumors can secrete a variety of chemokines, which contribute to the ratio of anti-tumor or pro-tumor immune cells recruited.[66] In addition to directly inhibiting T-cells and preventing APC recruitment, tumors can down-regulate their own MHC-I or inhibit type I

interferon signaling to prevent appropriate antigen presentation.[295] Finally, tumors can even physically exclude immune cells from the tumor microenvironment by altering their ECM and vasculature, preventing effective anti-tumor immune cell recruitment.[79,295] Immunotherapy strategies in cancer aim to circumvent these mechanisms of anti-tumor escape, or enhance T-cell killing ability.[81] Some tumors are better at evading the immune system, such as subtypes of breast cancer, while others are not, such as melanoma, two examples of tumors used in this dissertation to study connections between T-cell anti-tumor and anti-cardiac functions.

1.4.2 Subtypes of Cancer and Immunologic Status

Based on the immune microenvironment as detailed above, tumors can be classified into "hot" tumors, or those that have high anti-tumor immune cell infiltration such as $CD8^+$ T-cells,

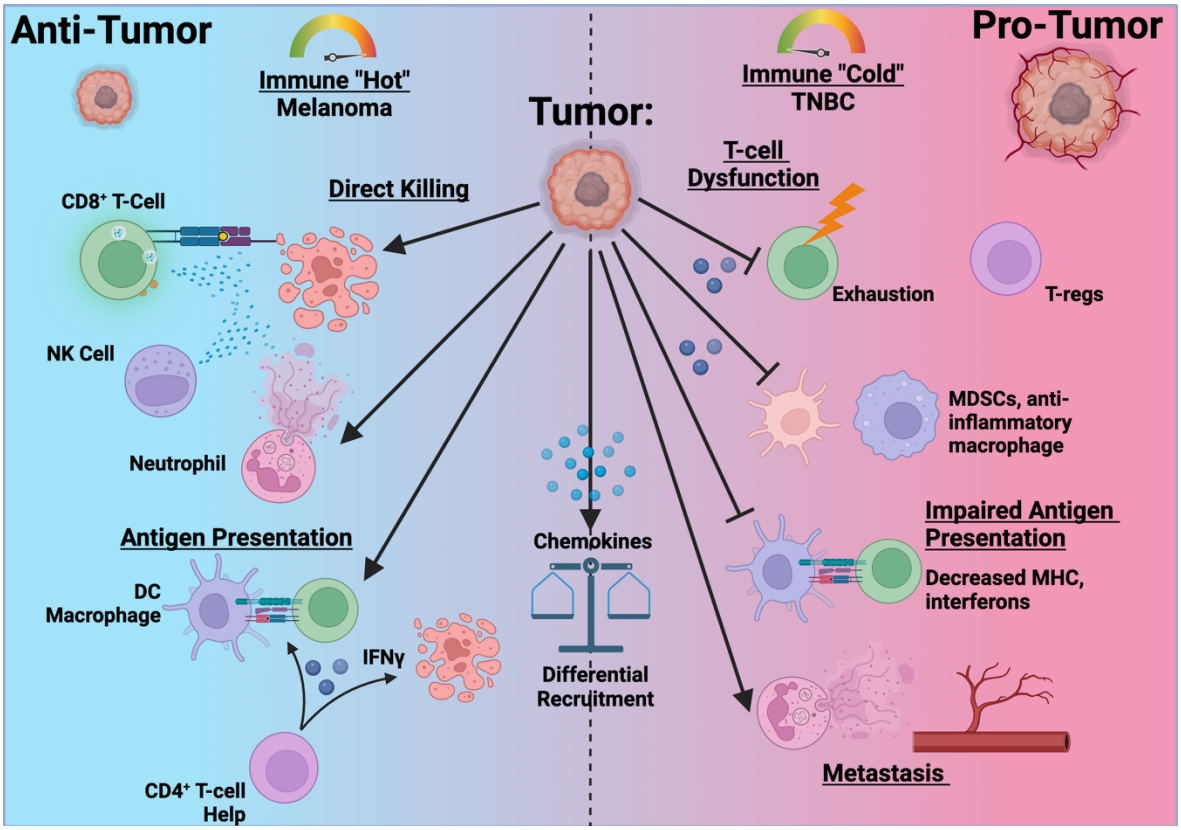


Figure 1-10 Inflammation and Immune Escape in Cancer
Overview of basic mechanisms of anti-tumor immunity and immune escape in cancer. NK = natural killer, DC = dendritic cell, TNBC = triple negative breast cancer, T-regs = regulatory T-cells, MHC = major histocompatibility complex. Figure made with Biorender.

NK cells, and professional APCs. Tumors can also be classified as “cold” tumors, which are either immune excluded (physically prevent $CD8^+$ T-cells from infiltrating the tumor) or immune deserted (lack $CD8^+$ T-cells in the tumor), and instead have higher MDSCs, T-regs, and anti-inflammatory macrophages (Figure 1-10).[296] Classifying tumors based on inflammatory profiles can have significant implications for the potential efficacy of immunotherapies, and significant effort has been put into transitioning tumors from “cold” to “hot”.[297] Traditionally, one example of a hot tumor is melanoma, a tumor of the pigment producing cells of the skin, which is used in Chapter 4 of this dissertation to study T-cell anti-tumor activity. Melanoma is easily surgically excised when it is localized to the skin, whereas once it metastasized it can be quite deadly.[298,299] Melanoma often has high T-cell infiltration and relatively lower MDSC/macrophage numbers, together being predictive of positive outcomes and therapeutic responses.[299–301] Indeed, melanoma was one of the first malignancies in which immune checkpoint inhibitors (ICIs) were shown to be effective at improving survival.[86,302]

In contrast, tumors such as breast tumors are more commonly considered “cold” tumors, although they can have quite variable levels of immune infiltration. In breast tumors that are triple negative – lacking estrogen receptor, progesterone receptor, and HER2 expression that limit chemotherapeutic options, T-cell infiltration can predict tumor progression.[303–305] Triple negative breast cancer (TNBC), the most aggressive subtype of breast cancer, can show the same spectrum of immune exclusion or desertion to immune infiltrated, however despite this clinical trials of ICIs have been less effective in these patients.[306,307] In appendix 9.2, I use TNBC in mice to compare the T-cell response against the tumor versus the heart in the context of chemotherapy and ICI induced cardiotoxicity. This also models newer efforts in patients, which attempt to utilize existing chemotherapy regimens that directly induce breast tumor cell death and promote the transition to a “hot tumor” prior to ICI

use.[304,308] However, as previously discussed, cancer induces a systemic inflammatory response and tumoral and cardiac inflammation are quite intertwined. As such, many treatment strategies, both chemotherapeutic and immunologic, can have negative consequences on the heart, leading to a goal of this dissertation which aims to interrogate the relationship between the two.[15,17,36]

1.4.3 Anthracycline Treatment and Cardiotoxicity

Anthracycline chemotherapies, including the drug Doxorubicin, are the most commonly prescribed class of chemotherapeutic drug and remain in first line regimens for both solid and hematologic malignancies such as TNBC. Doxorubicin acts as a topoisomerase inhibitor, intercalates into DNA, and causes oxidative stress, together inhibiting DNA replication to kill rapidly dividing tumor cells.[309,310] However, anthracyclines have a dose-dependent cardiotoxic effect, with an overall incidence of about 9% for any cardiac side effects and up to 30-40% in patients receiving the maximum allowable doses.[309,311,312] Patients can present with acute heart failure, myopericarditis, and arrhythmias, or can develop chronic LV dysfunction over time. [309,311,312] Histopathologically, cardiac samples show signs of cardiomyocyte atrophy, cardiomyocyte cell death, and fibrosis.[313] Several clinical trials have attempted to repurpose existing HF treatments such as ACE inhibitors, angiotensin receptor inhibitors, and beta blockers, in anthracycline treated patients. These trials have shown some efficacy in preventing LV dysfunction in some patients, however they are not widely effective in all patients across different trials, suggesting differing mechanisms driving cardiotoxicity in these patients.[314–317] Dexrazoxane is thus far the only approved drug for anthracycline cardiotoxicity, and while it has shown efficacy in cardio-protection, concerns including altering the effect of Doxorubicin or secondary malignancy development limit its' use.[318,319] Further, while classical biomarkers for HF such as pro-BNP

and Troponins are often elevated in anthracycline treated patients, these do not correlate with cardiotoxicity, highlighting the need for more specific biomarkers.[320]

Immunologic markers represent one potential avenue (Figure 1-11). Patients treated with anthracyclines have shown changes in circulating cytokines and chemokines such as CCL23, MIF, IL-10, sICAM-1, and sIL6r,[321–323] as well as altered TLR expression on circulating immune cells.[324] However, these studies have been small and observational, with no consistent inflammatory mechanism identified in patients with anthracycline cardiotoxicity. Preclinical animal models have revealed additional information about the cardiac inflammatory response induced by Doxorubicin. Rodents treated with Doxorubicin consistently show elevated cardiac IL-1β, IL-6, TNFα, IL-17, and IL-18.[325–328] Several toll-like receptors have been shown to play a functional role in this inflammation and subsequent cardiotoxicity, responding to DAMPs from cardiac cell death.[324,328–330] Doxorubicin has also been shown to activate the cGAS-STING pathway in several cardiac cell types, although the downstream inflammatory consequences have not yet been studied in depth.[133,331,332] Other studies have shown evidence of cardiac monocyte and macrophage infiltration,[325,333,334] splenic macrophage contraction,[335] and a neutrophil contribution to the cardiotoxic effects of Doxorubicin.[336,337] While these studies provide evidence of acute cardiac inflammation, thus far only one study has examined the adaptive immune response, outlining a role for B-cell antibody signaling and deposition in cardiac damage.[338] As no study has looked at the T-cell response in preclinical models of Doxorubicin cardiotoxicity, despite significant study of T-cells in other etiologies of HF, in this dissertation in Chapter 6 and 7, I characterize a mechanistic role for T-cells in mediating anthracycline cardiotoxicity.

1.4.4 Adoptive Cell Therapies

One of the first immunotherapies used in cancer treatment is adoptive cell therapy (ACT) most commonly with $CD8^+$ T-cells (Figure 1-11). In ACT, $CD8^+$ T-cells are isolated from

circulation or from tumor samples of cancer patients, then are expanded *ex vivo* in the presence of pro-survival and proliferative cytokines (IL-2, IL-7, IL-15). Patients usually undergo ablation of their existing immune cells, then the expanded T-cells are reinfused back into patients. Using this strategy, higher numbers of the patient's own tumor-specific T-cells can be utilized therapeutically.[82,339,340] ACT was first utilized in the treatment of melanoma, showing moderate success in tumor regression in a subset of patients.[341,342] However, several challenges limit the efficacy of ACT. First, bulk T-cells are used, which limits their antigen specificity, and does not take into account antigenic evolution of tumors. Additionally, generating high T-cell numbers is difficult, and once infused, T-cells often become exhausted by the tumor microenvironment and are unable to persist for long enough for effective tumor killing. Finally, ACT efficacy is limited in many solid tumors such as breast cancer, as they are still unable to infiltrate tumors.[339,343]

Several strategies have evolved to circumvent these challenges. Isolated T-cells have been transduced with exogenous TCR constructs designed for tumor antigens, however finding tumor-specific antigens remains difficult.[82,339] T-cells have also been modified to express chemokine receptors that allow for enhanced tumor infiltration, [166]or modified to delete immune checkpoint molecules such as PD-1.[344] Perhaps the most successful modification to ACT is chimeric antigen receptor T-cell therapy (CAR-T), in which an antigen-specific single chain variable fragment is fused to the intracellular domain of the TCR and co-stimulatory signaling receptors, allowing for T-cell activation in the absence of MHC or co-stimulation.[339,345] Multiple CAR-T therapies have been approved for B-cell lymphomas and multiple myeloma, but the same challenges remain for solid tumors.[83,345] Interestingly, ACT and CAR-T have relatively low rates of cardiovascular side effects. Several studies have reported arrythmias and LV dysfunction, all with an incidences ranging from 1-10%.[346–348] However, ACT and CAR-T therapies can have widespread systemic inflammatory side effects, such as dermatitis, colitis, uveitis, and neurotoxicity, due to systemic cytokine

release or off-target antigen effects.[349–351] Chapter 4 of this dissertation shows a novel example of modifying T-cells to improve adoptive cell therapies based on data from Chapter 2 in the context of cardiac inflammation.

1.4.5 Immune checkpoint inhibitors

Inhibitors of immune checkpoints (ICIs) on T-cells have revolutionized immunotherapy treatment in cancer. Thus far, ICIs have been approved consisting of antibodies targeting the molecules PD-1, PD-L1, CTLA-4, and LAG3, which prevents checkpoint induced T-cell exhaustion, overall increases T-cell activation, and improves anti-tumor T-cell activity.[146,352] Anti-CTLA-4 and anti-PD1 therapies were first approved in melanoma, showing significant efficacy in prolonging progression free survival as single agents,[86,353] and with greater efficacy seen more recently using combination ICI therapies.[302] Since then, ICIs have been approved for the treatment of a majority of solid and hematologic cancers, with up to 50% of cancer patients eligible for some form of ICI therapy.[354,355] However, systemic T-cell activation can result in a wide variety of immune related adverse events (IRAEs), which have been reported in most major organ systems (Figure 1-11). While not all are severe, the incidence of any IRAEs can reach up to 80-90% in various clinical trials depending on the specific ICI and malignancy studied.[356,357] These IRAEs include several types of cardiovascular disease, including myocarditis, pericarditis, arrythmias, and atherosclerosis, and are more common with combination ICI treatment.[358,359] ICI myocarditis, while rare, is the most lethal of the cardiovascular IRAEs, and is mediated by a massive influx of $CD8^+$ T-cells into the heart.[360] Recent studies have given mechanistic insight into the pathophysiology of the disease. Animal models and patients samples show expansion of antigen specific $CD8^+$ T-cell clones, which are often specific for cardiac α-myosin.[208,361] These T-cells exhibit cross-talk with pathogenic cardiac macrophages that express the chemokines CXCL9, CXCL10 in response to T-cell derived IFNγ, recruiting $CXCR3^+CD8^+$ T-

cells to the heart in feed forward loop. However, it is still unknown why certain patients develop ICI myocarditis and others do not, making further study of the exact mechanisms governing T-cell activation and cardiac infiltration necessary for therapeutic and preventative strategies.

1.5 Summary and Hypothesis

Inflammation is a central mechanistic connection in the initiation, progression, and treatment of cardiovascular disease and cancer, the top two causes of death across the world. The work presented in this dissertation provides continued study of both connections and distinctions in the inflammatory mechanisms in both diseases that will lead to improvements in the management of patients with cancer and heart failure. In this

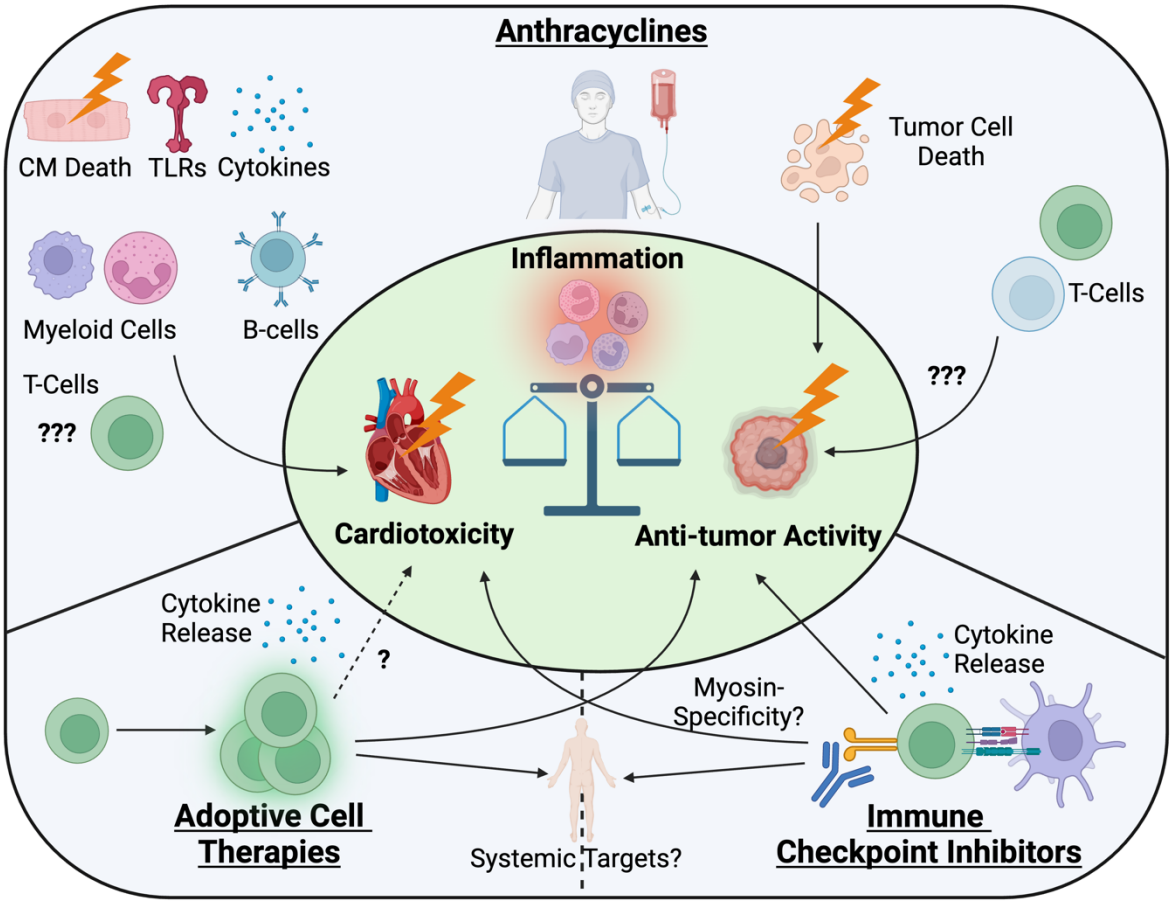


Figure 1-11 Cancer Treatment Balances Beneficial Anti-Tumor Effects and Cardiac Toxicities Through Inflammation
Selected cancer therapies and immunotherapies with associated mechanisms for anti-tumor efficacy and cardiac toxicities. These mechanisms often are a balance between positive effects on tumor regression with negative toxicities, with inflammation driving many of these processes. Figure made with Biorender.

dissertation, I hypothesized that novel mechanisms that regulate T-cell activation are conserved across models of cardiac injury and can be harnessed to improve anti-tumor immunotherapy. In depth mechanistic study of these signaling pathways including TLR-MyD88 signaling in T-cells will uncover potential targets to modulate T-cell mediated inflammation in the heart and tumor, and prevent maladaptive cardiac remodeling such as cardiac fibrosis. Further, I hypothesized that the function of TLR-MyD88 signaling is specific to each cell type, and that mechanistic studies comparing the function of MyD88 in innate, adaptive, and non-immune cells will provide novel insight into previous difficulties in modulating cardiac inflammation and uncover new, and cell-specific therapeutic targets. I also hypothesized that T-cell mediated inflammation contributes to chemotherapeutic cardiac injury in anthracycline treatment, which has yet to be studied, and I aimed to characterize a mechanistic role for T-cells in this disease. This included what T-cell subsets contribute to disease, how they are recruited to the heart, and whether previously characterized regulatory mechanisms for T-cell activation are relevant and targetable in anthracycline cardiotoxicity. Together this dissertation will increase our understanding of T-cell activation, T-cell effector function, cardiac fibrosis, and anti-tumor immunity across different contexts of cardiac injury or cancer, and will guide patient immunotherapeutic strategies moving forward.

Chapter 2 T-cell MyD88 is Novel Regulator of Cardiac Fibrosis Through Modulation of T-cell Activation

---

[1]Bayer, A.L., Smolgovsky, S., Ngwenyama, N., Hernández-Martínez, A., Kaur, K., Sulka, K., Amrute, J., Aronovitz, M., Lavine, K., Sharma, S., Alcaide, P. T-cell MyD88 is a Novel Regulator of Cardiac Fibrosis Through Modulation of T-cell Activation. *Circulation Research.* 133:5(412-419) 2023.

Reprinted here with permission of publisher.

2.1 Introduction

Cardiac inflammation and cardiac fibrosis are two intimately associated hallmarks of HF, however thus far anti-inflammatory therapies have shown limited success in clinical trials.[55,56,202] This suggests a more in depth study of specific inflammatory mechanisms is needed to improve anti-inflammatory therapies in HF. As cardiac damage ensues, the constant release of damage associated molecular patterns (DAMPs) activates resident myeloid cells to present antigen to T-cells in a continuous progression of worsening inflammation.[90,102] DAMPs, also known as “alarmins,” are increased in the heart during HF.[362,363] Most DAMP receptors, such as toll-like receptors (TLRs) and the IL-1 family of receptors, converge onto the adaptor protein Myeloid differentiation primary response protein 88 (MyD88), to initiate an innate immune response.[98,99] The persistent inflammation initiated through DAMP-myeloid-MyD88 signaling during HF suggests that intrinsic mechanisms must exist to resolve or mitigate a continuous subsequent T-cell immune response during cardiac maladaptive adaptations to stress.

We previously showed that antigen presentation by myeloid cells results in a type 1 helper T-cell (Th1 cells) response in mice subjected to transverse aortic constriction (TAC), characterized by cardiac Th1 infiltration and adhesion to cardiac fibroblasts (CFBs) through vascular adhesion molecule 1 (VCAM-1).[73,227,229] Further, while T-cell deficient mice, including *Tcra*$^{-/-}$ *or MhcII*$^{-/-}$, are protected from cardiac fibrosis in response to TAC, adoptive transfer of Th1 cells into these mice partially restored cardiac fibrosis.[73,229] This supports that effector T-cells exhibit sustained activation in the cardiac inflammatory environment, directly responding to stimuli induced by TAC. One of such stimuli is the presentation of ROS-induced cardiac neoantigen by antigen presenting cells (APCs), which induces T-cell activation and clonal expansion.[226,231] While we know that this process is potentiated by DAMP-MyD88 signaling in APCs,[99] whether direct effects of DAMPs on T-cells contribute to this response, as well as the T-cell intrinsic mechanisms necessary to prevent their

overactivation have yet to be characterized. Thus far, only one study has shown MyD88 to be partially protective in TAC, using global cardiac MyD88 deletion with Adeno-Associated Virus (AAV).[364] While DAMP receptors and MyD88 are predominantly expressed in innate immune cells and provide pro-inflammatory signaling, adaptive immune cells including T-cells express them as well,[105,107,365] but their function in cardiac inflammation is unknown.

We hypothesized that TCR activated T-cell sensing of DAMPs will activate MyD88 thus contributing to T-cell activation and cardiac fibrosis in response to TAC. To our surprise, this was not the case, and instead we found that MyD88 deletion in T-cells resulted in enhanced T-cell effector function and worsened fibrosis, revealing a novel T-cell intrinsic mechanism that limits TCR overactivation and tunes down inflammation in the onset of experimental HF.

2.2 Methods

2.2.1 Animals

All animal studies were approved by the Tufts University Institutional Animal Care and Use Committee. C57BL/6, CD45.1[366], and $Tcra^{-/-}$ mice[367] were bred and maintained under pathogen free conditions. $Myd88^{-/-}$ mice[368] were donated by Dr. Linden Hu (Tufts University, Boston MA), and maintained under specific pathogen free conditions as heterozygotes by crossing with C57BL/6J mice. $Myd88^{fl/fl}$ $CD4^{Cre}$ mice were generated by crossing $Myd88^{fl/fl}$ mice[369] with constitutive $CD4^{Cre}$ expressing mice[370] (Jackson Laboratory). MyD88 excision was determined by PCR (see Appendix 9.10 for primer sequences).

2.2.2 *In Vivo* Echocardiography:

Transthoracic echocardiography was 4 or 10 weeks post surgery, as previously described.[204] Mice were sedated using isoflurane on a heated stage in supine position. Heart rates and respiratory rates were continuously monitored via stage electrodes. Depilatory cream (Nair) was applied to the chest to remove fur, and ultrasonic gel was

applied to a 22-55 MHz echocardiography transducer (MS550D Vevo 2100, Fujifilm VisualSonics) to obtain parasternal short axis views of the left ventricle in M-mode with a target heart rate of 400-500 bpm. Cardiac parameters and heart rate were measured by averaging the values from 5 cardiac cycles. All analyses were performed blindly using Vevo 2100 software (see below)

2.2.3 Transverse Aortic Constriction Model:

Pressure overload was induced by minimally invasive TAC surgery to constrict the transverse aorta of mice as previously described.[226] Sham operated mice underwent the same operation without aortic constriction. 8-10 week old male *Tcrα*$^{-/-}$ mice underwent 25G TAC (for comparability to previous adoptive transfer studies[229,371]), then 10 million Th1 cells were injected intraperitoneally 2 days, and 2 weeks after surgery. 8-10 week old male and female *Myd88*$^{fl/fl}$*CD4*^{Cre} mice using Cre^{+} and Cre^{-} littermates underwent 27G TAC (most commonly performed by us and others).[372] Mice were euthanized 4 weeks after surgery and after visual confirmation of asystole tissues were harvested for analysis, or allowed to progress for survival studies up to 12 weeks. Exclusion criteria included WT TAC mice that exhibited no decrease in fractional shortening or LV hypertrophy or inconclusive genotyping. Randomization for each group was performed by a random number generator (https://www.calculator.net/random-number-generator.html), and all analysis were done blinded using an ID number assigned by a third party. Sample sizes are based on power calculations for the expected decrease in fractional shortening and increase in T-cell infiltration (http://powerandsamplesize.com/Calculators/Compare-2-Means/2-Sample-Equality), showing a minimum of 6 mice per group is needed to detect statistically significant changes with a power of 90%.

2.2.4 Generation and Culture of Th1 cells:

Spleens were excised and crushed through a 40 μM cell strainer, the strainer was rinsed with PBS + 0.5% BSA + 2 mM EDTA, pelleted at 300g, then red blood cell lysis was performed according to manufacturer's instructions (Biolegend 4210301). Naïve $CD4^+$ T-cells were isolated from the splenic cell suspension by positive selection using magnetic beads (Miltenyi 130-117-043). Cells were plated at 2 million cells / mL and differentiated in the presence of anti-CD3 (2.5 μg/mL, Biolegend 100253), anti-CD28 (1 μg/mL, Biolegend 102102), IL-12 (10 ng/mL, Peprotech 210-12), IL-2 (25U/mL, Miltenyi, 130-120-662) and, anti-IL4 (50 ng/mL, Biolegend 504102) for 3 days, expanded for 24 hours in IL-2 alone, then harvested for experiments. T-cells were cultured at 37°C in RPMI medium (Gibco, 11875-093) containing 10% fetal bovine serum (FBS – Atlanta Biologicals S11150), Glutamax (Gibco A12860-01), $NaHCO_3$ (Gibco 25080-094), Penicillin/Streptomycin (Gibco 15140122), 60μM β-mercaptoethanol (Sigma 444203), Sodium pyruvate (Gibco 11360-070). Where indicated T-cells were treated with 1 μM Myd88 inhibitor peptide or scramble peptide (NovusBio NBP2-29328) for 24 hours during activation. Purity and gating strategy for all *in vitro* T-cell use is shown in Figure 2-4.

2.2.5 Histologic Analysis and Immunohistochemistry:

LV samples from hearts were fixed in 10% formalin, embedded in paraffin, and cut in 6 μM sections. Slides were deparaffinized using xylenes (Sigma 534056) then hydrated using a decreasing ethanol gradient. Fibrosis was stained in 0.1% Direct Red 80 (Sigma 365548) in saturated picric acid (Sigma P6744) for 1 hour, after 1 min. hematoxylin counter stain (Sigma GHS2128). Slides were washed with 0.5% acetic acid twice before dehydration and mounting. Immunohistochemistry was performed in frozen LV sections: samples were fixed in ice cold acetone (Sigma 179124), blocked for 10 minutes each

with: 10% normal goat serum (Abcam 7481), biotin/avidin blocking kit (Vector labs SP-2001), and with 1% hydrogen peroxide (H1009). Samples were stained with primary antibody against CD4 (Biolegend 100402) for 1 hour (1:200 dilution) followed by incubation with goat anti-rat biotinylated secondary antibody (1:300 dilution, Jackson Immunoresearch 112-065-062). Sections were incubated with Streptavidin HRP (DAKO, K0675) and visualized using AEC Substrate (Sigma A5754), then nuclear counterstained with hematoxylin, and mounted using aqueous fluoromount G (Southern Biotech 0100-01. $CD4^+$ cells were counted manually.

2.2.6 Bulk RNA-Sequencing:

Cell lysis and RNA isolation was performed using an RNEasy kit according to manufacturer's instructions (Qiagen 74004). RNA samples that passed quality checks were used as input to prepare RNA-seq library using Illumina TruSeq stranded mRNA kit per manufacturer instruction. Libraries were sequenced on an Illumina HiSeq 2500 sequencer (Illumina) with a 75 base pair single-end reads format. Raw data in FASTQ format were processed for quality control using FastQC (https://www.bioinformatics.babraham.ac.uk/projects/fastqc/) then mapped to the mouse genome using STAR (http://code.google.com/p/rna-star/), and quantified by featureCounts (http://subread.sourceforge.net/). Using QluCore software, a heat map of differentially expressed genes using hierarchical clustering and a cutoff of $p<0.05$ and log(FC) of >1 for significance. Gene set enrichment analysis was performed against Mouse MSigDB collections (https://www.gsea-msigdb.org/gsea/msigdb/mouse/collections.jsp) using $p<0.05$ for significance.

2.2.7 Analysis of Single-Cell RNA Sequencing Data:

Raw data were downloaded from GEO: GSE122930. 1 and 4-week sham and TAC datasets, which include two replicates, were used for scRNAseq analysis. Well

established workflows based on the Seurat package were utilized for analysis. Briefly, datasets were downloaded, and Seurat objects were merged using the merge function, normalization and dimensional reduction were conducted with the scTransform v2 regularization function, and analyzed using basic Seurat (Version 4) functions.[373] T cells were identified based on *Thy1, Cd3e, Cd4, and Cd8a* expression and created a subset of T cells for analysis using the subset function for downstream analysis. *Cd4, CD8a*, and *Myd88* expression data were visualized using the FeaturePlot function in Seurat.

2.2.8 Analysis of CITE-seq Data:

T-cells were selected from a global object consisting of non-failing donors compared to heart failure of all causes.[374] The T-cells were represented in a UMAP embedding representation using weighted nearest neighbor clustering utilizing RNA and protein information. Differential RNA and protein expression were independently used to identify phenotypically distinct T-cell states within the major CD4, CD8, and NK cell groups. For differential expression analysis FindAllMarkers function from Seurat was used and a Wilcoxon Rank Sum test with a log2FC cut-off of 0.25 and a min.pct cut-off of 0.1 was used. Genes with a log2FC > 0.58 and adjusted p-value < 0.05 were used for annotating cell states.

2.2.9 Immunoblotting:

Cells were lysed in RIPA buffer (150 mM NaCl, 50 mM Tris pH 7.4, 1% NP-40, 0.1% SDS, 5 mM EDTA, 0.1% sodium deoxhycholate, 1 mM DTT) supplemented with protease andphosphatase inhibitors (Roche 4906845001, 4693159001), then cleared by centrifugation at 4°C at 13,000 g. Protein concentrations were determined using DC protein assay (BioRad 5000112) and equal concentrations of protein were subjected to SDS-PAGE in 10% resolving gels unless otherwise indicated, then transferred to PVDF membranes, followed by blocking with Tris buffered saline + 0.1% Tween20 containing

5% non-fat milk or bovine serum albumin (BSA) for 1 hour at room temperature. Immunoblotting was performed overnight at 4°C using antibodies diluted 1:1000 in 5% non-fat milk or BSA. Antibody sources: IL-1β (CST 12242), IL-33 (R&D AF3626), HMGB1 (Abcam 79823), TRIF (NovusBio NB120-13810SS), GAPDH (CST 2118), MyD88 (R&D AF3109), pERK (CST 9101), ERK (CST 9102), β-actin (Sigma A5441), pP38 (CST 4511), P38 (CST 9212), pP65 (CST 3033), P65 (CST 4764), pAKT (CST 4060), AKT (CST 4691), α-tubulin (CST 3873), α-smooth muscle actin (Sigma A2547), pZap70 (CST 2717), Zap70 (CST 3165), collagen 1 (Invitrogen PA529569) or CXCR3 (Bios 2209R). Blots were then incubated with the appropriate HRP-peroxidase conjugated secondary antibody (1:2000, Rabbit CST 7074, Mouse CST 7076, Goat ThermoFisher A15999) at room temperature for 1 hour, then developed using Pierce ECL (ThermoFisher 32106) and imaged using a ChemiDoc XRS+ System (Biorad). Band intensity was quantified using Image-J.

2.2.10 RT-qPCR:

Cell lysis and RNA isolation was performed using an RNEasy kit according to manufacturer's instructions (Qiagen 74004). For cardiac RNA isolation, LV samples were crushed in Trizol (Qiagen 79306), RNA was chloroform extracted and separated by centrifugation, then the aqueous phase was applied to RNAEasy columns. cDNA synthesis was performed using High-Capacity cDNA Reverse Transcription Kit (ThermoFisher 4368814), and qPCR was performed using SYBR Green (ThermoFisher A25741) on a QuantStudio 6 Flex Real-Time PCR Machine (ThermoFisher), then analyzed for fold change using ΔΔCt method. See Appendix 9.10 for primer sequences and for amplification conditions.

2.2.11 Flow Cytometry:

Cell suspensions from culture or lymphoid organs were stained using the following antibodies from Biolegend: APC-Cy7 or FITC CD4 (Biolegend 100414, 100406), FITC CD8 (Biolegend 100705), APC IFNγ(Biolegend 505810), PE IL-17 (Biolegend 506904), PerCP Tbx21 (Biolegend 644806), APC-Cy7 TCRβ (Biolegend 109220), BV421 or APC CD45.2 (Biolegend 109832, 109814), PE CD45.1 (Biolegend 110707), APC CD11a (Biolegend 101119), FITC CD49d (Biolegend 103606) PE TLR4 (Biolegend 145404) APC IL-1r (Biolegend 113509) PE-Cy7 IL-33r (Biolegend 145316), APC CD44 (Biolegend 103012), PE CD62L (Biolegend 104408), BV421 CD25 (Biolegend 102043), FITC CD69 (Biolegend 104506), APC CXCR3 (Biolegend 126512), APC MHCII (Biolegend 107613) APC-Cy7 CD11b (Biolegend 101225), PE CD11c (Biolegend 117307), BV421 Ly6G (Biolegend 127627), FITC CCR2 (Biolegend 150607). Other antibodies included APC Mefsk4 (Miltenyi 130-120-166) and PE Foxp3 (Invitrogen 14-5773-82). Samples were surface stained by incubation with the relevant antibodies diluted 1:50 in phosphate buffered saline (PBS) + 2% FBS for 20 minutes at 4°C. When intracellular cytokine staining was performed, samples were incubated for 4 hours at 37C in complete T-cell media (see above) including 50 ng/mL Phorbol Myristate Acetate (PMA, Sigma Aldrich P8139), 0.1% Ionomycin (Sigma 13909), 0.1% Brefeldin A (Biolegend 420601), and Monensin (Biolegend 420701), followed by surface staining as described. Samples were fixed for 15 minutes at RT with fixation buffer (Biolegend, 420801), then permeabilization by two washes with 1X Perm/Wash buffer (Biolegend, 421002, then stained intracellularly with the appropriate antibodies diluted 1:50 in PBS + 2% FBS for 20 minutes at 4°C. To detect Tbx21 or Foxp3, samples were surface stained as described, fixed using 1X FOXP3 Fix/Perm solution (Biolegend, 421401) for 20 minutes at RT, permeabilized for 15 minutes using 1X FOXP3 Perm solution (Biolegend,

421402), then stained intracellular for 20 minutes with the appropriate antibodies diluted 1:50 in PBS + 2% FBS for 20 minutes at 4°C. Data was acquired an a BD LSRII (BD Biosciences) and analyzed using FlowJo software.

2.2.12 Isolation of Cardiac Fibroblasts and Co-culture:

Adult mice (7-12 week old) were anesthetized, then hearts were excised, perfused with PBS, minced, and digested using 5 mg/mL Liberase TL (Roche, 05401020001) and TrypLE Express (Gibco, 12605036) for 30 minutes with agitation. Digested tissue was pelleted at 300g for 10 minutes, then resuspended in fibroblast growth media – DMEM (Gibco 11995-065) + 10% FBS, Penicillin/Streptomycin (ThermoFisher 15140122), Amphotericin B (Sigma A2411), insulin-transferrin-selenium (Sigma I3146, and plated on 0.1% gelatin coated plates for 2 hours at 37°C. After this time, non-adherent cells were removed and fresh media was added. Cells were used through passage 3. For co-culture experiments, fibroblasts were plated on 0.1% gelatin coated coverslips in 12 well plates at 200,000 cells / well. Once adherent, cells were serum starved in media containing 1% FBS overnight, then Th1 cells were added at 100,000 cells / well unless otherwise indicated by ratio, and cultured overnight, then washed with PBS to remove non-adherent T-cells. When indicated, Th1 cells were pretreated with 20 μg/mL anti-CD49d (Biolegend clones 9C10 and RI-2) or with 20. Where indicated 5 μg/mL anti-TGFβ (Thermofisher MA5-23795) was added to CFB prior to Th1 addition. Additionally when indicated, cells were washed with 5 mM EDTA to remove adherent T-cells.

2.2.13 T-cell Adhesion and Migration Studies Under Shear Flow Conditions:

T-cell adhesion was determined under defined laminar flow conditions in a parallel plate apparatus using video microscopy (20x objective) and Nikon Elements NIS software as previously described.[375] In brief, Th1 cells were generated as described above, treated with PMA (50 ng/mL, 5 min), and perfused at a concentration of 1 x 10^6 cells / mL at an

estimated shear stress of 1 dyne/cm^2 over immobilized ICAM-1 or VCAM-1 (20µg/mL, Biolegend 553006, 553706). Where indicated, Th1 cells were pretreated with 20 µg/mL anti-CD49d (Both Biolegend 103701, 103629) or anti-CD11a (Biolegend 101101) Adherent cells were quantified in 4-5 fields of view. For Transendothelial migration experiments, mouse heart endothelial cells (MHECs) were generated as described previously[375] and cultured on coverslips. MHECs were treated with 125 ng/mL TNFα for 4 hours prior to perfusion of 1 million Th1 cells at an estimated shear stress of 1 dyne/cm^2 with temperature controlled to 37°C. TEM was observed during 10 minutes.

2.2.14 T-cell Chemotaxis:

1 million Th1 cells were loaded on an 8µM transwell insert in complete T-cell media across either media alone of media supplemented with 2 µg/mL CXCL-10 (Peprotech 250-16). After 4 hours, the number of T-cells migrated across the transwell were counted manually.

2.2.15 ELISA:

Th1 cells were cultured in fresh T-cell media at a concentration of 2 million cells/mL for 24 hours, then pelleted at 13,000 rpm for 5', then culture supernatant was snap frozen. Supernatant was run undiluted (IL-2) or diluted 1:5 (TNFα), or 1:100 (IFNγ) Duoset ELISA kits according to manufacturer's instructions (R&D DY410, DY402, DY485).

2.2.16 T-cell Viability Assays:

Th1 cells were plated on 384 well black optical bottom plates (Nunc 142761) coated with 10 µg/mL αCD43 (Invitrogen, 14-0431-85) at 30,000 cells / well in complete T-cell media or media containing 1% FBS, including 10 µg/mL propidium iodide (Biolegend 421301). The Lionheart imager was used to maintain temperature at 37°C, 5% CO2, and humidity during the experiment. Kinetic microscopy was performed by the Lionheart imager to quantify propidium iodide uptake every 90 minutes over 72 hours. Wells containing 0.1%

Triton X-100 lysed cells were used as a positive control, with propidium iodide uptake baseline subtracted and normalized as % positive control.

2.2.17 T-cell Proliferation:

Naïve $CD4^+$ cells ($CD62L^{hi}CD44^{lo}$) were isolated using a FACS Aria (BD Biosciences). 1.5 million naïve $CD4^+$ cells were stained with 5 μM carboxyfluorescein diacetate succinimidyl ester (CFSE) for 15 minutes at 37°C, then cultured in Th1 polarizing conditions as described above. For proliferation of Th1 cells, 1.5 million pre-activated Th1 cells were stained with 5 μM CFSE for 15 minutes at 37C, then resuspended in T-cell media with fresh IL-2 (25 U/mL). Samples were analyzed by flow cytometry at the indicated time points in culture.

2.2.18 T-cell Activation Assay:

T-cells were generated as described above, and plated onto coverslips coated with anti-CD3 in the polarization conditions described above. At the indicated time points, or after being removed from stimulation for 24 hours, coverslips were removed from media, rinsed with cold PBS, then fixed for 15 minutes in 4% PFA. Immunofluorescence was performed as described in subsequent methods.

2.2.19 Immunofluorescence:

Coverslips or tissues were washed 2 x 10 min. with PBS, then fixed with 4% PFA for 15 minutes. Samples were washed with PBS, then incubated with PBS + 10% normal goat serum and/or 10% donkey serum (depending on species of secondary antibody), and 0.1% triton-X for intracellular staining for 1 hour at RT. Samples were incubated with the following primary antibodies where indicated: αCD4-AF594 (Biolegend 100446), α-alpha smooth muscle actin (αSMA, Sigma A2547), MyD88 (R&D AF3109), TCRβ (Biolegend 109220), CD31 (Biolegend 102520), PDGFrα (R&D AF1062), or Ki67 (Abcam Ab15580) at 1:100 in blocking buffer overnight at 4°C. Samples were washed with PBS then

incubated with the appropriate secondary antibody (Thermo A32766, Thermo A11055, Thermo A21432, Thermo A78966, CST 4413) at 1:200 in blocking buffer, then mounted in Vectashield with DAPI (Southern Biotech, 0100-20). For WGA staining, tissues were fixed for 15 minutes in 4% PFA, followed by blocking with PBS + 10% normal goat serum for 1 hour at RT. Tissues were stained with 5µg/mL FITC conjugated WGA (Sigma L4895) in PBS + 10% normal goat serum for 2 hours and mounted in Vectashield with DAPI. For TUNEL staining tissues were deparaffinized as described previously, then stained with *In Situ* cell death detection kit TMR red (Roche 12156792910) according to manufacturers instructions, and mounted in Vectashield with DAPI. Visualization was performed with a Nikon Ti inverted fluorescence microscope, or in Figure 2-13 using a Leica SP8 confocal microscope. Antibodies were validated based on comparison to unstained and secondary only controls.

2.2.20 Genomic DNA Isolation and PCR:

Tissues were perfused using PBS and then digested using proteinase K (Thermofisher) in Tris buffer at 60°C for 1 hour. DNA was Isopropanol precipitated then used for genotyping using GoTaq Green MasterMix (Promega), using primers listed in Appendix 9.10.

2.2.21 Statistical Analysis

Statistical analysis was performed using GraphPad Prism 9.4.1. All data is presented as mean ± SEM. Normality was assessed using the D'Agostino-Pearson Test or the Shapiro-Wilk Test. For any data that was determined to have a normal distribution, a T-test was used to compare 2 means, or for >2 means a one-way ANOVA with Tukey's multiple comparison test or two-way ANOVA with Sidak's multiple comparison test were used. For data that was determined not have a normal distribution, a Mann-Whitney Test was used to compare 2 means, or for >2 means a Kruskal-Wallis Test was used with

Dunn's multiple comparison test. Exact p values are shown in all graphs. Sample size was determined by power calculation using http://powerandsamplesize.com/Calculators.

2.2.22 Data Availability

The data, methods, and materials will be available to other researchers for the purposes of reproducing the results or replicating procedures. Detailed methods and any associated references are provided in the supplementary material.

2.3 Results

2.3.1 Adoptive Transfer of Myd88$^{-/-}$ Th1 cells into Tcra$^{-/-}$ Mice Induces Greater Cardiac Fibrosis and Systolic Dysfunction than WT Th1 Cells In Response to TAC

We have previously shown that transfer of WT Th1 cells induces cardiac fibrosis in *Tcra*$^{-/-}$ mice, otherwise protected from fibrosis and systolic dysfunction in the onset of TAC. Thus, we used this strategy (Figure 2-1A) to investigate the role of T-cell MyD88 in TAC-induced cardiac remodeling. At 4 weeks post-surgery, we found that *Tcra*$^{-/-}$ mice reconstituted with *Myd88*$^{-/-}$ Th1 cells had decreased fractional shortening (FS), in contrast to WT Th1 cells, which were unable to alter FS (Figure 2-1B), as we have previously described.[229] Despite this, both WT and *Myd88*$^{-/-}$ Th1 cells induced similar left ventricular hypertrophy, as measured by normalized left ventricular weight (Figure 2-1C) and wheat-germ agglutinin (WGA) histologic staining (Figure 2-1D-E). Interestingly, we found *Tcra*$^{-/-}$ mice reconstituted with *Myd88*$^{-/-}$ Th1 cells exhibited significantly greater cardiac fibrosis and cardiac T-cell infiltration compared to mice reconstituted with WT Th1 cells (Figure 2-1D-G). Further analysis showed that *Myd88*$^{-/-}$ Th1 cells induced higher cardiac transcript of *Col3* and *Tgfb1* after TAC, and a trend upward for *Col1* (Figure 2-1H-J). We confirmed equal reconstitution of both WT and *Myd88*$^{-/-}$ Th1 cells by flow cytometry quantification of TCRβ^{+}CD4^{+} cells, finding similar frequencies in the spleen and mediastinal lymph nodes (mLN) (Figure 2-2A-C). Together, these data demonstrate that MyD88 deletion in T-cells results in enhanced T-cell cardiotropism and has detrimental consequences in cardiac fibrosis and contractile function.

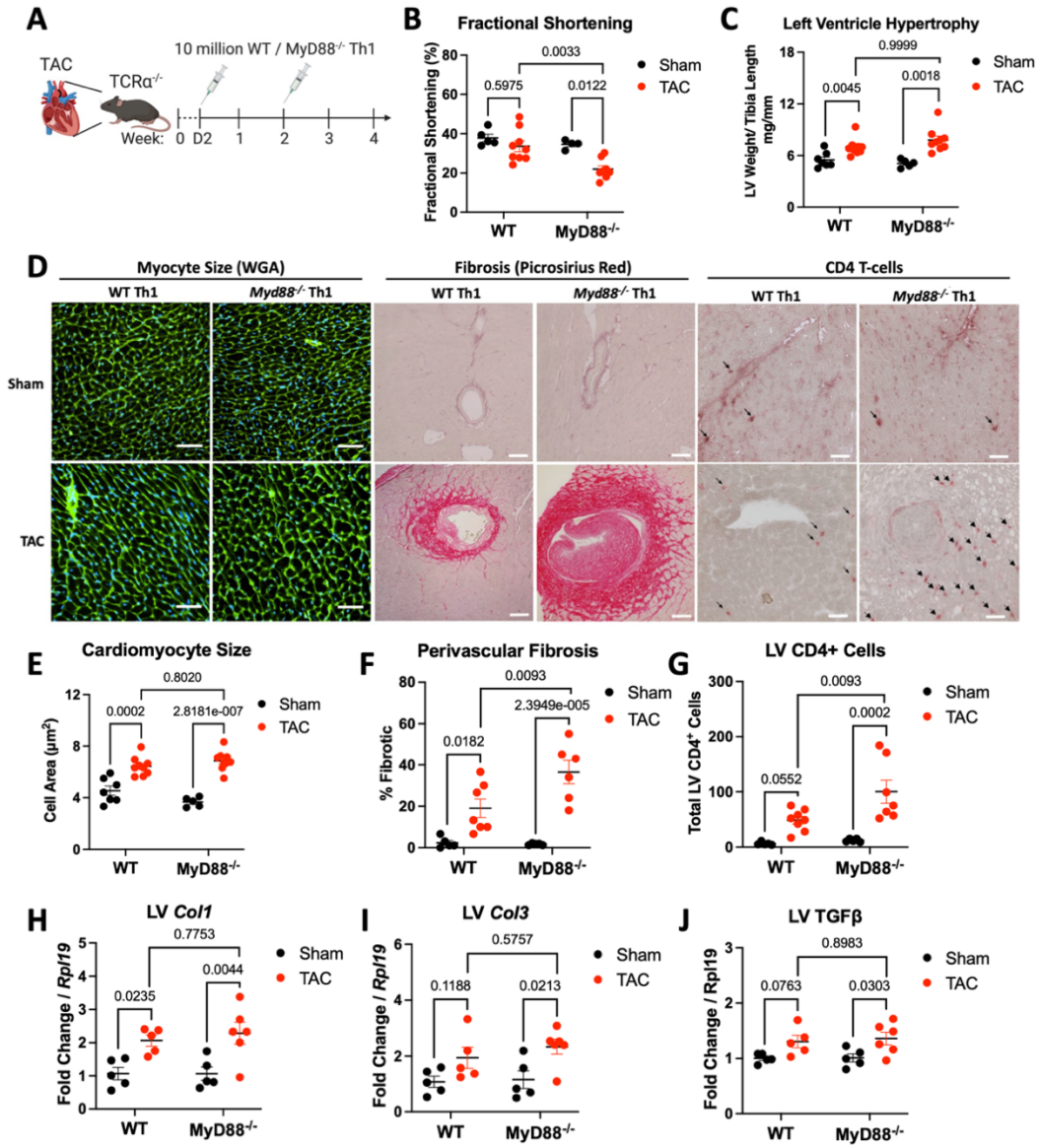


Figure 2-1 Tcra-/- Mice given Myd88-/- Th1 cells in the onset of TAC develop more cardiac fibrosis and systolic dysfunction

A. Schematic of experimental design, 8-10 week old male Tcra-/- mice underwent 25G TAC or Sham surgery then were reconstituted with 10 million WT or Myd88-/- Th1 cells 2 days, then 2 weeks post surgery, and tissues were harvested after 4 weeks. B. Fractional shortening as measured by echocardiography after 4 weeks. C. Measured weight of excised left ventricles normalized to tibia length. D. Representative images of LV of WGA (left), Picrosirius red (midde), and CD4 by IHC (right). Scale bars are 100 μM (middle) or 50 μM (left/right). E. Average cardiomyocyte size quantified using ImageJ on WGA stained sections. F. Left ventricular perivascular fibrosis quantified with ImageJ from Picrosirius red stained sections. G. CD4 infiltration was counted manually after IHC stain for CD4. H-J. RNA was isolated from the LV of each group of mice for gene expression analysis by RT-qPCR. Each data point is an individual mouse. Statistical analysis by 2-way ANOVA with Sidák's multiple comparison test for all panels except C, which used Kruskal-Wallis test with Dunn's multiple comparison test. P values shown.

2.3.2 Deletion of MyD88 in T-Cells Results in Enhanced Pro-Inflammatory Function

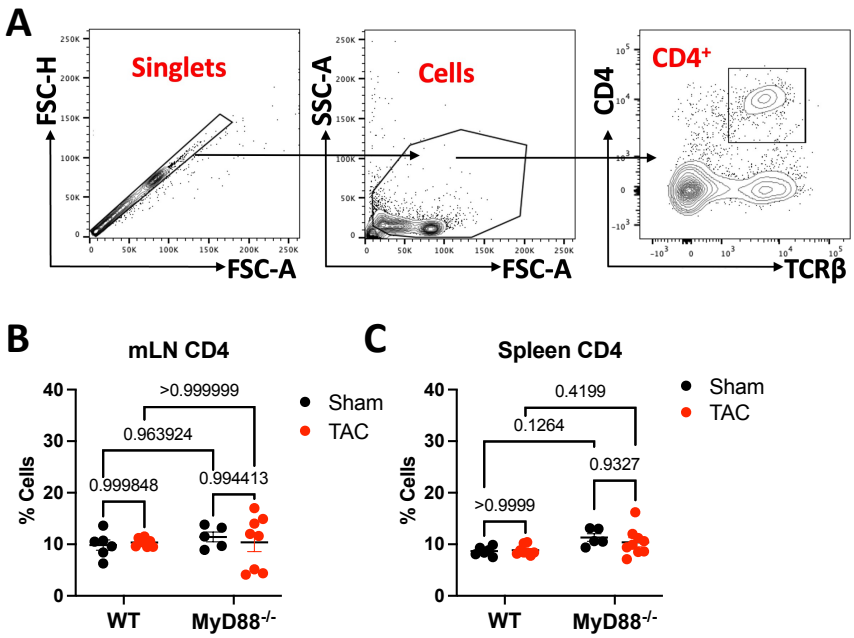


Figure 2-2 Reconstitution of TCRα Mice by Adoptive Transfer:
TCRa$^{-/-}$ Mice were reconstituted with WT or *Myd88*$^{-/-}$ Th1 cells in the onset of 25G TAC or sham surgery, and harvested after 4 weeks. A. Spleens or lymph nodes were crushed and stained for analysis by flow cytometry, gating strategy to identify CD4^{+} T-cells in lymphoid organs. B-C. Quantification of CD4^{+} T-cells from the mediastinal lymph nodes or spleens. Statistical analysis by 2-way ANOVA with Sidák's multiple comparison test, p values shown.

As an initial step to understand the intrinsic role MyD88 might play in cardiac T-cell function, we took an unbiased approach and compared the gene expression profile of WT and *Myd88*$^{-/-}$ Th1 cells by bulk RNA-sequencing. We found >100 differentially expressed genes when MyD88 was deleted in T-cells (Figure 2-3A). Gene set enrichment analysis (GSEA) revealed enriched genes for "MAPK3 Target genes" as well as decreased enrichment in "Apoptosis" and "Negative Regulation of T-cell Mediated Immunity" alongside the expected decreased enrichment for "TLR signaling pathways" (Figure 2-3B-E). We validated these pathways at the protein level and found not only increased phosphorylation of the MAPK effectors ERK and p38, but also increased NF-kB and AKT phosphorylation (Figure 2-3F-G) in *Myd88*$^{-/-}$ compared to WT Th1 cells. Each signal downstream of the TCR, and participate in clonal expansion, T-cell survival, and effector functions. However, we found similar expression of the Th1 signature cytokine, IFNγ, and transcription factor, Tbx21, at the protein and transcript level in WT and *Myd88*$^{-/-}$ Th1 cells (Figure 2-4B-D). Taken together, these data

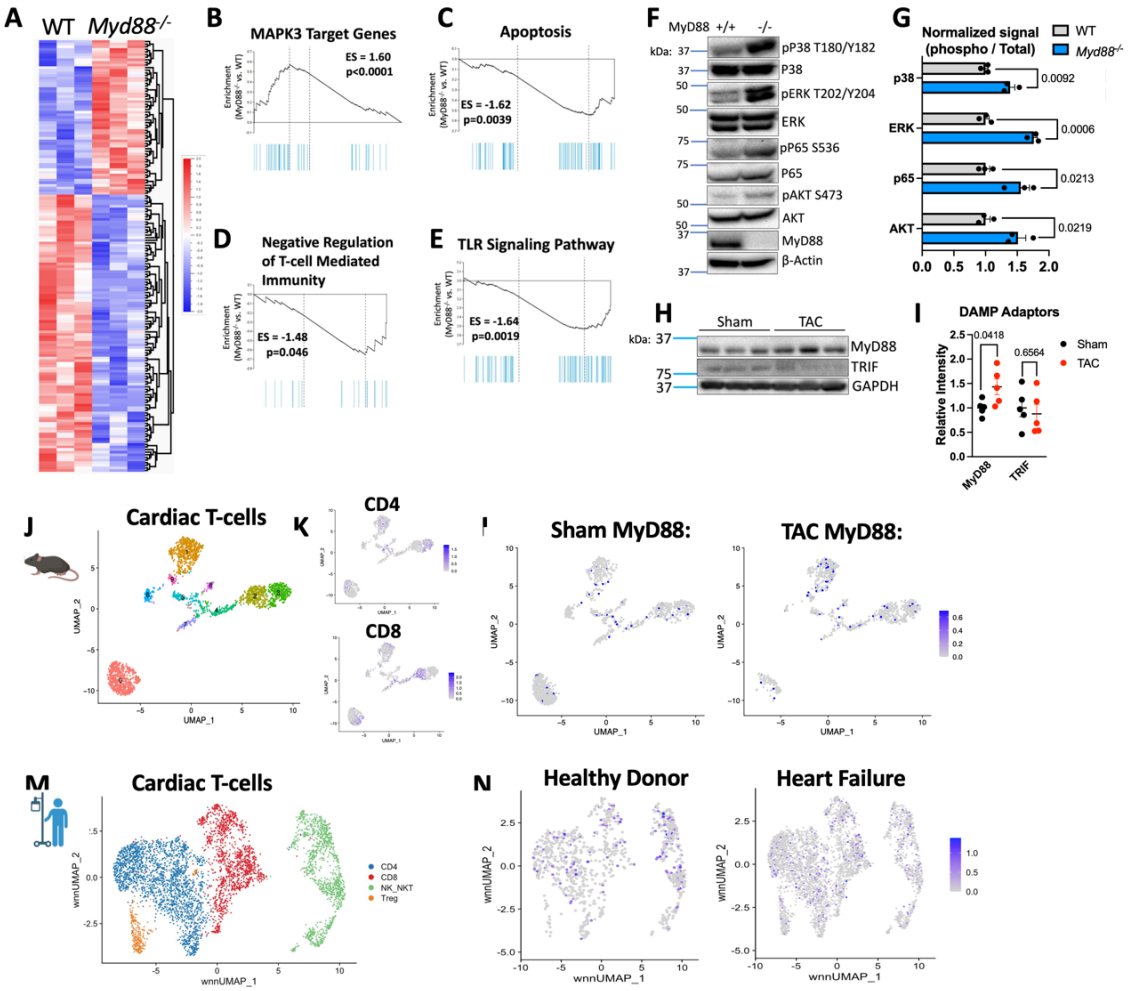


Figure 2-3 MyD88 Regulates T-cell Signaling In vitro and In the Heart

A. Bulk RNA sequencing was performed using RNA from n=3 WT or *Myd88*$^{-/-}$ Th1 cells, shown are differentially expressed genes with hierarchical clustering using p<0.05 for significance. B-E. Selected gene set enrichment analysis from Bulk RNA-seq data, shown enriched in *Myd88*$^{-/-}$ Th1 cells as compared to WT. F. Representative western blot from WT or *Myd88*$^{-/-}$ Th1 cells, quantified in G. from n=3 independent experiments and normalized to WT signal. H. Representative western blot from the LV WT mice after 4 weeks TAC or Sham surgery, quantified in I. for n=5 mice total. J. Pooled 4 week Sham and TAC UMAP of total cardiac T-cells with overlay of *Cd4* or *Cd8a* expression (K). M. Relative *Myd88* expression in Sham vs. TAC T-cells clusters. M. UMAP of T-cells from pooled patient heart samples. N. Relative expression of *Myd88* in healthy donors or patients with heart failure. Statistical analyses by multiple T-tests (panels G-I), p values shown.

demonstrate that MyD88 deletion in Th1 cells enhances TCR signaling pathways involved in T-cell activation and survival, supporting an anti-inflammatory role for MyD88 in T-cells, in contrast to its well established pro-inflammatory role in myeloid cells.

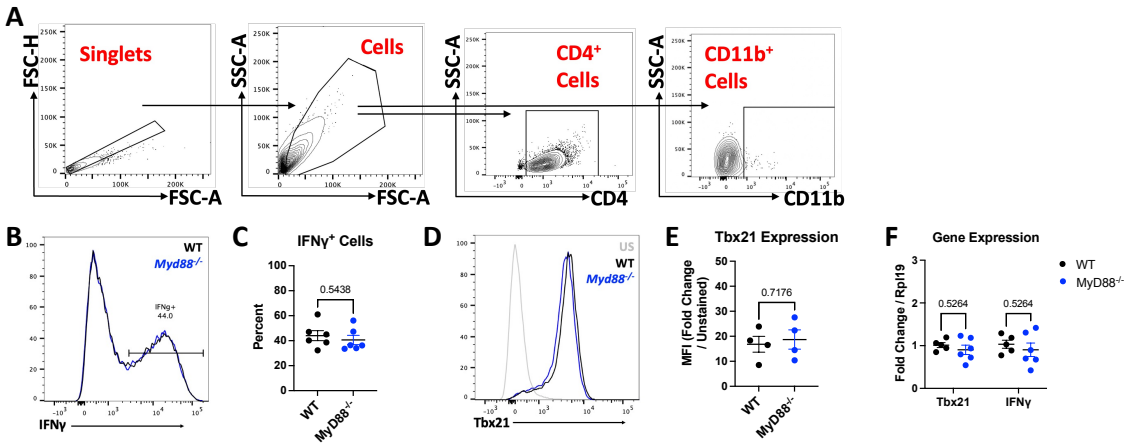


Figure 2-4 Gating Strategy for In vitro T-cell Experiments and Characterization of Myd88-/- Th1 cells

A. Gating strategy used for all *in vitro* T-cell experiments. B. WT or *Myd88*$^{-/-}$ Th1 cells were stained for IFN using intracellular cytokine staining, representative flow cytometry plots shown gated on CD4^{+} cells with quantification in C. from n=6 independent experiments. D. WT or *Myd88*$^{-/-}$ Th1 cells were stained intracellularly for Tbx21, representative flow cytometry plots shown gated on CD4^{+} cells with quantification in E. from n=4 independent experiments. F. RNA was collected from WT or *Myd88*$^{-/-}$ Th1 cells for qPCR, from n=6 independent experiments. Statistical analyses by T-tests, with p values shown.

2.3.3 Mouse and Human T-cells Express MyD88 in the Cardiac Inflammatory Environment

We hypothesized that constant stimuli in the cardiac inflammatory environment would require T-cells to have a mechanism controlled by MyD88 to limit T-cell overactivation. We found that MyD88 protein levels were increased in the LV of TAC mice compared to sham mice, however the parallel but less frequently used DAMP adaptor TRIF showed no changes in TAC vs. sham hearts (Figure 2-3H-2I). As this readout includes all cardiac cell types, we then turned to the existing single cell data collected from cardiac leukocytes isolated from sham and TAC hearts[376] to analyze the expression of MyD88 specifically in T-cells. We first re-clustered cardiac CD45^{+} cells to include only T-cells in both Sham and TAC mice 1 and 4 weeks post-surgery (Figure 2-3J-2K, Figure 2-5) and found that at 1 week post TAC surgery CD4^{+}MyD88-expressing cells began to infiltrate the heart, and by 4 weeks post-surgery the number of T-cells

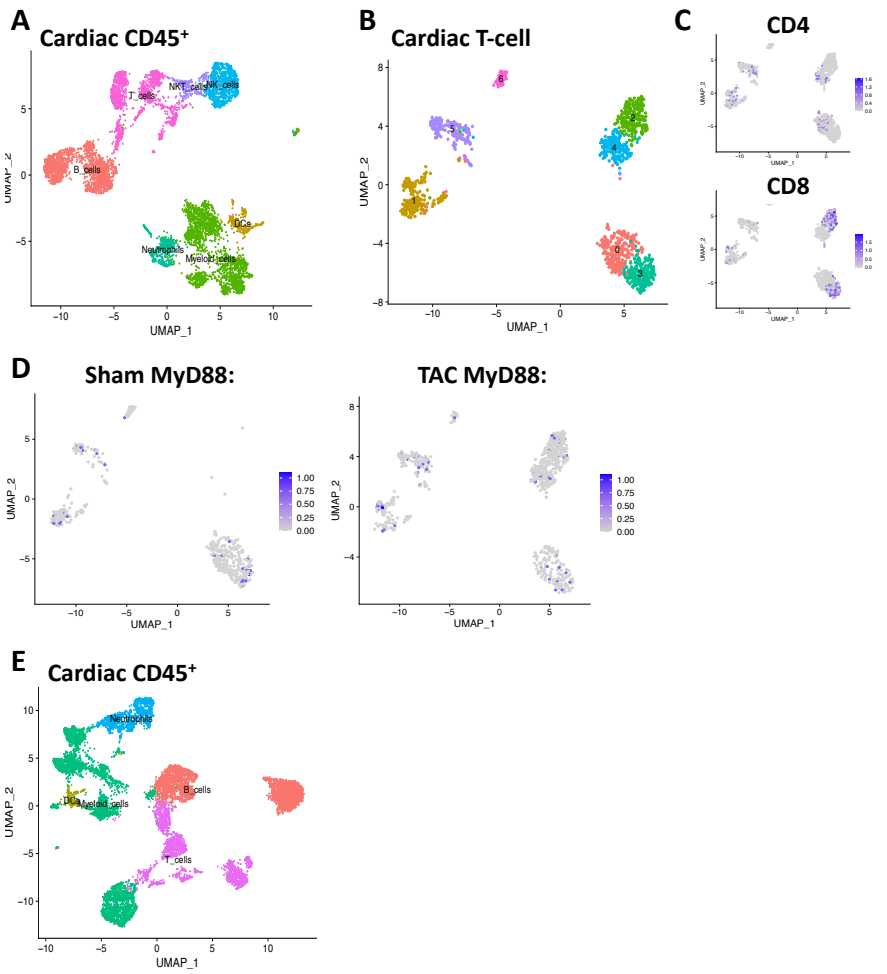


Figure 2-5 Cardiac MyD88+ T-cells Are Found at 1 week Post TAC. Pooled 1 week Sham and TAC UMAP of total cardiac CD45+ cells (A) or T-cells (B) with overlay of *Cd4* or *Cd8a* expression (C). D. Relative *Myd88* expression in Sham vs. TAC T-cell clusters. E. Pooled 4 week Sham and TAC UMAP of total cardiac CD45+ cells.

expressing *Myd88* was overall increased compared to Sham, as well as their relative expression of *Myd88* (Figure 2-3L, Figure 2-5). We then utilized published CITE-seq data[374] from human donors without HF and patients with HF to select T-cell subsets. Using RNA and protein markers, we annotated distinct T-cell states and found evidence of cardiac inflammation including a significant population of MyD88-expressing T-cells in failing hearts (Figure 2-3M-N). These data demonstrate that pro-inflammatory T-cells in mice and humans express MyD88 in the setting of cardiac inflammation and suggest a novel role for T-cell MyD88 in limiting the overactivation of T-cells in the inflamed heart.

2.3.4 T-cell MyD88 Deletion Results in Increased Adhesion to ICAM-1 and VCAM-1 and Primary Cardiac Endothelial Cells

As we observed increased cardiac infiltration of *Myd88*$^{-/-}$ Th1 cells compared to WT cells, we then sought to investigate whether MyD88 modulates T-cell interactions with adhesion molecules expressed by the inflamed endothelium required for T-cell extravasation. We used PMA to mimic TCR signaling and induce T-cell integrin activation to enhance adhesion to ICAM-1 and VCAM-1 under shear flow conditions. As expected, there was little adhesion to both ligands in the absence of PMA. However upon PMA treatment, higher numbers of *Myd88*$^{-/-}$ Th1 cells bound to both ICAM-1 and VCAM-1 compared to WT Th1 cells (Figure 2-6A-D). Adhesion was completely abrogated in the presence of anti-LFA-1 or anti-VLA-4 antibodies, the respective ligands of ICAM-1 and VCAM-1, demonstrating the increased adhesion of *Myd88*$^{-/-}$ Th1 cells occurred through canonical interactions (Figure 2-6A-D). Further, we did not observe any difference in the surface expression of LFA-1 and VLA-4 between WT and *Myd88*$^{-/-}$ Th1 cells (Figure 2-6E-F). These data support that MyD88 regulates the integrin activation status downstream of TCR signaling, rather than at the expression level, to modulate T-cell adhesion.

Myd88$^{-/-}$ Th1 cells also adhered to primary cardiac endothelial cells in higher numbers compared to WT Th1 cells (Figure 2-6G-H). However, despite the increased adhesion, the frequency of Th1 cells that transmigrated across the endothelial cells was similar between genotypes (Figure 2-6I). Because Th1 cell TEM requires chemokine signals for integrin activation, and the CXCL10-Th1 axis is central to T-cell cardiotropism in response to TAC [163,377], we next evaluated T-cell chemotaxis in response to CXCL10. We found no differences between WT and *Myd88*$^{-/-}$ Th1 cell migration (Figure 2-7A) or in the expression of the CXCL10 receptor CXCR3 by flow cytometry or western blot (Figure

2-7B-D). These data support that MyD88 regulates T-cell effector function by modulating signals downstream of the TCR that lead to T-cell adhesion to endothelial cells.

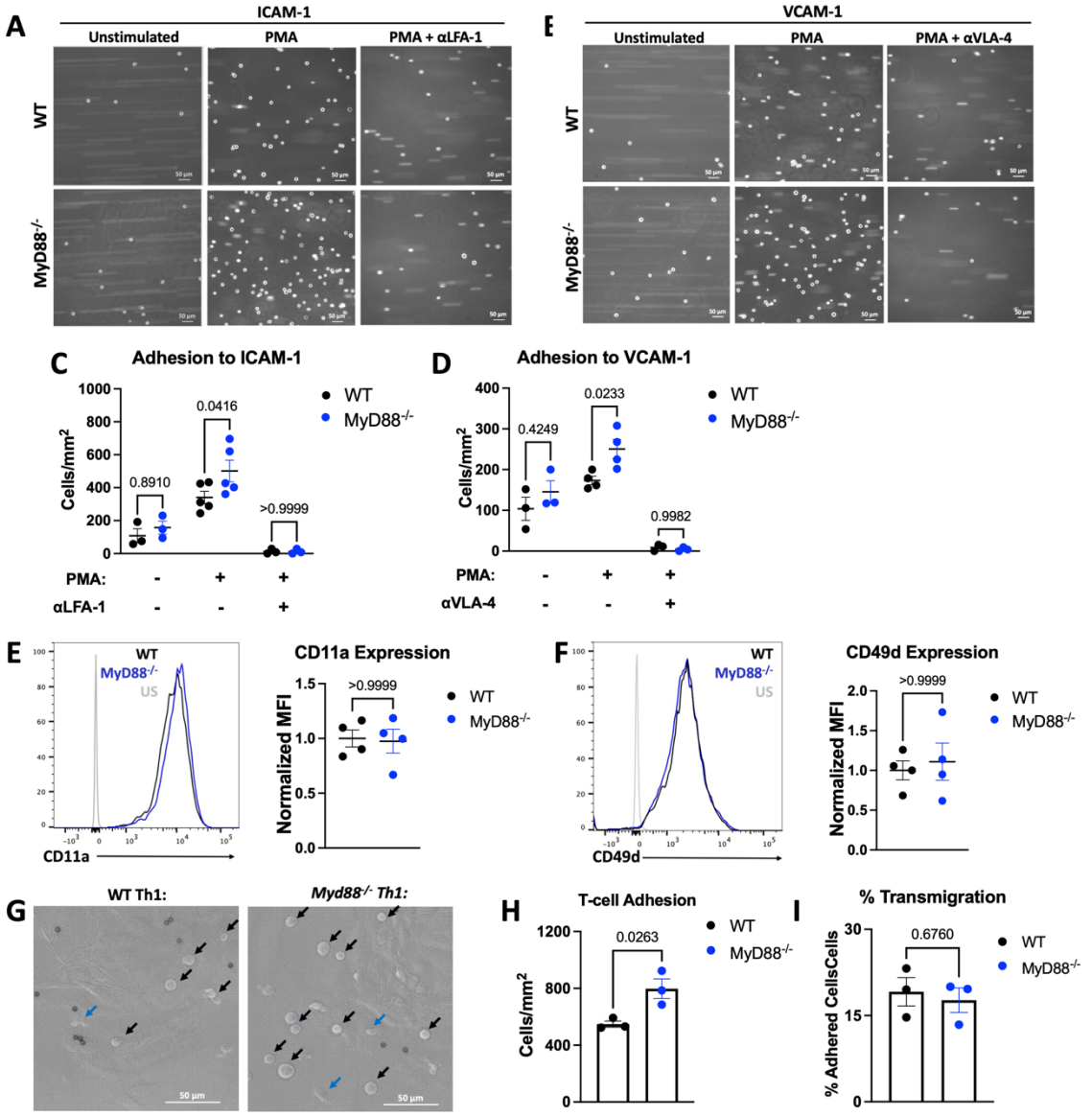


Figure 2-6 MyD88 Deletion Increases Th1 Adhesion Ability Without Impairment of Transendothelial Migration

A-D. WT or *Myd88*$^{-/-}$ Th1 cells were perfused at 1 million cells / mL at an estimated shear stress of 1 dyne / cm^2 over ICAM-1 or VCAM-1 after 5 minutes of treatment with 50 ng/mL PMA and/or 20 minutes of treatment with 20 μg/mL αLFA-1 or αVLA-4 where indicated, shown are representative images (A-B), quantified in C-D. E-F. Representative flow cytometry plots from WT or *Myd88*$^{-/-}$ Th1 cells shown with quantification of n=4 independent experiments. G. 1 million WT or *Myd88*$^{-/-}$ Th1 cells were perfused over mouse heart endothelial cells pre-treated with 125 ng/mL TNFα for 4 hours, at an estimated shear stress of 1 dyne / cm^2, at 37°C. TEM was monitored over 10 minutes and adhered vs. migrated cells were counted manually. Representative images of adhered cells (black arrows) vs. transmigrated cells (blue arrows) in G. with quantification of adhesion in H. and percent migration (migrated / adhered) in I. In all panels each data point is from an independent experiment. All scale bars are 50 μM. Statistical analysis by 2-way ANOVA with Sidák's multiple comparison test (C,D), Mann-Whitney Test (E, F) or T-test (H, I), p values shown.

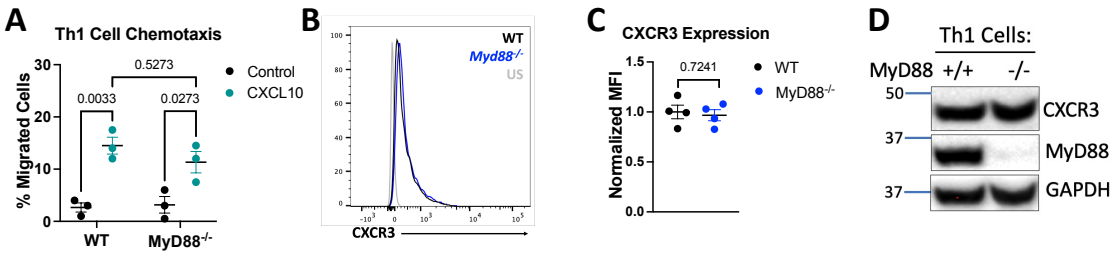


Figure 2-7 Myd88-/- Th1 cells Exhibit Similar Chemotaxis to CXCL10
A. 1 million WT or *Myd88*$^{-/-}$ Th1 cells were loaded onto Transwell inserts with or without a gradient of 2 µg/mL CXCL10, and T-cells migrated were counted manually after 4 hours from n=3 independent experiments. B-D. WT or *Myd88*$^{-/-}$ Th1 cells were collected for analysis of CXCR3 expression by flow cytometry, from n=4 independent experiments. Representative plot in B. quantified in C. or western blot (D). Statistical analysis by 2-way ANOVA with Sidák's multiple comparison test for A, or T-test for C. with p values shown.

2.3.5 T-cell MyD88 Deletion Results in Enhanced Th1 Cell Adhesion to Cardiac Fibroblast and Cardiac Fibroblast Transformation

Based on the high affinity for VCAM-1 that *Myd88*$^{-/-}$ Th1 cells displayed, and knowing that Th1 cells interact with CFB through the VLA-4/VCAM-1 interaction to induce myofibroblast transformation[229], we next investigated if T-cell MyD88 modulates CFB transformation through adhesion to VCAM-1. We co-cultured primary CFB with WT and *Myd88*$^{-/-}$ Th1 cells and detached the adhered T-cells to analyze CFB activation in isolation (Figure 2-8A). We found that fibroblasts that had been in contact with *Myd88*$^{-/-}$ Th1 cells expressed higher levels of alpha-smooth muscle actin (αSMA) and Collagen type 1, readouts of myofibroblast transformation, compared to those that had been in contact with WT Th1 cells (Figure 2-8B-D). As expected, WT Th1 cells adhered to CFB and induced αSMA expression, however, *Myd88*$^{-/-}$ Th1 cells adhered in higher numbers to CFB and induced greater levels of αSMA compared to WT Th1 cells (Figure 2-8E-G). Alteration of Th1:CFB ratio further demonstrated that WT and *Myd88*$^{-/-}$ Th1 cells adhered to and induced αSMA in CFB in a T cell dose dependent manner, with sustained enhancement of *Myd88*$^{-/-}$ Th1 cell adhesion and CFB transformation at all ratios (Figure 2-9). Moreover, inhibition of either the VLA-4/VCAM-1 interaction or TGFβ blunted

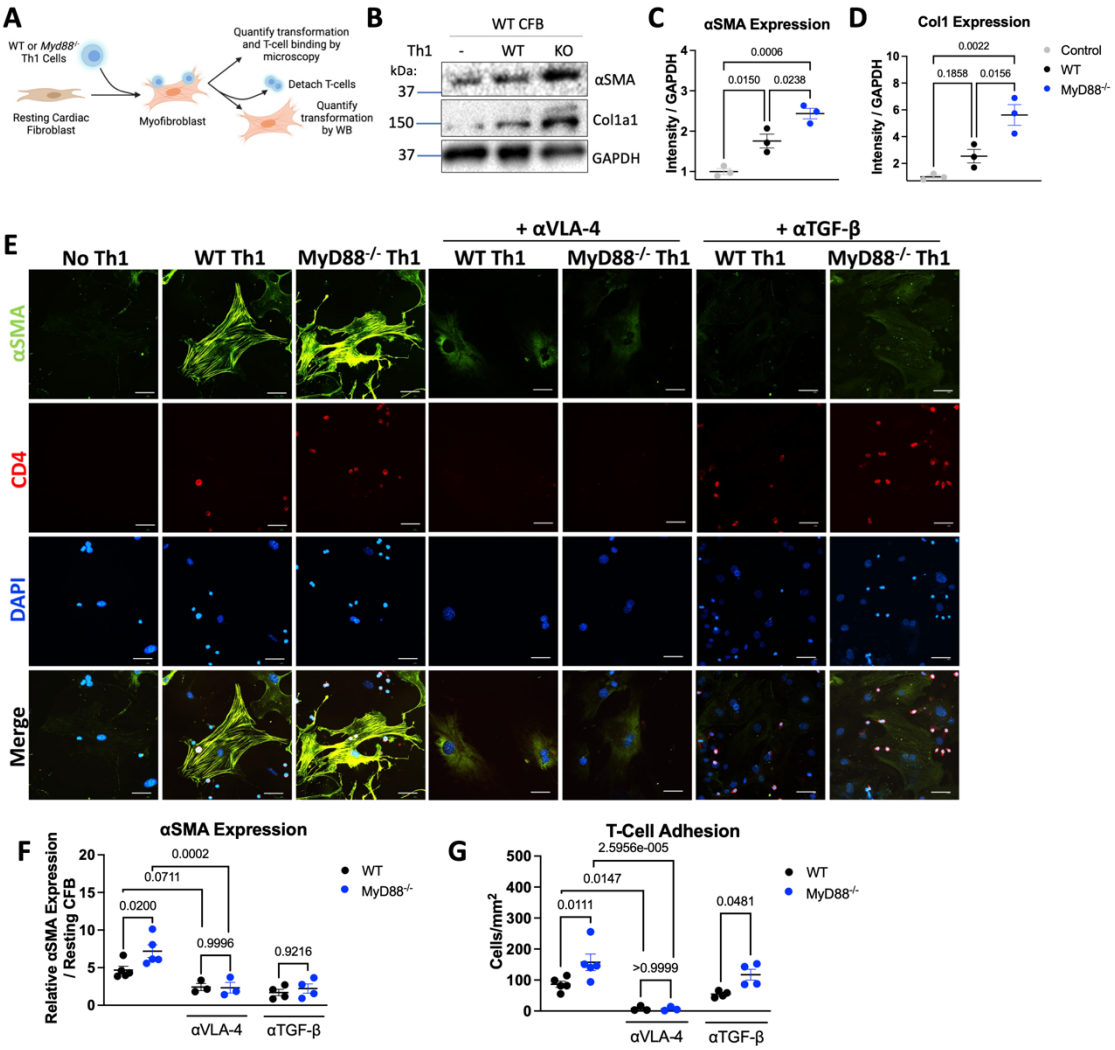


Figure 2-8 MyD88-/- Th1 Cells Exhibit Increased Binding to and Activation of Fibroblasts
A. Schematic of T-cell fibroblast co-cultures. WT cardiac fibroblasts were cultured with WT or *Myd88*$^{-/-}$ Th1 cells at a ratio of 2:1 CFB:Th1 for 16 hours with 20 μg/mL αVLA-4 or 5 μg/mL αTGFβ where indicated, non-adherent T-cells were washed off with PBS, and where indicated T-cells were detached with 5 mM EDTA. B. Representative western blot from cardiac fibroblasts after detaching WT or *Myd88*$^{-/-}$ Th1 cells, quantified using ImageJ for in C/D. E. Fibroblasts were stained for αSMA and CD4, and imaged by immunofluorescence microscopy. Representative images shown in E. αSMA was quantified using imageJ and normalized to untreated cells (F) and T-cells adhered were counted manually (G). Each data point represents an independent experiment. Scale bars are 50 μM. Statistical analysis by 1-way ANOVA with Tukey's multiple comparison test (C-D) or 2-way ANOVA with Sidák's multiple comparison test (F-G) with p values shown.

myofibroblast transformation by both genotypes, and the former blocked all T-cell adhesion, confirming that increased myofibroblast transformation induced by *Myd88*$^{-/-}$ T cells occurred through contact-dependent induction of TGFβ (Figure 2-8E-G). These data demonstrate that the enhanced binding of *Myd88*$^{-/-}$ Th1 cells to CFB VCAM-1

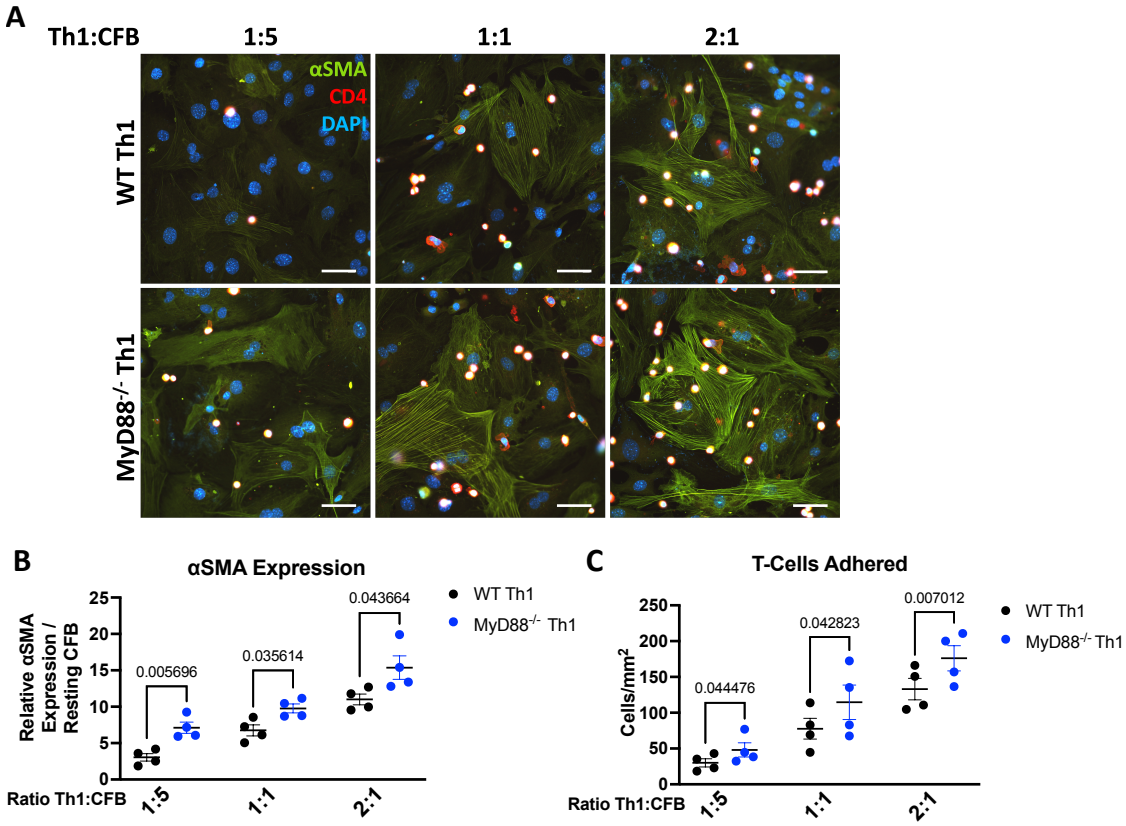


Figure 2-9 Myd88-/- and WT Th1 cells Exhibit Dose Dependent CFB Activation.
WT Fibroblasts were cultured with Th1 cells at the indicated ratio (Th1:CFB) for 16 hours, then non-adherent T-cells were washed off with PBS before staining for αSMA and CD4, then imaged by immunofluorescence microscopy. Representative images shown in A. αSMA was quantified using imageJ and normalized to untreated cells (B) and T-cells adhered were counted manually (C). Each data point represents an independent experiment. Scale bars are equal to 50 μm. Statistical analysis by paired T-tests, with p values shown.

results in increased CFB transformation in a TGFβ-dependent manner, a plausible mechanism to enhance cardiac fibrosis during TAC.

2.3.6 MyD88 Modulates T-Cell Activation through TCR Signaling

Based on our findings demonstrating overall improved T-cell effector function in the absence of MyD88, we then sought to dissect if MyD88 in T-cells modulated T-cell activation through DAMP receptors (TLRs/IL-1R) or through the TCR. We first found that relevant DAMPs which signal through MyD88 such as pro-IL-1β, IL-33, and HMGB1 were increased at the protein level in the LV of WT mice subjected to TAC compared to sham mice (Figure 2-10A-B). We then took TCR-activated Th1 cells, removed them from TCR stimulation, and treated them with cardiac lysate from TAC mice (containing

DAMPs) to test whether cardiac DAMPs can further activate T-cells in the absence of TCR signals. Cardiac DAMPs, or purified HMGB1 alone, were not sufficient to induce

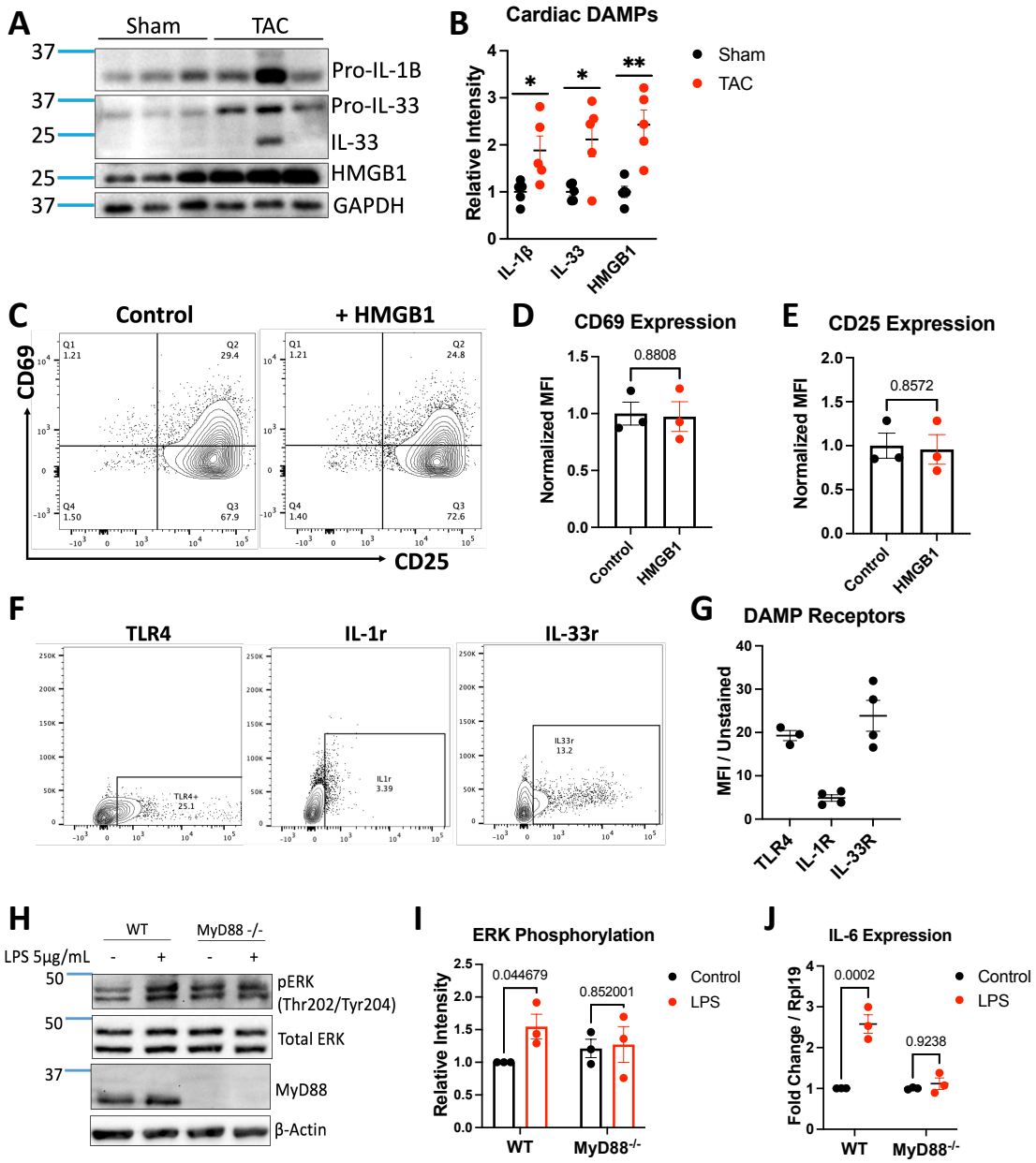


Figure 2-10 Characterization of Cardiac DAMPs and T-cell DAMP sensing
A.WT mice underwent 27 G TAC for 4 weeks, and LV samples were taken for western blot. Representative blot from 3 Sham or TAC mice, quantified in B. for n=5 mice total. C. Th1 cells were cultured in T-cell media lacking beta-mercapto-ethanol and treated with 10 µg/mL recombinant HMGB1 and 50 µM H2O2 for 24 hours, then cells were collected for flow cytometry. Representative plots shown with quantification in D-E from n=3 independent experiments. F. Representative flow cytometry plots of Th1 cells gated on $CD4^+$ cells, with quantification in G. for n=3 or n=4 independent experiments H. Th1 cells were treated with 2.5 µg/mL for 1 hour then protein was collected for western blot. Representative blot shown, quantified n=3 independent experiments in I. J. Th1 cells were treated with 2.5 µg/mL LPS for 16 hours then RNA was collected for analysis of cytokine expression by qPCR, data shown is normalized to control treated cells from n=3 independent experiments. Statistical analyses by T-tests (panels B-E) or 2-way ANOVA with Sidák's multiple comparison test (I-J), with p values shown.

the expression of the T-cell activation markers CD69 and CD25 (Figure 2-11A-C, 2-10C-E). However, the same dose of cardiac DAMPs was able to increase MHCII expression in dendritic cells (Figure 2-11D-E). To ensure that canonical DAMP signaling was functional in T-cells despite measuring low receptor expression (Figure 2-10F-G), we treated WT and *Myd88*$^{-/-}$ Th1 cells with LPS, a TLR4 ligand that signals through MyD88, and found LPS induced a MyD88-dependent increase in ERK phosphorylation and IL-6 expression (Figure 2-10H-J), both downstream of MyD88. These data demonstrate that despite a functional TLR-MyD88 axis in T-cells, signals through this pathway do not further induce CD69 or CD25 expression, prompting us to explore whether MyD88 modulation of T-cell activation occurs downstream of the TCR.

To do so, we measured phospho-ZAP70, a component of the TCR signaling complex that marks T-cell activation, using TCR stimulation *in vitro* using αCD3/αCD28, and found that *Myd88*$^{-/-}$ Th1 cells exhibited higher expression of pZAP70 compared to WT after activation but not at baseline (Figure 2-11F-G). Additionally, TCR activation of *Myd88*$^{-/-}$ Th1 cells resulted in higher levels of CD69 (Figure 2-11H-I), and increased secretion of the cytokines IL-2 and TNFα compared to WT Th1 cells (Figure 2-11J-K), confirming an overall enhanced activation status in *Myd88*$^{-/-}$ Th1 cells. Further, small molecule inhibition of MyD88 during T-cell activation in WT Th1 cells recapitulated both increased CD69 and pZAP70 (Figure 2-12). Interestingly, TCR activation of WT cells correlated with upregulation of MyD88 protein expression compared to inactivated cells, directly associating MyD88 expression with TCR signaling for the first time (Figure 2-11L-M). To further investigate how MyD88 modulates T-cell activation, we investigated the localization of MyD88 upon TCR engagement by immunofluorescence. We again confirmed increased expression of MyD88 upon TCR activation, alongside expected

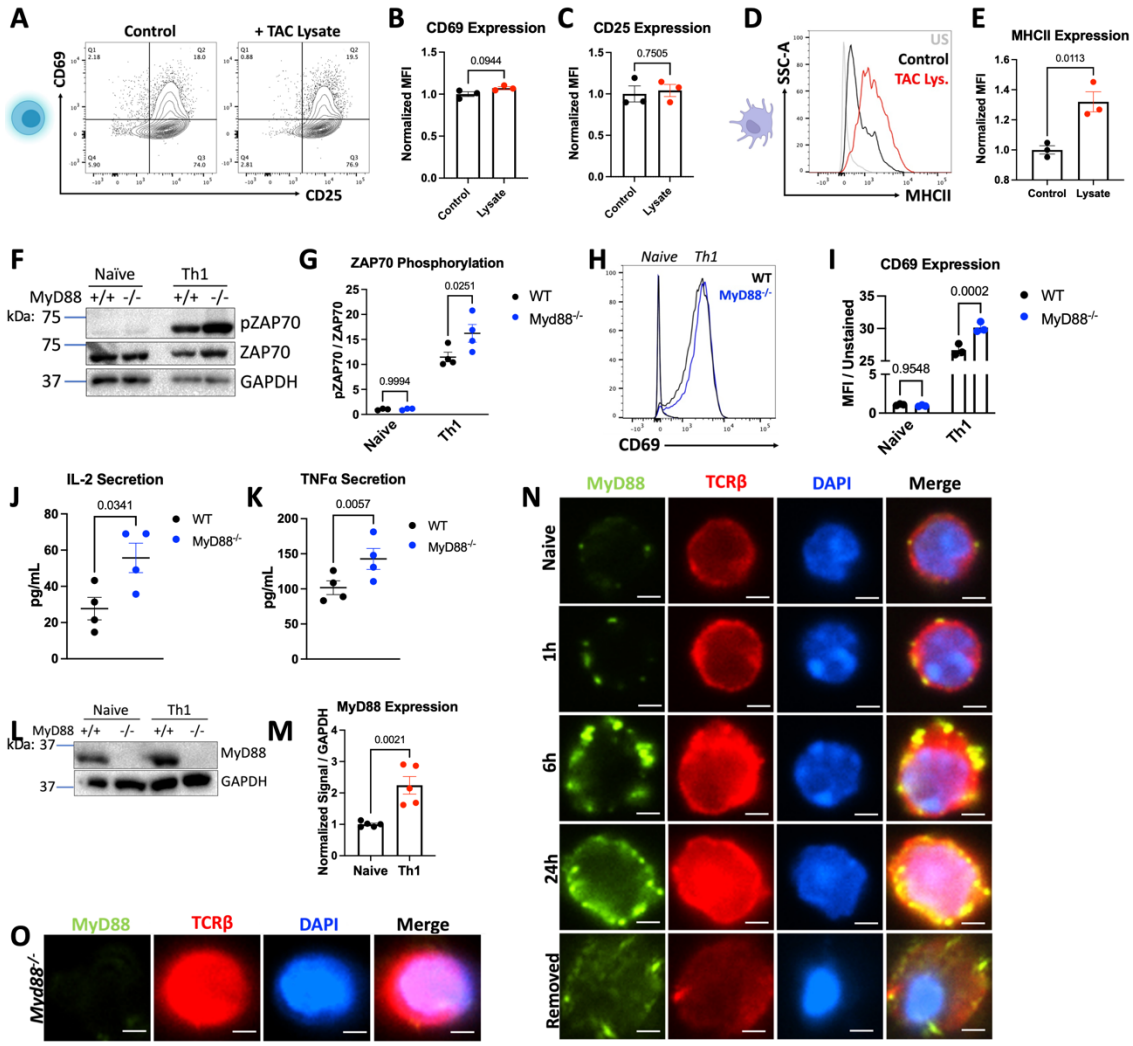


Figure 2-11 MyD88 Acts as a Break During T-cell Activation through TCR but not TLR signaling
Th1 cells were cultured in T-cell media with 10 μg/mL of lysate generated from the LV of WT TAC mice for 24 hours, then analyzed by flow cytometry. Example plots shown in in A. with quantification for n=3 independent experiments in B-C. D-E. BMDCs were cultured with 10 μg/mL of TAC lysate for 24 hours, then analyzed by flow cytometry. Representative plots shown in D, with quantification for n=3 independent experiments in E. F. Representative western blots from WT or *Myd88*$^{-/-}$ Th1 cells, quantified in G. WT or *Myd88*$^{-/-}$ Naive CD4^{+} splenocytes or Th1 cells were stained and analyzed by flow cytometry, with representative plots shown in H. quantified in I. from n=3 independent experiments. J-K. Supernatants were collected for ELISA from 1 million WT or *Myd88*$^{-/-}$ Th1 cells cultured in fresh T-cell media for 24 hours from n=4 independent T-cell preps. L. Representative western blots from WT or *Myd88*$^{-/-}$ Naive CD4^{+} or Th1 cells, quantified in M. from n=4 independent experiments. N-O. Naïve WT (N) or *Myd88*$^{-/-}$ (O) T-cells were plated on coverslips in the absence or presence of αCD3/CD28 for the indicated timepoints, or removed from stimulation for 24 hours, then stained with MyD88 and TCRβ for analysis by fluorescent microscopy. Scale bars are 2 μM. Statistical analysis by T-test (B,C, E, J, K, M), or 2-way ANOVA with Sidák's multiple comparison test (G, I) P values shown.

puncta of TCRβ clusters at the membrane during TCR-induced activation.[378] Strikingly, specific MyD88 signal colocalized in said TCRβ puncta (Figure 2-11N-O), and when T-cells were removed from TCR stimulation, MyD88 decreased at the membrane along with clustered TCRβ, albeit not back to the level of naïve T-cells. Interestingly, using

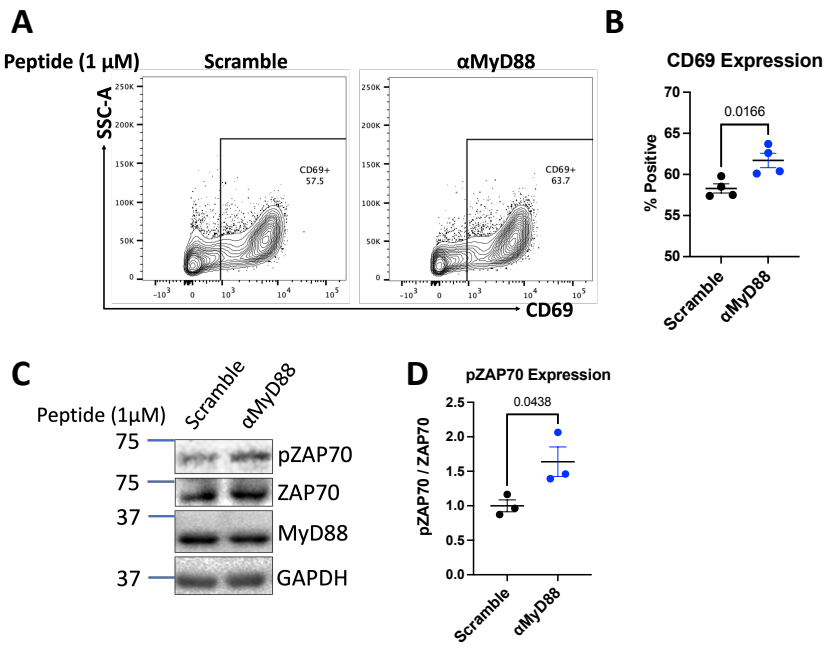


Figure 2-12 MyD88 Inhibition Increases Th1 Activation Status
WT CD4 cells were activated in the presence of 1 µM of MyD88 inhibitor peptide or scrambled peptide for 24 hours. A. Representative flow cytometry plots of CD69 expression with quantification (B). C. Representative western blot of inhibitor treated T-cells with quantification (D). Each data point represents an independent experiment. Statistical analysis by T-test, p values shown.

confocal microscopy

we found MyD88 to co-localize with TCRβ in multiple planes close and distal to the TCR engagement, and MyD88 was also found in isolation far from TCR engagement (Figure 2-13). Together, these data demonstrate that MyD88 co-localizes with the TCR at the membrane during TCR engagement and suggests that MyD88 functions as a brake of T-cell activation downstream of the TCR rather than through TLR-DAMP signaling.

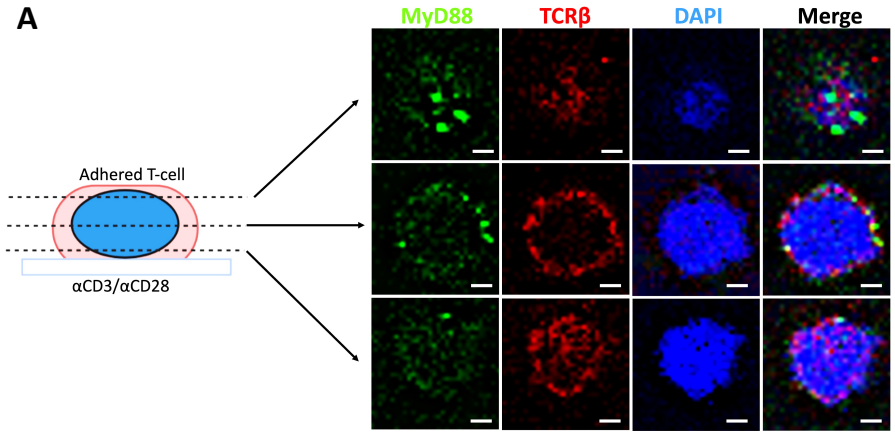


Figure 2-13 Analysis of MyD88 Expression in T-cells by confocal microscopy
A. WT CD4 T-cells were plated on coverslips in the presence of αCD3/CD28 for 24 hours, then stained with MyD88 and TCRβ for analysis by Confocal microscopy with Z-stack imaging. Scale bars are equal to 2 µM.

2.3.7 MyD88 Deletion Enhances T-Cell Survival:

As TCR signaling leads to optimal T-cell proliferation and survival, we next investigated the role of T-cell MyD88 in T-cell survival as another mechanism to explain increased cardiac T-cell presence, and therefore increased fibrosis. Th1 cells were cultured in the

absence of TCR engagement or cytokine stimulation as a way to induce steady T-cell death, and imaged in real time (Figure 2-14A). Interestingly, *Myd88*$^{-/-}$ Th1 cells exhibited decreased cell death over time compared to WT Th1 cells, a finding which was further exacerbated by serum starvation (Figure 2-14A-B). Moreover, we performed *in vivo* competitive survival experiments using equal numbers of adoptively transferred WT and *Myd88*$^{-/-}$ Th1 cells, carrying the CD45.1 and CD45.2 alleles respectively, into healthy *Tcra*$^{-/-}$ recipient mice (Figure 2-14C). We found that as early as 1 week post transfer, there were higher numbers of *Myd88*$^{-/-}$ Th1 cells in the spleen, and this survival advantage was sustained 2 and 4 weeks post transfer (Figure 2-14D-E). These data demonstrate a long-term survival benefit *in vivo for Myd88*$^{-/-}$ Th1 cells compared to WT

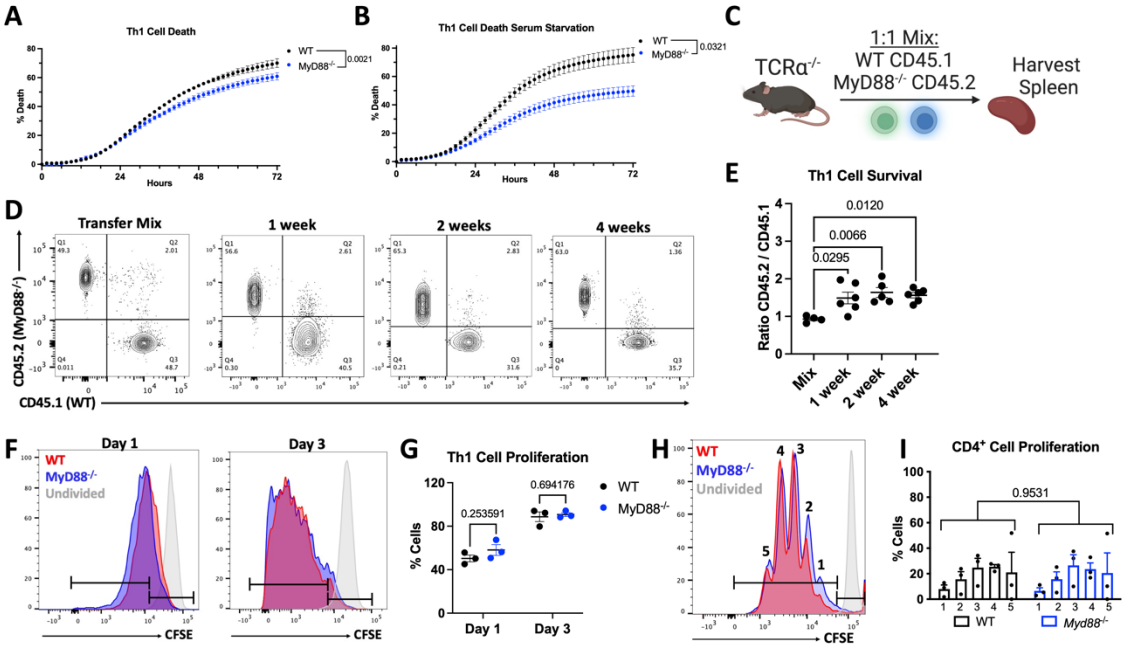


Figure 2-14 MyD88 Knockout Enhances Survival but Not Proliferation in Th1 Cells
A. WT or *Myd88*$^{-/-}$ Th1 cells were cultured on αCD43 coated plates (10 μg/mL) in the presence of 10 μg/mL PI in media with or without 10% FBS. PI incorporation was monitored for 72 hours, baseline subtracted, and normalized to a 100% death Triton-X treated control. C. Scheme of *in vivo* competitive survival, in which healthy *Tcra*$^{-/-}$ mice were reconstituted with 10 million WT CD45.1 and *Myd88*$^{-/-}$ CD45.2 Th1 cells in 1:1 abundance, then spleens were harvested at indicated time points. D. Example flow cytometry plots gated on CD4^{+}TCRβ^{+} cells from *in vivo* survival showing transfer mix, then splenocytes after 1, 2, and 4 weeks, quantified in E. from 5-6 mice / group. F. Activated Th1 cells were stained with CFSE then cultured in the presence of 25U/mL IL-2 and collected after 1 or 3 days, example flow cytometry plots shown in F. quantified in G. from n=3 independent experiments. H. Naïve CD4^{+} T-cells (CD62L^{hi}CD44^{low}) were sorted from splenocytes of WT or *Myd88*$^{-/-}$ mice, stained with 5 μM CFSE, then polarized to Th1 cells as described in methods and collected after 3 days activation, representative plot in H. quantified in I. from n=3 independent experiments. Statistical analysis by 2-way ANOVA with repeated measures (A, B), 2-way ANOVA with Sidák's multiple comparison test (I), 1-way ANOVA with Tukey's multiple comparison test (E), or multiple T-tests (G), with n.s. = no significance, p values shown.

cells and suggest that MyD88 modulation of T-cell survival in activated T-cells may be responsible for the increased cardiac T-cell presence during TAC.

To distinguish between survival and proliferative cues modulated by MyD88 upon TCR engagement, we next assessed the proliferative capacity of Th1 cells, and found that WT and *Myd88*$^{-/-}$ Th1 cells showed similar CFSE dilution as a measurement of proliferation in the presence of IL-2 after 1 and 3 days in culture (Figure 2-14F-G). We additionally isolated naïve CD4^{+} T-cells from WT and *Myd88*$^{-/-}$ mice and traced CFSE dilution as they differentiated into effector T-cells in response to TCR stimulation. We again found rapid but similar proliferation in the presence or absence of MyD88 (Figure 2-14H-I). From these data, we conclude that MyD88 acts at the TCR during active TCR signaling and its deficiency results in a T-cell survival advantage that may explain enhanced cardiac inflammation.

2.3.8 T-cell specific MyD88$^{-/-}$ mice develop more cardiac fibrosis and cardiac fibroblast activation

We next generated T-cell specific MyD88$^{-/-}$ mice (*Myd88*$^{fl/fl}$*CD4*^{Cre}) to investigate the intrinsic role of T-cell MyD88 in T-cell activation and adverse cardiac remodeling in response to TAC. We confirmed that *Myd88*$^{fl/fl}$*CD4*$^{Cre+}$ mice had excision of *Myd88* exon 3 and ablated Myd88 protein specifically in T-cells (Figure 2-15A-C). In response to TAC, we found higher levels of perivascular and interstitial fibrosis in *Cre*$^{+}$ mice (T-MyD88$^{-/-}$) compared to *Cre*$^{-}$ littermates (T-MyD88$^{+/+}$), but no baseline differences, suggesting TCR engagement is needed for MyD88 dependent fibrosis (Figure 2-15D-F). As observed in our adoptive transfer model, each group of mice developed similar cardiac hypertrophy by LV weight and WGA staining, and neither group developed significant cell death, determined by TUNEL staining (Figure 2-16). In line with the pro-fibrotic phenotype, we found TAC induced similar increases in *Col1* and *Tgfb1* but greater cardiac expression of

Col3 and *Fn1* (Fibronectin) in T-MyD88$^{-/-}$ mice (Figure 2-15G-J). Interestingly, we found a significant increase in total MEFSK4^{+} CFBs in the hearts of T-MyD88$^{-/-}$ but not T-MyD88$^{+/+}$ mice in response to TAC (Figure 2-15K-L). Further co-staining of αSMA with PDGFRα and CD31 determined that the majority of αSMA^{+} cells were also PDGFRα and

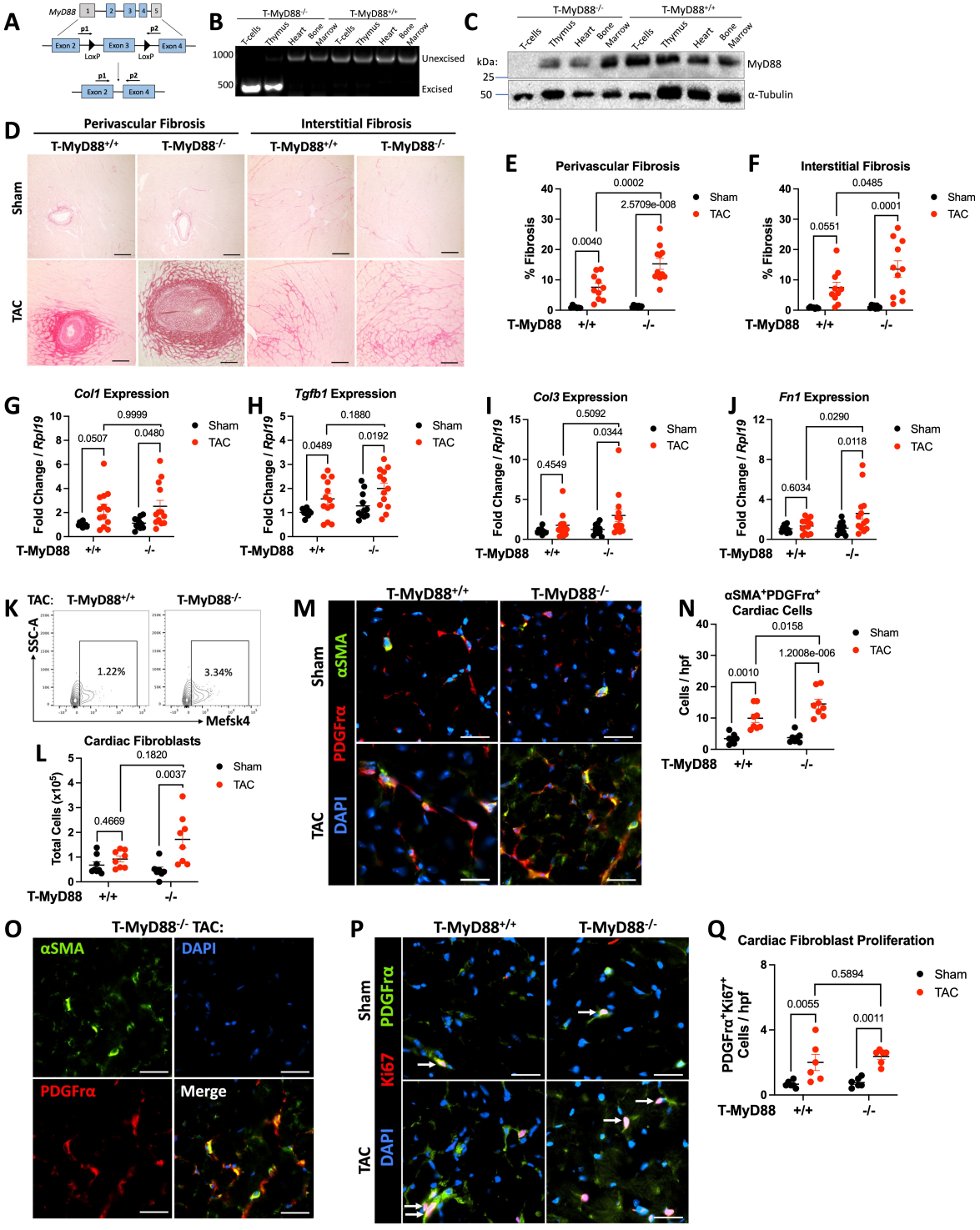


Figure 2-16 T-Cell Specific MyD88 Knockout Mice Show Increased Cardiac Fibrosis with Increased Cardiac Fibroblast Activation and Proliferation

A. Schematic showing *Myd88* floxed exon 3 and primers used to detect Cre-mediated excision. B. Genomic DNA was isolated from $CD4^+$ T-cells and control tissues and amplified to detect *Myd88* excision by PCR. C. Western blot of $CD4^+$ T-cells and control tissues for MyD88 deletion. D. 8-10 week male and female $Myd88^{fl/fl}CD4^{Cre}$ mice using Cre^+ and Cre^- littermates underwent 27G TAC or Sham surgery. Representative images from LV samples stained with Picrosirius, scale bars are 100 μM. E-F. ImageJ was used to quantify fibrosis F in perivascular or interstitial regions respectively. G-J. RNA was isolated from the LV of each group of mice for gene expression analysis by RT-qPCR. K. The LV of each group of mice was enzymatically and mechanically digested for analysis of cardiac fibroblasts ($CD45^-Mefsk4^+$) by flow cytometry, shown are representative plots from TAC mice (K) with quantification (L). M-N. Representative images from LV samples stained for αSMA and PDGFrα, scale bars are 25 μM, with quantification in N. and individual channels shown in O. for a Cre+ TAC example. P-Q. Representative images from LV samples stained for PDGFrα and Ki67, scale bars are 25 μM, with quantification in Q. Each data point represents an individual mouse. Statistical analysis by 2-way ANOVA with Sidák's multiple comparison test (E,F,H,J,L), Kruskal-Wallis Test with Dunn's multiple comparisons test (G,I,N,Q), p values shown.

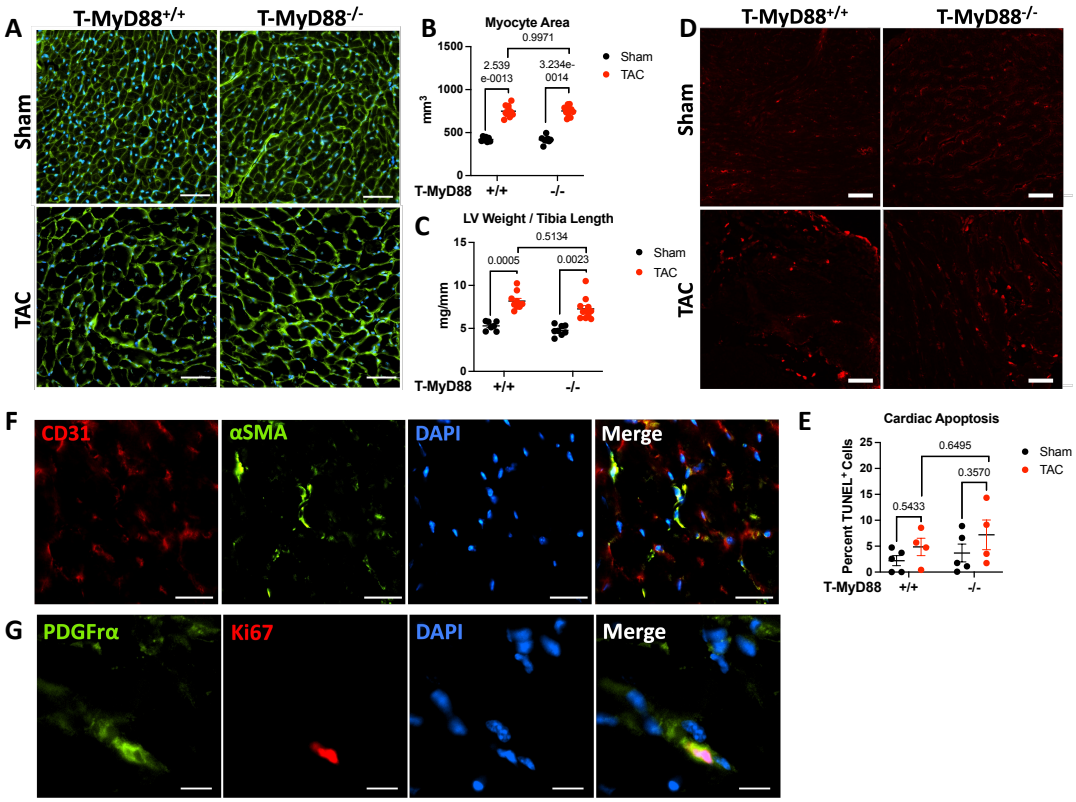


Figure 2-15 T-MyD88-/- Mice Exhibit Similar Hypertrophy and Little Cardiac Cell Death After TAC

8-10 week male and female $Myd88^{fl/fl}CD4^{Cre}$ mice using Cre^+ and Cre^- littermates underwent 27G TAC or Sham surgery and were harvested after 4 weeks. A-B. LV sections were stained with WGA and quantified with ImageJ. C. LV weight was measured and normalized to Tibia length. D-E. LV sections were TUNEL stained and quantified with ImageJ. F. LV sections were stained with CD31 and αSMA, example image from a Cre+ TAC mouse G. LV sections were stained with PDGFrα and Ki67, example image from a Cre- Sham mouse. Scale bars shown for are 50 μM (A, D) 25 μM (F), 10 μM (G). Each data point represents an individual mouse. Statistical analysis by 2-way ANOVA with Sidák's multiple comparison test (B,C) or Kruskal-Wallis test with Dunn's multiple comparison tests (C), p values shown.

that $PDGFR\alpha^+$ αSMA^+ cardiac fibroblasts were increased in TAC $T\text{-}MyD88^{-/-}$ compared to $T\text{-}MyD88^{+/+}$ mice (Figure 2-15M-O). We also observed limited, yet still present,

expression of αSMA in CD31+ vessels (Figure 2-16F). Moreover, to visualize proliferating and non proliferating fibroblasts, we stained with Ki67 and found that while TAC increased the numbers of PDGFRα^{+}Ki67^{+}cells in both genotypes, T cell MyD88 deficiency did not alter the presence of proliferating fibroblasts at this time point (Figure 2-15P-Q, and Figure 2-16G). Together, these confirm that mice deficient in T-cell MyD88 have increased cardiac fibrosis in response to TAC alongside with increased CFB co-expressing αSMA and PDGFRα, yet similar number of proliferating CFBs at this time point.

2.3.9 T-cell specific MyD88$^{-/-}$ mice have increased T-cell cardiac infiltration, TCR activation, and decreased survival to TAC

We next characterized the inflammatory profile of T-MyD88$^{-/-}$ mice in response to TAC, finding increased cardiac CD4^{+} T-cells compared to T-MyD88$^{+/+}$ mice (Figure 2-17A-B), however when we quantified effector T-cells (defined as CD62L^{lo}CD44^{hi}, gating strategy in Figure 2-18A), we found similar increases in mLN CD4^{+} effector T-cells but increased splenic effector T-cells in T-MyD88$^{-/-}$ mice, a sign of enhanced systemic inflammation (Figure 2-17C-D). Additionally, only T-MyD88$^{-/-}$ mice exhibited increased cardiac CD8^{+} T-cells after TAC (Figure 2-18D). We further quantified CD69 expression in cardiac T cells to probe TCR engagement in the cardiac inflammatory environment and found increased numbers of both CD4^{+} and CD8^{+} T-cells expressing CD69 in the hearts of T-MyD88$^{-/-}$ mice (Figure 2-17E, Figure 2-18E). Moreover, splenic CD4^{+} T cells from T-MyD88$^{-/-}$ mice showed enhanced levels of pZAP70 compared to T-MyD88$^{+/+}$ mice in response to TAC, with no differences observed in pZAP70 in sham mice between groups (Figure 2-17F-G), demonstrating enhanced TCR activation induced by TAC in T-MyD88$^{-/-}$ mice. Despite this, and similar to *in vitro* differentiated Th1 cells, T-cells from T-MyD88$^{-/-}$ mice had comparable levels of IFNγ to those from MyD88+/+ control mice in the onset of

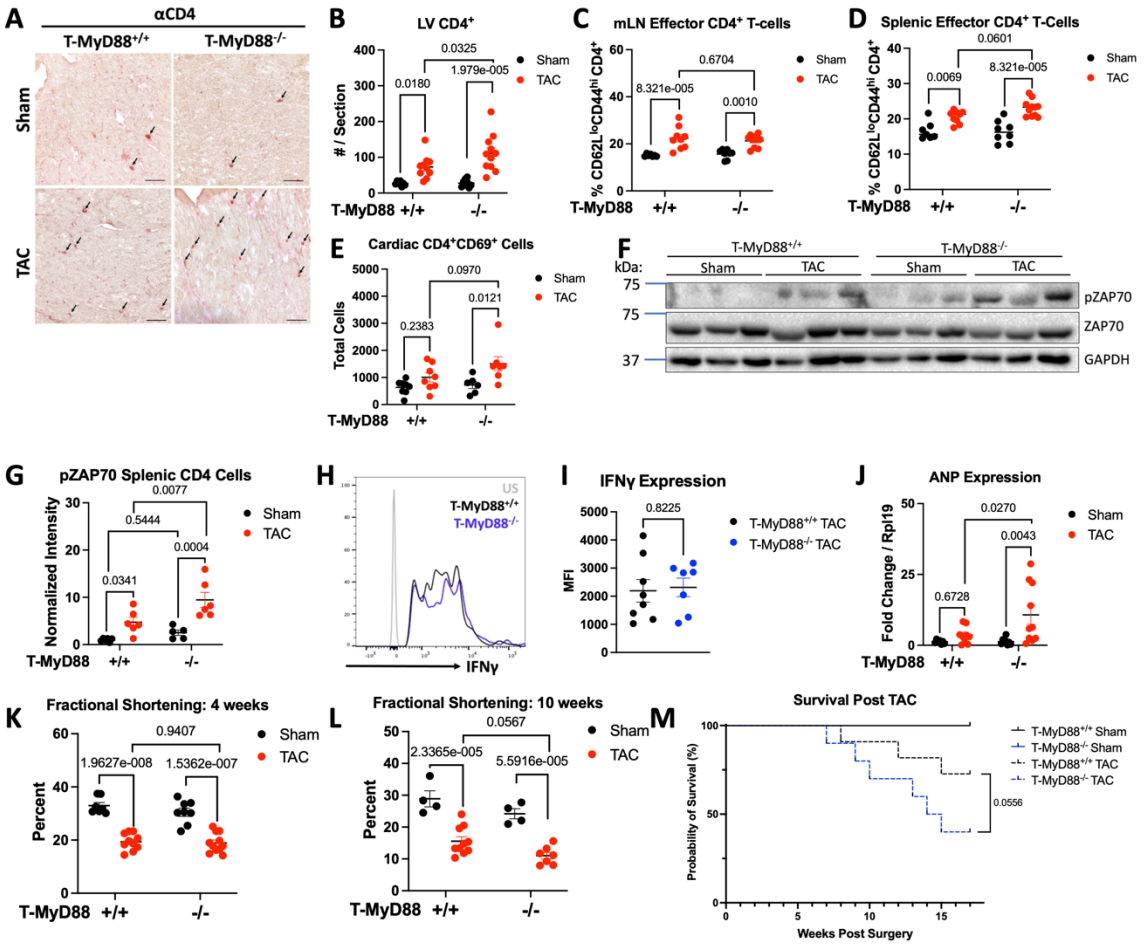


Figure 2-17 T-Cell Specific MyD88 Knockout Mice Show Increased T-cell Activation, Cardiotropism, Systolic Decline, and Survival

A. 8-10 week male and female *Myd88$^{fl/fl}$CD4^{Cre}* mice using Cre^{+} and Cre^{-} littermates underwent 27G TAC. Representative images from LV samples stained for CD4 with IHC, scale bars are 50 μM, with quantification in B. C-D. The mediastinal lymph nodes and spleen of each group of mice was digested and effector T-cells (TCRβ^{+}CD4^{+}CD62L^{lo}CD44^{hi}) were quantified by flow cytometry. E. The LV of each group of mice was enzymatically and mechanically digested for analysis of cardiac T-cell reactivation (CD45^{+}CD4^{+}CD69^{+}) by flow cytometry. F-G. Splenic CD4^{+} cells were isolated from each group of mice for analysis of Zap70 phosphorylation, shown is a representative blot from 3 mice / group (F) with quantification of 6 mice (G). H-I. The mediastinal lymph nodes were digested and stimulated with PMA, Ionomycin, Brefeldin, and Monensin A for 4 hours before analysis of IFNγ expression by flow cytometry, shown are representative plots (H) with quantification in I. J. RNA was isolated from the LV of each group of mice for gene expression analysis by RT-qPCR. K-L. Fractional shortening was measured by echocardiography at 4 weeks post surgery (K.) or 10 weeks post surgery (L). Each data point represents an individual mouse. M. Survival of *Myd88$^{fl/fl}$CD4^{Cre}* mice after 27G TAC analyzed by Mantel-Cox test. (n=4 Sham mice per each genotype, n=11 T-MyD88$^{+/+}$ TAC, n=10 T-MyD88$^{-/-}$ TAC). Statistical analysis by 2-way ANOVA with Sidák's multiple comparison test (All except I) or T-test (I), p values shown.

TAC (Figure 2-17H-I). Moreover, T-MyD88$^{-/-}$ mice also exhibited increased cardiac CD11b^{+}CD11c^{+}MHC-II^{+} dendritic cells and CD11b^{+}CCR2^{+}MHC-II^{+} myeloid cells, but similar neutrophils (Figure 2-19A-D), and we did not observe changes in splenic or mediastinal T-regs at baseline or during TAC (Figure 2-19F-G).

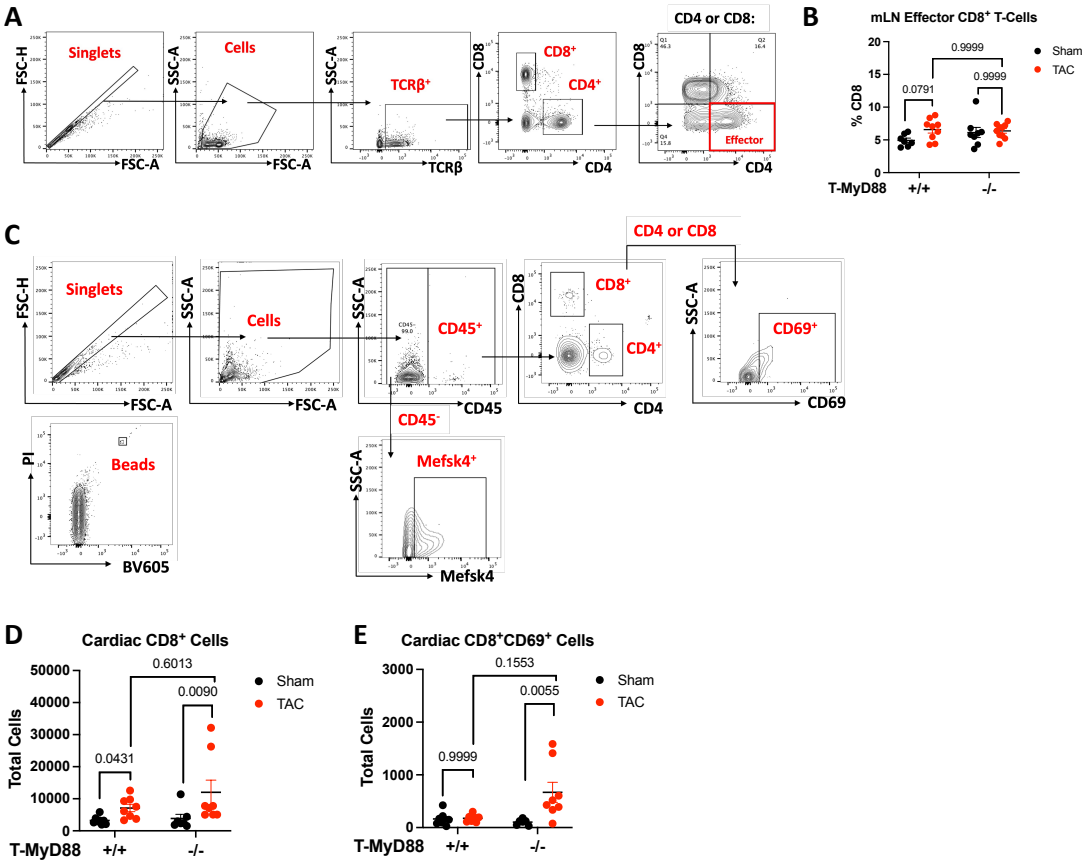


Figure 2-18 Flow Cytometric Analysis of Cardiac Inflammation in Myd88$^{fl/fl}$CD4^{Cre} mice
8-10 week male and female *Myd88$^{fl/fl}$CD4^{Cre}* mice using Cre^{+} and Cre^{-} littermates underwent 27G TAC or Sham surgery and were harvested after 4 weeks.. A. Lymph nodes or spleen were crushed followed by staining for analysis by flow cytometry, shown is gating strategy for effector CD4 and CD8 T-cells. B. Quantification of effector CD8 cells in the mLN. C. The LV of each group of mice was enzymatically and mechanically digested for analysis by flow cytometry, shown is gating strategy for cardiac T-cells and fibroblasts. D-E. Quantification of cardiac CD8 cells and CD69 expression. Each data point represents an individual mouse. Statistical analysis by Kruskal-Wallis test with Dunn's multiple comparison tests, p values shown

Overall increases in cardiac inflammation co-existed with increased levels of cardiac *Anp* in T-MyD88$^{-/-}$ TAC mice compared to T-MyD88$^{+/+}$, suggestive of cardiac damage (Figure 2-17J). Lastly, the decline in fractional shortening in response to TAC at 4 weeks was comparable between genotypes, despite the increased cardiac fibrosis and inflammation (Figure 2-17K). However, at 10 weeks post TAC, T-MyD88$^{-/-}$ mice had lower fractional shortening compared to T-MyD88$^{+/+}$, demonstrating enhanced systolic decline long term after TAC (Figure 2-17L). Moreover, survival post TAC was significantly decreased in T-MyD88$^{-/-}$ mice compared to T-MyD88$^{+/+}$ littermates (Figure 2-17M). Taken together, T-MyD88$^{-/-}$ mice subjected to TAC have unrestrained systemic and cardiac TCR activation

characterized by enhanced P-ZAP-70 expression as well as enhanced presence of CD69^{+} T cells and MHC-II^{+} myeloid cells. This demonstrates a central role for T-cell MyD88 in limiting T-cell activation through the TCR to modulate cardiac inflammation in HF.

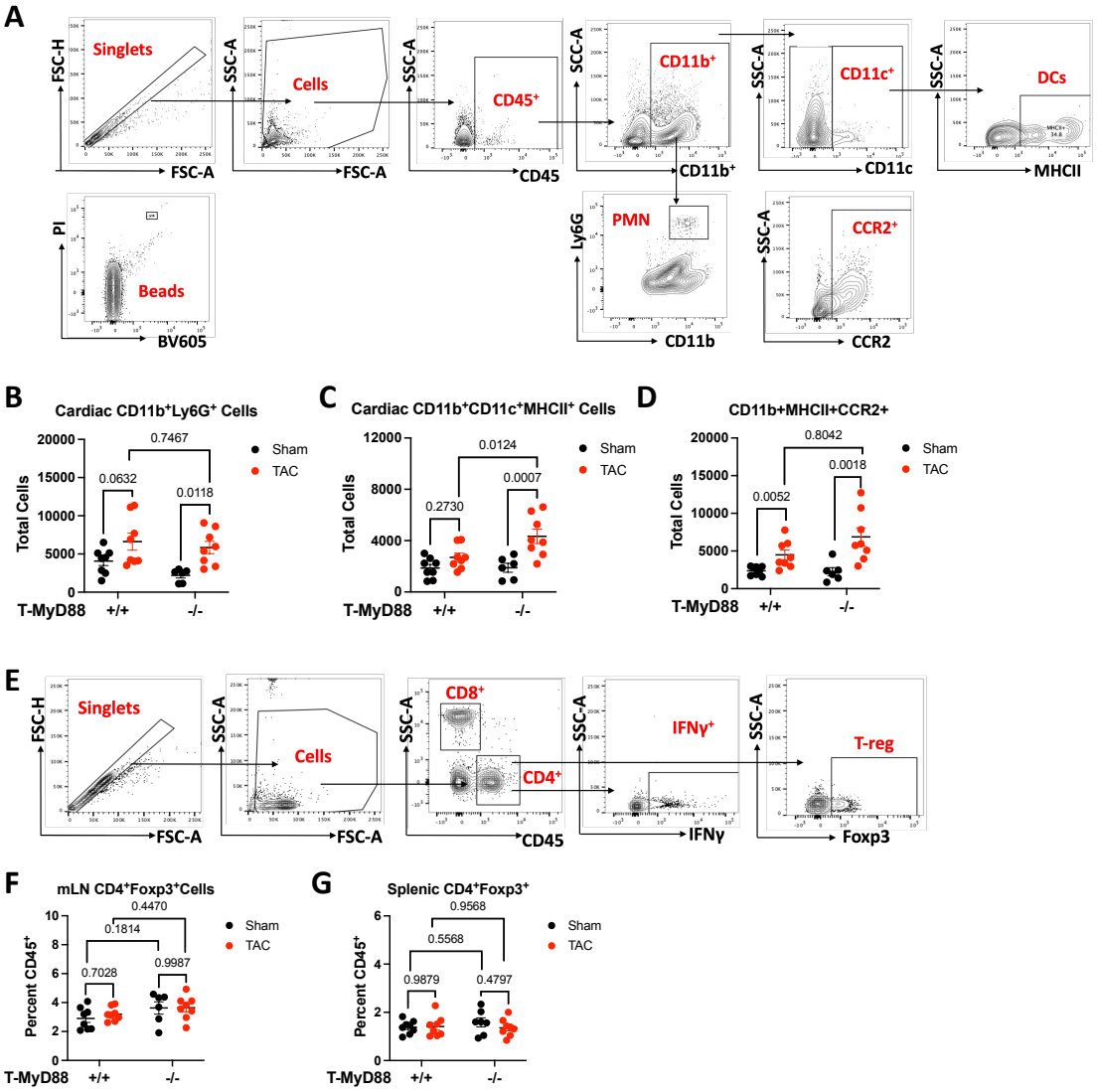


Figure 2-19 Continued Flow Cytometric Analysis of Cardiac Inflammation in Myd88$^{fl/fl}$CD4^{Cre} mice
8-10 week male and female *Myd88$^{fl/fl}$CD4^{Cre}* mice using Cre^{+} and Cre^{-} littermates underwent 27G TAC or Sham surgery and were harvested after 4 weeks. A. The LV of each group of mice was enzymatically and mechanically digested for analysis by flow cytometry, shown is gating strategy for cardiac myeloid populations, quantified in B-D. E. Lymph nodes or spleen were crushed followed by staining for analysis by flow cytometry, shown is gating strategy for in vivo IFNγ and Foxp3 expression, quantification of T-regs in F. mediastinal lymph nodes and G. spleen. Each data point represents an individual mouse. Statistical analysis by 2-way ANOVA with Sidák's multiple comparison test (B,C) or Kruskal-Wallis test with Dunn's multiple comparison tests (D), p values shown.

2.4 Discussion

Here we report that deletion of MyD88 in T-cells is detrimental for the heart and for survival in experimental non-ischemic heart failure. We find that Th1 cells, major drivers of cardiac fibrosis in response to TAC, survive longer, are more inflammatory, have enhanced cardiotropism, and greater adhesion to cardiac endothelial cells and fibroblasts when lacking MyD88. We demonstrate for the first time, to our knowledge, the expression of MyD88 in cardiac mouse and human T-cells, and its localization to the TCR upon TCR engagement. Moreover, we show evidence that MyD88 functions as a brake of T-cell activation upon TCR signaling, rather than solely modulating TLR signaling induced by DAMPs, its classical function in innate cells. This represents a novel T-cell modulatory mechanism involved in cardiac inflammation, fibrosis, and dysfunction in experimental HF.

The pro-inflammatory role of MyD88 in myeloid cells is well established. It triggers pro-inflammatory cytokine secretion, and induces the expression of major histocompatibility complex type II (MHC-II) in antigen presenting cells for an optimal T-helper cell immune response.[99] In contrast, its role in adaptive immune cells is not well understood, and even less so in the context of cardiac inflammation. The only study investigating a role for MyD88 in pressure-overload induced HF showed that global cardiac MyD88 deletion conferred a partial protection in response to TAC. However this used a non-cell specific approach, and therefore protection was likely conferred through inhibition of DAMP signaling in innate immune cells.[364] Our data provide evidence that in contrast to its role in innate immune cells in cardiac inflammation, in T-cells, MyD88 plays an anti-inflammatory role, which we hypothesize contributes to the partial protection was observed with global cardiac MyD88 deletion.

We have previously shown that Th1 cell production of IFNγ is essential for the induction of cardiac fibrosis in TAC[229], therefore we hypothesized that MyD88 might modulate IFNγ expression in addition to T-cell activation. However, our findings

demonstrate that the lack of MyD88 did not result in changes to Th1 identify, as seen by IFNγ or Tbx21 levels in *in vitro* differentiated T cells as well as *in* vivo during TAC. This somewhat differs from a described role for T cell MyD88 in the Th1/Th17 response to LPS injection and ovalbumin (OVA) immunization.[379] Isolated T cells from LPS and OVA treated mice re-stimulated and expanded for OVA *ex vivo* had decreased IFNγ and IL-17 expression, despite similar proliferation and T-reg frequency. While the proliferation and T-reg frequency are in line with our results in mice subjected to TAC, the differences in the IFNγ response could be attributed to different TCR stimuli *in vitro* (OVA vs anti-CD3/anti-CD28) and different inflammatory conditions *in vivo* (LPS/OVA vs TAC). Moreover, we show that cardiac DAMPs do not further induce activation marker expression on T cells, while LPS, used in that report, is a more potent activator of TLR4. Thus, the context of T-cell activation may differently influence the outcome of MyD88-TCR signaling in these two distinct inflammatory settings. Along these lines, our results demonstrating that MyD88 functions as a brake for T cell effector function is in agreement with studies showing that T-MyD88$^{-/-}$ mice had slowed growth of melanoma.[118] When MyD88 was deleted using the *Foxp3* Cre driver, authors reported no difference in T-reg numbers, in line with our results, but worse allograft survival, potentially a result of enhanced T-cell effector function.[155]

While T-cell effector function was broadly enhanced in the absence of MyD88, we mainly found functions regulated directly by TCR signaling to be enhanced in *Myd88*$^{-/-}$ Th1 cells. For example, TCR signaling directly influences cytokine secretion, cell survival, and T-cell adhesion,[378] and specifically, p-AKT signaling has been previously shown to regulate integrin activation on T-cells.[380] Thus, we propose that the increased adhesion to protein ligands, endothelial cells, and CFBs observed in *Myd88*$^{-/-}$ Th1 cells is a direct result of MyD88 modulation of TCR induced AKT signaling. This is further supported by our *in vitro* studies showing that enhanced adhesion to ICAM-1 and VCAM-1 of *Myd88*$^{-/-}$ Th1 cells was dependent on PMA treatment, a mimic of active TCR stimulation known to induce p-AKT.

We hypothesize increased T-cell endothelial interaction might further contribute to perivascular fibrosis. On the contrary, the lack of alteration to Th1 polarization or chemotaxis to CXCL10 in *Myd88*$^{-/-}$ Th1 cells would be explained by the fact that these two are more dependent on cytokine receptor or G-protein coupled receptor signaling, respectively, both of which operate mostly independently from the TCR.[381,382] Further studies depicting how MyD88 specifically regulates these signals are needed to explain why many, but not all T-cell effector functions are enhanced in *Myd88*$^{-/-}$ Th1 cells. TCR signaling is intimately associated with cell survival, and as such, we found that *Myd88*$^{-/-}$ Th1 cells exhibited a survival advantage both *in vivo* and *in vitro.* However, we have yet to fully elucidate the mechanism of cell death regulated by MyD88, whether that be apoptosis as suggested by our RNA-seq results, or other pathways including inflammatory cell death. In contrast to the survival advantage conferred by MyD88 deletion in T-cells that we outline here, we were surprised to see similar cellular proliferation in response to CD3/CD28 stimulation or IL-2 *in vitro*. While MyD88 might be more specific to pro-survival signaling, it is possible that MyD88 modulates proliferation *in vivo* in a more complex inflammatory environment with DAMPs and TCR co-stimulation.

While we originally thought that sensing of cardiac DAMPs would be a major factor influencing Th1-MyD88 signaling, we found that DAMPs either alone or in combination were unable to modulate T-cell activation *in vitro.* One study has shown a protective role for HMGB1 in TAC, however other studies have disputed this.[218,383] Our RNA-seq data and *in vitro* studies stimulating T-cells with cardiac lysate and DAMPs suggest that this is not the case during sterile inflammation in the heart. Our results demonstrate that the absence of MyD88 alters T-cell effector function in response to TCR engagement and in the absence of TLR stimulation *in vitro.* Additionally, it has been well described that TLR ligation can act as a co-stimulatory signal for T-cell activation and influence T-cell polarization.[148,149] While we did not explicitly test this, it is possible that in a more complex scenario *in vivo,* DAMP

agonism of TLRs in Th1 cells among other cells also contribute to cardiac fibrosis and inflammation, in line with studies reporting that DAMP sensing by CFB can contribute to fibrosis.[384,385] More work in the field is warranted to investigate potential crosstalk between TLR / DAMP receptors and TCR signals through MyD88 or other adaptors in distinct inflammatory and infectious settings.

To our knowledge, this is the first investigation of a T-cell specific deletion for MyD88 in sterile cardiac inflammation, which we characterized using both adoptive transfer and endogenous genetic deletion. In the T-MyD88$^{-/-}$ mouse, we found no baseline changes in cardiac function or T-cell subsets in the heart and lymphoid organs, and no baseline expression of P-ZAP70 in T cells, immediately downstream TCR engagement. The increased phosphorylation of ZAP-70 in T-MyD88$^{-/-}$ mice compared to T-MyD88$^{+/+}$ control littermates in the onset of TAC further support that MyD88 modulates T-cell cardiac inflammation through TCR mediated activation secondary to cardiac insult, rather than non-specific DAMP induced signals. One limitation of this mouse model is that the CD4-Cre driver also excises MyD88 from double positive CD4/CD8 T-cells during thymic development, thus MyD88 is also deleted in CD8^{+} T-cells. And indeed, we found increases in CD8^{+}CD69^{+} T-cells in the heart. Our adoptive transfer approach of Th1 cells into T-cell deficient mice eliminates any confounding effects from other T-cell subtypes, and in fact showed earlier systolic decline than the T-MyD88$^{-/-}$ mice post TAC. Moreover, our observation that T-MyD88$^{-/-}$ mice have worsened survival to TAC further emphasizes the necessity of T-cell MyD88 in limiting chronic inflammation in HF in the context of a fully intact immune system.

Both our adoptive transfer and genetic approach for MyD88 deletion in T-cells showed significantly increased cardiac fibrosis, which we attribute to increased T-cell survival and enhanced fibroblast activation. We have previously shown that CD4 cells co-localize with CFB *in vivo*[226] and that their contact is required for myofibroblast

transformation *in vitro.*[229] As such, we conclude while IFNγ was not enhanced on a per cell basis, the overall increased presence of highly inflammatory T-cells resulted in greater T-cell fibroblast cross-talk and as such, greater fibrosis. Moreover, our findings in T-MyD88$^{-/-}$ mice provide evidence that the fibrotic response resulting by the lack of MyD88 in T cells is in part due to overactivated CD4^{+} and CD8^{+} T cells unable to tune down TCR signals, as seen by increased P-ZAP70 and CD69. However enhanced T-cell function further contributed to an overall increased proinflammatory and profibrotic milieu consisting of increased MHC-II^{+} myeloid cells, able to continue to reactivate T-cells. Together, this potent inflammatory environment increased fibrosis. While to thoroughly determine whether T-cell MyD88 modulates CFB proliferation and/or myofibroblast transformation, Periostin-Cre lineage tracing would be required,[386,387] our results suggest that the lack of MyD88 in T cells results in enhanced CFB activation given the increased presence of PDGFRα^{+} αSMA^{+} CFBs, rather than increased proliferation at this time post TAC. It is possible that T-cell MyD88 modulates CFB proliferation at earlier time points post TAC[388]and thus we see more total activated CFBs at this time point. Nevertheless, the increased T cell activation and survival of MyD88$^{-/-}$ T cells results in a heightened fibrotic response dependent on TGFβ, collagen III and fibronectin. It is further plausible that enhanced binding by MyD88$^{-/-}$ Th1 cells increases fibroblast transformation due to stronger collective mechanical force, and while we did not explicitly test this, future studies aim to further define mechanisms of T-cell CFB interaction.

Despite these interesting and novel findings, our study has some limitations we would like to outline. Given the altered fibrotic response and the worsened survival to cardiac stress observed in the absence of T-cell MyD88, one can speculate that cardiac stiffness may lead to diastolic dysfunction and contributes to less survival to TAC, in addition to the systolic dysfunction we report, yet we have not performed hemodynamics studies to thoroughly characterize the role of T-cell MyD88 in cardiac relaxation. While we

demonstrate a modulatory role for T-cell MyD88 in pressure overload HF, this role may be different in other models of sterile or infectious inflammation. We focus on Th1 cells, but our data indicate that MyD88 might contributes similarly to $CD8^+$ T-cell activation, which has other implications in contexts more dependent on a cytotoxic T-cell response, such as cancer or immune checkpoint-induced myocarditis.[208,389] Mechanistically, while we demonstrate the first evidence that MyD88 co-localizes with the TCR during active TCR engagement and modulates immediate downstream signals such as ZAP70 and AKT, the exact molecular binding partner(s) that recruit or limit MyD88 access to the TCR signaling complex to modulate T-cell activation remain an ongoing area of investigation. We hypothesize that the strength of TCR stimulation alongside other signals that recruit MyD88 will influence the degree of MyD88 localization to the TCR vs. other locations or outcomes.

The different role we report for MyD88 in T-cells vs. innate immune cells in the context of DAMP signals might explain the limited of efficacy of clinical trials targeting DAMPs such as IL-1β, whereas a more targeted approach modulating the signaling effectors such as MyD88 might prove more effective[55,390].

2.5 Author contributions

A.L.B designed the project, performed experiments, analyzed data, and wrote the manuscript. S.S. and K.K. performed experiments and edited the manuscript. N.N. and A.H. designed and performed experiments. M.A. performed all TAC surgeries. K.L. and J.A. generated and analyzed the human single cell data, and K.S. and S.S. analyzed the mouse single cell data. P.A. designed the project, provided intellectual support, and edited the manuscript.

2.6 Acknowledgements

This work was supported by National Institute of Health (NIH) Grants R01 HL123658 and R01 HL144477 (P.A.), American Heart Association (AHA) Pre-Doctoral Fellowship

906361 (A.L.B.), NIH F30 Grant HL162200 (A.L.B.), F31 Grant HL159907A (S.S), and NIH F31 Grant HL140883 (N.N.), and AHA Pre-Doctoral Fellowship 826325 (J.M.A). K.L is supported by: NIH Grants P30AR073752, R01 HL138466, R01 HL139714, R01 HL151078, R01 HL161185, and R35 HL161185, Leducq Foundation Network (#20CVD02), Burroughs Welcome Fund (1014782), and Children's Discovery Institute of Washington University and St. Louis Children's Hospital (CH-II-2015-462, CH-II-2017-628, PM-LI-2019-829), Foundation of Barnes-Jewish Hospital (8038-88), and generous gifts from Washington University School of Medicine. S.S. and K.S. are supported by R01 AI142005-01. Additional thanks to Albert Tai at Tufts University for help in analyzing bulk RNA-seq data, and the Poltorak lab for assistance with *in vitro* cell death assays. Biorender was used to generate figures. The authors declare no competing interests.

Chapter 3 Cardiac Fibroblast MyD88 Regulates TGFβ-Induced Myofibroblast Transformation

---

Bayer, A. L., Smolgovsky, S., Theall, B., Emig, R., & Alcaide, P. Cardiac Fibroblast MyD88 Regulates TGFβ Induced Myofibroblast Transformation. *In Preparation.*

3.1 Introduction

When cardiac tissue is damaged or undergoes stress, cardiac fibroblasts (CFB) aid in an immediate response to repair insults of a wide variety. In the case of chronic hypertension leading to heart failure (HF), CFB quickly adapt to increased myocardial stress by differentiating into myofibroblasts and promoting fibrosis, which includes the deposition of extracellular matrix and subsequent cardiac wall stiffening.[243,391] Hypertensive stress activates a variety of pathways systemically, including the renin-angiotensin-aldosterone system.[392] Angiotensin II not only is hypertensive itself, but can directly act on CFB to transform to myofibroblasts, secrete collagen, and produce the pro-fibrotic cytokine TGFβ.[393–395] TGFβ is one of the most potent triggers of myofibroblast transformation,[254] however clinical trials targeting TGFβ have largely been unsuccessful in cardiovascular disease,[396] indicating additional mechanistic studies of the CFB response to TGFβ are needed.

Systemic inflammation has become a hallmark in most etiologies of HF, which includes both the innate and adaptive immune responses.[397] Specifically, the activation of T-cells and subsequent infiltration into cardiac tissue is a critical driver of adverse cardiac remodeling under stress, including their ability to promote cardiac fibrosis through secretion of pro-fibrotic factors or direct interaction with CFB.[231,244,398] In turn, CFB participate in the propagation of cardiac inflammation through cytokine and chemokine production, antigen presentation, and direct recognition of immunologic triggers.[194] CFB have been shown to express a variety of pathogen recognition receptors (PRRs) including Toll-Like Receptors (TLRs) and their central adaptor, Myeloid Differentiation Response Factor 88 (MyD88).[270,271] In myeloid cells, MyD88 mediates the response to pathogen associated molecular patterns (PAMPs) or damage associated molecular patterns (DAMPs) to initiate an innate inflammatory response.[397] While in CFB, TLR-MyD88 signaling axis is functional in response to cardiac PAMPs and DAMPS,[270,399] increasing evidence has shown that MyD88 can act in

different roles in a cell specific manner. Our group has shown in multiple settings of sterile inflammation that T-cell MyD88 acts as an anti-inflammatory break to limit T-cell overactivation,[220,400] and we recently showed the ability of MyD88 to bind with non-canonical signaling partners in T-cells (CITE JI). Further, MyD88 has been implicated in TGFβ signaling in non-cardiac cell types.[401,402] However, if MyD88 plays an additional role outside of TLR signaling in the CFB response to TGFβ has not yet been studied.

We hypothesized that MyD88 mediates myofibroblast transformation downstream of TGFβ signaling and regulates cardiac fibrosis. Using preclinical mouse models of cardiac fibrosis, we show only partially T-cell dependent fibrosis, leading to myofibroblasts that downregulate MyD88 expression in the failing heart and in response to TGFβ. TGFβ acts both transcriptionally and through the Ubiquitin Proteasome System (UPS) to downregulate MyD88, which in turn enhances downstream TGFβ signaling through interaction with SMAD4. We show that deletion of MyD88 *in vitro* or *in vivo* increases TGFβ responsiveness and subsequent fibrotic remodeling, and together provide novel mechanistic insight into fibrotic transformation with several potential novel therapeutic targets.

3.2 Methods

3.2.1 Animals, PE-ANGII, and TAC Models:

All animal studies were approved by the Tufts University Institutional Animal Care and Use and Care Committee. C57BL/6J, global MyD88$^{-/-}$ mice, [369] and TCR-/- mice[367] were bred and maintained under pathogen free conditions. Tcf21^{Cre+}-Myd88$^{l/fl}$ mice (CFB-MyD88$^{-/-}$) were generated by crossing Myd88$^{fl/fl}$ mice [369] with Tcf21^{Cre+} mice.[231] All CFB-MyD88$^{-/-}$ mice were given 75 mg/kg Tamoxifen by IP injection for 5 days prior to experimental use. Myd88 excision was determined by polymerase chain reaction (See Appendix 9.10 for primer sequences). For phenylephrine / angiotensin II model, male and female mice aged 8-12 weeks old underwent osmotic minipump implantation (Alzet Model 2004) and were infused with 1.5 mg/kg/day angiotensin II (Selleckchem P1085 and 50 mg/kg/day phenylephrine (Sigma P6126) compared to sterile saline, then tissues were harvested after 28 days. For transverse aortic constriction, pressure overload was induced by minimally invasive TAC surgery to constrict the transverse aorta using a 27G needle, then tissues were harvested after 28 days. Sham operated mice underwent the same operation without aortic constriction. A minimum sample size of 6 mice per group was calculated to detect statistically significant changes in cardiac function with a power of >80% and $\alpha = 0.05$. Randomization for each group was performed by a random number generator (https://www.calculator.net/random-number-generator.html), and all analyses were done blinded using an ID number assigned by a third party.

3.2.2 Flow Cytometry:

Hearts were excised from mice and perfused with PBS, then minced and digested enzymatically with 0.895 mg/mL collagenase II (Gibco 17101-015). Single cell suspensions were generated from cells in culture or lymphoid organs using a 40 μm cell strainer. Blood samples were first RBC lysed using RBC lysis buffer (Biolegend 420302)

according to the manufacturer's instructions, then leukocytes were pelleted before staining. Samples were stained using the following antibodies from Biolegend: CD4 APC-Cy7 (100414), CD8 BV711 (103057), CD8 Percp (100732), CD31 FITC (102406), CD45.2 BV421 (109832), CD11b Percp (101230), CD44 APC (103012), CD62L PE (104408), CD4 Spark UV 387 (100492), CD3 APC-Cy7 (100222), CD3 BV605 (100237), PDGFrα APC (139507), or other sources: CD45.2 BUV805 (BD 569200), AF350 FAP (R&D FAB9727U). Samples were surface stained by incubation with the relevant antibodies listed above diluted 1:100 in phosphate buffered saline (PBS) + 2% FBS for 20 minutes at 4°C. Data was acquired on a Cytek Aurora spectral cytometer (Cytek Biosciences) and analyzed using FlowJo software Version 10.10.0. For FACS sorting of cardiac fibroblasts, hearts were digested to single cell suspensions as described above, pooled 2 hearts per sample, then stained with the following antibodies: CD31 FITC (102406), CD45.2 BV421(109832), APC Mefsk4 (Miltenyi 130-120-166) then sorted on CD31-CD45-Mefsk4+ cells using a Thermofisher Bigfoot with 5 laser configuration.

3.2.3 Echocardiography:

Mice were sedated using isoflurane on a heated stage in supine position. Heart rate and respiratory rate were continuously monitored via stage electrodes. Depilatory cream (Nair) was applied to the chest to remove fur, and ultrasonic gel was applied to a 22-55 MHz echocardiography transducer (MS550D Vevo 2100, Fujifilm VisualSonics) to obtain parasternal short axis views of the left ventricle in M-mode with a target heart rate of 400-500 bpm. Cardiac parameters and heart rate were measured by averaging the values from 5 cardiac cycles. All analyses were performed blindly using Vevo 2100 software version 2.2.0 (Build 12089).

3.2.4 Histologic Analysis:

Picrosirius Red (PSR): Cardiac samples were fixed in 10% formalin, embedded in paraffin, and cut in 6 μm sections. Collagen was stained in 0.1% Direct Red 80 (Sigma 365548) in saturated picric acid (Sigma P6744) for 1 hour, followed by hematoxylin counter stain (Sigma GHS2128) for 1 minute. Slides were washed with 0.5% acetic acid twice before dehydration and mounting. Fibrosis was quantified by positive threshold on ImageJ (Version 1.53t) to exclude non-specific signal from counter-stained nuclei. **H&E:** Formalin fixed cardiac samples were stained with hematoxylin (Sigma GHS2128) followed by 1% Eosin Y solution (source) before dehydration and mounting. Cardiomyocyte size was measured by ImageJ (Version 1.53t) in axial areas including nuclei.

3.2.5 Analysis of scRNA-seq:

Single cell data was downloaded from the following datasets: PE-ANGII (GSE218392)[52], TAC (GSE133054)[403], Human (GSE218392 – only donor and non-ischemic cardiomyopathy).[52] Seurat objects were created using Seurat Version 4, then normalization and dimensional reduction were conducted using scTransform V2 function and analyzed using basic Seurat functions. Fibroblasts were identified using *Pdgfra* expression and additional ECM transcripts. *Postn, Myd88,* and *Smurf2* expression were visualized using FeaturePlot or VlnPlot functions. Cells were subsetted based on *Postn* expression greater or less than 3.0, then differential gene expression analysis was performed using FindMarkers with a significance cutoff of $p < 0.05$.

3.2.6 Culture of Primary Cardiac Fibroblasts:

Adult mice (7-12 week old) were anesthetized, then hearts were excised, perfused with PBS, minced, and digested using 2 mg/mL Collagenase I (Gibco17100016) for 30 minutes with intermittent agitation. Digested tissue was pelleted at 300g for 10 minutes,

then resuspended in fibroblast growth media – DMEM (Gibco 11995-065) + 10% FBS, Penicillin/streptomycin (ThermoFisher 15140122), insulin-transferrin-selenium (Sigma I3146), and plated on 0.1% gelatin coated plates for 2 hours at 37°C. After this time, non-adherent cells were removed and fresh media was added. Cells were used through passage 3. Where indicated, cells were treated with 100 ng/mL recombinant TGFβ (Peprotech 100-21-10ug) or 10 nm Bortezomib (Sigma 5043140001). Healthy human LV fibroblasts were purchased from Promocell (C-12375) or gifted from Dr. Navin Kapur at Tufts Medical Center, isolated from LVAD core samples taken from patients with diagnosed heart failure.

3.2.7 siRNA Knockdown:

Primary mouse cardiac fibroblasts were cultured as described above. 50 pm siRNA (See Table 1 for sequences) was transfected using Lipofectamine 3000 (Sigma L3000015) according to manufacturers instructions, then cells were collected after 48 hours for analysis. Where indicated cells were treated with 100 ng/mL recombinant TGFβ beginning 24 hours after transfection for an additional 24 hours.

3.2.8 Immunoblotting:

Cells were lysed in RIPA buffer supplemented with protease and phosphatase inhibitors then cleared by centrifugation at 4°C at 13,000 xg. For fractionation: Cells were lysed for membrane fractions with with 50 mM Tris pH 8.0, 2.5 mM EDTA, 0.1% NP40 and 10% glycerol, then nuclei were pelleted and lysed with 50 mM Tris pH 8.0, 2.5 mM EDTA, and 0.25% SDS. Protein concentrations were determined using DC protein assay (BioRad 5000112) and equal amounts of protein were subjected to SDS-PAGE, then transferred to PVDF membranes, followed by blocking with Tris buffered saline + 0.1% Tween20 containing 5% non-fat milk for 1 hour at room temperature. Immunoblotting was performed overnight at 4°C using antibodies diluted 1:1000 in 5% non-fat milk or 5%

BSA for phosphor-antibodies. Antibody sources: pSMAD2 (CST), SMAD2 (CST), SMAD4 (CST), Smurf2 (NovusBio), Ubiquitin (Santa Cruz), Beta-Actin (CST), Histone H3 (CST), GAPDH (CST 2118) aSMA (Thermo), MyD88 (CST), MyD88 (R&D), Collagen I (Thermo) Blots were then incubated with the appropriate HRP peroxidase conjugated secondary antibody (1:2000, Rabbit CST 7074, Mouse CST 7076, Goat) at room temperature for 1 hour, then developed using Pierce ECL (ThermoFisher 32106) and imaged using a ChemiDoc XRS+ System (Biorad). Band intensity was quantified using Image-J.

3.2.9 Immunoprecipitation:

For Ub/MyD88 Denaturing IPs: Cells were lysed in 50 mM Tris pH 7.1, 150 mM NaCl, 0.5% NP-40, 1% SDS for denaturing conditions, followed by dilution 1:10 in lysis buffer without SDS. For SMAD4 IP: Cells were lysed in 50 mM Tris-HCl (pH 7.2-7.4) with 1% NP-40, 0.1% Triton X-100, 150 mM NaCl, 1 mM EDTA, 1 mM EGTA, supplemented with protease and phosphatase inhibitors (Roche 4906845001, 4693159001). All lysates were incubated for 30 minutes on ice before clearing by centrifugation at 4°C at 13,000 g. Protein concentrations were determined using DC protein assay (BioRad 5000112). Protein A/G beads (Thermofisher 88802) were incubated with antibodies against SMAD4 , MyD88, or Ub (see above) for 2 hours rotating at 4°C. Equal concentrations of cell lysate were incubated rotating with antibody bound beads overnight at 4°C. Beads were separated by magnet, washed 3 times with lysis buffer, then eluted with SDS loading buffer for 20 minutes at 95°C before SDS-PAGE, followed by immunoblotting as described above.

3.2.10 RT-qPCR:

Cell lysis and RNA isolation was performed using an RNeasy kit according to manufacturer’s instructions (Qiagen 74004). For cardiac RNA isolation, LV samples were

crushed in Trizol (Qiagen 79306), RNA was chloroform extracted and separated by centrifugation, then the aqueous phase was combined with 70% ethanol and applied to RNAeasy columns. cDNA synthesis was performed using High-Capacity cDNA Reverse Transcription Kit (ThermoFisher 4368814), and qPCR was performed using SYBR Green (ThermoFisher A25741) on a QuantStudio 6 Flex Real-Time PCR Machine (ThermoFisher). See Appendix 9.10 for primer sequences.

3.2.11 Gel Contraction:

Primary cardiac fibroblasts were cultured as described above. Cells were passaged and 100,000 cells were embedded in Collagen Matrix (Advanced Biomatrix 5074) in a 24 well plate, which was allowed to solidify at 37C for 30 minutes. Gels were then released, where indicated 100 ng/mL recombinant TGFβ was included in culture media, then gels were monitored for 24 hours, after which they were imaged and ImageJ was used to quantify area to calculate percent contraction.

3.2.12 MyD88 Overexpression:

Adenoviral vectors and were designed with VectorBuilder, and virus was produced by VectorBuilder. Viruses contained codon-optimized MyD88 cDNA under the control of a CMV promoter and eGFP tag, compared to empty vectors with eGFP alone. Fibroblasts were plated at 100,000 cells per well of a 6 well plate, then virus was added at an MOI of 1:250 in serum free media for 6 hours, then supplemented with 2% FBS media overnight, followed by a complete media change after 24 hours. When indicated, cells were treated with 100 ng/mL TGFβ, and collected after an additional 24 hours.

3.2.13 Immunofluorescence:

Coverslips or tissues were washed 2 x 10 min. with PBS, then fixed with 4% PFA for 15 minutes. Samples were washed with PBS, then incubated with PBS + 10% normal goat serum and/or 10% donkey serum (depending on species of secondary antibody), and

0.1% triton-X for intracellular staining for 1 hour at RT. Samples were incubated with the following primary antibodies where indicated: α-alpha smooth muscle actin (αSMA, Sigma A2547), mouse PDGFrα (R&D AF1062), Human PDGFrα (R&D AF-307-NA), MyD88 (CST 4283), Smad4 (CST 46535) at 1:100 in blocking buffer overnight at 4°C. Samples were washed with PBS then incubated with the appropriate secondary antibody (Thermo A32766, Thermo A11055, Thermo A21432, Thermo A78966, CST 4413) at 1:200 in blocking buffer, then mounted in Vectashield with DAPI (Southern Biotech, 0100-20). Visualization was performed with a Nikon Ti inverted fluorescence microscope or a Leica DMi8 inverted fluorescence microscope.

3.2.14 Statistical Analysis:

Statistical analysis was performed using GraphPad Prism 9.4.1. All data are presented as mean ± standard error of the mean (SEM). Statistical analysis was done by Student's unpaired or paired t-test (where indicated) for two group analysis. Multiple group comparisons were done using one-way ANOVA with Tukey's multiple comparison test or two-way ANOVA with Sidak's multiple comparison test. Differences were considered statistically significant at $p \leq 0.05$.

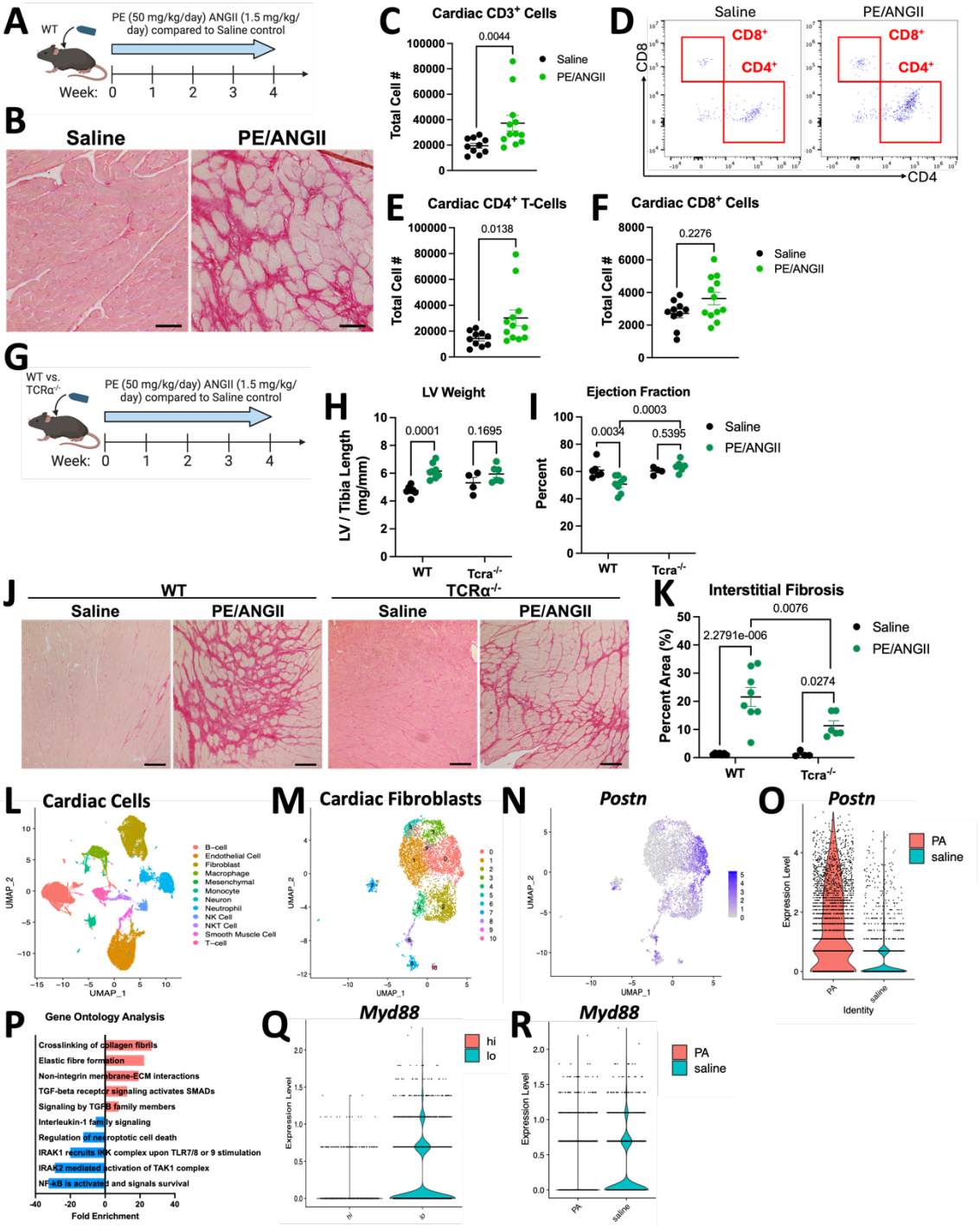
3.2.15 Data Availability;

The data, methods, and materials will be available to other researchers for the purposes of reproducing the results or replicating procedures.

3.3 Results

3.3.1 PE-ANGII Infusion Induces Partially T-cell Independent Fibrosis:

As T-cells have been shown to participate in the fibrotic response to Angiotensin-induced hypertension,[232,234] we first evaluated cardiac T-cell infiltration in the well-established Phenylephrine/Angiotensin II (PE/ANGII) infusion model of fibrosis (Figure 3-1A). We implanted PE/ANGII-secreting osmotic minipumps in wild type (WT) mice and after 4 weeks, we observed the significant interstitial fibrosis by picrosirius red staining in mice given PE/ANGII compared to saline controls, as expected. (Figure 3-1B). We then used flow cytometry on left ventricular (LV) samples from these mice and measured cardiac immune cells, finding an increase in $CD3^+$ T-cells in PE/ANGII mice (Figure 3-1C, 3-2A) but no changes to overall $CD11b^+$ myeloid cells at this time point (Figure 3-2B). When we further evaluated T-cell subtypes, we found a significant increase in cardiac $CD4^+$ T-cells with a trending increase in $CD8^+$ T-cells as well (Figure 3-1D-F) in PE/ANGII mice compared to saline. We next sought to evaluate if chronic fibrosis was dependent on cardiac T-cell infiltration, as we have shown in pressure overload.[244,404] We subjected WT and *Tcra*$^{-/-}$ mice to PE/ANGII infusion (Figure 3-1G), and found that while both WT and T-cell deficient mice developed cardiac hypertrophy in response to PE/ANGII (Figure 3-1H), only WT mice developed a significant drop in ejection fraction as measured by echocardiography (Figure 3-1I). Further, when we measured cardiac fibrosis, we found that while *Tcra*$^{-/-}$ mice developed significantly less cardiac fibrosis than WT mice, they still developed a considerable amount of fibrosis (Figure 3-1J-K). These data evidence that while T-cells contribute to cardiac fibrosis, other T-cell independent mechanisms contribute to fibroblast activation and the fibrotic response.



3.3.2 Cardiac Fibroblasts Downregulate Inflammatory MyD88 Signaling in Response to PE-ANGII:

To probe for potential mechanisms intrinsic to fibroblast that might contribute to fibrosis in *Tcra*$^{-/-}$ mice, we leveraged a publicly available single cell RNA-sequencing

Figure 3-1 PE-ANGII Induces Partially T-cell Independent Fibrosis and Downregulates MyD88-Associated Inflammatory Signaling
A. WT mice aged 8-10 weeks (n=10-12 / group) were implanted with osmotic minipumps secreting 50 mg/kg/day phenylephrine and 1.5 mg/kg/day angiotensin II or saline, then euthanized after 4 weeks. B. Representative LV section stained with picrosirius red, scale bars are 50 uM. C-F. LVs were digested enzymatically and mechanically, then analyzed for cardiac T-cells by flow cytometry. Representative flow cytometry plots gated on CD3+CD11b- cells shown in D, with quantification for CD3+ cells (C), CD4+ T-cells (E) , or CD8+ T-cells (F). G. WT or Tcra$^{-/-}$ mice (n=6-8 / group) were implanted with osmotic minipumps secreting phenylephrine and angiotensin II or saline. H. Normalized LV weight. I. Ejection fraction was measured by echocardiography. J. Representative LV sections stained with picrosirius red, quantification shown in K, scale bars are 100 uM. L. UMAP display of all cardiac cells. M. UMAP of reclustered cardiac fibroblasts based on Pdgfra expression. N. Periostin expression of re-clustered cardiac fibroblasts. O. Violin plot of fibroblast Periostin expression in saline compared to phenylephrine/angiotensin II treated mice. P. Selected gene ontology analysis of Periostin hi compared to periostin lo fibroblasts. Q. Myd88 expression in Periostin hi compared to periostin lo fibroblasts. R. MyD88 expression in saline compared to phenylephrine/angiotensin II treated mice. Statistical analysis by Mann-Whitney test (C, E, F) or 2-way ANOVA with Sidak's multiple comparison test (H-K). P-values shown.

dataset from whole heart in mice subjected to PE/ANGII.[52] We first subsetted and re-clustered cardiac fibroblasts from all cardiac cells based on *Pdgfra* expression (Figure 3-1L-M). We then probed for *Postn* expression as a marker of myofibroblast transformation, finding several clusters to express high levels of *Postn* (Figure 3-1N), with overall highly increased *Postn* in PE/ANGII fibroblasts compared to saline (Figure 3-1O). We then subsetted fibroblasts based on their *Postn* expression, and performed differential gene expression analysis in *Postn*^{hi} compared to *Postn*^{low} cells. As expected, when we characterized differentially expressed genes by gene ontology analysis,

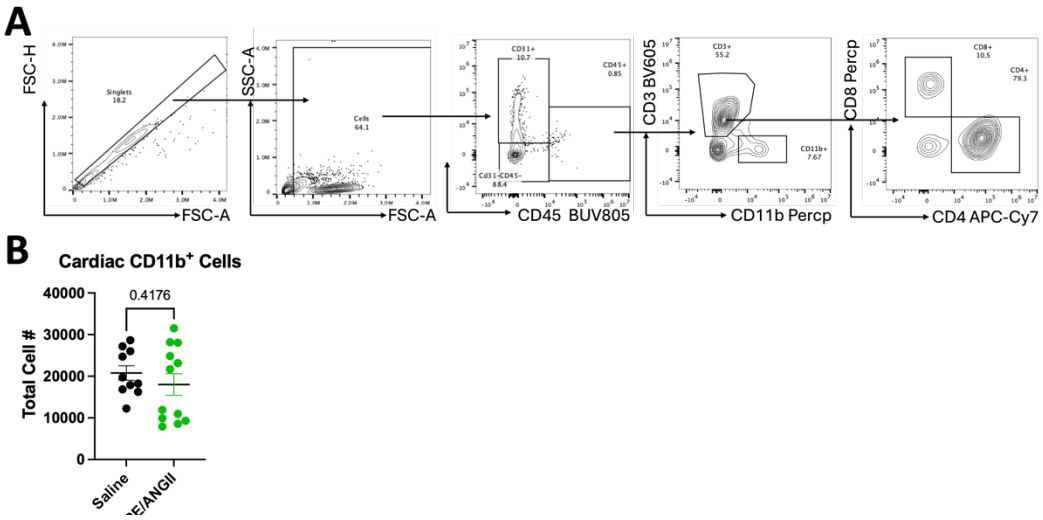


Figure 3-2 Gating Strategy for Cardiac T-cells
A. WT mice aged 8-10 weeks (n=10-12 / group) were implanted with osmotic minipumps secreting 50 mg/kg/day phenylephrine and 1.5 mg/kg/day angiotensin II or saline, then euthanized after 4 weeks. LVs were digested enzymatically and mechanically, then analyzed for cardiac T-cells by flow cytometry, shown is gating strategy. B.Cardiac CD11b cells quantified by flow cytometry. Statistical analysis by Mann-Whitney test. P-value shown.

fibroblasts from PE/ANGII mice had significant upregulation of genes involved in cardiac fibrosis and extracellular matrix production, as well as TGFβ signaling (Figure 3-1P). Interestingly, these cells had a downregulation of several different inflammatory pathways, including TLR, IL1, and NF-kB signaling, overall suggesting a transcriptomic shift from inflammatory to fibrotic (Figure 3-1P). The adaptor protein MyD88 is a central hub to all of these downregulated pathways and has further been implicated in TGFβ signaling in immune cells,[401] and as such we next probed for fibroblast *Myd88* expression. There was higher *Myd88* transcript in *Postn*^{low} compared to *Postn*^{hi} cells (Figure 3-1Q), and overall a downregulation of *Myd88* expression in PE/ANGII mice compared to saline (Figure 3-1R). This overall positioned MyD88 as a potential regulator of inflammatory to pro-fibrotic states of cardiac fibroblasts.

3.3.3 MyD88$^{-/-}$ CFB Exhibit Increased Transformation and Contractile Function at Baseline and in Response to TGFβ:

To test the hypothesis that MyD88 regulates fibroblast transformation, we evaluated the functional consequence of deleting MyD88 in fibroblasts. When we cultured MyD88$^{-/-}$ CFB *in vitro,* we found significantly elevated collagen I and α-smooth muscle actin (αSMA) at baseline in their lysates compared to WT, indicating increased myofibroblast transformation (Figure 3-3A-C). We observed enhanced αSMA stress fiber formation in MyD88$^{-/-}$ CFB compared to WT by immunofluorescence at baseline, which was further accentuated upon treatment after TGFβ treatment to induce transformation (Figure 3-3D-E). Similarly, TGFβ treatment induced greater *asma* and *postn* transcription in MyD88$^{-/-}$ compared to WT CFB (Figure 3-3F-G). While these data show increased myofibroblast markers in the absence of MyD88, we then used a gel contraction assay to evaluate myofibroblast contractility. We found that after 24 hours, untreated MyD88$^{-/-}$ fibroblasts set in collagen discs showed greater disc contraction then WT cells. Further,

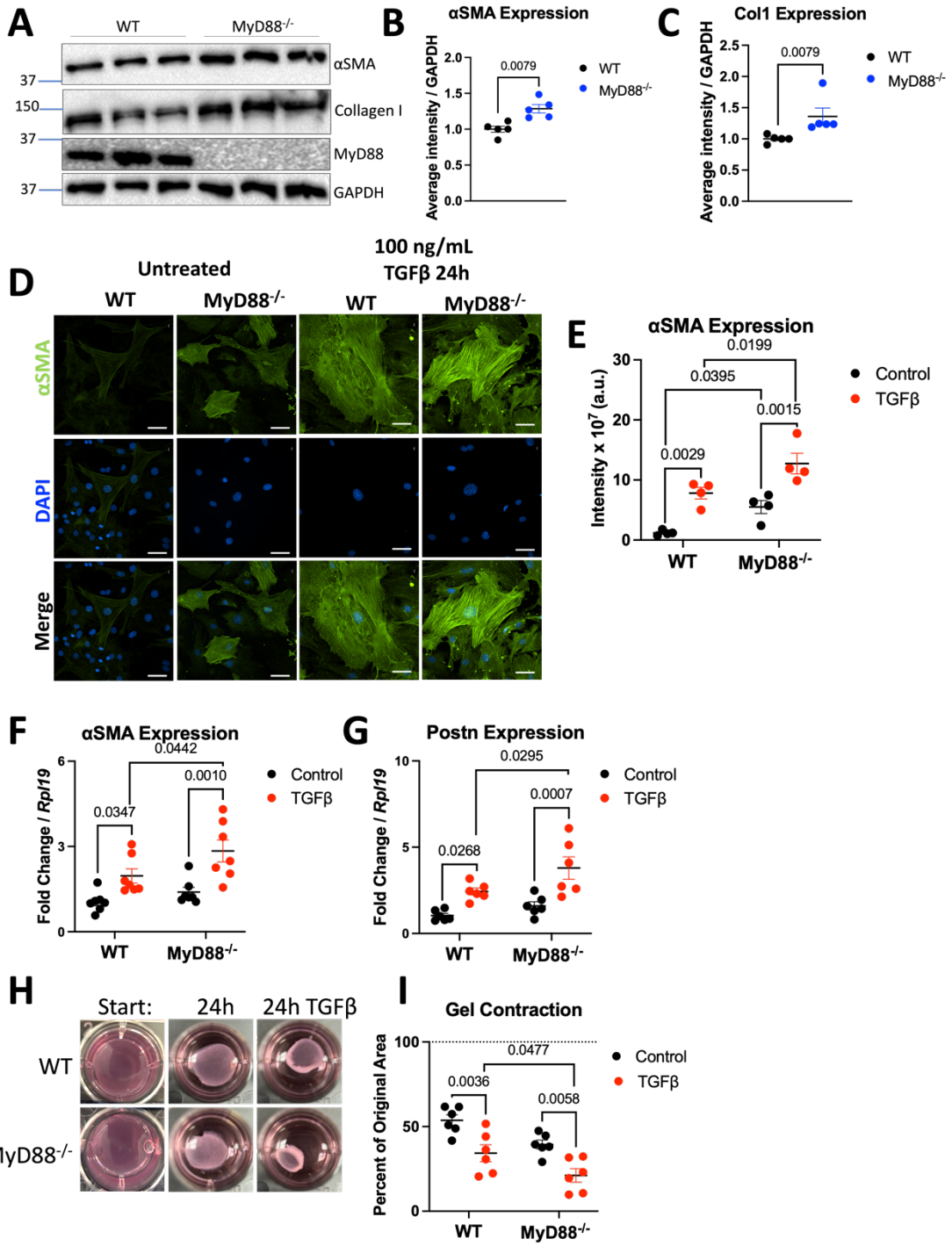


Figure 3-1 MyD88-/- CFB Exhibit Increased Transformation and Contractile Function at Baseline and In Response to TGFβ

A. Lysate was generated from cultured WT and MyD88$^{-/-}$ fibroblasts and analyzed by western blot. Quantification shown for n=5 independent experiments for aSMA (B) and collagen I (C). D-G. WT and MyD88$^{-/-}$ fibroblasts were treated with 100 ng/mL of TGFβ and stained for aSMA by immunofluorescence, representative images shown in D (Scale bars are 50 um), with quantification from n=4 independent experiments in E. RT-qPCR was used to measure expression of aSMA (F) or Postn (G) from n=6 independent experiments. H. WT or MyD88$^{-/-}$ fibroblasts were seeded in collagen matrix and treated with 100 ng/mL of TGFβ where indicated. Representative collagen discs shown with quantification shown in I for n=6 independent experiments. Statistical analysis by Mann-Whitney test (B-C), or 2-way ANOVA with Sidaks multiple comparison test (E, F, G, I). P-values shown.

while TGFβ treatment increased the contractile function of both cell types, MyD88$^{-/-}$

fibroblasts showed significantly enhanced gel contraction than WT (Figure 3-3H-I). Overall, these data confirmed enhanced myofibroblast differentiation and function in the absence of MyD88.

3.3.4 TGFβ Induced Myofibroblast Transformation Decreases MyD88 Levels:

To understand why MyD88 ablation enhanced myofibroblast function, we hypothesized that downregulation of MyD88 occurs during canonical myofibroblast differentiation. We found that TGFβ treatment *in vitro* significantly decreased MyD88 over 24 hours at the protein level (Figure 3-4A-B). Interestingly, there was also a moderate decrease in *Myd88* transcription in response to TGFβ (Figure 3-5), indicating regulation at the transcript and potentially post-transcriptional levels. We then used immunofluorescence to visualize MyD88 in TGFβ-treated fibroblasts and strikingly we observed that strongly αSMA expressing cells had very little detectable MyD88 (Figure 3C-white arrows), and that neighboring undifferentiated αSMA^- cells expressed much higher MyD88 (blue arrows).

We then sought to use the PE-ANGII model to evaluate if myofibroblast transformation decreases MyD88 protein *in vivo.* After 4 weeks of PE-ANGII, WT mice exhibited systolic dysfunction and LV hypertrophy as expected (Figure 3-4D-E), and LV tissue showed significantly elevated *Tgfb* (Figure 3-4F). We then FACS-sorted $CD45^-$ $CD31^-MEFSK4^+$ fibroblasts from these hearts, finding increased fibroblast numbers in PE-ANGII treated mice (Figure 3-4G-H, Figure 3-6). CFB sorted from PE-ANGII hearts also showed elevated Collagen I and αSMA, indicating strong myofibroblast transformation, and importantly, had a significant decrease in MyD88 protein (Figure 3-4I-3). Further, in left ventricular sections analyzed by immunofluorescence, we found that neighboring $PDGFr\alpha^+$ fibroblasts that stained positive for αSMA were distinct from those

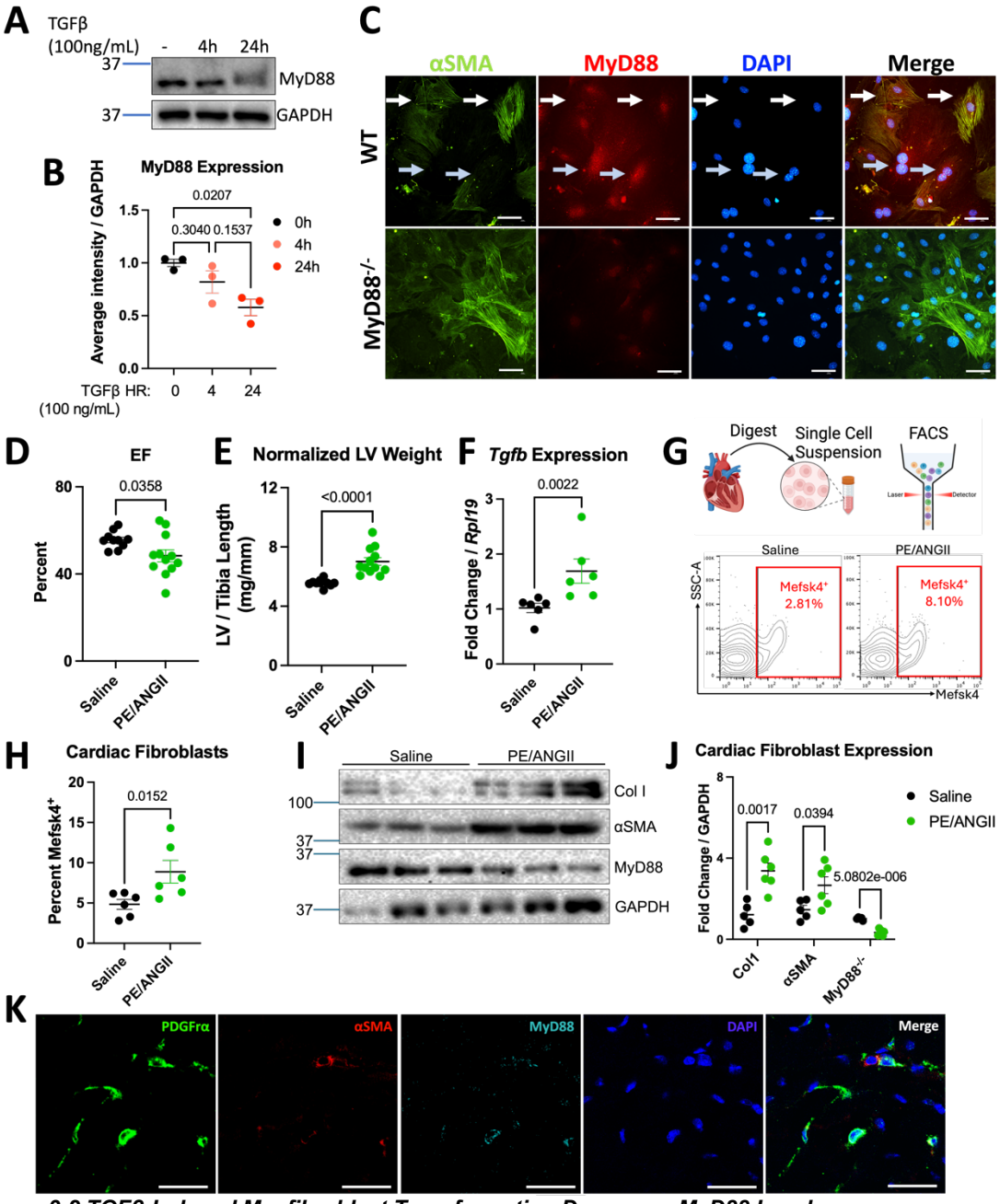


Figure 3-2 TGFβ-Induced Myofibroblast Transformation Decreases MyD88 Levels

A. WT fibroblasts were treated with 100 ng/mL TGFβ for the indicated time points then analyzed by western blot. Shown is representative blot, with quantification in B. for n=3 independent experiments. C. WT or MyD88$^{-/-}$ fibroblasts were treated with 100 ng/mL TGFβ for 24 hours, then immunofluorescence was used to visualize aSMA and MyD88. White arrows indicate aSMA+ myofibroblasts, blue arrows indicate MyD88+ fibroblasts. Scale bars are 50 um. D-J. WT mice aged 8-10 weeks (n=10-12 / group) were implanted with osmotic minipumps secreting 50 mg/kg/day phenylephrine and 1.5 mg/kg/day angiotensin II or saline, then euthanized after 4 weeks. D. Ejection fraction was measured with echocardiography. E. Normalized LV weight. F. RNA was isolated from LV samples and then RT-qPCR was used to measure Tgfb expression. G. 2 hearts / group were pooled and then Mefsk4+CD45-CD31- cells were sorted, shown are representative flow cytometry plots of Mefsk4+ cells, quantified in H. I. Sorted fibroblasts were analyzed by western blot, shown is representative blot with quantification in J for n=6 pooled samples. K. LV sections were stained by immunofluorescence. Statistical analysis by 1-way ANOVA with Tukey's multiple comparison test (B), Mann-Whitney test (D-H), and t-tests (J). P-values shown.

that stained positive for MyD88 (Figure 3-4K). These data provide strong evidence that

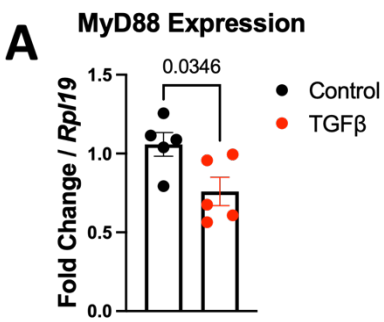


Figure 3-4 TGFβ Decreases MyD88 at the transcriptional level
A. WT fibroblasts were treated with 100 ng/mL of TGFβ for 24 hours, then analyzed by RT-qPCR for MyD88 expression. Statistical analysis by T-test, p=value shown.

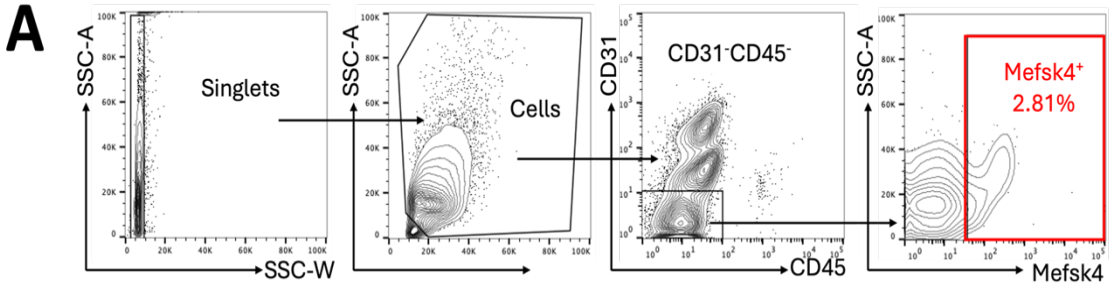


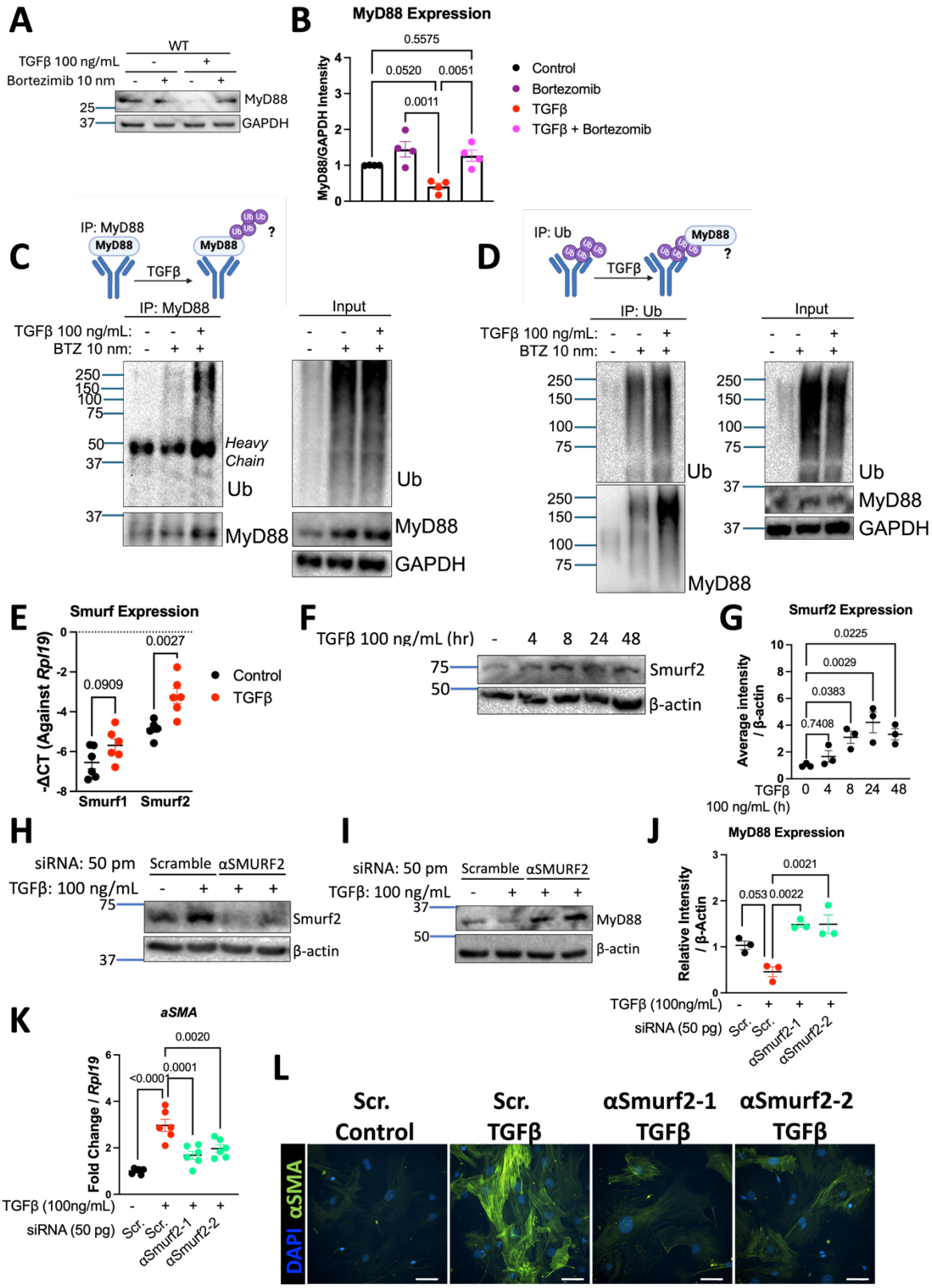
Figure 3-3 Fibroblast sorting Gating Strategy
WT mice aged 8-10 weeks (n=10-12 / group) were implanted with osmotic minipumps secreting 50 mg/kg/day phenylephrine and 1.5 mg/kg/day angiotensin II or saline, then euthanized after 4 weeks. Gating strategy for sorting, Mefsk4+CD45-CD31- cells were sorted.

decreased MyD88 is a characteristic of TGFβ-induced myofibroblast transformation.

3.3.5 TGFβ Induces Proteasomal Degradation of MyD88 Through SMURF2:

Next, we sought to further probe the mechanism of TGFβ-induced MyD88 loss. We first included a proteasome inhibitor alongside TGFβ treatment to test if the ubiquitin proteasome system is responsible for the degradation of MyD88. At baseline, Bortezomib (BTZ) treatment did not significantly alter MyD88 levels, however the co-treatment of BTZ and TGFβ completely restored the decrease in MyD88 induced by TGFβ alone (Figure 3-7A-B). We then looked for evidence of MyD88 ubiquitination using immunoprecipitation strategies. First, we immunoprecipitated MyD88 in denaturing conditions comparing untreated cells to proteasomal inhibition with or without TGFβ. While MyD88 was immunoprecipitated similarly in the presence or absence of TGFβ and BTZ, there was significant high molecular weight signal for Ubiquitin when proteasome inhibition was performed in TGFβ-treated cells (Figure 3-7C). Similarly, when we

immunoprecipitated all ubiquitinated proteins under the same set of conditions, we found



a high molecular weight signal for MyD88 that increased with BTZ, and further increased

Figure 3-5 TGFβ Induces Proteasomal Degradation of MyD88 through Smurf2
A. WT fibroblasts were treated with 100 ng/mL TGFβ and 10 nM Bortezomib for 16 hours where indicated. Shown is representative western blot, with quantification from n=4 independent experiments in B. C-D. WT fibroblasts were treated with 100 ng/mL and 10 nM Bortezomib for 16 hours where indicated, then denaturing immunoprecipitation was performed for MyD88 (C) or Ubiquitin (D), and then samples were analyzed by western blot. Shown are schematics for each experiment and representative western blots. E. WT fibroblasts were treated with 100 ng/mL TGFβ then analyzed by RT-qPCR for n=6 independent experiments. F. WT fibroblasts were treated with 100 ng/mL TGFβ at the indicated time points, shown is representative western blot with quantification in G for n=3 independent experiments. H-L. WT fibroblasts were transfected with 50 ng scramble or Smurf2 siRNA, then treated with TGFβ where indicated. H. Representative western blot showing Smurf2 knockdown. I. Representative western blot for MyD88, with quantification in J for n=3 independent experiments. K. RT-qPCR was used to analyze aSMA expression. L. Immunofluorescence was used to measure aSMA expression, scale bar = 50 um. Statistical analysis by 1-way ANOVA with Tukey's multiple comparison test (B, G, J, K) or T-tests (E). P-values shown.

with TGFβ and BTZ (Figure 3-7D), collectively showing that TGFβ is able to increase MyD88 ubiquitination to target it to the proteasome.

We then sought to find the E3 ligase that was responsible for targeting MyD88 to the proteasome. Smurf1 and Smurf2 have previously been shown to ubiquitinate MyD88 in myeloid cells[401], as such, we tested if TGFβ induced Smurf expression to degrade MyD88. WT CFB treated with TGFβ for 24 hours had a significant increase in Smurf2 but not Smurf1 at the transcript level, and overall higher Smurf2 expression compared to Smurf1 at baseline (Figure 3-7E). Additionally, Smurf2 increased significantly at the protein level with TGFβ treatment over time (Figure 3-7F). Next, we sought to test if Smurf2 was functionally responsible for MyD88 ubiquitination. We designed siRNAs against Smurf2 and confirmed that transfection of these siRNAs decreased Smurf2 transcript (Figure 3-8A) and knockdown at the protein level compared to scramble siRNA (Figure 3-7H). We then treated CFB with TGFβ after Smurf2 knockdown, and found that while TGFβ decreased MyD88 level in CFB transfected with scramble siRNA, both Smurf2 siRNAs completely prevented MyD88 degradation (Figure 3-7I-J). We also evaluated myofibroblast transformation in these cells, and found that Smurf2 knockdown blunted TGFβ-induced *aSMA* and *Postn* transcript, and decreased αSMA protein and spindle fiber formation (Figure 3-7K-L, Figure 3-8B). This identified Smurf2 as the E3 ligase responsible for the proteasomal degradation of MyD88 in response to TGFβ and

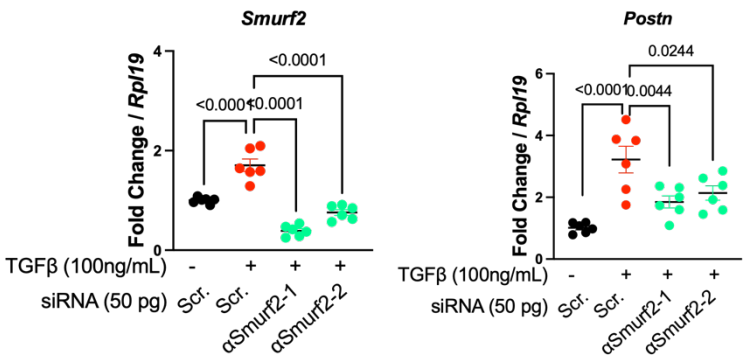


Figure 3-6 Smurf2 Knockdown Decreases Fibroblast Transformation
WT fibroblasts were transfected with 50 ng scramble or Smurf2 siRNA, then treated with TGFβ where indicated. Cells were analyzed by RT-qPCR for Smurf (A) or POSTN (B). Statistical analysis by 1-way ANOVA with Tukey's multiple comparison test. P-values shown.

provided evidence that MyD88 degradation is necessary for myofibroblast transformation.

3.3.6 MyD88 Binds to Smad4 to Impair Nuclear Translocation in Response to TGFβ

We then hypothesized that MyD88 negatively regulated TGFβ signaling downstream of the TGFβ receptor, the mechanism explaining why MyD88 degradation is necessary for myofibroblast transformation. To test this, we treated WT and MyD88$^{-/-}$ CFB with TGFβ and monitored SMAD2 phosphorylation over time as a readout of canonical TGFβ receptor activation (Figure 3-9A). To our surprise, we found very similar induction of p-SMAD2 after TGFβ treatment in both WT and MyD88$^{-/-}$ CFB, as well as unchanged expression of the co-transcription factor SMAD4 (required for the transcriptional activity of pSMAD2/3) in either genotype or TGFβ treated time point (Figure 3-9B-D). To interrogate the TGFβ pathway farther, we performed nuclear fractionation to test translocation of the SMAD complex after TGFβ treatment. As expected, we found TGFβ treatment significantly increased nuclear translocation of SMAD4 and pSMAD2 in WT CFB, however there was significantly greater nuclear SMAD4 and pSMAD2 in TGFβ treated MyD88$^{-/-}$ CFB (Figure 3-9E-G). To confirm this finding, we performed immunofluorescence for SMAD4 and observed greater nuclear signal in MyD88$^{-/-}$ CFB compared to WT both at baseline and in response to TGFβ (Figure 3-9H). Finally, we asked if MyD88 directly bound SMAD4 to prevent association with SMAD2/3 and

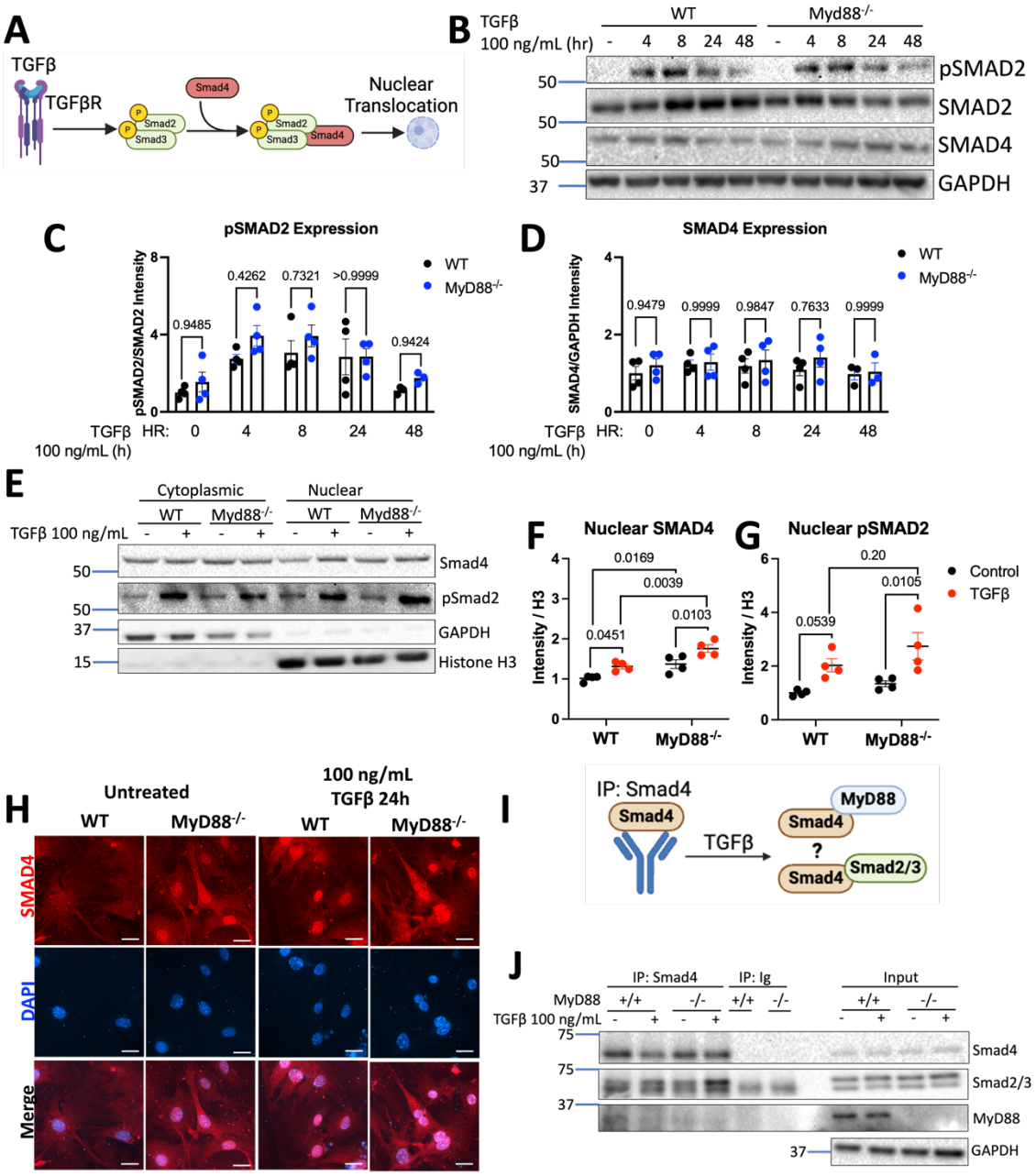


Figure 3-7 MyD88 Binds SMAD4 to Impair Complex Nuclear Translocation In Response to TGFβ
A. Schematic of canonical TGFβ signaling. B-D. WT or MyD88$^{-/-}$ fibroblasts were treated with 100 ng/mL TGFβ for the indicated time points, representative blot shown with quantification from n=4 independent experiments in for pSMAD2 (C) and SMAD4 (D). E. WT or MyD88$^{-/-}$ fibroblasts were treated with 100 ng/mL TGFβ for 24 hours, then cytosolic and nuclear fractions were isolated, shown is a representative western blot with quantification in F (Smad4) and G (pSMAD2) from n=4 independent experiments. H. Representative immunofluorescence for SMAD4, scale bars are 50 uM. J. Representative immunoprecipitation for SMAD4. Statistical analysis by 2-way ANOVA with Sidak's multiple comparison test, p-values shown.

subsequent nuclear translocation (Figure 3-9I). When we immunoprecipitated SMAD4, we found that MyD88 co-precipitated at baseline, which was abrogated by TGFβ treatment alongside an increase in SMAD2/3 co-precipitation (Figure 3-9J). In the

absence of MyD88, TGFβ treatment induced much greater SMAD4 – SMAD2/3 binding (Figure 3-9J), together confirming that MyD88 degradation by TGFβ or genetic deletion allows for increased SMAD4-SMAD2/3 complex formation and transcriptional activity, one mechanism for MyD88 regulating fibroblast transformation.

3.3.7 Fibroblast Specific Ablation of MyD88 Increases the Fibrotic Response to PE/ANGII:

We next sought to delete MyD88 in cardiac fibroblasts and test the fibrotic response to cardiac injury. We crossed *Myd88*$^{fl/fl}$ mice to the fibroblast specific *Tcf21*^{iCre} mice (Figure 3-10A) to generate inducible CFB-MyD88$^{-/-}$ mice (iCre^{+}) alongside CFB-MyD88$^{+/+}$ littermate mice (iCre^{-}), confirming Tamoxifen to excise MyD88 at the gene level (Figure 3-10B) and protein level (Figure 3-10C). We then subjected these mice to PE/ANGII for 4 weeks and evaluated fibrosis and cardiac dysfunction (Figure 3-10D). Interestingly, while both sets of mice developed significant gross left ventricular hypertrophy (Figure 3-10E), only CFB-MyD88$^{-/-}$ mice developed systolic dysfunction after PE/ANGII, with no detectable baseline differences in cardiac function (Figure 3-10F). We also found greater ventricular wall diameter in CFB-MyD88$^{-/-}$ mice (Figure 3-10G), and as such further characterized cardiac hypertrophy at the cellular level. CFB-MyD88$^{-/-}$ mice had greater cardiomyocyte area compared to littermate CFB-MyD88$^{+/+}$ mice treated with PE/ANGII (Figure 3-11A-B), and also expressed significantly greater BNP transcript (Figure 3-11C). We then characterized cardiac fibroblast populations in the hearts of these mice by flow cytometry, and found that while PE/ANGII induced fibroblast proliferation similarly in both mice (Figure 3-10H, 3-12), there were significantly more FAP^{+} fibroblasts in PE/ANGII treated CFB-MyD88$^{-/-}$ mice (Figure 3-10I) indicating greater myofibroblast transformation. In line with this, picrosirius red staining revealed a significantly greater induction of cardiac fibrosis after PE/ANGII in CFB-MyD88$^{-/-}$ mice compared to littermate CFB-

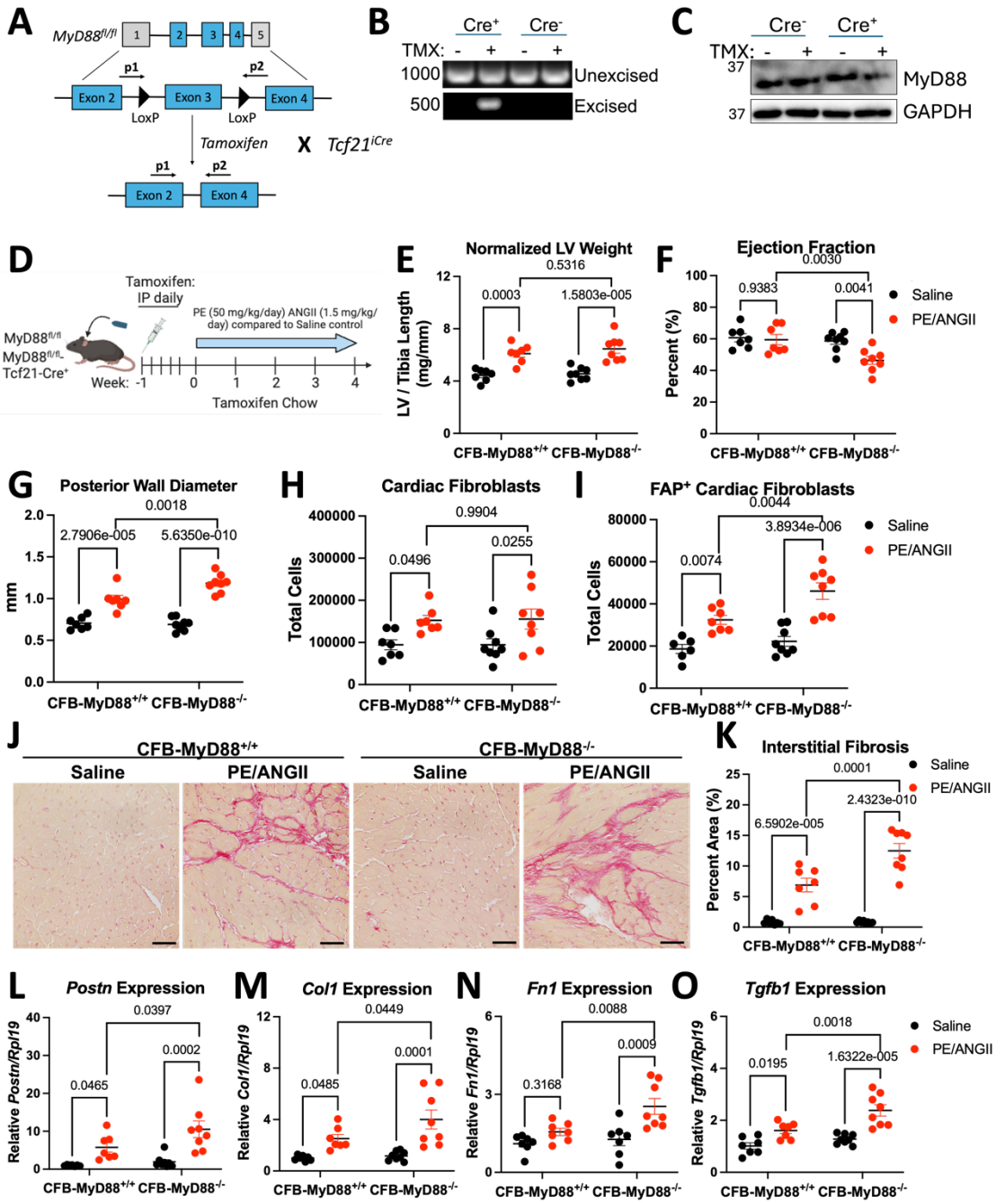


Figure 3-8 Fibroblast Specific Ablation of MyD88 Increases the Fibrotic Response to PE/ANGII

A. Schematic showing floxed Myd88 and excision by Tcf21 Cre and primers for detection of gene excision. B. MyD88 Tcf21$^{fl/fl}$Cre$^{+/-}$ mice were injected IP with 80mg/kg Tamoxifen for 5 days, then genomic DNA from hearts was isolated and analyzed by PCR for MyD88 excision. C. Fibroblasts were isolated from MyD88 Tcf21$^{fl/fl}$Cre$^{+/-}$ mice and treated for 48h with 1 uM 4'OH-Tamoxifen, then analyzed by western blot. D. MyD88 Tcf21$^{fl/fl}$Cre$^{+/-}$ mice were injected with Tamoxifen for 5 days, then implanted with osmotic minipumps secreting 50 mg/kg/day phenylephrine and 1.5 mg/kg/day angiotensin II or saline (n=7-9 / group), then euthanized after 4 weeks. E. Normalized LV weight. F. Ejection fraction was measured by echocardiography. G. Ventricular wall diameter was measured by echocardiography. H-I. LV samples were digested enzymatically and mechanically, then analyzed by flow cytometry for Mefsk4+ fibroblasts (H) and FAP+ fibroblasts (I). J. LV sections were stained with Picrosirius red, shown are representative images (scale bar = 100 um) with quantification in K. L-O. RNA was isolated from LV samples, and RT-qPCR was used to measure expression of Postn (L), Col1 (M), Fn1 (N) and Tgfb (O). Statistical analysis by 2-way ANOVA with Sidak's multiple comparison test. P-values shown.

MyD88$^{+/+}$ mice (Figure 3-10J-K). Further, we found broad increases in pro-fibrotic

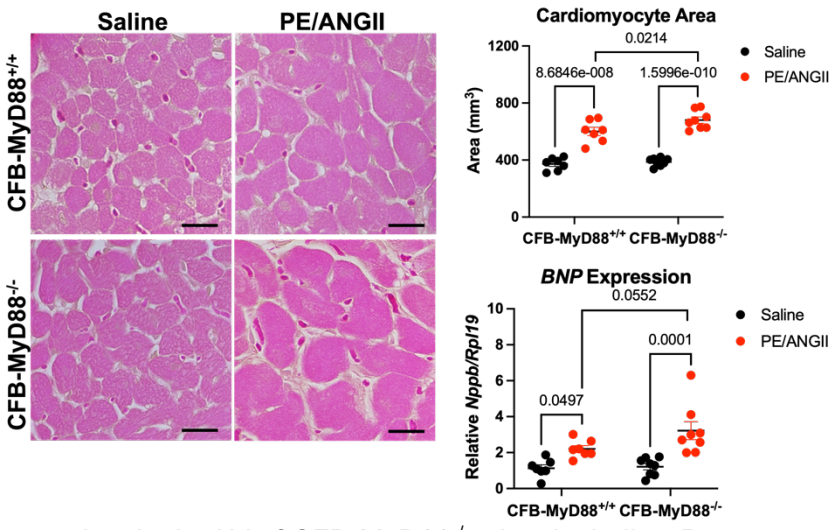


Figure 3-9 CFB-MyD88 Mice Have Increased Hypertrophy Compared to WT
MyD88 Tcf21$^{fl/fl}$Cre$^{+/-}$ mice were injected with Tamoxifen for 5 days, then implanted with osmotic minipumps secreting 50 mg/kg/day phenylephrine and 1.5 mg/kg/day angiotensin II or saline (n=7-9 / group), then euthanized after 4 weeks. A. LV sections were stained by H&E and cardiomyocyte area was measured using ImageJ. Representative images shown, with quantification in B. C. RNA was isolated from LV samples, and RT-qPCR was used to measure expression of BNP. Statistical analysis by 2-way ANOVA with Sidak's multiple comparison test. P-values shown.

transcripts in the LV of CFB-MyD88$^{-/-}$ mice, including *Postn* (myofibroblast transformation), *Col1* and *Fn1* (ECM production) and *Tgfb1* (Figure 3-10L-O). We then sought to evaluate if CFB MyD88 regulated the cardiac T-cell response. Interestingly, we found increased effector CD4^{+} T-cells in the lymphoid organs of only CFB-MyD88$^{+/+}$ mice (Figure 3-12A-E), however we only found trending increases in CD4^{+} or CD8^{+} T-cells in either genotype with PE/ANGII (Figure 3-12F-H). This suggested that increased fibrosis was more strongly regulated by fibroblast MyD88 than by altered T-cell recruitment. Together these data confirm that fibroblast-specific ablation of MyD88 is detrimental to the development of fibrosis in PE/ANGII by enhancing fibroblast transformation.

3.3.8 Fibroblast MyD88 Regulates Cardiac Fibrosis in Transverse Aortic Constriction

We then subjected CFB-MyD88$^{-/-}$ mice to transverse aortic constriction to test if fibroblast MyD88 broadly regulated the fibrotic response across models of fibrosis (Figure 3-13A). After 4 weeks, CFB-MyD88$^{-/-}$ mice exhibited a greater drop in ejection fraction than CFB-MyD88$^{+/+}$ littermates, in the presence of similar LV hypertrophy (Figure 3-13B-C). Flow cytometry analysis of the LVs of these mice also revealed greater increase in relative fibroblast number and FAP+ fibroblasts in CFB-MyD88$^{-/-}$ mice

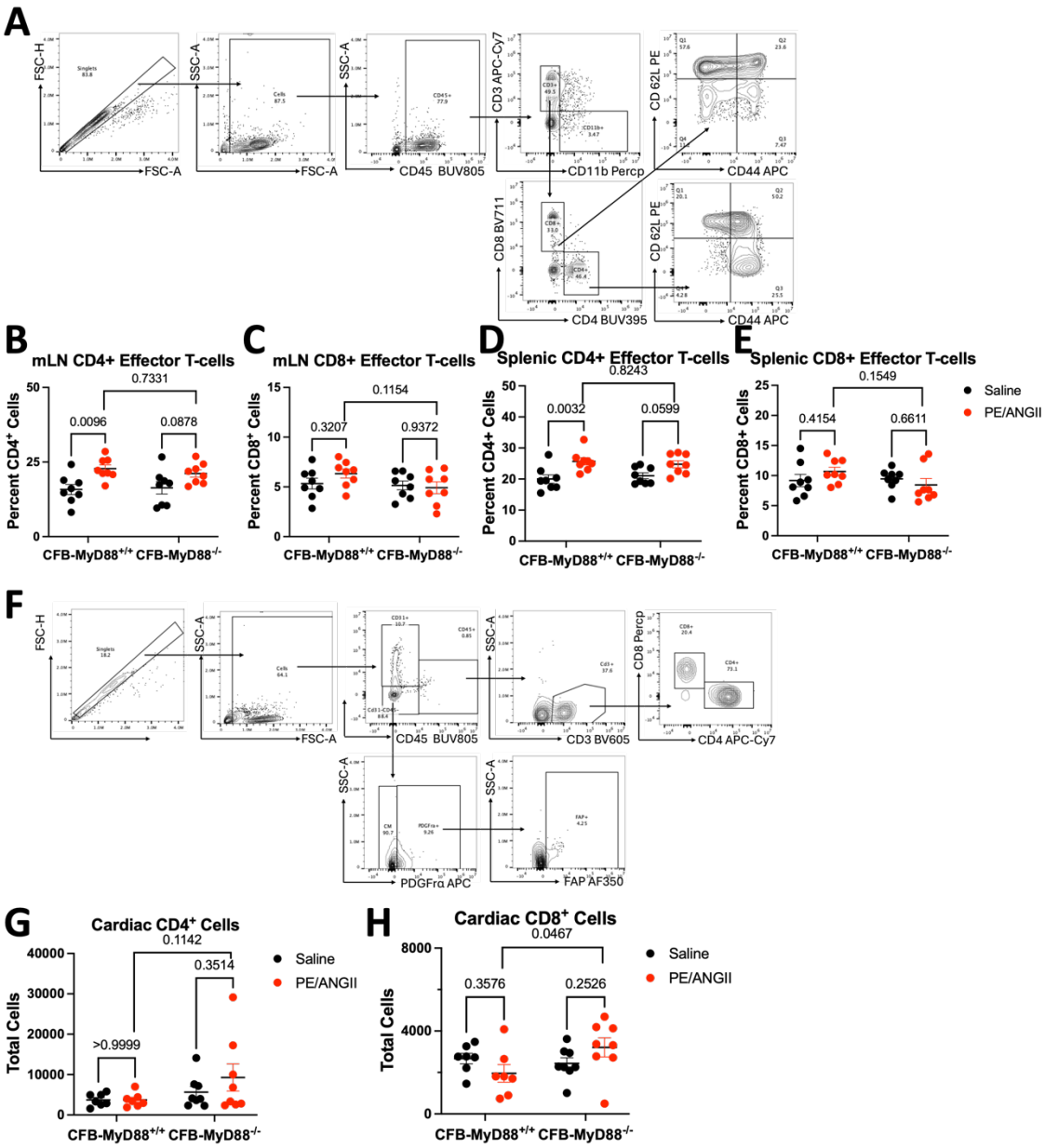


Figure 3-10 PE AngII Induces Lymphoid CD4+ T-cell activation but not cardiotropism in WT Mice
A. MyD88 Tcf21$^{fl/fl}$Cre$^{+/-}$ mice were injected with Tamoxifen for 5 days, then implanted with osmotic minipumps secreting 50 mg/kg/day phenylephrine and 1.5 mg/kg/day angiotensin II or saline (n=7-9 / group), then euthanized after 4 weeks. mLN or spleen samples were digested to a single cell suspension then analyzed using flow cytometry. Shown is the gating strategy, with effector T-cells quantified in B-C (mLN) and D-E (spleen). Hearts were digested enzymatically and mechanically and analyzed by flow cytometry. Shown is the gating strategy, with quantification for cardiac CD4+ T-cells (G) and CD8+ T-cells (H). Statistical analysis by 2-way ANOVA with Sidak's multiple comparison test. P-values shown.

subjected to TAC compared to sham mice or littermate controls. (Figure 3-13D-E). This occurred again in the absence of enhanced CD4$^+$ T-cell recruitment to the heart, as both groups of mice had similar elevated LV T-cells (Figure 3-13F). As we observed using the PE/ANGII model, we found increased cardiac fibrosis by picrosirius red staining,

primarily in the perivascular region as we have previously shown (Figure 3-13G-H). We

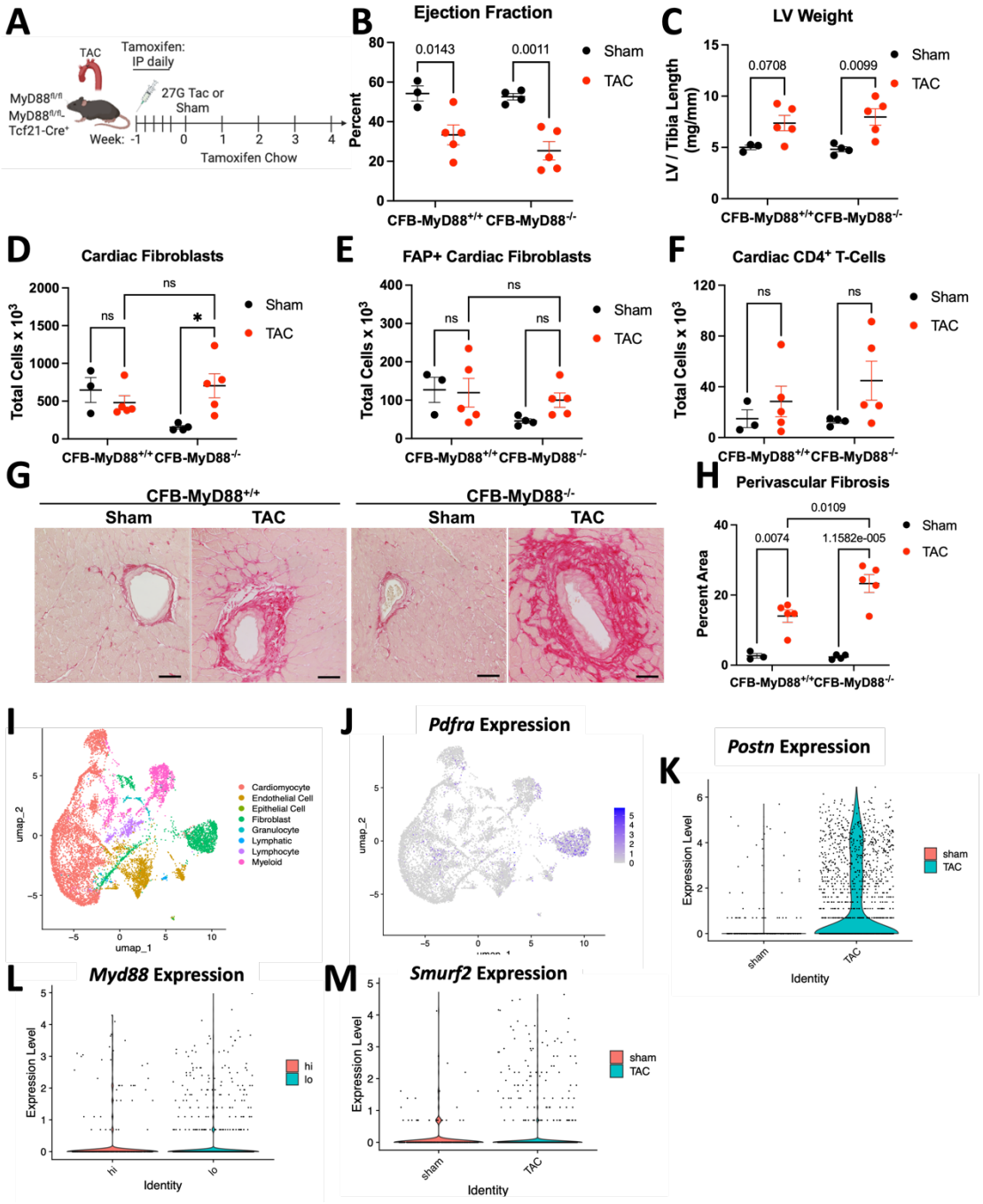


Figure 3-11 Fibroblast MyD88 Regulates Fibrosis in Transverse Aortic Constriction
A. MyD88 Tcf21$^{fl/fl}$Cre$^{+/-}$ mice were injected with Tamoxifen for 5 days, then underwent 27G TAC surgery or sham surgery, then were euthanized after 4 weeks. B. Ejection fraction was measured by echo-cardiography. C. Normalized LV weight. D-F. LV samples were digested enzymatically and mechanically, then analyzed by flow cytometry for Mefsk4+ fibroblasts (D), FAP+ fibroblasts (E), or CD4+ T-cells (F). G. LV sections were stained with Picrosirius red, shown are representative images (scale bar = 100 um) with quantification in H. I. UMAP display of all cardiac cells. J. UMAP of Pdgfra expression showing cardiac fibroblasts. K. Violin plot of fibroblast Periostin expression in TAC compared to Sham mice. L. Myd88 expression in Periostin hi compared to periostin lo fibroblasts. M. Smurf2 expression in TAC compared to Sham mice. Statistical analysis by 2-way ANOVA with Sidak's multiple comparison test. P-values shown

then utilized a publicly available scRNA-seq data[403] of Sham vs. TAC mice as done with PE/ANGII to evaluate changes in cardiac fibroblast MyD88 levels after TAC. We first identified cardiac fibroblasts by *Pdgfra* expression from all cardiac cells (Figure 3-13I-J). Fibroblasts from TAC hearts expressed much higher *Postn* than those from Sham hearts, as expected, and when we subsetted cells based on *Postn* level as done previously, $Postn^{hi}$ cells had lower expression of *Myd88* than $Postn^{lo}$ cells (Figure 3-13K-M). Further, fibroblasts from TAC hearts expressed higher *Smurf2* than sham (Figure 3-13M), additional evidence that TAC induces similar downregulation of MyD88 through both transcriptional and proteasomal regulation in myofibroblasts.

3.3.9 Aged MyD88$^{-/-}$ Mice Have Mildly Increased Interstitial Fibrosis and Myofibroblast Number:

We then asked if a pro-fibrotic stimulus was required for increased fibrosis in the absence of fibroblast MyD88. We aged WT and MyD88$^{-/-}$ mice to 1 year, and then collected LV samples to evaluate cardiac fibrosis. We found that MyD88$^{-/-}$ mice had mildly increased interstitial but not perivascular fibrosis compared to aged WT mice (Figure 3-14A-C). To confirm if this occurred alongside myofibroblast activation, we performed immunofluorescence in LV samples, and found aged MyD88$^{-/-}$ mice to have increased αSMA^{+}PDGFrα^{+} cardiac fibroblasts compared to WT mice (Figure 3-14D-E). Despite this, we found no changes to ejection fraction in these mice (Figure 3-14F), indicating that while MyD88 deletion results in increased baseline fibroblast transformation over time, challenge with cardiac stress that induces pro-fibrotic signals like TGFβ is required for overt systolic dysfunction and more significant fibrosis.

3.3.10 Overexpression of MyD88 Prevents Myofibroblast Transformation:

Our data thus far show that deletion of MyD88 or proteasomal degradation through TGFβ promotes myofibroblast transformation, so we next tested if overexpression of

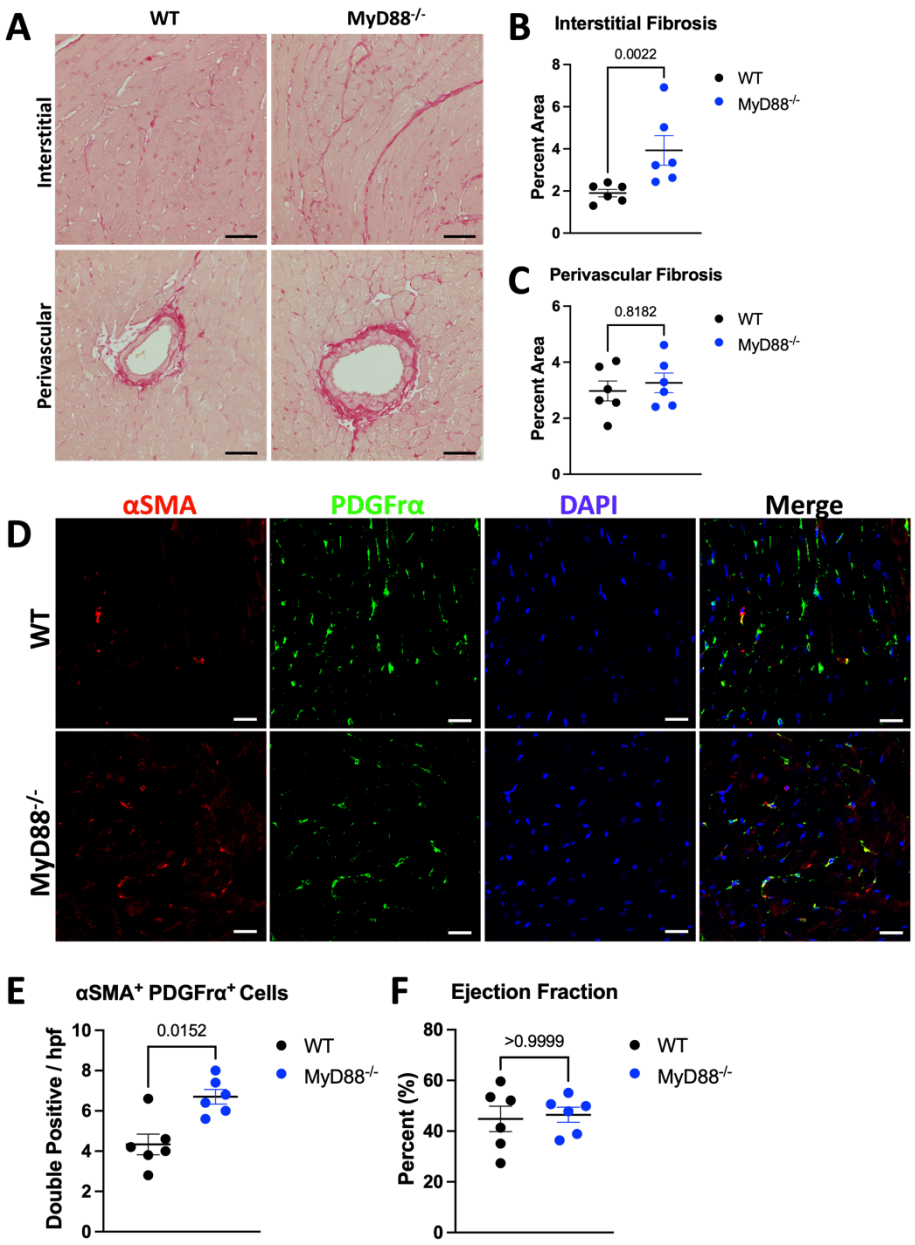


Figure 3-12 Aged MyD88-/- Mice Have Mildly Increased Interstitial Fibrosis and Myofibroblast Number

A. LV samples from 1 year old WT and MyD88$^{-/-}$ mice (n=6 / group) were stained with picrosirius red, shown are representative images (scale bars = 50 um), quantification in insterstitial areas (B) and perivascular areas (C). D. LV samples were analyzed by immunofluorescence (scale bars = 50 um) with quantification of double positive cells in E. F. Echocardiography was used to measure ejection fraction. Statistical analysis by Mann-Whitney test. p-values shown.

MyD88 would prevent TGFβ-induced transformation. We generated Adenovirus to overexpress MyD88 (Figure 3-15 – Myd88^{OE}-GFP) compared to an empty GFP vector and transduced resting WT CFB. There was a significant overexpression of MyD88 at the transcript and protein level (Figure 3-15A-C), and cells transduced with MyD88^{OE}-GFP virus or GFP virus both showed similar GFP expression (Figure 3-15D) indicating similar efficacy. We then measured the response of transduced fibroblasts to TGFβ by staining for αSMA expression. While GFP transduced cells had a significant increase in αSMA expression by immunofluorescence, MyD88^{OE}-

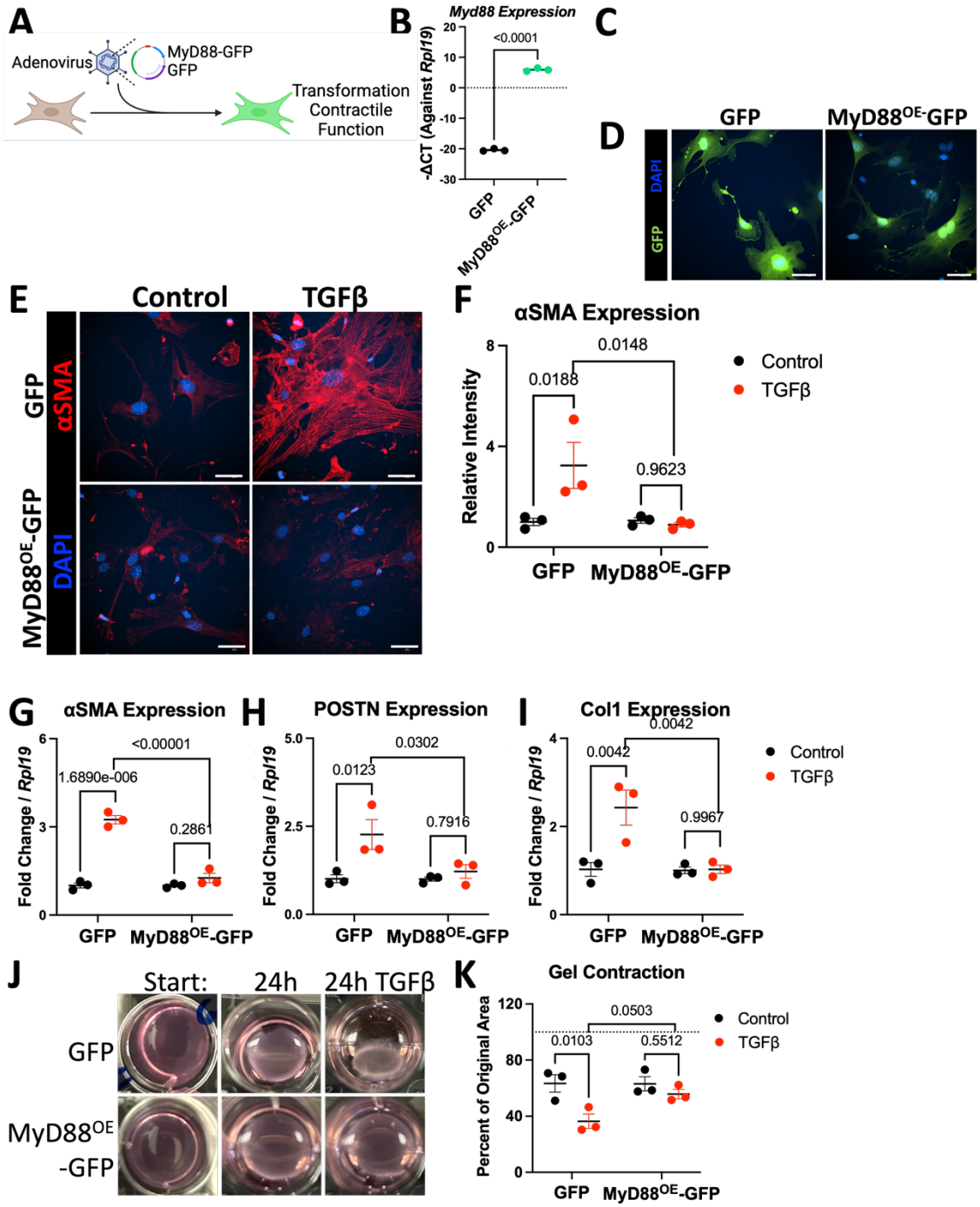


Figure 3-13 Overexpression of MyD88 Prevents Myofibroblast Transformation

A. Schematic showing adenovirus induced overexpression of MyD88. WT fibroblasts were transduced with GFP or MyD88-OE Adenovirus at an MOI of 1:250, then collected after 48 hours. Cells were treated with 100 ng/mL of TGFβ for 24 hours where indicated. B. RT-qPCR was used to measure Myd88 expression. C. Representative western blot showing MyD88 overexpression. D. Cells were imaged after transduction to show GFP expression, scale bars = 50 um. E. Cells were analyzed by immunofluorescence for aSMA, representative images shown (scale bars = 50 um) with quantification in F. for n=3 independent experiments. G-I. RT-qPCR was used to measure aSMA expression (G), POSTN expression (H), or Collagen I expression (I). J. Fibroblasts were seeded in collagen matrix and treated with 100 ng/mL of TGFβ where indicated. Representative collagen discs shown with quantification shown in K. for n=3 independent experiments. Statistical analysis by 2-way ANOVA with Sidak's multiple comparison test. P-values shown.

GFP transduced cells were not able to increase αSMA after TGFβ, indicating impaired

myofibroblast transformation (Figure 3-15E-F). As additional evidence of this, we found that TGFβ only increased the transcript levels of *aSMA, Postn,* and *Col1* in GFP transduced cells, but not MyD88 overexpressing cells (Figure 3-15G-I). Finally, we evaluated the contractile ability of control or MyD88^{OE} cells. TGFβ treatment significantly increased the contractile function of GFP-transduced cells, however MyD88^{OE} cells did not (Figure 3-15-K). These data show that endogenous overexpression of MyD88 is able to prevent myofibroblast transformation and contractile function in response to TGFβ.

3.3.11 MyD88 Regulates Human Fibroblast Transformation:

To evaluate if MyD88 plays a similar regulatory role for myofibroblast transformation in human cardiac fibroblasts, we first cultured LV cardiac fibroblasts from patients with HF and treated them with TGFβ *in vitro.* TGFβ treatment resulted in a significant decrease in MyD88 at the protein level alongside increased αSMA (Figure 3-16A-B), and decreased *Myd88* transcript (Figure 3-16C), re-capitulating what we have observed thus far in mouse fibroblasts. We next asked if fibroblasts sourced from HF patients would express less MyD88 if they are more transformed then healthy fibroblast. Lysates HF patient fibroblasts expressed greater αSMA and collagen I compared to purchased healthy CFB, as expected (Figure 3-16D-E). Importantly, we found HF-derived CFB to express significantly lower MyD88 than healthy CFB (Figure 3-16D-E). Next, we stained LV sections from human HF patients to evaluate fibroblast MyD88 *in situ* in the failing heart. Similar to mice, we observed that PDGFrα^{+} fibroblasts that stained positive for MyD88 (red arrows) were distinct from αSMA^{+} fibroblasts (cyan arrows) (Figure 3-16F). To further evaluate the dynamics of MyD88 expression in human HF patients, we leveraged published scRNA-seq data from human heart samples.[52] We first subsetted only non-ischemic cardiomyopathy vs. control donor cells and identified cardiac fibroblasts through PDFRA expression (Figure 316G-H). We then plotted POSTN

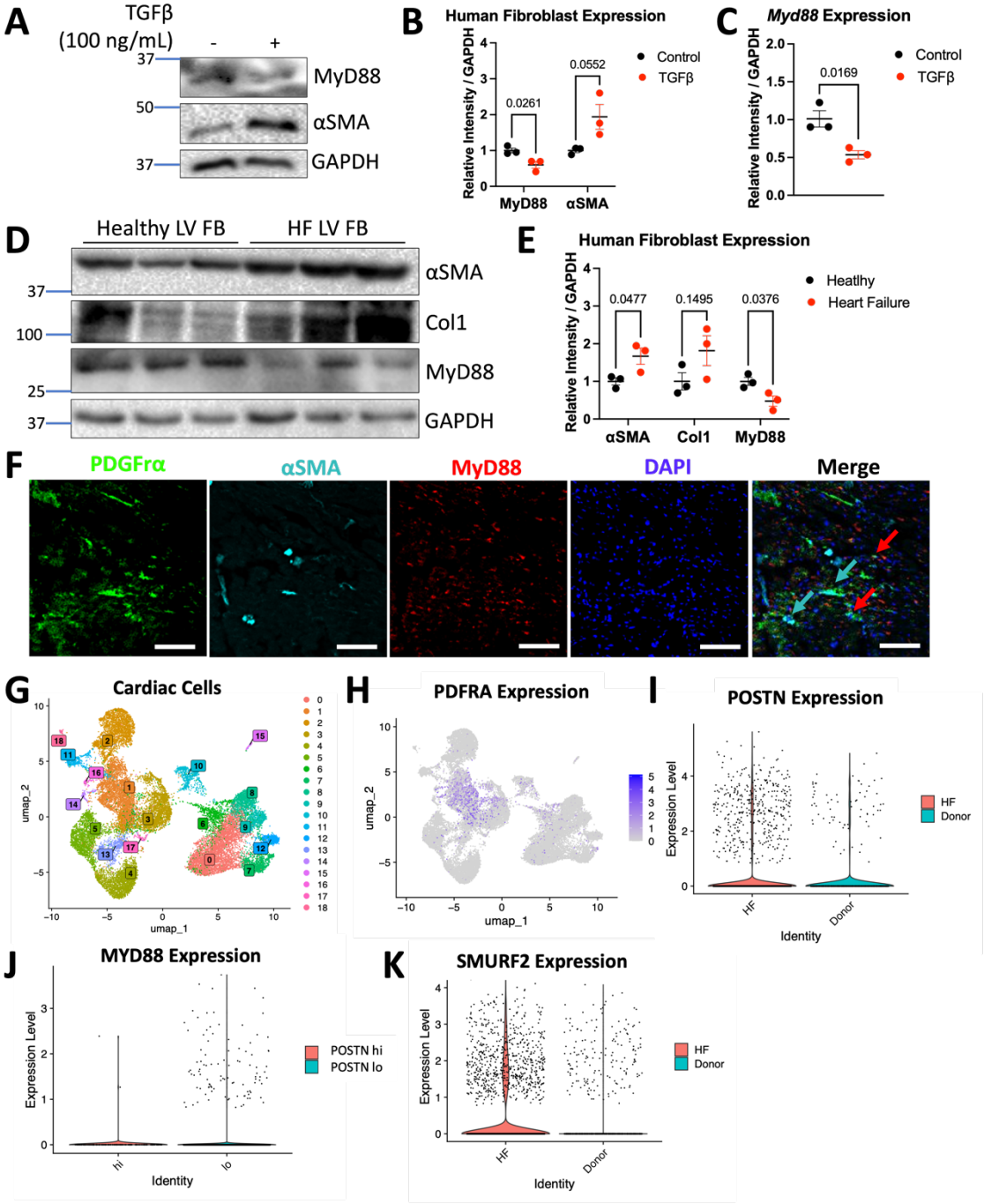


Figure 3-14 MyD88 Regulates Human Fibroblast Transformation

A. Human LV fibroblasts were treated with 100 ng/mL of TGFβ, shown is representative western blot with quantification in B. from n=3 patients. E. Human heart failure patient LVs were analyzed by immunofluorescence. Scale bars are 25 um. Cyan arrows indicate aSMA+ fibroblasts, red arrows indicate MyD88+ fibroblasts. F. UMAP projection of total cardiac cells from jealthy donor hearts and non-ischemic cardiomyopathy hearts. G. PDGFRA expression on UMAP showing fibroblasts. H. Violin plot showing POSTN expression in fibroblasts from HF vs healthy donor hearts. I. Violin plot showing MyD88 expression in fibroblasts subsetted by POSTN expression. J. Violin plot showing SMURF2 expression in fibroblasts form HF vs. healthy donor hearts. Statistical analysis by T-tests, p-values shown.

expression in these cells, finding an increase in POSTN^{+} fibroblasts in HF patients

compared to healthy donors (Figure 3-16I), then subsetted cells based on POSTN expression as done previously. $POSTN^{lo}$ fibroblasts expressed higher MYD88 than $POSTN^{hi}$ cells, in which MYD88 was barely detectable, in line with our results thus far in mice (Figure 3-16J). We also found that fibroblasts from HF patients expressed much higher SMURF2 than donor controls, evidence that SMURF2 induced degradation is likely occurring in human cells as well (Figure 3-16K). Based on our *in vitro* data and evidence from LV sections and sequencing, we conclude that in humans, fibroblast MyD88 decreases with myofibroblast transformation and acts in a similar regulatory role as what we outline thus far in mouse fibroblasts.

3.4 Discussion

Here we present new insight into the molecular mechanisms that regulate pro-fibrotic cardiac fibroblast transformation in response to TGFβ. We show that MyD88 is downregulated in myofibroblasts at the transcript level and at the protein level *in vitro,* in multiple pre-clinical models of cardiac fibrosis, and in human fibroblasts. As such, deletion of MyD88 in mice results in enhanced myofibroblast transformation and fibrotic responses. Mechanistically, we found that TGFβ induces Smurf2 expression, resulting in proteasomal degradation of MyD88 and allowing for enhanced Smad4/Smad2/3 complex translocation to the nucleus. Restoration of MyD88 through Smurf2 knockdown or overexpression of MyD88 prevented appropriate myofibroblast transformation, evidence that modulation of MyD88 levels represents a potential anti-fibrotic therapeutic approach.

While it is well established that MyD88 modulates pro-inflammatory PRR signaling in innate immune cells, our previous work showing MyD88 is anti-inflammatory in T-cells has expanded the functions for MyD88 in different cell types, [220,400] and further shows that MyD88 can interact with different binding partners depending on the cell type.[510] Previously, MyD88 has been shown to bind to Smad4 in macrophages and hepatocytes, regulating Smad4 levels.[402] Here we show that while MyD88 also binds Smad4 in fibroblasts, rather than regulate Smad4 expression, their interaction restrains translocation into the nucleus to regulate TGFβ signaling. This further expands our understanding of MyD88 functionality in different cell types. Additionally, this work elucidates a novel regulatory mechanism in the TGFβ signaling cascade. Smad signaling downstream of TGFβR ligation is well characterized, however as resting cardiac fibroblasts produce a baseline level of TGFβ, little is known about what prevents spontaneous myofibroblast transformation. Our work showing increased αSMA and collagen production in untreated MyD88$^{-/-}$ fibroblasts provides evidence that the presence of MyD88 and its' interaction with Smad4 is one mechanism

safeguarding fibroblast homeostasis. This positions MyD88 and TGFβ induced degradation as a new component in physiologic and pathologic TGFβ signaling.

Using the PE-ANGII model of cardiac fibrosis, we also show that while $CD4^+$ T-cells are activated and infiltrate the heart in response to PE/ANGII treatment, mice lacking T-cells still develop cardiac fibrosis. Previous work has shown that T-cells are required for the development of hypertension in response to Angiotensin,[232,234,405] however T-cells have not been thoroughly studied in combined PE-ANGII treatment. While the decrease in cardiac fibrosis is likely a result of blunted hypertensive stress, the remaining fibrosis indicates other mechanisms regulate fibroblast transformation in this model. Further, our results in TAC mice show that fibroblast MyD88 can still regulate fibrosis in a model in which T-cells are fully required for fibrosis. Our results indicate that decreased inflammatory signaling, especially decreased MyD88, represent one such mechanism. Interestingly, while we found decreased *Myd88* transcription in myofibroblasts from scRNA-sequencing data from PE-ANGII, TAC, and human HF, we also show post-translational regulation of MyD88 through the ubiquitin proteasome system. As proteasomal inhibition or Smurf2 knockdown restored MyD88 expression after TGFβ treatment, we believe post-translational regulation is the main mechanism regulating MyD88 in fibroblasts, however TGFβ directly decreased *Myd88* transcription, and both the functional relevance and mechanism remain an ongoing area of investigation.

While we show that fibroblast MyD88 decreases in multiple preclinical models of fibrosis and human non-ischemic cardiomyopathy, the broader application of this mechanism remains unclear. It is plausible this applies mostly to cardiac fibrosis, but TGFβ is widely implicated across fibrotic diseases,[254] necessitating the study of fibroblast MyD88 in other disease contexts and organs. Further, in the context of myocardial infarction (MI), in which fibroblasts create the fibrotic scar necessary for acute survival but also mediate chronic pathologic fibrosis, the role of MyD88 might be more complicated. While we hypothesize that

in MI the TGFβ-MyD88 axis still occurs, genetic manipulation might have differing results in different phases of healing. Additionally, the massive necrotic cardiomyocyte death induced by MI can induce TLR-MyD88 signaling[270] which might alter the MyD88-Smad4 binding. This inflammatory signaling through TLRs also highlights the potential for MyD88 in mediating other inflammatory functions in fibroblasts, such as antigen presentation or chemokine secretion. Future studies will further characterize how deletion or overexpression of MyD88 impacts this.

Targeting TGFβ has not yet shown success context of cardiovascular disease, necessitating other anti-fibrotic therapeutic approaches.[396] Additionally, inhibition of other pro-fibrotic cytokines such as IL-1β have not been broadly effective in improving patient outcomes in HF.[55,58,59] We hypothesize that as MyD88 functions differently in innate immune cells, adaptive immune cells, and now stromal cells, this could be one reason why IL-1β inhibition is not yet successful. However, this also suggests that inhibition of MyD88 broadly would not represent a therapeutic approach. Our data imply that modulation of the level of MyD88 in specific cell types such as cardiac fibroblasts could be more fruitful in preventing fibrosis in HF. Inhibition of Smurf2 could allow for the preservation of fibroblast MyD88 even in a high TGFβ environment, preventing myofibroblast transformation and keeping the innate immune function of MyD88 intact. However, as Smurf2 inhibitors have yet to be established, their potential as anti-fibrotic therapies and any off-target effects in other cell types remain unknown.

While our work has elucidated a novel mechanism in TGFβ induced myofibroblast transformation, it has several limitations we would like to address. This study uses hypertensive or pressure overload induced fibrotic models, and as such it is not clear how broadly applicable this mechanism is across all etiologies of cardiac fibrosis. Additionally, *Myd88* transcript was relatively low in each single cell RNA-seq dataset we utilized, and while we consistently found downregulated *Myd88* supporting our hypothesis, we believe

that single cell proteomics, once more widely available, will better capture the full post-translational regulation of MyD88 in cardiac fibroblasts. We also show that MyD88 overexpression prevents TGFβ induced fibroblast transformation, however thus far we have only shown proof of concept experiments *in vitro.* Futures studies will employ *in vivo* MyD88 overexpression utilizing fibroblast specific AAV vectors to further test the hypothesis that modulating MyD88 levels can prevent cardiac fibrosis. This will be further tested in the future using fibroblast conditional knockout of Smurf2 as an additional method of preserving MyD88. Finally, while we have shown *in vitro* and *in vivo* that myofibroblasts downregulate MyD88, we mainly use αSMA and POSTN as readouts for myofibroblast differentiation. We acknowledge that there is large heterogeneity of myofibroblasts themselves, and future unbiased multi-omics experiments will help delineate which subsets of fibroblasts use MyD88 in this regulatory fashion. Despite these limitations, we believe that the data presented here outline an important new mechanism in fibroblast biology.

In summary, here we characterize a novel regulatory mechanism in the myofibroblast transformation TGFβ in which MyD88 is degraded in response to TGFβ through the Ubiquitin Proteasome system, allowing increased Smad translocation to the nucleus. Our data highlight the increasing diversity of functions for MyD88 outside of innate immune cells and increase our understanding of TGFβ signaling with broadly applicable implications. Together this evidences that modulation of MyD88 levels in fibroblasts could be a novel therapeutic approach in preventing cardiac fibrosis.

3.5 Author Contributions

A.L.B. designed the project, performed experiments, analyzed data, and wrote the manuscript. S.S., B.P.T., and R.E. performed experiments, provided intellectual input, and

edited the paper. P.A. designed the project, provided intellectual support, and contributed to writing and editing of the manuscript.

3.6 Acknowledgements

Thank you to Navin Kapur at Tufts Medical Center for providing human LV HF fibroblasts.This work was supported by National Institute of Health (NIH) Grants R01 HL144477 and HL165725 (P.A.), NIH F30 Grant HL162200 (A.L.B.), Equipment Grant NIH S10OD032201.

Chapter 4 Deletion of T-cell MyD88 Improves Anti-Tumor Immunity in Melanoma[400]

Bayer, A. L., Padilla-Rolon, D., Smolgovsky, S., Hinds, P. W. & Alcaide, P. Deletion of MyD88 in T Cells Improves Antitumor Activity in Melanoma. *The American Journal of Pathology* **194**, 1007–1019 (2024).

Reprinted here with permission of the publisher.

4.1 Introduction:

The progression of cancer is tightly regulated by a fine balance between the anti-tumor immune response, and the tumor pro-survival and proliferative signals determined by immune cell-tumor cell interactions in the tumor microenvironment.[81,280] The immune response is required to prevent tumor growth, yet cancer cells perpetuate suppressive mechanisms for immune evasion and uncontrolled growth. The overall goal of immunomodulatory therapy against cancer is to shift the tumor microenvironment to favor anti-tumor immunity and T-cell cytotoxicity by preventing the suppressive signals that tumor cells imprint on immune cells. One method of anti-tumor immunotherapy is the expansion of patient-derived cytotoxic T-cells *ex vivo* which are then transferred back into the patient,[81,82] however this is hindered by the ability of T-cells to survive in the anti-inflammatory tumor microenvironment. Another successful approach in melanoma is the inhibition of immune checkpoint molecules such as programmed death ligand-1 (PD-1), expressed on T-cells to prevent their over activation and effector functions at steady state.[82,352,406] Inhibitors of these checkpoints have demonstrated efficacy in enhancing T-cell anti-tumor activity in melanoma and other cancers.[407] However these inhibitors are not effective in all patients, with a maximum response rate in melanoma rarely higher than 50%.[408,409] This suggests that other intrinsic mechanisms must exist to limit cytotoxic T-cell activity that could be targeted to improve anti-tumor immunity.

An optimal anti-tumor immune response requires recognition of tumor damage-associated molecular patterns (DAMPs) by antigen presenting cells (APCs) that become activated and present tumor-antigens to $CD4^+$ and $CD8^+$ T-cells.[410,411] Tumor killing is in part mediated by a coordinated $CD4^+$ helper T-cell response that helps $CD8^+$ T-cell cytotoxicity characterized by degranulation of perforin and granzymes as well as IFNγ production (Type I cytotoxic T-cells – Tc1) resulting in direct tumor cell killing.[91,154] DAMP signals from dying tumor cells converge onto the adaptor protein Myeloid differentiation response 88

(MyD88).[410] While in innate immune cells MyD88 signals are central to pro-inflammatory immune responses,[410] in T-cells the antigen specificity and strength of the T-cell receptor (TCR) determines how MyD88 contributes to adaptive immune responses.[118,412] We recently reported that $CD4^+$ T-cell MyD88 limits helper $CD4^+$ T-cell activation by tuning down T-cell receptor signaling in the context of cardiac inflammation[398]. However, the contribution of MyD88 to $CD8^+$ T-cell cytotoxicity is unknown. We hypothesized that if a similar mechanism takes place, modulating $CD8^+$ T-cell MyD88 could be used for immunomodulation in cancer.

Here we tested this hypothesis using adoptive transfer strategies and T-cell specific genetic deletion of MyD88 in mice bearing antigen non-specific and specific melanoma tumors, as well as *in vitro* mechanistic studies of T-cell cytotoxicity. We found that MyD88 restrains $CD8^+$ T-cell activation and that deletion of MyD88 in T-cells enhances T-cell cytotoxicity against melanoma through mechanisms involving T-cell activation, degranulation, and cell survival.

4.2 Methods:

4.2.1 Animals:

All animal studies were approved by the Tufts University Institutional Animal Care and Use Committee. C57BL/6, *Tcra*$^{-/-}$[367], OTI[413], and CD4^{Cre} x MyD88$^{fl/fl}$ mice[398] were bred and maintained under pathogen free conditions. MyD88$^{-/-}$ mice were bred and maintained under specific pathogen free conditions, and MyD88$^{-/-}$ OTI mice were generated by breeding OTI to MyD88$^{-/-}$ mice under specific pathogen free conditions. MyD88 excision was determined by PCR (see Appendix 9.10 for primer sequences).

4.2.2 Cell Culture:

SM1-750 cells[414] and B16-OVA cells[415] were cultured in RPMI with 10% fetal bovine serum (FBS – Atlanta Biologicals S11150), and 1% penicillin streptomycin (Gibco 15140122). B16-OVA cells were switched to DMEM with 10% FBS 24 hours prior to implantation in tumor studies.

4.2.3 Generation of Tc1 Cells:

CD8^{+} T-cells were isolated from splenic cell suspensions by positive selection using magnetic beads (Miltenyi 130-117-044). Cells were plated at 2 million cells / mL and differentiated in the presence of anti-CD3 (2.5 µg/mL, Biolegend 100253), anti-CD28 (1 µg/mL, Biolegend 102102), IL-12 (10 ng/mL, Peprotech 210-12), IL-2 (25U/mL, Miltenyi, 130-120-662) and, anti-IL4 (50 ng/mL, Biolegend 504102) for 3 days, expanded for 24 hours in IL-2 alone, then harvested for experiments. T-cells were cultured at 37°C in RPMI medium (Gibco, 11875-093) containing 10% FBS, Glutamax (Gibco A12860-01), NaHCO3 (Gibco 25080-094), Penicillin/Streptomycin (Gibco 15140122), 60µM β-mercaptoethanol (Sigma 444203), Sodium pyruvate (Gibco 11360-070).

4.2.4 Melanoma Models and Adoptive Transfer:

SM1-750 or B16-OVA cells were trypsinized (Thermofisher 12604013) and resuspended in cold PBS. 2 million SM1-750 cells or 1 million B16-OVA cells were injected subcutaneously in the left flank of *Tcra*$^{-/-}$ or CD4^{Cre} x MyD88$^{fl/fl}$ mice. Once palpable, tumor growth was monitored with caliper measurement using the formula [(π/6)*Length*Width^2]/2. Mice were euthanized when indicated or when tumor volume reached 1.5 cm^3 or when tumors measured 2 cm in any direction. For adoptive transfer, 10 million WT or MyD88$^{-/-}$ Tc1 cells were resuspended in cold PBS and injected intraperitoneally once tumors were palpable, then again 10 days later. 5 million OTI or MyD88$^{-/-}$ OTI Tc1 were resuspended in cold PBS and injected intraperitoneally once tumors were palpable. Mice were randomized by random number generator, and all harvest of tissues and analysis was performed blinded.

4.2.5 Tumor Digestion and Flow Cytometry:

Tumors were excised, and divided with one piece digested mechanically and enzymatically 30 minutes using 1 mg/mL collagenase 1 (Thermofisher 17100017), 250 u/mL hyaluronidase (Sigma H3506), and 100 µg/mL DNAse1 (Signa DN25). Spleens and lymph nodes were excised and crushed through a 40 µm strainer to generated single cell suspensions. Cell suspensions were stained using the following antibodies from Biolegend: APC-Cy7 or FITC CD4 (Biolegend 100414, 100406), FITC CD8 (Biolegend 100705), APC IFNγ(Biolegend 505810), PE IL-17 (Biolegend 506904), PerCP Tbx21 (Biolegend 644806), APC-Cy7 TCRβ (Biolegend 109220), BV421 or APC CD45.2 (Biolegend 109832, 109814), PE CD45.1 (Biolegend 110707), APC CD44 (Biolegend 103012), PE CD62L (Biolegend 104408), BV421 CD25 (Biolegend 102043), FITC CD69 (Biolegend 104506), APC MHCII (Biolegend 107613) APC-Cy7 CD11b (Biolegend 101225), PE CD11c (Biolegend 117307), BV421 Ly6G (Biolegend 127627),

FITC CCR2 (Biolegend 150607), or APC PD1 (Biolegend 135210). Samples were surface stained by incubation with the relevant antibodies diluted 1:50 in phosphate buffered saline (PBS) + 2% FBS for 20 minutes at 4°C. When intracellular cytokine staining was performed, samples were incubated for 4 hours at 37C in complete T-cell media (see above) including 50 ng/mL Phorbol Myristate Acetate (PMA, Sigma Aldrich P8139), 0.1% Ionomycin (Sigma 13909), 0.1% Brefeldin A (Biolegend 420601), and Monensin (Biolegend 420701), followed by surface staining as described. Samples were fixed for 15 minutes at RT with fixation buffer (Biolegend, 420801), then permeabilization by two washes with 1X Perm/Wash buffer (Biolegend, 421002, then stained intracellularly with the appropriate antibodies diluted 1:50 in PBS + 2% FBS for 20 minutes at 4°C. To detect Tbx21, samples were surface stained as described, fixed using 1X FOXP3 Fix/Perm solution (Biolegend, 421401) for 20 minutes at RT, permeabilized for 15 minutes using 1X FOXP3 Perm solution (Biolegend, 421402), then stained intracellular for 20 minutes with the appropriate antibodies diluted 1:50 in PBS + 2% FBS for 20 minutes at 4°C. Data was acquired an a BD LSRII (BD Biosciences) and analyzed using FlowJo software. Tumor infiltrating immune cells were normalized to the weight of the digested tumor.

4.2.6 Immunofluorescence:

Frozen tissues were washed 2 x 10 min. with PBS, then fixed with 4% PFA for 15 minutes. Samples were washed with PBS, then incubated with PBS + 10% normal goat serum (Abcam Ab7481), 10% donkey serum (Southern Biotech 0030-01), and 0.1% triton-X (Sigma X100) for 1 hour at RT. Samples were incubated αCD8 (Biolegend 100701) and αCleaved Caspase 3 (CST 9661) at 1:100 in blocking buffer overnight at 4°C. Samples were washed with PBS then incubated with either anti-rat AF568 (A78946) or anti-rabbit AF488 (A11008) at 1:200 in blocking buffer, then mounted in Vectashield

with DAPI (Southern Biotech, 0100-20) before imaging on an Nikon Ti inverted fluorescence microscope, then quantified using ImageJ version 1.53t (https://imagej.net/ij/download.html, last accessed 2/15/24).

4.2.7 Immunoblotting:

Cells were lysed in RIPA buffer (150 mM NaCl, 50 mM Tris pH 7.4, 1% NP-40, 0.1% SDS, 5 mM EDTA, 0.1% sodium deoxycholate, 1 mM DTT) supplemented with protease and phosphatase inhibitors (Roche 4906845001, 4693159001), then cleared by centrifugation at 4°C at 13,000 RCF. Protein concentrations were determined using DC protein assay (BioRad 5000112) and equal concentrations of protein were subjected to SDS-PAGE in 10% resolving gels unless otherwise indicated, then transferred to PVDF membranes, followed by blocking with Tris buffered saline + 0.1% Tween20 containing 5% non-fat milk or bovine serum albumin (BSA) for 1 hour at room temperature. Immunoblotting was performed overnight at 4°C using antibodies diluted 1:1000 in 5% non-fat milk or BSA. Antibody sources: GAPDH (CST 2118), MyD88 (R&D AF3109), Cleaved Caspase 3 (CST 9661), Caspase 8 (CST 4927), Cleaved Caspase 8 (CST 8592), Caspase 9 (CST 9508), pERK (CST 9101), ERK (CST 9102), β-actin (Sigma A5441), α-tubulin (CST 3873), α-smooth muscle actin (Sigma A2547), pZap70 (CST 2717), Zap70 (CST 3165), Blots were then incubated with the appropriate HRP-peroxidase conjugated secondary antibody (1:2000, Rabbit CST 7074, Mouse CST 7076, Goat ThermoFisher A15999) at room temperature for 1 hour, then developed using Pierce ECL (ThermoFisher 32106) and imaged using a ChemiDoc XRS+ System (Biorad). Band intensity was quantified using Image-J.

4.2.8 Real Time Cell Imaging:

Tc1 cells were plated on 384 well black optical bottom plates (Nunc 142761) coated with 10 μg/mL αCD43 (Invitrogen, 14-0431-85) at 30,000 cells / well in complete T-cell media

or media containing 1% FBS, including 10 μg/mL propidium iodide (Biolegend 421301). The Lionheart imager was used to maintain temperature at 37°C, 5% CO_2, and humidity during the experiment. Kinetic microscopy was performed by the Lionheart imager to quantify propidium iodide uptake every 90 minutes over 72 hours. Wells containing 0.1% Triton X-100 lysed cells were used as a positive control, with propidium iodide uptake baseline subtracted and normalized as % positive control.

4.2.9 In Vitro Killing:

SM1-750 or B16-OVA cells were plated at a concentration of 100,000 cells per well in a 12 well plate, then Tc1 cells were added in ratios from 1:5 (Tc1:Melanoma) up to 1:1. For SM1-750 killing assays cultures were harvested after 4 hours of co-culture, whereas B16-OVA killing assays were harvested after 16 hours of co-culture. Samples were stained with Annexin V AF647 (Biolegend 650912) in PBS + 2% FBS, 10 mM HEPES (Thermofisher 15630080), 2.5 mM $CaCl_2$ and 1.0 mM $MgCl_2$ for 30 minutes at 4 deg. C, then stained with CD8 BV421 (Biolegend 100753) and 7AAD (Biolegend 420403) in PBS + 2% FBS for 20 minutes at 4 deg. C.

4.2.10 RT-qPCR:

Cell lysis and RNA isolation was performed using an RNEasy kit according to manufacturer's instructions (Qiagen 74004). cDNA synthesis was performed using High-Capacity cDNA Reverse Transcription Kit (ThermoFisher 4368814), and qPCR was performed using SYBR Green (ThermoFisher A25741) on a QuantStudio 6 Flex Real-Time PCR Machine (ThermoFisher), then analyzed for fold change using ΔΔCt method. See Appendix 9.10 for primer sequences.

4.2.11 T-cell Degranulation Assay:

Tc1 cells were generated as described above, pelleted, and resuspended in complete T-cell media where indicated containing 50 ng/mL Phorbol Myristate Acetate (PMA, Sigma

Aldrich P8139) and 0.1% Ionomycin (Sigma 13909) for 1 or 5 hours in the presence of 1:100 PE CD107a antibody (Biolegend 121612).

4.2.12 Statistical Analysis:

Statistical analysis was performed using GraphPad Prism 9.4.1. All data is presented as mean ± SEM. Statistical analysis was done by Student's unpaired or paired t-test (where indicated) for two group analysis. Multiple group comparisons were done using one-way ANOVA with Tukey's multiple comparison test or two-way ANOVA with Sidak's multiple comparison test. Differences were considered statistically significant at $p \leq 0.05$.

4.2.13 Data Availability:

The data, methods, and materials will be available to other researchers for the purposes of reproducing the results or replicating procedures.

4.3 Results:

4.3.1 Adoptive Transfer of MyD88$^{-/-}$ Tc1 Cells into Melanoma Bearing Mice Slows Tumor Growth Compared to WT Tc1 Cells.

To investigate the intrinsic role for CD8^{+} T-cell MyD88 in anti-melanoma activity, we implanted SM1-750 melanoma cells, an aggressive murine BRAF mutant line, into *Tcra*$^{-/-}$ mice, lacking T-cells and thus highly permissive to tumor growth, and adoptively transferred either WT or MyD88$^{-/-}$ Tc1 cells once tumors were palpable (Figure 4-1A). We detected similar frequencies of WT and MyD88$^{-/-}$ CD8^{+}TCRβ^{+} cells in the draining lymph nodes, confirming successful reconstitution of both genotypes of T-cells (Figure 4-1B), and no alteration of CD11b^{+} myeloid cells in lymphoid organs (Figure 4-2A-C). WT Tc1 cells modestly reduced tumor growth and total tumor weight by ~30% compared to mice receiving no Tc1 cells (Figure 4-1C-D). Strikingly, mice given MyD88$^{-/-}$ Tc1 cells had significantly slower tumor growth than either other group, showing ~70% decreased tumor size and weight (Figure 4-1C-D). To investigate whether the observed decreased tumor growth was a result of enhanced anti-tumor immune activity, we next analyzed tumor immune cell infiltration. We found adoptively transferred WT and MyD88$^{-/-}$ CD8^{+} cells in each tumor, however, MyD88$^{-/-}$ CD8^{+} T-cells infiltrated tumors in significantly higher numbers than WT CD8^{+} T-cells (Figure 4-1E). MyD88$^{-/-}$ Tc1 cells also induced elevated intratumoral populations of CD11b^{+} monocyte/macrophages, CD11b^{+}Ly6G^{+} neutrophils, and CD11b^{+}CD11c^{+}MHCII^{+} dendritic cells compared to either group, whereas none of these populations were elevated in mice given WT Tc1 cells compared to mice receiving no T-cells. (Figure 4-2F-I). Next we analyzed tumor sections by immunofluorescence to corroborate our findings and again found elevated intratumoral CD8^{+} T-cells in tumors from mice given MyD88$^{-/-}$ Tc1 cells compared to either group (Figure 4-1F-G). We then probed for co-localization of intratumoral CD8^{+} T-cells with

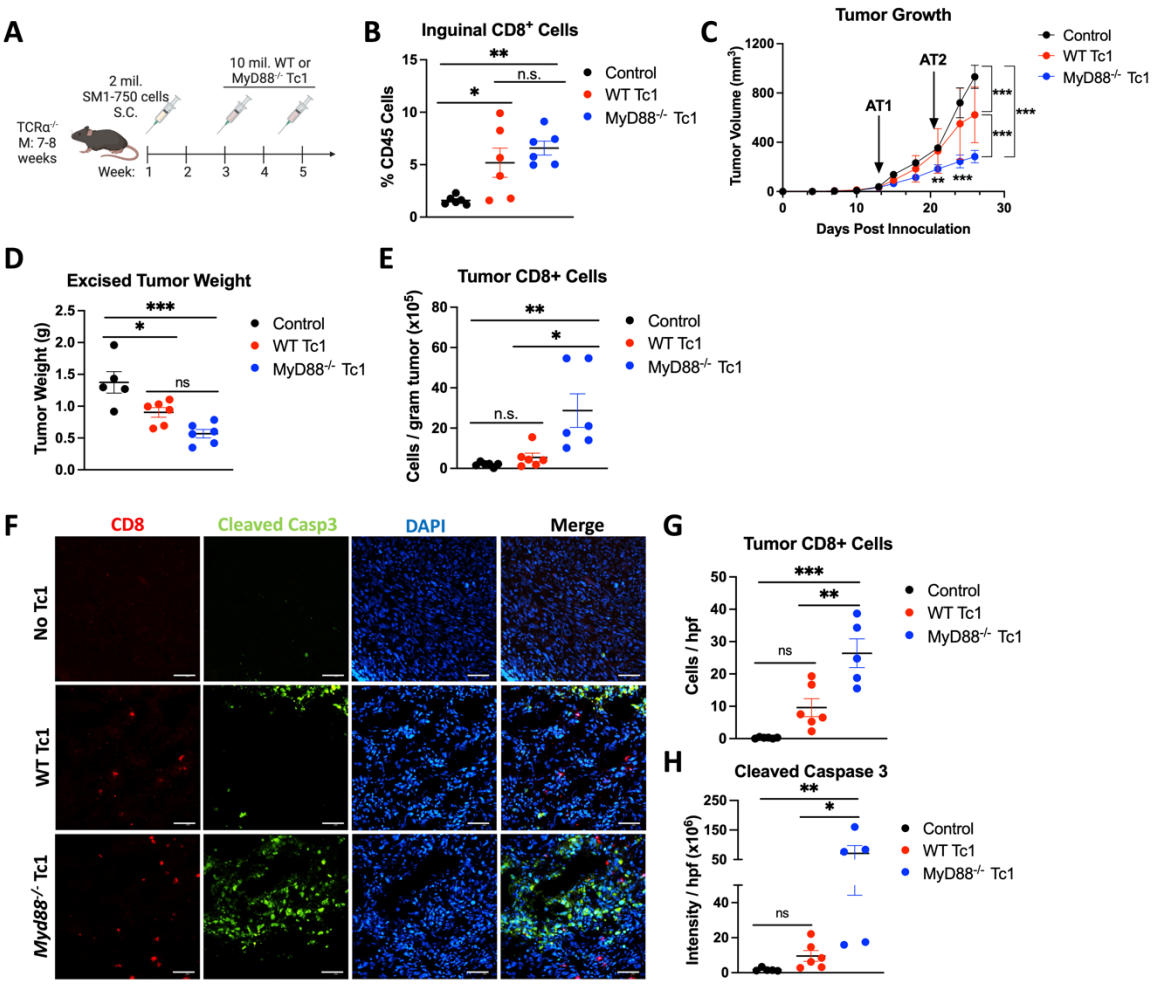


Figure 4-1 Adoptive Transfer of MyD88-/- Tc1 Cells into Melanoma Bearing Mice Slows Tumor Growth Compared to WT Tc1 Cells.

A. Schematic of tumor experiment in which male Tcra$^{-/-}$ mice were given 2 million subcutaneous SM1-750 cells, then 10 million WT or MyD88$^{-/-}$ Tc1 cells were transferred at the indicated time points by intraperitoneal injection once tumors were palpable (n=6-7 mice / group). B. Inguinal lymph nodes were digested and analyzed by flow cytometry for CD8 T-cells. C. Tumors were measured every 3-4 days by calipers, tumor volume was calculated with the formula $V = [(\pi/6) \times L \times W^2] / 2$. After 26 days tumor were excised and weighted (D) then digested enzymatically and mechanically, then analyzed by flow cytometry for CD8 T-cells (E). F-H. Frozen sections of tumor were stained for CD8 and Cleaved Caspase 3 by immunofluorescence microscopy (scale bars = 50 μm), G. T-cells were counted manually from an average of 5 fields of view (hpf = high powered field), H. Caspase 3 signal intensity was analyzed using imageJ from 5 fields of view. Statistical analysis was performed by 1-way ANOVA with Tukey's multiple comparison test (B, D, E, G, H) or by 2-way ANOVA with repeated measures (C), ns = no significance, * = $p < 0.05$, ** = $p < 0.01$, *** = $p < 0.001$.

tumor cell death by analyzing cleaved caspase 3 intensity. We found only modest cleaved caspase 3 near WT Tc1 cells, but significantly greater cleaved caspase 3 colocalized with MyD88$^{-/-}$ Tc1 cells, indicating greater melanoma cell death induced by these T-cells (Figure 4-1F, H). These data demonstrate that deletion of MyD88 in CD8^{+} T-cells results in greater tumor infiltration and melanoma cell death.

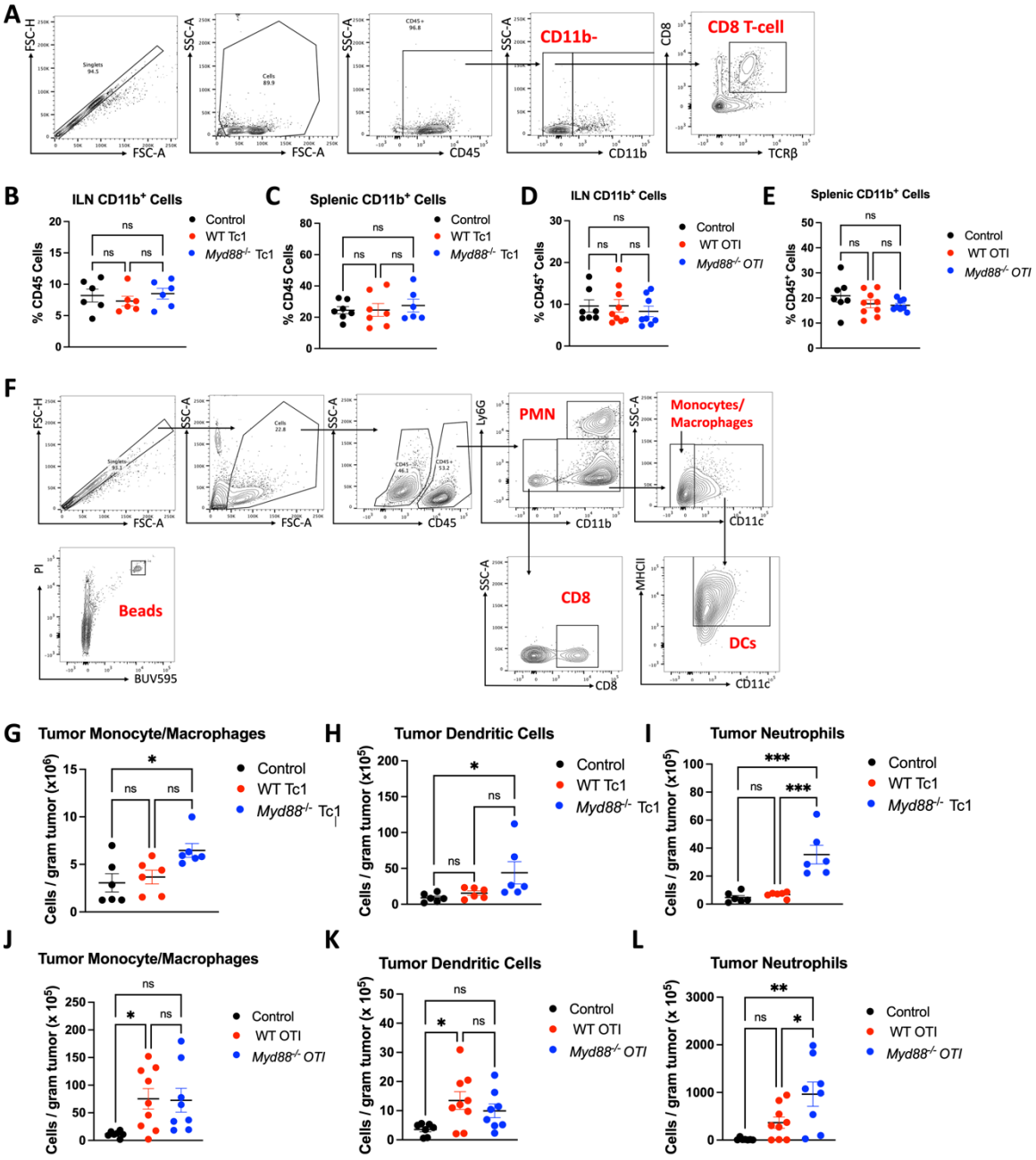


Figure 4-2 Gating for Adoptive Transfer and Tumor Myeloid Populations.
A. Inguinal lymph nodes or spleens were digested and analyzed by flow cytometry. Gating strategy for analysis of T-cell reconstitution and CD11b+ cells in Figure 4-1 and Figure 4-3, with quantification in for mice with SM1-750 tumors (B-C), or mice with B16 tumors (D-E). Tumors were digested enzymatically and mechanically, then analyzed by flow cytometry. F. Gating strategy for analysis of tumor immune populations in Figure 4-1 and Figure 4-3, with quantification for SM1-750 tumors (Figure 4-1) of Monocyte/Macrophages (G), Dendritic cells (H), or neutrophils (I) and for B16 tumors (Figure 4-3) of Monocyte/Macrophages (J), Dendritic cells (K), or neutrophils (L). Statistical analysis by 1-way ANOVA with Tukey's multiple comparison test. ns = no significance, * = $p < 0.05$, ** = $p < 0.01$, *** = $p < 0.001$.

4.3.2 MyD88 Deletion in OTI Tc1 Cells Improves Antigen Specific Anti-Tumor Immunity.

We next asked if MyD88 was able to further modulate the anti-tumor immune response in the context of a tumor-specific antigen. To do so, we generated $CD8^+$ T-cell antigen restricted WT and $MyD88^{-/-}$ mice by crossing $MyD88^{-/-}$ mice with OTI mice that have a transgenic TCR specific for ovalbumin ($MyD88^{-/-}$ OTI and $MyD88^{+/+}$-WT-OTI - Figure 4-3A). We adoptively transferred either WT OTI Tc1 cells or $MyD88^{-/-}$ OTI Tc1 cells into *Tcra*$^{-/-}$ mice bearing tumors from the OVA expressing melanoma cell line B16-OVA once tumors were palpable (Figure 4-3B). Staining for $CD8^+TCR\beta^+$ cells showed similar frequencies of WT or $MyD88^{-/-}$ OTI cells in the spleen (Figure 4-3C). However, the draining lymph nodes had significantly higher $MyD88^{-/-}$ OTI cells compared to WT (Figure 4-3D), suggesting greater T-cell expansion. We did not observe alterations to myeloid cells in the spleen or lymph nodes (Figure 4-2D-E). Both groups of mice receiving T-cells specific for tumor antigen showed significantly slower tumor growth compared to mice

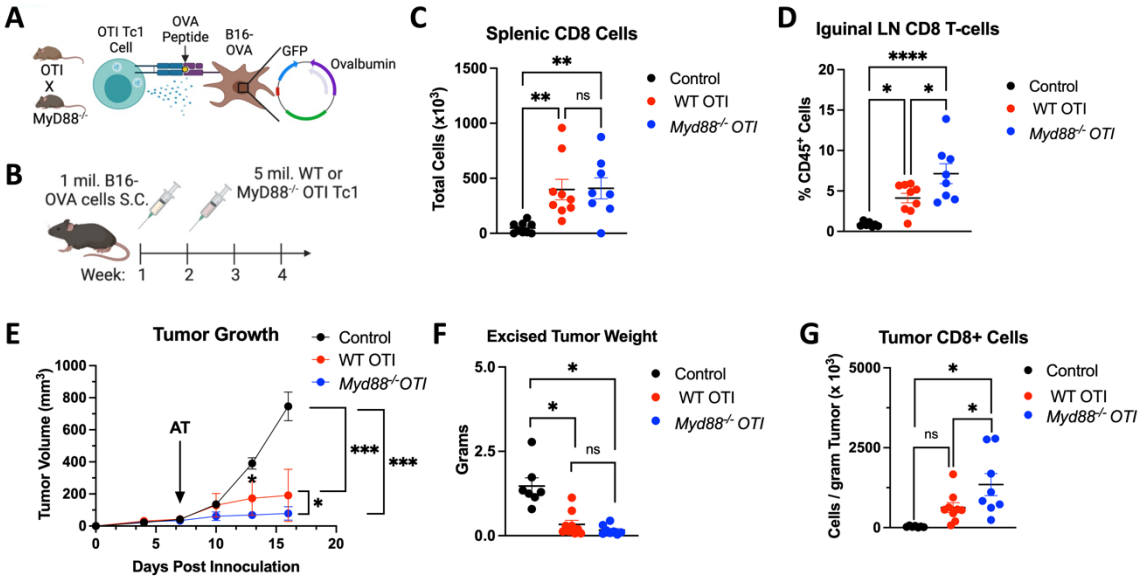


Figure 4-3 MyD88 Deletion in OTI Tc1 Cells Improves Antigen Specific Anti-Tumor Immunity in Melanoma

A. Schematic of antigen specific cancer model in which OTI T-cells recognize OVA expressed by B16 melanoma cells. B. Schematic of tumor experiment in which male $Tcra^{-/-}$ mice were given 1 million subcutaneous B16-OVA cells, then 5 million WT or $MyD88^{-/-}$ OTI Tc1 cells were transferred at the indicated time points by intraperitoneal injection once tumors were palpable (n=7-9 mice / group). B-C. Spleens and inguinal lymph nodes were digested and analyzed by flow cytometry for CD8 T-cells. E. Tumors were measured every 3-4 days by calipers, tumor volume was calculated with the formula $V = [(\pi/6) \times L \times W^2] / 2$. Tumors were excised after 16 days and weighted (F) then digested enzymatically and mechanically then analyzed by flow cytometry for CD8 T-cells (G). Statistical analysis was performed by 1-way ANOVA with Tukey's multiple comparison test (C, D, F, G) or by 2-way ANOVA with repeated measures (E), ns = no significance, * = $p < 0.05$, ** = $p < 0.01$, *** = $p < 0.001$, **** = $p < 0.0001$.

that received no T-cells. However, mice receiving MyD88$^{-/-}$ OTI Tc1 showed a ~90% decrease in tumor size while WT OTI Tc1 cells showed a ~75% decrease compared to mice that did not receive T-cells (Figure 4-3E). Both WT and MyD88$^{-/-}$ OTI cells were able to significantly decrease excised tumor weights (Figure 4-3F). The immune infiltrate of these tumors revealed significantly higher accumulation of intratumoral MyD88$^{-/-}$ OTI cells compared to WT OTI cells (Figure 4-3G), alongside similarly elevated monocyte, macrophage, and dendritic cell numbers in tumors of mice receiving either group of T-cells (Figure 4-2J-K), with slightly elevated neutrophils in mice given MyD88$^{-/-}$ OTI cells (Figure 4-2L). Taken together, these results demonstrate that antigen specific MyD88$^{-/-}$ Tc1 cells exhibit a stronger anti-tumor effect than antigen specific WT Tc1 cells.

4.3.3 MyD88 Limits CD8^{+} T-cell Activation Status and Survival.

We next investigated if the absence of MyD88 altered CD8^{+} T-cell activation as one mechanism for enhanced anti-tumor effector functions. We generated WT or MyD88$^{-/-}$ Tc1 cells *in vitro* and found that MyD88$^{-/-}$ cells expressed significantly higher phospho-ZAP70, immediately downstream of TCR activation (Figure 4-4A-B) as well as the early T-cell activation surface marker CD69 (Figure 4-4C-D) compared to WT-cells. In contrast, the protein and transcript levels of IFNγ, the signature Tc1 cytokine, and Tbx21, the master transcription factor for Tc1 cells were not altered by MyD88 deletion (Figure 4-5A-E), neither was PD-1 expression, a marker of T-cell exhaustion targeted by immune checkpoint inhibitors (Figure 4-5F). We next asked whether in addition to MyD88 modulating TCR signaling, it also mediates canonical Toll-Like Receptor (TLR) signals, as in innate cells, we treated naïve WT or MyD88$^{-/-}$ CD8^{+} cells with the TLR4 ligand LPS and found an increase in ERK phosphorylation (Figure 4-5G) and IL-6 expression (Figure 4-5H), both downstream of MyD88, in only WT-cells. This confirmed

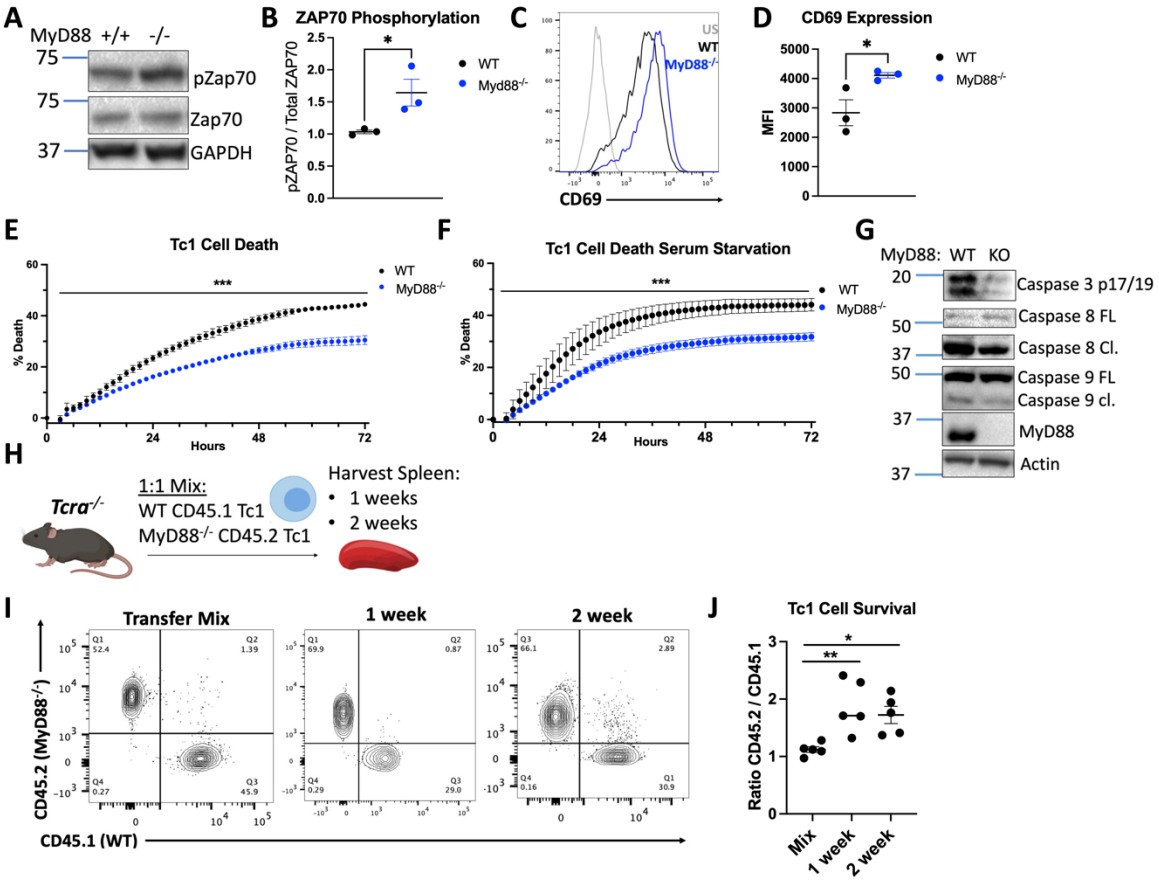


Figure 4-4 MyD88 Limits CD8+ T-cell Activation Status and Survival.
Tc1 cells were collected after 3 days of activation by 2.5 μg/mL αCD3 and 1.0 μg/mL αCD28 for analysis by western blot, representative blot in A. and quantification from n=3 independent experiments in B, or collected for analysis by flow cytometry, representative histograms in C. and quantification from n=3 independent experiments in D. E-F. WT or *Myd88*$^{-/-}$ Tc1 cells were cultured on αCD43 coated plates (10 μg/mL) in the presence of 10 μg/mL propidium iodide (PI) in media with (E) or without 10% FBS (F). PI incorporation was monitored for 72 hours, baseline subtracted, and normalized to a 100% death Triton-X treated control, representative graphs shown from n=4 independent experiments. G. WT or MyD88$^{-/-}$ Tc1 cells were collected after 3 days of activation followed by 1 day of serum starvation for analysis by western blot. H. Scheme of *in vivo* competitive survival, in which healthy *Tcra*$^{-/-}$ mice were reconstituted with 10 million WT CD45.1 and *Myd88*$^{-/-}$ CD45.2 Tc1 cells in 1:1 abundance, then spleens were harvested at indicated time points. I. Representative flow cytometry plots gated on CD8^{+}TCRβ^{+} cells from *in vivo* survival showing transfer mix prior to transfer, and splenic T-cells after 1 or 2 weeks post transfer, quantified in J. from 5-6 mice / group. Statistical analysis was performed by T-test (B, D), 2-way ANOVA with repeated measures (E,F) or 1-way ANOVA with Tukey's multiple comparison test (J), ns = no significance, * = $p < 0.05$, ** = $p < 0.01$, *** = $p < 0.001$.

MyD88 is functional as a DAMP receptor in addition to a novel role in modulating CD8^{+} T-cell activation through TCR signaling.

We next tested whether increased T-cell activation in MyD88$^{-/-}$ Tc1 cells also resulted in enhanced T-cell survival as one mechanism leading to T-cell persistence in tumors and stronger anti-tumor immunity. We cultured T-cells in the absence of TCR or cytokine stimulation to induce T-cell death as done previously,[398] and imaged propidium

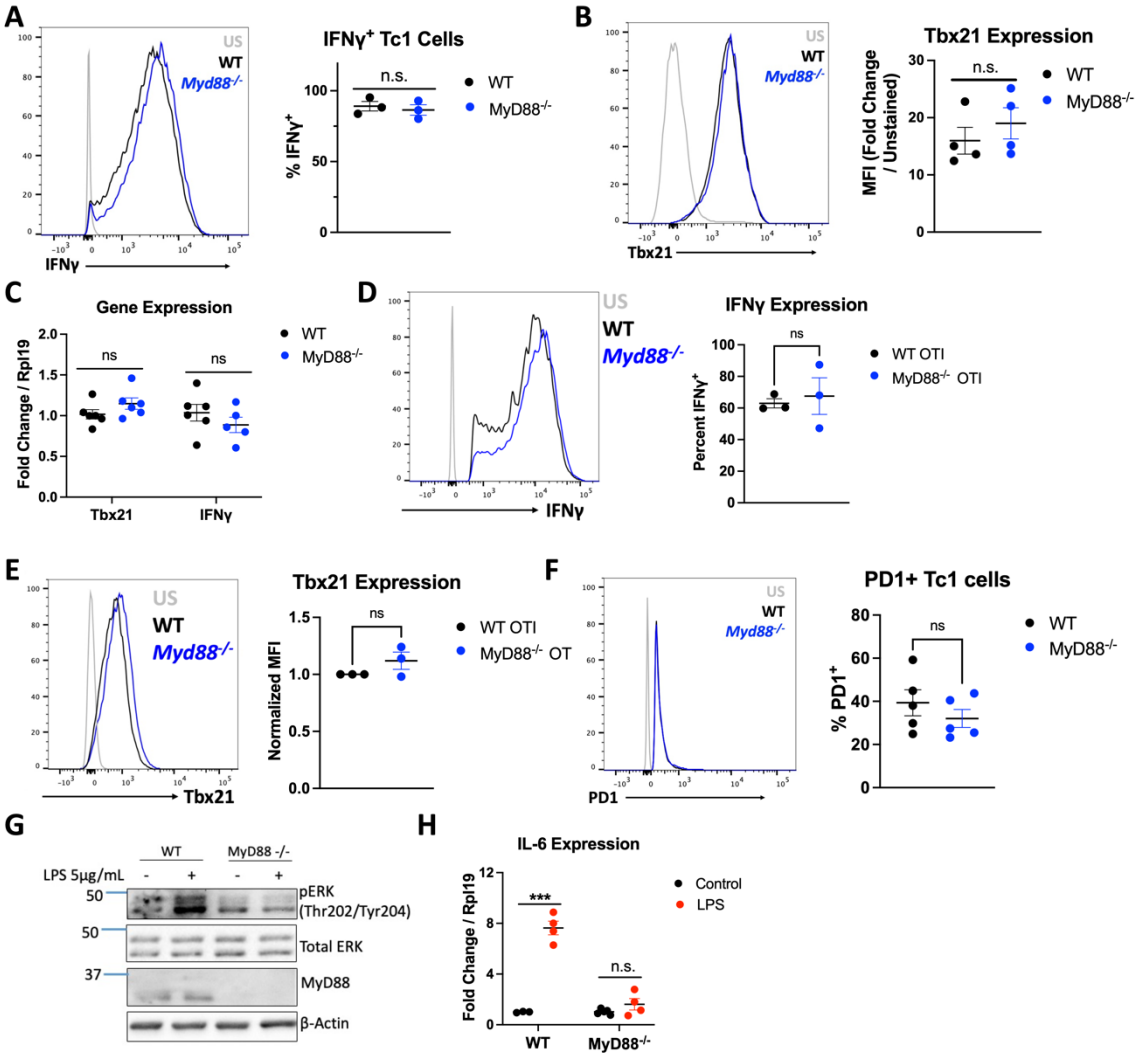


Figure 4-5 MyD88 Mediates TLR Signaling in Tc1 Cells but does not contribute to Tc1 Polarization
A-C. WT or MyD88$^{-/-}$ Tc1 cells were isolated from splenocytes and activated as described in the methods. A. Representative flow cytometry plots for IFNγ expression with quantification from n=3 independent experiments. B. Representative flow cytometry plots for Tbx21 expression with quantification from n=4 independent experiments. C. RNA was isolated from WT or MyD88$^{-/-}$ Tc1 cells for analysis by RT-qPCR. D-E. WT or MyD88$^{-/-}$ OTI Tc1 cells were isolated from splenocytes and activated as described in the methods. D. Representative flow cytometry plots for IFNγ expression with quantification from n=3 independent experiments. E. Representative flow cytometry plots for Tbx21 expression with quantification from n=4 independent experiments. F. Representative flow cytometry plots for PD1 expression with quantification from n=5 independent experiments. G.WT or MyD88$^{-/-}$ Tc1 cells were treated with 2.5 ug/mL LPS for 16 hours than analyzed by western blot (G) or RT-qPCR (H). Statistical analysis by T-tests (A-F) or 2-way ANOVA with Sidak's multiple comparison test (H) ns = no significance, *** = $p < 0.001$.

iodide incorporation in real time. Strikingly, *Myd88*$^{-/-}$ Tc1 cells exhibited improved survival over time compared to WT Tc1 cells, and this was also observed in conditions of serum starvation that increase T-cell death (Figure 4-4E-F). In line with this, we found decreased levels of several cleaved caspases, which coordinate cell death, in the lysates of serum starved MyD88$^{-/-}$ Tc1 cells compared to WT Tc1 cells. We then

performed *in vivo* competitive survival assays using equal numbers of adoptively transferred WT and *Myd88*$^{-/-}$ Tc1 cells, carrying the CD45.1 and CD45.2 alleles respectively, into healthy *Tcra*$^{-/-}$ recipient mice (Figure 4-4H). We found higher frequencies of *Myd88*$^{-/-}$ Tc1 cells compared to WT in the spleen at both 1- and 2-weeks post transfer (Figure 4-4I-J). Taken together, these data demonstrate a role for MyD88 in modulating Tc1 activation through the TCR as well as survival *in vitro* and *in vivo.*

4.3.4 Deletion of MyD88 Affords Tc1 Cells Enhanced Anti-Melanoma Cytotoxic Activity.

Given the striking anti-tumor activity of MyD88$^{-/-}$ CD8^{+} T-cells observed *in vivo,* we next directly tested the killing activity of WT and MyD88$^{-/-}$ CD8^{+} T-cells in *in vitro* assays. We first evaluated Tc1 killing of SM1-750 melanoma cells (Figure 4-6A) and co-cultured melanoma cells with Tc1 cells at different ratios. At each ratio tested, MyD88$^{-/-}$ Tc1 cells had increased cytotoxicity against SM1-750 cells compared to WT Tc1 cells. (Figure 4-6B-C). We then sought to perform a similar analysis using antigen restricted T-cells and melanoma cells, which we expected to exhibit more robust killing. As such, we performed the same experiment with WT and MyD88$^{-/-}$ OTI Tc1 cells in culture with B16-OVA cells. As expected, the antigen specific OTI cells resulted in far greater killing of B16-OVA cells compared to SM1-750 death (Figure 4-6D). At low ratios of T-cells to melanoma cells, MyD88$^{-/-}$ OTI cells had improved cytotoxic killing ability compared to WT OTI cells, while this difference diminished at the highest ratio tested, in line with overall greater baseline cytotoxicity (Figure 4-6E) observed *in vitro* and in the tumor model *in vivo* (Figure 4-3). To further understand the mechanism of increased killing ability in MyD88$^{-/-}$ compared to WT Tc1 cells, we measured the intracellular levels of the cytotoxic mediators Perforin 1 and Granzyme B in both cell types. We found that MyD88$^{-/-}$ Tc1 cells expressed higher levels of Granzyme B at the transcript level (Figure 4-6F) and

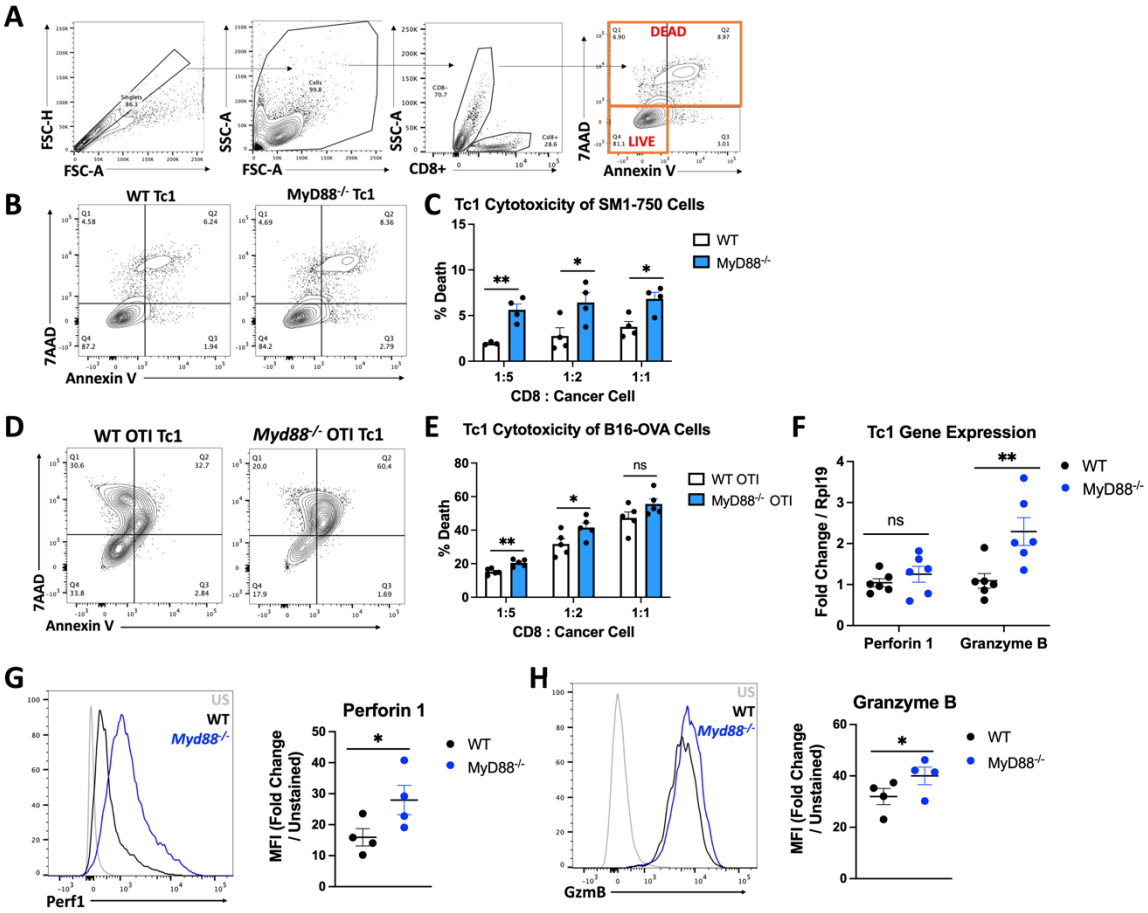


Figure 4-6 Deletion of MyD88 Affords Tc1 Cells Enhanced Anti-Melanoma Cytotoxic Activity
A. Gating strategy for analysis of melanoma cell death in *in vitro* cytotoxicity experiments, with red box for "Live" indicating Annexin V^{-}7AAD^{-} and red box "Dead" indicating 7AAD+. B. Representative flow cytometry plots of CD8- melanoma cells showing cell death by WT and MyD88$^{-/-}$ Tc1 cells at 1:2 ratio T-cell:cancer cell, with quantification in C. From n=4 independent experiments. D. Representative flow cytometry plots of CD8- melanoma cells showing cell death by WT and MyD88$^{-/-}$ OTI Tc1 cells at 1:2 ratio T-cell:cancer cell, with quantification in E. From n=4 independent experiments. F-H. WT or MyD88$^{-/-}$ Tc1 cells were collected after 3 days of activation by αCD3/αCD28 for analysis by qPCR (F) or flow cytometry, representative blot and quantification shown for Perforin 1 (G) or Granzyme B (H). Statistical analysis by T-tests, ns = no significance, * = $p < 0.05$, ** = $p < 0.01$.

expressed higher Perforin 1 and Granzyme B at the protein level than WT Tc1 cells (Figure 4-6G-H). These data demonstrate that deletion of MyD88 in cytotoxic T-cells improves their ability to kill melanoma cells through increased expression of cytotoxic molecules.

4.3.5 MyD88$^{-/-}$ Tc1 Cells Exhibit Increased Degranulation and ERK Signaling:

To better understand the mechanism of increased killing ability afforded by the loss of MyD88 and given our observation of increased intracellular Granzyme and Perforin

levels in MyD88$^{-/-}$ Tc1 cells compared to WT Tc1 cells, we next evaluated their ability to degranulate, or release these cytotoxic molecules. We analyzed CD107a expression, a cytotoxic granule marker that is displayed on the surface of a T-cell when a granule fuses with the plasma membrane as a readout of degranulation.[416] As expected, treatment with the TCR signaling stimuli PMA and Ionomycin increased CD107a expression in both WT and MyD88$^{-/-}$ Tc1 cells compared to unstimulated cells, which expressed very little at baseline (Figure 4-7A). However, upon 1 and 5 hours of PMA and Ionomycin stimulation, MyD88$^{-/-}$ Tc1 cells expressed higher CD107a compared to activated WT-cells, indicative of increased degranulation (Figure 4-7B). As expected, PMA and Ionomycin decreased intracellular Granzyme B in both WT and MyD88$^{-/-}$ Tc1 cells, as it was released from granules. This intracellular decrease in Granzyme B was significantly greater in MyD88$^{-/-}$ Tc1 cells compared to WT-cells, additional evidence of increased degranulation into the extracellular space (Figure 4-7C-D). We have previously shown that TCR activated MyD88$^{-/-}$ helper CD4^{+} T-cells express higher phospho-ERK compared to WT-cells.[398] ERK signaling downstream of the TCR has been directly associated with degranulation.[417,418] As such we asked if the increased activation status of MyD88$^{-/-}$ Tc1 cells promoted ERK activation. While at baseline we did not observe any significant changes to ERK phosphorylation, in response to PMA/Ionomycin stimulation, MyD88$^{-/-}$ Tc1 cells expressed higher phospho-ERK, trending up at 1 hour and becoming significant by 5 hours of treatment (Figure 4-7E-F). Together, these data provide evidence that the absence of MyD88 results in elevated ERK activation and subsequent increased degranulation in response to TCR stimulation by PMA and Ionomycin, as one mechanism of improved CD8^{+} T-cell cytotoxicity.

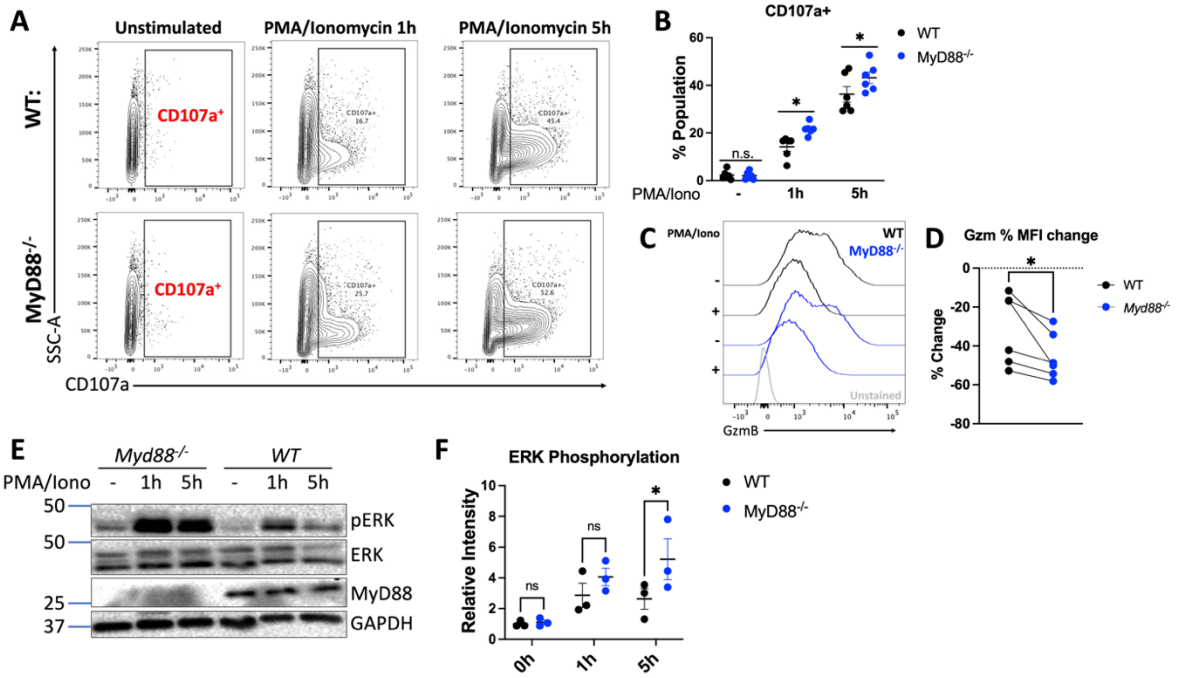


Figure 4-7 MyD88-/- Tc1 Cells Exhibit Increased Degranulation and ERK Signaling.
WT or MyD88$^{-/-}$ Tc1 cells were treated with 50 ng/mL PMA and 0.1% Ionomycin for 1 or 5 hours in the presence of PE anti-CD107a or were collected for western blot. A. Representative flow cytometry plots showing CD8+ T-cell CD107a expression, quantified in n=6 independent experiments in B. C. Representative flow cytometry histograms after PMA/Ionomycin showing Granzyme B expression, quantified in D. for n=5 independent experiments. E. Representative western blot after PMA/Ionomycin treatment of n=3 independent experiments quantified in F. Statistical analysis by 2-way ANOVA with Sidak's multiple comparison test (B, F) or paired T-tests (D), ns = no significance, * = $p < 0.05$.

4.3.6 Genetic Deletion of MyD88 in T-cells Delays Melanoma Growth by Increased T-cell Activation, Tumor Infiltration, and Cytotoxicity.

To understand how deletion of T-cell MyD88 impacts the endogenous T-cell anti-tumor response, we implanted B16-OVA melanomas on T-cell specific MyD88 knockout mice, using the constitutive CD4-Cre driver which deletes MyD88 on both CD4^{+} and CD8^{+} T-cells (CD4^{Cre}MyD88$^{fl/fl}$)[398]. While tumors initiated in similar frequencies in both Cre^{+} knockout animals (T-MyD88$^{-/-}$) and Cre^{-} littermate controls (T-MyD88$^{+/+}$), we observed significantly slowed growth in the T-MyD88$^{-/-}$ mice (Figure 4-8A) and smaller excised tumor weight upon euthanasia of the animals (Figure 4-8B). We found that T-MyD88$^{-/-}$ mice had a significant increase in intratumoral CD8^{+} T-cells compared to T-MyD88$^{+/+}$ mice (Figure 4-8C), but no changes to CD4^{+} T-cells or any tumor myeloid population

(Figure 4-9B). We then evaluated T-cell activation in the tumor draining lymph nodes, and interestingly found elevations in both effector $CD8^+$ and $CD4^+$ T-cells (defined as $CD62^{lo}CD44^{hi}$) in T-$MyD88^{-/-}$ mice compared to T-$MyD88^{+/+}$ mice (Figure 4-8D-E). Thus, deletion of MyD88 in T-cells increases endogenous T-cell activation in the onset of melanoma i*n vivo* as well. We found no changes in overall myeloid populations in the draining lymph node, suggesting the increased T-cell activation was not a result of altered APC activity (Figure 4-9D-E). Lastly, we measured melanoma cell death by Caspase 3 cleavage in tumor sections, and strikingly found increased intratumoral cleaved Caspase 3 in areas of $CD8^+$ T-cell infiltration (Figure 4-8F, H) as well as

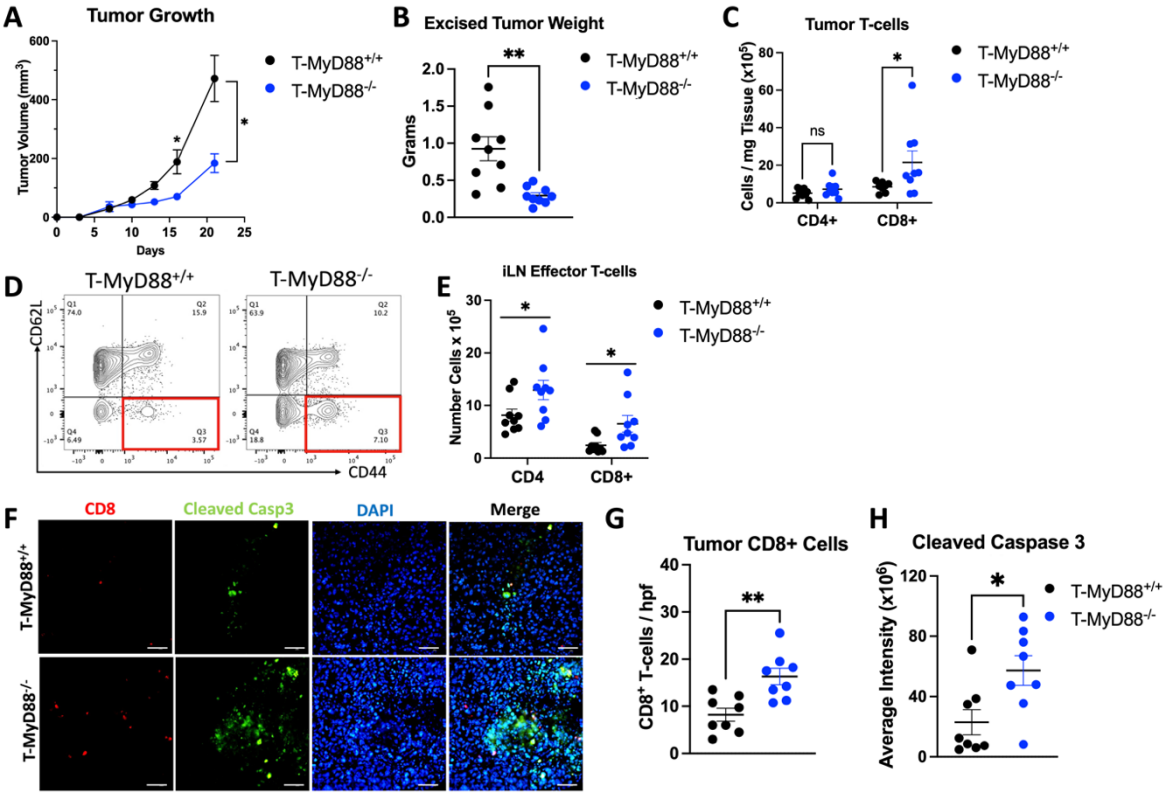


Figure 4-8 Genetic Deletion of MyD88 in T-cells Delays Melanoma Growth by Increased T-cell Activation, Tumor Infiltration, and Cytotoxicity

A. Tumors were measured every 3-4 days by calipers, tumor volume was calculated with the formula $V = [(\pi/6) \times L \times W^2] / 2$, n=8-9 mice / group. Tumors were excised after 21 days and weighed (B) then digested enzymatically and mechanically then analyzed by flow cytometry for CD8 or CD4 T-cells (C). D-E. Inguinal lymph nodes were digested and analyzed by flow cytometry for T-cell activation, representative plots in E. gated on CD45+CD11b-CD8+ cells, quantified in E. F-H. Frozen sections of tumor were stained for CD8 and Cleaved Caspase 3 by immunofluorescence microscopy, (scale bars = 50 μm). G. T-cells were counted manually from an average of 5 fields of view (hpf = high powered field), H. Caspase 3 signal intensity was analyzed using imageJ from 5 fields of view. Statistical analysis was performed by 2-way ANOVA with repeated measures (A), or by T-tests (B, C, F, H, I) ns = no significance, * = $p < 0.05$, ** = $p < 0.01$.

increased intra-tumoral CD8^{+} T-cells (Figure 4-8G) in T-MyD88$^{-/-}$ mice as compared to T-MyD88$^{+/+}$ mice. Overall, these data demonstrate a dominant role for T-cell MyD88 in limiting CD8^{+} T-cell activation and anti-tumor activity in melanoma.

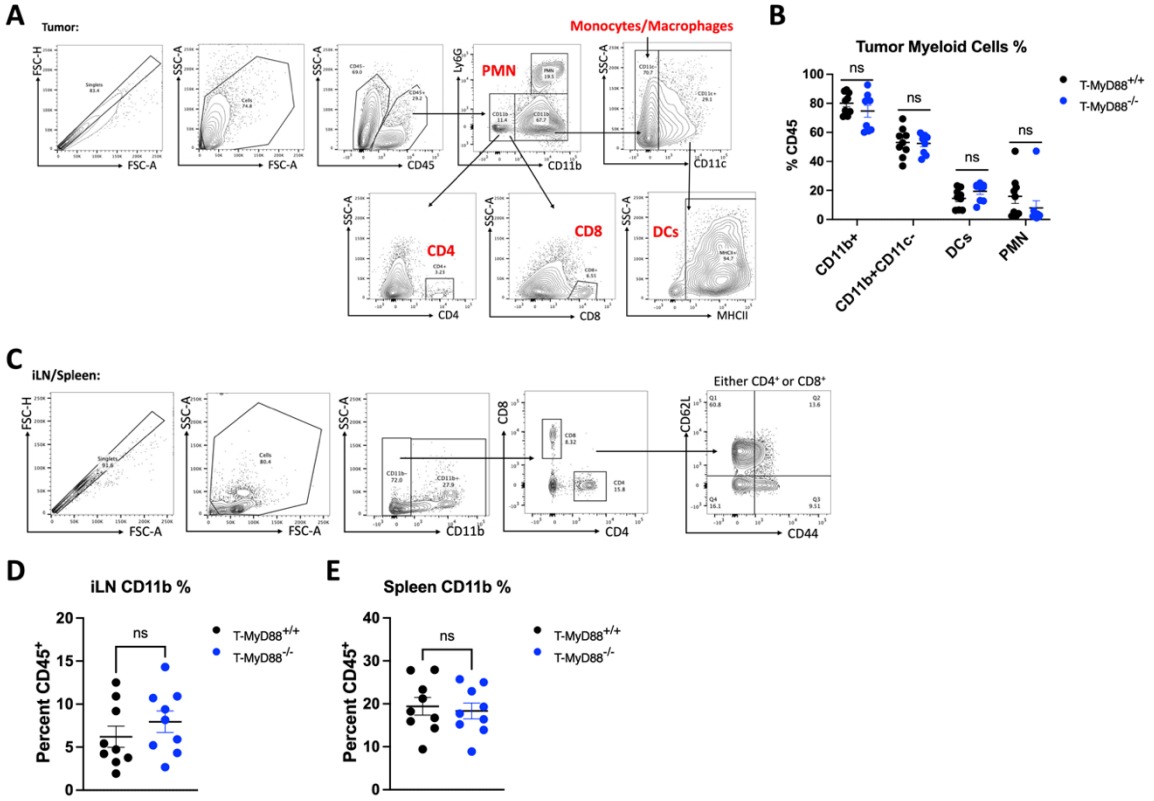


Figure 4-9 Gating for T-MyD88-/- B16 Tumors and Myeloid Cell Populations
Tumors were digested enzymatically and mechanically, then analyzed by flow cytometry. A. Gating strategy for analysis of tumor immune populations in Figure 6 with quantification of the indicated myeloid populations shown in B. C. inguinal lymph nodes or spleens were digested and analyzed by flow cytometry. Gating strategy for analysis of T-cell activation and CD11b+ cells in Figure 4-8, with quantification of CD11b+ cells in D-E. Statistical analysis by T-tests. ns = no significance.

4.4 Discussion:

Here we show a powerful role for MyD88 in cytotoxic T-cells that depresses cytotoxicity towards melanoma by restraining T-cell activation, degranulation, and cell survival. We used two preclinical models of melanoma, one Tc1 antigen independent (SM1-750) and one Tc1 antigen dependent (B16-OVA) and adoptive transfer of WT and MyD88$^{-/-}$ Tc1 cells, as well as mice genetically modified to lack MyD88 in T-cells. These models uncovered that deletion of T-cell MyD88 results in overactivation of Tc1 cells with enhanced cytotoxicity and ability to decrease tumor burden. MyD88$^{-/-}$ Tc1 cells have increased survival and tumor infiltration compared to WT Tc1 cells and show greater activation in the tumor draining lymph nodes compared to littermate controls. Our *in vitro* mechanistic studies demonstrate that deletion of MyD88 affords Tc1 cells enhanced killing of melanoma cells associated with increased cytotoxic granule release upon TCR signaling.

Our *in vivo* results using *T-MyD88*$^{-/-}$ mice and adoptive transfer of MyD88$^{-/-}$ Tc1 cells support that MyD88 restrains CD8+ anti-tumor activity, and are in line with a study demonstrating that T-MyD88$^{-/-}$ mice had slower tumor growth in a chemically induced melanoma model through keratinocyte signaling, yet T-cell function was not investigated as a potential contributor of such phenotype.[118] The role of MyD88 in in the field of cancer, however, was initially described by its gain of function mutation (L265P) as a driver of plasma cell neoplasms.[419] Additionally, several studies have shown that MyD88/TLR4 signaling determines the metastatic potential, and show that MyD88 knockout colorectal cancer cells exhibit reduced proliferation, migration and invasion.[420–422] However, none of these studies specifically investigated the cell specificity *in vivo* of

such response, which could arise from the tumor cells themselves, or from myeloid cells relying on TLR4 signaling, which is well established to be pro-inflammatory.

We have recently demonstrated that TCR activation of $CD4^+$ T-cells induces MyD88 expression and co-localization of MyD88 with the TCR, resulting in enhanced CD4+ T-cell activation. Such activation was characterized by a global enhancement of downstream pro-inflammatory and pro-survival pathways, including MAP Kinase signaling and AKT signaling[398]. Our results herein demonstrate that $MyD88^{-/-}$ $CD8^+$ T-cells exhibit increased surface CD69 and phospho-ZAP70 expression compared to WT upon TCR activation as compared to MyD88 sufficient T-cells. We also find that stimulation downstream of the TCR using PMA/Ionomycin also results in enhanced ERK phosphorylation in $MyD88^{-/-}$ compared to WT Tc1 cells. Thus, both helper and cytotoxic T-cells share a common mechanism of MyD88 modulating T-cell activation and survival. This is further supported by the shared increase in activation and tissue infiltration of both $CD4^+$ and $CD8^+$ T-cells in T-$MyD88^{-/-}$ mice locally and systemically, whether we are using a cardiac inflammation model system in which cardiac CD4+ T-cells play a predominant inflammatory role[244,398], or melanoma, with $CD8^+$ cytotoxic cells dominating the anti-tumor response, as demonstrated here. While we observed no obvious cardiac phenotype at baseline in the T-$MyD88^{-/-}$ mice or in tumor bearing mice, the potential for non-specific cardiac infiltration of $MyD88^{-/-}$ Tc1 cells must be evaluated.

Interestingly, it was recently shown that CAR-T-cell therapy could be enhanced using a constitutively active MyD88 linked to non-native binding partners, suggesting that gain of function, in lieu of loss of function, enhances anti-tumor activity of CAR-T-cells.[423] Our results demonstrating enhanced TCR signaling and activation in the absence of MyD88 suggest that alterations of MyD88 and possibly intracellular partners in endogenous T-cells in the onset of melanoma, are distinct from the engineered CAR-T model system. This also suggests that the exact stimuli and binding partners that recruit MyD88 impact

functional outcome, highlighted by studies using LPS treatment and activation of T-cells *ex vivo.*[412] These signals downstream of the TCR might also differ in the context of a helper T-cell vs. a CAR-T or Tc1 cell that must trigger rapid degranulation of cytotoxic molecules in response to TCR stimulation. However, the molecular partner or partners that limit overactivation of T-cells through MyD88 at the TCR signaling complex remains unknown and is an ongoing area of investigation.

By showing that MyD88$^{-/-}$ T-cells have greater anti-tumor effector function using both a genetic model and adoptive transfer approach, we provide evidence that MyD88 can regulate both intrinsic T-cell activation in response to tumor antigens as well cytotoxicity and survival in the tumor itself. This suggests that deletion of MyD88 in patient derived T-cells might improve adoptive T-cell therapy against solid tumors, in which many clinical and technical limitations still remain including the ability to generate long lasting functional T-cells in high numbers.[424] An additional challenge includes preventing T-cell exhaustion in the tumor microenvironment, and while immune checkpoint inhibitors targeting T-cell exhaustion are increasingly used in the context of melanoma, they are not effective in all patients[408], making improvement of other treatment options such as adoptive cell therapy vital. While we show no changes to PD1 expression between WT and MyD88$^{-/-}$ Tc1 cells *in vitro*, it remains plausible that MyD88 is able to regulate T-cell exhaustion, which remains an area of ongoing investigation as part of the mechanism of enhanced T-cell activation. Interestingly, while we show that in an antigen specific model (B16-OVA with OTI Tc1 cells) deletion of MyD88 improved tumor burden and *in vitro* killing, we observed a less dramatic effect compared to the antigen independent model (SM1-750). This might suggest that in antigen-specific adoptive cell therapy, such as in CAR-T therapy with a defined tumor antigen, such robust T-cell cytotoxicity might limit the benefit of MyD88 modification. However, we did not explicitly evaluate MyD88 deletion in CAR-T-cells, something we plan to test in future studies. With additional

mechanistic information, patient derived T-cells or CAR-T cells could be modified to delete MyD88 to enhance their anti-tumor ability, an area of future investigation that we plan to evaluate pre-clinically using patient derived xenograft models.

Despite these interesting and novel findings, our study has some limitations that we would like to address. First, we only evaluated melanoma using subcutaneous injections, which while they are widely used, have some limitations in their translatability, especially in that they rarely produce metastases, a hallmark of melanoma progression.[425] Our data still support that T-cell function could still be readily tested by subcutaneous injection in a dermatologic neoplasm. We also studied T-cell MyD88 in the context of melanoma, and as such, we cannot assume this phenotype would extend to all solid malignancies, which will require additional studies. Further, we use the constitutive CD4-Cre driver for our genetic model, which excises MyD88 in CD4 and CD8 T-cells, as well as a very small population of dendritic cells expressing CD4 during development.[426] While we believe that MyD88$^{-/-}$ helper CD8+ T-cells with CD4+ T-cell help are the main drivers of the potent anti-tumor immunity we observe in vivo, supported by our in vitro mechanistic tumor killing assays, it is possible that the in vivo effect is not uniquely due to cytotoxic T-cells. We have previously reported strong MyD88 expression in bone marrow myeloid cells in CD4^{Cre+}MyD88$^{fl/fl}$ mice (T-MyD88$^{-/-}$ mice used here)[398], therefore we do not expect MyD88 in myeloid cells being dominant contributors to melanoma decreased growth. Additionally, we show by flow cytometry and immunofluorescence increased numbers of intratumoral T-cells in the absence of T-cell MyD88, although we were only able to analyze a portion of the tumor by flow cytometry and as such present cell numbers normalized to weight. This also does not explicitly distinguish whether increased T-cell numbers are a result of increased recruitment, proliferation, or survival. Our results show a survival benefit of Tc1 cells with MyD88 deletion in this study, yet this is not in the context of the tumor microenvironment. Our previous work demonstrated

that MyD88$^{-/-}$ Th1 cells adhered to primary endothelial cells with greater frequency,[398] so it is plausible that Tc1 cells behave similarly, although we did not explicitly test that for Tc1 cells in this study. Lastly, due to the aggressive tumor formation of the cell lines used, we only evaluated short term anti-tumor immunity after a singular tumor challenge. It remains plausible that MyD88 can regulate the long term memory T-cell response and continue to enhance anti-tumor immunity in a subsequent rechallenge. Alternatively, tumor heterogeneity or immunoediting could allow tumors to outpace the enhanced activity of MyD88$^{-/-}$ cytotoxic T-cells, extensions of the current study that we plan to evaluate moving forward.

4.5 Author Contributions:

A.L.B. designed the project, performed experiments, analyzed data, and wrote the manuscript. D.P. performed experiments and analyzed data. S.S. performed experiments and edited the paper. P.W.H. provided intellectual and technical support, the SM1-750 cell line, and edited the paper. P.A. designed the project, provided intellectual support, and contributed to writing and editing the manuscript.

4.6 Acknowledgements:

This work was supported by National Institute of Health (NIH) Grants R01 HL144477 and HL165725 (P.A.), Tufts Cancer Collaborates Award (A.L.B.) NIH F30 Grant HL162200 (A.L.B.), NIH F31 Grant HL159907A (S.S), AHA Pre-Doctoral Grant 906561 (S.S.), and NIH R25 HL007785 (D.P.).Additional thanks to Dr. Marisol Soengas for graciously providing the B16-OVA cell line.

Chapter 5 MyD88 Determines T-cell Fate Through BCAP-PI3K Signaling

---

Bayer, A. L., Magri, Z., Muendlein, H., Poltorak, A. & Alcaide, P. MyD88 Determines T-cell Fate Through BCAP-PI3K Signaling. *The Journal of Immunology. In press* (2025). Reprinted here with permission of the publisher.

5.1 Introduction

An inflammatory response initiates when signals of pathogens or cellular damage, known as pathogen or damage associated molecular patterns (PAMPs or DAMPs) are recognized by cells of the innate immune system using pattern recognition receptors (PRRs) such as Toll-like receptors (TLRs) [89,96,97]. These cells then present antigen to the T-cell receptor (TCR) and trigger complex signaling cascades including the phosphorylation of ZAP70, PI3K, AKT, and promote T-cell activation and effector function [427,428]. Effector T-cells receive survival stimuli and when inflammation subsides they die by programmed cell death or apoptosis [91,167]. T-cell death can result from a lack of pro-survival stimuli, also known as "neglect-induced" death, or from direct stimulation of pro-death pathways involving Fas-FasL interaction[168].

Most TLRs signal through the adaptor protein "Myeloid differentiation primary response 88" (MyD88), which serves as a central signaling hub vital to pro-inflammatory function in innate immune cells [397]. MyD88 and TLRs are expressed in adaptive immune cells as well [397,429,430], where it plays an alternative, anti-inflammatory role tuning down inflammation in both helper $CD4^+$ and cytotoxic $CD8^+$ T-cells in experimental models of sterile inflammation [220,400]. TLR stimulation of T-cells has been shown to activate MyD88 and enhance T-cell activation and survival [431–433], whereas TCR stimulation results in MyD88 co-localization with the T-cell receptor and limits activation [220].

In support of this concept, we demonstrated that deletion of T-cell MyD88 resulted in enhanced T-cell effector function and improved T-cell survival in activated T-cells [220,400]. Thus, the subcellular localization of T cell MyD88 between the TCR and TLR signaling complexes dictates the T cell activation and survival status and the molecular partners and signals governing these processes need to be elucidated. MyD88 has been shown to bind proteins distinct from TLR complexes through its various domains [434,435]. In antigen presenting cells, MyD88 has been shown to interact with the "B-cell activating protein"

(BCAP). The BCAP adaptor protein is also expressed on T cells and activates PI3K-AKT downstream of the TCR [428,436]. We hypothesized that MyD88 similarly interacts with BCAP in T cells to modulate downstream TCR signals that determine T cell activation and survival.

Here we report a novel mechanistic insight into the role for MyD88 in adaptive immunity and T-cell activation and cellular death that is regulated by MyD88 in a TCR-BCAP-PI3K dependent manner. We find that T cell activation by the TCR and TLR dictates MyD88 subcellular localization and BCAP binding and has consequences in T cell fate.

5.2 Methods

5.2.1 Generation and Culture of Primary Mouse T-cells:

Spleens were excised and crushed through a 40 µM cell strainer, the strainer was rinsed with PBS + 0.5% BSA + 2 mM EDTA, pelleted at 300g, then red blood cell lysis was performed according to manufacturer's instructions (Biolegend 4210301). Naïve $CD4^+$ T-cells were isolated from the splenic cell suspension by positive selection using magnetic beads (Miltenyi 130-117-043). Cells were plated at 2 million cells / mL and differentiated to Th1 cells in the presence of anti-CD3 (2.5 µg/mL, Biolegend 100253), anti-CD28 (1 µg/mL, Biolegend 102102), IL-12 (10 ng/mL, Peprotech 210-12), IL-2 (25U/mL, Miltenyi, 130-120-662) and, anti-IL4 (50 ng/mL, Biolegend 504102) for 3 days, expanded for 24 hours in IL-2 alone, then harvested for experiments. T-cells were cultured at 37°C in RPMI medium (Gibco, 11875-093) containing 10% fetal bovine serum (FBS – Atlanta Biologicals S11150), Glutamax (Gibco A12860-01), NaHCO3 (Gibco 25080-094), Penicillin/Streptomycin (Gibco 15140122), 60µM β-mercaptoethanol (Sigma 444203), Sodium pyruvate (Gibco 11360-070). When indicated, T-cells were cultured in serum free media, or treated with 50 µM Caspase 3/7 inhibitor (Cayman Chemical 14464), 50 µM Necrostatin 1 (Selleckchem S8037), 2.5 µM Buparlisib (Selleckchem S2247), or 2.5 µM MK2206 (Selleckchem S1078), 1 µg/mL LPS (Invivogen NC0202558), or 20 ng/mL FasL (Adipogen G-40B-0130-C010).

5.2.2 Generation and Culture of Primary Mouse Bone Marrow Derived Macrophages:

Bone marrow was isolated from mice aged 6-12 weeks old, filtered through a 100 µM cell strainer, followed by red blood cell lysis was performed according to manufacturer's instructions (Biolegend 4210301). Bone marrow cells were plated at a concentration of 1 x 10^7 cells in a 10 cm dish and cultured in RPMI medium containing 10% FBS,

Glutamax, Penicillin/Streptomycin, 60μM β-mercaptoethanol, Sodium pyruvate, and 20% L929 cell conditioned media. Where indicated macrophages were plated on 20 μg/mL mouse IgG (Biolegend 401408).

5.2.3 Flow Cytometry:

Cell suspensions from culture were stained using the following antibodies from Biolegend: BV421 CD25 (Biolegend 102043), FITC CD69 (Biolegend 104506), AF647-Annexin V (Biolegend 640912), Propidium Iodide (Biolegend 421301), CD45 BV711 (Biolegend 109847), CD3 BV605 (Biolegend 100351), CD4 PE(Biolegend 100512), or Fas FITC (Biolegend 152606). Samples were surface stained by incubation with the relevant antibodies diluted 1:50 in phosphate buffered saline (PBS) + 2% FBS for 20 minutes at 4°C. Data was acquired an a BD LSRII (BD Biosciences) and analyzed using FlowJo software.

5.2.4 Cellular Viability Imaging:

T-cells were plated on 384 well black optical bottom plates (Nunc 142761) coated with 10 μg/mL αCD43 (Invitrogen, 14-0431-85) at 30,000 cells / well in complete T-cell media or media containing 1% FBS, including 10 μg/mL propidium iodide (Biolegend 421301). The BioTek Lionheart Fx imager (Agilent) was used to maintain temperature at 37°C, 5% CO_2, and humidity during the experiment. Kinetic microscopy was performed by the Lionheart imager to quantify propidium iodide uptake every 90 minutes over 72 hours. Wells containing 0.1% Triton X-100 lysed cells were used as a positive control, with propidium iodide uptake baseline subtracted and normalized as % positive control.

5.2.5 Immunoblotting:

Cells were lysed in RIPA buffer (150 mM NaCl, 50 mM Tris pH 7.4, 1% NP-40, 0.1% SDS, 5 mM EDTA, 0.1% sodium deoxycholate, 1 mM DTT) supplemented with protease and phosphatase inhibitors (Roche 4906845001, 4693159001), then cleared

by centrifugation at 4°C at 13,000 g. Protein concentrations were determined using DC protein assay (BioRad 5000112) and equal concentrations of protein were subjected to SDS-PAGE, then transferred to PVDF membranes, followed by blocking with Tris buffered saline + 0.1% Tween20 containing 5% non-fat milk or bovine serum albumin (BSA) for 1 hour at room temperature. Immunoblotting was performed overnight at 4°C using antibodies diluted 1:1000 in 5% non-fat milk or BSA. Antibody sources: Cleaved Caspase 3 (CST 9661), Cleaved Caspase 7 (CST 9492), Caspase 8 (CST 4927), Cleaved Caspase 8 (CST 8592), Caspase 9 (CST 9508), Bcl2 (CST 2870) Bcl-XL (CST 2764), pBIM (CST 4550) BIM (CST 2933), pRIP1K (CST 31122), RIP1K (CST 3493) pMLKL (Abcam ab196436) , MLKL(Sigma MABC1634), Caspase 1 (CST 24232), Gasdermin D (Abcam ab209845), pPI3K (CST 4228), PI3K (CST 4257), BCAP (R&D AF4851), GAPDH (CST 2118), MyD88 (R&D AF3109), pERK (CST 9101), ERK (CST 9102), β-actin (Sigma A5441), pAKT (CST 4060), AKT (CST 4691), pZAP70 (CST 2717), Zap70 (CST 3165), Blots were then incubated with the appropriate HRP peroxidase conjugated secondary antibody (1:2000, Rabbit CST 7074, Mouse CST 7076, Goat ThermoFisher A15999) at room temperature for 1 hour, then developed using Pierce ECL (ThermoFisher 32106) and imaged using a ChemiDoc XRS+ System (Biorad). Band intensity was quantified using Image-J.

5.2.6 In Vivo Induction of Apoptosis by FasL:

All animal studies were approved by the Tufts University Institutional Animal Care and Use Committee. T-MyD88$^{+/+}$ or littermate T-MyD88$^{-/-}$ mice [220,400] were injected with 0.3 µg of Multimeric FasL (Adipogen) or sterile saline by tail vein injection. 24 hours later, the spleens of mice were excised, digested to a single cell suspension, RBC lysed (see above), and analyzed by flow cytometry or CD4^{+} T-cells were isolated by MACS (see above).

5.2.7 Immunoprecipitation:

T-cells were lysed in 50 mM Tris-HCl (pH 7.2-7.4) with 1% NP-40, 0.1% Triton X-100, 150 mM NaCl, 1 mM EDTA, 1 mM EGTA, supplemented with protease and phosphatase inhibitors (Roche 4906845001, 4693159001) for 30 minutes on ice before clearing by centrifugation at 4°C at 13,000 g. Protein concentrations were determined using DC protein assay (BioRad 5000112). Protein A/G beads (Thermofisher 88802) were incubated with antibodies against MyD88 or BCAP (see above) for 2 hours rotating at 4°C. Equal concentrations of cell lysate were incubated rotating with antibody bound beads overnight at 4°C. Beads were separated by magnet, washed 3 times with lysis buffer, then eluted with SDS loading buffer for 20 minutes at 95°C before SDS-PAGE, followed by immunoblotting as described above.

5.2.8 Immunofluorescence:

T-cells were cultured on glass coverslips, washed 2 x 10 min. with PBS, then fixed with 4% PFA for 15 minutes. Samples were washed again with PBS, then incubated with PBS + 10% normal goat serum and/or 10% donkey serum (depending on species of secondary antibody), and 0.1% triton-X for intracellular staining for 1 hour at RT. Samples were incubated with the following primary antibodies where indicated: MyD88 (R&D AF3109), TCRβ (Biolegend 109220), pZAP70 (CST 2717) 1:100 in blocking buffer overnight at 4°C. Samples were washed with PBS then incubated with the appropriate secondary antibody (Thermo A32766, Thermo A11055, Thermo A21432, Thermo A78966, CST 4413) at 1:200 in blocking buffer, then mounted in Vectashield with DAPI (Southern Biotech, 0100-20) before imaging on an Nikon Ti inverted fluorescence microscope.

5.2.9 Lentiviral Transduction of T-cells with αBCAP shRNA:

Spleens were excised and crushed through a 40 μM cell strainer, the strainer was rinsed with PBS + 0.5% BSA + 2 mM EDTA, pelleted at 300g. Naïve $CD4^+$ T-cells were isolated from the splenic cell suspension by negative selection using magnetic beads (Miltenyi 130-104-453). Cells were plated at 1 million cells / mL and activated to Th0 cells for 16 hours in the presence of anti-CD3 (5.0 μg/mL, Biolegend 100253), anti-CD28 (5.0 μg/mL, Biolegend 102102), IL-2 (200U/mL, Miltenyi, 130-120-662), 4 μg/mL αIL-12 (Biolegend 505308), 4 μg/mL αIL-4 (Biolegend 504102), and 10 μg/mL αIFNγ (Biolegend 517906) Cells were then transduced with eGFP expressing lentivirus (designed and purchased from VectorBuilder – see Table 5-1 for shRNA sequences) at an MOI of 1:10 by spinning at 2800 rpm at 37 deg. C in the presence of 1 ug/mL polybrene (Vectorbuilder) for 90 minutes. Fresh media with the antibody cocktail listed above was added to the cells for 24 hours, then plain media with 200 U/mL IL-2 was added and cells were cultured for 24 hours before purification by sorting for $eGFP^+7AAD^-$ cells a Thermofisher Bigfoot with 5 laser configuration before use in experiments.

Target	Sequence	VectorBuilder ID
BCAP shRNA	GAAACCACCGTCAGCTATTAT	VB230207-1214pjk
Scramble shRNA	CCTAAGGTTAAGTCGCCCTCGCTC	VB230207-1221svm

Table 5-1 shRNA sequences

5.2.10 Statistical Analysis:

Statistical analysis was performed using GraphPad Prism 9.4.1. All data is presented as mean ± SEM. Statistical analysis was done by Student's unpaired or paired t-test (where indicated) for two group analysis. Multiple group comparisons were done using one-way ANOVA with Tukey's multiple comparison test or two-way ANOVA with Sidak's multiple comparison test. Differences were considered statistically significant at $p \leq 0.05$.

5.2.11 Data Availability:

The data, methods, and materials will be available to other researchers for the purposes of reproducing the results or replicating procedures.

5.3 Results

5.3.1 MyD88 Deletion Confers a Survival Advantage to CD4+ T-cells Dependent on T-cell Receptor Activation:

We previously showed that MyD88 deficiency promoted survival of TCR activated T-cells [220,400], therefore we sought to test if MyD88 regulated cell death after activation in a TCR dependent manner. We compared WT and MyD88$^{-/-}$ naïve CD4^{+} T-cells to those activated to Th1 cells – a dominant T-cell subset in which MyD88 contributes to tuning down activation upon TCR engagement(Act.) in serum starvation conditions (serum free media) to induce T-cell death by neglect, analyzing viability by flow cytometry. As we have previously shown, serum starvation induced significant death of activated T cells of both genotypes after 72 hours as measured by propidium iodide (PI) and Annexin V stain, and greater survival was observed in MyD88$^{-/-}$ compared to WT T cells (Figure 5-1A-B). In contrast, naïve T-

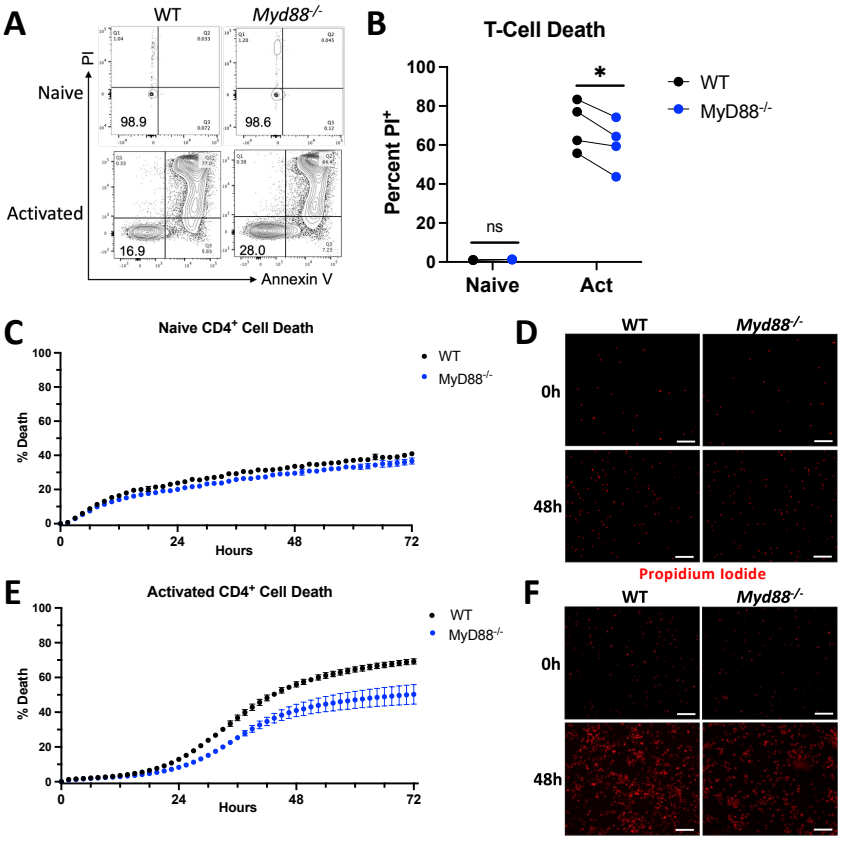


Figure 5-1 MyD88 Deletion Confers a Survival Advantage to CD4+ T-cells Dependent on T-cell Receptor Activation: A. WT or MyD88-/- CD4+ splenic T-cells were isolated and stained with propidium iodide and Annexin V before (naïve) or after 3 days of activation in Th1 polarizing conditions (Act), representative flow cytometry plots shown with quantification in B. C. Propidium iodide incorporation was monitored with the lionheart cell imager over 72 hours in naïve WT or MyD88-/- CD4+ splenic T-cells cultured in serum free media, with representative images shown in D. scale bars are 100 microns. E. Propidium iodide incorporation was monitored the lionheart cell imager over 72 hours in activated WT or MyD88-/- CD4+ splenic T-cells cultured in serum free media, with representative images shown in F. scale bars are 100 microns. Statistical analysis by 2-way ANOVA (B). Ns = no significance, * = $p < 0.05$

cells of either genotype exhibited no observable differences in survival, and very little cell death overall (Figure 5-1A-B). We then sought to monitor viability over time using live cell imaging and PI incorporation in serum starved naïve or activated WT and MyD88$^{-/-}$ T-cells over 72 hours. Similar to our results by flow cytometry, we observed no difference in survival between WT and MyD88$^{-/-}$ naïve CD4^{+} T-cells over the full duration of 72 hours (Figure 5-1C-D). In contrast, TCR activated CD4^{+} T-cells exhibited progressively less cell death in MyD88$^{-/-}$ T-cells compared to WT over the course of 72 hours (Figure 5-1E-F). We found no difference in cell death between WT and MyD88$^{-/-}$ Bone marrow derived macrophages (BMDM) after 48 hours in culture in serum starvation conditions, or when activated through Fc receptor stimulation (Figure 5-2). Together these data confirm that the survival advantage conferred by MyD88 deletion is specific to T-cells and is dependent on T-cell activation through the T-cell receptor.

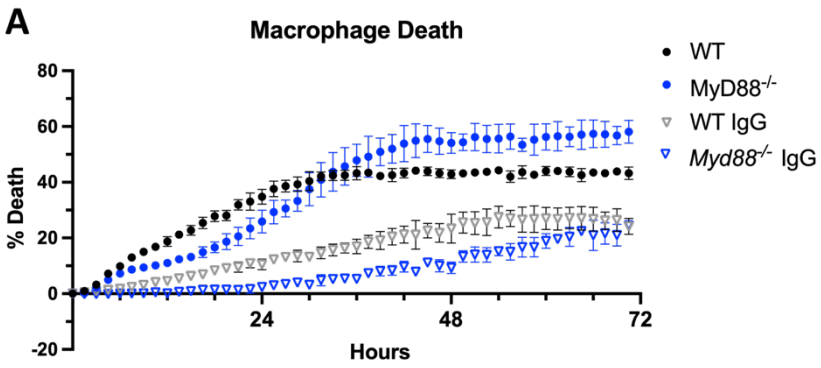


Figure 5-2 MyD88-/- Macrophages Have Similar Survival As WT at baseline and after FcgR activation A. WT or MyD88 bone marrow derived macrophages were generated and plated with or without 20 ug/mL mouse IgG, and then propidium iodide incorporation was monitored over 48 hours in culture in serum free media.

5.3.2 MyD88 Regulates Starvation Induced Apoptosis in Activated CD4^{+} T-cells:

We then tested if the difference in starvation-induced T-cell death between WT vs. MyD88$^{-/-}$ T-cells could be explained by differential activation of the effectors of apoptotic cell death. To this end, we tested for Caspase 3 and 7 cleavage as readouts of broad apoptotic activity, and Caspase 8 and 9 cleavage for further analysis of apoptotic pathways, comparing WT and MyD88$^{-/-}$ naïve and activated T-cells after 24 hours in culture in serum free media (Figure 5-3A). We found that naïve T-cells of either genotype

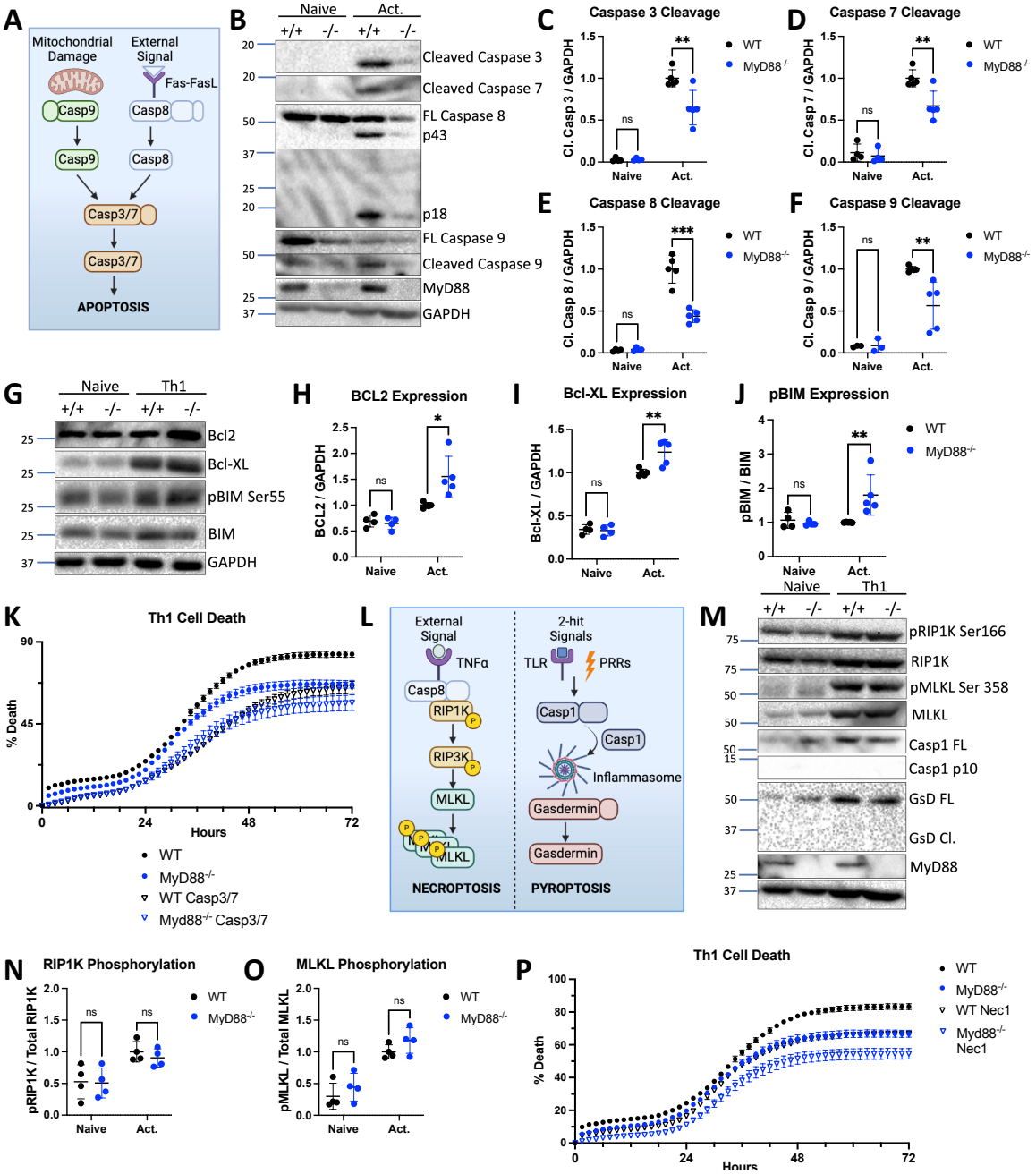


Figure 5-3 MyD88 Controls Starvation Induced Apoptosis in Activated CD4+ T-cells:
A. Schematic showing effectors tested to measure apoptotic cell death. B-N. WT or MyD88-/- CD4+ splenic T-cells were isolated before (naïve) or after 3 days of activation in Th1 polarizing conditions (Act) and culture in serum free media, then lysates were generated for western blot B. Representative western blot of caspase cleavage from naïve or activated T-cell lysates, with quantification for caspase 3 cleavage (C), caspase 7 cleavage (D), caspase 8 cleavage (E), or caspase 9 cleavage (F). G. Representative western blot of BCL family apoptotic mediator from naïve or activated T-cell lysates with quantification for BCL2 (H), for BCL-XL (I), or for BIM phosphorylation (J). K. Propidium iodide incorporation was monitored using the Lionheart live cell imager in activated WT or MyD88-/- T-cells treated with 50 μM caspase 3/7 inhibitor in serum free media. L Schematic showing effectors tested to measure necroptotic and pyroptotic cell death. M. Representative western blot of necroptotic and pyroptotic effectors from naïve or activated T-cell lysates with quantification for RIP1K phosphorylation (N), or MLKL phosphorylation (O). P. Propidium iodide incorporation was monitored using the Lionheart live cell imager in activated WT or MyD88-/- T-cells treated with 50 μM necrostatin 1 in serum free media. Statistical analysis by 2-way ANOVA, ns = no significance, * = $p < 0.05$, ** = $p < 0.01$, *** = $p < 0.001$.

exhibited little to no caspase cleavage from either arm of the apoptotic pathways (Figure

5-3B). Interestingly, TCR-activated T-cells expressed cleaved caspases 3, 7, 8, and 9, including both the p48 and p18 fragments of cleaved caspase 8, strong evidence of apoptotic cell death (Figure 5-3B). However, MyD88$^{-/-}$ T-cells had significantly decreased cleavage for all caspases tested, indicating impaired apoptotic activity in the absence of MyD88 only after TCR stimulation (Figure 5-3B-F). We next tested the expression of the anti-apoptotic BCL2 family members in each cell type, and found that MyD88 deletion resulted in increased expression of Bcl2, Bcl-XL, and phosphorylated BIM (Figure 5-3G-J) in TCR activated but not naïve T-cells. To test whether the observed difference in survival between WT and MyD88$^{-/-}$ T-cells was a result of altered apoptotic activity, we analyzed cell death by propidium iodide incorporation in the presence of a pharmacologic caspase 3/7 inhibitor which specifically inhibits apoptosis. Inhibition of Caspase 3/7 only slightly decreased T-cell death over 72 hours, however it fully reversed the MyD88-dependent difference in survival (Figure 5-3K). Taken together, these data demonstrate that activated T cell apoptosis is dependent on MyD88 and that TCR stimulation in the absence of MyD88 shifts T-cells toward an anti-apoptotic status.

5.3.3 Activated MyD88$^{-/-}$ T-cells Undergo Similar Necroptotic Cell Death to WT and No Pyroptotic Cell Death:

As T-cells treated with an inhibitor of apoptosis still exhibited significant cell death in serum starvation conditions, we then asked if other pathways of cell death contributed to the difference in survival between WT and MyD88$^{-/-}$ T-cells (Figure 5-3L). We found a mild induction of phosphorylated RIP1K and significant phosphorylated MLKL in activated T-cells, evidence of active necroptosis, however there was no difference in either protein between WT and MyD88$^{-/-}$ T-cells (Figure 5-3M-O). Interestingly, we did not detect any cleaved caspase 1 or Gasdermin D in either genotype of T-cell, ruling out

a significant contribution of pyroptosis (Figure 5-3M). Finally, to dismiss the contribution of necroptosis in MyD88-dependent cell death, we treated T-cells with the necroptosis inhibitor Nec1 and monitored survival over time. Nec1 had only a minor effect on T-cell death, with a detectable difference between WT and MyD88$^{-/-}$ T-cells, indicating that MyD88 did not regulate necroptosis in T-cells and it was not a major pathway of cell death in these conditions (Figure 5-3P).

5.3.4 Loss of T-cell MyD88 Impairs CD4+ T-cell Death In Response to FasL *In vivo* and *In vitro:*

Having confirmed the role of MyD88-dependent "death by neglect" in T-cells, , we next sought to test the response of MyD88$^{-/-}$ T-cells to an active extrinsic apoptotic stimulus. We treated TCR activated WT and MyD88$^{-/-}$ T-cells with Fas-ligand (FasL), known to induce rapid apoptosis in T-cells. FasL induced cell death in both genotypes, however the death response to FasL was decreased in MyD88$^{-/-}$ T-cells compared to WT (Figure 5-4A) despite similar surface expression of the Fas receptor in WT and MyD88$^{-/-}$ T-cells (Figure 5-4B-C). We next evaluated the *in vivo* cell death response to FasL stimulation by injecting T-cell specific MyD88$^{-/-}$ mice (T-MyD88$^{+/+}$ or T-MyD88$^{-/-}$) with low dose recombinant FasL by tail vein injection to avoid hepatic toxicity, and evaluated splenic T-cell death by flow cytometry (Figure 5-4D). We found a detectable increase in splenic CD4^{+}Fas^{+}AnnexinV^{+} in only T-MyD88$^{+/+}$ mice but not littermate T-MyD88$^{-/-}$ mice compared to saline injected mice, further evidence that loss of T-cell MyD88 impairs the apoptotic response induced by FasL (Figure 5-4E-F). We also isolated splenic CD4^{+} T-cells to evaluate *in vivo* caspase cleavage in response to FasL injection. As expected, we found very little caspase cleavage in saline injected mice from either genotype, however T-MyD88$^{+/+}$ mice injected with FasL had significantly greater cleaved caspase 3,

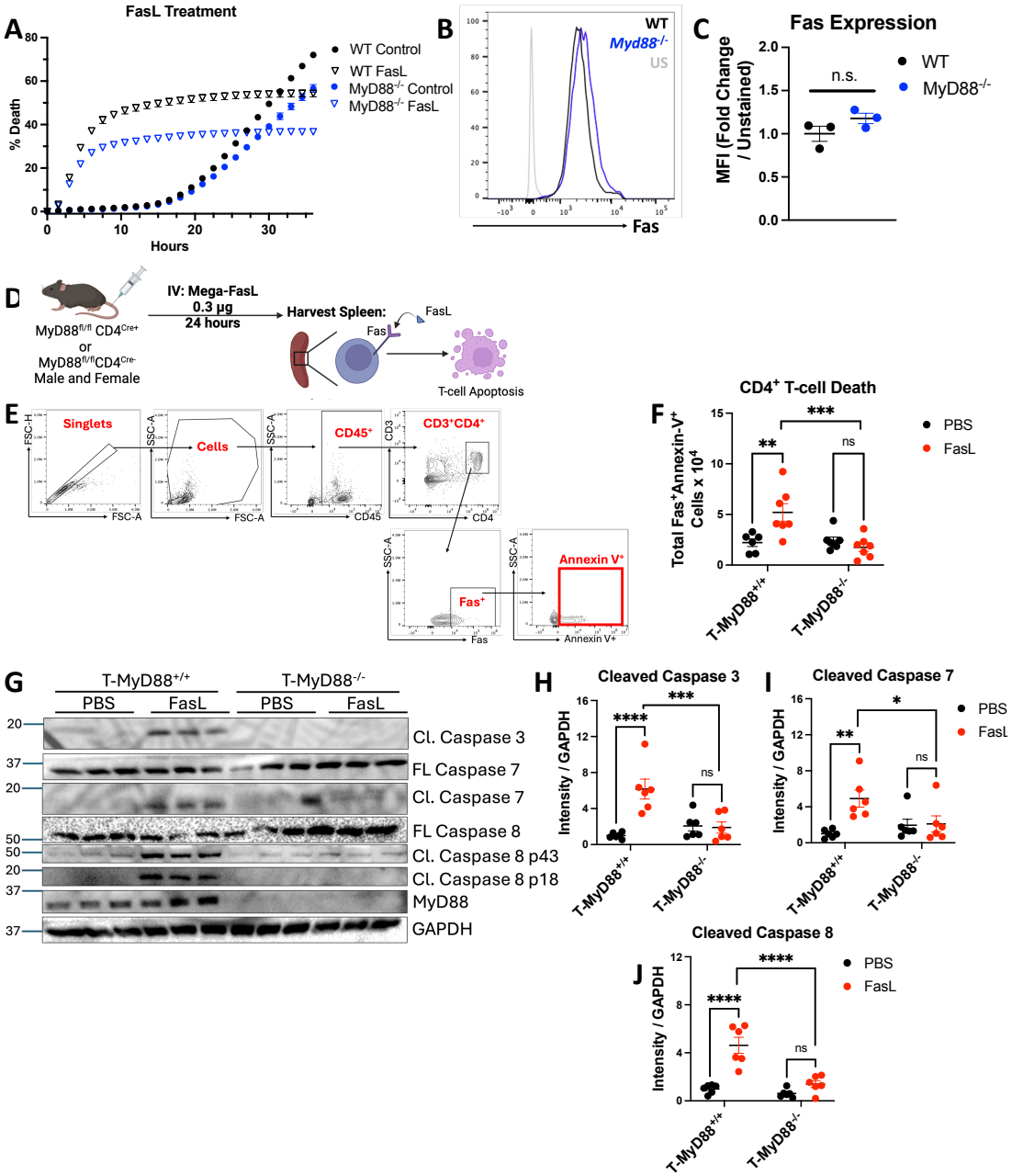


Figure 5-4 Loss of T-cell MyD88 Impairs CD4+ T-cell Death In Response to FasL In vivo and In vitro:

A. Propidium iodide incorporation was monitored using the Lionheart live cell imager in activated WT or MyD88-/- T-cells after 3 days of activation in Th1 polarizing conditions, then treated with 20 ng/mL Fas ligand. B-C. Activated WT or MyD88-/- T-cells were analzyed by flow cytometry for surface Fas expression, representative plots compared to unstained T-cells in B. with quantification in C. D. Schematic for in vivo Fas ligand treatment of T-MyD88-/- mice, in which 0.3 µg of Fas ligand was administered by tail vein injection to 7-8 week old littermate T-MyD88-/- or T-MyD88+/+ mice, then spleens were harvested 24 hours later, digested to a single cell suspension, red blood cell lysed, then analyzed by flow cytometry . E. Gating strategy for analysis of CD4+ T-cell death in response to Fas ligand. F. Total number of splenic CD3+CD4+Fas+Annexin V+ T-cells quantified by flow cytometry. G-J. CD4+ T-cells were isolated by magnetic sorting from the spleens of Fas ligand injected mice then lysed for analysis by western blot. G. Representative blot from n=3 mice / group, with quantification for n=6 mice of Cleaved Caspase 3 (H), Cleaved Caspase 7 (I), or Cleaved Caspase 8 (J). Statistical analysis by 2-way ANOVA with Sidak's multiple comparison test. ns = no significance, * = $p < 0.05$, ** = $p < 0.01$, *** = $p < 0.001$, **** = $p < 0.0001$.

cleaved caspase 7, and cleaved caspase 8 compared to FasL injected T-MyD88$^{-/-}$

littermates (Figure 5-4G-H). Together these data confirm that T-cell MyD88 promotes apoptosis in conditions of passive starvation as well as active death stimuli.

5.3.5 The Pro-Survival Effect of MyD88 Deletion is Dependent on PI3K-AKT Signaling:

Our data thus far indicate that MyD88 promotes cell death upon TCR stimulation, suggesting MyD88-specific interactions downstream of the TCR. Based on the well-established pro-survival role of AKT in regulating T-cell survival [427,437], and our previous findings demonstrating enhanced AKT phosphorylation in TCR activated MyD88$^{-/-}$ T-cells

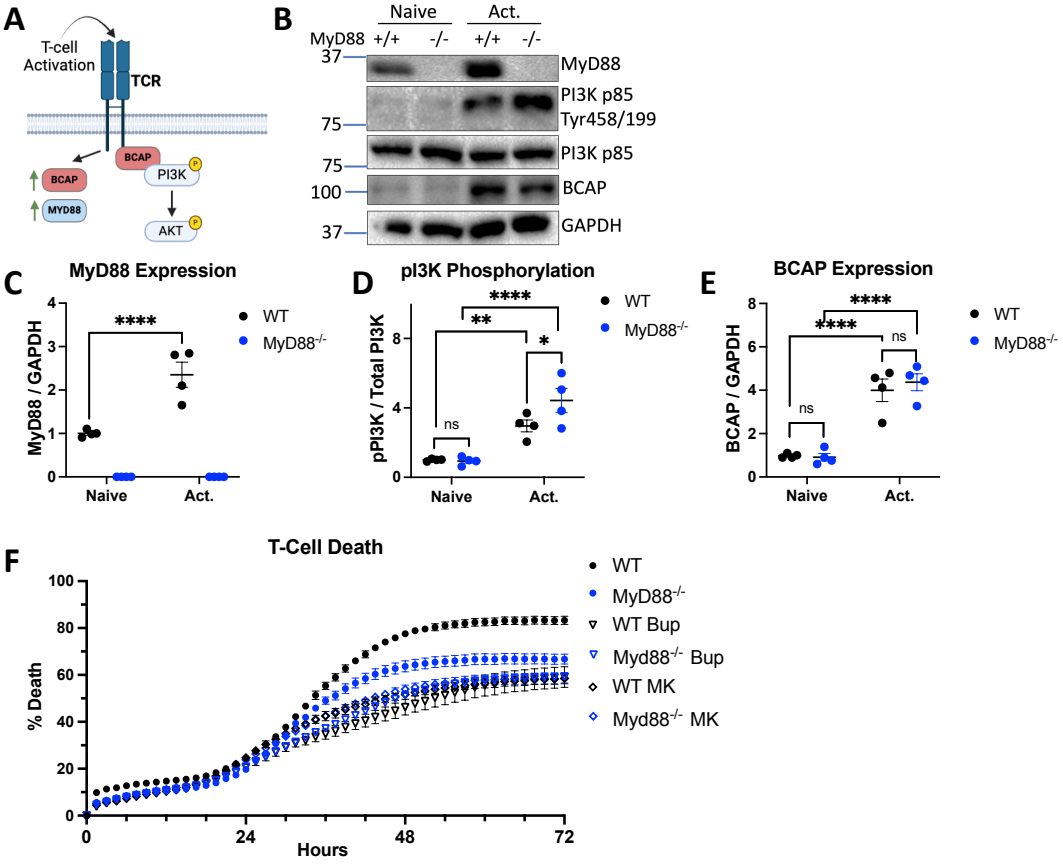


Figure 5-5 The Pro-Survival Role of MyD88 Deletion is Dependent on PI3K-AKT Signaling
A. Schematic of BCAP-PI3K-AKT signaling downstream of T-cell receptor stimulation. B-E. WT or MyD88-/- CD4+ splenic T-cells were isolated before (naïve) or after 3 days of activation in Th1 polarizing conditions (Act), then lysates were generated for western blot B. Representative western blot from T-cell lysates, with quantification for MyD88 (C), pI3K phosphorylation (D) or BCAP (E). F. Propidium iodide incorporation was monitored using the lionheart cell imager over 72 hours in activated WT or MyD88-/- CD4+ splenic T-cells cultured in the presence of 2.5 μM Buparlisib or 2.5 μM MK2206 in serum free media. Statistical analysis by 2-way ANOVA, ns = no significance, * = $p < 0.05$, ** = $p < 0.01$, **** = $p < 0.0001$.

[220], we next examined the possibility that the PI3K-AKT pathway is involved in MyD88 modulation of T cell apoptosis. We focused on BCAP, a major regulator of PI3K-AKT signaling, known to interact with MyD88 in dendritic cells [428,435,438]. As such, we first examined the BCAP-PI3K signaling axis in response to TCR activation in WT compared to MyD88$^{-/-}$ T-cells (Figure 5-5A). As expected, T-cell activation increased MyD88 expression at the protein level (Figure 5-5B-C). Importantly, we found that activated MyD88$^{-/-}$ T-cells exhibited increased PI3K phosphorylation compared to WT T-cells (Figure 5-5B, 5-5D). Further, while T-cell activation significantly upregulated BCAP expression, there was no difference in BCAP expression between WT and MyD88$^{-/-}$ T-cells (Figure 5-5B, 5-5E). To test the functional significance of enhanced PI3K-AKT signaling in MyD88$^{-/-}$ T-cells on cell death, we treated activated WT and MyD88$^{-/-}$ T-cells with the PI3K inhibitor Buparlisib, and the pan-AKT inhibitor MK2206, and monitored survival over time. Treatment with either Buparlisib or MK2206 normalized the difference in survival between WT and MyD88$^{-/-}$ T-cells (Figure 5-5F). These data confirm in the context of TCR induced-activation, MyD88 promotes cell death via enhanced PI3K-AKT signaling, potentially through the BCAP-PI3K axis.

5.3.6 T-cell Receptor and Toll-like Receptor Stimulation Differentially Regulate MyD88-BCAP-PI3K Binding

Given the observed TCR-dependent upregulation of both MyD88 and BCAP, and that deletion of MyD88 enhanced PI3K activation downstream of BCAP, we next tested whether MyD88 and BCAP associate with each other in response to TCR stimulation. We performed immunoprecipitation for MyD88 after a time course of TCR activation in WT T-cells compared to naïve T-cells, and blotted for BCAP after MyD88 pull down. As expected, we pulled down greater MyD88 in T-cells over the course of activation, with a

maximum at 24 hours (Figure 5-6A). Strikingly, BCAP co-immunoprecipitated with MyD88 as soon as 1 hour after T-cell activation, increasing progressively over 24 hours (Figure 5-6A-C). Next, we asked if the absence of MyD88 altered the ability of BCAP to bind to its downstream partner PI3K after 24 hours of T-cell activation during peak MyD88-BCAP binding. We performed immunoprecipitation of BCAP, finding significantly greater BCAP pulldown in activated T-cells but no difference in the absence of MyD88 (Figure 5-6D-E). We first showed significantly greater MyD88 association with BCAP in TCR activated WT T-cells compared to naïve T-cells (Figure 5-6D, 5-6G). We also found

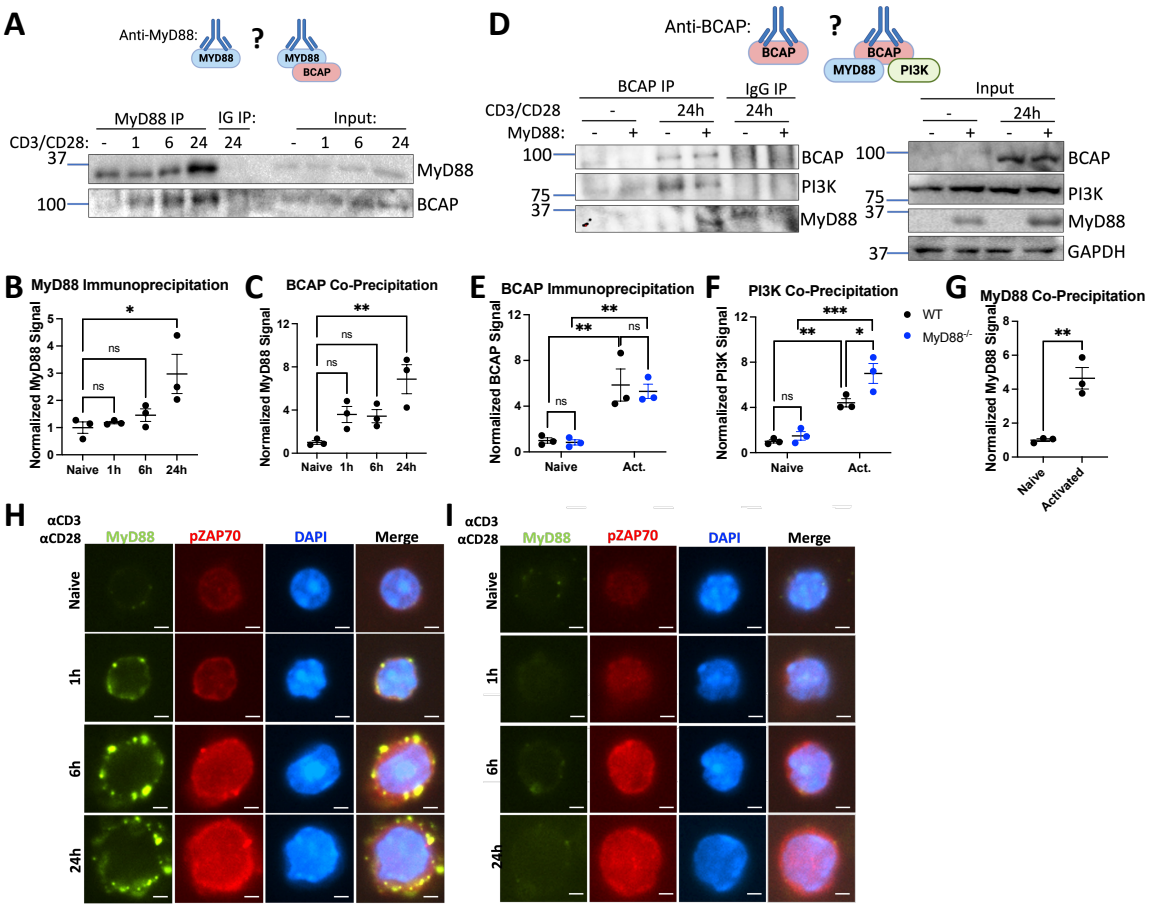


Figure 5-6 T-Cell Receptor Stimulation Induces A MyD88-BCAP-PI3K complex at the TCR
A. Wildtype CD4+ splenic T-cells were activated for the indicated number of hours in Th1 polarizing conditions, then lysed for co-immunoprecipitation, representative blot in A quantified in B-C for n=3 independent experiments. D. Wildtype or MyD88-/- CD4+ splenic T-cells were lysed before or after activation for 24 hours then used for co-immunoprecipitation, representative blot in D. quantified in E-G for n=3 independent experiments. Wildtype (H) or Myd88-/- (I) CD4+ splenic T-cells were activated for the indicated number of hours by 2.5 μg/mL αCD3 and 1.0 μg/mL αCD28 on coverslips before immunofluorescence staining. Representative images shown, scale bar = 2 μm. Statistical Analysis by 1-way ANOVA (B-C) 2-way ANOVA (E-F), or T-test (G), 2-way ANOVA, ns = no significance, * = $p < 0.05$, ** = $p < 0.01$, *** = $p < 0.001$.

significantly greater PI3K association with BCAP in MyD88$^{-/-}$ T-cells compared to WT (Figure 5-6D, 5-6F), supporting that MyD88 sequesters BCAP from PI3K and prevents TCR activation of PI3K-AKT. We further evaluated MyD88 localization by immunofluorescence during T-cell activation, and found that MyD88 increased in abundance at the plasma membrane and co-localized with phospho-zap70, starting as soon as 1 hour post activation and increasing significantly by 24 hours (Figure 5-6H-I), likely indicating the site of MyD88-BCAP interaction.

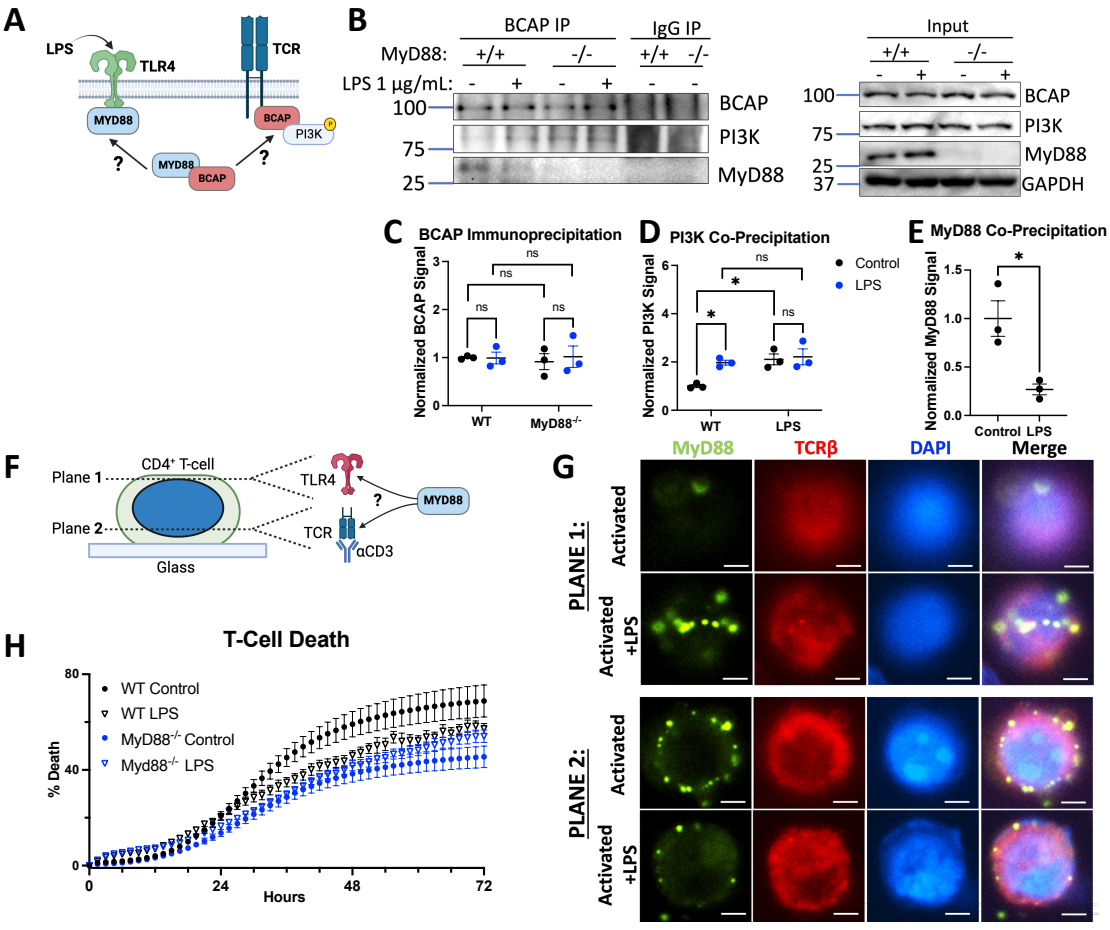


Figure 5-7 T-cell Receptor and Toll-like Receptor Stimulation Differentially Regulate MyD88-BCAP-PI3K Binding and Cell Death

A. Wildtype or MyD88-/- CD4+ splenic T-cells were activated for 24 hours in Th1 polarizing conditions in the absence or presence of 1 µg/mL LPS, then lysed for co-immunoprecipitation, representative blot in B quantified in C-E for n=3 independent experiments. F. Schematic of immunofluorescence strategy in T-cells to analyze MyD88 co-localization. G Wildtype CD4+ splenic T-cells were activated for 24 hours in the absence or presence of 1 µg/mL LPS on coverslips before immunofluorescence staining. Representative images shown, scale bar = 2 µm. H. Propidium iodide incorporation was monitored using the lionheart cell imager over 72 hours in activated WT or MyD88-/- CD4+ splenic T-cells cultured in the presence or absence of 1.0 µg/mL LPS in serum free media. Statistical analysis by 2-way ANOVA (C-D), or T-test (E), 2-way ANOVA, ns = no significance, * = $p < 0.05$, ** = $p < 0.01$, *** = $p < 0.001$.

We then asked if MyD88-BCAP binding was modulated by TLR agonism, which would signal MyD88 to form the Myddosome complex at active TLRs rather than at the TCR (Figure 5-7A). We treated activated WT and MyD88$^{-/-}$ T-cells with the TLR4 ligand LPS, and similarly performed immunoprecipitation for BCAP (Figure 5-7B-C). While LPS had no effect on BCAP expression or pull-down, strikingly, we found that LPS treatment abrogated MyD88 co-immunoprecipitation with BCAP in WT T-cells (Figure 5-7C), and in turn significantly increased PI3K binding to BCAP, and had no effect on BCAP-PI3K co-immunoprecipitation in MyD88$^{-/-}$ T-cells, as expected (Figure 5-7C-E). Finally, we examined whether TLR-mediated activation of MyD88 would affect its co-localization at the T-cell receptor signaling complex (Figure 5-7F). When we activated WT T-cells with and without LPS, we found that MyD88 aggregated in plane of view distinct from the TCR only in the presence of LPS. Accordingly, in a plane of view of TCR stimulation, LPS treatment decreased the co-localization of MyD88 with the TCR (Figure 5-7G). Importantly, LPS treatment was also able to fully normalize the difference in survival between WT and MyD88$^{-/-}$ T-cells over time, improving WT T-cell viability (Figure 5-7H) These data demonstrate that T-cell activation induces MyD88-BCAP binding at the TCR, and this is prevented by TLR stimulation.

5.3.7 BCAP Knockdown Inhibits the Modulation of Cell Death and T-cell Activation by MyD88:

To test if the MyD88-BCAP interaction does in fact impair T-cell survival and activation, we used shRNA mediated knockdown of BCAP in WT and MyD88$^{-/-}$ T-cells by lentivirus during T-cell activation to Th0 cells. We first showed a greater than 80% knockdown of BCAP in both genotypes of T-cell transduced with αBCAP shRNA compared to a scramble shRNA transduced cells (Figure 5-8A). We then tested whether BCAP

knockdown impacted T-cell activation markers that we previously have shown to be increased in the absence of MyD88 [220]. As expected, in scramble shRNA transduced cells, MyD88$^{-/-}$ T-cells exhibited higher surface CD69 expression and higher ZAP70 phosphorylation compared to WT, both indications of increased T-cell activation status (Figure 5-8B-D). However, the differences in activation of CD69 and pZAP70 between WT and MyD88$^{-/-}$ T-cells were attenuated upon BCAP knockdown (Figure 5-8B-D).

We next evaluated T-cell survival in transduced T-cells by PI incorporation over 48 hours. As previously shown, MyD88$^{-/-}$ T-cells exhibited significantly less cell death than WT T-cells over time when transduced with scramble shRNA. In contrast, cell death

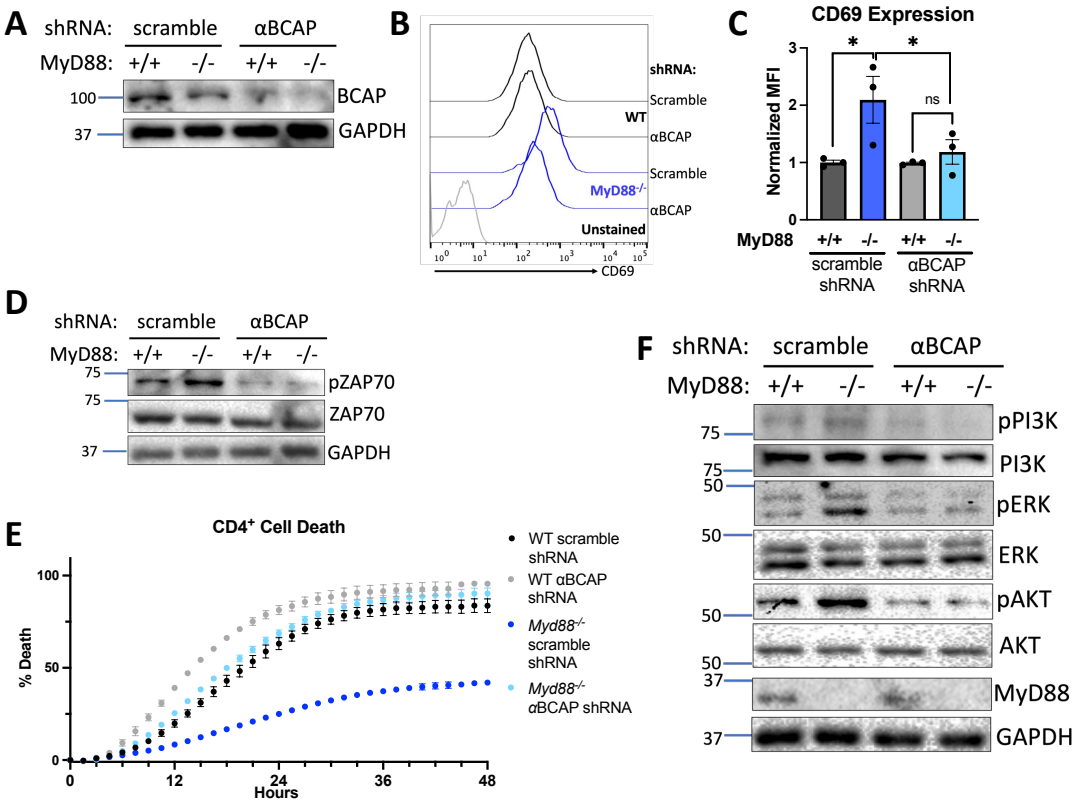


Figure 5-8 BCAP Knockdown Inhibits the Modulation of Cell Death and T-cell Activation by MyD88

A. Wildtype or MyD88-/- naïve CD4+ splenic T-cells were transduced with either scramble or BCAP targeting shRNA during activation with 2.5g μg/mL αCD3 and 1.0 μg/mL αCD28 for 3 days, then lysed for western blot. B-C. Transduced T-cells were analyzed b flow cytometry for CD69 expression, representative plots in B. with quantification from n=3 independent experiments in C. D. Transduced T-cells were lysed and analyzed by western blot. E. Propidium iodide incorporation was monitored using the lionheart cell imager over 72 hours in transduced activated WT or MyD88-/- CD4+ splenic T-cells in cultured in serum free media. F. Transduced T-cells were lysed and analyzed by western blot. Statistical analysis by 2-way ANOVA with Sidaks multiple comparison test. ns = no significance, * = $p < 0.05$

increased significantly in MyD88$^{-/-}$ T-cells transduced with αBCAP shRNA, nearly to the level of WT αBCAP shRNA transduced cells, which also increased moderately (Figure 5-8E). We then sought to test mechanistic signaling pathways downstream of BCAP after knockdown. We found that BCAP knockdown normalized the difference in phosphorylation of the direct binding partner of BCAP, pI3K, as well as both downstream pathways AKT and ERK in WT and MyD88$^{-/-}$ T-cells (Figure 5-8F). Together these data confirm that MyD88 is able to regulate T-cell activation, survival, and signaling downstream of the TCR in a BCAP dependent manner.

5.4 Discussion

Here we show evidence that MyD88 limits T-cell survival upon T-cell receptor engagement and signaling through its interaction with its novel binding partner BCAP. We further demonstrate that the survival advantage afforded by MyD88 deficiency consists of inhibition of apoptotic pathways only after activation through the T-cell receptor that prompts BCAP towards AKT-PI3K pro-survival signals and T-cell activation. T-cells activated in the absence of MyD88 exhibit increased PI3K phosphorylation and increased BCAP-PI3K interaction. This is further supported by the observed binding of MyD88 to BCAP in response to T-cell activation in WT T-cells. Our observation that TLR4 stimulation with LPS decreases the MyD88-BCAP interaction, altering co-localization of MyD88 with the TCR, and normalizing the survival difference of WT and MyD88$^{-/-}$ T-cells further supports the modulatory concept of MyD88 for T-cell activation and survival when TCR signals take place. These data provide the first molecular mechanism of MyD88 regulation of T-cell activation and survival and a novel role for the MyD88-BCAP-PI3K axis in fine tuning T-cell receptor signaling.

In response to activation through the TCR by APCs, T-cells undergo a rapid and powerful signaling cascade that allows them to effectively respond to antigens without becoming overactivated and causing non-specific cellular damage. Further, to resolve inflammation, T-cells must undergo apoptotic death when antigenic and cytokine stimulation are withdrawn. Our previous work has shown that mice lacking T-cell MyD88 have significantly enhanced inflammatory responses during sterile cardiac inflammation [220] as well as in the anti-tumor response to melanoma [400] in part due to increased T-cell activation status and improved survival at the site of the cardiac and melanoma immune response. Our data here further demonstrate that increased T-cell activation and improved survival *in vitro* occur in both Th1 and Th0 cells. This suggests a global role for T cell MyD88 in dictating the activation and/or survival status of T-cells in response to an inflammatory

trigger. Our results herein define now the specific molecular mechanism by which MyD88 modulates the T-cell receptor signaling complex and subsequent effects on T cell survival and activation upon TCR activation. While targeting T-cell MyD88 would only be beneficial depending on the context of inflammation, such as enhancing the anti-tumor response, this study suggests that more precise control over the expression level of MyD88 and its TCR functionality would have therapeutic implications in other T-cell mediated diseases. We have previously shown TCR activation results in enhanced expression of MyD88 protein in effector $CD4^+$ and $CD8^+$ cells and speculated this is a natural response to tune down overactivation of T cells. Uncovering the pathways and transcription factors regulating MyD88 expression downstream of the TCR will reveal additional ways to modulate MyD88 as a potential therapeutic approach.

Our data also support a role for MyD88 in specifically regulating apoptotic cell death, whereas necroptosis was unaffected by MyD88 deletion and T-cells underwent little pyroptosis at baseline. Previously, MyD88 has been studied in macrophages as a regulator of apoptosis in response to UV radiation [439], however it has never been studied in the context of T-cell death. Interestingly, in macrophages MyD88 has also been shown to be dispensable for pyroptotic/caspase 8 mediated cell death [331]. Our data in both resting and activated macrophages showing no difference between WT and $MyD88^{-/-}$ cells further support that the role of MyD88 in apoptosis is specific to TCR activated T cells and does not apply to resting or activated macrophages. This further is in line with our results in T-cells, as macrophages do not have the same TCR-BCAP functionality that T-cells do. Our data show enhanced AKT phosphorylation in activated T-cells, and AKT signaling has been shown to upregulate Bcl family members and inhibit apoptosis [440,441]. As such, it is plausible that enhanced BCAP-PI3K-AKT signaling down stream of TCR stimulation in the absence of MyD88 promotes the apoptotic regulation that we observe. Interestingly, there were only minor alterations in cell death in the onset of Caspase3/7 or AKT by small molecule

treatment, which we believe to be compensatory upregulation of other forms of cell death such as necroptosis, a phenomenon occurring in macrophages as well [439]. While we show that MyD88$^{-/-}$ T-cells express higher levels of Bcl family members, the exact mechanisms of cell death remain an ongoing area of investigation.

It has been well established that TLR ligands are able to act in a co-stimulatory manner for T-cell activation, increasing cytokine secretion, activation markers and proliferation [442–445]. Importantly, these phenotypes are only reported when stimulating MyD88-dependent TLRs, whereas the one study using TLR3 stimulation, known to only signal through TRIF and not MyD88, did not impact T-cell activation and function [442]. Our work provides a specific molecular mechanism by which MyD88 modulates TLR effects on T-cell activation that involves the TCR complex, demonstrating that TLR stimulation is able to alter the co-localization of MyD88 away from the TCR in T-cells, decreasing its binding to BCAP, and normalizing the difference in viability between WT and MyD88$^{-/-}$ T-cells. This suggests that one mechanism for TLR induced co-stimulatory function acts by impairing MyD88-BCAP binding as opposed to exclusively a broad increase in pro-inflammatory signaling downstream of MyD88 triggered by the TLR. This highlights the concept that the function of MyD88 is both cell and context dependent, especially considering the different domains of MyD88 allow for different binding partners. The death domain (DD) of MyD88 predominantly drives inflammatory function [410], whereas the TIR domain was shown to bind to BCAP [446], opening up the possibility that different binding partners can influence the functionality of MyD88. Future studies are needed to investigate whether the DD is responsible for regulating apoptosis and if MyD88-BCAP binding allows for altered complex formation at the DD. We believe these findings provide an avenue to further explore this novel molecular crosstalk mechanism between TLR and TCR activation in T-cells to bring new approaches that fine tune T-cell activation, either by specifically modulating T cell TLR4 or by directly

targeting the MyD88-BCAP-PI3K complexes downstream of the TCR during aberrant T cell activation.

While this study broadens our understanding of T-cell biology as well as carries significant therapeutic implications, it has several limitations we would like to address. We show that MyD88 and BCAP interaction downstream of TCR signaling and that the BCAP-PI3K complex is regulated by MyD88, yet the exact location of this complex in the TCR signalosome remains unknown. Additionally, immunoprecipitation of BCAP does not distinguish if BCAP binds to MyD88 and PI3K separately or if a tertiary complex forms. The shRNA used to knock down BCAP was highly effective in in normalizing the differences in pro-inflammatory signaling, activation, and cell death between WT and MyD88$^{-/-}$ T-cells, but whether other shRNAs or genetic ablation of MyD88, BCAP, will be incorporated in future studies to further characterize this mechanism. Lastly, we previously have shown a similar pro-survival phenotype for MyD88$^{-/-}$ CD4^{+} and CD8^{+} T-cells, and herein we provide a novel mechanism that applies to CD4^{+} T-cells. While BCAP performs a similar function in CD8^{+} T-cells [438], it remains to be seen if the exact molecular mechanism differs between T-cell subtypes and if the MyD88-BCAP interaction is relevant in other immune cell types. Despite these limitations, our work outlines a novel role for MyD88 in limiting BCAP-PI3K signaling downstream of the TCR that can be modulated with TLR stimulation with powerful downstream effects on T-cell viability.

5.5 Author Contributions

A.L.B. designed the project, performed experiments, analyzed data, and wrote the manuscript. H.M. and Z.M. assisted with experiments, data analysis, intellectual support, and edited the manuscript. A.P. provided intellectual support. P.A. designed the project, wrote and edited the manuscript.

5.6 Acknowledgements

This work was supported by National Institute of Health (NIH) Grants R01 HL144477 and HL165725 (P.A.), NIH F30 Grant HL162200 (A.L.B.), NIH R01 AI056234 and AI167245 (A.P). Equipment Grant NIH S10OD032201. We would also like to acknowledge Dr. Xudong Li, from Tufts University, Department of Immunology, for sharing protocols and helping optimize the knockdown experiments in T cells.

Chapter 6 Cytotoxic T-cells Drive Doxorubicin Induced Cardiac Fibrosis and Systolic Dysfunction

---

Bayer AL, Zambrano MA, Smolgovsky S, Robbe ZL, Ariza A, Kaur K, Sawden M, Avery A, London C, Asnani A, et al. Cytotoxic T cells drive doxorubicin-induced cardiac fibrosis and systolic dysfunction. *Nat Cardiovasc Res*. 2024;3:970–986.

Reprinted here with permission of publisher.

6.1 Introduction

Doxorubicin (DR) is the most widely used chemotherapeutic agent, used in first line regimens for solid and hematologic tumors in humans and in the treatment of canine lymphoma.[311,312,447] Patients commonly exhibit dose-dependent cardiotoxicity with an average incidence ~9% [309,312] and respond differently to heart failure (HF) treatments.[448] Systemic inflammation is associated with HF [45,449] and with DR cardiomyopathy in patients[321,323,324], yet the underlaying immune mechanisms elicited by DR are limited.

DR inhibits Topoisomerase II in cancer dividing cells[310]. However, it induces reactive oxygen species (ROS) which are detrimental to cardiomyocytes and pro-inflammatory.[310,312,450] Hallmarks of the inflamed heart in HF imply cross-talk between the cardiac immune and fibrotic responses[231,243,391,451]. Specifically, $CD4^+$ and $CD8^+$ T-cells have been implicated in myocarditis, ischemic and non ischemic HF.[15199,220,404,452–455] While fibrosis, cardiac pro-inflammatory cytokines, innate cell activation pathways, and immune cells co-exist in the heart in DR cardiomyopathy[311,312,456,325,332,336,338], mechanistic depth is lacking. $CD8^+$ T-cells contribute to anti-tumor immunity in part by degranulation and granzyme release. Thus far, no studies have investigated if T-cells are cardiotoxic and pro-fibrotic in DR cardiomyopathy. Here we show that DR induces cardiac directed $CD8^+$ T-cells and enhances activation and degranulation that contributes to off-target cardiac toxicity and fibrosis. The DR induced $CD8^+$ T-cell response is observed in mice, canines, and humans with cardiomyopathy.

6.2 Methods

6.2.1 Animals and Doxorubicin Model:

All animal studies were approved by the Tufts University Institutional Animal Care and Use Committee. C57BL/6J, *Tcra*$^{-/-}$[367], and OTI[457] mice were bred and maintained under pathogen free conditions and in a 14h light/10h dark cycle, at an ambient temperature of

70-74 deg. F, with humidity between 30-70% RH. Male mice (unless otherwise indicated) aged 8-10 weeks old were given 5.0 mg/kg Doxorubicin (Selleckchem) by intraperitoneal injection once weekly to mimic cumulative doses in patients for the indicated lengths of time. A minimum sample size of 6 mice per group was calculated to detect statistically significant changes in cardiac function with a power of >80% and $\alpha = 0.05$. For antibody depletion, mice were given 100 µg of anti-CD8 antibody (Biolegend 100763) or anti-CD4 antibody (Biolegend 100457) by intraperitoneal injection every 4 days starting 2 days prior to first Doxorubicin injection. For adoptive transfer, Tc1 cells were generated from wild type mouse spleens (see below for protocol) and transferred 1 day after first DR injection and again 2 weeks later by intraperitoneal injection of 10 million Tc1 cells per mouse. Randomization for each group was performed by a random number generator (https://www.calculator.net/random-number-generator.html), and all analyses were done blinded using an ID number assigned by a third party.

6.2.2 *In Vivo* Echocardiography:

Transthoracic echocardiography was performed one day before tissue harvest, as previously described.[204] Mice were sedated using isoflurane on a heated stage in supine position. Heart rate and respiratory rate were continuously monitored via stage electrodes. Depilatory cream (Nair) was applied to the chest to remove fur, and ultrasonic gel was applied to a 22-55 MHz echocardiography transducer (MS550D Vevo 2100, Fujifilm VisualSonics) to obtain parasternal short axis views of the left ventricle in M-mode with a target heart rate of 400-500 bpm. Cardiac parameters and heart rate were measured by averaging the values from 5 cardiac cycles. All analyses were performed blindly using Vevo 2100 software version 2.2.0 (Build 12089).

6.2.3 Flow Cytometry:

Hearts were excised from mice and perfused with PBS, then minced and digested enzymatically with 0.895 mg/mL collagenase II (Gibco 17101-015). Single cell suspensions were generated from cells in culture or lymphoid organs using a 40 μm cell strainer. Blood samples were first RBC lysed using RBC lysis buffer (Biolegend 420302) according to the manufacturer's instructions, then leukocytes were pelleted before staining. Samples were stained using the following antibodies from Biolegend: APC-Cy7 or FITC CD4 (Clone GK1.5); FITC, BV421, PerCP, or BV711 CD8 (Clone 53-6.7); BV421, FITC, PE, or APC CD45.2 (Clone 104); APC or BV711 CD44 (Clone IM7); PE CD62L (Clone MEL-14); BV421 or BV711 CD25 (Clone PC61); FITC CD69 (Clone H1.2F3); FITC CCR2 (Clone SA203G11); BV421 Ly6G (Clone 1A8); APC MerTK (Clone 2B1OC42); PerCP or APC-Cy7 CD11b (Clone M1/70); APC or FITC MHCII (Clone M5/114.15.2); BV421 CTLA-4 (Clone UC10-4B9); APC PD-1 (Clone 29F.1A12); PE or BV421 CD11c (Clone N418); FITC ICAM1 (Clone YN1/1.7.4); PE CD107a (Clone 1D4B); PE VCAM1 (Clone 429), or the following human antibodies: BV605 CD45 (Clone 2D1), PerCP-Cy5.5 CD3 (Clone OKT3), BV421 CD8 (Clone SK1), AF647 CXCR3 (Clone G025H2), or APC-Cy7 CD4 (BD Clone RPA-T4). When indicated, samples were stained with 7AAD diluted 1:25 in staining buffer (Biolegend 420404). Samples were surface stained by incubation with the relevant antibodies listed above diluted 1:50 in phosphate buffered saline (PBS) + 2% FBS for 20 minutes at 4°C. When intracellular cytokine staining was performed, samples were incubated for 4 hours at 37C in complete T-cell media (see below for details) including 50 ng/mL Phorbol Myristate Acetate (PMA, Sigma Aldrich P8139), 0.1% Ionomycin (Sigma 13909), 0.1% Brefeldin A (Biolegend 420601), and 0.1% Monensin (Biolegend 420701), followed by surface staining as described. Samples were then fixed for 15 minutes at RT with fixation buffer (Biolegend, 420801), permeabilized by two washes with 1X Perm/Wash buffer (Biolegend, 421002, and

stained intracellularly with the following antibodies from Biolegend: APC IFNγ (Clone XMG1.2), Percp Granzyme B (Clone QA16A02), APC Human IFNγ (Clone 4S.B3), or PE Human Granzyme B (BD Clone GB11) diluted 1:50 in 1x Perm/Wash buffer for 20 minutes at 4°C. To detect transcription factors, samples were surface stained as described, fixed using 1X FOXP3 Fix/Perm solution (Biolegend 421401) for 20 minutes at RT, permeabilized for 15 minutes using 1X FOXP3 Perm solution (Biolegend 421402), then stained intracellular for 20 minutes with the following antibodies PerCP Tbx21 (Biolegend Clone 4B10), FITC GATA3 (BD Pharm. Clone L50-823), APC RORgt (Invitrogen Clone B2D), PE FOXP3 (Invitrogen Clone FJK-16s), or Pacblue Helios (Biolegend Clone 22F6) diluted 1:50 in 1x Perm solution for 20 minutes at 4°C. Data was acquired on a BD LSRII (BD Biosciences) and analyzed using FlowJo software Version 10.10.0

6.2.4 Histologic Analysis:

Picrosirius Red (PSR): Cardiac samples were fixed in 10% formalin, embedded in paraffin, and cut in 6 μm sections. Collagen was stained in 0.1% Direct Red 80 (Sigma 365548) in saturated picric acid (Sigma P6744) for 1 hour, followed by hematoxylin counter stain (Sigma GHS2128) for 1 minute. Slides were washed with 0.5% acetic acid twice before dehydration and mounting. Fibrosis was quantified by positive threshold on ImageJ (Version 1.53t) to exclude non-specific signal from counter-stained nuclei.
TUNEL: Formalin fixed cardiac samples were stained using *In Situ* Cell Death Detection kit TMR red (Sigma 12156792910) according to the manufacturer's protocol. **Reactive Oxygen Species (ROS): 10 um** frozen cardiac sections were hydrated with PBS and stained with 10 μM DCFDA (Thermofisher D399) for 30 minutes at 37°C, then DAPI counterstained before imaging by fluorescence microscopy.

6.2.5 Immunohistochemistry:

Immunohistochemistry was performed in 10 um frozen LV sections: samples were fixed in ice cold acetone (Sigma 179124), blocked for 10 minutes each with: 10% normal goat serum (Abcam 7481), biotin/avidin blocking kit (Vector labs SP-2001), and 1% hydrogen peroxide (H1009). Samples were stained with primary antibody against CD8 for 1 hour (1:200 dilution, Biolegend 100702) followed by incubation with goat anti-rat biotinylated secondary antibody (1:300 dilution, Jackson Immunoresearch 112-065-062). Sections were incubated with Streptavidin HRP (DAKO K0675) and visualized using AEC Substrate (Sigma A5754), then nuclear counterstained with hematoxylin for one minute, and mounted using aqueous fluoromount G (Southern Biotech 0100-01).

6.2.6 ELISA:

Cardiac lysate was generated from heart tissue by lysis in RIPA buffer (150 mM NaCl 50 mM Tris pH 7.4, 1% NP-40, 0.1% SDS, 5 mM EDTA, 0.1% sodium deoxycholate, 1 mM DTT) supplemented with protease and phosphatase inhibitors (Roche 4906845001, 4693159001), then cleared by centrifugation at 4°C at 13,000 xg. Protein concentrations were determined using DC protein assay (BioRad 5000112) and equal amounts of protein were input into the following ELISA kits according to the manufacturer's instructions: CXCL9 (R&D DY492) CXCL10(R&D DY466), and Granzyme B(R&D DY1865).

6.2.7 Generation and Culture of Activated T-cells and Tc1 Cells:

$CD4^+$ or $CD8^+$ T-cells were isolated from splenic cell suspensions by positive selection using magnetic beads (Miltenyi 130-117-043 or 130-117-044). Cells were plated at 2 million cells / mL and activated in the presence of anti-CD3 antibody (2.5 µg/mL, Biolegend 100253) and anti-CD28 antibody (1 µg/mL, Biolegend 102102), for 3 days then harvested for experiments. For Tc1 cells, cells were also cultured with IL-12 (10

ng/mL, Peprotech 210-12) and, anti-IL4 (50 ng/mL, Biolegend 504102). T-cells were dosed with the indicated concentration of Doxorubicin where indicated. T-cells were cultured at 37°C in RPMI medium (Gibco 11875-093) containing 10% fetal bovine serum (FBS – Atlanta Biologicals S11150), Glutamax (Gibco A12860-01), $NaHCO_3$ (Gibco 25080-094), Penicillin/Streptomycin (Gibco 15140122), 60μM β-mercaptoethanol (Sigma 444203), and Sodium pyruvate (Gibco 11360-070).

6.2.8 RT-qPCR:

Cell lysis and RNA isolation was performed using an RNeasy kit according to manufacturer's instructions (Qiagen 74004). For cardiac RNA isolation, LV samples were crushed in Trizol (Qiagen 79306), RNA was chloroform extracted and separated by centrifugation, then the aqueous phase was combined with 70% ethanol and applied to RNAeasy columns. cDNA synthesis was performed using High-Capacity cDNA Reverse Transcription Kit (ThermoFisher 4368814), and qPCR was performed using SYBR Green (ThermoFisher A25741) on a QuantStudio 6 Flex Real-Time PCR Machine (ThermoFisher). See appendix 9.10 for primer sequences.

6.2.9 Isolation of Cardiac Fibroblasts and Co-culture:

Adult mice (7-12 week old) were anesthetized, then hearts were excised, perfused with PBS, minced, and digested using 2 mg/mL Collagenase I (Gibco17100016) for 30 minutes with intermittent agitation. Digested tissue was pelleted at 300g for 10 minutes, then resuspended in fibroblast growth media – DMEM (Gibco 11995-065) + 10% FBS, Penicillin/streptomycin (ThermoFisher 15140122), insulin-transferrin-selenium (Sigma I3146), and plated on 0.1% gelatin coated plates for 2 hours at 37°C. After this time, non-adherent cells were removed and fresh media was added. Cells were used through passage 3. For co-culture experiments, fibroblasts were plated on 0.1% gelatin coated coverslips in 12 well plates at 100,000 cells / well. Once adhered, fibroblasts were

pretreated with the indicated dose of Doxorubicin for 24 hours, and washed prior to addition of Tc1 cells when indicated at 25,000 cells / well, and cultured overnight, then washed with PBS to remove non-adherent T-cells. When indicated, Th1 cells and co-cultures were pretreated with 20 µg/mL anti-CD49d (Biolegend clones 9C10 and RI-2) or 20 µg/mL anti-CD11a (Biolegend clone MI7/4).

6.2.10 Immunofluorescence:

Fibroblasts and Cardiac Samples: Samples were washed 2 x 10 minutes with PBS, then fixed in 4% PFA for 15 minutes. Non-specific binding was prevented by incubation with PBS + 10% normal goat serum and normal donkey serum for 1 hour at RT with 0.1% triton-X for permeabilization. Samples were stained overnight at 4C with 1:100 anti-αSMA (Sigma A2547) and 1:200 anti-CD8 (Biolegend), washed in PBS, then stained 1:500 with goat anti-mouse AF-488 (Invitrogen A11071) and donkey anti-rat AF594 (Invitrogen A21209) for 2 hours, washed in PBS, then mounted in mounting media with DAPI (Southern Biotech, 0100-20). **Wheat Germ Agglutinin (WGA):** Tissues were fixed for 15 minutes in 4% PFA, followed by blocking with PBS + 10% normal goat serum for 1 hour at RT. Tissues were stained with 5µg/mL FITC conjugated WGA (Sigma L4895) in PBS + 10% normal goat serum for 2 hours and mounted in mountging media with DAPI. Visualization was performed with a Nikon Ti inverted fluorescence microscope.

6.2.11 Cytokine Array:

Sera from 3 PBS or DR treated mice was pooled and used to probe the Proteome Profiler Mouse Cytokine Array Kit (R&D, ARY007) according to manufacturer's instructions, before exposure to Pierce ECL (Thermofisher 32106) and quantification using ImageJ.

6.2.12 Western Blotting:

Cells were lysed in RIPA buffer supplemented with protease and phosphatase inhibitors

then cleared by centrifugation at 4°C at 13,000 xg. Protein concentrations were determined using DC protein assay (BioRad 5000112) and equal amounts of protein were subjected to SDS-PAGE, then transferred to PVDF membranes, followed by blocking with Tris buffered saline + 0.1% Tween20 containing 5% non-fat milk for 1 hour at room temperature. Immunoblotting was performed overnight at 4°C using antibodies diluted 1:1000 in 5% non-fat milk. Antibody sources: Collagen 1 (Thermofisher PA5-29569), Collagen 3(ABclonal A0817), Cleaved Caspase 3 (CST 9661), SERCA (CST 4388), GAPDH (CST 2118), IsoLG D11 (Provided by Dr. Annet Kirabo[458]). Blots were then incubated with the appropriate HRP peroxidase conjugated secondary antibody (1:2000, Rabbit CST 7074, Mouse CST 7076, Goat ThermoFisher A15999) at room temperature for 1 hour, then developed using Pierce ECL (ThermoFisher 32106) and imaged using a ChemiDoc XRS+ System (Biorad). Band intensity was quantified using Image-J.

6.2.13 Canine Patient Samples:

Data was generated from pet dogs with diffuse large B cell lymphoma (DLBCL) enrolled in an open label non-randomized clinical trial. Dogs were eligible if they had a diagnosis of $CD21^{+}/CD5^{-}$ lymphocytosis/ B-cell lymphoproliferative disease on flow cytometric evaluation of lymph node fine needle aspirate samples confirmed as B-cell lymphoma on lymph node biopsy and had not received any prior therapy. Additional details of eligibility and enrollment are provided in the referenced manuscripts.[459,460] The animal protocol associated with this study was approved by the Tufts University Institutional Animal Care and Use Committee (IACUC, #G2017-110, #G2020-82). As part of this prospective clinical trial, all pet dogs received the canine chimeric monoclonal anti-CD20 antibody (1E4-cIgGB) in combination the anthracycline doxorubicin to treat their DLBCL.[461] Blood was taken prior to or after anthracycline initiation at the indicated time points, additional

patient information found in Supplemental Table 3. Immunophenotyping of canine patients was performed as previously described.[462] 500 µl of blood was lysed using 1 ml of ACK lysis buffer (0.15M NH_4CL, 1M KHO_3, O.1 mM Na_2EDTA, 1N HCL at a pH of 7.2-7.4) in a 1.5 ml microfuge tube for 5 minutes at RT. Samples were centrifuged at 1000 xg for 3 minutes at RT and lysed a second time with 1 ml of lysis buffer. Cells were then resuspended in 200 µl of PBS with 2% FBS. Twenty-five µl of cell suspension was added to each of 5 individual wells of a 96-well round bottom polystyrene plate together with 25 µl of the following antibody cocktail: APC CD5 (Biorad MCA1037APC), Pacific Blue CD4 (Biorad MCA1038PB), and AF700 CD8 (Biorad MCA1039A700). Samples were incubated for 15 minutes at room temperature and then washed with PBS twice. Samples then were resuspended in PBS-2% FBS with 10 µg/ml of propidium iodide (Sigma P4170) for dead cell exclusion and analyzed on a Gallios Flow Cytometer (Beckman Coulter) within 3 hours. The gating strategy is shown in Figure S13.

6.2.14 Human Patient Samples:

Patients were recruited prospectively and consecutively and enrolled at Beth Israel Deaconess Medical Center (BIDMC) for flow cytometry analyses, and from Massachusetts General Hospital and McGill University for Somascan data[463]. All study procedures were approved by the Dana-Farber/Harvard Cancer Center institutional review board in conjunction with the BIDMC Cancer Clinical Trials Office, and all patients provided informed consent. Individuals aged 18 years and older were eligible based on the following criteria: 1) planned treatment with anthracycline-based chemotherapy, and 2) at least one risk factor for cardiotoxicity, including age > 65 years, hypertension, treatment for aggressive non-Hodgkin lymphoma, planned cumulative doxorubicin dose ≥ 300 mg/m^2 (or equivalent of an alternative anthracycline), planned treatment with an anti-HER2 agent, or prior chest irradiation. Patients with a left ventricular ejection

fraction (LVEF) of less than 50% before chemotherapy initiation, or those who were unwilling to provide informed consent were excluded at the time of enrollment. Whole blood samples were collected at baseline (prior to chemotherapy) and after a 3-month follow-up. Additionally, we interrogated the CXCL9/10-CXCR3 axis in a previously published data set that used an aptamer-based proteomics platform (SomaScan®) to profile 1,317 plasma proteins in patients treated with anthracyclines for breast cancer.[463]

6.2.15 Statistical Analysis:

Statistical analysis was performed using GraphPad Prism 9.4.1. All data are presented as mean ± standard error of the mean (SEM). Statistical analysis was done by Student's unpaired or paired t-test (where indicated) for two group analysis. Multiple group comparisons were done using one-way ANOVA with Tukey's multiple comparison test or two-way ANOVA with Sidak's multiple comparison test. Differences were considered statistically significant at $p \leq 0.05$.

6.2.16 Data Availability:

The data, methods, and materials will be available to other researchers for the purposes of reproducing the results or replicating procedures. Detailed methods, all raw source data, and any associated references are provided in the supplementary material.

6.3 Results

6.3.1 Doxorubicin Increases Cardiac and Systemic Cytotoxic T-cells

Innate and adaptive immune cells were analyzed in wild type (WT) mice in response to DR treatment (Figure 6-1A). 4 weeks and 8 weeks after DR initiation, we found increased cardiac $CD8^+$ T-cells compared to PBS controls and similar frequency and number of $CD4^+$ T-cells (Figure 6-1B-F). We also found intramyocardial $CD8^+$ T-cells by immunohistochemistry (Figure 6-1G), which co-existed with the expected reduced ejection fraction, progressive ventricular wall thinning, cardiac atrophy and cardiac

TUNEL positivity (Figure 6-1H-L). Overall cardiac myeloid cells and $CCR2^{+}$ monocytes were unchanged, and $CD11b^{+}Ly6G^{+}$ neutrophils were slightly elevated only at 4 weeks

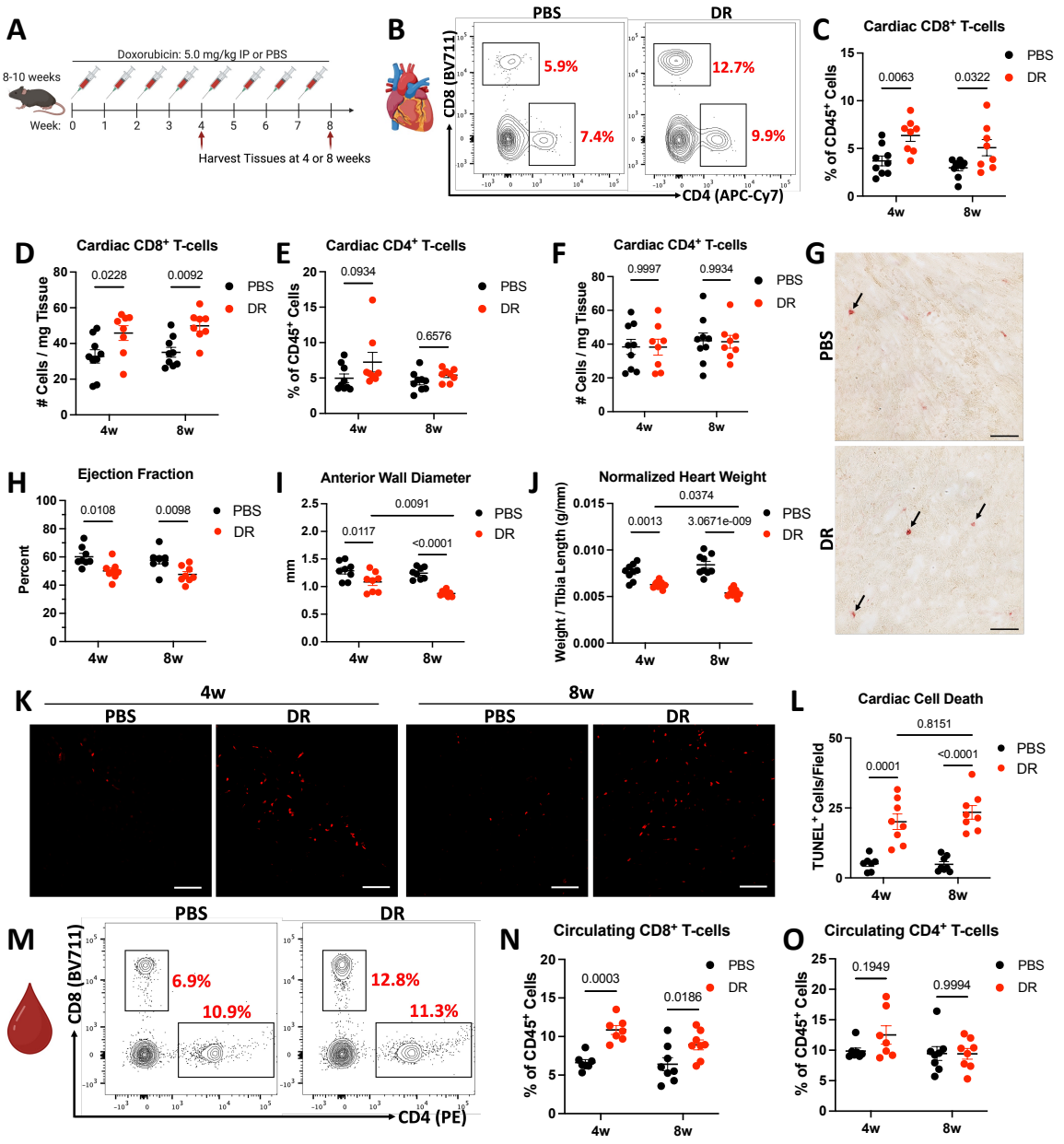


Figure 6-1 CD8 T-Cells Infiltrate the Heart Concurrently with Doxorubicin Induced Cardiac Pathology and Systemic Inflammation

A. Schematic of Doxorubicin (DR) treatment. All data in figure include n=8-10 mice per group. B-F. Hearts from wild type PBS or DR treated mice were digested and analyzed by flow cytometry. Representative plots showing cardiac T-cells (gated on CD45+CD11b- cells) in 8 week treated mice shown in B, quantified by frequency (C, E) or total number per tissue digested (D, F) at 4 and 8 weeks. G. Representative immunohistochemistry for CD8 in cardiac sections of PBS or 8 week DR treated mice. Scale bars are 50 μm. H-I. Echocardiography was used to measure ejection fraction and wall thickness 1 day before tissue harvest. J. Whole heart weight normalized to tibia length. K. Formalin fixed cardiac samples were stained with TUNEL, representative images shown in K with scale bars of 50 μm quantified using ImageJ in L. M-O. Whole blood from PBS or DR treated mice was analyzed by flow cytometry. Representative plots showing circulating T-cells (gated on CD45+CD11b- cells) in 8 week treated mice shown in M, quantified in N-O at 4 and 8 weeks. All data shown are mean±SEM. Statistical analysis by 2-way ANOVA with Sidak's multiple comparison test, exact p-values shown.

(Figure 6-2). Systemically, DR resulted in increased frequency of circulating CD8⁺ T-

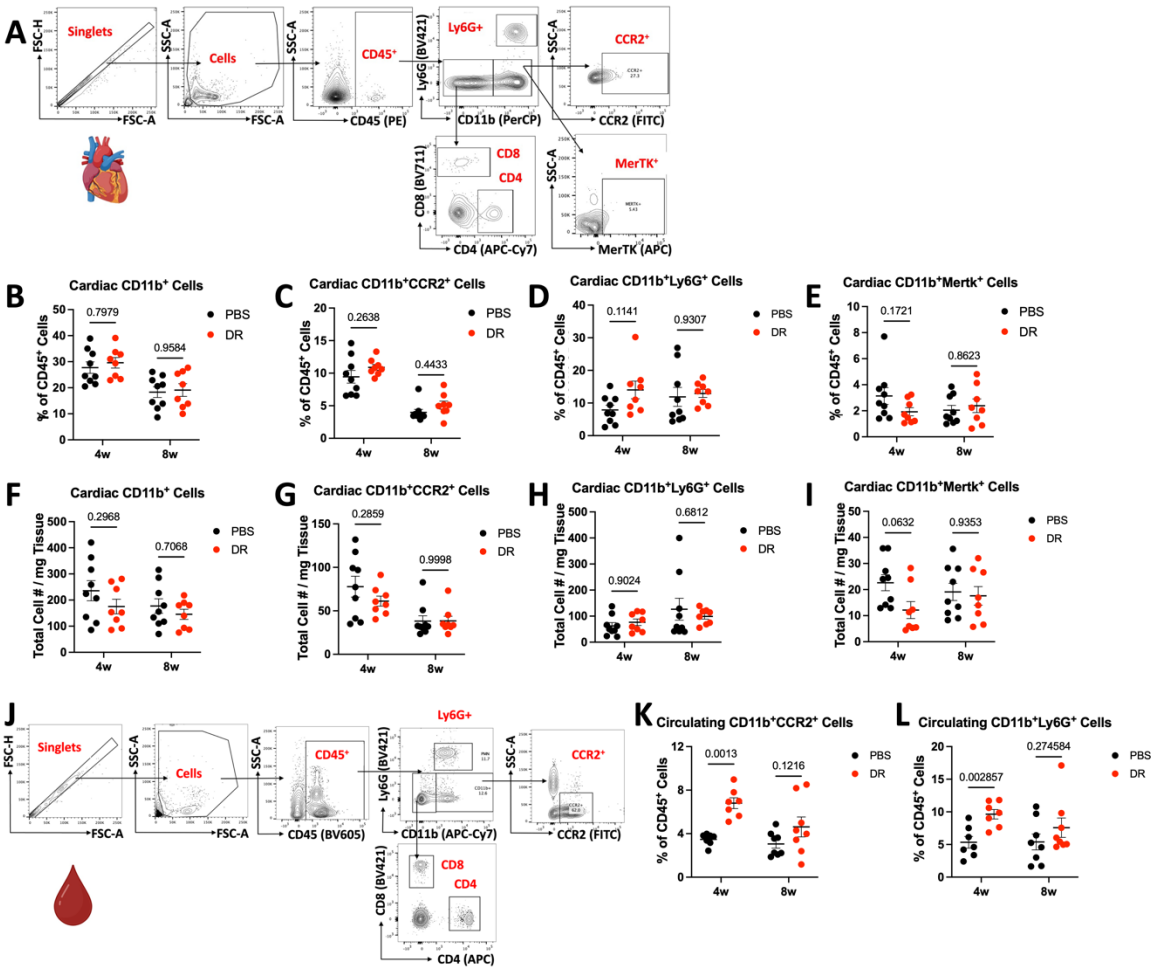


Figure 6-2 Doxorubicin Effects on Cardiac and Circulating Myeloid Populations
WT mice were treated with PBS or 5.0 mg/kg DR for 4 or 8 weeks (n=7-10 mice / group). A. Hearts were digested and analyzed by flow cytometry, shown is the gating strategy used for T-cells and myeloid populations, and quantification by frequency or total cell number for CD11b+ cells (B,F), CD11b+CCR2+ cells (C,G), CD11b+Ly6G- cells (D,H), or CD11b+MertK+ cells (E, I). J. Whole blood was analyzed by flow cytometry, shown is gating strategy for T-cells and myeloid populations, and quantification for CD11b+CCR2+ cells (K), or CD11b+Ly6G- cells (L). All data shown are mean±SEM. Statistical analysis by 2-way ANOVA with Sidak's multiple comparison test, exact p-values shown.

cells, and not $CD4^+$ T-cells (Figure 6-1M-O), and elevated $CCR2^+$ monocytes and $CD11b^+Ly6G^+$ neutrophils at 4 and not at 8 weeks, indicative of early systemic inflammation (Figure 6-2J-L). Moreover, we found widely elevated levels of pro-inflammatory cytokines and chemokines in serum, including several produced by T-cells such as IFNγ, IL-4, and IL-17 as well as the T-cell chemoattractants CXCL9 and CXCL10, also confirmed by ELISA (Figure 6-3). We also treated WT female mice (Figure 6-4A) and similarly found decreased ejection fraction, ventricular wall thinning, cardiac

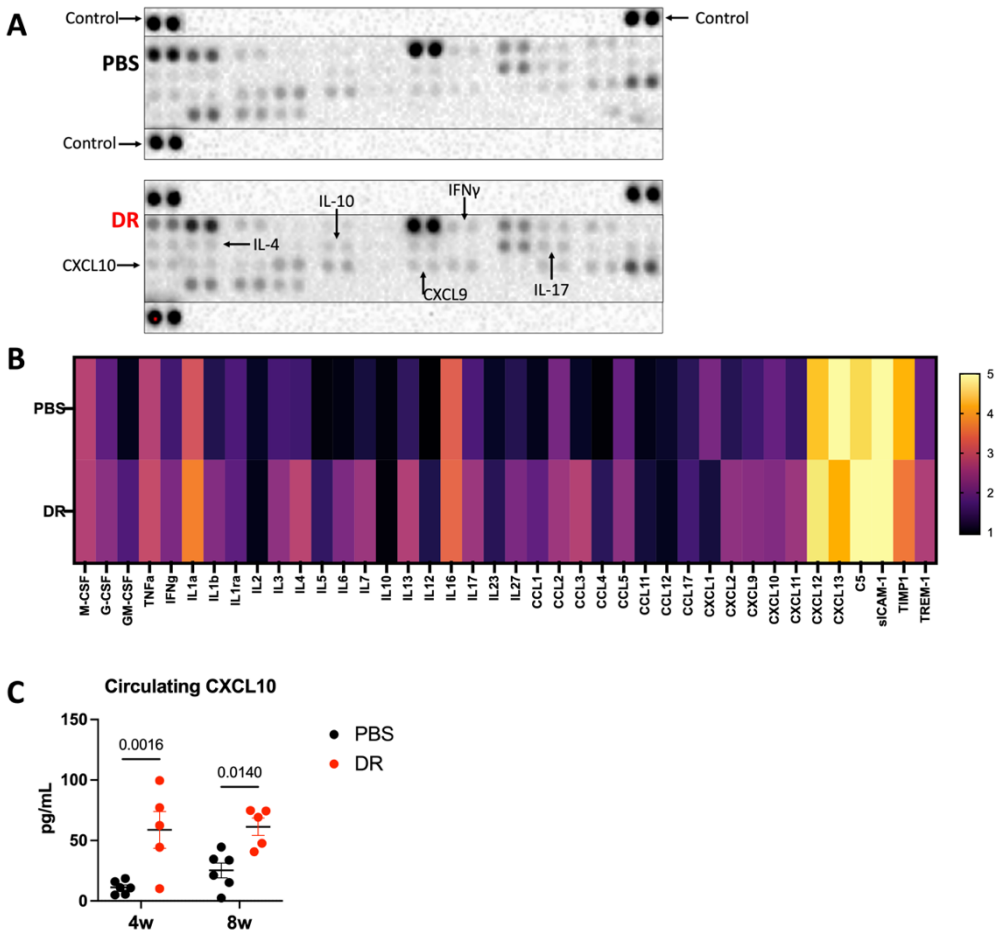


Figure 6-3 Doxorubicin Induces Systemic Inflammation
A. Pooled sera from n=3 mice each treated with 4 week of PBS or DR was used to probe a cytokine array. Shown are representative blots for the array, with the inlay showing a higher exposure compared to control spots labeled in corners. Selected relevant cytokines and chemokines labeled on each blot. **B.** Arrays were quantified using ImageJ and normalized to control signal. **C.** Sera from n=6 mice / group was analyzed by ELISA for CXCL10. All data shown are mean±SEM. Statistical analysis by 2-way ANOVA with Sidak's multiple comparison test, exact p-values shown.

atrophy, and increased TUNEL^{+} cells in DR compared to PBS (Figure 6-4B-F). While cardiac CD8^{+} T-cells but not CD4^{+} T-cells were also increased by DR in female mice (Figure 6-4G-J), circulating CD8^{+} or CD4^{+} T-cells were not (Figure 6-4K-L). Taken together, cardiac and systemic CD8^{+} T cells are induced by DR, and the systemic inflammatory response to DR is less severe in female mice.

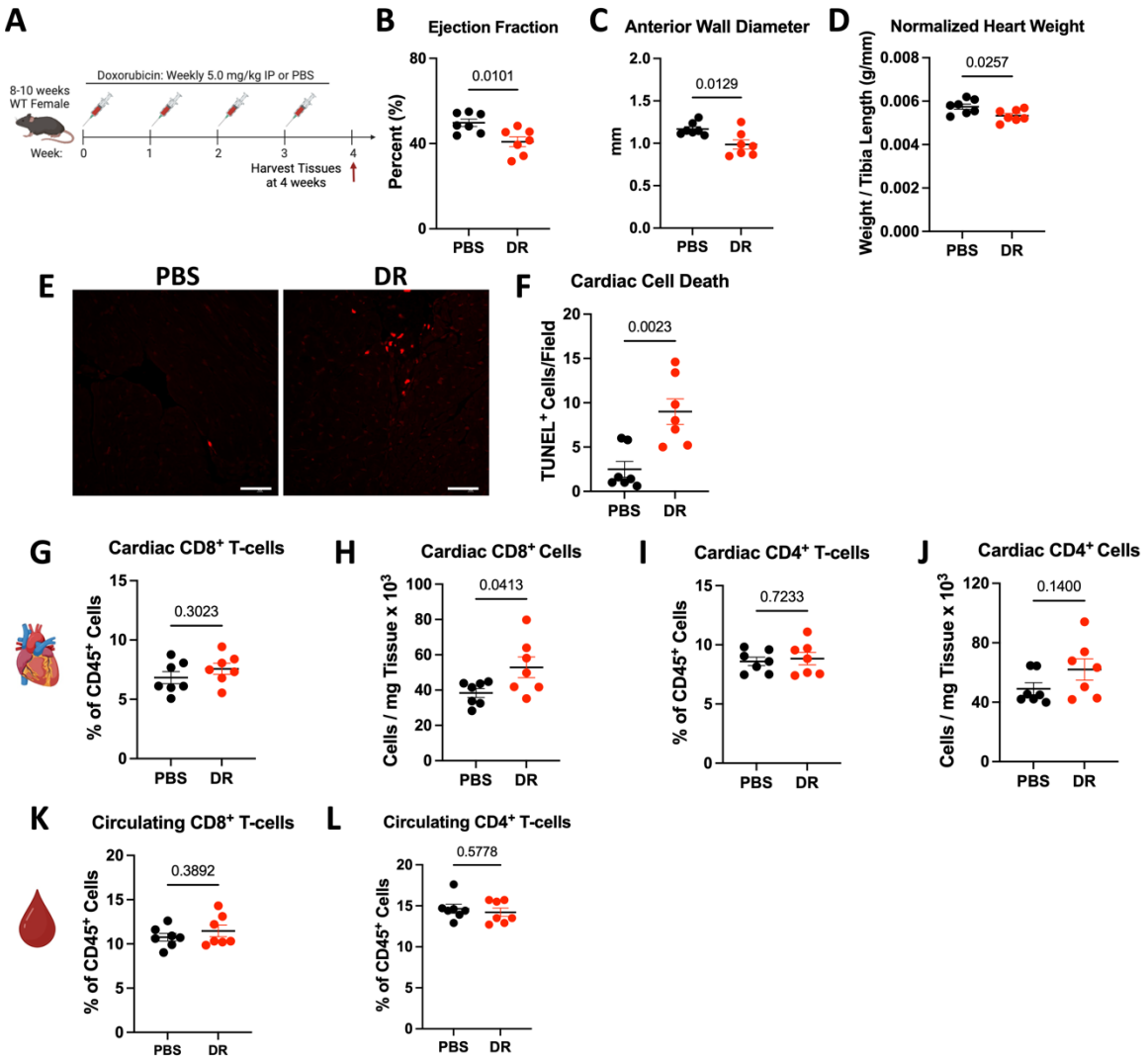


Figure 6-4 Female Mice Treated with Doxorubicin Exhibit Cardiotoxicity and Cardiac CD8+ T-cell Infiltration

A. Schematic of DR treatment in female mice (n=7 mice / group). **B-C.** Echocardiography was used to measure ejection fraction and wall thickness one day prior to tissue collection. **D.** Whole heart weight normalized to tibia length. **E-F.** Formalin fixed cardiac samples were stained with TUNEL, **r**epresentative images shown in **E** with scale bars of 50 μm quantified using ImageJ in **F. G-J.** Hearts were enzymatically and mechanically digested and analyzed for cardiac T-cells by flow cytometry (gating strategy in Figure 6-2). Quantification by frequency shown in **G, I** and by total cell number in **H, J. K-L.** Whole blood was analyzed by flow cytometry for circulating T-cells (gating strategy in Figure S1) quantified in **K-L.** All data shown are mean±SEM. Statistical analysis by 2 sided T-tests, exact p-values shown.

6.3.2 DR Induces a Type-1 CD8$^+$ T-cell Response:

We next analyzed T-cells in lymphoid organs and found that DR increased effector CD8$^+$CD62L^{lo}CD44^{hi} in the mediastinal lymph nodes at both timepoints (mLN) (Figure 6-5A-C) and the spleen at 4 weeks, which subsided by 8 weeks (Figure 6-5D-E). Interestingly, memory CD8$^+$CD62L^{hi}CD44^{hi} cells emerged after DR (Figure 6-6B-E), as

well as the frequency of CD4$^+$ T-cells, supporting a CD4$^+$ T-cell helper response alongside CD8$^+$ T-cell expansion in the lymphoid organs (Figure 6-6F-J). We also analyzed T-cell exhaustion markers (Figure 6-7A) and found that mLN CD4$^+$ T-cells expressed lower levels of PD-1 and CTLA-4 compared to controls, whereas CD8$^+$ T-cells did not (Figure 6-7B-G), and this was not observed in splenic T-cells (Figure 6-7H-K).

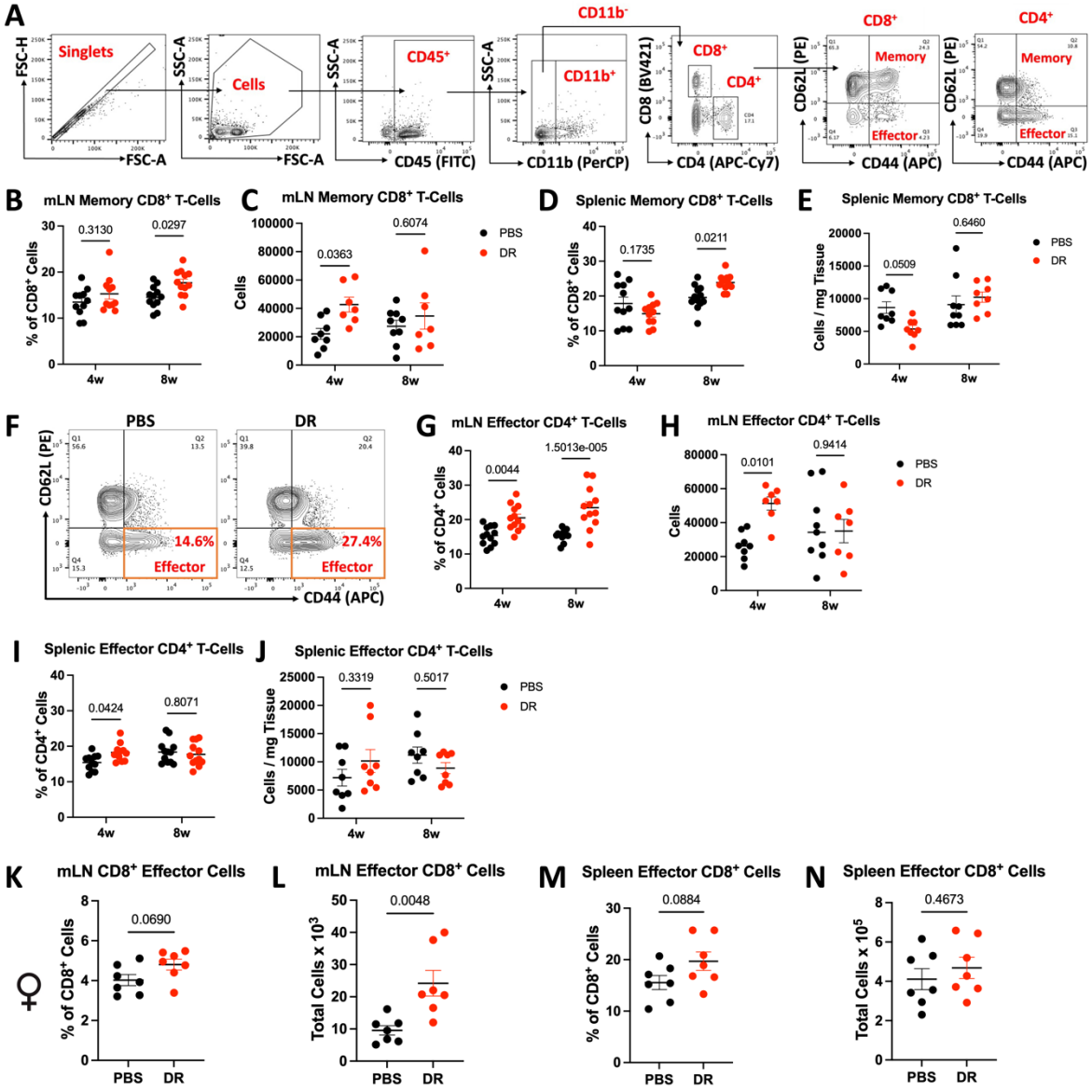


Figure 6-5 Gating Strategies for Lymphoid Organ Effector Populations
WT mice were treated with PBS or 5.0 mg/kg DR for 4 or 8 weeks (n=7-10 mice / group). **A.** Mediastinal lymph nodes or spleens were digested and analyzed by flow cytometry. Shown is gating strategy for effector and memory T-cells. **B-E.** Quantification of memory CD8$^+$ T-cells by frequency (**B**,**D**) and total number (**C**,**E**) in the mLN and spleen. **F.** Representative plots for CD4$^+$ effector T-cells from 8 week treated mice (gated on CD45+CD11b-CD4+ cells), with quantification for mLN (**G-H**) or splenic T-cells (**I-J**). **K-N.** Quantification of mLN and splenic effector CD8$^+$ T-cells from female mice treated with DR for 4 weeks. All data shown are mean±SEM. Statistical analysis by 2-way ANOVA with Sidak's multiple comparison test (**B-J**) or 2 sided T-test (**K-N**), exact p-values shown

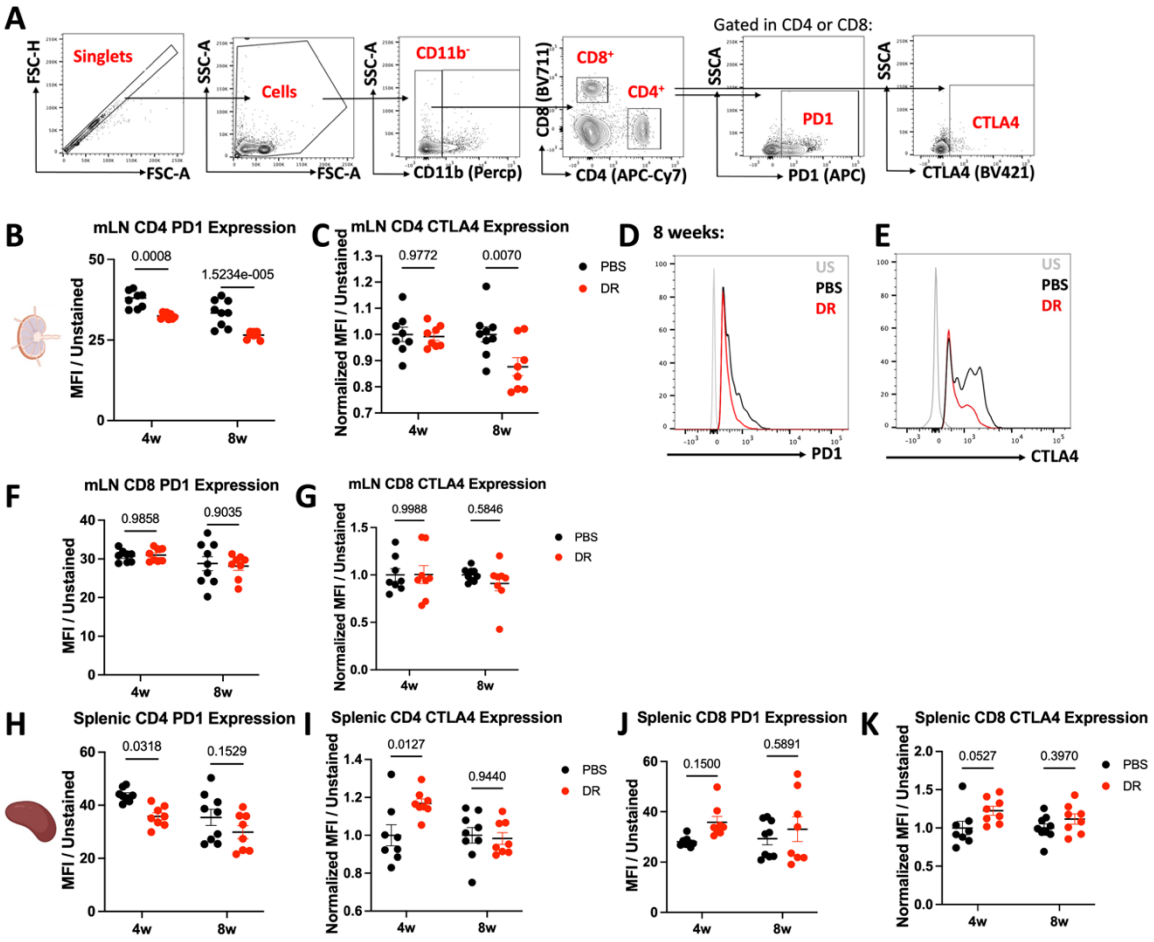


Figure 6-6 Lymphoid T-cells Do Not Increase Exhaustion Markers in Response to Doxorubicin
WT mice were treated with PBS or 5.0 mg/kg DR for 4 or 8 weeks (n=7-9 mice per group), and mediastinal lymph nodes or spleens were digested and analyzed by flow cytometry. **A.** Gating strategy for T-cell PD-1 and CTLA-4 expression. **B-C** Quantification of relative mLN CD4+ T-cell PD-1 and CTLA-4 expression, with representative plots shown in **D-E. F-G.** Quantification of relative mLN CD8+ T-cell PD1 and CTLA4 expression. **H-I.** Quantification of relative splenic CD4+ T-cell PD-1 and CTLA-4 expression. **J-K.** Quantification of relative splenic CD8+ T-cell PD-1 and CTLA-4 expression. All data shown are mean±SEM. Statistical analysis by 2-way ANOVA with Sidak's multiple comparison test, exact p-values shown.

Intracellular staining of T cells (Figure 6-8A-B) demonstrated higher levels of mLN and splenic $CD8^+Tbx21^+$ and $CD8^+IFN\gamma^+$ cells (Figure 6-5F-H) in DR treated mice, indicative of a type 1 cytotoxic T-cell response (Tc1). (Figure 6-5I-J). Splenic $CD4^+$T-cells had slightly increased Tbx21, Gata3, and RorγT positivity (Figure 6-8C-I). In line with an IFNγ-driven T-cell response, cardiac *Ifng* transcript progressively increased after DR treatment (Figure 6-5K), which also resulted in increased cardiac *Cxcl9* and *Cxcl10* gene and protein expression (Figure 6-5L-O), similarly increased in sera (Figure 6-3).

Together, these data outline a DR driven IFNγ-Tbx21^{+}CD8^{+} T-cell response that results in elevated T-cell chemoattractants.

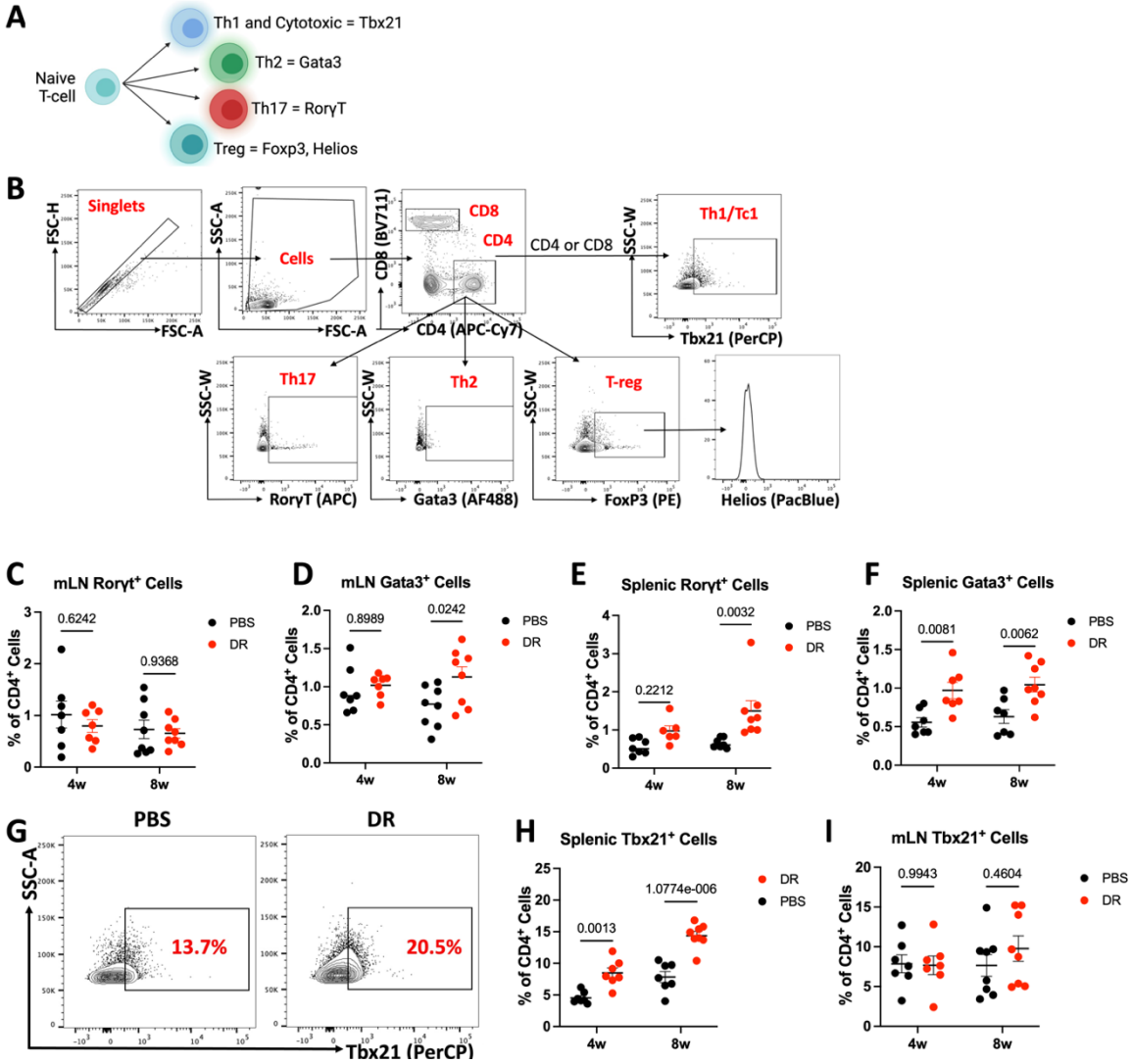


Figure 6-7 Doxorubicin Increases Multiple Helper T-cell Subtypes in Lymphoid Organs
A. Schematic showing helper T-cell differentiation and transcription factors probed to quantify each subtype (n=7-9 mice / group). **B.** Gating strategy used to identify T-cell transcription factors in digested mediastinal lymph nodes (mLN) or spleens form PBS or DR treated mice, with quantification of mLN Th17 cells (**C**), mLN Th2 cells (**D**), splenic Th17 cells (**E**), or splenic Th2 cells (**F**). **G.** Representative plots of splenic CD4+ Tbx21 staining from 8 week treated mice (gated on CD45+CD11b-CD4+ cells), with quantification for splenic Th1 cells (**H**) or mLN Th1 cells (**I**). All data shown are mean±SEM. Statistical analysis by 2-way ANOVA with Sidak's multiple comparison test, exact p-values shown.

6.3.3 DR Induces CD8^{+} T-cell IFNγ Expression and Degranulation

To better understand the direct effect of DR on T-cells, we isolated primary CD8^{+} and CD4^{+} T-cells from WT mice and activated them with αCD3/αCD28 in the presence of low and high dose DR. Only high dose DR decreased viability by about 30% in CD8^{+} T-cells

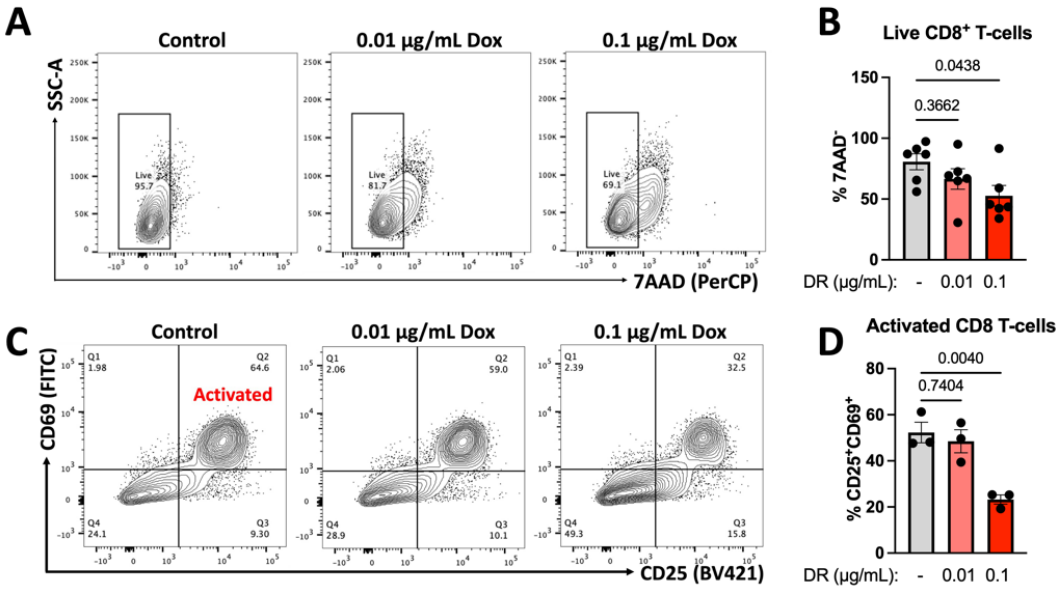


Figure 6-8 Doxorubicin Does Not Increase T-cell Activation Markers In Vitro
WT CD8+ T-cells were activated using αCD3 and αCD28 for 3 days in the presence or absence of the indicated concentration of DR, then analyzed by flow cytometry. **A.** Representative viability plots by 7AAD positivity, quantified in **B** from n=6 independent experiments**. C.** Gating strategy and representative plots for activation markers gated on live cells, with quantification in **D** from n=3 independent experiments**.** All data shown are mean±SEM. Statistical analysis by 1-way ANOVA with Tukey's multiple comparison test , exact p-values shown.

(Figure 6-9A-B). Live T-cells showed increased gene and protein IFNγ expression compared to control (Figure 6-10A-C) yet similar expression of the activation markers CD25 and CD69 (Figure 6-9 C-D). *In vivo*, DR induced the expression of cardiac Granzyme B in WT but not *Tcra*$^{-/-}$ mice treated with 8 weeks of DR, indicating CD8^{+} T-cell degranulation occurs in the cardiac inflammatory environment (Figure 6-10D). We also found that DR directly caused T-cell degranulation, showed by the enhanced expressed of surface CD107a, a granule marker that fuses with the membrane upon degranulation, compared to controls(Figure 6-10E-F). This effect was recapitulated in the cardiac inflammatory environment, as CD8^{+} cardiac T-cells in mice treated with DR also expressed higher CD107a at both timepoints compared to PBS controls (Figure 6-10G-I). Further, cardiac Granzyme B^{+}CD8^{+} T-cells were increased at 4 and 8 weeks post DR

treatment (Figure 6-10J-L). Together this provides evidence of DR directly modulating CD8$^+$ T-cell effector functions *in vitro* and in the context of cardiac inflammation.

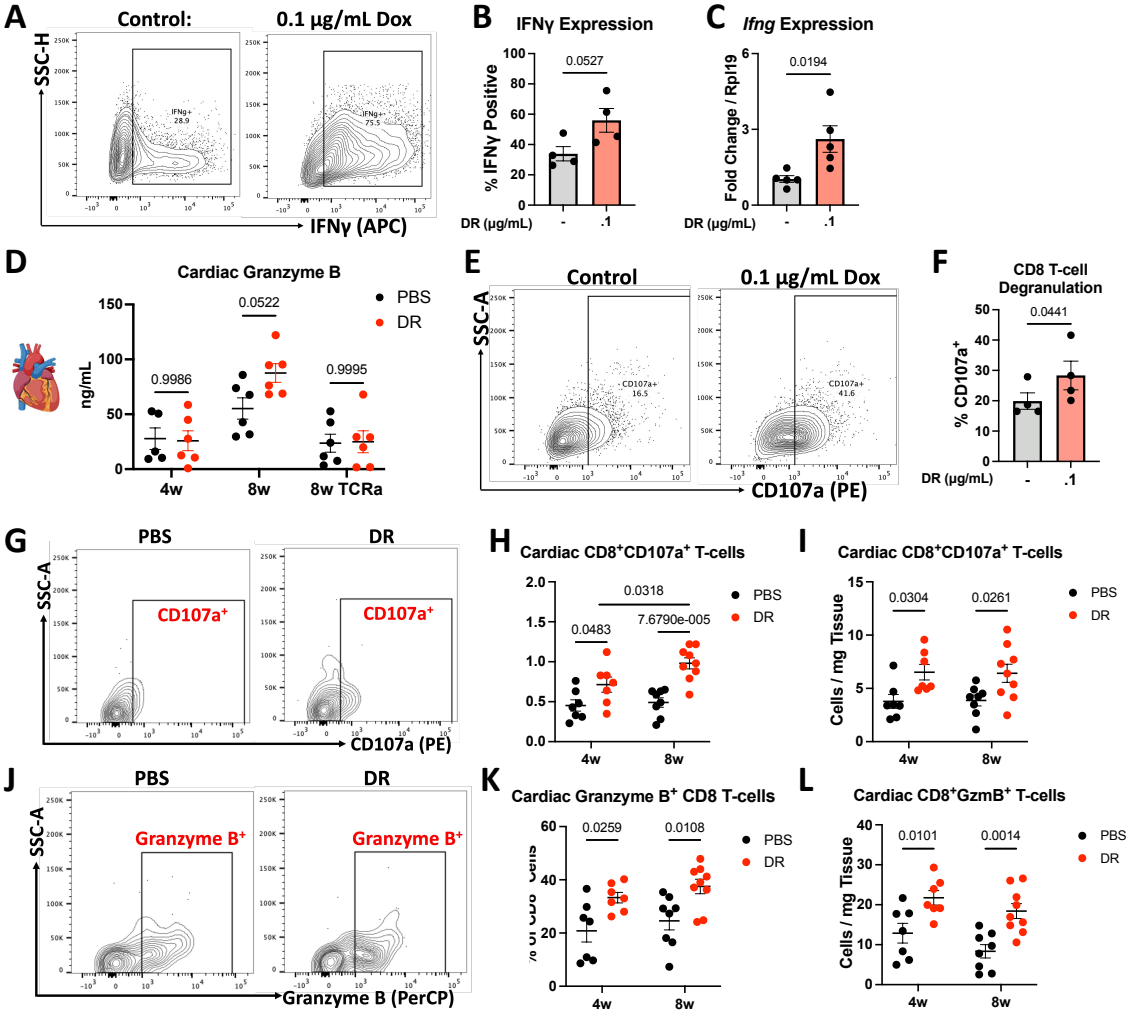


Figure 6-9 Doxorubicin Directly Increases Cytokine Secretion and CD8 T-cell Degranulation
A-B. WT CD8+ T-cells were activated using αCD3 and αCD28 for 3 days in the presence or absence of DR, then analyzed by flow cytometry. Representative plots for IFNγ staining gated on live cells shown in A and quantified in B. from n=4-5 independent T-cell cultures. C. WT CD8+ T-cells activated in the presence or absence of DR were analyzed for *Ifng* transcript by RT-qPCR. D. Whole heart lysate from n=6 WT PBS or DR treated mice for 4 or 8 weeks and TCRa$^{-/-}$ mice treated for 8 weeks were analyzed for Granzyme B by ELISA. E-F. WT CD8+ T-cells were activated, then rested in complete T-cell media overnight before treatment for 5 hours with DR in the presence of PE-αCD107a then analyzed by flow cytometry, representative CD107a staining shown in E, quantified gated on live cells in F from n=4 independent T-cell cultures. G-L. Hearts from n=7-10 WT PBS or DR treated mice were digested then analyzed using flow cytometry. Representative plots (gated on CD45+CD11b-CD8+ cells) shown for 8 week treated mice, CD107a staining shown in G and quantified at 4 and 8 weeks by frequency in H or total cell number per mg tissue digested in I. Granzyme B staining shown in J. and quantified at 4 and 8 weeks by frequency in K or total cell number per mg tissue digested in L. All data shown are mean±SEM. Statistical analysis by 2 sided T-test (B, C, F) or 2-way ANOVA with Sidak's multiple comparison test (D, H-L), exact p-values shown.

6.3.4 $CD8^+$ T-cells Drive DR Cardiotoxicity and Cardiac Fibrosis

Given the strong induction of $CD8^+$ T-cell activation and cardiotropism in response to DR with some evidence of a $CD4^+$ T-cell response, we next tested the functional relevance of each T-cell subset in DR cardiotoxicity. We treated mice with αCD4 and αCD8 antibodies before initiating DR treatment to selectively deplete $CD4^+$ and $CD8^+$ T-cells and evaluated cardiotoxicity after 4 weeks of DR (Figure 6-11A). T-cell subset depletion was confirmed in blood, mLN, and spleens of each group of mice (Figure 6-11B-D, Figure 6-12A-F). Depletion of $CD8^+$ T-cells resulted in a striking protection from systolic dysfunction, and ventricular wall thinning after 4 weeks of DR treatment, with similar gross cardiac atrophy in all DR treated mice (Figure 6-11E-G). However, CD8-depletion prevented DR-induced cardiomyocyte toxicity at the cellular level and the pathologic increase in expression of β-myosin heavy chain (MHC) compared to α-MHC, further supporting a role for $CD8^+$ T-cells in pathologic cardiomyocyte changes (Figure 6-11H, Figure 6-12G-H).

Interestingly, depletion of $CD4^+$ T-cells did not provide protection, and in fact caused a trend towards worse systolic function and increased $CD8^+$ effector T-cells, with no effect on memory T-cells between groups (Figure 6-11I-4). This correlated with increased cardiac $CD8^+$ cells in CD4-depleted mice (Figure 6-12I-J), suggesting a role for $CD4^+$ T-cells in regulating CD8 activity in the onset of DR. To test this, we measured levels of regulatory T-cells (T-regs) in WT mice treated with DR and found that DR treatment resulted in increased $CD4^+Foxp3^+$ cells in the mLN as well as T-reg expression of Helios, a marker of T-reg suppressive activity, at 4 and 8 weeks compared to PBS treated mice (Figure 6-8, Figure 6-13A-C). Depletion of $CD8^+$ or $CD4^+$ T cells showed similar cardiac TUNEL positivity and cardiac caspase 3 cleavage as non-depleted mice in response to DR (Figure 6-13D-G). Strikingly, depletion of $CD8^+$ cells abrogated both interstitial and

perivascular cardiac fibrosis, while depletion of CD4$^+$ cells trended towards more

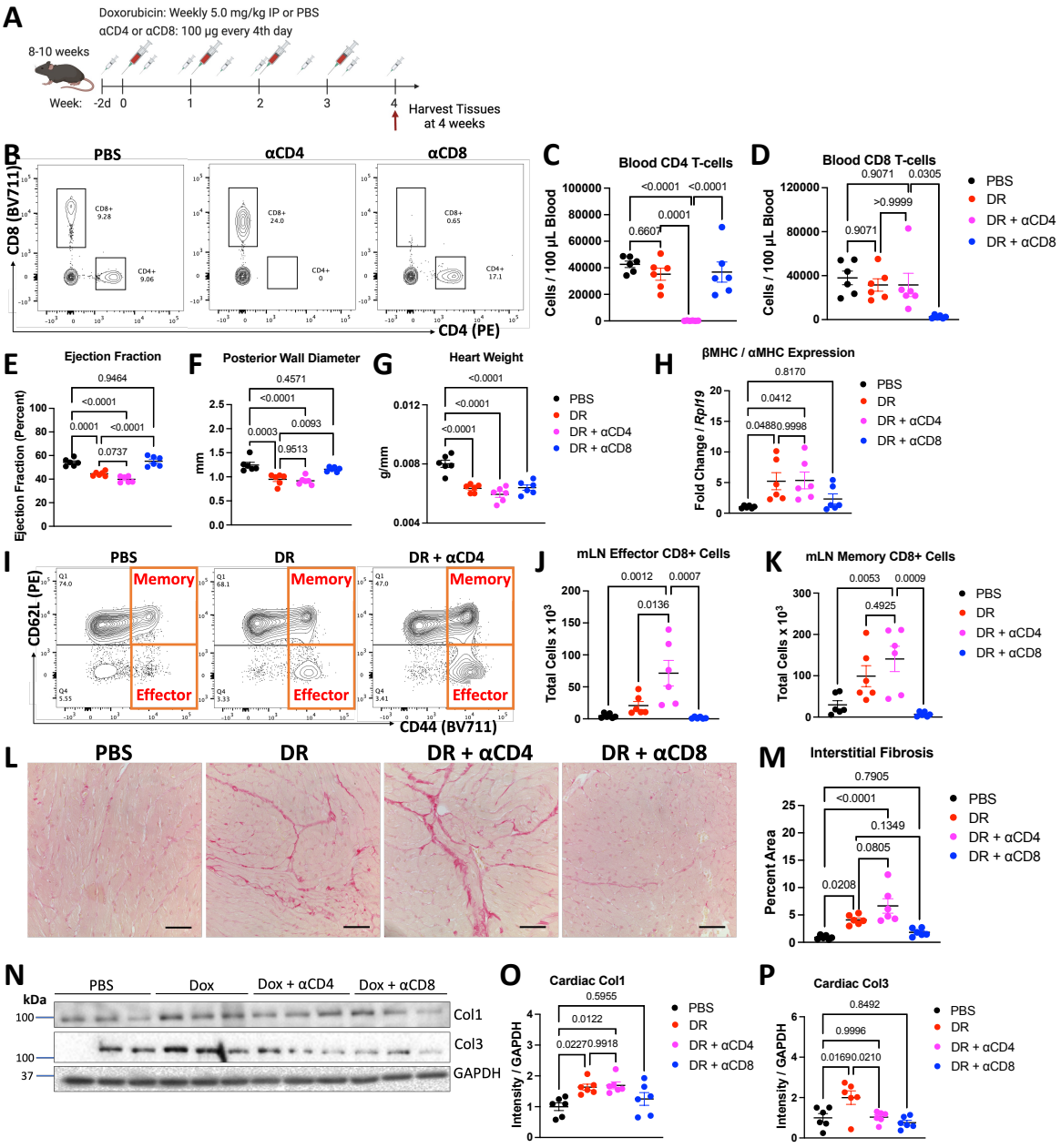


Figure 6-10 CD8 but not CD4 T-cells Drive Cardiac Fibrosis and Systolic Dysfunction in Response to Doxorubicin

A. Schematic of DR treatment and antibody depletion, all data shown are from n=6 mice. B-D. Whole blood was analyzed by flow cytometry for circulating T-cells, shown in B are representative plots (gated on CD45+CD11b- cells) quantified in C-D. E-F. Echocardiography was used to measure ejection fraction and wall thickness one day prior to tissue collection. G. Whole heart weight normalized to tibia length. H. Cardiac RNA was isolated and analyzed by RT-qPCR for beta and alpha myosin. I-K. Mediastinal lymph nodes were digested and analyzed by flow cytometry. Representative plots and gating strategy for effector and memory T-cells (gated on CD45+CD11b-CD8+ cells) shown in I and quantified by total cell number in J-K. L-M. Formalin fixed cardiac samples were stained with picrosirius red, representative images shown in L with scale bars of 50 μm quantified using ImageJ in M. N. Cardiac lysate was analyzed by western blot for collagens, with representative blots from 3 mice shown in N quantified for n=6 mice in O-P. All data shown are mean±SEM. Statistical analysis by 1-way ANOVA with Tukey's multiple comparison test, exact p-values shown.

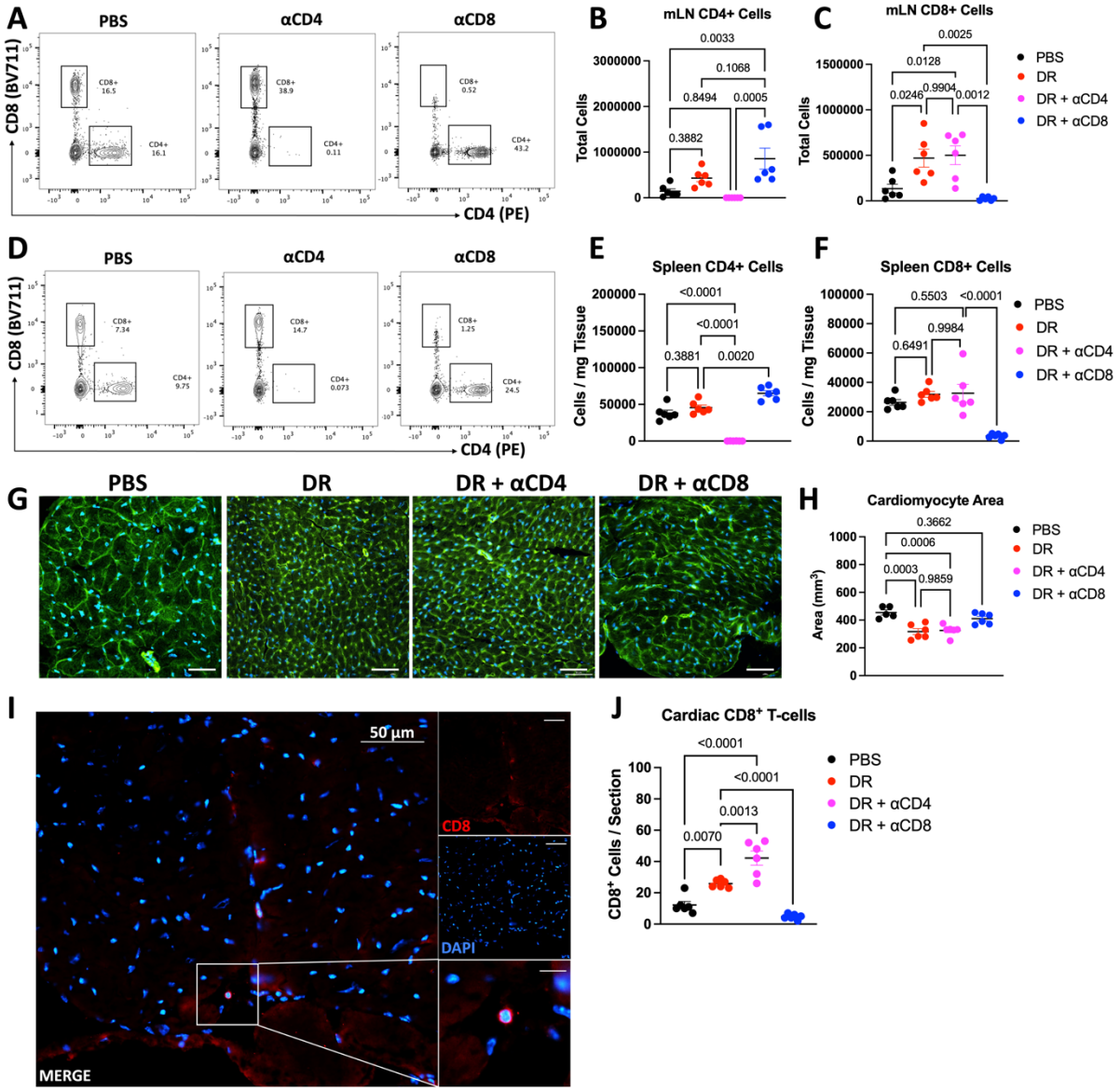


Figure 6-11 Analysis of Doxorubicin Treatment in Antibody Depleted Mice
WT mice were treated with Doxorubicin alongside anti-CD4 and anti-CD8 antibody depletion (see Figure 6-11, n=6 mice / group). **A-C.** mLN were digested and analyzed by flow cytometry, representative plots shown in **A** with quantified CD4+ T-cells (**B)** or CD8+ T-cells (**C**). **D-F.** Spleens were digested and analyzed by flow cytometry, representative plots shown in **D** with quantified CD4+ T-cells (**E)** or CD8+ T-cells (**F**). **G-H.** Cardiac sections were stained with wheat-germ agglutinin to measure cardiomyocyte area, representative images in **G** with scale bars of 50 µm, quantified using ImageJ in **H. I-J.** Cardiac sections were stained with anti-CD8 and analyzed by immunofluorescence, representative image identifying CD8+ T-cells shown in **I.** T-cells were counted manually and quantified in **J.** All data shown are mean±SEM. Statistical analysis by 1-way ANOVA with Tukey's multiple comparison test, ns = no significance, exact p-values shown.

fibrosis, cardiac Collagen 1 and 3, which were reduced in $CD8^+$ cells depleted mice (Figure 6-11L-P, Figure 6-13H-I). Thus, $CD8^+$ T-cells drive DR-induced cardiac fibrosis and systolic dysfunction, while $CD4^+$ T-reg attempt to modulate the $CD8^+$ T-cell pathogenic and pro-fibrotic response.

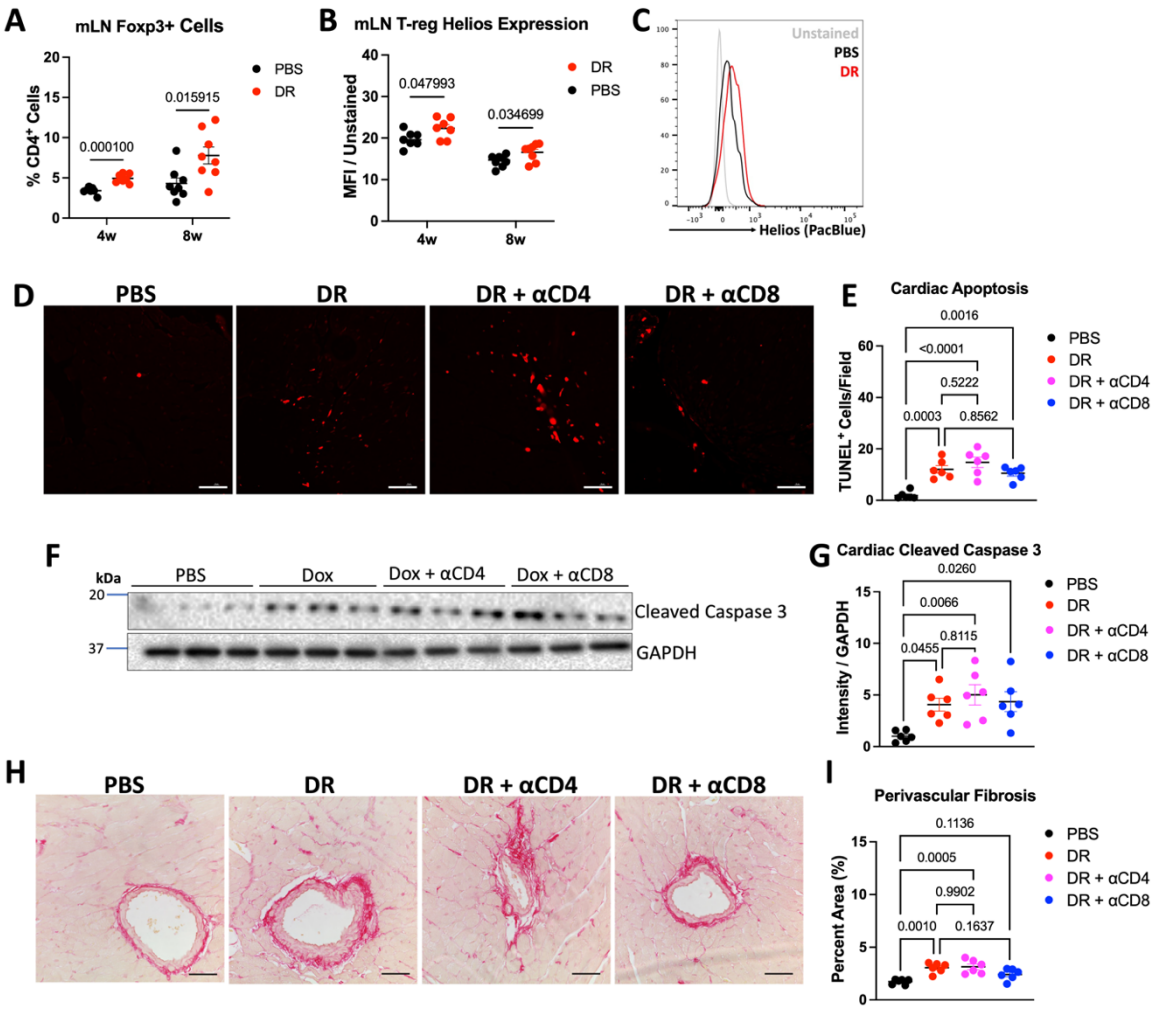


Figure 6-12 Analysis of Doxorubicin Treatment in Antibody Depleted Mice Cont
A-C. WT mice were treated with Doxorubicin for 4 or 8 weeks (n=7-9 mice / group), mLN were digested and analyzed by flow cytometry, (gating strategy in Figure S6). A. Frequency of Foxp3+CD4+ T-cells. B. Relative intensity of Helios expression in Foxp3+CD4+ T-cells, with representative plots for Helios staining in C. D-I. WT mice were treated with Doxorubicin alongside CD4 and CD8 antibody depletion (see Figure 6-11, n=6 mice / group). D-E. Cardiac sections were stained with TUNEL, representative images in D. with scale bars of 50 μm, quantified using ImageJ in E. F-G. Cardiac lysate was analyzed by western blotting for cleaved caspase 3, representative blot for n=3 mice shown in F. quantified for n=6 mice in G. H-I Cardiac sections were stained with picrosirius red, representative images in H. with scale bars of 50 μm, quantified using imageJ in I. All data shown are mean±SEM. Statistical analysis by 2 sided T-test (A-B), or 1-way ANOVA with Tukey's multiple comparison test (E-I), exact p-values shown.

6.3.5 DR Induces An Antigen Specific CD8$^+$ T-cell Response

We next asked whether the CD8$^+$ T-cell response to DR is antigen dependent. We treated ovalbumin-antigen restricted OTI mice with DR with or without systemic immunization with the cognate antigenic OVA peptide (Figure 6-14A). Unimmunized OTI mice treated with DR were fully protected from systolic dysfunction, ventricular wall

thinning, and cardiac atrophy, evidence that endogenous antigen drives T-cell activation and cardiac pathology (Figure 6-14B-D). Further, immunization of OTI mice with OVA alongside DR treatment, thus artificially activating $CD8^+$ T-cells as would occur in a WT mouse with endogenous antigen, resulted in the recurrence of DR-induced systolic dysfunction and cardiac toxicity (Figure 6-14B-D). Moreover, while DR alone was unable to induce T-cell activation in OTI mice, OVA immunization in the absence or presence of DR resulted in a robust increase of splenic $CD8^+CD44^+$ T-cells (Figure 6-14E-F). We also found that OVA immunization increased mLN $CD8^+CD44^+$ T-cells in PBS treated mice, despite the lack of systolic dysfunction, evidence that OVA immunization is a potent stimulus of $CD8^+$ T-cell activation in this model as expected (Figure 6-14G). Importantly, we found that while OTI mice treated with either DR or OVA immunization alone did not show cardiac $CD8^+$ T-cell infiltration, combined DR treatment and OVA led to activated $CD8^+$ T-cell cardiotropism (Figure 6-14H). Together these data confirm that both endogenous antigen specific $CD8^+$ T-cell activation and DR induced cardiac damage are required for cardiac T-cell infiltration. In line with this, we found that OTI mice treated with DR did not develop significant cardiac fibrosis or increased cardiac collagens by western blot, whereas OVA immunized mice treated with DR did (Figure 6-14I-N). Finally, DR alone induced a trending increase in $TUNEL^+$ cells with no detectable cleaved caspase 3, indicator of cell death, compared to OVA immunization mice which exhibited significant DR induced cardiac cell death (Figure 6-14I, L, O-P). Thus, these data support that endogenous neoantigens that arise in response to DR are responsible of CD8+ T cell activation and subsequent cardiomyopathy, which can be further enhanced by immunization with cognate peptide.

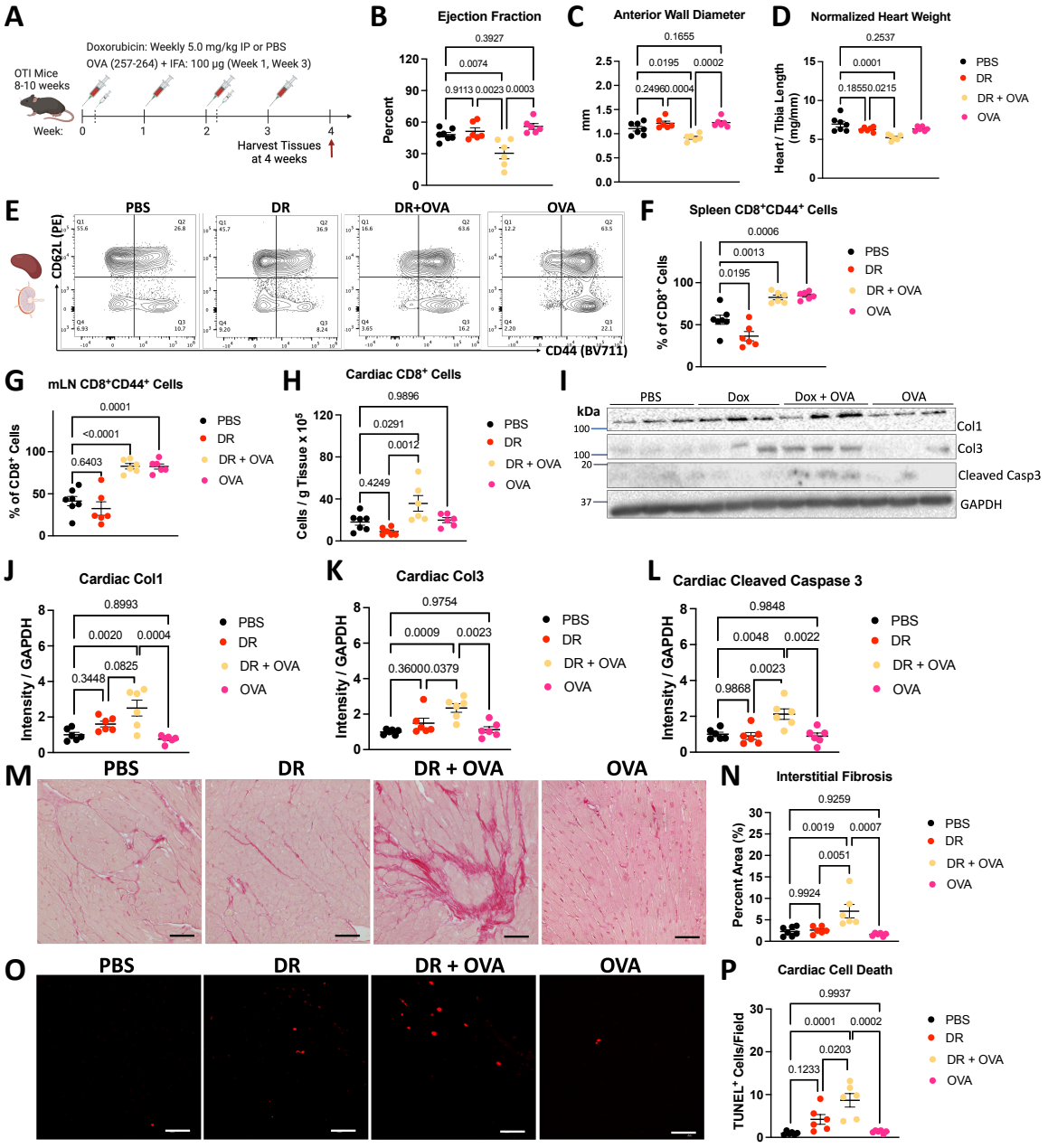


Figure 6-13 Doxorubicin Induces Antigen Specific CD8+ T-cell Activation Required for Cardiac Fibrosis and Systolic Dysfunction:

A. Schematic of DR treatment of OTI mice and vaccination with OVA, all data include n=6 mice / group. B-C. Echocardiography was used to measure ejection fraction and wall thickness one day prior to tissue collection. D. Whole heart weight normalized to tibia length. E-G. Mediastinal lymph nodes or spleens were digested and analyzed by flow cytometry. Representative plots and gating strategy for activated CD44+ T-cells (gated on CD45+CD11b-CD8+ cells) shown in E and quantified for spleen (F) or mediastinal lymph nodes (G). H. Hearts were digested enzymatically and mechanically and analyzed by flow cytometry for CD8+ T-cells, shown as total number normalized to mass of digested tissue. I-L. Cardiac lysate was analyzed by western blot for collagens and cleaved caspase 3 with representative blots from n=3 mice in I and quantification from n=6 mice in J-L. M-N. Formalin fixed cardiac samples were stained with picrosirius red, representative images shown in M with scale bars of 50 µm quantified using ImageJ in N. O-P. Formalin fixed cardiac samples were stained with TUNEL, representative images shown in O with scale bars of 50 µm quantified using ImageJ in P. All data shown are mean±SEM. Statistical analysis by 1-way ANOVA with Tukey's multiple comparison test, exact p-values shown.

6.3.6 *Tcra*$^{-/-}$ Mice are Partially Protected from DR Cardiotoxicity:

Thus far our data implicate $CD8^+$ T-cells as pathogenic after DR treatment while $CD4^+$ T-cells are protective. As such, we sought to next understand the effects of DR in the absence of both T-cell subsets by treating *Tcra*$^{-/-}$ mice, lacking both, with DR. *Tcra*$^{-/-}$ mice were protected from systolic dysfunction and partially protected from ventricular wall thinning at 4 and 8 weeks compared to WT (Figure 6-15A-B, Figure 6-16A-B), suggesting the protective effects of T-regs are negated in the absence of $CD8^+$ T-cells. However, *Tcra*$^{-/-}$ mice exhibited similar cardiac atrophy as WT mice determined by heart weight and cardiomyocyte area at both 4 and 8 weeks post DR treatment (Figure 6-15C, Figure 6-16C-F). At 4 weeks, we found a similar number of cardiac $TUNEL^+$ cells in WT and *Tcra*$^{-/-}$ mice treated with DR (Figure 6-16G-H), demonstrating that T-cells do not contribute considerably to the early induction of cardiomyocyte damage induced by DR. However, *Tcra*$^{-/-}$ mice had less $TUNEL^+$ cells, cleaved caspase 3, and *Anp* gene expression than WT mice after 8 weeks of DR treatment, all markers of cardiomyocyte damage (Figure 6-15D-F, K). We also found that WT but not *Tcra*$^{-/-}$ mice exhibited increased cardiac β-myosin heavy chain (MHC) compared to α-MHC mRNA, and decreased cardiac SERCA protein levels, indicative of dysfunctional cardiomyocytes, in response to DR (Figure 6-16I-L). We then found decreased reactive oxygen species (ROS) generation, a driver of cardiomyocyte apoptosis, and cardiac Isolevuglandin (IsoLG), resulting from cardiac oxidative stress[450,464], in the hearts of DR treated *Tcra*$^{-/-}$ mice (Figure 6-16I-O). These data demonstrate that T-cells are dispensable for the early induction of cardiomyocyte death and that chronic DR administration induces myocyte death and dysfunction through both T-cell dependent and independent mechanisms.

While cardiac fibrosis was not observed in *Tcra*$^{-/-}$ mice after 4 weeks of DR treatment (Figure 6-17), signs of interstitial and perivascular collagen deposition developed in *Tcra*$^{-}$

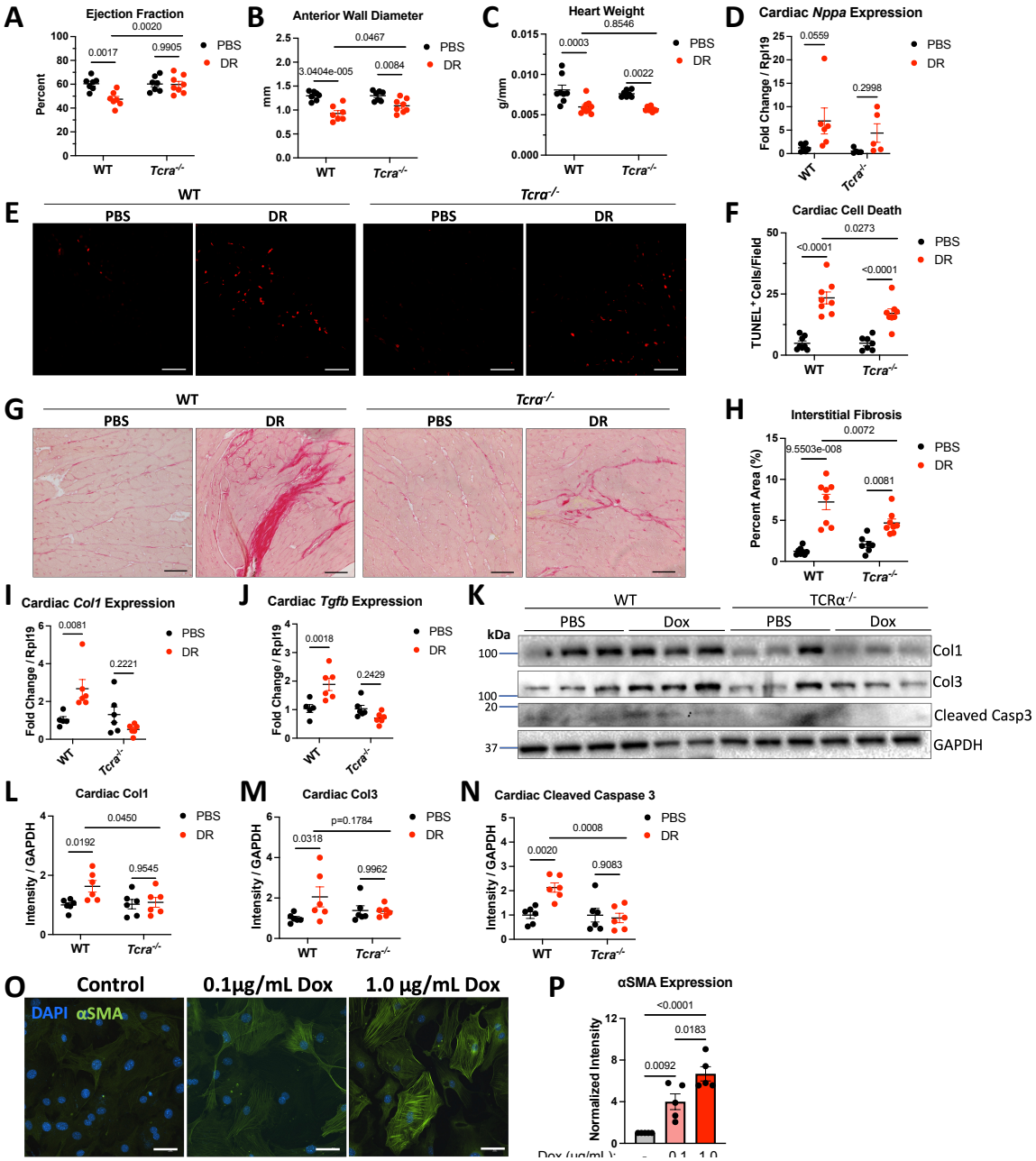


Figure 6-14 T-Cell Deficient Mice are Partially Protected from Doxorubicin Cardiomyopathy and Develop Less Fibrosis than WT

Age matched WT or Tcra$^{-/-}$ mice were treated with DR or PBS for 8 weeks (n=7-8 mice / group). A-B. Echocardiography was used to measure ejection fraction and wall thickness one day prior to tissue collection. C. Whole heart weight normalized to tibia length. D. Cardiac RNA was isolated and analyzed by RT-qPCR for *Anp* from n=6 mice / group. E-F. Formalin fixed cardiac samples were stained with TUNEL, representative images shown in E with scale bars of 50 μm quantified using ImageJ in F. (TCR samples compared to 8w WT from Figure 6-1) G-H. Formalin fixed cardiac samples were stained with picrosirius red, representative images shown in G with scale bars of 50 μm quantified using ImageJ in H. I-J. Cardiac RNA was analyzed by RT-qPCR for *Col1* or *Tgfb* from n=6 mice / group. K-N. Cardiac lysate was analyzed by western blot for collagens and cleaved caspase 3 with representative blots from n=3 mice in K and quantification from n=6 mice in L-N. O-P. Primary cardiac fibroblasts were treated for 16 hours with DR as indicated, then fixed and stained for aSMA using immunofluorescence microscopy, representative images with scale bars of 50 μm shown in O and quantified using ImageJ in P from n=5 independent experiments. All data shown are mean±SEM. Statistical analysis by 2-way ANOVA with Sidak's multiple comparison test (A-N) or 1-way ANOVA with Tukey's multiple comparison test (P) , exact p-values shown.

$^{-/-}$ mice at 8 weeks, albeit significantly less than in WT mice (Figure 6-15G-H, Figure 6-

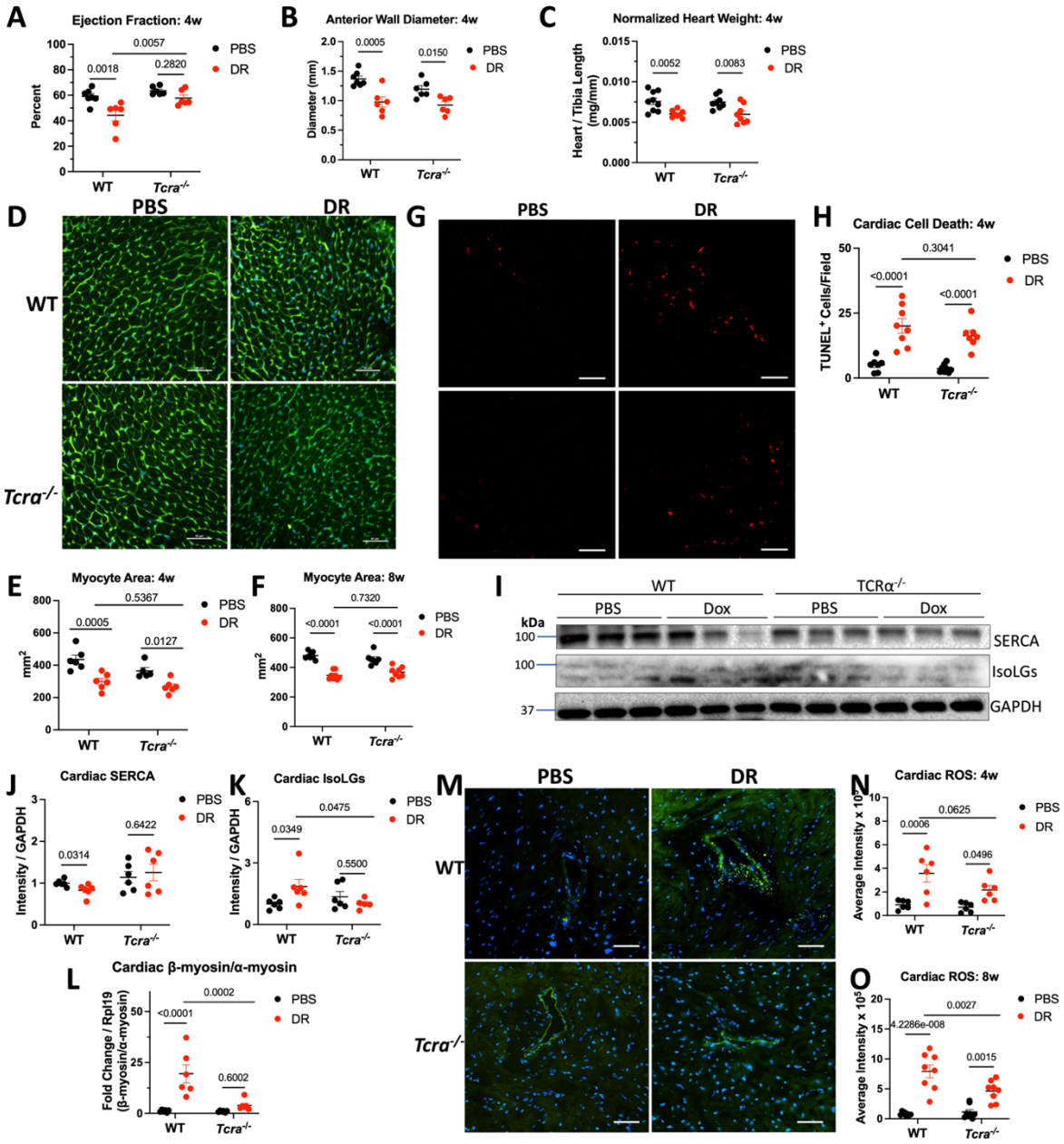


Figure 6-15 TCRa mice Are Partially Protected from Doxorubicin Cardiomyopathy
Age matched WT or Tcra$^{-/-}$ mice were treated with DR or PBS for 4 weeks (n=6-8 mice / group). A-B. Echocardiography was used to measure ejection fraction and wall thickness one day prior to tissue collection. C. Whole heart weight normalized to tibia length. D. Frozen cardiac samples were stained with Wheat Germ Agglutinin (WGA), representative images shown in D with scale bars of 50 μm quantified using ImageJ in E-F. G-H. Formalin fixed cardiac samples were stained with TUNEL, representative images shown in G with scale bars of 50 μm quantified using ImageJ in H (TCR samples compared to 4w WT from Figure 6-1). I-K. Cardiac lysate from PBS or 8w DR treated mice was analyzed by western blot for SERCA or IsoLG expression, representative blots for n=3 mice show in I with quantification from n=6 mice in J-K. L. Cardiac RNA was analyzed by RT-qPCR for alpha and beta myosin. M. Frozen cardiac samples were stained with DCFDA, representative images shown in M. with scale bars of 50 μm quantified using ImageJ in N-O. All data shown are mean±SEM. Statistical analysis by 2-way ANOVA with Sidak's multiple comparison test.

17), suggesting a direct pro-fibrotic effect by DR on cardiac stromal cells. In line with

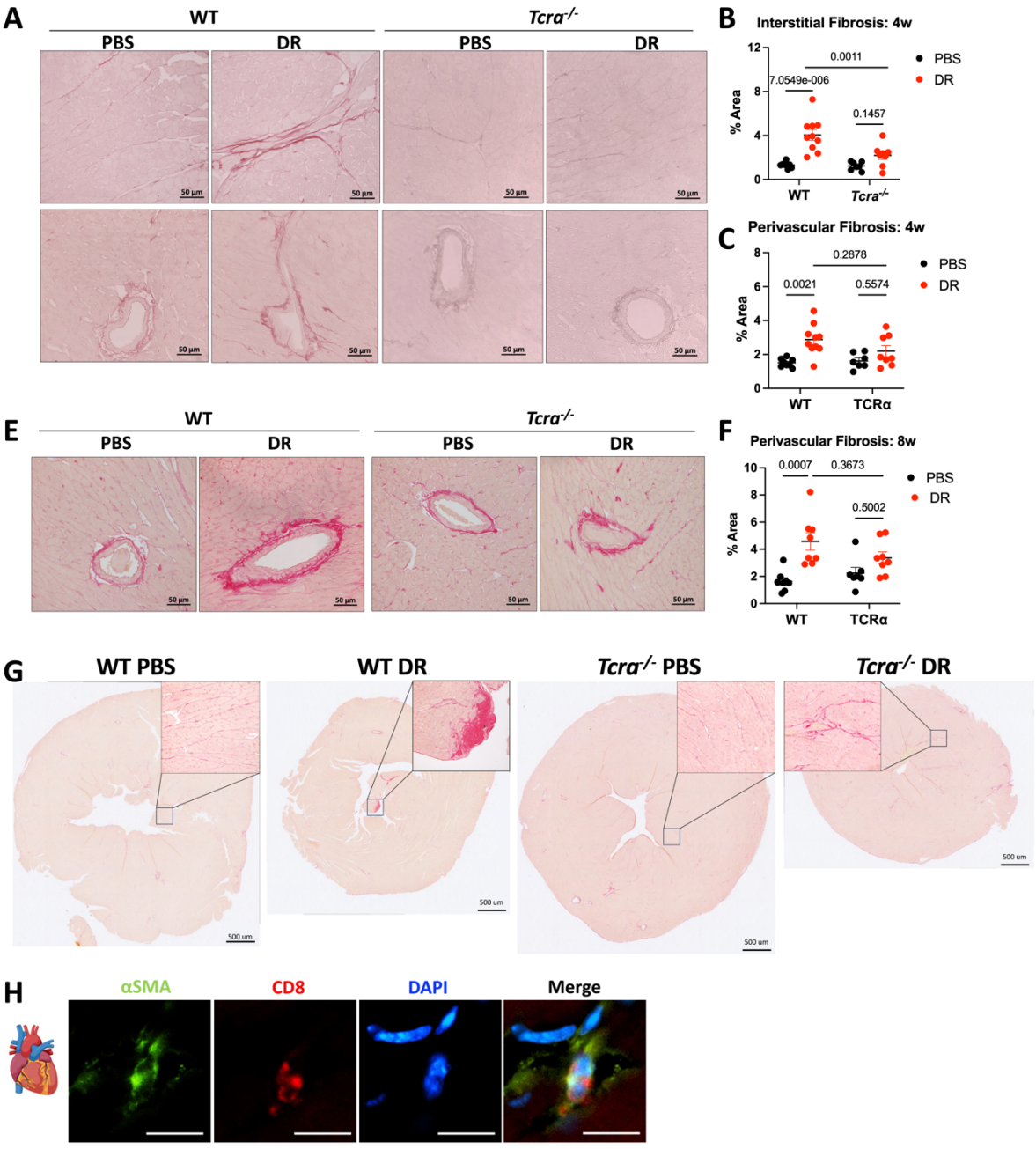


Figure 6-16 Tcra-/- mice Are Partially Protected from Cardiac Fibrosis
Age matched WT or Tcra$^{-/-}$ mice were treated with DR or PBS for 4 or 8 weeks (n=7-10 mice / group). Cardiac sections were stained with picrosirius red for cardiac fibrosis. A. Representative images from 4 week treated mice, scale bars are 50 µm, with quantification in the interstitial region (B) or perivascular region (C). E. Representative images from 8 week treated mice, scale bars are 50 µm, with quantification in the perivascular region (F). G. Whole cardiac section imaging of 8 week matched WT or Tcra$^{-/-}$ mice stained with picrosirius red with zoomed in inlays at 40x, scale bars are 500 µm. H. Cardiac samples from 4 week WT DR treated mice were stained for CD8 and αSMA, example images shown with scale bars of 10 µm. All data shown are mean±SEM. Statistical analysis by 2-way ANOVA with Sidak's multiple comparison test , exact p-values shown.

these data, cardiac *Col1* and *Tgfb* gene expression, as well as cardiac Collagen 1 and 3 protein were induced by DR in WT but not *Tcra*$^{-/-}$ mice (Figure 6-15I-M). We next

interrogated whether delayed fibrosis in the absence of T-cells is induced by DR effects on cardiac fibroblasts. DR induced a dose dependent increased of αSMA expression in primary cardiac fibroblasts *in vitro* (Figure 6-15O-P). Together, these data outline a role for T-cells in cardiac fibrosis and late-stage myocyte damage as T-cells accumulate, alongside direct pro-fibrotic effects on cardiac fibroblasts.

6.3.7 Adoptive Transfer of Tc1 Cells Restores DR Cardiotoxicity:

To further test the hypothesis that Tc1 are responsible for DR cardiotoxicity, we adoptively transferred activated WT Tc1 cells into *Tcra*$^{-/-}$ mice in the onset of 4 weeks of DR treatment. Strikingly, *Tcra*$^{-/-}$ mice receiving Tc1 cells with DR had a significant drop in EF compared to those treated with DR alone, with similar ventricular wall thinning and cardiac atrophy (Figure 6-18A-D). As expected, Tc1 cells repopulated the mLN and spleen after adoptive transfer, and we also found that a significant number of Tc1 cells infiltrated the heart, confirming that DR treatment results in Tc1 cell cardiotropism in reconstituted *Tcra*$^{-/-}$ mice (Figure 6-18E-H). We found increased interstitial and perivascular fibrosis in mice receiving Tc1 cells compared to those treated with DR alone, whereas both groups of mice had significant TUNEL^{+} cardiac cells (Figure 6-18I-N). This confirmed that Tc1 cell cardiotropism induces cardiac fibrosis and systolic dysfunction in recipient *Tcra*$^{-/-}$ mice, which are otherwise partially protected from DR cardiomyopathy.

6.3.8 DR Induces Cardiac Fibroblast/CD8 T-cell Crosstalk

We next investigated the potential interaction between CD8^{+} T-cells and cardiac fibroblasts (CFB) as a contributor of fibrosis. Co-staining for CD8 and αSMA in the hearts of mice treated with DR for 4 weeks showed evidence of CD8^{+} cells co-localizing with

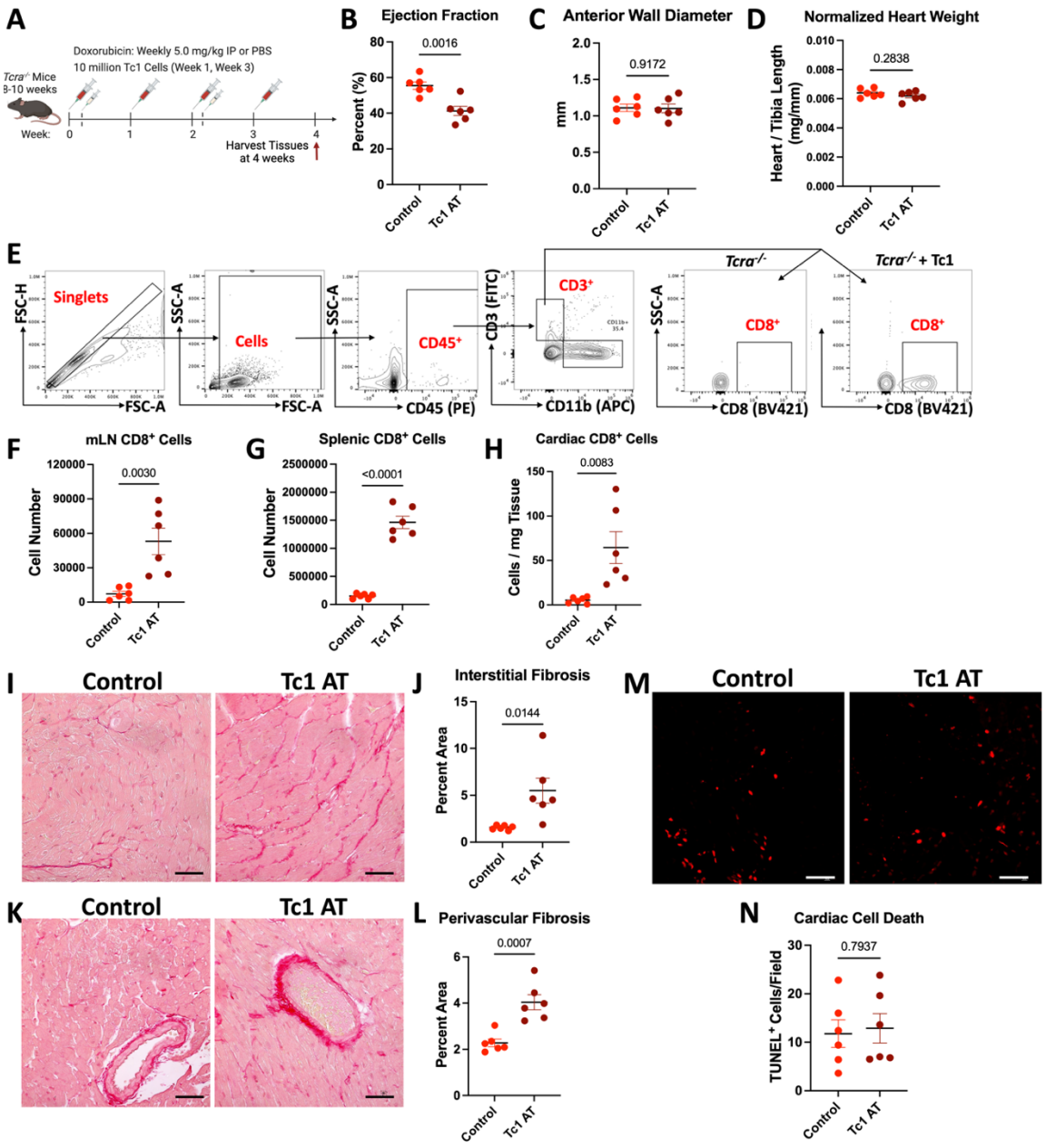
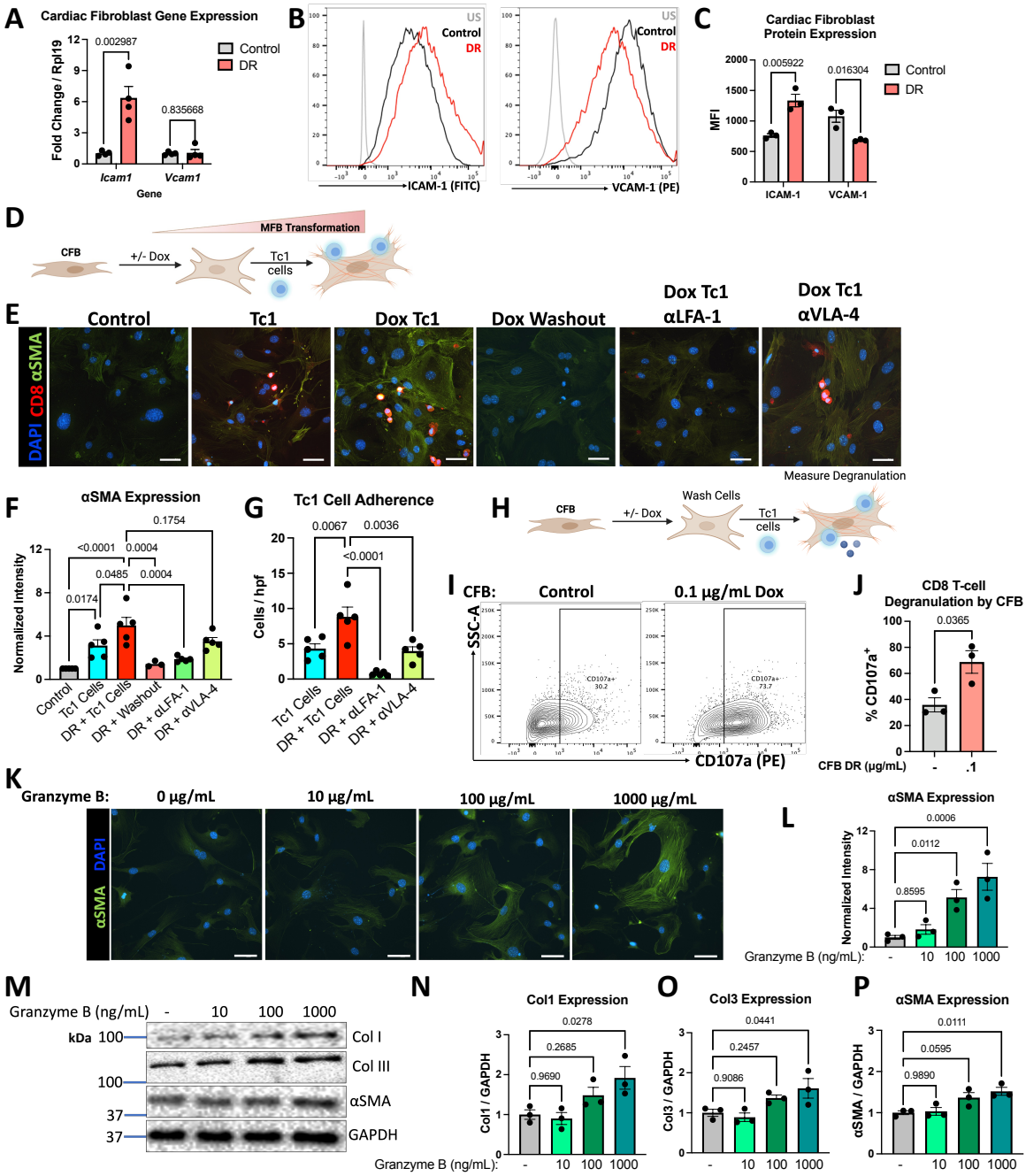


Figure 6-17 Adoptive Transfer of Tc1 Cells Restores Doxorubicin Cardiotoxicity
A. Schematic of DR treatment in Tcra$^{-/-}$ mice alongside adoptive transfer of Tc1 cells (n=6 mice / group). B-C. Echocardiography was used to measure ejection fraction and wall thickness one day prior to tissue collection. D. Whole heart weight normalized to tibia length. E. Gating strategy for identification of CD8+ T-cells in the heart of lymphoid organs. Quantification of CD8+ T-cell number in the mediastinal lymph nodes (F), spleen (G), or heart (H). I-L. Formalin fixed cardiac samples were stained with picrosirius red, representative images shown in I/K. with scale bars of 50 μm quantified using ImageJ in the interstitial region (J), or perivascular region (L). M-N. Formalin fixed cardiac samples were stained with TUNEL, representative images shown in M. with scale bars of 50 μm quantified using ImageJ (N). All data shown are mean±SEM. Statistical analysis by 2 sided T-tests, exact p-values shown.

αSMA^{+} cells (Figure 6-17). As we already showed a direct effect of DR on CFB αSMA expression, we investigated whether DR primes CFB to interact with Tc1 cells. We found



that DR significantly increased CFB expression of ICAM-1 but not VCAM-1 at the transcript and protein level (Figure 6-19A-C), ligands for the integrins LFA-1 and VLA-4 on T-cells respectively, which participate in CD4^{+}-CFB interactions[244]. Co-culture experiments of Tc1 cells with DR treated or untreated CFB (Figure 6-19D) demonstrated that Tc1 cells adhered to DR treated CFB in higher numbers than to untreated CFB, and induced enhanced expression of αSMA (Figure 6-19E-G). DR treated CFB that were

Figure 6-18 Doxorubicin Induces Cardiac Fibroblast ICAM-1 Increasing CD8 T-cell Adhesion and Contact Dependent Degranulation
A-C. WT primary cardiac fibroblasts (n=3-4 independent experiments) were treated for 16 hours with 0.1 μg/mL DR then collected and analyzed for ICAM-1 and VCAM-1 transcript by RT-qPCR (A), or stained for ICAM-1 and VCAM-1 for flow cytometry analysis. Representative plots in B, quantified in C. D. Schematic of T-cell fibroblast co-culture with proposed activation mechanism. E-G. WT primary cardiac fibroblasts were pre-treated with 0.1 μg/mL DR for 16 hours where indicated and WT $CD8^+$ (Tc1) cells were added at a ratio of 1:5 CFB:Tc1 where indicated, or switched to regular media (Dox washout), or included αLFA-1 / αVLA-4 blocking antibodies at 20 μg/mL where indicated, then stained for CD8 and αSMA. Shown are representative images with scale bars at 50 μm (E). αSMA was quantified with ImageJ (F), and T-cells were counted manually (G) from n=3-5 independent experiments. H. Representative schematic of fibroblast pre-treatment strategy to induce T-cell degranulation, in which fibroblasts were pre-treated for 16 hours with 0.1 μg/mL DR, washed, and then Tc1 cells were added at a ratio of of 1:5 CFB:Tc1 for 5 hours in the presence of PE-CD107a, then analyzed by flow cytometry. Representative plots shown in I with quantification from n=3 independent experiments in J. K-P. WT cardiac fibroblasts were treated with recombinant Granzyme B at the indicated concentrations and stained for αSMA by immunofluorescence from n=3 independent experiments, representative images with scale bars at 50 μm in K quantified in L. Representative western blots of granzyme B treated fibroblasts in M with quantification in N-P. All data shown are mean±SEM.

changed to fresh media (DR free) for 24 hours, showed that αSMA returned to baseline levels (labeled washout). Moreover, blocking LFA-1 and VLA-4 on Tc1 cells, the integrin binding partners of ICAM-1 and VCAM-1, respectively, demonstrated that Tc1 adhesion and CFB transformation was dependent on LFA-1/ICAM1 and not VLA-4/VCAM1 interactions, since only anti-LFA-1 significantly decreased both αSMA expression and T-cell adhesion (Figure 6-19E-G). As we showed T-cell contact with CFB induced transformation, we then asked whether this contact in turn induced T-cell degranulation (Figure 6-19H). Adhesion of Tc1 cells to DR treated CFB resulted in greater degranulation of Tc1 cells, determined by the increased surface CD107a expression compared to the Tc1 cells in contact with untreated CFB (Figure 6-19I-J). To understand the mechanism by which CFB-induced T-cell degranulation resulted in pro-fibrotic CFB transformation, we tested if Granzyme B released during degranulation contributed to CFB transformation. We found that treatment of CFB *in vitro* with recombinant Granzyme B increased expression of αSMA in a dose dependent manner (Figure 6-19K-L), becoming significant at the concentration found in the heart by ELISA (Figure 6-10). Further, the same concentration of Granzyme B was able to induce CFB expression of collagen 1, collagen 3, and αSMA at the bulk protein level by western blot (Figure 6-19M-P). Together these data demonstrate that DR primes CFB to interact with $CD8^+$ T-

cells through increased ICAM-1 expression, resulting in myofibroblast transformation and $CD8^+$ T-cell degranulation, and that degranulated Granzyme B directly contributes to cardiac fibroblast transformation.

6.3.9 DR Induces a $CD8^+$ T-cell Response Across 3 Species:

To evaluate if the T-cell response induced by DR in mice translates to patients treated with anthracyclines, we first characterized T-cell counts in 36 canine lymphoma patients treated with anthracyclines, who received 3-4 doses of 25 mg/m^2 of DR (see Table 6-1 for patient characteristics and Figure 6-21A for gating strategy). We found elevated circulating $CD8^+$ T-cells at around 1 month after initiating Doxorubicin, which remained significantly elevated nearly 4 months later (Figure 6-20A-B). Despite this, we found no significant changes to $CD4^+$ T-cell numbers at either time point (Figure 6-20C-D). We then characterized T-cells in the blood of 5 human patients with hematologic malignancy before or 3 months after initiating anthracyclines (Gating Strategy in Figure 6-21B). Patients were white non-Hispanic individuals (2 females and 3 males) with an average age of 52 ± 15 years. The average cumulative DR dose was 385.66 ± 90.9 mg/m^2 (Further patient characteristics found in Figure 6-2). Similar to mice and canines treated with DR, we found expanded circulating $CD8^+$ T-cells but not $CD4^+$ T-cells after anthracycline treatment (Figure 6-20E-G). Further, we found significantly higher numbers of $IFN\gamma^+CD8^+$ and near significantly higher $GranzymeB^+CD8^+$ T-cells after anthracycline treatment (Figure 6-20H-I, Figure 6-21C-D). Additionally, a greater percent of the circulating $CD8^+$ T-cells expressed CXCR3, the receptor for CXCL9 and CXCL10 (Figure 6-20J-K), which we found to be increased in the hearts of DR treated mice.

To further investigate the potential relevance of the CXCL9/10-CXCR3 axis in anthracycline treated patients, we utilized our team's previously published dataset in which plasma proteins were profiled in patients before and 3 months post anthracycline

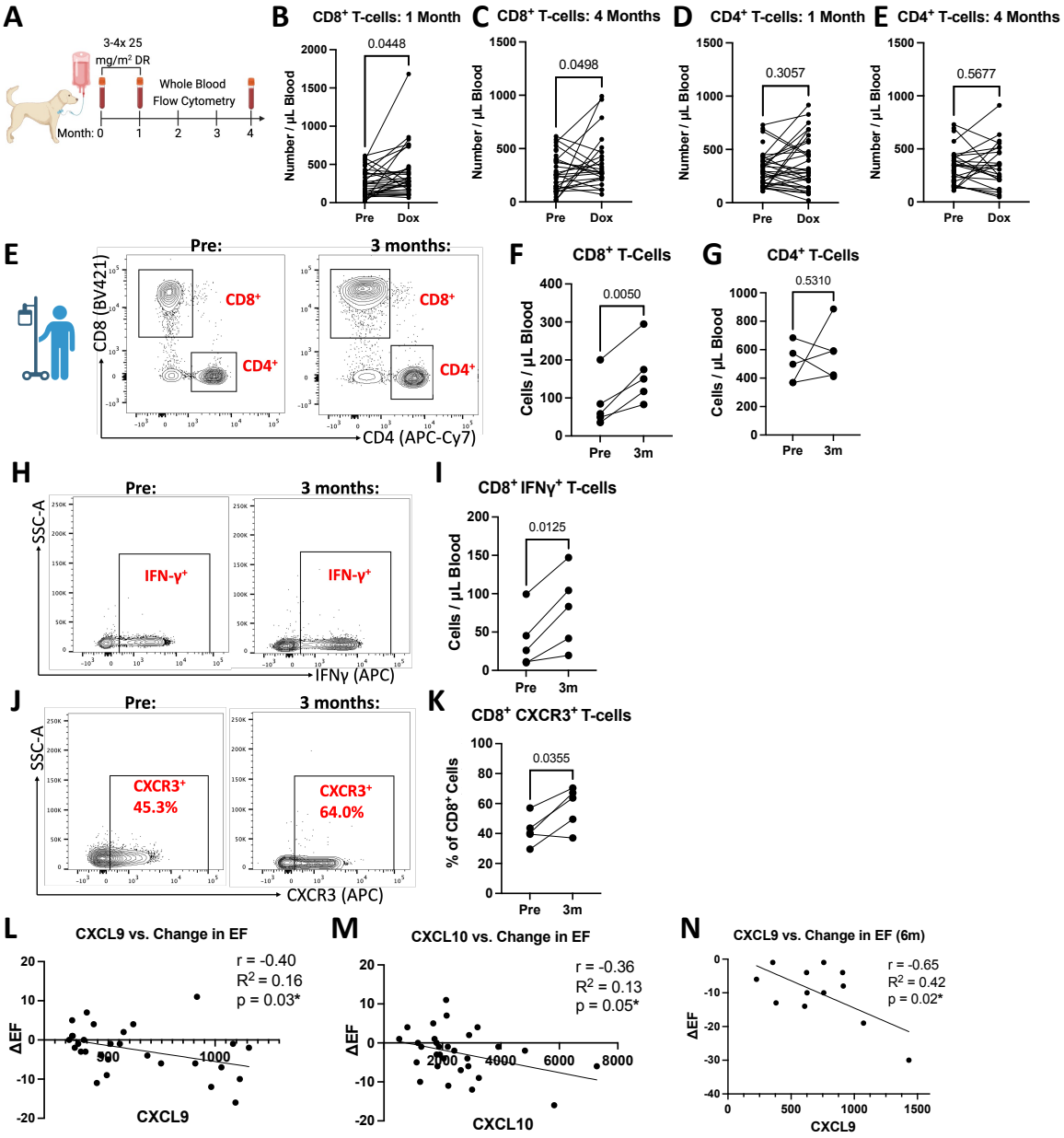
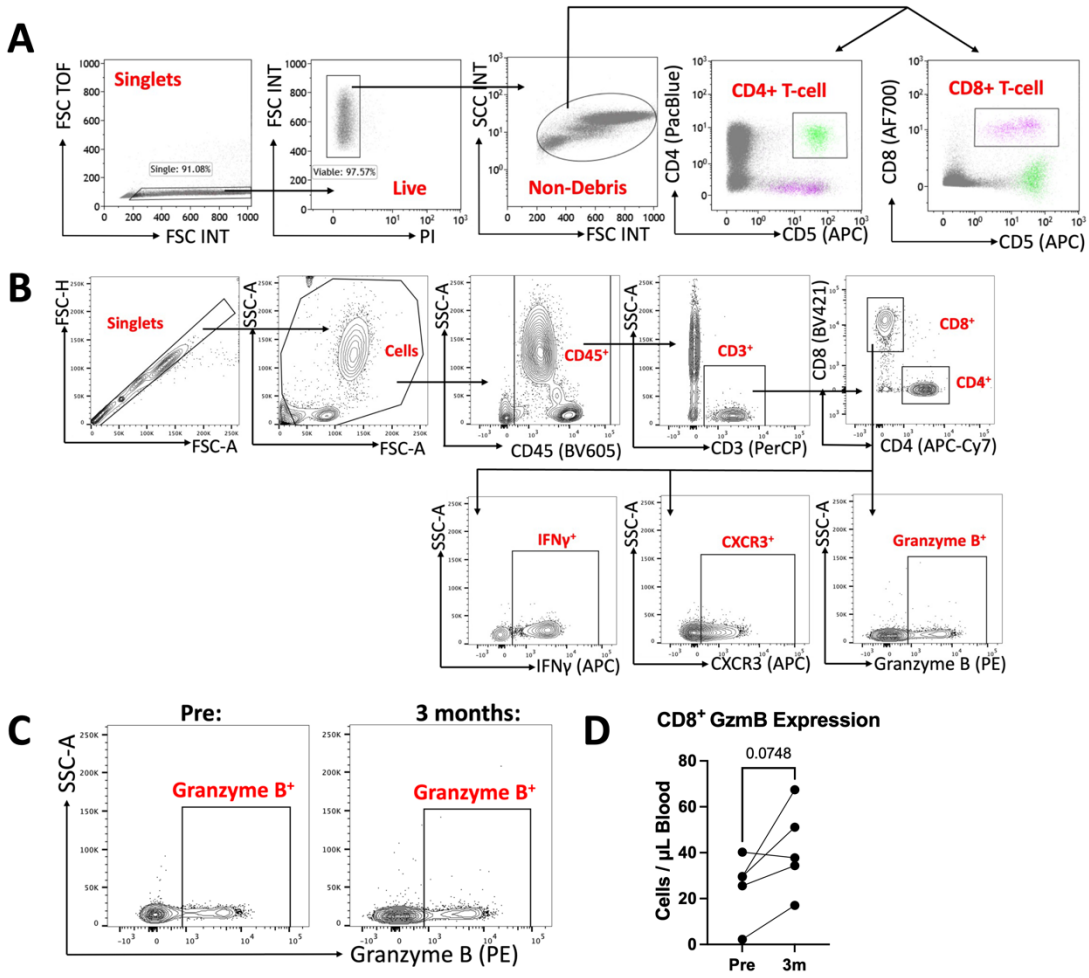


Figure 6-19 Canine and Human Patients Treated with Anthracyclines Develop a Progressive CD8+ T-cell Response

A-D. Whole blood was analyzed by flow cytometry from n=36 canine patients before (pre) or after anthracycline initiation at timepoints listed. CD8+ T-cells at 1 month post treatment (A) or 4 months post treatment (B), CD4+ T-cells at 1 month post treatment (C) or 4 months post treatment (D). E-K. Whole blood was analyzed by flow cytometry from n=5 patients before (pre) or 3 months (3m) after anthracycline initiation. Shown are representative plots for T-cells (gated on CD45+CD3+) in E, quantified in F-G. Representative plots (gated on CD45+CD3+CD8+) for CD8+ T-cell IFNγ (H) or CXCR3 expression (J) quantified in I, K. L-N. Change in ejection fraction (EF) by echocardiography plotted against plasma levels of CXCL9 or CXCL10 measured using Somascan in patients 3 months (L-M) or 6 months (N) after anthracycline initiation (Ref. 30). All data shown are individual patients, B-K show paired before/after. Statistical analysis 2 sided T-tests (A-D), 2 sided paired T-tests (F-K) or Pearson's correlation with r value, R squared, and p values shown. (L-N), n.s. = no significance, * = p ≤ 0.05, ** = p < 0.01, or p-value shown. Patient characteristics can be found in Supplementary Tables 3 and 4.

initiation.[463] We found that plasma levels of CXCL9 and CXCL10 at 3 months correlated



s

Whole blood was analyzed by flow cytometry from canine or human patients before or after anthracycline initiation. A. Gating strategies for T-cells from canine patients. B. Gating strategies for T-cells and additional markers from human patients. C. Representative plots for CD8 T-cell Granzyme B expression (gated on CD45+CD3+CD8+ cells), with quantification in D. Data from n=5 patients shown paired before/after treatment. Statistical analysis by paired 2 sided T-test, p-value shown.

with decreased ejection fraction between baseline and 3 months of anthracycline treatment (Figure 6-20L-M). A small number of patients followed up to 6 months post anthracycline treatment showed a greater drop in ejection fraction that still correlated with increased CXCL9 levels (Figure 6-20N).

	n=36 Total, Number (Percent)
Average Age	7.941666667
Sex	
Male	20 (55)
Female	16 (45)
Neuter Status	3 (8)
Average Weight (kg)	25.525
Breed	
Whippet	1 (2.8)
Shepherd	1 (2.8)
Pitbull	5 (13.9)
Mastiff	1 (2.8)
Labrador	5 (13.9)
Terrier	4 (11.1)
Pug	2 (5.6)
Shetland Sheepdog	1 (2.8)
Cocker Spaniel	2 (5.6)
Schnauzer	1 (2.8)
Boxer	1 (2.8)
Golden Retreiver	2 (5.6)
Border Collie	1 (2.8)
Doberman	1 (2.8)
Shiba Inu	1 (2.8)
Beagle	2 (5.6)
German Shepherd	1 (2.8)
Basset Hound	1 (2.8)
Mix	3 (8.3)
Drug:	
Doxorubicin	36 (100)
αCD20	36 (100)
KPT9274 (PAK4-NAMPT inhibitor)	19 (53)
RV1001 (PI3Kδ inhibitor)	18 (50)
TAK-981 (sumo activator)	10 (28)

Table 6-1 Canine Patient Characteristics
Selected characteristics, listed is either mean +/- standard error or number (Percent).

	Proteomics Data (Ref. 27) n=30, Number (Percent)	Flow Cytometry Cohort n=5 Number (Percent)
Age	50 ± 12	52 ± 15
Body mass index (kg/m^2)	26 ± 4	27 ± 4
Systolic Blood Pressure (mm Hg)	120 ± 18	129 ± 15
Diastolic Blood Pressure (mm Hg)	72 ± 10	79 ± 5
Sex		
Female	30 (100)	2 (40)
Male	0 (0)	3 (60)
Treatment		
Doxorubicin	26 (87)	5 (100)
Epirubicin	4 (13)	0 (0)
Cyclophosphamide	30 (100)	3 (60)
Taxane	30 (100)	0 (0)
Trastuzumab	30 (100)	0 (0)
Radiotherapy	17 (57)	0 (0)
Rituximab	0 (0)	3 (60)
Vincristine	0 (0)	5 (100)
Prednisone	0 (0)	4 (80)
Vinblastine	0 (0)	5 (100)
Dacarbazine	0 (0)	1 (20)
Nivolumab	0 (0)	1 (20)
Cancer		
Breast	30 (100)	0 (0)
Non-Hodgkin's Lymphoma	0 (0)	4 (80)
Hodgkins Lymphoma	0 (0)	1 (20)
Cardiovascular Risk Factors		
Hypertension	12 (40)	2 (40)
Diabetes mellitus	1 (3)	1 (20)
Hyperlipidemia	8 (27)	1 (20)
Smoking	2 (7)	2 (40)
Baseline LVEF	0.64 ± 0.05	0.61 ± 0.05

Table 6-2 Human Patient Characteristics
Selected characteristics, listed is either mean +/- standard error or number (Percent).

6.4 Discussion

Here we show that Doxorubicin induces a $CD8^+$ T-cell cardiac immune response that contributes to cardiac fibrosis and cardiotoxicity. We report in depth characterization of the inflammatory response in the heart, lymphoid organs, and circulation using a preclinical mouse model of DR cardiotoxicity, and outline a key role for IFNγ-producing $CD8^+$ T-cells and a strong correlation of this signature across species in anthracycline treated human and canine patients. We demonstrate that antibody targeted depletion of $CD8^+$ but not $CD4^+$ T-cells protects mice from systolic dysfunction and cardiac fibrosis, and that the $CD8^+$ T-cell response to DR is dependent on endogenous antigens induced by DR. Mechanistically, we demonstrate that DR induces alterations on CFB, including the expression of ICAM-1, resulting in $CD8^+$ T-cell adhesion, contact dependent cardiac fibroblast transformation, and $CD8^+$ T-cell degranulation of Granzyme B, which induces CFB transformation. Our data in canine and human cancer patients treated with anthracyclines support a central, pathogenic and cardiotoxic role for $IFN\gamma^+CD8^+$ T cells and the $CXCR3^/$CXCL9/CXCL10 axis in anthracycline cardiotoxicity.

While several studies thus far have shown increased cytokine expression in the hearts of DR treated mice,[327,329,332] and others have shown increases in various innate immune cells,[326,332,336] no study has specifically characterized T-cell adaptive immune responses in response to DR. As such, this work provides evidence that DR induces a $CD8^+$ T-cell immune response. Unlike in other forms of HF, our data show cardiac pathology is $CD8^+$ T-cell dependent, and that IFNγ production, together with degranulation of granzyme B, promotes cytotoxicity and fibrosis as a central component of DR cardiotoxicity. This makes the DR response different from other forms of non-ischemic HF which are predominantly $CD4^+$ T-cell driven.[244,404] Interestingly, we find the activated $CD4^+$ T-cells induced by DR are $Foxp3^+$ T-regs, explaining why depletion of $CD4^+$ T-cells results in increased $CD8^+$ T-cell activation in the onset of DR treatment.

Because T-regs play central roles in the tumor microenvironment and limiting off target inflammation[156,465], understanding the mechanistic driver of T-reg expansion induced by DR will help determine the possibility of manipulating T-reg activity to protect the heart while allowing for anti-tumor cytotoxicity.

DR has been well characterized to cause direct myocardial cell death[310]. Our data showing similar TUNEL staining and substantial ROS production at 4 weeks of treatment in *Tcra*$^{-/-}$ mice confirm that DR has early toxic actions that are T-cell independent, such as those on CFB. We show *in vitro* that DR alone induces CFB expression of αSMA, which is reversible without the addition of T-cells, suggesting *in vivo* cardiac fibrosis is potentiated by triggering a co-existing T-cell immune response. Moreover, after 8 weeks of treatment we find greater TUNEL staining in WT mice compared to *Tcra*$^{-/-}$ mice, supporting that sustained DR exposure induces a potent T cell immune response that potentiates DR induced cardiac damage. In line with this hypothesis, we found a progressive and strong dependence on T-cells for cardiac fibrosis. To our surprise, CD8^{+} T-cells were more dependent on binding to ICAM-1 for interaction with CFB, while we have previously shown CD4^{+} T-cells are more dependent on VCAM-1 and bind independently of ICAM-1.[244] These data support a bidirectional cross-talk between CFB and T-cells induced by DR, that differ from other forms of HF.[231,466] Our data showing direct co-localization of CD8^{+} T-cells and αSMA^{+} fibroblasts in cardiac sections provide evidence of this interaction *in vivo,* although higher powered microscopic and multi-omic techniques currently underway will provide stronger evidence of this interaction. Moreover, our data show that T-cell contact with CFB induces myofibroblast transformation through two mechanisms: direct contact as well as subsequent CD8^{+} T-cell degranulation which releases Granzyme B, a immunologic contributor to the pro-fibrotic mechanism of DR. This is line with other reports of Granzyme B having pro-fibrotic activity in Angiotensin II or in post-ischemia cardiac fibrosis.[467,468] While it is

further possible that in vivo granzyme B released by $CD8^+$ T cells induces cardiomyocyte death and a rapid compensatory fibrotic response, our data showing direct pro-fibrotic effects of granzyme B on cardiac fibroblasts *ex vivo* identifies an additional mechanism of action that triggers collagen synthesis through pathways in the fibroblast that remain to be explored. Future studies will interrogate the exact mechanism by which Granzyme B activates CFB and if it can be targeted therapeutically. Further, we show evidence that systolic dysfunction induced by DR is T-cell dependent, and importantly that DR decreases cardiac SERCA and increases the ratio of β-myosin heavy chain to α-myosin heavy chain expression in a T-cell dependent manner. While this alteration is also observed in models of cardiomyopathy that cause hypertrophic remodeling, our data demonstrate myocyte alterations in response to Doxorubicin, in line with previous work in non-hypertrophic models including a model of cardiac atrophy, similar to what we observe with chronic DR treatment.[469,470] This suggests communication between $CD8^+$ T-cells and cardiomyocytes, which has been implicated previously in the context of chemotherapy[471] and is an ongoing area of investigation.

To our knowledge, this is the first report of DR inducing a T-cell immune response in patients similar to what we have found in a pre-clinical model. Prior studies of patients treated with DR are quite limited, and have focused on downstream effects on circulating cytokines, with even more limited studies in canines.[321,323] Building upon these prior data, we show $CD8^+$ T-cells increase in response to DR in both canines and humans, and further narrow in humans a specific subset of $CD8^+$ T-cells that express IFNγ and the chemokine receptor CXCR3. CXCR3 serves as the receptor for the T-cell chemo-attractants CXCL9/10, which we show correlate with systolic dysfunction post-anthracycline treatment, outlining a potentially targetable chemokine axis in anthracycline cardiotoxicity that has already been implicated in other types of HF[472]. Ongoing studies will determine the mechanism and cellular source of CXCL9 and

CXCL10 in pre-clinical models and unveil the best practices to neutralize them as a therapeutic approach, as well as expanding patient studies to determine their potential utility as biomarkers. Further, as these patients have not yet developed signs of cardiotoxicity, longer time points and additional patients are needed to determine if $CD8^+$ T-cell expansion is causative in cardiotoxic disease progression.

Our data demonstrate the contribution of $CD8^+$ T-cells to DR cardiotoxicity. However, $CD8^+$ T-cells are also vital to anti-tumor immunity, making targeting this subset therapeutically to treat cardiotoxicity challenging in the context of cancer.[473] In one clinical trial of patients with breast cancer, the presence of $CD8^+$ T-cells in tumors was associated with greater benefit from anthracyclines.[474] Similarly, in mouse models of breast adenocarcinoma and fibrosarcoma, the presence of intratumoral $CD8^+$ T-cells was associated with increased efficacy of doxorubicin treatment.[475] These studies, also showed enrichment of γδ T-cells, interleukin (IL)-1β, and IL-17 cytokines, supporting that doxorubicin's antitumor effect was not exclusively mediated by $CD8^+$ T cells. Additionally, one study showed that inhibition of IFNγ does not impact anti-tumor immunity and has beneficial effects on cardiac damage, [23] which we build upon by showing $CD8^+$ T-cells as the source of this IFNγ. These data suggest that therapies targeted against $IFN\gamma^+CD8^+$ T-cells might remain a valid approach by leveraging differences in the immune responses in the heart or tumor. More mechanistic depth on the direct effects of DR on T-cells is needed to determine how the anti-tumor effects of DR can be manipulated without further damaging the heart. These studies will include tools to determine whether the $CD8^+$ antigen specificity that is pathogenic for the heart, as supported by our data in antigen restricted OT-I mice, is distinct of the $CD8^+$ antigen specificity for the tumor. A recent study of immune checkpoint inhibitor myocarditis showed antigen specific $CD8^+$ T-cell expansion against cardiac alpha-myosin heavy chain,[453] indicating plausibility for a cardiac-specific T-cell response in parallel with an anti-tumor response a question we

plan to distinguish by location-specific TCR-sequencing. Moreover, we report that $CD8^+$ T-cells are pathogenic in the heart by active interactions with cardiac fibroblasts. Whether tumor $CD8^+$ T-cells similarly engage with tumor-associated fibroblasts remains unknown. The plasticity and heterogeneity of tumor-associated fibroblasts parallels that of the cardiac environment - some function as antigen presenting cells to T-cells and some become profibrotic, and while they can protect from tumor cell expansion and metastasis, other studies show that they impair chemotherapy and immune infiltration into the tumor.[478,479] Determining how DR may alter $CD8^+$ T-cells to interact with tumor-associated fibroblasts similarly to what we present here for cardiac fibroblasts will be critical in future studies. It is also plausible that $CD8^+$ T-cells are recruited differently across the tumor vasculature than cardiac vasculature, something we plan to investigate. Further study of the exact mechanism and timing of the T-cell cardiac immune response in comparison to the T-cell anti-tumor response will help elucidate the best immunomodulatory prevention strategies in DR cardiotoxicity. Preventive strategies aimed at the innate immune response leading to subsequent $CD8^+$ T-cell activity might also be fruitful. One such example is the cGAS-STING pathway, shown recently to be triggered by DR and a powerful inducer of T-cell immunity.[133,332]

While we have uncovered insight into the inflammatory response elucidated by DR, our work has some limitations that we would like to address. Our study only uses time points immediately following the cessation of DR treatment, and targeted antibody depletion was performed at an acute timepoint. As such, longer studies might be needed to better understand the chronic inflammation observed after anthracycline treatment has been completed in patients. It is further plausible that inflammation subsides post DR treatment in mice and patients, making it more of a driver of acute cardiotoxicity rather than chronic. Additionally, while our depletion studies demonstrate a causative role for CD8+ T-cells in DR cardiotoxicity, we acknowledge that other immune cells,

especially dendritic cells that present antigen to CD8+ T-cells may contribute to cardiac inflammation. Ongoing transcriptomic analyses will help determine the full landscape of this inflammatory response.

Further, while DR did not lead to increased T-cell activation markers *in vitro*, we found that the T-cell response to DR is antigen dependent using ovalbumin restricted OTI mice, similar to that of pressure overload.[450] However, the endogenous antigen that T-cells respond to remains an ongoing area of investigation. We also measured T-cell exhaustion markers in local and peripheral lymphoid organs, which did not increase with DR treatment, however it is plausible T-cells become exhausted in the cardiac inflammatory environment. Importantly, while we show the extent and location of collagen deposition is altered by cytotoxic T-cells in the context of DR, we use picrosirius red staining and western blot for collagen to determine this, and it is possible that other extracellular matrix proteins are modulated by $CD8^+$ T-cells, which merits further investigation. In this study, immune responses were assessed in peripheral plasma or blood obtained from patients. We focused on the T-cell compartment due to our compelling pre-clinical data, however it is plausible that there are alterations to myeloid cells especially in the context of combined chemotherapy treatment, such as potential neutropenia commonly observed[136]. Due to the associated procedural risks, it is challenging to obtain cardiac samples from patients treated with anthracyclines who do not have substantial comorbidities that could obfuscate DR induced cardiac inflammation. It is thus possible that the expanded circulating $IFN\gamma^+CXCR3^+CD8^+$ T-cells and chemokine-ejection fraction correlation we show in patients after anthracycline treatment do not imply the same cardiac T-cell cardiotropism we show in mice. However, we provide strong evidence of T-cell mediated inflammation paralleled across mice, canines, and humans, necessitating further study of the mechanism of inflammation in these patients. In doing so, we can better evaluate if immunomodulatory therapies

targeting $CD8^+$ T-cells or the CXCL9/10-CXCR3 axis can prevent or treat DR cardiomyopathy. In summary, we outline a critical role for the adaptive immune response, specifically IFNγ-producing $CD8^+$ T-cells, in the development of cardiac fibrosis and systolic dysfunction after DR treatment. Our data implicate the CXCL9/10-T-cell axis in DR-induced cardiac toxicity, setting the stage for future studies on how to immunomodulate cardiotoxic inflammation in the onset of cancer and define the delicate balance between cardiotoxicity and tumor toxicity. Our results highlight the need for a better understanding of inflammation in cancer patients treated with anthracyclines to improve outcomes and provide novel preventative therapies.

6.5 Author Contributions

A.L.B. designed the project, performed experiments, analyzed data, and wrote the manuscript. M.A.Z., S.S., Z.L.R., and M.S. performed experiments, provided intellectual support and edited the paper. K.K. provided intellectual and technical support and edited the paper. A.Ar. and A.As. recruited human patients and assisted in collecting patient data, provided intellectual support, and edited the paper. A.Av. and C.L. recruited and treated canine patients, collected and analyzed flow cytometry data, and provided intellectual support. P.A. designed the project, provided intellectual support, and contributed to writing and editing the manuscript.

6.6 Acknowledgements

We thank the Tufts University Histology Core, Flow Cytometry Core, and CMS Animal Facility for their support in this work. We also thank our collaborators at BIDMC and CSU and the support of their institutions. We would also like to acknowledge Shruti Sharma, from Tufts University School of Medicine, for the use of the microscope to image full heart cross section. All graphic figures were created with BioRender.com. This work was supported by National Institute of Health (NIH) Grants R01 HL144477 and HL165725

(P.A.), Tufts Springboard Tier 1 grant (P.A and C.L), American Heart Association (AHA) Pre-Doctoral Fellowship 906361 (A.L.B.), NIH F30 Grant HL162200 (A.L.B.), NIH 3R01HL144477-04S1 grant (M.A.Z.), NIH F31 Grant HL159907A (S.S), AHA Pre-Doctoral Grant 906561 (S.S.), NIH U01CA272268 (C.L. and A.Av.), NIH K08HL145019 (A.As.) and NIH R01 HL163172 (A.As.).

Chapter 7 Cell Specific STING Activity Differentially Modulates Cardiac Inflammation and Fibrosis in Doxorubicin Cardiotoxicity

---

Bayer, A. L., Sanders, E., Smolgovsky, S., Wagner, N., & Alcaide, P. Cell Specific STING Activity Differentially Modulates Cardiac Inflammation and Fibrosis in Doxorubicin Cardiotoxicity. *In Preparation.*

7.1 Introduction

Doxorubicin (DR) is the most commonly prescribed chemotherapeutic drug, although its use is limited by dose-dependent cardiotoxicity and progression to chronic heart failure (HF).[309,310] Due to it's function as a topoisomerase II inhibitor and through induction of reactive oxygen species (ROS), DR can lead to DNA damage and subsequent cell death as one mechanism of it's anti-tumor activity.[481,482] However, the concurrent accumulation of DR in cardiomyocytes (CM) leading to CM apoptosis is one proposed mechanism for it's cardiotoxicity.[483] However, Dexrazoxane, an iron chelator that prevents ROS and CM apoptosis is not widely effective in all patients,[318,484] implying that further processes downstream of cardiac cell death contribute to chronic cardiotoxicity after DR treatment.

Recent work has positioned cardiac inflammation as central to the initiation and progression of DR cardiotoxicity. Both innate immune cells such as neutrophils and macrophages[333,336] as well as adaptive immune cells including B- and T-lymphocytes [338,485] have been implicated in the cardiac immune response to DR using animal models. Specifically, we previously showed that $CD8^+$ cytotoxic T-cells are required for systolic dysfunction and cardiac fibrosis in DR treated mice, and that patients treated with DR had expanded circulating $CD8^+$ T-cells. Further, the systolic function of DR-treated patients correlated significantly with the T-cell chemoattractants CXCL9/10, had circulating T-cells expressed high CXCR3, the receptor for this ligands.[485] Overall, this suggests the CXCL9/10-CXCR3 axis, which has been implicated in other causes of cardiac inflammation,[472,486] as a potential therapeutic target, however the source of CXCL9/10 remains unknown.

DNA damage and intracellular DNA can be recognized by cyclic GMP-AMP synthase (cGAS) which activates the stimulator of interferon genes (STING), a potent inducer of type I interferon mediated inflammation, including the release of interferon stimulated genes such as CXCL9/10.[125,487] Thus far, STING has been implicated in the response to DR induced

DNA damage in several cardiac cell types[133,332,488], however the inflammatory response induced by DR downstream of STING activation has yet to be characterized. Further, the relative contributions of individual cell types have not be thoroughly outlined. We hypothesized that DR activates STING in stromal, vascular, and immune cells leading to CXCL9/10 expression and cardiac $CD8^+$ T-cell infiltration. Here we utilize global and cell specific ablation of STING *in vivo* as well as *in vitro* primary cell culture systems to outline a critical role for endothelial and macrophage STING in promoting CD8+ cardiotropism after DR treatment through CXCR3, whereas cardiac fibroblast STING contributed to myofibroblast transformation in both mouse and human cells. Together this positions the STING-CXCL9/10 axis as a potential therapeutic target for DR cardiotoxicity.

7.2 Methods

7.2.1 Animals and Doxorubicin Model:

All animal studies were approved by the Tufts University Institutional Animal Care and Use and Care Committee. C57BL/6J, global STING$^{-/-}$ mice,[489] Vecad^{Cre+}-STING$^{fl/fl}$ mice,[487] Tcf21^{Cre+}-STING$^{fl/fl}$ mice and LysM^{Cre+}-STING$^{fl/fl}$ mice (generously donated by Dr. Shruti Sharma) were bred and maintained under pathogen free conditions. Tcf21^{Cre+}-STING$^{fl/fl}$ mice were generated by crossing STING$^{fl/fl}$ mice[487] with Tcf21^{Cre+} mice.[231] All mice were given 75 mg/kg Tamoxifen by IP injection for 5 days prior to experimental use. STING excision was determined by polymerase chain reaction (See Appendix 9.10 for primer sequences). Male mice aged 8-12 weeks old were given 5.0 mg/kg Doxorubicin (Selleckchem) by intraperitoneal injection once weekly for 4 weeks before echocardiography and tissue harvest. A minimum sample size of 6 mice per group was calculated to detect statistically significant changes in cardiac function with a power of >80% and α= 0.05. Randomization for each group was performed by a random number generator (https://www.calculator.net/random-number-generator.html), and all analyses were done blinded using an ID number assigned by a third party.

7.2.2 In Vivo Echocardiography:

Mice were sedated using isoflurane on a heated stage in supine position. Heart rate and respiratory rate were continuously monitored via stage electrodes. Depilatory cream (Nair) was applied to the chest to remove fur, and ultrasonic gel was applied to a 22-55 MHz echocardiography transducer (MS550D Vevo 2100, Fujifilm VisualSonics) to obtain parasternal short axis views of the left ventricle in M-mode with a target heart rate of 400-500 bpm. Cardiac parameters and heart rate were measured by averaging the values from 5 cardiac cycles. All analyses were performed blindly using Vevo 2100 software version 2.2.0 (Build 12089).

7.2.3 Flow Cytometry:

Hearts were excised from mice and perfused with PBS, then minced and digested enzymatically with 0.895 mg/mL collagenase II (Gibco 17101-015). Single cell suspensions were generated from cells in culture or lymphoid organs using a 40 μm cell strainer. Blood samples were first RBC lysed using RBC lysis buffer (Biolegend 420302) according to the manufacturer's instructions, then leukocytes were pelleted before staining. Samples were stained using the following antibodies from Biolegend: CD45.2 BV605 (109841), CD45.2 PE-Cy7 (109830), CD11b Percp (101230), CD11c PE (117308), CD11c BV421 (117330), MHCII APC (107614), MHCII FITC (107606), CD8 BV711 (100748), CD8 BV421 (100737), CD4 APC-Cy7 (100414), CD4 PE (100408), CXCR3 APC (126511), CD62L PE (104408), CD44 BV711 (103057), CD25 BV421 (101923), CD69 FITC (104506), F4/80 AF647 (123122), F4/80 PE-Cy7 (123114), CD31 APC-Cy7(102440), CD31 FITC (102406), PDGFrα APC (135907), ICAM1 FITC (116106), CCR4 PE-Cy7 (131214) or other sources: CD11b ef506 (Invitrogen 69-0112-82), APC Mefsk4 (Miltenyi 130-120-166), CD45.2 BUV805 (BD 569200). Samples were surface stained by incubation with the relevant antibodies listed above diluted 1:100 in phosphate buffered saline (PBS) + 2% FBS for 20 minutes at 4°C. When intracellular cytokine staining was performed, samples were incubated for 4 hours at 37C in complete T-cell media (see below for details) including 50 ng/mL Phorbol Myristate Acetate (PMA, Sigma Aldrich P8139), 0.1% Ionomycin (Sigma 13909), 0.1% Brefeldin A (Biolegend 420601), and 0.1% Monensin (Biolegend 420701), followed by surface staining as described. Samples were then fixed for 15 minutes at RT with fixation buffer (Biolegend, 420801), permeabilized by two washes with 1X Perm/Wash buffer (Biolegend, 421002, and stained intracellularly with the following antibodies from Biolegend: APC IFNγ (Clone XMG1.2) diluted 1:50 in 1x Perm/Wash buffer for 20 minutes at 4°C. To detect pIRF3, samples were surface stained as described, fixed using

fixation buffer (Biolegend, 420801) for 20 minutes at 37°C, then 1 mL of ice cold TruePhos perm buffer (Biolegend 425401) was added while vortexing, before samples were incubated for 1 hour at -20°C. Samples were washed with staining buffer and then stained for 30 minutes at RT with 1:25 PE-pIRF3 (CST 53539). Data was acquired on a Cytek Aurora spectral cytometer (Cytek Biosciences) and analyzed using FlowJo software Version 10.10.0.

7.2.4 Histologic Analysis:

Picrosirius Red (PSR): Cardiac samples were fixed in 10% formalin, embedded in paraffin, and cut in 6 μm sections. Collagen was stained in 0.1% Direct Red 80 (Sigma 365548) in saturated picric acid (Sigma P6744) for 1 hour, followed by hematoxylin counter stain (Sigma GHS2128) for 1 minute. Slides were washed with 0.5% acetic acid twice before dehydration and mounting. Fibrosis was quantified by positive threshold on ImageJ (Version 1.53t) to exclude non-specific signal from counter-stained nuclei.

TUNEL: Formalin fixed cardiac samples were stained using *In Situ* Cell Death Detection kit TMR red (Sigma 12156792910) according to the manufacturer's protocol. Visualization was performed with a Nikon Ti inverted fluorescence microscope.

Immunofluorescence:

Coverslips or tissues were washed 2 x 10 min. with PBS, then fixed with 4% PFA for 15 minutes. Samples were washed with PBS, then incubated with PBS + 10% normal goat serum and/or 10% donkey serum (depending on species of secondary antibody), and 0.1% triton-X for intracellular staining for 1 hour at RT. Samples were incubated with the following primary antibodies where indicated: α-alpha smooth muscle actin (αSMA, Sigma A2547), CD8 (Biolegend 100702), PDGFrα (R&D AF1062) at 1:100 in blocking buffer overnight at 4°C. Samples were washed with PBS then incubated with the appropriate secondary antibody (Thermo A32766, Thermo A11055, Thermo A21432,

Thermo A78966, CST 4413) at 1:200 in blocking buffer, then mounted in Vectashield with DAPI (Southern Biotech, 0100-20). Visualization was performed with a Nikon Ti inverted fluorescence microscope.

7.2.5 Immunoblotting:

Cells were lysed in RIPA buffer supplemented with protease and phosphatase inhibitors then cleared by centrifugation at 4°C at 13,000 xg. Protein concentrations were determined using DC protein assay (BioRad 5000112) and equal amounts of protein were subjected to SDS-PAGE, then transferred to PVDF membranes, followed by blocking with Tris buffered saline + 0.1% Tween20 containing 5% non-fat milk for 1 hour at room temperature. Immunoblotting was performed overnight at 4°C using antibodies diluted 1:1000 in 5% non-fat milk or 5% BSA for phosphor-antibodies. Antibodies were purchased from CST: pIRF3 (4947), IRF3 (4302) , pSTING (72971), STING (50494), α-Tubulin (3873) pTBK1 (5483), TBK1 (3504), cGAS (31659), GAPDH (2118). Blots were then incubated with the appropriate HRP peroxidase conjugated secondary antibody (1:2000, Rabbit CST 7074, Mouse CST 7076) at room temperature for 1 hour, then developed using Pierce ECL (ThermoFisher 32106) and imaged using a ChemiDoc XRS+ System (Biorad). Band intensity was quantified using Image-J.

7.2.6 RT-qPCR:

Cell lysis and RNA isolation was performed using an RNeasy kit according to manufacturer's instructions (Qiagen 74004). For cardiac RNA isolation, LV samples were crushed in Trizol (Qiagen 79306), RNA was chloroform extracted and separated by centrifugation, then the aqueous phase was combined with 70% ethanol and applied to RNAeasy columns. cDNA synthesis was performed using High-Capacity cDNA Reverse Transcription Kit (ThermoFisher 4368814), and qPCR was performed using SYBR

Green (ThermoFisher A25741) on a QuantStudio 6 Flex Real-Time PCR Machine (ThermoFisher). See Appendix 9.10 for primer sequences.

7.2.7 ELISA:

Cardiac lysate was generated from heart tissue by lysis in RIPA buffer (150 mM NaCl 50 mM Tris pH 7.4, 1% NP-40, 0.1% SDS, 5 mM EDTA, 0.1% sodium deoxycholate, 1mM DTT) supplemented with protease and phosphatase inhibitors (Roche 4906845001, 4693159001), then cleared by centrifugation at 4°C at 13,000 xg. Protein concentrations were determined using DC protein assay (BioRad 5000112) and equal amounts of protein were input into the following ELISA kits according to the manufacturer's instructions: CXCL9 (R&D DY492) CXCL10(R&D DY466), and cGAMP (Cayman Chemical 501700).

7.2.8 Generation and Culture of Primary Cardiac Fibroblasts and Co-culture:

Adult mice (7-12 week old) were anesthetized, then hearts were excised, perfused with PBS, minced, and digested using 2 mg/mL Collagenase I (Gibco17100016) for 30 minutes with intermittent agitation. Digested tissue was pelleted at 300g for 10 minutes, then resuspended in fibroblast growth media – DMEM (Gibco 11995-065) + 10% FBS, Penicillin/streptomycin (ThermoFisher 15140122), insulin-transferrin-selenium (Sigma I3146), and plated on 0.1% gelatin coated plates for 2 hours at 37°C. After this time, non-adherent cells were removed and fresh media was added. Cells were used through passage 3. For co-culture experiments, fibroblasts were plated on 0.1% gelatin coated coverslips in 12 well plates at 100,000 cells / well. Once adhered, fibroblasts were pretreated with the indicated dose of Doxorubicin for 24 hours, and then where indicated washed prior to addition of Tc1 cells when indicated at 25,000 cells / well, and cultured overnight, then washed with PBS to remove non-adherent T-cells. Human LV CFB were

cultured under similar conditions, used till passage 4, and treated with the same dose of Doxorubicin.

7.2.9 Generation and Culture of Primary Cardiac Endothelial Cells:

Hearts were digested from young mice (2-4 weeks old) as described above, and then Pecam1+ cells were isolated by magnetic selection (Biolegend 102502). Cells were plated on 0.1% gelatin coated plates and cultured in DMEM (Gibco 11995-065) + 10% FBS, Penicillin/streptomycin (ThermoFisher 15140122) and 0.1% mouse endothelial cell growth factors (Corning 356006) After confluence, cells were passed and Icam2+ cells were isolated by magnetic selection (Biolegend 105602) before use in experiments. Where indicated cells were pre-treated with DR. For transendothelial migration, cells were cultured on coverslips, treated with 0.1 µg/mL DR overnight prior to perfusion of 1 million Tc1 cells at an estimated shear stress of 1 dyne/cm^2 with temperature controlled to 37°C. TEM was observed during 10 minutes by live microscopy.

7.2.10 Culture of Human Umbilical Vein Endothelial Cell:

HUVEC were isolated from 2–5 umbilical cord veins, pooled, and established as primary cultures in M199 containing 20% FCS (Hyclone).[490] HUVEC were serially passaged (1:4 split ratio) and maintained in M199 containing 10% FBS, endothelial cell growth factor (Biomedical Technologies, BT-203), porcine intestinal heparin (Sigma, H-3933), ascorbic acid (Sigma, A4403), hydrocortisone (Sigma, H6909), and penicillin/streptomycin (Thermo Fisher, 15140122) on 1% gelatin-coated (Sigma, G1393) plates. Experiments were performed at passage 1 or 2 using confluent cells 24hr post seeding.

7.2.11 Generation and Culture of Primary Mouse Tc1 cells:

CD8$^+$ T-cells were isolated from splenic cell suspensions by positive selection using magnetic beads (Miltenyi or 130-117-044). Cells were plated at 2 million cells / mL and activated in the presence of anti-CD3 antibody (2.5 µg/mL, Biolegend 100253) and anti-

CD28 antibody (1 µg/mL, Biolegend 102102), IL-12 (10 ng/mL, Peprotech 210-12) and, anti-IL4 (50 ng/mL, Biolegend 504102) for 3 days then harvested for experiments. T-cells were dosed with the indicated concentration of DR where indicated. T-cells were cultured at 37°C in RPMI medium (Gibco 11875-093) containing 10% fetal bovine serum (FBS – Atlanta Biologicals S11150), Glutamax (Gibco A12860-01), $NaHCO_3$ (Gibco 25080-094), Penicillin/Streptomycin (Gibco 15140122), 60µM β-mercaptoethanol (Sigma 444203), and Sodium pyruvate (Gibco 11360-070).

7.2.12 Generation and Culture of Primary Mouse Macrophages:

Bone marrow was isolated from mice aged 6-12 weeks old, filtered through a 100 µM cell strainer, followed by red blood cell lysis was performed according to manufacturer's instructions (Biolegend 4210301). Bone marrow cells were plated at a concentration of 1 x 10^7 cells in a 10 cm dish and cultured in RPBI medium containing 10% FBS, Glutamax, Penicillin/Streptomycin, 60µM β-mercaptoethanol, Sodium pyruvate, and 20% L929 cell conditioned media.

7.2.13 Generation of Thp1 Derived Macrophages:

Thp1 cells were cultured in suspension in RPMI medium (Gibco 11875-093) containing 10% fetal bovine serum (FBS – Atlanta Biologicals S11150), Glutamax (Gibco A12860-01), $NaHCO_3$ (Gibco 25080-094), Penicillin/Streptomycin (Gibco 15140122), 60µM β-mercaptoethanol (Sigma 444203), and Sodium pyruvate (Gibco 11360-070). Cells were plated in 6 well dishes and treated for 48 hours with 200 ng/mL PMA (Sigma P8139) and 100 ng/mL LPS (Invitrogen 103576-100) before treatment with DR as described previously.

7.2.14 Transwell Migration Assay:

Primary fibroblasts, endothelial cells, or macrophages were plated in a 24 well plate and treated overnight with 1.0 µg/mL DR. The media was changed and then 500,000 CFSE

(Invitrogen C34554) labeled Tc1 cells were loaded on a 3μM transwell insert in complete T-cell media. After 4 hours, the number of T-cells migrated was determined by flow cytometry for CFSE+ cells.

7.2.15 Statistical Analysis:

Statistical analysis was performed using GraphPad Prism 9.4.1. All data are presented as mean ± standard error of the mean (SEM). Statistical analysis was done by Student's unpaired or paired t-test (where indicated) for two group analysis. Multiple group comparisons were done using one-way ANOVA with Tukey's multiple comparison test or two-way ANOVA with Sidak's multiple comparison test. Differences were considered statistically significant at $p \leq 0.05$.

7.2.16 Data Availability:

The data, methods, and materials will be available to other researchers for the purposes of reproducing the results or replicating procedures.

7.3 Results

7.3.1 Doxorubicin Induces STING Dependent CXCR3+CD8+ Cardiac Inflammation alongside Cardiotoxicity:

We first treated global STING$^{-/-}$ mice with DR alongside wild type (WT) age matched mice to test if STING ablation altered the cardiac immune response to DR (Figure 7-1A). After 4 weeks of DR treatment, WT mice had significantly increased cardiac CD8^{+} T-cells alongside the expected decrease in systolic function and ventricular wall thinning (Figure 7-1B-D, Figure 7-2A) compared to PBS treated mice as previously shown.[485] However, STING$^{-/-}$ mice treated with DR were fully protected from cardiac CD8^{+} T-cell infiltration, systolic dysfunction, and exhibited less ventricular wall thinning (Figure 7-1B-D) despite showing similar cardiac atrophy (Figure 7-1E). We characterized several innate immune populations as well, and found no significant changes to the number of cardiac CD11b^{+} cells or dendritic cells in response to DR in either genotype (Figure 7-2B-C).

As we previously showed cardiac IFNγ^{+}CD8^{+} T-cells to drive the expression of the T-cell chemoattractants CXCL9/10, we then asked if impaired cardiotropism in STING$^{-/-}$ mice also lead to decreased CXCL9/10 expression. In ventricular tissue, we found that only WT but not STING$^{-/-}$ mice increased *Cxcl9* and *Cxcl10* transcript after DR treatment (Figure 7-1G-H). We then characterized the expression of CXCR3, the receptor for CXCL9/10 on cardiac CD8^{+} T-cells, and found that DR treatment significantly increased cardiac CXCR3^{+}CD8^{+} T-cells in WT but not STING$^{-/-}$ mice (Figure 7-1I-J). We then characterized the systemic T-cell response in blood from these mice, and found significant increases in circulating CD8^{+} T-cells in WT but not STING$^{-/-}$ mice treated with DR (Figure 7-1I, Figure 7-3B). Further, a higher frequency of these circulating T-cells

expressed CXCR3 (Figure 7-1J) in DR treated WT mice only, a finding that was specific

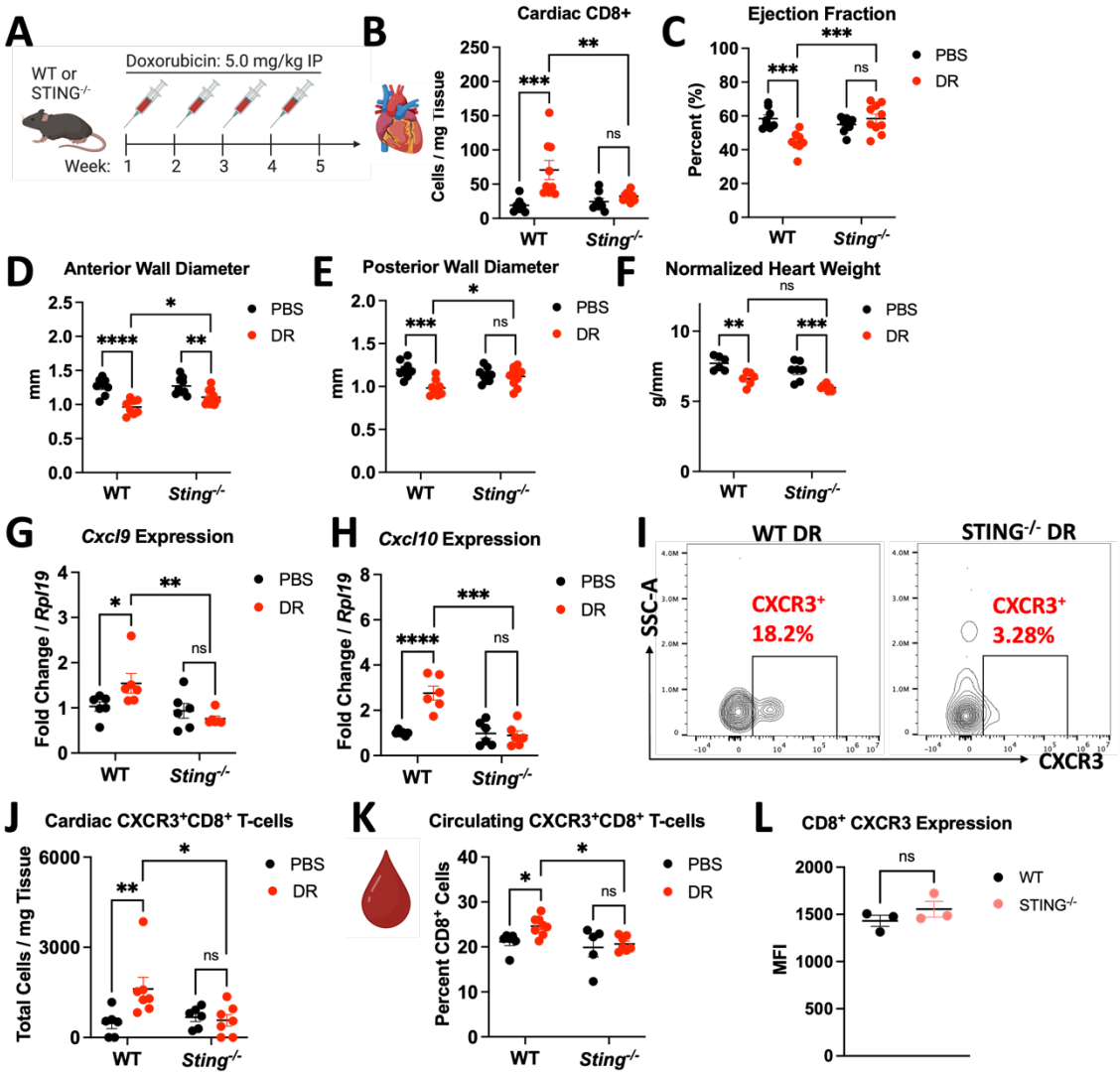


Figure 7-1 Doxorubicin Induces STING Dependent CXCR3+CD8+ Cardiac Inflammation alongside Cardiotoxicity

A. 8-10 week old WT or STING$^{-/-}$ mice were treated with 5.0 mg/kg Doxorubicin or saline weekly for 4 weeks before euthanasia (8-10 mice / group). B. Hearts were digested mechanically and enzymatically then analyzed by flow cytometry for CD8^{+} T-cells. C-E. Echocardiography was used to measure ejection fraction (C), anterior wall thickness (D), or posterior wall thickness (E). F. Heart weight was normalized to tibia length. G-H. RNA was isolated from heart samples and analyzed by RT-qPCR for *Cxcl9* (G) or *Cxcl10* (H) expression. I. Hearts were digested mechanically and enzymatically then analyzed by flow cytometry for CXCR3+CD8+ T-cells, shown are representative flow cytometry plots for CXCR3 gated on CD11b^{-}CD8^{+} cells, quantified in J. K. Blood samples were analyzed by flow cytometry for CXCR3^{+}CD8^{+} T-cells. L. WT and STING$^{-/-}$ CD8^{+} T-cells were activated *in vitro* by αCD3/αCD28 and CXCR3 expression was measured by flow cytometry. Statistical analysis by 2-way ANOVA with Sidak's multiple comparisons test (B-K) or T-test (L). Ns = no significance, * = $p < 0.05$, ** = $p < 0.01$, *** = $p < 0.001$, **** = $p < 0.0001$

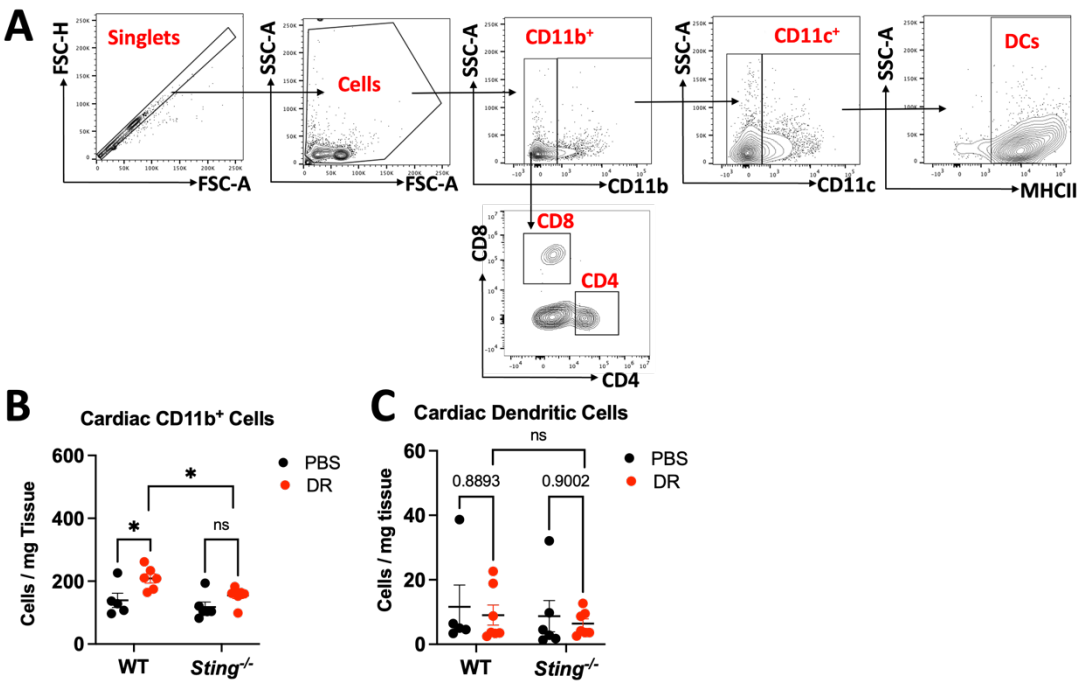


Figure 7-2 STING Knockout Decreases DR Induced Cardiac Myeloid Infiltration but not Cardiac or lymphoid Dendritic Cells

8-10 week old WT or STING$^{-/-}$ mice were treated with 5.0 mg/kg Doxorubicin or saline weekly for 4 weeks before euthanasia (8-10 mice / group). Hearts were digested mechanically and enzymatically then analyzed by flow cytometry. A. Gating strategy for cardiac T-cells and myeloid cells. B. Cardiac CD11b+ cells quantified. C. Cardiac CD11b+CD11c+MHCII+ dendritic cells quantified.

to CXCR3, as there was no changes to CCR4, another common chemokine receptor expressed by T-cells (Figure 7-3C). Additionally, we activated WT and STING$^{-/-}$ CD8^{+} T-cells *in vitro* by αCD3/αCD28and found similar CXCR3 expression (Figure 7-1K), confirming that STING deficiency does not impair CXCR3 expression and that DR drives a STING dependent cardiac and systemic CXCR3^{+}CD8^{+} T-cell response in mice.

7.3.2 STING Knockout Mice Have Decreased Cardiac Toxicity and Fibrotic Responses to DR:

We then evaluated how STING deficiency and the impaired T-cell inflammatory response impacted DR induced cardiac pathology. We first performed TUNEL staining on cardiac sections, and found that while DR induced significant cardiac cell death in

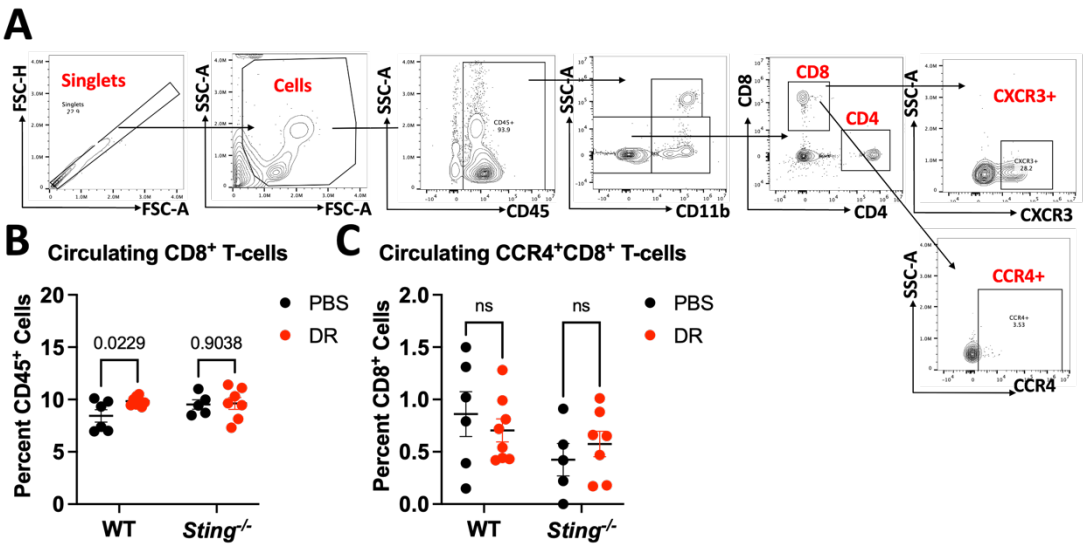


Figure 7-3 Flow Cytometry Analysis of Blood T-cells and Gating Strategy
8-10 week old WT or STING$^{-/-}$ mice were treated with 5.0 mg/kg Doxorubicin or saline weekly for 4 weeks before euthanasia (8-10 mice / group). Blood samples were RBC lysed then analyzed by flow cytometry. A. Gating strategy for blood T-cells and chemokine receptors. B. Circulating CD8+ T-cells quantified. C. Circulating CCR4+CD8+ T-cells quantified.

both WT and STING$^{-/-}$ mice, STING deficiency significantly blunted the number of TUNEL positive cells (Figure 7-4A-B). Further, we measured ANP expression as a readout of cardiac damage (as previously shown[485]) by RT-qPCR and found only WT mice treated with DR to have increased ANP (Figure 7-4C). Our previous work implicated T-cells in shaping the cardiac fibrotic response after DR treatment, therefore we next asked if STING ablation impacted cardiac fibrosis and fibroblast activation. Strikingly, while WT mice developed significant interstitial fibrosis in response to DR, STING$^{-/-}$ mice were fully protected from detectable cardiac fibrosis (Figure 7-4D-E). To further probe the fibrotic response we probed for PDGFrα^{+} cardiac fibroblast populations by immunofluorescence and co-stained for αSMA to detected fibrotic myofibroblasts. In line with STING dependent cardiac fibrosis, we found DR to increase PDGFrα^{+}αSMA^{+} fibroblasts in only WT but not STING$^{-/-}$ mice, evidence that STING is a powerful regulator of both cardiotoxicity and fibrosis in response to DR.

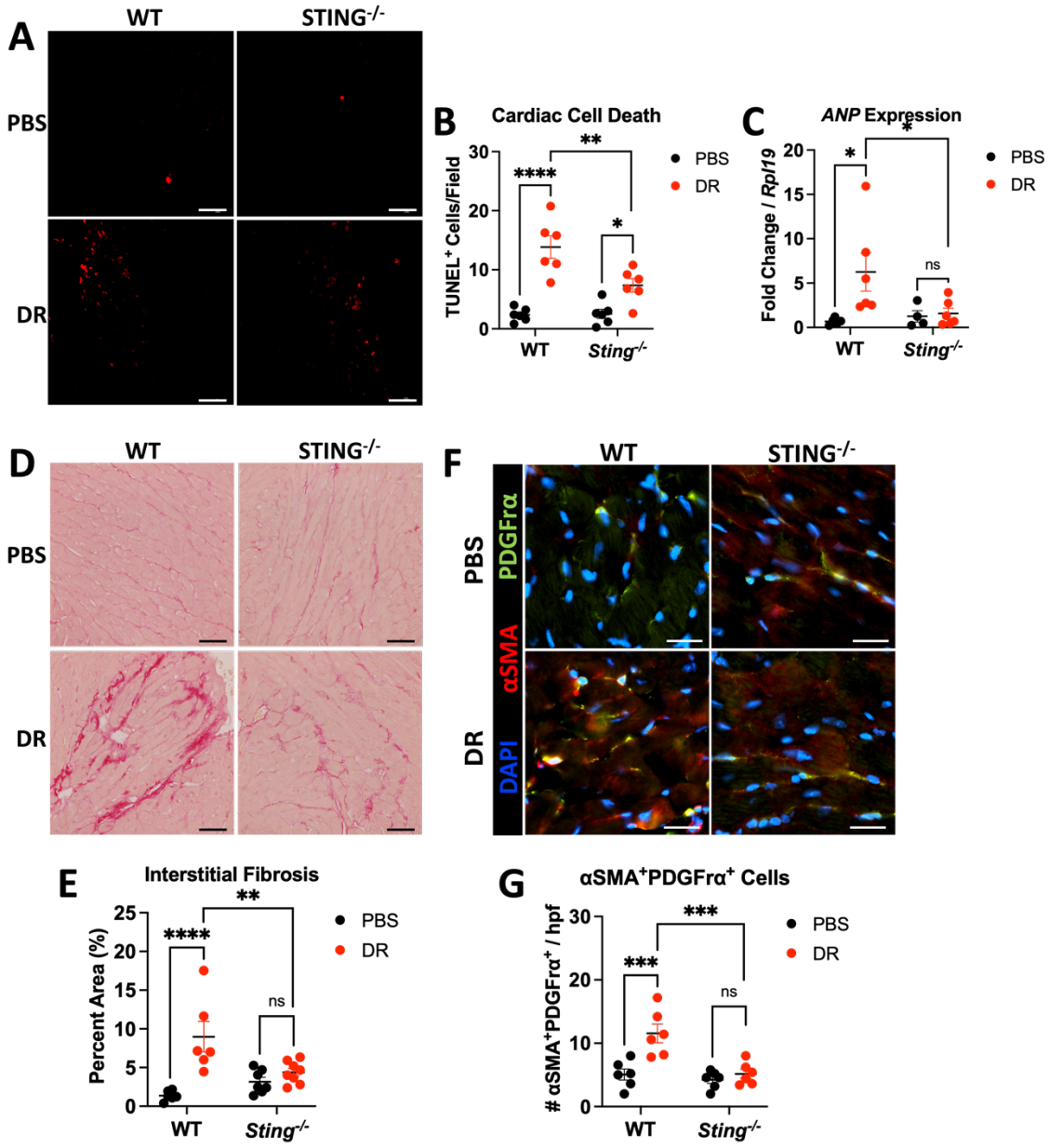


Figure 7-4: STING Knockout mice have decreased cardiac toxicity and fibrotic responses to Doxorubicin

8-10 week old WT or STING$^{-/-}$ mice were treated with 5.0 mg/kg Doxorubicin or saline weekly for 4 weeks before euthanasia (6 mice / group). A. Heart samples were stained using TUNEL for cell death, shown are representative images (scale bars = 50 um). B. TUNEL+ cells were counted manually per field of view. C. RNA was isolated from cardiac samples and analyzed by RT-qPCR for ANP expression. D. Heart samples were stained by picrosirius red for fibrosis, shown are representative images (scale bars = 50 um). E. E. ImageJ was used to quantify percent fibrosis. F. Heart samples were stained by immunofluorescence for αSMA and PDGFRα , shown are representative images (scale bars = 50 um). G. Double positive cells were counted manually. Statistical analysis by 2-way ANOVA with Sidak's multiple comparisons test. Ns = no significance, * = $p < 0.05$, ** = $p < 0.01$, *** = $p < 0.001$, **** = $p < 0.0001$.

7.3.3 STING Knockout T-cells Exhibit Decreased Activation in Response to DR *In Vivo* But Similar Activation *In vitro*

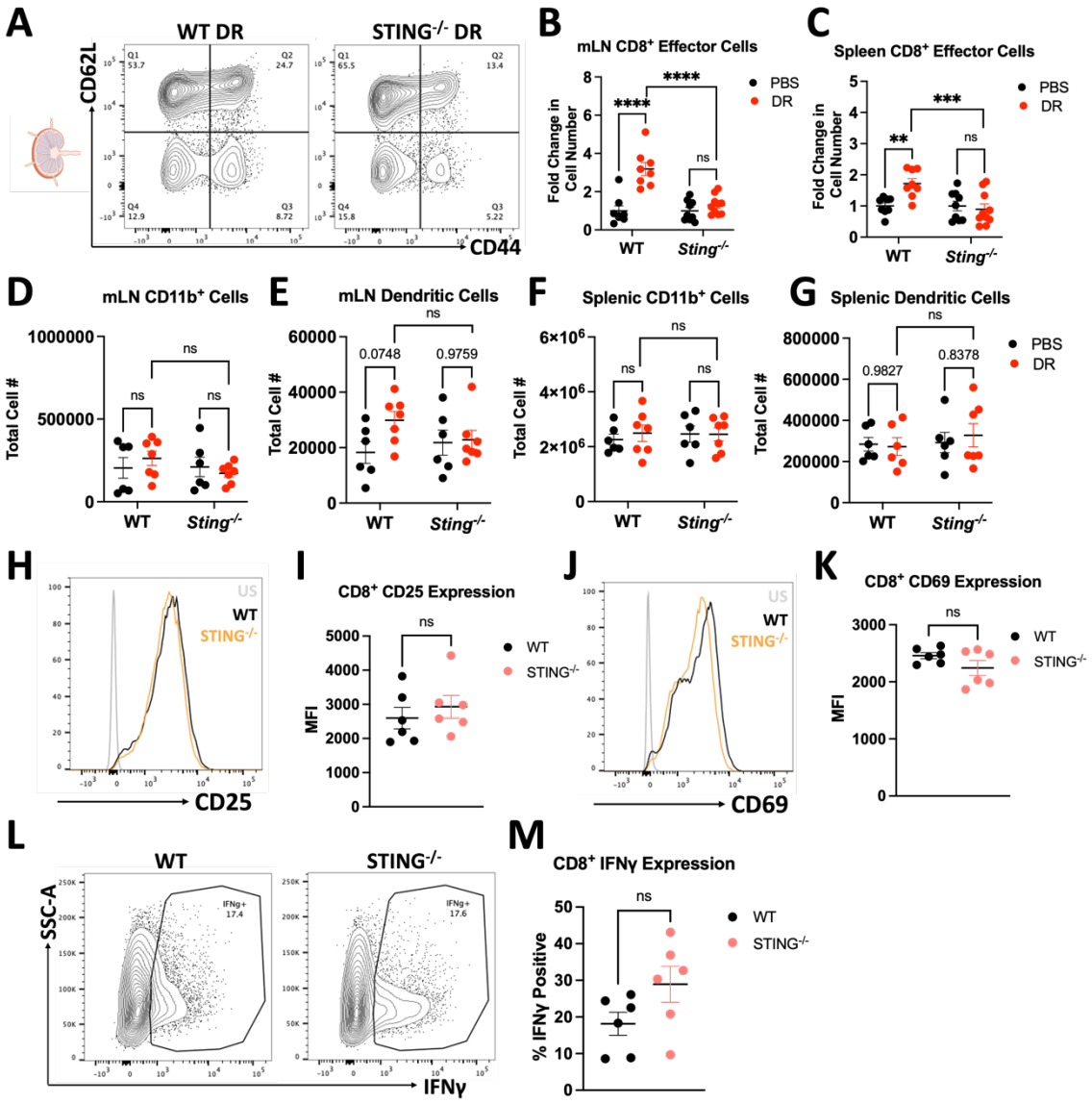


Figure 7-5 STING Knockout T-cells Exhibit Decreased Activation in Response to DR In Vivo But Similar Activation In vitro

8-10 week old WT or STING$^{-/-}$ mice were treated with 5.0 mg/kg Doxorubicin or saline weekly for 4 weeks before euthanasia (6-8 mice / group). A. Mediastinal lymph nodes (mLN) and spleens were digested and analyzed by flow cytometry for effector T-cells (CD8^{+}CD44^{hi}CD62L^{lo}), shown are representative flow cytometry plots for lymph nodes, quantified in B, or in the spleen in C. Quantification of mLN CD11b+ myeloid cells (D), mLN CD11b+CD11c+MHCII+ dendritic cells (E), splenic CD11b+ myeloid cells (F), mLN CD11b+CD11c+MHCII+ dendritic cells (G). H-M. WT and STING$^{-/-}$ CD8^{+} T-cells were activated *in vitro* by αCD3/αCD28, then analyzed by flow cytometry for CD25 and CD69 expression, shown are representative flow cytometry plots for CD25 (H) and quantification (I), or for CD69 (J) with quantification (K). L-M. Intracellular cytokine staining was used to measure IFNγ levels, shown are representative flow cytometry plots with quantification in M. Statistical analysis by 2-way ANOVA with Sidak's multiple comparisons test (B-G) or T-test (I-M). Ns = no significance, * = $p < 0.05$, ** = $p < 0.01$, *** = $p < 0.001$, **** = $p < 0.0001$.

We next asked if STING deficiency impaired CD8^{+} T-cell activation in lymphoid organs after DR treatment as one explanation for decreased cardiotropism and cardiotoxicity. We evaluated T-cell activation in the mediastinal lymph nodes (mLN) and

spleen, and found elevated $CD62L^{lo}CD44^{hi}CD8^{+}$ T-cells in both locations in WT mice treated with DR but not $STING^{-/-}$ mice (Figure 7-5A-C). Interestingly, we did not find any alterations to mLN and splenic myeloid cells or dendritic cells (Figure 7-5D-G), making altered antigen presenting cell function less likely to explain decreased effector T-cells in response to DR treatment. We then tested if STING ablation impairs T-cell activation *in vitro.* WT and $STING^{-/-}$ $CD8^{+}$ T-cells activated *in vitro* had similar expression of the T-cell activation markers CD25 and CD69 (Figure 7-5H-K), and expressed similar IFNγ by intracellular cytokine staining (Figure 7-5L-M). From these data we conclude STING deficiency impairs T-cell activation *in vivo* in response to DR with no sign of intrinsic T-cell impairment, prior to subsequent decreased cardiotropism.

7.3.4 STING is Activated in Immune, Vascular, and Stromal Cells in Doxorubicin Injured Hearts:

After seeing striking effects on DR-induced cardiotoxicity and inflammation in STING-deficient animals, we sought to characterize what components of STING signaling are activated in response to DR (Figure 7-6A). We generated cardiac lysate from WT and $STING^{-/-}$ mice treated with PBS or DR and found elevated 2'3'-cGAMP, the small molecule produced by cGAS that activates STING, in both sets of mice treated with DR (Figure B). Further downstream, we also observed DR to induce phosphorylated STING and IRF3 in only WT mice (Figure 7-6C-E), while overall levels of pTBK1 and cGAS were unchanged (Figure 7-74A-C). Overall cardiac STING pathway activation after DR treatment lead to the transcription of IFNβ in WT but not $STING^{-/-}$ mice (Figure 7-6F), as well as several examples of interferon stimulated genes (ISGs) including *Oasl2, Irf9,* and *Ifnar* (Figure 7-6G, Figure 7-7D-E). Thus far as we have showed cardiac STING activation in the onset of DR cardiotoxicity after 4 weeks of treatment, we treated WT

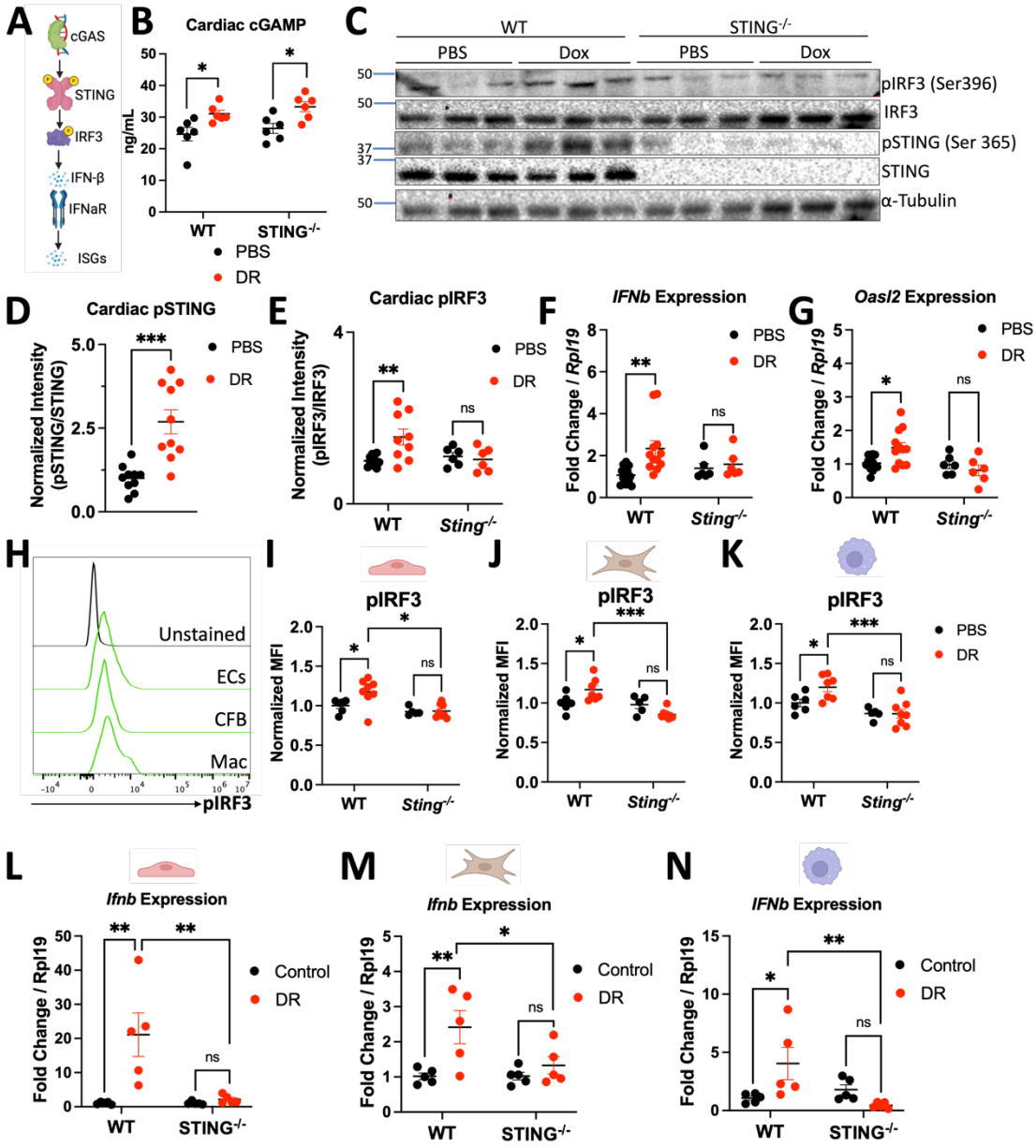


Figure 7-6 Doxorubicin activates STING in immune and stromal cells in Doxorubicin injured hearts
A. Schematic of the canonical cGAS-STING pathway. B. 8-10 week old WT or STING$^{-/-}$ mice were treated with 5.0 mg/kg Doxorubicin or saline weekly for 4 weeks before euthanasia (6 mice / group). Cardiac samples were analyzed by ELISA for 2,3-cGAMP. C. Cardiac samples were analyzed by western blot for cGAS-STING signaling components, shown is a representative blot from n=3 mice / group, with quantification for pSTING in WT mice in D, or pIRF3 in WT or STING$^{-/-}$ mice in E. F-G. RNA was isolated from cardiac samples, and RT-qPCR was used to measure expression of Ifnb (F) or Oasl2 (G). H-K. Cardiac samples were digested enzymatically and mechanically, then analyzed by flow cytometry with intracellular staining for pIRF3. Shown are example plots (H) with quantification for pIRF3 gated on CD31+ endothelial cells (Ecs - I), PDGFrα+ Fibroblasts (CFB – J), or CD45+CD11b+F4/80+ macrophages (Mac – K) compared to unstained cells. L. WT or STING$^{-/-}$ primary mouse endothelial cells were treated with 1.0 μg/mL Doxorubicin then analyzed by RT-qPCR for Ifnb expression. M. WT or STING$^{-/-}$ primary mouse fibroblasts were treated with 1.0 μg/mL Doxorubicin then analyzed by RT-qPCR for Ifnb expression. L. WT or STING$^{-/-}$ primary mouse macrophages were treated with 1.0 μg/mL Doxorubicin then analyzed by RT-qPCR for Ifnb expression. Statistical analysis by 2-way ANOVA with Sidak's multiple comparisons test, or T-test (D). Ns = no significance, * = $p < 0.05$, ** = $p < 0.01$, *** = $p < 0.001$, **** = $p < 0.0001$.

mice with DR for 8 weeks to test for any temporal regulation of STING activity. At this

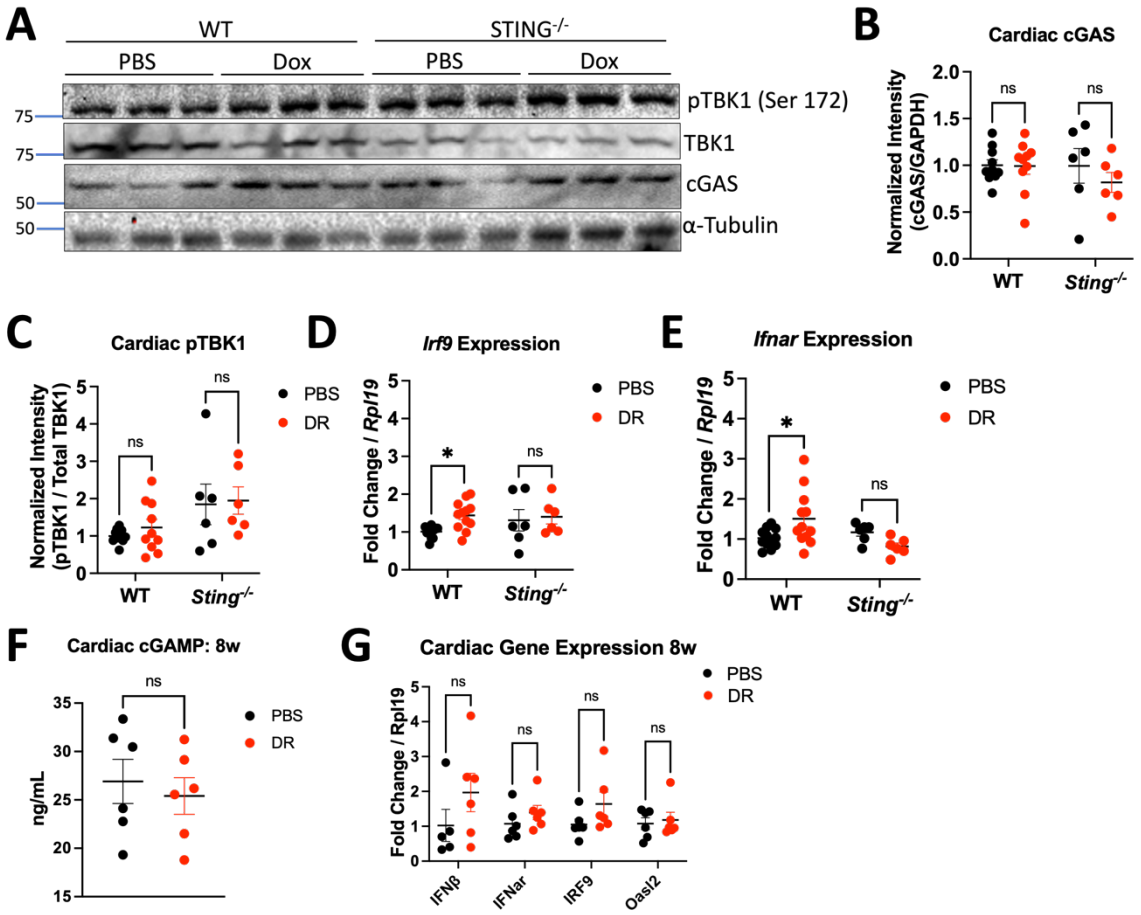


Figure 7-7 Additional Characterization of STING Activation in the heart at 4 weeks and 8 weeks
A. 8-10 week old WT or STING$^{-/-}$ mice were treated with 5.0 mg/kg Doxorubicin or saline weekly for 4 weeks before euthanasia (6 mice / group). Cardiac samples were analyzed by western blot for cGAS-STING signaling components, shown is a representative blot from n=3 mice / group, with quantification for cGAS in B, or pTBK1 in C. D-E. RNA was isolated from cardiac samples, and RT-qPCR was used to measure expression of Irf9 (D) or Ifnar (E). F. WT mice were treated with 5.0 mg/kg Doxorubicin or saline weekly for 8 weeks before euthanasia (6 mice / group). Cardiac samples were analyzed by ELISA for 2,3-cGAMP. G. RNA was isolated from 8 week Doxorubicin treated cardiac samples, and RT-qPCR was used to measure expression of listed ISGs. Statistical analysis by 2-way ANOVA with Sidak's multiple comparisons test (B-E), or T-tests (F-G). Ns = no significance, * = $p < 0.05$, ** = $p < 0.01$, *** = $p < 0.001$, **** = $p < 0.0001$.

chronic timepoint, we found no elevated 2'3'-cGAMP (Figure 7-7F) or IFNβ/ISGs in hearts treated with DR (Figure 7-7G), suggesting STING activation plays a more significant role in the acute inflammatory response to DR.

We then asked which cell types exhibited STING activation in response to DR, using the downstream signaling molecule pIRF3 as a readout of STING activity *in vivo* by flow cytometry (Figure 7-8A). Strikingly, we found that after 4 weeks of DR treatment, WT mice exhibited elevated pIRF3 in cardiac endothelial cells, fibroblasts, and macrophages, whereas STING$^{-/-}$ mice showed no changes to IRF3 phosphorylation *in*

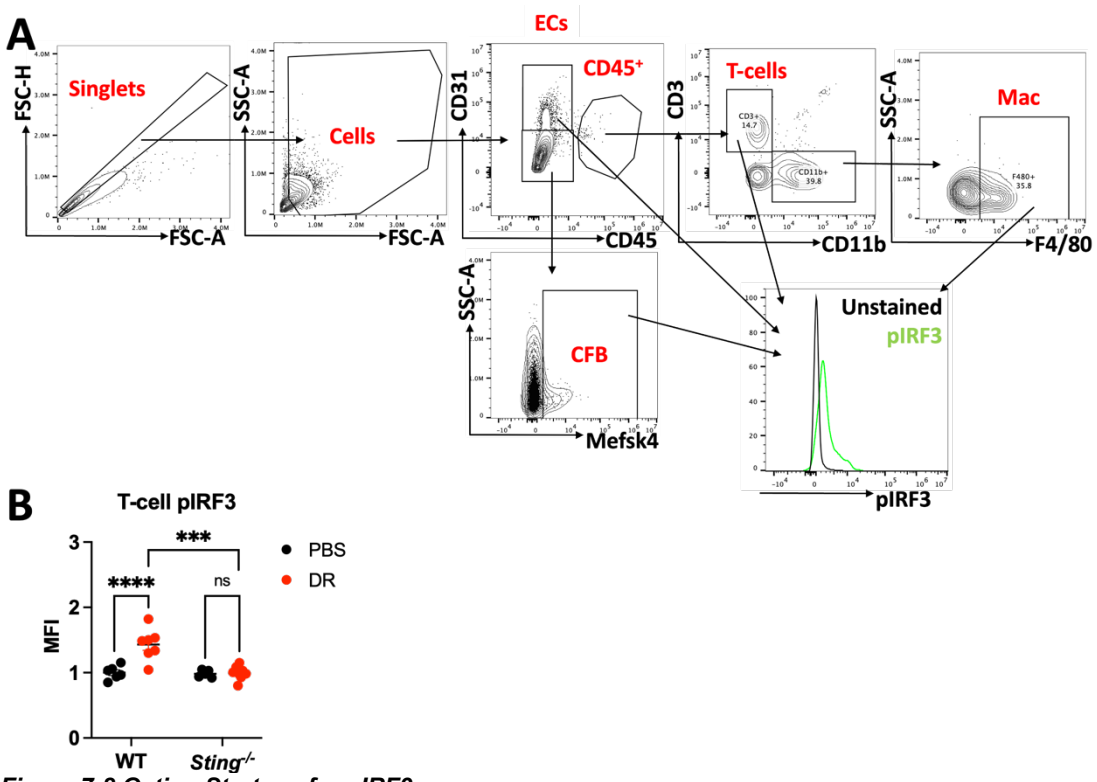


Figure 7-8 Gating Strategy for pIRF3

A. 8-10 week old WT or STING$^{-/-}$ mice were treated with 5.0 mg/kg Doxorubicin or saline weekly for 4 weeks before euthanasia (6 mice / group). Cardiac samples were digested enzymatically and mechanically, then analyzed by flow cytometry with intracellular staining for pIRF3. Shown is the gating strategy used in Figure 7-6. B. Normalized MFI of pIRF3 in CD3+ T-cells. Statistical analysis by 2-way ANOVA with Sidak's multiple comparisons test. Ns = no significance, *** = $p < 0.001$, **** = $p < 0.0001$.

vivo (Figure 7-6H-K). Interestingly, T-cells also had STING-dependent IRF3 phosphorylation after DR treatment, even though STING-deficiency did not alter T-cell activation (Figure 7-5, 7-8). We then tested if *in vivo* activation of STING was a direct cellular response to DR. We treated primary mouse endothelial cells, fibroblasts, and macrophages with DR *in vitro* and found that DR induced STING-dependent IFNβ expression in all 3 cell types, albeit to different degrees (Figure 7-6L-N). Together these data evidence DR is able to activate canonical STING signaling in vascular, immune, and stromal cells both *in vitro* and *in vivo*.

7.3.5 Cell Specific Deletion of STING Protects Against DR Cardiotoxicity and CXCL9/10 Driven CD8 Cardiotropism:

After observing STING activation in multiple cell compartments, we tested the consequences of cell specific ablation of STING on DR cardiotoxicity. We treated

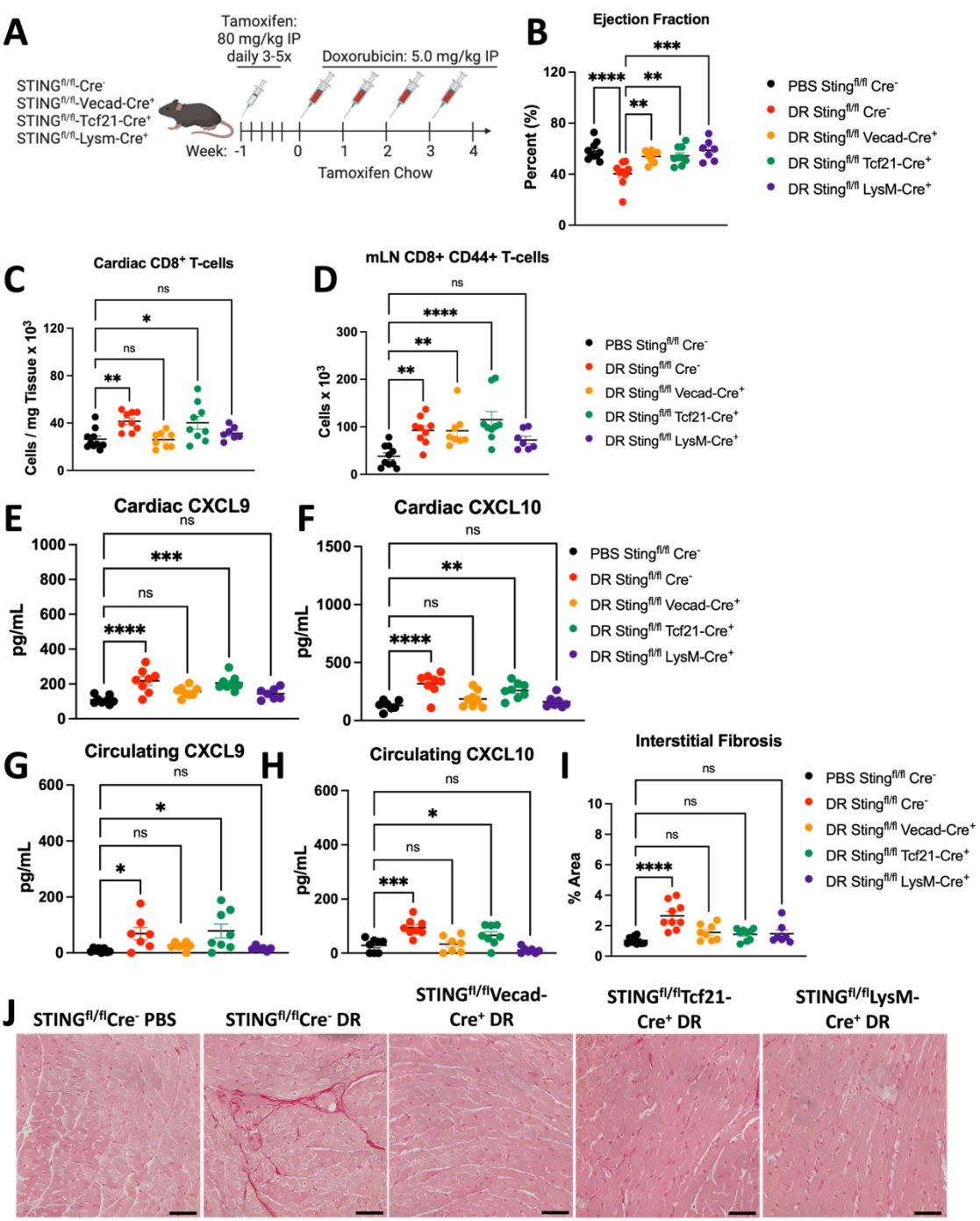


Figure 7-9 Cell Specific Deletion of STING Protects Against DR Cardiomyopathy and CXCL9/10 Driven CD8 Cardiotropism

A. 8-10 week old male STING$^{fl/fl}$, STING$^{fl/f}$Vecad-Cre^{+}, STING$^{fl/f}$Tcf21-Cre^{+}, or STING$^{fl/f}$LysM-Cre^{+} were given Tamoxifen then 5.0 mg/kg Doxorubicin for 4 weeks before euthanasia. B. Echocardiography was used to measure ejection fraction. C. Hearts were digested mechanically and enzymatically then analyzed by flow cytometry for CD8^{+} T-cells. D. Mediastinal lymph nodes (mLN) were digested then analyzed by flow cytometry for CD8^{+}CD44^{+} T-cells. E-F. ELISA was used on cardiac lysate to measure CXCL9 (E) or CXCL10 (F). G-H. ELISA was used on plasma to measure circulating CXCL9 (G) or CXCL10 (H). I-J. Cardiac sections were stained using picrosirius red for fibrosis, then quantified with ImageJ (I), shown in J are representative images (scale bars = 50 um). Statistical analysis by 1-way ANOVA with Tukey'ss multiple comparisons test. Ns = no significance, * = $p < 0.05$, ** = $p < 0.01$, *** = $p < 0.001$, **** = $p < 0.0001$.

STING$^{fl/fl}$Cre^{-} mice (WT equivalent) with endothelial STING$^{-/-}$ mice (STING$^{fl/fl}$Vecad-Cre^{+}),

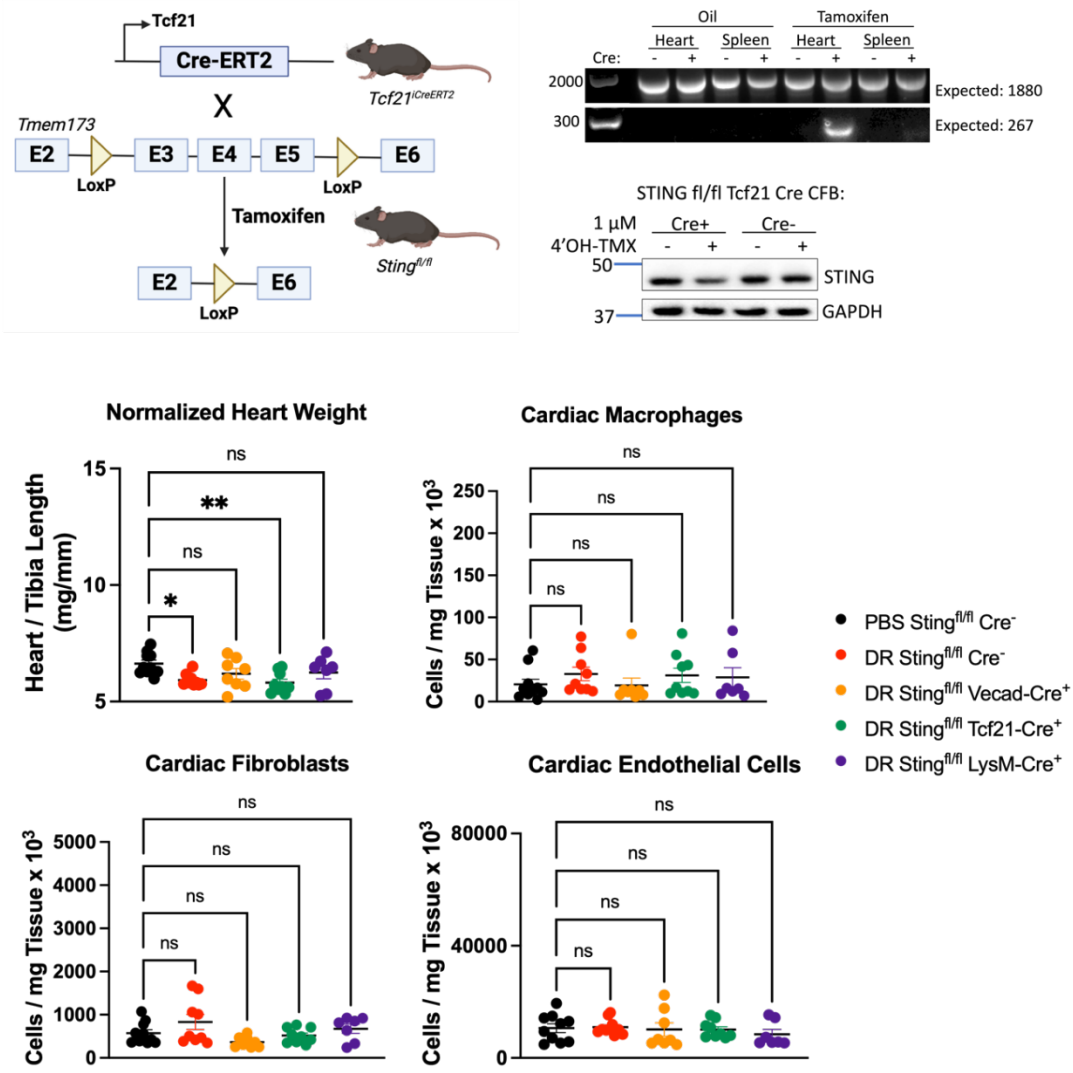


Figure 7-10 Characterization of STING-Tcf21 Mice and Cardiac Phenotyping of Cell Specific STING KO Mice

A. Schematic showing excision of STING by Tcf21-driven Cre recombinase. B. STING$^{fl/fl}$ or STING$^{fl/f}$Tcf21-Cre^{+} mice were injected with Tamoxifen or vehicle for 5 days by IP injection, then genomic DNA was isolated from hearts or spleens and PCR was used to visualize intact or excised STING. C. Cardiac fibroblasts were isolated from STING$^{fl/fl}$ or STING$^{fl/f}$Tcf21-Cre^{+} mice, then treated with 1 µm 4'OH-Tamoxifen for 48 hours, then STING expression was analyzed by western blot. D-G. 8-10 week old male STING$^{fl/fl}$, STING$^{fl/f}$Vecad-Cre^{+}, STING$^{fl/f}$Tcf21-Cre^{+}, or STING$^{fl/f}$LysM-Cre^{+} were given Tamoxifen then 5.0 mg/kg Doxorubicin for 4 weeks before euthanasia. D. Heart weight normalized to tibia length. E-G. Hearts were digested mechanically and enzymatically then analyzed by flow cytometry for CD45+CD11b+F4/80+ macrophages (E), CD45-CD31-PDGFrA+ fibroblasts (F) or CD31+CD45- endothelial cells (G). Statistical analysis by 1-way ANOVA with Tukey'ss multiple comparisons test. Ns = no significance, * = $p < 0.05$, ** = $p < 0.01$, *** = $p < 0.001$, **** = $p < 0.0001$.

fibroblast STING$^{-/-}$ mice (STING$^{fl/fl}$Tcf21-Cre^{+} - see Figure 7-10 for confirmation of gene excision), and myeloid/macrophage STING$^{-/-}$ mice (LysM$^{fl/fl}$Vecad-Cre^{+}) with DR for 4 weeks (Figure 7-9A). While WT mice showed the expected drop in ejection fraction after DR treatment, all 3 cell-specific STING$^{-/-}$ mice were fully protected from systolic

dysfunction after DR treatment (Figure 7-9B). Interestingly, only WT and fibroblast STING$^{-/-}$ mice developed detectable cardiac atrophy by gross heart weight (Figure 7-10D). We then characterized the CD8^{+} T-cell response in these mice. While all cell-specific knockout mice had a preserved ejection fraction, only WT and fibroblast STING$^{-/-}$ mice exhibited cardiac CD8^{+} T-cell infiltration after DR treatment, whereas endothelial and myeloid STING$^{-/-}$ mice did not (Figure 7-9C), indicating differing mechanisms of protection. Despite cell specific STING regulating cardiotropism differently, WT, endothelial, and fibroblast STING$^{-/-}$ mice treated with DR had elevated mLN CD44+CD8^{+} T-cells, whereas myeloid STING$^{-/-}$ mice only trended up (Figure 7-9D), indicating that T-cell activation was unaffected by endothelial and fibroblast STING, whereas myeloid STING plays a minor role. Importantly, each cell-specific ablation of STING did not alter the number of cardiac macrophages, fibroblasts, or endothelial cells (Figure 7-10E-G). To explain the observed differences in cardiotropism, we measured levels of cardiac and circulating CXCL9/10 to test if endothelial and macrophage STING promoted CXCL9/10 secretion WT and fibroblast STING$^{-/-}$ mice exhibited increased CXCL9 and CXCL10 in the heart and plasma after DR treatment, whereas endothelial and myeloid STING$^{-/-}$ mice had non-significant increases in the levels of these chemokines (Figure 7-9E-H). Finally, we evaluated the effects of each cell-specific knockout of STING on DR-induced cardiac fibrosis and found that only WT mice had an increase in detectable fibrosis (Figure 7-9I-J). We conclude from these data that endothelial and macrophage STING contribute to CD8^{+} T-cell cardiotropism through CXCL9/10 production while fibroblast STING acts through a different mechanism.

7.3.6 Doxorubicin Induces STING Dependent Chemotaxis Through CXCR3 towards Endothelial Cells and Macrophages

To further evaluate the role for endothelial cell and macrophage STING in inducing $CD8^+$ T-cell recruitment after DR treatment, we first measured the chemokine production of each cell type *in vitro* in response to DR. After 24 hours of treatment, we found that DR directly increased the expression of *Cxcl9* and *Cxcl10* in WT primary mouse heart endothelial cells (MHECs) and bone marrow derived macrophages (BMDMs), however $STING^{-/-}$ MHECs and BMDMs did not upregulate either chemokine (Figure 7-11A-B). Both WT and $STING^{-/-}$ primary mouse cardiac fibroblasts (CFBs) upregulated *Cxcl9* and *Cxcl10* expression similarly in response to DR (Figure 7-11C), in line with the T-cell infiltration results from the cell-specific knockout mice *in vivo*. Based on the chemokine expression, we then sought to test the ability of each cell type to induce T-cell chemotaxis, a critical step in T-cell infiltration into tissues. We plated WT and $STING^{-/-}$ MHECs, BMDMs, and CFBs underneath a Transwell and treated them with DR to induce CXCL9 and CXCL10, then added activated WT $CD8^+$ T-cells above the Transwell, also including a STING inhibitor (H151) and pretreating some T-cells with a blocking antibody to CXCR3 (Figure 7-11D). In both MHECs and BMDMs, DR pre-treatment induced significant T-cell chemotaxis across the Transwell in WT cells that was ablated by STING inhibition or CXCR3 blockade, whereas $STING^{-/-}$ cells were unable to induce significant increases in chemotaxis (Figure 7-11E-F). Pre-treatment of WT and $STING^{-/-}$ CFBs with DR induced similar $CD8^+$ T-cell chemotaxis that was unaffected by STING inhibition but still ablated with CXCR3 blockade (Figure 7-11G). Together these data confirm that DR directly induces STING-dependent chemokine secretion in MHECs and BMDMs that allows for $CD8^+$ T-cell migration through CXCR3 recognition, whereas CFB chemokine secretion can induce chemotaxis that is not STING dependent.

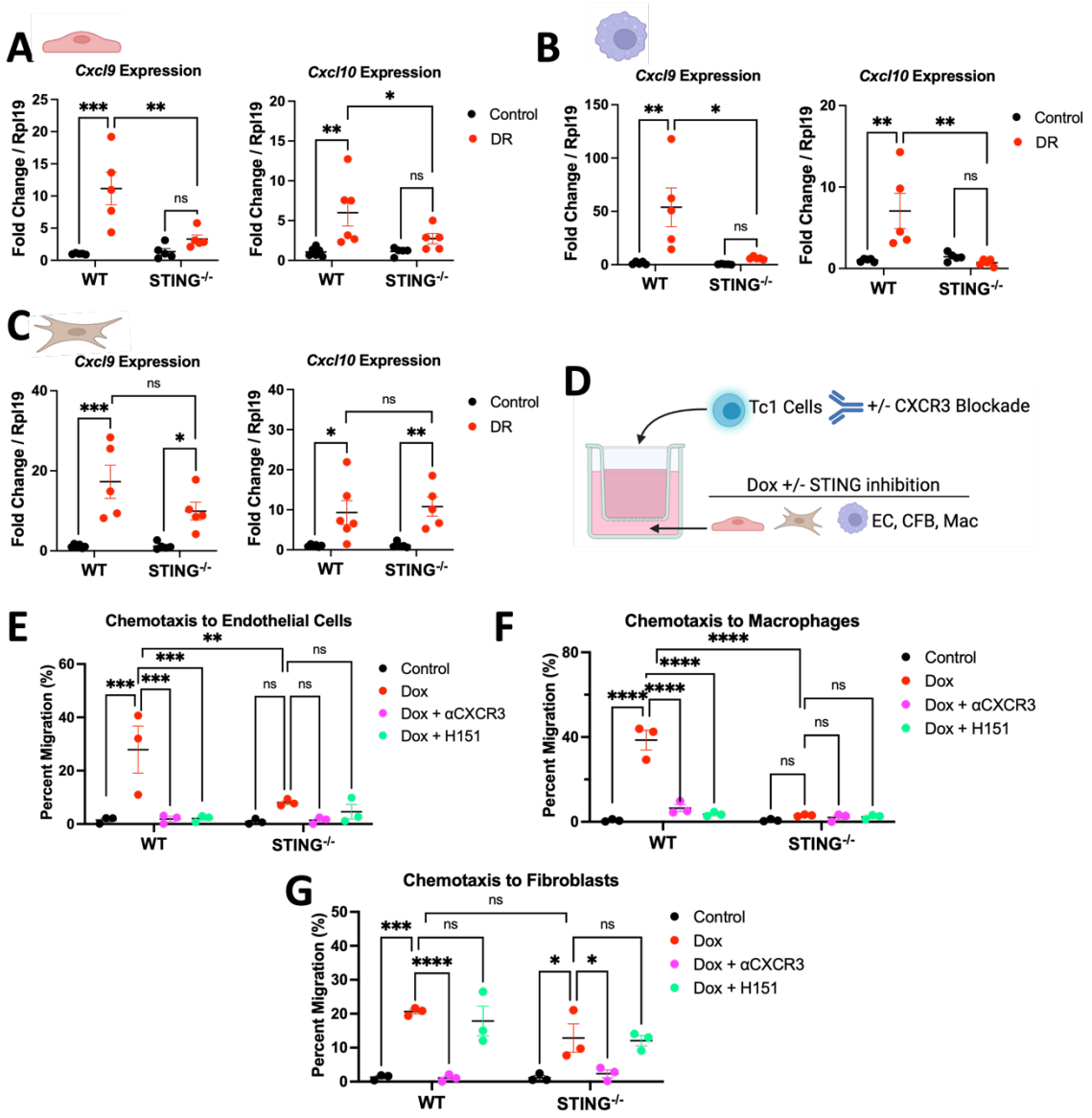


Figure 7-11 Doxorubicin Induces STING and CXCR3 Dependent Chemotaxis towards Endothelial Cells and Macrophages

Primary WT and STING$^{-/-}$ mouse cells were treated with 1.0 μg/mL DR for 24 hours, then RNA was collected for analysis of *Cxcl9/10* expression by RT-qPCR in primary heart endothelial cells (A), primary bone marrow derived macrophages (B) or primary cardiac fibroblasts (C). D. Schematic of Transwell T-cell migration experiment, in which primary WT and STING$^{-/-}$ mouse cells were plated below the Transwell, treated with 1.0 μg/mL DR for 24 hours in the presence of absence of 1 μm H151. 500,000 WT activated CD8+ T-cells labeled with CFSE were loaded on top of the Transwell, and where indicated were treated with 10 μg/mL αCXCR3 inhibiting antibody, then migrated cells were counted with by flow cytometry, done for primary heart endothelial cells (E), primary bone marrow derived macrophages (F) or primary cardiac fibroblasts (G). Statistical analysis by 2-way ANOVA with Sidak's multiple comparisons test, Ns = no significance, * = $p < 0.05$, ** = $p < 0.01$, *** = $p < 0.001$, **** = $p < 0.0001$.

7.3.7 Doxorubicin Induces STING Dependent Transendothelial Migration:

While we have outlined a role for MHEC and BMDM STING in CD8^{+} T-cell chemotaxis in response to DR, as MHECs are the major regulator of immune cell entry

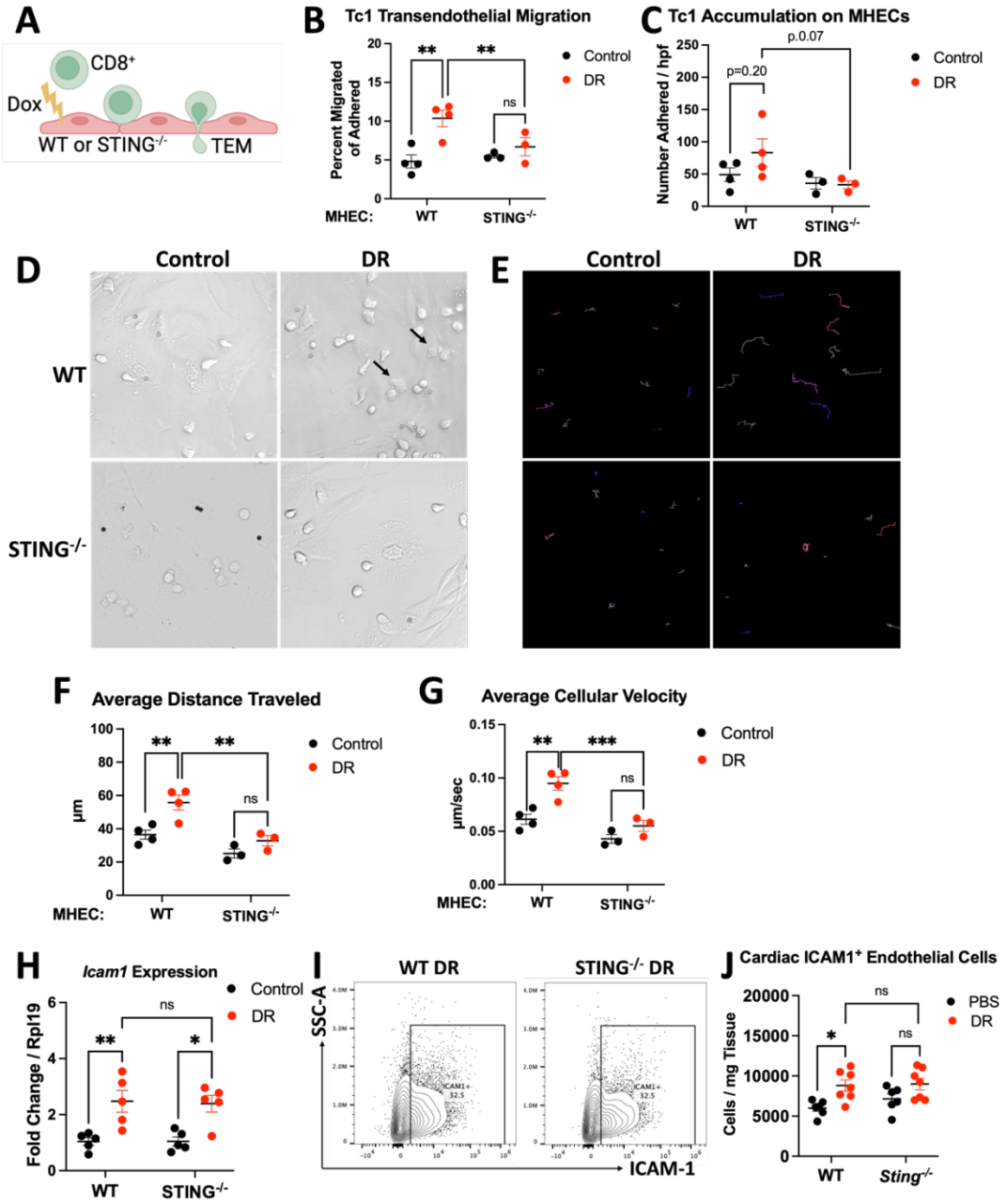


Figure 7-12 Doxorubicin induces STING dependent transendothelial migration

A. Primary WT and STING$^{-/-}$ mouse heart endothelial cells were treated with 1.0 µg/mL DR for 24 hours, then 1 million activated WT CD8+ T-cells were perfused across endothelial cells at a shear stress of 1.0 dyne/cm^2 at 37 deg. C and monitored by live microscopy. B. T-cells that underwent transendothelial migration were counted manually. C. Adhered T-cells were counted manually. D. Representative images showing T-cell accumulation on endothelial monolayers, black arrows indicate transmigrated T-cells. E. Manual Tracking plugin on ImageJ was used to analyze the path and movement of 10 randomly selected T-cells, shown are example paths traveled highlighted in color. The manual tracking plugin was used to analyze average distance traveled (F) or average cellular velocity (G). H. Primary WT and STING$^{-/-}$ mouse heart endothelial cells were treated with 1.0 µg/mL DR for 24 hours then RNA was collected to measure *icam1* expression by RT-qPCR. I. 8-10 week old WT or STING$^{-/-}$ mice were treated with 5.0 mg/kg Doxorubicin or saline weekly for 4 weeks before euthanasia (5-7 mice / group), hearts were digested mechanically and enzymatically then analyzed by flow cytometry for ICAM-1 expression on CD31+ endothelial cells, shown is a representative plot of ICAM-1 expression, quantified in J. Statistical analysis by 2-way ANOVA with Sidak's multiple comparisons test, Ns = no significance, * = $p < 0.05$, ** = $p < 0.01$, *** = $p < 0.001$, **** = $p < 0.0001$.

in tissue we then directly evaluated transendothelial migration (TEM). We pretreated WT

and STING$^{-/-}$ MHECs with DR and then perfused WT CD8^{+} T-cells across the endothelial monolayers under shear stress conditions (Figure 7-12A) then monitored CD8^{+} T-cell adhesion and TEM by live microscopy. We found that DR treatment enhanced CD8^{+} T-cell TEM across WT but not STING$^{-/-}$ MHECs (Figure 7-12B, D), and resulted in a trending increase in T-cell accumulation on the endothelium (Figure 7-12C, D). As T-cell accumulation only trended up with DR treatment, and our previous data indicate that DR directly modulates endothelial chemokine secretion, we used the CellTracker function to measure CD8^{+} T-cell movement while interacting with the endothelium by tracking individual cell paths before undergoing TEM. DR treatment resulted in increased distance traveled by CD8^{+} T-cells across WT but not STING$^{-/-}$ endothelial monolayers (Figure 7-12E-F), and increased the average velocity of T-cell movement on only WT MHECs as well (Figure 7-12G). We next measured the expression of ICAM-1, involved in the adhesion of T-cells to MHECs prior to TEM. DR treatment increased *Icam1* expression similarly in WT and STING$^{-/-}$ MHECs *in vitro* (Figure 7-12H). Further, we treated WT and STING$^{-/-}$ mice with DR and stained for CD31^{+}ICAM-1^{+} cells by flow cytometry, and found a similar increase in activated ICAM1^{+} endothelial cells in both mice (Figure 7-12I). Together these data show that DR can induce CD8^{+} TEM, which endothelial STING modulates specifically through enhancing chemotaxis and not firm adhesion.

7.3.8 STING Knockout Cardiac Fibroblasts Exhibit Impaired Transformation in Response to DR but not TGFβ:

While thus far we showed that EC STING and Macrophage STING mediate recruit of T-cells across the cardiac endothelium, CFB STING did not contribute to T-cell cardiotropism despite CFB-STING$^{-/-}$ mice remaining protected from DR cardiotoxicity. As such, we hypothesized that STING regulates CFB transformation and fibrosis. We have

previously shown that DR can directly induce myofibroblast transformation, so we first treated WT and STING$^{-/-}$ CFB with DR and measured myofibroblast markers. DR treatment significantly increased *aSMA* and *Postn* gene expression in WT but not

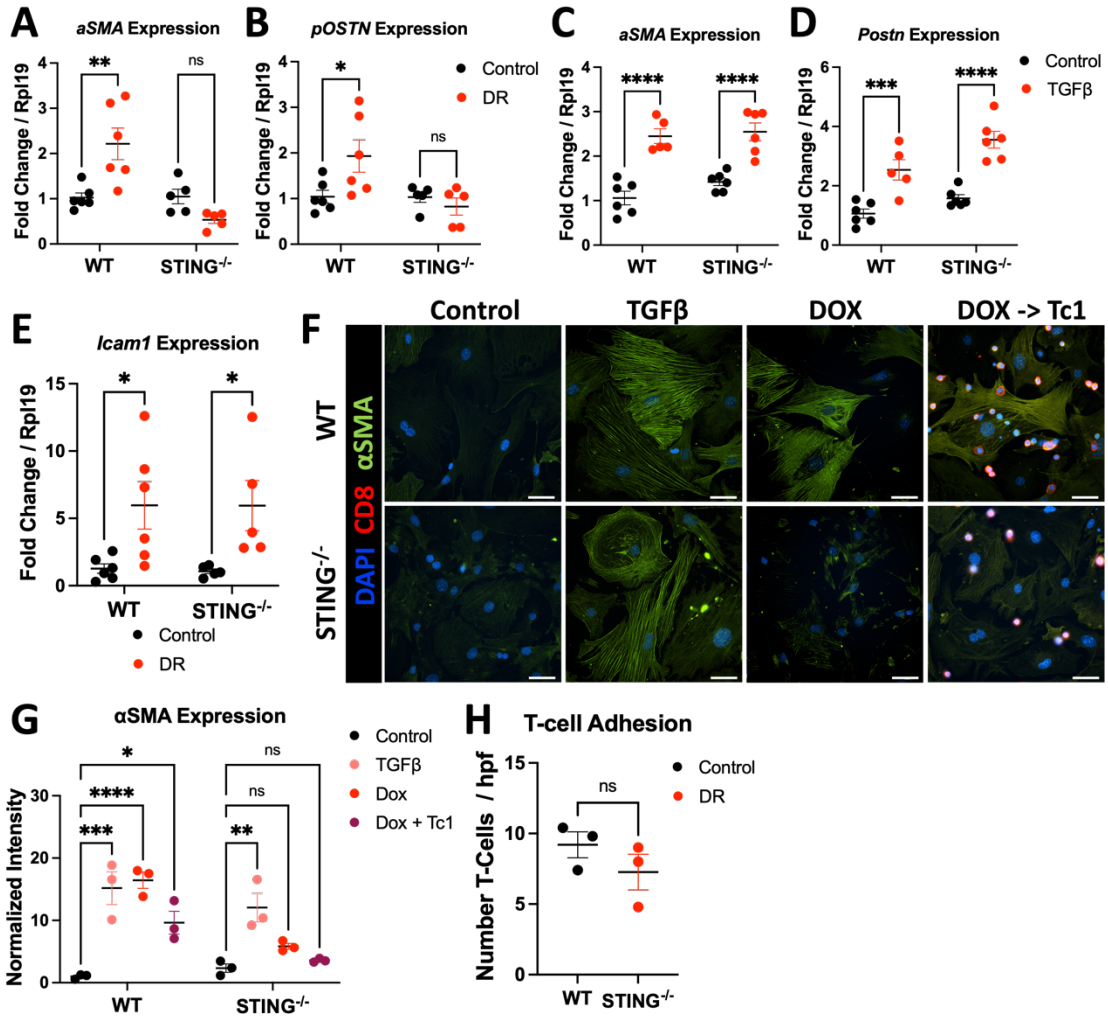


Figure 7-13 STING-/- Cardiac Fibroblasts Exhibit Impaired Transformation in Response to Doxorubicin

WT or STING$^{-/-}$ primary mouse cardiac fibroblasts were treated with 1.0 µg/mL DR for 24 hours, then RNA was isolated and RT-qPCR was used to measure aSMA expression (A) or Postn expression (B). WT or STING$^{-/-}$ primary mouse cardiac fibroblasts were treated with 100 ng/mL TGFβ for 24 hours, then RNA was isolated and RT-qPCR was used to measure aSMA expression (C) or Postn expression (D). E. Icam1 expression was measured by RT-qPCR in DR treated WT or STING$^{-/-}$ cardiac fibroblasts. F. WT or STING$^{-/-}$ fibroblasts were treated with 1.0 µg/mL DR or 100 ng/mL TGFβ for 24 hours, or pre-treated with DR before the addition of WT CD8+ T-cells at a ratio of 1:5 CFB:Tc1 cells, then cells were stained using immunofluorescence of aSMA and CD8. G. aSMA intensity was analyzed by ImageJ. H. T-cells were counted manually. Statistical analysis by 2-way ANOVA with Sidak's multiple comparisons test (A-G) or T-test (H), Ns = no significance, * = $p < 0.05$, ** = $p < 0.01$, *** = $p < 0.001$, **** = $p < 0.0001$.

STING$^{-/-}$ CFB (Figure 7-13A-B). To test if STING deficiency broadly impaired fibroblast transformation, we then treated both sets of CFB with TGFβ, and found a similar

induction of *aSMA* and *Postn* independent of STING (Figure 7-13C-D). To further corroborate this, we performed both DR and TGFβ treatment WT and STING$^{-/-}$ CFB and measured αSMA by immunofluorescence, again observing that while WT CFB upregulated αSMA in response to both stimuli, STING$^{-/-}$ CFB could only respond to TGFβ (Figure 7-13F-G). Our previous work further showed that DR induces CFB ICAM-1, which CD8^{+} T-cells adhere to and induce further myofibroblast transformation. Interestingly, both WT and STING$^{-/-}$ CFB upregulated *Icam1* similarly after DR treatment (Figure 7-13E), indicating T-cell adhesion would not be impacted by STING deficiency. To test this, we treated WT and STING$^{-/-}$ CFB with DR followed by co-culture with activated CD8^{+} T-cells and co-stained for αSMA and CD8. While T-cells bound to WT and STING$^{-/-}$ CFB at similar frequencies (Figure 7-13H), only WT CFB in contact with T-cells increased αSMA expression. Taken together with our *in vivo* data showing CFB-STING$^{-/-}$ are protected from DR induced systolic dysfunction and fibrosis, this provides evidence of a role for STING in modulating CFB transformation.

7.3.9 Doxorubicin Activates STING in Human Cells:

We then wanted to corroborate our findings in primary mouse cardiac cells with human cells. To do so, we used human vein umbilical cells (HUVEC), primary left ventricular cardiac fibroblasts (LV CFB), and Thp1 cell derived macrophages, and treated each cell type with DR as well as the pharmacologic STING inhibitor H151. In all 3 cell types, we found that DR increased the expression of IFNα and IFNβ, which was abrogated by co-treatment with H151 (Figure 7-14A-C). We next measured expression of CXCL9 and CXCL10 to evaluate if human cells could similar contribute to human T-cell migration. As seen in primary mouse cells, DR induced significant CXCL9 and CXCL10 in all 3 cell types, and H151 prevented upregulation of both chemokines in HUVECs and Thp1 macrophages (Figure 7-14D-F). In primary LV CFB, H151 blunted

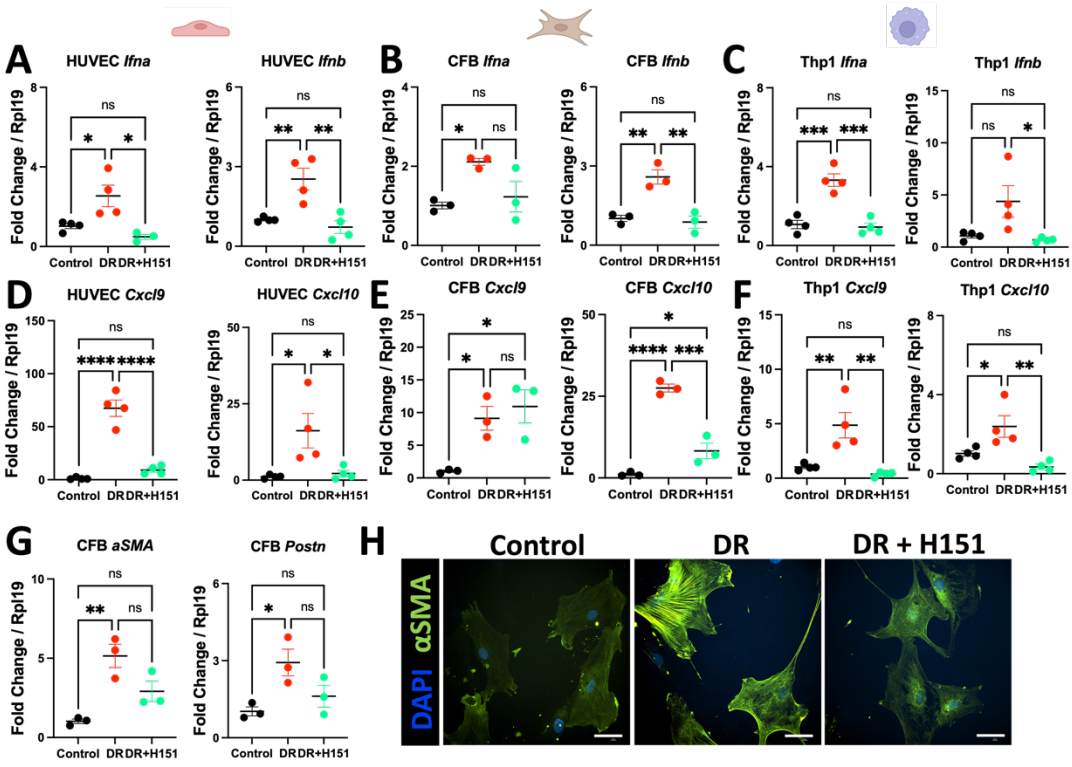


Figure 7-14 Doxorubicin Activates STING and Induces Chemokine Expression and Fibroblast Transformation in human cells

Cells were treated with 1.0 µg/mL DR for 24 hours in the presence of absence of 1 µm H151, then RNA isolated and used to analyze Ifna and Ifnb expression by RT-qPCR in HUVEC cells (A), primary human LV fibroblasts (B) or Thp1 derived macrophages (C). RT-qPCR was used to analyze Cxcl9 and Cxcl10 expression in HUVEC cells (D), primary human LV fibroblasts (E) or Thp1 derived macrophages (F). G. RT-qPCR was used to analyze aSMA and Postn expression in primary human LV fibroblasts. H. Fibroblasts were stained with aSMA by immunofluorescence, representative images shown (scale bars = 50 um). Statistical analysis by 1-way ANOVA with Tukey's multiple comparisons test, * = $p < 0.05$, ** = $p < 0.01$, *** = $p < 0.001$, **** = $p < 0.0001$.

CXCL10 but not CXCL9 expression, in line with less STING-dependency for CFB chemokine production observed in mouse CFB (Figure 7-14E). Next, we evaluated if DR caused LV CFB transformation. We found that DR increased *aSMA* and *Postn* transcript as well as aSMA protein by immunofluorescence in LV CFB, however H151 was only able to cause a trending decrease in the expression of these transformation markers (Figure 7-14G-H). Overall, this shows a similar effect of DR on STING activation, chemokine secretion, and fibroblast transformation across multiple human cell types.

7.4 Discussion

In this study we outline a critical role for STING in regulating the cardiac $CD8^+$ T-cell immune response to anthracycline treatment, in which we further specify several cell specific roles – chemokine production for cardiotropism by endothelial cells and macrophages and regulation of the fibrotic response by CFB. We show that DR directly activates STING in these 3 cell types both *in vitro* and *in vivo*, contributing to cardiac and systemic inflammation, and that global or cell specific deletion of STING in mice is protective against DR cardiotoxicity. Further we expand upon our previous work by showing cellular sources for the chemokines CXCL9 and CXCL10 induced by DR, and provide evidence that cardiac $CD8^+$ T-cells are recruited through CXCR3 in both mouse models and patients treated with anthracyclines.

Here we compare side by side the activation of STING by DR in 3 cardiac cell types, and show cardiac protection using cell specific ablation of STING in each. Previous work has only used global knockout of STING or focused on only specific cell type, whereas our work provides the first evidence directly comparing the contribution of STING in stromal and immune cells. Importantly, our work also shows that even though multiple cell-specific STING knockout mice were protected from DR, the mechanisms of protection differ for each cell type. Two studies have shown DR to activate STING in cardiac fibroblasts and endothelial cells, [133,332] however our work builds upon this by connecting STING activation to chemokine production and $CD8^+$ T-cell cardiotropism. We previously showed $CD8^+$ T-cells as critical drivers of DR cardiotoxicity and fibrosis,[485] which is illustrated further by the cardio-protection observed in our EC and Myeloid STING knockout mice. Additionally, we generated the first CFB-specific knockout of STING and showed protection from DR cardiotoxicity. Further, previous work by Lei *et al* elegantly showed DR induces mitochondrial DNA damage in cardiomyocytes activating STING,[488] however as cardiomyocytes are not potent producers of CXCL9 and CXCL10 we did not focus on them.

Interestingly, we observed a complete lack of T-cell activation in the mLN of DR treated global STING$^{-/-}$ mice, whereas we did not see the same phenotype in cell specific STING mice. This suggests a role for STING in T-cell activation in an additional cell type. While our work showed STING$^{-/-}$ T-cells expressed similar activation markers as WT *in vitro,* it is plausible STING internally regulates T-cell activation *in vivo*. STING has been previously shown to be functional in T-cells and regulate their inflammatory response and cell death.[491] Additionally, our prior work showed DR induces an antigen specific T-cell response, and we hypothesize that cardiomyocyte STING might contribute to cardiac neoantigen production induced by DR.

We show evidence of STING activation *in vivo* after DR broadly in the heart as well as in specific cell types at the 4 week time point, however by 8 weeks of DR treatment we did not see STING pathway activation. This suggests that STING mediates the acute inflammatory response to DR, and might play less of a role in propagating chronic inflammation once CD8^{+} T-cells have already infiltrated. While DR directly induced *Cxcl9* and *Cxcl10* expression, IFNγ is a potent trigger of both chemokines,[492] and our prior work showed cardiac CD8^{+} T-cells to express high IFNγ after DR treatment, leading us to hypothesize that after STING signaling resolves, cardiac T-cells might propagate chemokine expression and further T-cell cardiotropism through IFNγ expression. Future time course studies and transcriptomic analyses will further allow us to delineate the exact timing of STING signaling in each cell type after DR treatment. Further, we show elevated cardiac cGAMP after DR treatment at the 4 week time point, which indicates canonical cGAS induced STING signaling. However, it is plausible that cGAS is not driving STING activation in all cell types. Prior work has shown global cGAS$^{-/-}$ mice to be protected from DR cardiotoxicity, and shown signs of cGAS activation in several cell types *in vitro.*[133,332,488] However, STING can be activated independent of cGAS from mitochondrial stress, DNA damage, or the unfolded

protein response, all of which can be explored as potential mechanistic avenues in each cell type.[128,129]

While DR activated CFB STING, DR-treated CFB were still able to produce some CXCL9 and CXCL10 and mediate $CD8^+$ T-cell recruitment *in vivo* and *in vitro.* This suggests that additional mechanisms in CFB regulate chemokine production, and further, other DNA sensing mechanisms such as NLRs, RLRs, or endosomal TLRs might compensate for the lack of STING signaling in this cell type, [120] whereas STING is the dominant DNA sensor in other cell types. In contrast, STING regulated CFB transformation in response to both DR and $CD8^+$ T-cell co-culture after DR treatment. Interestingly, T-cell adhesion to $STING^{-/-}$ CFB in co-culture was comparable to WT cells, further evidenced by similar ICAM-1 expression in response to DR, indicating a specific defect in the CFB transformation pathway. We previously showed T-cell derived Granzyme-B induces myofibroblast transformation, however the mechanism of extracellular Granzyme sensing remains under debate.[493] As DR is known to cause DNA damage and oxidative stress[482,488], it is plausible that canonical or non-canonical STING signaling can lead to myofibroblast transformation. Whether this induces TGFβ-mediated transformation and what specific signaling pathways drive this phenotype is an ongoing area of investigation.

We previously showed that CXCL9 and CXCL10 correlate with systolic decline in patients treated with anthracyclines[485], and this work further implicates T-cell recruitment through the CXCL9/10-CXCR3 axis. This strongly suggests that targeting this chemokine/receptor axis could be a viable therapeutic option in patients to prevent T-cell cardiotropism. Further, there is some evidence that the anti-tumor effects of DR are not fully tied to intratumoral T-cell function[477], which would allow for immunomodulatory cardioprotective therapy without compromising the anti-tumor efficacy of DR. This study showed IFNγ blockade to be cardioprotective but not promote tumor progression, which we hypothesize is in part a result of inhibiting further CXCL9 and CXCL10 production, limiting

ongoing cardiac T-cell infiltration. Anti-CXCL10 therapies are already in clinical trials for autoimmune disease,[494,495] as are CXCR3 antagonists[496,497], which we think could be a viable protective strategy for DR induced cardiotoxicity. However, significant study would be needed to ensure inhibition of DR induced cardiotropism did not also impair T-cell anti-tumor immunity.

While our study provides novel insight into the cell specific functions of STING in response to DR treatment and implicates the CXCR3 pathway as a therapeutic target, it has several limitations we would like to address. We utilized global and cell-specific STING$^{-/-}$ mice, but did not fully characterize the functional role of cGAS, IFNaR, or other DNA sensors in our model. Further, while we showed macrophages to help recruit cardiac T-cells after DR treatment, we utilized a LysM Cre driver, which is not specific to macrophages, and as such future studies will use additional Cre drivers and unbiased transcriptomics approaches to better delineate myeloid cell STING functionality. While we only used genetic modulation strategies, other studies have used a pharmacologic STING inhibitor for protection against DR in animal models[332], and future work will employ this among CXCR3 pathway inhibitory strategies. Finally, while we were able to show human cells to respond similarly *in vitro*, and find CXCR3+ T-cells in human cancer patient cardiac samples, all of the *in vivo* work for this study was performed in non-tumor bearing mice. As we continue to work on translating cardioprotective strategies, future work will employ tumor-bearing mice to test cardio-protection in the context of a tumor and evaluate effects on tumor progression. Despite these limitations, we believe this work furthers our understanding of the inflammatory response in DR cardiotoxicity and opens up novel avenues for immune-modulatory therapies.

In summary, we build upon existing knowledge in implicating the STING inflammatory pathway in responding to DR induced cardiac damage by outlining a role for myeloid and endothelial STING in contributing to DR-induced CD8^{+} T-cell cardiotropism through

CXCL9/10 produdction. We also provide evidence of a novel role for STING in mediating myofibroblast transformation after DR treatment. Together these data evidence that targeting the STING-chemokine axis in patients treated with anthracyclines could be a viable approach to treating or preventing chronic cardiac inflammation and cardiotoxicity.

7.5 Author Contributions

ALB designed the project, performed experiments, analyzed data, and wrote the manuscript. ES, NW, and SS performed experiments and helped edit the manuscript.

7.6 Acknowledgements

Thank you to Navin Kapur at Tufts Medical Center for providing LV human fibroblasts. Additional thanks to Shruti Sharma at Tufts University for graciously providing $STING^{flox}LysM^{Cre}$ mice. This work was supported by National Institute of Health (NIH) Grants R01 HL144477 and HL165725 (P.A.), Tufts Springboard Tier 1 Grant (P.A.) NIH F30 Grant HL162200 (A.L.B.)

Chapter 8 Discussion

8.1 MyD88 Plays Different Roles in Different Cell Types:

8.1.1 Introduction to Diverse MyD88 Functionality

The adaptor protein MyD88 has been well characterized in innate immune cells such as a macrophages for it's pro-inflammatory role in mediating signaling downstream of TLRs and the IL-1r family.[498,499] As such, deletion of MyD88 leads to loss of PAMP/DAMP signaling and high susceptibility to infection in mice,[500–502] and MyD88 mutation in humans, although rare, significantly increases the risk of infection.[104] As most of the preclinical studies use global deletion, for a long time the role of MyD88 was presumed to be limited to innate immune cells and canonical PAMP/DAMP signaling. However, as MyD88 is widely expressed throughout the body, it became known that non-innate immune cells could also respond through PRRs and signal through MyD88, contributing to both sterile and infectious inflammation.[503–505] This opened up the concept that TLR-MyD88 signaling might in fact have a more diverse set of roles in additional cell types beyond the well characterized innate immune response. In this dissertation, I uncovered novel molecular roles for MyD88 in both T-cells and cardiac fibroblasts which contribute to sterile inflammation in both the heart and in cancer.

8.1.2 T-cell MyD88 Function is Dependent on Inflammatory Context:

To test a functional role for T-cell MyD88, $CD4^{Cre}$ T-cell deficient MyD88 mice (T-$MyD88^{-/-}$) or bone marrow chimera approaches have previously been used several times, showing impaired T-cell response to bacterial and viral pathogens through decreased cytokine secretion and T-cell activation.[506–509] My results showed the opposite effect in the context of sterile inflammation in the heart or tumor, suggesting that the context of inflammation a T-cell experiences strongly impacts it's functional outcome (Figure 8-1). This means T-$MyD88^{-/-}$ mice could have impaired anti-pathogen responses

but accentuated sterile inflammatory functions. One group did show enhanced anti-tumor immunity in squamous cell carcinoma using T-MyD88 mice, in line with my results.[118] These differences are further illustrated by the fact that cardiac DAMPs did not alter T-cell activation in our hands,[398] but LPS treatment could alter T-cell signaling and survival.[510] Indeed, another study using OVA-vaccination with LPS treatment *in vivo* showed impaired T-cell activation and cytokine secretion in the absence of MyD88,[379] again evidence that the inflammatory context, especially molecular signals from pathogens, has in impact. The models used in this dissertation all induced Th1 or Tc1 responses, and as such it is further plausible that MyD88 is differentially regulated or

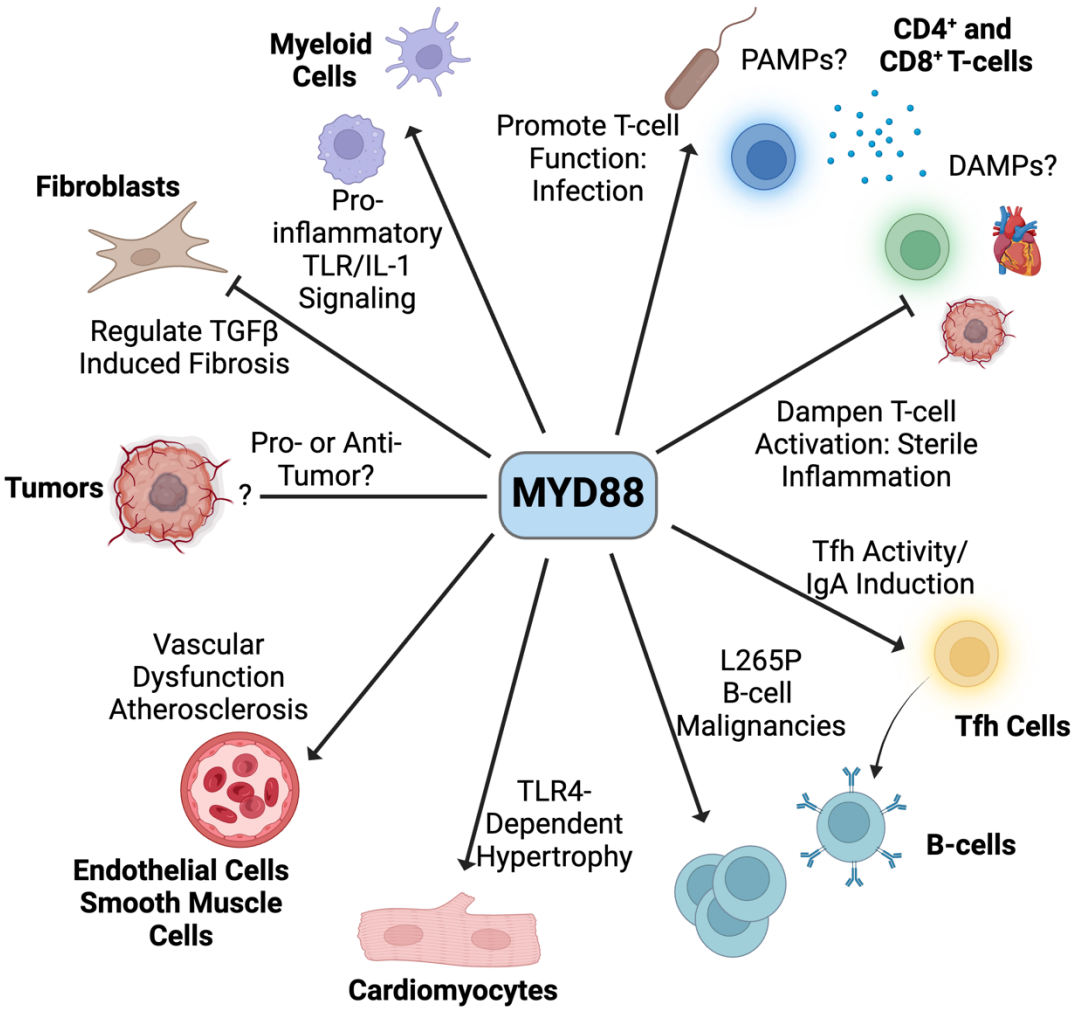


Figure 8-1 Cell Specific Functions of MyD88
Overview of functions that MyD88 plays specific to each cell type. Cell types shown in bold, with arrow alongside summary of each function. Figure created with Biorender.

plays a different role in a T-cell subset dependent manner. The literature in fact supports this theory, as Foxp3^{Cre} (T-reg) MyD88$^{-/-}$ mice did not exhibit altered T-cell function, while other groups reported T-MyD88$^{-/-}$ mice to have impaired Th17 differentiation and IL-17 production while having preserved IFNγ production in the context of inflammatory bowel disease or skin malignancy.[118,511] My data did not show MyD88 deletion to impact Tbx21 levels, but it could regulate other transcription factors. Together this highlights the need for additional mechanistic studies of T-cell MyD88 across T-cell subsets and models.

8.1.3 T-cell MyD88 Acts through BCAP and is Modulated by TLR Signaling

The most well-established role for MyD88 in T-cells is that of mediating TLR-induced co-stimulatory functions. Several studies have treated T-cells with agonists against TLR2, TLR4, TLR9, etc. and shown enhanced T-cell activation, cytokine secretion, and survival, which is dependent on the presence of MyD88.[431,512–515] This work describes TLR ligation as an “enhanced co-stimulatory signal” and shows increases in pro-inflammatory signaling pathways such as ERK, NF-kB, and PI3K, all known to be downstream of the TCR signaling cascade, but no full molecular mechanism had been discovered for this phenomenon.[431,512–515] Interestingly, my work reproduced alterations to these pathways using MyD88$^{-/-}$ CD4^{+} or CD8^{+} T-cells, as I have shown increased activation markers, cytokine expression, and enhanced survival.[398,400,510] This implies that as MyD88 deletion and MyD88 recruitment to TLRs share enhanced activation phenotypes, the mechanism including BCAP binding presented in this dissertation could be applied broadly to previous studies. As the enhanced function of MyD88$^{-/-}$ T-cells was dependent on TCR-activation, and I had shown MyD88 co-localization to the TCR during T-cell activation, this strongly suggests a role for MyD88 directly in TCR signaling. The mechanism that I outlined in Chapter 5 thus far consists of MyD88 sequestering BCAP, a signaling molecule upstream of PI3K-AKT in the TCR cascade, therefore in its absence,

we observe enhanced pathway activation and effector function. This study also showed TLR4 stimulation through LPS treatment could decrease MyD88-BCAP binding.[510] As such, I hypothesize that the previous studies of TLR co-stimulation in T-cells act through a similar mechanism, in which MyD88 is recruited away from the TCR and BCAP leading to enhanced T-cell activation. However, it remains plausible that MyD88 has additional binding partners in the TCR signaling cascade that could directly effect other pathways. One such is also Smad4, which can regulate $CD8^+$ T-cell function [434] and which I showed MyD88 binds to in cardiac fibroblasts (Chapter 3). There is also evidence of MyD88 directly interacting with PI3K,[514] however BCAP knockdown eliminated the signaling differences between WT and $MyD88^{-/-}$ T-cells (Chapter 5), evidence that BCAP independent effects on PI3K signaling are not the primary mechanism. Future work can use unbiased pull-down proteomics techniques to fully characterize the binding partners of MyD88 during the course of T-cell activation. Additionally, while my work showed MyD88-BCAP interaction, the exact location of this binding remains unknown, and future studies can delineate whether this interaction occurs in the cytosol, at the TCR, or elsewhere.

8.1.4 MyD88 Shapes the Humoral Immune Response:

Interestingly, T-cell MyD88 has also been shown to shape the humoral immune response through altered follicular helper T-cell function, IgA secretion, and subsequent gut dysbiosis (Figure 8-1).[516–518] This begs the broader question of how MyD88 can regulate the other arm of adaptive immunity. In fact, the primary role of BCAP is that of activating PI3K downstream of the B-cell receptor in B-cells,[436] although MyD88-BCAP binding has yet to be studied in this cell type. As B-cells express high levels of TLRs and can act as APCs responding to PAMPs/DAMPs, MyD88 acting at the BCR similarly to the TCR might be less significant, and rather it might act more similarly to innate immune

cells. MyD88 in B-cells has been traditionally associated with the MyD88 L265P mutation, which drives B-cell lymphomas and Waldenström's Macroglobulinemia. However, this mutation results in constitutively activated canonical Myddosome signaling, and as such is not indicative of an endogenous role for MyD88 in B-cells.[419] B-cell MyD88$^{-/-}$ mice using CD79^{Cre}, CD20^{Cre}, Mb1^{Cre} or adoptive transfer of MyD88$^{-/-}$ B-cells have all been challenged with vaccination models, autoimmune models, or even atherosclerosis, and each time showed impaired antibody secretion and B-cell function.[519–522] However, the exact molecular mechanisms for these has not yet been determined, as TLR functionality was shown to contribute to only some of these phenotypes.

8.1.5 MyD88 Plays Diverse Roles in Cardiac and Tumor Cells

With more examples of cell-specific functions for MyD88 across the immune system, understanding broadly the role that it plays in both cardiac cells and tumor cells will help determine the feasibility of MyD88-related therapeutics (Figure 8-1). In cardiomyocytes, it is well established that TLRs are expressed and functional in the failing heart.[209] In line with this, expression of a dominant negative MyD88 (containing just the TIR domain) in pressure overload decreased cardiomyocyte hypertrophy,[364] TLR4 deletion in cardiomyocytes protected against PE/ANGII induced hypertrophy,[523] and inhibition of cardiomyocyte MyD88-TLR4 is protective against diabetic cardiomyopathy.[524,525] Despite this, cardiomyocyte specific expression of full MyD88 or a MyD88 lacking just the INT domain induced baseline hypertrophy,[526,527] suggesting that different domains of MyD88 induce differential function in cardiomyocytes.

Far less is known about the role of vascular MyD88. MyD88 promotes endothelial activation of NF-kB and cytokines such as IL-1β and IL-6 in response to TLR stimulation, and one study showed endothelial MyD88 knockout is protective against atherosclerotic

disease.[528–531] Similarly TLR4 signaling promoted vascular smooth muscle dysfunction in aging, atherosclerosis, and angiotensin infusion.[532–534] While this makes targeting vascular MyD88 a promising target, the role of MyD88 in fibroblast functionality complicates this further. My data shows that MyD88-fibroblast deletion promotes cardiac fibrosis (Chapter 3) and impairs several fibroblast inflammatory functions (Appendix 9.1). In line with this, in MI, deletion of fibroblast MyD88 resulted in a loss of fibroblast mediated inflammatory function through IL-1 signaling.[271] Additionally, MyD88 deletion in zebrafish promoted fibrosis in heart development, although this model was not cell-specific.[535] However, multiple studies by Jinhua Zhang's group showed liver and colonic myofibroblast MyD88 promotes fibrosis, inflammation, and even colon cancer, again limiting the therapeutic potential of targeting fibroblast MyD88 with contrasting roles across organ systems.[536–538]

This then brings up the question of if any sort of modulation of MyD88 levels systemically could promote malignancy, even while having beneficial effects in CVD. While all of the previously discussed roles for immune MyD88 apply in most malignancies, such as our finding showing MyD88 deletion in T-cells promotes anti-melanoma activity,[400] MyD88 acts in cancer cells themselves. MyD88 and TLR4 expression correlate with worse survival in ovarian, breast, and colorectal cancers.[116,117,421] As such, activation of MyD88 promotes cancer cell invasiveness, and deletion of MyD88 prevents tumor progression in multiple malignancies.[116,421,422,539,540] However, in the case of colon cancer, MyD88 has been reported to protect against tumorigenesis.[420,541] With such variable and contrasting roles in both cardiac cell types and across malignancies, the broad inhibition or activation of MyD88 would prove inefficient with widespread side effects. If MyD88 inhibitors progress into clinical trials for

either cardiovascular disease or antineoplastics, significant monitoring of cardiac side effects or long term malignancy would be required.

8.2 Factors that Determine the Function of MyD88

8.2.1 Expression of Receptors:

To reconcile the differing functions across contexts or cell types, it is necessary to consider the factors that might regulate how MyD88 acts functionally. One such example is what receptors that utilize MyD88 are expressed or ligated in a given cell. It has been shown that across immune and non-immune cell types, and in different organs, there is a very wide variety of TLR expression.[114,542] In a myeloid cell acting as an APC, very high TLR expression might draw most of the MyD88 to act canonically in forming Myddosomes and acting in a proinflammatory manner. However, in T-cells that express lower TLRs, while the TLRs remain functional, more MyD88 would remain free to be recruited to the TCR.[105] This further highlights discrepancies in the functional outcomes of PRR ligation. As previously discussed in section 8.1.2, in the context of infection, T-cell MyD88 is more pro-inflammatory, whereas in sterile inflammation it can be anti-inflammatory. Different PAMP and DAMP signals are likely to mediate this difference across different cell types. In immune and non-immune cells, a variety of studies have shown that activation of different TLRs that all signal through MyD88 can induce different cytokine responses, and further that different combinations of TLR co-stimulation can have synergistic effects.[543–546] As such, the exact combinations of molecular signals (DAMPs/PAMPs) in an infection, in cardiovascular disease, or in cancer could lead to widely variable recruitment of MyD88 to PRRs and subsequent differences in downstream signaling.

8.2.2 Spatial Localization of MyD88

This concept also implies that the sub-spatial localization of MyD88 can determine its' functional outcome. Our work shows that MyD88 co-localizes with the TCR during T-cell

activation through CD3 stimulation, which then disperses after removing T-cells from this stimulus.[220] Further, TLR4 activation decreases TCR-colocalization of MyD88, evidence that triggering different receptors can alter the location of MyD88 and can impact it's function (Chapter 5). A recent study outlined a novel concept in TLR signaling – that the Myddosome actually dissociates from TLRs after complex formation and promotes signaling from the cytosol. This work also characterized co-localization of MyD88 with a variety of other organelles and signaling molecules, including mitochondria, autophagosomes, cGAS, and inflammasomes,[547] implying an even wider array of potential functions in novel cellular locations for MyD88 than previously known.

8.2.3 MyD88 Binding Partners and Domains

Each domain of the MyD88 protein is involved in binding to a variety of other proteins, one additional layer of regulation of it's function (Figure 8-2). Both the cellular expression of potential binding partners and alternative splicing of *Myd88* can impact what complexes form and downstream effects. MyD88 contains a C-terminal Toll-interleukin-1 receptor (TIR) domain, which primarily allows it to bind to TLRs and IL-1r, an unstructured intermediate domain (INT), a death domain (DD) for MyD88 oligomerization, and N-terminal domain (NTD-Figure 8-2).[99,397] In canonical TLR signaling, MyD88 uses its' DD to both bind to itself and bind to the DD of IRAK4 and IRAK2, forming the Myddosome.[548] Mutations of the DD in humans result in immunodeficiency through impaired IRAK recruitment, although these are quite rare.[549] MyD88 can also recruit TIRAP (or MAL) among other Leucine Rich Repeat (LRR) proteins through its TIR domain, which helps facilitate TLR2 and TLR4 complex formation and downstream signaling.[550,551] Finally, the N-terminal domain of MyD88 binds to IRF7 to help mount a type I interferon response from endosomal TLRs.[552] Similar to differential TLR expression, innate immune cells will express higher levels of the canonical

MyD88-binding machinery to facilitate TLR signaling, while some cell types preferentially express other binding partners of MyD88.

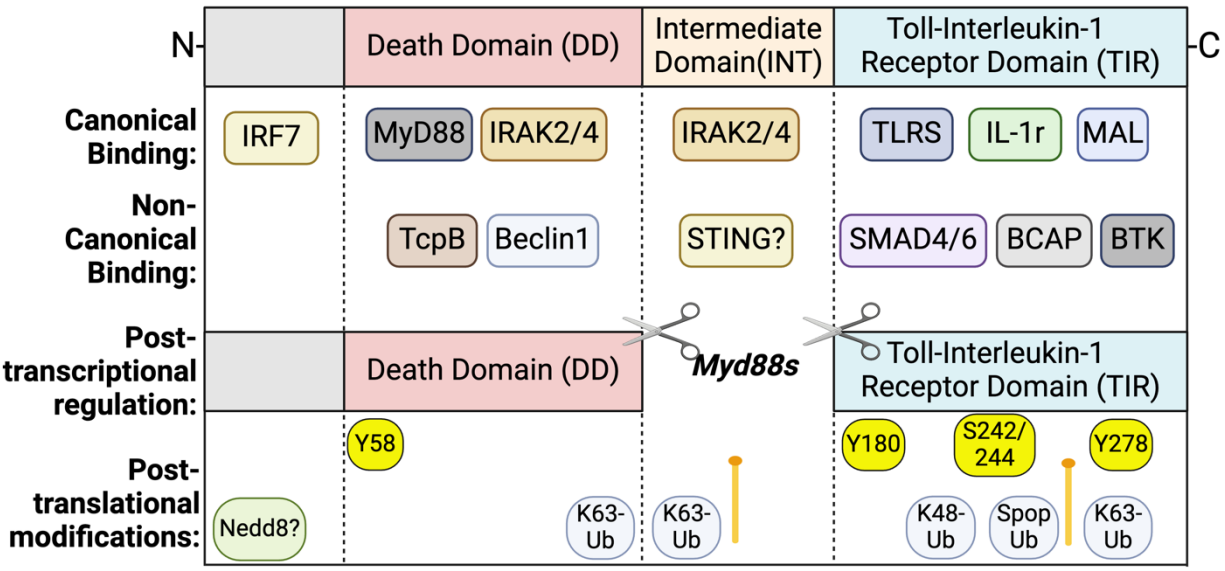


Figure 8-2 MyD88 Domains, Binding Partners, and Modifications
Schematic showing the 3 characterized and 1 uncharacterized domains of MyD88, as well as the proteins that bind each domain in canonical MyD88 signaling versus in non-canonical functions. Splicing of MyD88 into MyD88s is shown, as well as post translational modifications. Yellow = phosphorylation with residue and sites indicated. Lipid molecule indicates palmitoylation, and ubiquitination sites and chain types (if known) are indicated. Figure created with Biorender.

The work in this dissertation highlights the function of two non-canonical MyD88 binding partners: BCAP in T-cells (Chapter 3) and Smad4 in cardiac fibroblasts (Chapter 5). Both of these, however, have been previously described in other cell types. MyD88 was shown to bind Smad4 through its TIR domain in hepatocytes, enhancing it's expression to promote TGFβ family member activity. MyD88 was also shown to be degraded by Smurf1 via Smad6 binding to MyD88 TIR domain to limit overactivity.[401,402] In contrast, we show in fibroblast that MyD88 limits Smad4 activity and TGFβ signaling, and it's degradation by Smurf2 is a necessary step for full myofibroblast transformation. Presumably, a difference in expression or functional regulation of Smurf1 vs. Smurf2 would mediate this cell specific difference. Our work also outlined that MyD88 bound BCAP in T-cells to sequester it from enhancing TCR signaling and T-cell activation (Chapter 5). Previously BCAP has been shown in myeloid cells to bind to MyD88 through its TIR domain as well, this time to negatively regulate TLR signaling by impairing Myddosome formation and MAL interactions, which decreases

cytokine expression and dendritic cell maturation.[435,446,553] This interaction, while occurring similarly in different cell types, could have variable effects given the lack of a TCR in myeloid cells, as such the primary role for BCAP would be at a TLR rather than at the TCR. Another example of regulation of TLR signaling through MyD88 can be found in Brucella infection, where the pathogenic TcpB protein inhibits MyD88 DD dimerization and subsequent TLR signaling,[554] suggesting targeting this domain therapeutically might limit inflammation without effects on BCAP or SMAD4 binding.

MyD88 has been shown to bind several other proteins outside of the work presented in this dissertation, which very well might be relevant in T-cells or fibroblasts (Figure 8-2). In macrophages and monocytes, MyD88 can bind to STING, preventing it's autophagic degradation and promoting anti-viral activity downstream of TLR signaling. While the binding domains remain unknown, the structure of the C-terminal loop of STING is unknown,[555] which suggests potential binding of the unstructured intermediate domain of MyD88. As STING signaling promoted fibroblast transformation by Doxorubicin (Chapter 7, appendix 9.4), MyD88 might be involved in this process as well. Additionally, the function of STING in T-cells is not well understood, making it plausible that MyD88-STING can drive anti-viral T-cell activity, although this has not been studied. However, another study showed that DD of macrophage MyD88 interacts Beclin1 to induce autophagy,[556] in contrast to the regulation of STING, meaning MyD88 could selectively modulate degradation of specific targets. Interestingly, in malignant B-cells MyD88 bound to activated Bruton's Tyrosine Kinase (BTK),[419,557] which was enhanced by the L265P mutation, one mechanism for MyD88 driven B-cell malignancies. As MyD88-BTK interact through the TIR domain at the BCR similar to MyD88-BCAP at the TCR, it remains to be seen if the L265P mutation impacts T-cells or increases risk of cardiovascular disease.

Interestingly, TLR4 signaling in myeloid cells induces a splice variant of MyD88 (MyD88s) that lacks the INT domain.[558,559] MyD88s is unable to recruit and activate IRAKs to

the Myddosome due to missing an essential Tyrosine residue in the INT domain. This terminates pro-inflammatory signaling downstream of TLRs and IL-1r as a method of resolving inflammation, especially by decreasing NF-kB activation.[560–562] Importantly, one study showed feasibility of using oligonucleotide transfection to manipulate MyD88 splicing and cytokine responses to IL-1r stimulation, representing an additional way of modulating MyD88 expression.[563] However, the cell specificity of this remains unknown, as all of these studies used immortalized cell lines or primary macrophages. The oligonucleotide was dosed to mice *in vivo*, and while *Myd88* transcript decreased and *Myd88s* transcript increased in multiple tissues, no MyD88s protein was detected, one limitation of this approach.[563] While I have not found evidence of MyD88s in T-cell, fibroblast, or cardiac lysates in the conditions outlined throughout this dissertation, I have not used primers specific to detect MyD88s, leaving open the possibility that MyD88s expression regulates MyD88 and TLR activity in either of these cell types.

8.2.4 Post-Translational Modification of MyD88 and Regulation of Expression

Several post-translational modifications of MyD88 have been described that regulate it's expression and activity at TLRs (Figure 8-2). In neutrophils, MyD88 is palmitoylated in the INT and TIR domains, necessary for Myddosome complex formation.[564] Additional, several tyrosine and serine phosphorylation sites in the DD and TIR domain have been identified that promote Myddosome complex assembly and MyD88 oligomerization,[565–568] including one site that promotes MyD88 oligomerization in the L265P mutation.[569] TCR signaling promotes the activity of a variety of kinases, making MyD88 phosphorylation a distinct possibility downstream of T-cell activation. As the TIR domain of MyD88 binds BCAP, post-translational modification such as phosphorylation might regulate the binding of MyD88 to BCAP after TCR activation, as discussed in Chapter 5.

Several examples in the literature and the work outlined in Chapter 3 of this dissertation show that MyD88 can be ubiquitinated. It has been previously shown in macrophages that TGFβ stimulation causes Smurf1/2 induce K48 ubiquitination in MyD88's TIR domain with subsequent degradation.[401] This is in line with my results, showing that TGFβ upregulates Smurf2 in fibroblasts to degrade MyD88, with Smurf2 knockdown alone sufficiently rescuing MyD88 expression, in contrast to in macrophages in which both Smurf1/2 participate. This difference might simply be differences in relative Smurf expression between cell types, or other regulators of E3 ligase activity. Several other E3 ligases ubiquitinate MyD88 including SIAH1, NRDP1, SPOP, and RNF138, building K48 or K63 ubiquitin chains in each domain of MyD88.[570–573] OTUD4 can further de-ubiquitinate K63 chains MyD88, and Neddylation of MyD88 (site unknown) has been described to antagonize ubiquitination.[574,575] While several of these mechanisms mostly apply to L265P driven lymphomas,[572,573] differential cell expression of these E3 ligases and de-ubiquitinases likely contributes to differential cellular expression and functions of MyD88.

In the context of this thesis, I have characterized a TGFβ-inducible ubiquitination mechanism controlling MyD88 expression in fibroblasts (Chapter 3). However, TGFβ also decreased *Myd88* transcript *in vitro*, and I found evidence of decreased *Myd88* transcript in myofibroblasts across several single cell data sets in mice and humans. The mechanism of this transcriptional regulation remains unknown, and more careful study of both the MyD88 promoter as well as potential epigenetic regulators of MyD88 expression could uncover an additional mechanism prior to ubiquitin-proteasome mediated degradation. In endothelial cells, histone acetylation has been shown to regulate LPS induced MyD88 expression,[576] however epigenetic control of MyD88 is poorly understood across cell types. In both $CD4^+$ and $CD8^+$ T-cells, activation through the TCR increased MyD88 expression at the protein level, however I have yet to uncover the transcription factors regulating this. As TCR signaling increases the activity of many pro-inflammatory transcription factors, one or

multiple of these could regulate *Myd88* transcription in addition to epigenetic regulation. It is also plausible that any of the post-translational regulatory mechanisms such as ubiquitination are altered downstream of TCR signaling, although this has not yet been studied.

8.3 The Translatability of MyD88 Modulation

This dissertation outlines the breadth of functions that MyD88 can participate in across cell types in different inflammatory contexts. As such, broad activation or inhibition of MyD88 would not only likely not prove effective in either cancer or HF, but also could lead to a variety of off-target side effects. In the case of T-cell MyD88, therapeutic intervention would require more precise control over the expression of MyD88 and it's interaction with BCAP (Figure 8-3). Increasing T-cell MyD88 levels as well as MyD88-BCAP binding would impair T-cell effector function and potentially protect from chronic cardiac inflammation and fibrosis in the case of HF. However, assuming shared mechanisms across $CD4^+$ and $CD8^+$ T-cells, the inhibition of $CD8^+$ T-cell activity could put patients at higher risk for cancer. This also brings up the question of how widely applicable my work on T-cell MyD88 is in other settings of inflammation. The finding that T-MyD88$^{-/-}$ mice have worsened systolic dysfunction and fibrosis in both the TAC model (Chapter 2) and Doxorubicin treatment (Appendix 9.3), and further that T-MyD88$^{-/-}$ mice have improved anti-tumor immunity (Chapter 4) would suggest that MyD88 is involved in any sterile setting in which TCR-dependent T-cell activation occurs. However, the literature in infectious immunity suggests that T-cell MyD88 plays a pro-inflammatory role, and that T-MyD88$^{-/-}$ mice would be protected from cardiac remodeling secondary to a pathogen, such as *Trypanosoma Cruzi* or Coxsackie virus. This also highlights the possibility that inhibition of T-cell MyD88 might put patients at higher risk of infection. Pharmacologic, rather than genetic manipulation of T-cell MyD88 would partially mitigate these risks by only putting patients at risk for the duration of their treatment, a

strategy that would only work in the case of acute diseases such as planned anthracycline treatment or the period following myocardial infarction, not chronic non-ischemic heart failure secondary to HTN.

One potential translational avenue for T-cell MyD88 in patients is that of adoptive cell therapy in the treatment of cancer, as shown in Chapter 4. Two studies now show that mice deficient in T-cell MyD88 exhibit enhanced anti-tumor immunity in melanoma.[118,400] However, in patients, T-cells would need to be modified *ex-vivo,* to avoid the risks discussed previously and off-target effects or MyD88 deletion in non T-cells. Interestingly, several pre-clinical studies in mice have employed CD40-MyD88 fusion proteins to enhance co-stimulatory signaling in CAR-T cells and improve anti-tumor efficacy in both solid and

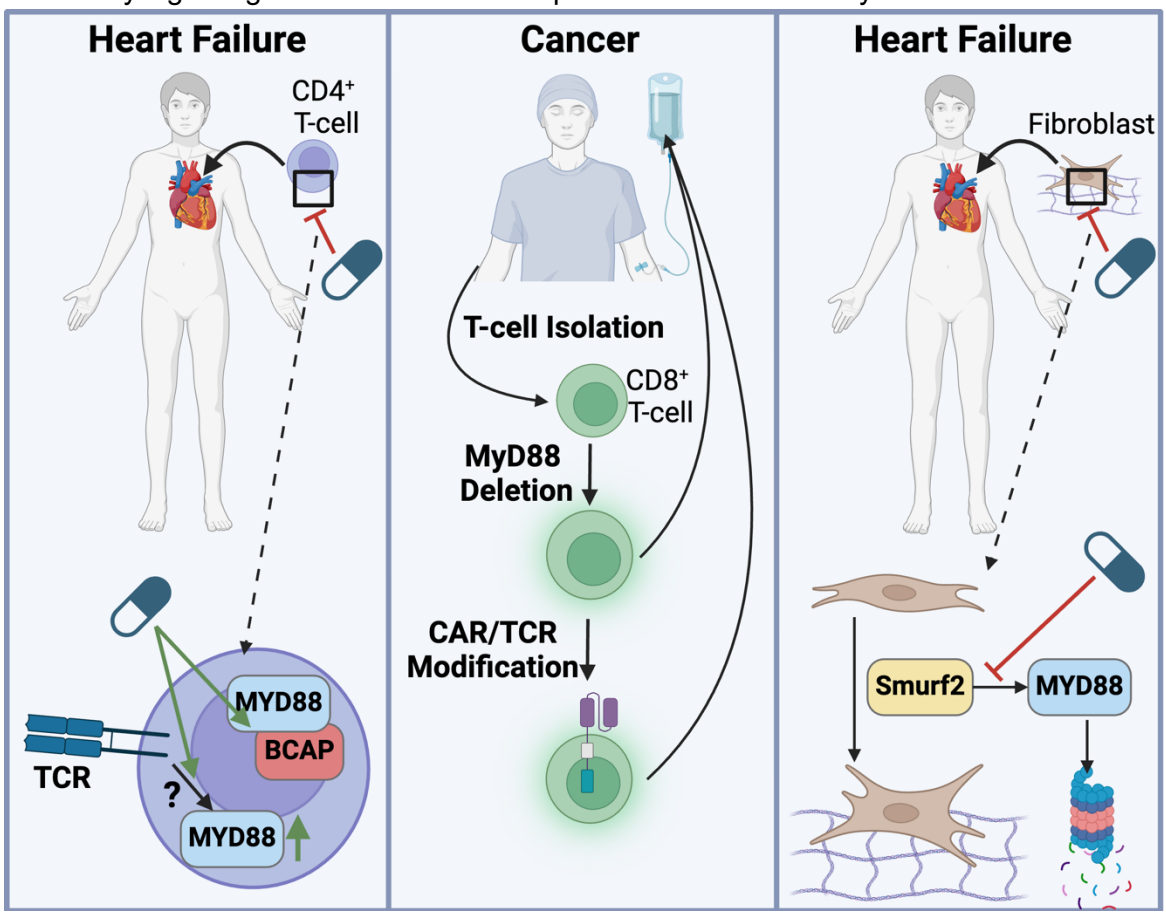


Figure 8-3 Potential Therapeutic Approaches in Heart Failure and Cancer Involving MyD88
Schematic showing therapeutic strategies for MyD88 suggested by the work in this thesis. Left: increasing T-cell MyD88 expression and/or promoting MyD88-BCAP binding would dampen T-cell activation in HF (Chapter 2/5). Middle: Deletion of T-cell MyD88 would enhance ant-tumor activity of ACT or CAR-T therapy (Chapter 4). Right: Inhibition of Smurf2-mediated MyD88 degradation would prevent cardiac fibrosis in HF. Figure made with Biorender.

hematologic malignancies, however all of these engineer MyD88 to force non-canonical signaling functions.[423,577,578] This more closely resembles the L265P activating mutation of MyD88, raising the concern of secondary T-cell malignancy in this strategy. A different group overexpressed TLR2 in T-cells, which amplified melanoma killing, likely through a similar mechanism in which I employed in Chapter 4 by which TLR stimulation diminishes BCAP-MyD88 binding.[579] A different approach could be taken in patients, in which a patient's T-cells could be isolated and expanded, MyD88 could be deleted by CRISPR, then upon re-infusion, I would hypothesize T-cell anti-tumor activity to be enhanced (Figure 8-3). If effective, this strategy could be used synergistically with CAR modification, TCR modification, or any other genetic manipulation in ACT. As T-cells require specific chemokine signals to infiltrate the heart, such as CXCL9/10 in pressure overload or anthracycline cardiomyopathy, there would likely be a low risk of cardiac side effects to this therapeutic strategy. However, in my work shown in Chapter 4 of this thesis, I did not check for increased cardiac T-cells, therefore the possibility of cardiotoxicity remains.

Control over fibroblast MyD88 expression could also represent an anti-fibrotic therapeutic approach in multiple etiologies of HF. My data in Chapter 3 of this dissertation show that CFB-MyD88$^{-/-}$ mice have increased fibrosis in both TAC and PE/ANGII induced HF, and that this mechanism applies to human fibroblasts. While fibrosis across HF models is not identical, I hypothesize that MyD88 regulating fibroblast activation is a conserved mechanism in HF and non-cardiac fibrosis. As such, the restoration of MyD88 expression through inhibition of Smurf2 could prevent the chronic development of fibrosis (Figure 8-3). This could not be used in all HF, as inhibiting fibrosis acutely in MI could be dangerous due to risk of cardiac rupture. There is further a chance this could impair wound healing by altering skin fibroblasts, although this risk could be considered minor compared to the mortality of HF. Further, in the case of anthracycline induced cardiac fibrosis, inhibiting fibroblast activation could prove beneficial in anti-tumor immunity by blunting ECM

production by cancer associated fibroblasts in the tumor impairing T-cell infiltration. However, the function of cancer-associated fibroblasts is complicated, and as such potential off-target effects of Smurf2 inhibition in cancer patients would need to be closely monitored.

8.4 Fibroblast States and Function

8.4.1 Comparison of Fibroblast Activation Across Models

As discussed in section 1.3.5, cardiac fibroblasts are a plastic cell type that can exhibit specific functions depending on the state they are in.[245,253] The work presented in this dissertation outlines several new mechanisms regulating the transition of quiescent fibroblasts to pro-fibrotic myofibroblasts. First, this work builds upon the previous finding that Th1 cells can induce TGFβ-dependent myofibroblast transformation through binding to VCAM-1 on fibroblasts.[229] I show that MyD88$^{-/-}$ Th1 cells, which exhibit enhanced activation through the TCR, are more adept at binding to VCAM-1 on fibroblasts or on coverslips (Chapter 2), which results in enhanced fibroblast transformation. Additionally, my data shows that MyD88$^{-/-}$ fibroblasts exhibit increased transformation in response to TGFβ signaling due to increased Smad translocation to the nucleus (Chapter 3). Interestingly, I show that Doxorubicin is able to directly activate myofibroblasts (Chapters 6&7) through a TGFβ independent mechanism (Appendix 9.4). However, Doxorubicin also primes fibroblasts to interact with Tc1 cells by increasing ICAM-1, which Tc1 cells bind to promoting TGFβ-dependent transformation, similar to Th1 cells (Chapters 6 and Appendix 9.4). The breadth of this work outlines the diverse triggers that fibroblasts are able to recognize and thereby induce subsequent fibrosis (Figure 8-4). As discussed below, while the work presented here outline regulators of myofibroblast state and inflammatory fibroblast state, the heterogeneity and plasticity of fibroblast biology make possible these states are not equivalent, and include transitional or overlapping states.

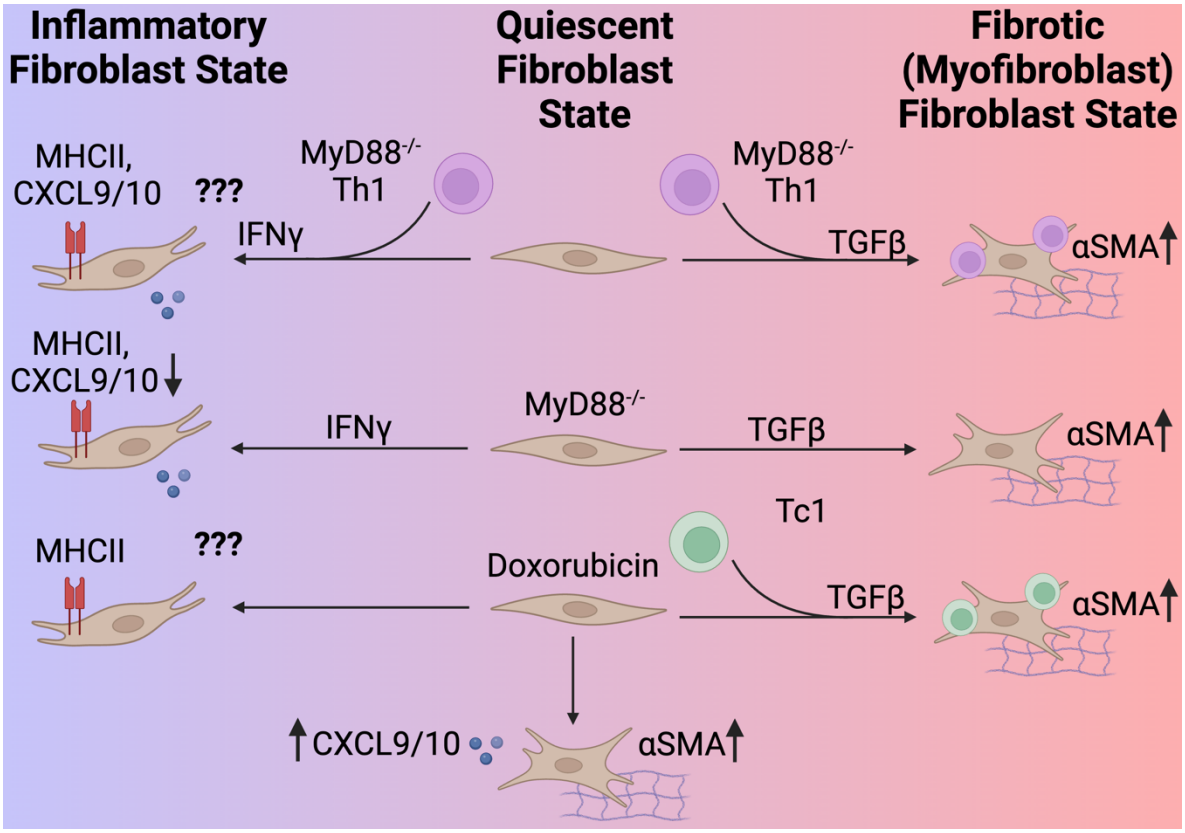


Figure 8-4 Summary of Mechanisms Regulating Fibroblast State Studied in This Dissertation.
Figure made with Biorender.

8.4.2 T-cell Fibroblast Cross-talk

This work shows two independent examples of T-cell fibroblast cross-talk, and highlights that different immune cells can use different ligands to interact with fibroblasts. Additional examples of immune cell fibroblast cross-talk have been shown in both models of pressure overload and in human heart failure, especially that of macrophages. The mechanisms of such cross-talk can also include soluble factor secretion, not only physical contact.[52,194,580] In this example, MyD88 deletion or inhibition might impair macrophage secretion of IL-1β, decreasing fibrosis, whereas MyD88 deletion in T-cells increases fibrosis, highlighting need for cell-specific therapies and mechanisms. As Doxorubicin did not increase VCAM-1, the ligand for $CD4^+$ T-cells, and Th1 cells do not accumulate in the hearts of mice treated with Doxorubicin, this supports that $CD8^+$ T-cells are the major immune driver of fibrosis. It also

remains unknown if macrophage or other immune cell interactions with fibroblasts promote fibrosis in anthracycline cardiotoxicity, in addition to $CD8^+$ T-cells. One remaining question in our work on T-cell fibroblast cross-talk is the cellular mechanism downstream of ICAM-1 or VCAM-1. Several signaling pathways downstream of these molecules could promote TGFβ secretion, such as AKT or MAPK, but this remains an ongoing area of investigation.[581,582] As my data points to both TGFβ dependent and independent mechanisms of fibrosis, the clinical relevance of drugs like Pirfenidone in preventing anthracycline induced cardiac fibrosis could be limited, and rather other pathways could more adequately block fibrosis. Further, previous work by our lab showed a requirement of $CD4^+$ cell IFNγ for promoting fibrosis in TAC, however the *in vitro* work in Appendix 9.4 suggests that $CD8^+$ IFNγ is not required for cross-talk after Doxorubicin treatment. While I showed cardiac T-cells increase IFNγ expression in the heart after Doxorubicin treatment, blocking studies would be required to delineate the function of IFNγ signaling in promoting fibroblast transformation or other elements of cardiotoxicity.

8.4.3 Inflammatory Fibroblast States and Fibroblast Heterogeneity

Our group has shown T-cell sourced IFNγ promotes cardiac fibroblasts to become antigen presenting cells, an “inflammatory” state of fibroblasts.[231] As anthracyclines induce Tc1 cells with high IFNγ expression, it is quite plausible that $MHCII^+$ fibroblasts play a mechanistic role in cardiac inflammation after Doxorubicin treatment. While $CD4^+$ depletion at 4 weeks did not show protection, at more chronic timepoints fibroblast antigen presentation could expand a pathogenic $CD4^+$ T-cell subset in the heart. Alternatively, $MHCII^+$ fibroblasts could also cross-present antigen to cardiac $CD8^+$ T-cells, something that has been shown in the context of cancer.[583] Further, we have shown that in pressure overload, fibroblasts secrete CXCL9/10 to promote $CD4^+$ T-cell cardiotropism. This mirrors the data shown in Chapter 7, in which Doxorubicin treatment induces fibroblast CXCL9/10

expression that contributes $CD8^+$ T-cell cardiotropism. This would suggest that pressure overload and Doxorubicin treatment induce a similar inflammatory state in fibroblasts characterized by chemokine secretion. While T-cell sourced IFNγ would further enhance chemokine secretion, as chemokines precede T-cell infiltration, an additional molecular trigger must exist that could be shared between the models.

However, in the case of Doxorubicin, my *in vitro* data support that the fibroblasts that secrete chemokine are also αSMA positive, whereas in pressure overload it is not known if these are distinct populations or not. The concept that fibroblasts could simultaneously exhibit inflammatory and fibrotic functions highlight the complexity, and potential plasticity of fibroblast states. A majority of my work in this dissertation uses αSMA and POSTN as markers of myofibroblast transformation, however there are limitations to these markers, and heterogeneity in $\alpha SMA^+/POSTN^+$ exists, especially likely with different triggers. One example shown here is that washout of Doxorubicin results in the reversal of αSMA expression, whereas TGFβ induced αSMA expression is not usually reversible,[584] indicating a different "myofibroblast" state. Understanding the specific molecular changes DR induces in fibroblast would help determine this. Likely, distinct pathways from those induced by T-cell contact are activated in fibroblasts by Doxorubicin directly, and in Appendix 9.4 I show that Doxorubicin treatment induces AKT, NF-kB, MAPK, STING, and p53 activation, although the functional significance of each pathway has not yet been tested. However, $STING^{-/-}$ fibroblasts did not increase αSMA, and CFB-$STING^{-/-}$ mice were protected from fibrosis, indicating this pathway as critical in mediating DR induced fibrotic activity, whether that be a true myofibroblast state or not. It is also unknown if immunologic fibroblast states such as MHCII expression or chemokine secretion are reversible, whether that be in response to IFNγ or Doxorubicin. For a more thorough characterization of fibroblast state, unbiased single-cell sequencing techniques could be used in both pressure overload and anthracycline models. This would allow for a transcriptional comparison of $\alpha SMA^+/POSTN^+$ fibroblasts across

models, as well as delineate different inflammatory, fibrotic, and potentially novel subsets of fibroblast contributing to each disease. Further, characterization of fibroblast subsets after withdrawal of pressure overload or Doxorubicin would help determine reversibility and chronic risks for patients.

8.4.4 MyD88 Regulation of Fibroblast State:

The work in this dissertation presents three examples of MyD88 modulating cardiac fibroblast state. T-cell Myd88 dampening myofibroblast activation through inhibition of T-cell activation and fibroblast binding (Chapter 2), fibroblast MyD88 inhibiting myofibroblast activation through limiting Smad translocation downstream of TGFβ (Chapter 3), and fibroblast MyD88 decreasing IFNγ responsiveness and inflammatory functions (Appendix 9.1). I would hypothesize that T-cell MyD88 would be limited to regulation of myofibroblast state and not inflammatory functions, as WT and MyD88$^{-/-}$ Th1 cells secreted similar IFNγ. However, these data alone highlight the need to understand cell-specific functions of MyD88, and evidence why broad MyD88 or PAMP/DAMP inhibition would not be an effective therapeutic approach. This concept is further highlighted by examples in the literature using global MyD88 deletion. One group showed MyD88$^{-/-}$ mice to have decreased scar size and cardiac cytokine expression compared to WT in MI,[585] whereas another group found MyD88$^{-/-}$ zebrafish to have enhanced cardiac fibrosis and inflammation.[535] Whether fibroblast MyD88 mediates Doxorubicin induced αSMA expression is unknown, however as this appears to be TGFβ independent (Appendix 9.4), likely the answer would be no.

Other studies have shown fibroblast MyD88 to alter state and other contexts. In macrophages, MyD88 stabilized IFNγ inducible transcripts, and deletion decreased IFNγ responsiveness, in line with my results in Appendix 9.1[586] siRNA knockdown of MyD88 in gingival fibroblasts altered the cytokine profile after TLR stimulation, suggesting a shift in inflammatory state.[587] In a liver fibrosis model, MyD88 deletion in fibroblasts instead

decreased myeloid cell recruitment, cytokine and chemokine expression including CXCL10, and overall fibrosis.[588] The impaired inflammatory state the authors observe is in line with the data shown in Appendix 9.1. However, decreased fibrosis could be a difference in liver fibroblasts vs. cardiac, or instead that the authors used an αSMA Cre driver rather than our Tcf21 driver, bypassing the regulatory role for MyD88 in fibroblast transformation and deleting it only once fibroblasts became activated. This deepens the role for fibroblast MyD88 by suggesting it not only regulates fibroblast states themselves, but has different functional roles as well.

The most well-studied context for fibroblast MyD88 is in cancer models. Three independent studies show that deletion of fibroblast MyD88 decreases tumorigenesis in the liver and colon.[536–538] This work again shows decreased inflammatory cytokines and altered macrophage polarization, suggesting that the inflammatory function of MyD88 in fibroblasts is more widely conserved. However, these studies also show decreased αSMA in the absence of MyD88, but again using different Cre drivers. Whether the differences is a Cre driver, organ specific, or even that αSMA expression is driven by a non-TGFβ dependent mechanism remains unknown. An additional question remains when studying fibroblast function in cancer models: are the various inflammatory or fibrotic phenotypes observed a result of resident fibroblasts, or altered “tumor associated fibroblasts” which play varying roles in cancer progression?[589] It is entirely plausible that MyD88 contributes to fibrotic activity in hepatic stellate cells, for example, but also mediates inflammatory function in hepatocellular carcinoma-associated fibroblasts. This could be distinguished using single-cell transcriptomics or spatial transcriptomics on tissue samples that include healthy tissue and cancer tissue.

8.5 Remaining Questions on the T-cell Response in Anthracycline Cardiomyopathy

8.5.1 Potential Antigens in Anthracycline Cardiotoxicity

My data characterize a cardiac directed $CD8^+$ T-cell response after anthracycline treatment in mice and patients (Chapter 6/7). Using antigen restricted OTI mice, I found that $CD8^+$ T-cell activation, cardiotropism, and pathology are dependent on the presence of an antigen. This concept is further supported by the finding that T-$MyD88^{-/-}$ mice exhibit worsened cardiotoxicity in response to Doxorubicin (Appendix 9.3), as MyD88 modulates TCR-dependent signaling, implying antigen recognition through the TCR in the context of Doxorubicin treatment. However, my work has not yet delineated what antigen(s) these T-cells respond to (Figure 8-5). One possibility is the formation of neo-antigen in the heart. Our group has previously shown that pressure overload induced by TAC results in oxidative stress, and the subsequent formation of Isolevuglandin species (IsoLGs), proteins with oxidized lipid adducts that stimulate a $CD4^+$ T-cell response.[450] As Doxorubicin causes oxidative stress in the heart,[310,485] it is plausible that similar IsoLGs form and drive the $CD8^+$ T-cell response that I observe. However, TAC induces primarily a Th1 response, whereas Doxorubicin induces a Tc1 response, indicating if IsoLGs were the antigen, other factors would help shape the T-cell response.

Others have shown various epitopes in cardiomyocyte α-myosin heavy chain (aMHC) can induce $CD8^+$ and $CD4^+$ T-cell activation in the context of ICI myocarditis, myocardial infarction, and autoimmune myocarditis.[208,455,590,591] This response stems from the finding that aMHC is not expressed in the thymus during T-cell development, leading to potential auto-reactive clones that can be triggered by a break in tolerance, such as ICI therapy.[208] Other antigens inducing a cardiac T-cell response have been described, including the β-adrenergic receptor or mitochondrial enzymes.[592,593] However, in either case the question still remains of why Doxorubicin induces a break in tolerance that triggers a T-cell response. Genetic risk

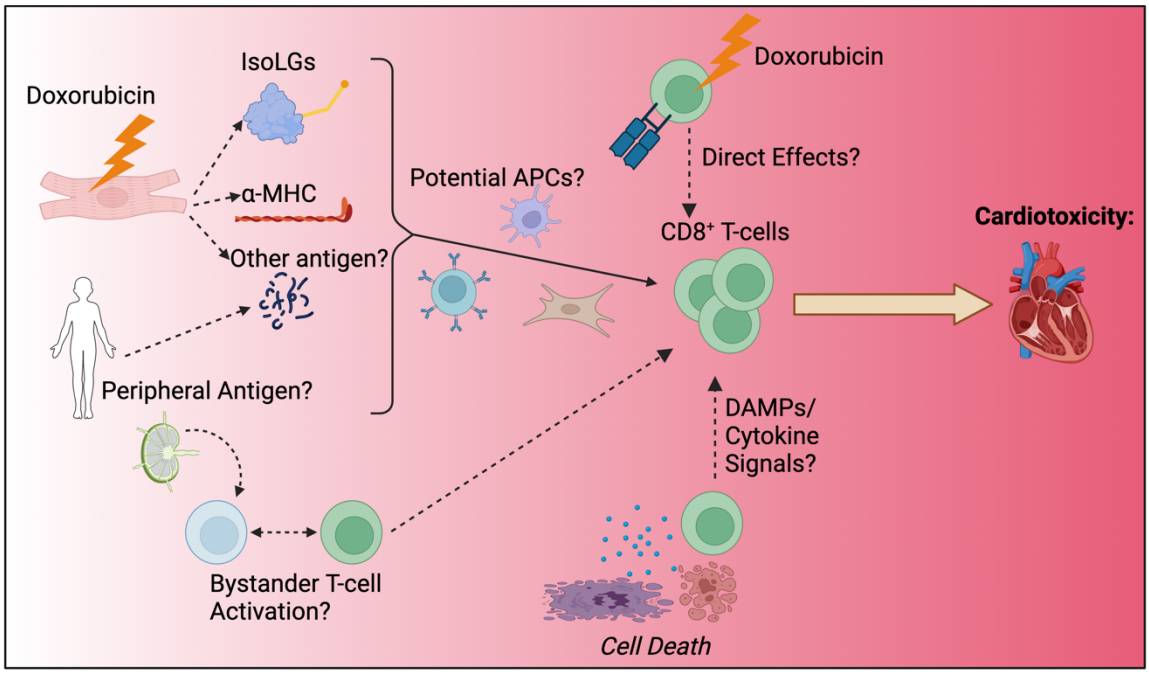


Figure 8-5 Potential Antigens and Mechanisms of T-cell Activation in Doxorubicin Cardiotoxicity
Schematic showing potential antigens – Isolevuglandins (IsoLGs), alpha-mysoin heavy chain (aMHC) or other antigens in the heart/periphery. The antigen presenting cell (APC) and mechanisms of bystander activation or direct effects from Doxorubicin on T-cells are not fully known. Figure made with Biorender.

factors have been associated with anthracycline cardiotoxicity,[594,595] and while HLA alleles have not yet been studied, patients might inherit specific HLA haplotypes that make presentation of anthracycline-associated antigens to T-cells more likely. Another possibility includes direct effects of Doxorubicin on T-cells. While my work showed Doxorubicin to induce T-cell cytokine secretion and degranulation, the exact molecular effects of Doxorubicin on T-cells are somewhat unknown. Doxorubicin could alter pathways involved downstream of the TCR that elevate TCR signaling above the threshold that self-antigens normally would induce, leading to full activation rather than anergy. In appendix 9.6 I show Doxorubicin activates p53 and HIF1α signaling, which could be broader mechanisms regulating T-cell activity in DR cardiotoxicity. Additionally, I showed that Doxorubicin increases mLN Foxp3^{+} T-regs, but it is plausible that these T-regs are dysfunctional in the setting of Doxorubicin cardiotoxicity. Dysfunctional T-regs have already been shown to contribute to atherosclerosis and myocardial infarction,[596,597] and as such future studies of

Doxorubicin induced T-regs could provide insight into potential auto-reactive $CD8^+$ T-cell escape.

8.5.2 Mechanisms of T-cell Activation and Adaptive Immunity in Doxorubicin Cardiotoxicity

In addition to the antigen that T-cells respond to, the exact mechanisms leading to T-cell activation have not been discovered (Figure 8-5). My work showed increased effector T-cells in both the spleen and the mediastinal lymph nodes (mLN), implying T-cell activation occurring in those sites. I did not see striking changes to the myeloid compartment in the heart, spleen, or mLN of mice treated with Doxorubicin, leaving unknown the potential antigen presenting cells involved in $CD8^+$ T-cell activation. I did observe a non-significant trend down in overall cardiac $CD11b^+$ cells after Doxorubicin treatment, therefore I hypothesize that dendritic cells migrating with cardiac antigen from the heart to the lymph nodes could activate $CD8^+$ T-cells.

A recent study also implicated B-cells in the development of Doxorubicin cardiotoxicity. These authors showed Ig deposition in Doxorubicin treated mice as well as a protective effect from B-cell depletion in the onset of Doxorubicin treatment.[338] While antibody deposition could induce complement dependent killing of cardiomyocytes, the exact mechanisms of B-cell induced cardiac damage were not fully explored in this paper. It is possible that in addition to antibody secretion, B-cells are acting as antigen presenting cells for $CD8^+$ T-cells in Doxorubicin treated mice. In this scenario, B-cell/T-cell cross-talk could also shape the humoral immune response. As Ig deposition was shown to occur alongside cardiotoxicity, $CD8^+$ T-cell cytokine secretion could in then influence activated B-cells to differentiate into IgG^+ antibody secreting cells. Both my study and this study did not look for increased cardiac B-cells after Doxorubicin treatment, leaving open the possibility that B-cells can directly induce cardiac damage, or simply that they act through antigen

presentation and antibody secretion alone. Our lab's work has also shown fibroblasts to present antigen to $CD4^+$ T-cells after T-cell derived IFNγ recognition.[231] As I have shown $CD8^+$ T-cells to express high IFNγ in Doxorubicin injured hearts, it is similarly plausible that fibroblasts can reactivate $CD8^+$ (or $CD4^+$) T-cells through antigen presentation after trafficking to the heart.

There is also the possibility of antigen-independent T-cell activation co-occurring in this model, such as bystander T-cell activation. While our work showed that Doxorubicin was not able to directly induce T-cell activation (Chapter 6), it could aid in activation through other mechanisms. Doxorubicin causes apoptosis of cardiomyocytes, but can induce cell death through different mechanisms in different cell types.[483] While I have shown that T-cells did not respond to cardiac DAMPs in the setting of TAC (Chapter 2), there is much greater cardiac cell death in this model, making it possible that DAMP-induced bystander activation is occurring. Additionally, *in vitro* studies show that Doxorubicin causes T-cell death as well as increases cytokine secretion. This suggests that T-cell death might drive the activation of neighboring T-cells through DAMP signaling, explaining the co-occurrence of cell death and increased effector functions, and proposed in other contexts.[598] However, these two possibilities are less likely, considering that T-cell MyD88 deletion is not protective but worsens Doxorubicin cardiotoxicity (Appendix 9.3). However, it is not known yet if the antigen driving cardiotoxicity is cardiac or derived from elsewhere in the periphery. It is plausible that systemic antigen might initiate T-cell activation in lymphoid organs, but Doxorubicin among other signals could drive secondary bystander T-cell activation, and this subset of T-cells then drives cardiac pathology (Figure 8-5).

8.5.3 The Role of $CD4^+$ T-cells

The data presented in Chapters 6 and 7 implicate $CD8^+$ T-cells as the pathogenic T-cell subset involved in anthracycline cardiotoxicity. When $CD4^+$ T-cells were depleted in short

term Doxorubicin treatment, the mice trended towards worse systolic dysfunction and fibrosis, which I attributed to loss of T-regs that help to dampen $CD8^+$ function. However, it remains to be seen the mechanism by which Doxorubicin induces T-regs *in vivo.* While I did show increased $Foxp3^+CD4^+$ T-cells in the mLN Doxorubicin treated mice, $CD4^+$ T-cells might play diverse roles beyond just a localized T-reg response. Increased mLN T-regs does not mean broadly increased T-regs, therefore the $CD4^+$ T-cells in the heart might not be anti-inflammatory. While I only observed a trending increase in cardiac $CD4^+$ T-cells in mice treated with Doxorubicin, they might change in character, rather than number. It is also more likely they were not recruited in the same manner as $CD8^+$ T-cells, as increased cardiac CXCL9/10 could potently recruit Th1 cells that express high CXCR3.[472] If a cardiac $IFN\gamma^+CD4^+$ T-cell population appeared with longer Doxorubicin treatments, longer term depletion might instead show protection. This could potentially be attributed to localized antigen presentation in the heart secondary to increased cardiac IFNγ whether that be by professional APCs or fibroblasts. As the highest site of Tc1 expansion was the mLN, where T-reg expansion also occurred, this is suggestive that both $CD8^+$ and $CD4^+$ T-cells are both responding to the same antigen. In future studies that seek to define the antigen(s) in Doxorubicin treated mice, we can delineate whether that antigen can induce co-existing $CD8^+$ activation and $CD4^+$ T-reg induction.

While Doxorubicin directly increased $CD8^+$ T-cell IFNγ production and degranulation, I did not investigate the effects of Doxorubicin on $CD4^+$ T-cells. The same effect on IFNγ might be recapitulated in *in vitro* $CD4^+$ T-cells treated with Doxorubicin. Previous work has shown that Doxorubicin increased $CD4^+$ T-cell expression of CD40 and 4-1BB, *in vitro* leading to increased activation.[599] This study, however, showed no effect on T-regs *in vivo* and *in vitro.* This suggests that Doxorubicin itself is likely not inducing the T-reg phenotype that I observed, and instead might result in chronic changes to existing $CD4^+$ T-cells. Interestingly, while the data I collected from patients showed increased $CD8^+$ T-cells but no

change to $CD4^+$ T-cells, another study showed decreased $CD4^+$ T-cells and T-regs in breast cancer patients treated with Doxorubicin.[600] The authors comment that this overall increased the $CD8^+/CD4^+$ T-cell ratio, which is what I observe, however this also could be a malignancy specific effect, as the patients from my study were hematologic malignancies. This is made more likely by their finding that $Her2^+$ breast cancer patients had a higher $CD8^+/CD4^+$ ratio than $Her2^-$, indicating an effect by the malignancy.[600] However, as the role for $CD4^+$ T-cells in anthracycline cardiotoxicity is overall less understood thus far, future studies will help determine if broad T-cell targeting would be a viable strategy, or if $CD8^+$ specific therapies would be safer to avoid depletion of protective T-reg cells.

8.5.4 Age and Temporal Regulation of the T-cell Response

Throughout the Doxorubicin experiments shown in Chapters 6 and 7, I utilized treatment for 4 and 8 weeks to show potential changes in the inflammatory response over time. While some changes were consistent across both time points, such as systolic dysfunction, or overall cardiac $CD8^+$ T-cells, readouts such as effector $CD8^+$ T-cells and memory $CD8^+$ T-cells were regulated across the two time points. Additionally, while at 4 weeks of treatment the TUNEL positivity in the hearts was not significantly different between WT and *Tcra*$^{-/-}$ mice, at 8 weeks there was a significant difference. Examples such as these imply that the T-cell response is not simply turned on or off with Doxorubicin treatment, but is progressive and shaped over time during the course of treatment (Figure 8-6).

Additional time points might elucidate more information about the characteristics of the T-cell response. One question that remains is how early lymphoid $CD8^+$ T-cell activation and cardiotropism occurs? If these changes occur prior to cardiomyocyte death or systolic dysfunction, there is a potential for early intervention to prevent cardiotoxicity with anti-inflammatory agents. That also suggests that the T-cells might respond to a non-cardiac antigen, or that the initial triggering even might not be antigen dependent. Earlier time points

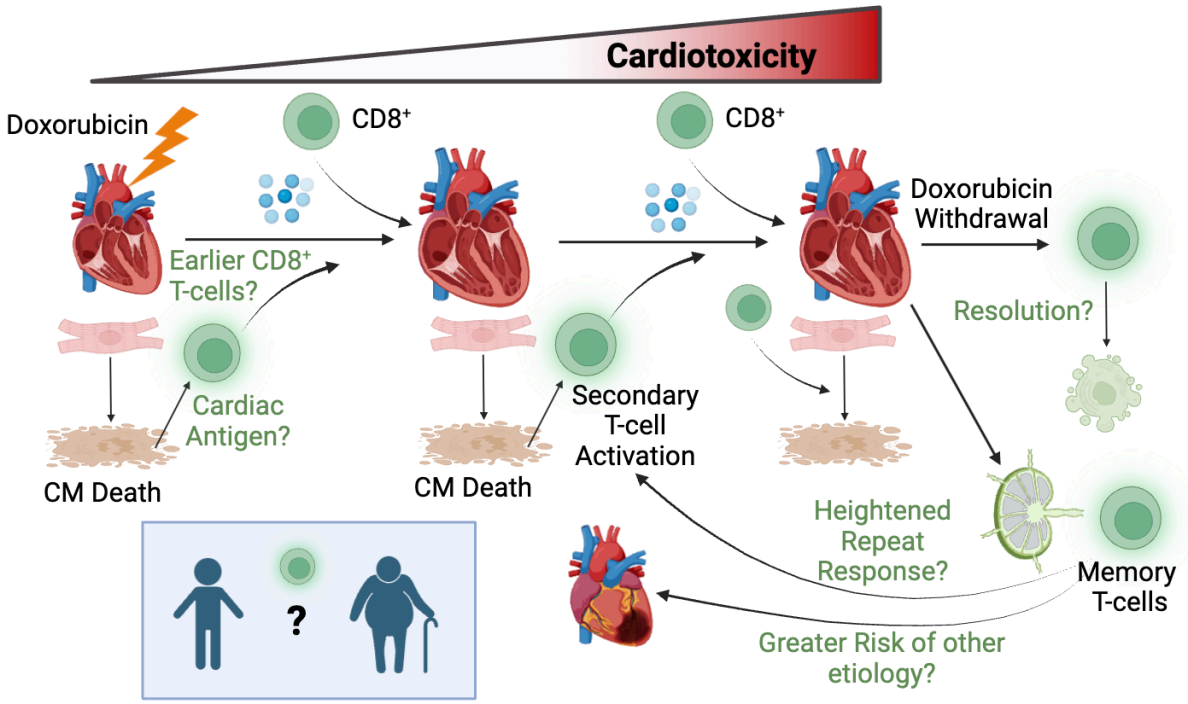


Figure 8-6 Temporal Regulation of the T-cell Response to Doxorubicin
Schematic showing what is known and what remains unknown about temporal regulation of T-cell activity in Doxorubicin treatment. T-cells infiltrate at early and late stages of Doxorubicin treatment, and contribute to later cardiomyocyte (CM) death. How early they infiltrate, what antigens induce them, resolution or repeat activation, and how age effects the response remain unknown. Figure made with Biorender.

in OTI mice would further answer this question. Alternatively, if the T-cell response coincides with the initiation of systolic dysfunction and cardiotoxicity, this makes a cardiac antigenic response more likely. The finding that T-cell dependent cardiomyocyte death occurs with 8 weeks of treatment does imply that some T-cell functionality occurs secondary to cardiac damage. This parallels the chronic T-cell response seen in MI, where cardiac necrotic cell death precedes antigen specific $CD4^+$ T-cell responses.[591,601]

After 8 weeks, even when Doxorubicin was stopped in mice, rapid mortality occurred (data not shown).To study longer time points, Doxorubicin would need to be stopped after fewer doses, or potentially a different dosing strategy employed. This would also help answer if the T-cell response subsides after Doxorubicin is withdrawn and could determine risk of T-cell driven cardiotoxicity long term in patients. I would hypothesize that ongoing T-cell recruitment and activation would diminish in this scenario. Chemokine expression is partially driven by Doxorubicin itself, and assuming cardiac antigen drives some degree of T-

cell activation, this would dampen ongoing recruitment to the heart. My data showed elevated T-cells at 3-4 months after anthracycline initiation in humans and canines. These time points are still relatively recent after treatment, and following these patients with serial blood samples for longer would help characterize chronic inflammation better. However, the finding that memory T-cells increased at 8 weeks of Doxorubicin treatment in mice does imply that chronic inflammation can persist. Memory T-cells could mediate several elements of chronic cardiotoxicity. First, patients usually receive anthracycline containing chemotherapy in 21 day cycles.[602] Once anthracycline-induced memory T-cells are formed, this could make the subsequent T-cell response to the next cycle heightened, one mechanistic explanation for the dose-dependent cardiotoxicity. Additionally, memory T-cells could put patients at higher risk of other forms of cardiovascular disease. While many studies show chronic elevated risk for HF in anthracycline treated patients[603], it is not known if this is from direct cardiac damage of anthracyclines or generally elevated risk. It is plausible that secondary cardiac insult such as hypertension or MI could reactive Doxorubicin-induced memory T-cells, especially if they are cardiac antigen directed.

Finally, all of my pre-clinical studies used mice at around 8 weeks of age, when they reach sexual maturity. This would roughly model adolescence in human patients. Pediatric cancer patients treated with anthracyclines can develop both acute, and chronic cardiotoxicity many years after their cancer treatment.[604,605] While many of the mechanisms of Doxorubicin apply to both children and adults, it is unknown if the immune response is affected by age. Using mice of varying ages, especially older mice, would determine if the T-cell response is similar across age and if potential immunotherapies could be more or less beneficial in certain populations. In the small patient cohort that I collected, the ages ranged from 28 to 66, and all patients had elevated $CD8^+$ T-cells in circulation. While this is a wide age range, this finding cannot necessarily be applied to pediatric patients. An additional consideration in pediatric patients is that of thymic T-cell development. While a majority of T-

cells develop early in life, T-cell development continues and thymic involution occurs during adolescence.[172] It has also been shown that impairing T-cell development impairs thymic involution.[606] There is potential that Doxorubicin could impair T-cell development or alter the process of involution, leading to increased risk for cardiac inflammation in pediatric patients later in life. On the other hand, it is well established that T-cells from aged patients undergo significant changes compared to T-cells from young patients, including exhaustion, alterations to metabolism, senescence, and more, another potential regulator of the cardiac inflammatory response to Doxorubicin in older vs. younger individuals.[607,608]

8.5.5 T-cell Cross-talk with Cardiac Cells

In Chapter 6, I outline $CD8^+$ T-cell cardiac fibroblast cross-talk that contributes to cardiac fibrosis after anthracycline cardiomyopathy. I showed that fibroblast transformation and $CD8^+$ T-cell binding was dependent on Doxorubicin induced ICAM-1 expression. However, as previously discussed, the fibroblast intracellular signaling in response to T-cell contact is not yet known. While my work showed T-cell sourced Granzyme B to be a pro-fibrotic factor, additional signals downstream of ICAM-1 or other T-cell ligands could help induce fibrotic transformation. The use of Granzyme B knockout T-cells or conditional knockout mice could help elucidate the contribution of Granzyme B to fibrosis *in vivo.* Granzyme B has been shown to be pro-fibrotic in other contexts of CVD.[467,468] However, what remains unknown in these contexts or in Doxorubicin treatment is the potential cleavable targets or extracellular mechanisms[493] of Granzyme B that induce fibroblast transformation. Further study of the pro-fibrotic activity of Granzyme B would help support it as a potential therapeutic target. My data also suggests that Granzyme B release is dependent on T-cells, and can be induced by direct contact with fibroblasts. However, as the main mechanism for triggering degranulation of $CD8^+$ T-cells is TCR ligation,[609] this implies either cross-presentation of antigen by fibroblasts or a novel signal induced by Doxorubicin treated fibroblasts. Surprisingly, despite

increased release of cytotoxic molecules, I did not observe significant fibroblast death in co-culture experiments. Together this shows that fibroblasts are somewhat resistant to T-cell killing and instead respond by inducing fibrosis.

While fibroblasts are not killed by T-cell degranulation, cardiomyocytes are much more susceptible. Indeed, after longer Doxorubicin treatment I saw T-cell dependent cardiac TUNEL positivity, evidence that T-cells are directly killing myocytes. Whether that be by Granzyme or by direct death receptor ligation, such as Fas/FasL, remains unknown. While cardiomyocyte apoptosis is directly induced by Doxorubicin itself, they express many death receptors that could be triggered by $CD8^+$ T-cells.[610] The role of $CD8^+$ T-cell cardiomyocyte cross-talk might also extend beyond T-cell induction of myocyte death. In the TAC model, stressed cardiomyocytes induced $CD8^+$ T-cell degranulation and fibrosis by triggering NKG2D, and as such a similar mechanism could further induce degranulation in the context of Doxorubicin treatment.[451] Doxorubicin also induces cardiomyocyte atrophy. While most of my data showed that this was not overtly T-cell dependent, it is still plausible that chronic inflammation can contribute to cardiomyocyte remodeling. Several pathways have been implicated in the development of cardiomyocyte atrophy, such as the unfolded protein response, FOXO signaling, and IGF-1 signaling,[611,612] all of which could potentially be regulated by T-cells. I did show T-cell dependent changes in myosin expression and SERCA expression, the mechanisms for which remain unknown. However, it has been shown that IFNγ can regulate SERCA expression, cardiac atrophy, and myosin expression, and as such secretion of this cytokine might be critical in T-cell induced cardiomyocyte dysfunction.[613,614]

The final cardiac cell type I found that interacts with T-cells in the context of anthracycline treatment is endothelial cells. As endothelial cells regulate all immune cell infiltration into the heart,[159] I showed in Chapter 7 that Doxorubicin increases T-cell chemotaxis on endothelial cells and subsequent transendothelial migration. This point of interaction is critical for $CD8^+$ T-cell induced cardiotoxicity, as $STING^{-/-}$ mice and $STING^{-/-}$

endothelial cells had impaired migration and as such were protected. Other interactions might exist between T-cells and endothelial cells. While Doxorubicin induces the initial chemokine driven T-cell cardiotropism, both T-cell derived IFNγ and TNFα likely further increase endothelial activation and T-cell recruitment. Additionally, Doxorubicin has been shown to induce endothelial to mesenchymal transformation (EMT) in cancer cells.[615] EMT has not yet been explored in the context of Doxorubicin cardiotoxicity, but as I observed perivascular fibrosis dependent on T-cells, both signals from T-cells and Doxorubicin might induce EMT. Finally, many other cell types in the heart might participate in the pathophysiology of Doxorubicin cardiotoxicity that I did not explore. $CD8^+$ T-cell derived IFNγ regulates smooth muscle cell activity in atherosclerosis,[616] and could similarly cause cardiac vascular dysfunction in Doxorubicin cardiotoxicity. Pericytes have a diverse secretome and could also help recruit $CD8^+$ T-cells to the heart. Unbiased single cell transcriptomics paired with receptor-ligand prediction analysis could help uncover many mechanistic interactions between $CD8^+$ T-cells and other cardiac cells.

8.5.6 DNA Damage and the T-cell Response

Doxorubicin is well known to cause DNA damage, which can be a potent trigger of inflammation. As such, several studies have looked at the DNA damage response as a mechanism for Doxorubicin cardiotoxicity. Previously, Doxorubicin has been shown to activate STING in cardiac fibroblasts, endothelial cells, and cardiomyocytes, and each has been proposed as a cell-specific target. [133,332,617] As STING is ubiquitously expressed in all cell types,[125] I hypothesized Doxorubicin would activate STING in most cell types. Previous studies not only focused in on STING in one cell type, using cell-specific knockouts of each one, but also did not study the inflammatory response as a whole. As the chemokines CXCL9/10 that my previous work had implicated (Chapter 6) can be downstream of STING-mediated type I interferons, I chose to study STING in the context of T-cell recruitment. My

work showed that in fibroblasts, endothelial cells, and myeloid cells, Doxorubicin activated STING and induced CXCL9/10 expression (Chapter 7, Figure 8-7). Likely, most other cell types have some degree of STING activation in response to Doxorubicin, and additional cell-specific knockout mice could help answer this question, or snRNA seq could provide transcriptomic evidence of the degree of STING activation in each type. Interestingly, STING knockout both *in vitro* or using cell-specific mouse models only prevented $CD8^+$ T-cell recruitment in macrophages or endothelial cells, but not in fibroblasts. $STING^{-/-}$ fibroblasts were still able to produce CXCL9/10 and induce $CD8^+$ T-cell cardiotropism. This suggests that in fibroblasts, other DNA sensors can compensate for the loss of STING, such as NLRs, RLRs, endosomal TLRs, or AIM2, whereas in other cell types STING is the primary DNA sensing mechanism.[121] The role of additional DNA sensing machinery in Doxorubicin is not

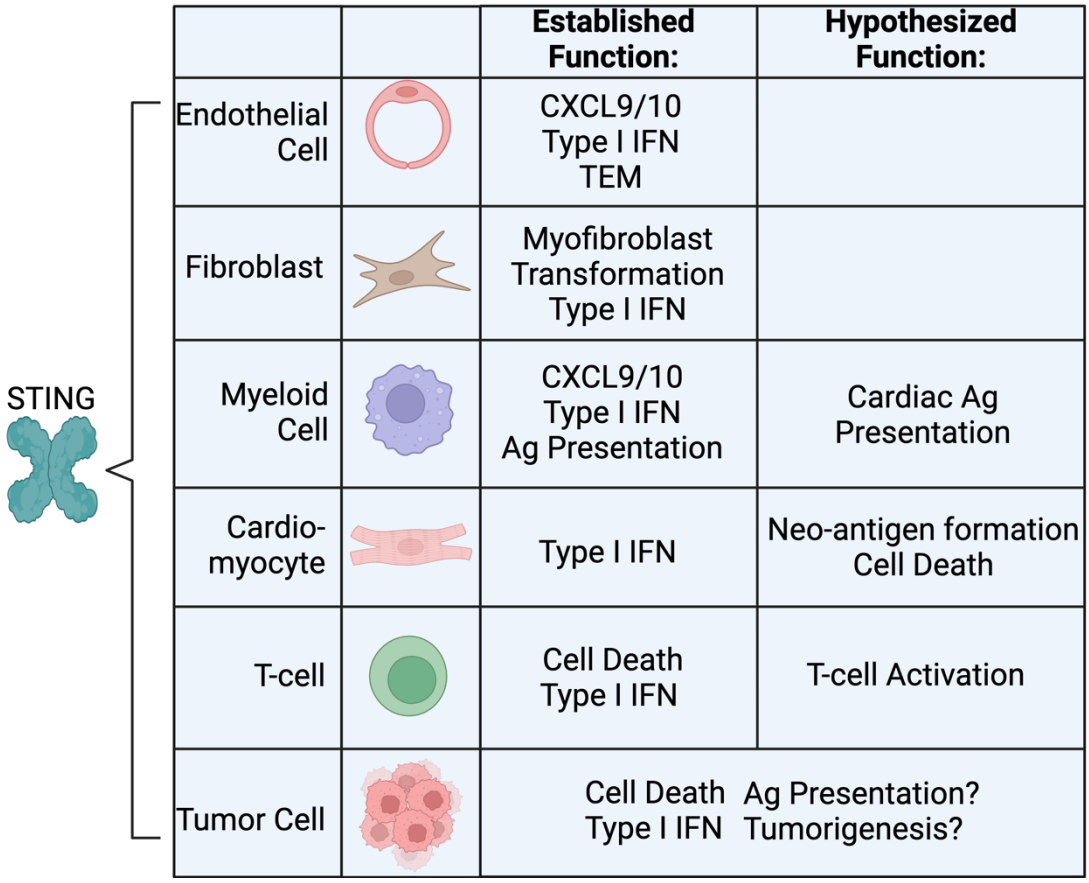


Figure 8-7 Established and Suggested Functions of STING in Selected Cell Types
Chart showing immunologic functions for STING in cardiac and tumor cell types, including what is shown in this dissertation, the literature, and potential hypothesized function. IFN = interferon, TEM = transendothelial migration, Ag = antigen. Figure made with Biorender.

yet known.

One outstanding question in my work is the mechanism of STING activation. Previous work in the literature has shown in each cell type, STING activation took place downstream of cGAS, leading us to believe that intracellular DNA is driving STING activation.[133,332,617] Whether this comes from the mitochondria or nucleus has only been shown in cardiomyocytes thus far.[617] However, as STING can be activated independent of cGAS through mitochondrial stress and the unfolded protein response[128,129], the relevance of these pathways in each cell type has not been fully studied. It is possible that in fibroblasts, for example, cGAS-STING signaling drives chemokine expression, but cGAS independent STING signaling drives fibroblast activation. Use of cGAS knockout mice and cells will help determine this. Knowing the exact triggers of STING in each cell type could help determine if cell specific STING therapies would be more effective than targeting STING broadly.

In global STING$^{-/-}$ mice, there was impaired CD8^{+} T-cell activation in the mLN, whereas each cell-specific STING mouse that I used did not alter mLN activation. While I tested activating STING$^{-/-}$ T-cells *in vitro,* which expressed similar activation markers and cytokines compared to WT, this does not rule out a role for STING in T-cells themselves. STING has previously been shown to regulate IFN production and cell death in T-cells,[491] but whether this contributes to the T-cell response in DR is not known. Alternatively, STING in other cell types could regulate T-cell activation. Impaired antigen presentation by myeloid cells could explain this, and while in global STING$^{-/-}$ mice there were no obvious changes to dendritic cell numbers in the heart or lymphoid organs, STING has already been tied to antigen presentation capability.[618] Another explanation could be downstream of cardiomyocyte STING. If we assume the T-cells are responding to cardiac antigen (as previously discussed), STING could mediate either cardiomyocyte death, as shown in Chapter 7 and in the other models[134], or could help induce cardiac neoantigens. In either case, in the absence of STING, we would observe decreased antigen for CD8^{+} T-cell activation.

Overall, while the exact cell-specific functions and mechanisms of STING in response to anthracyclines are still under study, the data presented in this dissertation and in previous studies support the use of broad STING inhibition to prevent Doxorubicin cardiotoxicity, through multiple cellular mechanisms. However, in patients with cancer, the effects on the tumor would be unclear. Activation of STING is a therapeutic approach to promote anti-tumor immunity, through type I interferons and increased antigen presentation.[619] However STING in cancer cells can promote tumorigenesis, but later stage tumors can downregulate STING for immune invasion.[135,619] Some pre-clinical data even show that STING inhibitors can sensitize tumors to other chemotherapeutic agents.[139] Overall, this highlights the need for further study of potential inflammatory modulating therapies for anthracycline treatment in the context of a tumor, not just in healthy hearts.

8.6 T-cell Therapies in Doxorubicin Cardiomyopathy

8.6.1 Anthracycline Induced Cardiac vs. Tumor T-cell Responses:

The work outlined in Chapters 6 and 7 of this dissertation show a critical role for $CD8^+$ T-cells in the development of systolic dysfunction and fibrosis in anthracycline chemotherapy. This suggests that targeting T-cells, or preventing them from trafficking to the heart could be a viable immunotherapeutic strategy in preventing cardiotoxicity from anthracyclines. However, as T-cells are a main anti-tumor immune cell,[81] it would be necessary to ensure that any therapy modulating cardiac T-cell activity does not impair anti-tumor activity, therefore worsening the progression of the patient's cancer. As much of the work presented thus far was done in healthy mice, this highlights the necessity of incorporating tumor bearing mice into pre-clinical studies of cardio-toxicity, as done in Appendix 9.2.[16] This would both better model the systemic inflammation of cancer patients, and would allow for simultaneous study of cardiac interventions and their effects on tumor progression.

Broad inhibition of T-cells through depletion or systemic immunosuppression is much more likely to have negative consequences on the tumor. This has been shown in mice,[620] and in patients while immunosuppression does not always increase the risk of developing cancer, it can have an impact on existing cancer's progression.[621–623] However, this brings up an important question regarding the T-cell response in anthracycline treated patients or mice. Is the anti-cardiac $CD8^+$ T-cell response targeting a distinct antigen from the anti-tumor $CD8^+$ T-cell response? The data generated in Appendix 9.2 suggest yes, as Doxorubicin induced cardiac $CD8^+$ T-cell infiltration in mice bearing melanoma and breast tumors, whereas Doxorubicin only effectively treated breast tumors. However, the only study of antigen specific T-cells I performed used antigen restricted OTI mice (Chapter 6), and as such the potential cardiac antigen currently remains unknown. If the cardiac antigen is distinct from tumor antigens, this would likely make inhibition of cardiac T-cell inflammation a more feasible protective strategy, whereas if no, this would be significantly more challenging. In the case of ICI myocarditis, work from Javid Moslehi's group has shown that $CD8^+$ T-cells target epitopes in α-myosin, a cardiac protein not expressed by cancer cells. In this work, they used TCR-sequencing to show the expansion of specific T-cell clones in ICI myocarditis, although tumor bearing mice again were not used. This strategy has been employed in the context of ICI myocarditis across tumor, heart, and blood, which revealed mostly non-overlapping TCR clones.[624] This could be similarly performed in tumor bearing mice treated with anthracyclines, or in anthracycline treated patients to determine shared clonality or not. However, currently approved anti T-cell therapies are able to target subsets of T-cells based on their antigen specificity, so even in the case of parallel, separate antigens, newer technologies must be developed or other approaches would have to be taken to specifically inhibit cardiac T-cells but not tumor T-cells. If both a cardiac neo-antigen was discovered and distinct from that of a tumor, study of the molecular mechanisms

triggering neo-antigen formation might lead to it's inhibition and the subsequent T-cell response (Figure 8-8).

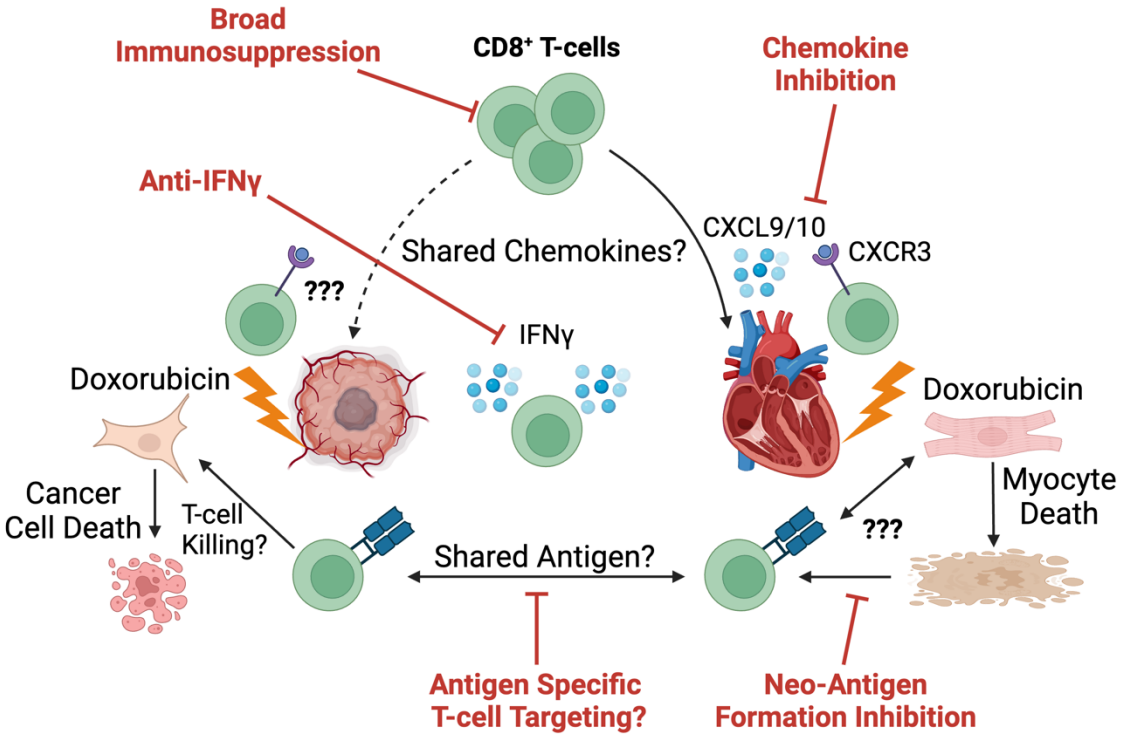


Figure 8-8 Opportunities for T-cell Anti-Inflammatory Therapy in Anthracycline Cardiotoxicity
Schematic showing the T-cell response in anthracycline cardiotoxicity and the anti-tumor response. Red text indicates potential places to inhibit cardio-toxic T-cell responses. Figure made with Biorender.

8.6.2 The Role for T-cells in Doxorubicin's Anti-Tumor Function

The second question when considering anti-T-cell therapies in anthracycline cardiotoxicity is if T-cells are even required for the anti-tumor effects? The main anti-tumor mechanism of action is through inhibition of DNA replication in tumor cells by Topoisomerase II inhibition.[310,625] However, there is some evidence of additional effects of Doxorubicin enhancing anti-tumor immunity, whether that be through directly altering immune cell function or secondary to tumor cell death.[475,625] The finding that Doxorubicin sensitizes tumor cells to both T-cell and NK cell mediated killing has been shown across multiple types of cancer including breast cancer.[626,627] Additionally, in both mouse models and patient cultures, Doxorubicin killed MDSCs, allowing for enhanced T-cell and NK cell killing of tumor cells.[628] Further studies have shown that Doxorubicin can increase $CD4^+$ T-cell activation,

through direct modulation of co-stimulatory signaling or through enhanced B-cell antigen presentation.[599,629] However, neither study showed a direct effect of Doxorubicin on $CD8^+$ T-cell activation or function. My data in Chapter 6 show that Doxorubicin causes $CD8^+$ T-cells to increase IFNγ expression and degranulation of Granzyme B. However, Doxorubicin did not increase intratumoral T-cells, and in fact increased T-cell exhaustion (Appendix 9.2) While these data together only suggest that Doxorubicin can enhance T-cell anti-tumor immunity, previous work has characterized roles for other immune cells, especially NK-cells. This implies that if an anti-T-cell therapy showed cardio-protection but impacted T-cell anti-tumor immunity, other immune cells such as NK cells could compensate for the loss of $CD8^+$ T-cells in the tumor microenvironment.

My work specifically characterized IFNγ expressing $CD8^+$ T-cells as the major drivers of cardiotoxicity in response to anthracyclines. IFNγ can also drive the expression of CXCL9/10, suggesting that targeting this cytokine might prevent ongoing T-cell recruitment to the heart after Doxorubicin treatment. *In vitro*, IFNγ was not required for $CD8^+$ T-cell activation of myofibroblasts after Doxorubicin treatment (Appendix 9.4), however I did not study the significance of IFNγ itself *in vivo* in the context of cardiotoxicity. Several other groups have attempted to utilize IFNγ blockade in anthracycline treated mice, with conflicting results. One group showed that in breast cancer bearing mice treated with Doxorubicin, IFNγ blockade preserved cardiac function in the absence of worsened tumor progression.[477] Others have shown IFNγ blockade with Doxorubicin worsened tumor progression in breast cancer, squamous cell carcinoma and cervical cancer.[475,630,631] These differences can be attributed in some circumstances to different types of tumors, which might have drastically different tumor microenvironments. Another explanation is that the first group only performed IFNγ blockade after Doxorubicin treatment was completed, while the others used longer term IFNγ inhibition or *in vitro* models. This implies that the cardiotoxic effects of IFNγ might take longer than the anti-tumor effects, and as such careful

study of *when* IFNγ inhibition is performed might make this a viable cardio-protective strategy.

8.6.3 Chemokine Therapies and Biomarkers

In Chapters 6 and 7, I showed increased $CXCR3^+$ $CD8^+$ T-cells in both mice and humans treated with Doxorubicin. While these studies did not use inhibition of this axis *in vivo*, *in vitro* CXCR3 blockade prevented T-cell chemotaxis towards Doxorubicin treated cells. This strongly suggests a functional role for CXCL9/10 in promoting cardiotropism after anthracycline treatment, and opens up the possibility that blocking this axis could prevent cardiotoxicity and ongoing T-cell recruitment. Antibodies to inhibit CXCR3 and CXCL10 have already been shown to be effective in many pre-clinical models of autoimmune diseases as well as ICI myocarditis.[486,496,497,632,633] Thus far, clinical trials have used CXCL10 antibodies in autoimmune disease, and shown mixed success, as one author wrote "The high production rate of CXCL10 makes it difficult to achieve drug levels that lead to sustained neutralization of the chemokine."[494,634] Together, I conclude that CXCR3 blockade would be a potential therapeutic approach in patients treated with anthracyclines, as Doxorubicin directly induces chemokines in cardiac cells, the patients would likely only need temporary CXCR3 blockade. However, this raises the same concern as discussed in section 8.5.3, if CXCR3 blockade would impact anti-tumor immunity. Interestingly, there are many examples of CXCR3 both promoting and inhibiting tumor progression[635–637], and while again this might be tumor or patient specific, this really highlights the need for deeper mechanistic studies of this chemokine axis in both cardiotoxicity and tumor immunity.

Interestingly, increased CXCL9 and CXCL10 correlated with systolic dysfunction in patients treated with anthracyclines (Chapter 6). However, to support CXCL9 and CXCL10 as potential biomarkers, this finding would need to be replicated in larger cohorts as well as tested to see if this was breast cancer specific or conserved across different malignancies.

We also performed similar analysis in a small cohort of B-cell lymphoma patients and did not find CXCL9/10 to correlate with systolic dysfunction (Data not shown), suggesting a malignancy dependent phenotype. Interestingly, neither dataset showed a strong correlation for cardiac function with IFNγ levels (Data not shown). This suggests that the direct increase in chemokine expression by Doxorubicin is a stronger trigger than T-cell sourced IFNγ, or that the temporal regulation of IFNγ is different than that of CXCL9/10. This is further suggested by one study that measured inflammatory markers in breast cancer patients treated with Doxorubicin, in which they found that patients with decreased LVEF had lower CXCL9 and IFNγ. This study only utilized plasma directly after the first and second cycles of chemotherapy, whereas I showed CXCL9 to correlate with cardiac dysfunction at both 3 and 6 months post initiation of anthracyclines. Overall though, there are strong preliminary data suggesting the utility of CXCL9 and CXCL10 as biomarkers in anthracycline cardiotoxicity.

8.6.4 Anthracycline Immune Checkpoint Inhibitor Cross-talk

As discussed in section 8.5.2, the functional role for T-cells in anti-tumor immunity after Doxorubicin treatment is debatable. As shown in Appendix 9.2, Doxorubicin does not increase the number of intra-tumoral $CD8^+$ T-cells in either breast cancer or melanoma bearing mice. However, in mice with breast cancer, I observed increased $PD1^+CD8^+$ T-cells after Doxorubicin treatment, as well as several cell types with increased PD-L1, suggesting a potential synergistic effect between ICI therapy and Doxorubicin treatment. In patients, the KEYNOTE-522 trial showed Pembrolizumab, an αPD-1 inhibitor had enhanced efficacy when combined with Doxorubicin containing chemotherapy in triple negative breast cancer[638], and smaller trials in other malignancies show potential for the same effect.[639,640] Indeed, when I co-treated mice with Doxorubicin and either αPD-1 or αPD-L1, I found that Doxorubicin + αPD-1 exhibited a synergistic effect, resulting in smaller tumors than either treatment alone. Interestingly, Doxorubicin + αPD-L1 did not synergize for

anti-tumor effects, but instead synergized to increase cardiotoxicity in mice compared to Doxorubicin or αPD-L1 alone, or compared to Doxorubicin + αPD-1. No published clinical trials thus far have used Doxorubicin + αPD-L1, or compared different ICIs in combination with Doxorubicin. Additionally, current clinical trials often do not monitor for all cardiotoxic effects, and rather only report fulminant myocarditis or cardiac death rather than serial echocardiography, cardiac biomarkers, or other cardiac tests. Interestingly, one published retrospective, small study of sarcoma patients receiving Doxorubicin with or without αPD-L1 showed a potential synergistic effect on LVEF decline, in line with my results.[641] Together, this highlights the necessity for both better cardiac monitoring in anthracycline-containing clinical trials as well as more combinatorial clinical trials.

Why did each ICI show different synergistic effects with Doxorubicin? In the case of Doxorubicin + αPD-1, the increased tumor PD1+CD8$^+$ T-cells likely indicate T-cell exhaustion, which blockade of PD-1 prevented, enhancing cytotoxic activity. T-cells can commonly become exhausted in the tumor microenvironment, whether that be from high signaling after tumor cell death by Doxorubicin or from constant antigenic stimulation in the tumor itself.[294,475] Doxorubicin has also been shown to upregulate PD-L1 in several cancer types, another mechanistic explanation for how Doxorubicin treatment increased T-cell exhaustion. [642–644] However, it is plausible that these mechanisms also increase PD-L2 expression, which is understudied,[645] explaining why PD-L1 inhibition did not further inhibit anti-tumor activity. On the other hand, in the case of cardiotoxicity, my data show that Doxorubicin increases PD-L1 expression on multiple cell types including endothelial cells, fibroblasts, and myeloid cells (Appendix 9.2). This increase could be mediated directly by Doxorubicin, however IFNγ can increase PD-L1, suggesting Tc1 T-cell recruitment might contribute to increased cardiac PD-L1 expression.[643,646] However, as the number of cardiac T-cells did not change significantly between Doxorubicin alone or Doxorubicin + αPD-L1 treated mice, this suggests that endothelial PD-L1 modulation of T-cell recruitment is not a

major contributor. Instead, I found that inhibition of PD-L1 *in vitro* increased $CD8^+$ T-cell degranulation when in contact with Doxorubicin treated fibroblasts, leading to enhanced fibrotic responses, whereas the function of myeloid PD-L1 in the heart remains unknown. While increased T-cell-fibroblast cross-talk would explain increased systolic dysfunction in the co-treated mice, inhibition of PD-1 should similarly increase T-cell degranulation and cardiotoxicity *in vivo,* which was not observed. This suggests there might be a role for PD-L1 intrinsically in cardiac fibroblasts, or even non-canonical PD-L1 signaling to $CD8^+$ T-cells after Doxorubicin treatment. Despite these remaining gaps in knowledge, these data together are strong pre-clinical evidence for further study of specific combinations consisting of Doxorubicin and newer ICI therapies.

8.7 Conclusion:

Overall, the data presented in this dissertation outline several new mechanisms that regulate T-cell activation and function that are conserved across different models of cardiovascular injury and can be applied into models of cancer. Further, this expands into several mechanistic studies of fibroblast function and T-cell fibroblast cross-talk, elucidating inflammatory regulation of fibrosis in said models. This includes the discovery that T-cell MyD88 acts as a brake on T-cell activation by acting at the T-cell receptor in sterile inflammation, such that it's deletion results in worsened cardiovascular injury and fibrosis but enhanced anti-tumor immunity. Further, degradation of MyD88 in fibroblasts by the proteasome mediates TGFβ-induced fibroblast transformation, uncovering a novel potential therapeutic target for fibrosis. One important conclusion from this work and moving forward in cardiovascular research is the concept that inflammation that is pathogenic for the heart can often be beneficial in anti-tumor immunity. This highlights the need for stronger pre-clinical modeling and study of cardiac function and toxicities in the context of tumors. Using pre-clinical models and patient samples with malignancies, this dissertation also outlined a

novel cardiac T-cell immune response that contributes to anthracycline cardiotoxicity, triggered from a DNA damage response through STING, chemokine directed cardiotropism, and antigen specific T-cells. Several elements of this work represent potential therapeutic targets or potential biomarkers, and as such future translational studies in humans will further support this. As patients with cancer and cardiovascular disease share risk factors and pathology, this work has furthered our understanding of the connections between the two diseases and mechanisms T-cell mediated inflammation that intertwine their pathobiology.

Chapter 9 Appendices and Supplemental Data

9.1 MyD88 Regulates the IFNγ Response and Inflammatory Functions in Cardiac Fibroblasts

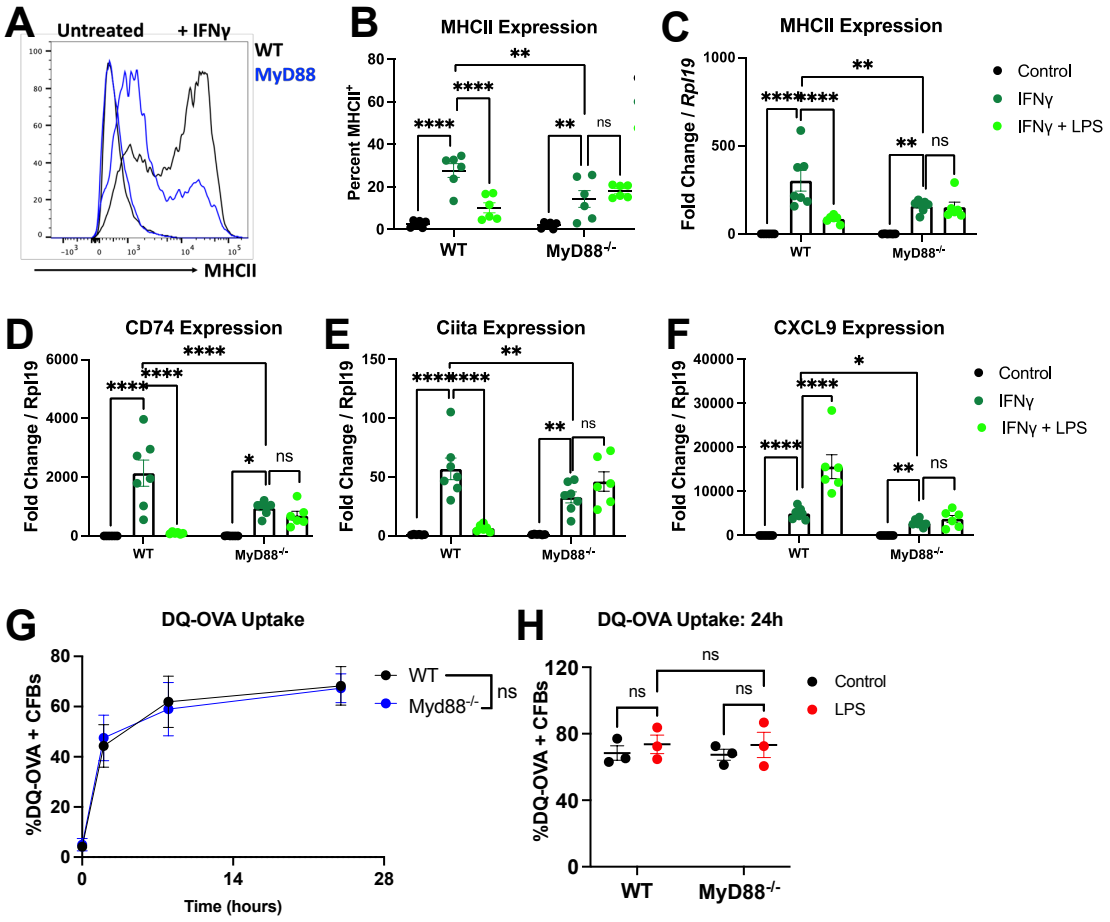


Figure 9-1 MyD88 Deletion or TLR4 Stimulation Decrease IFNγ Responsiveness Without Altering Antigen Processing

WT or MyD88$^{-/-}$ fibroblasts were treated daily for 3 days with 100 U/mL IFNγ with or without 1.0 μg/mL LPS. A-B. MHCII was measured by flow cytometry, representative histograms shown with quantification from n=6 independent experiments. C-F. RNA was isolated from treated fibroblasts and indicated gene was measured by RT-qPCR for 6 independent experiments. G-H. Fibroblasts were treated with ____ FITC-tagged DQ-OVA for the indicated time points with or without LPS, shown is FITC expression over time, or 24h expression with and without LPS treatment. Statistical analysis by 2-way ANOVA, ns = no significance, * = $p < 0.05$, ** = $p < 0.01$, *** = $p < 0.001$, **** = $p < 0.0001$.

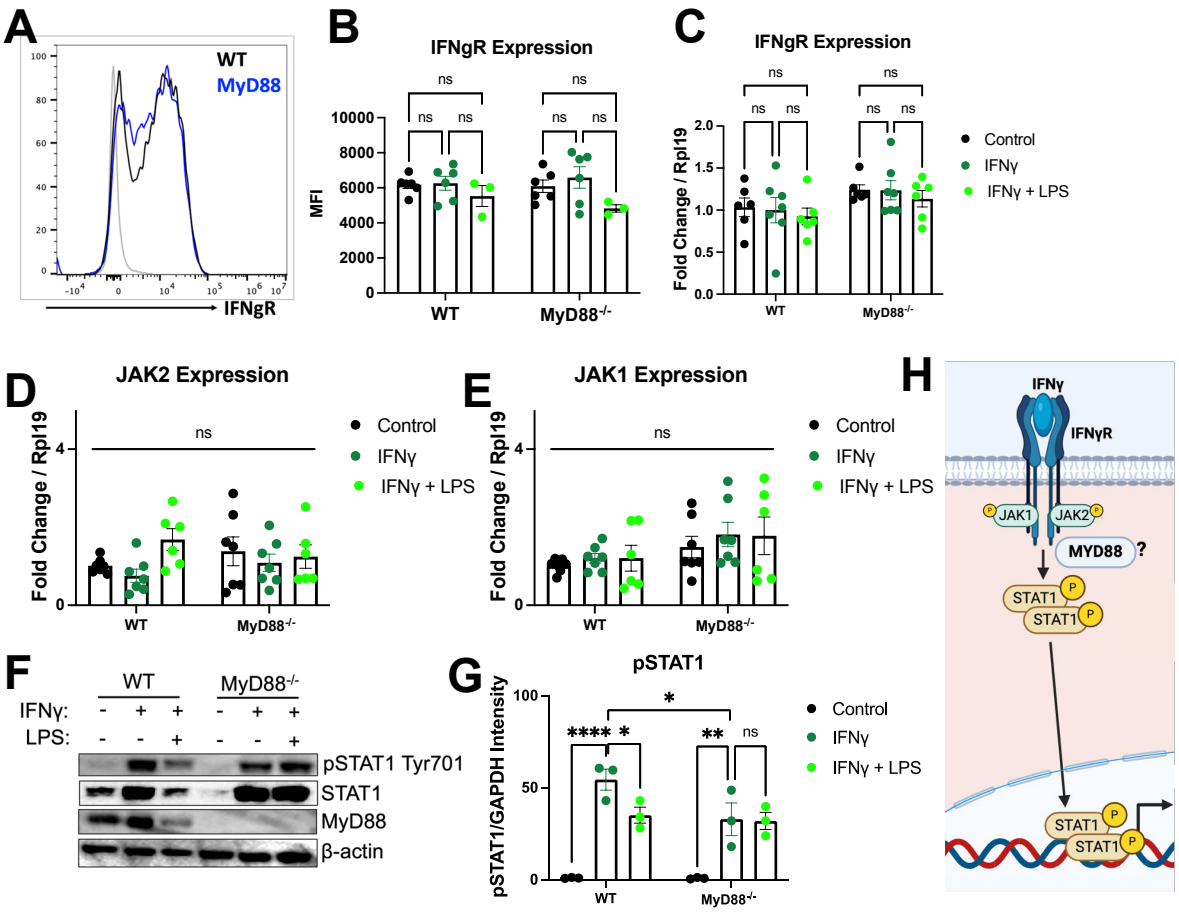


Figure 9-2 MyD88 and TLR4 Stimulation Do Not Alter IFNγR or JAK expression, but Decrease STAT1 phosphorylation

WT or MyD88$^{-/-}$ fibroblasts were treated daily for 3 days with 100 U/mL IFNγ with or without 1.0 μg/mL LPS. A-B. I IFNγR was measured by flow cytometry, representative histograms shown with quantification from n=3-6 independent experiments. C-E. RNA was isolated from treated fibroblasts and indicated gene was measured by RT-qPCR for 6 independent experiments. F-G. Western blot was performed for STAT1 phosphorylation after treatment of fibroblasts, shown is representative blot with quantification from n=3 independent experiments. H. Schematic showing potential role for MyD88 downstream of IFNγR. Statistical analysis by 2-way ANOVA, ns = no significance, * = $p < 0.05$, ** = $p < 0.01$, *** = $p < 0.001$, **** = $p < 0.0001$.

9.2 Doxorubicin Impacts the Anti-Tumor and Cardiotoxic Effects of Immune Checkpoint Inhibitors

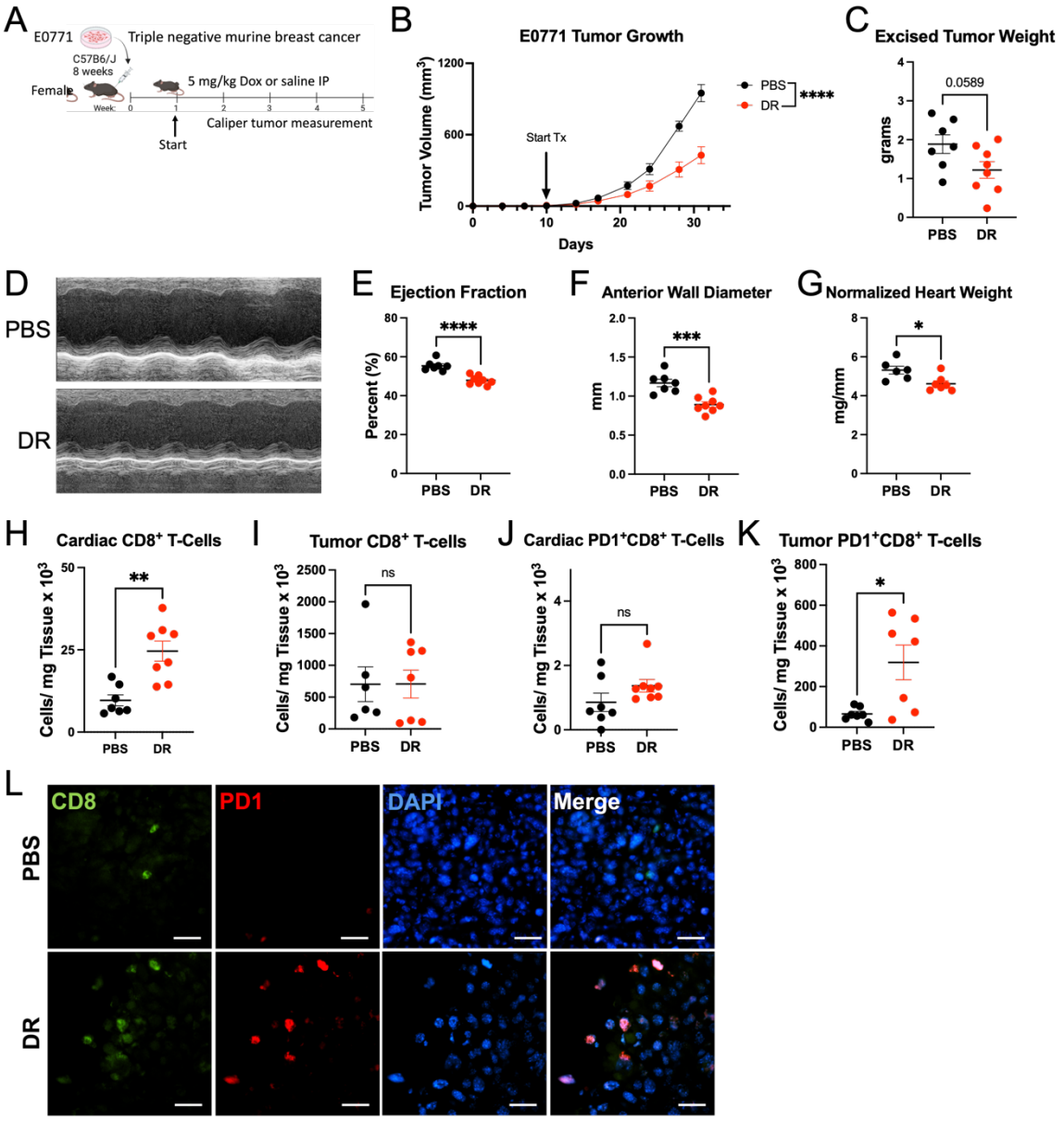


Figure 9-3 Doxorubicin Treatment of Breast Cancer Induces Cardiotoxicity, Cardiac Inflammation, and Intratumoral T-cell Exhaustion

A. 200,000 E0771 cells were implanted in the 4th mammary fat pad of female WT mice, then 5 mg/kg Doxorubicin was given weekly starting 1 week after tumor implantation when tumors were palpable. B. Tumor growth was measured with calipers. C. Excised tumor weight. D. Echocardiography was used to evaluate cardiac function, representative echocardiograph's shown in M-mode, with quantification for ejection fraction (E) or anterior wall diameter (F). G. Heart weight normalized to tibia length. H-I. Hearts were mechanically and enzymatically digested then analyzed by flow cytometry for cardiac CD8$^+$ T-cells (H) or cardiac CD8$^+$PD1$^+$ T-cells (I). J-K. Tumors were mechanically and enzymatically digested then analyzed by flow cytometry for tumor CD8$^+$ T-cells (J) or tumor CD8$^+$PD1$^+$ T-cells (K). L. Tumor sections were stained by immunofluorescence for PD1 and CD8, representative images shown (scale bars = 25 μm). Statistical analysis by 2-way ANOVA with repeated measures (B) or T-test (C-K). ns = no significance, * = $p < 0.05$, ** = $p < 0.01$, *** = $p < 0.001$, **** = $p < 0.0001$.

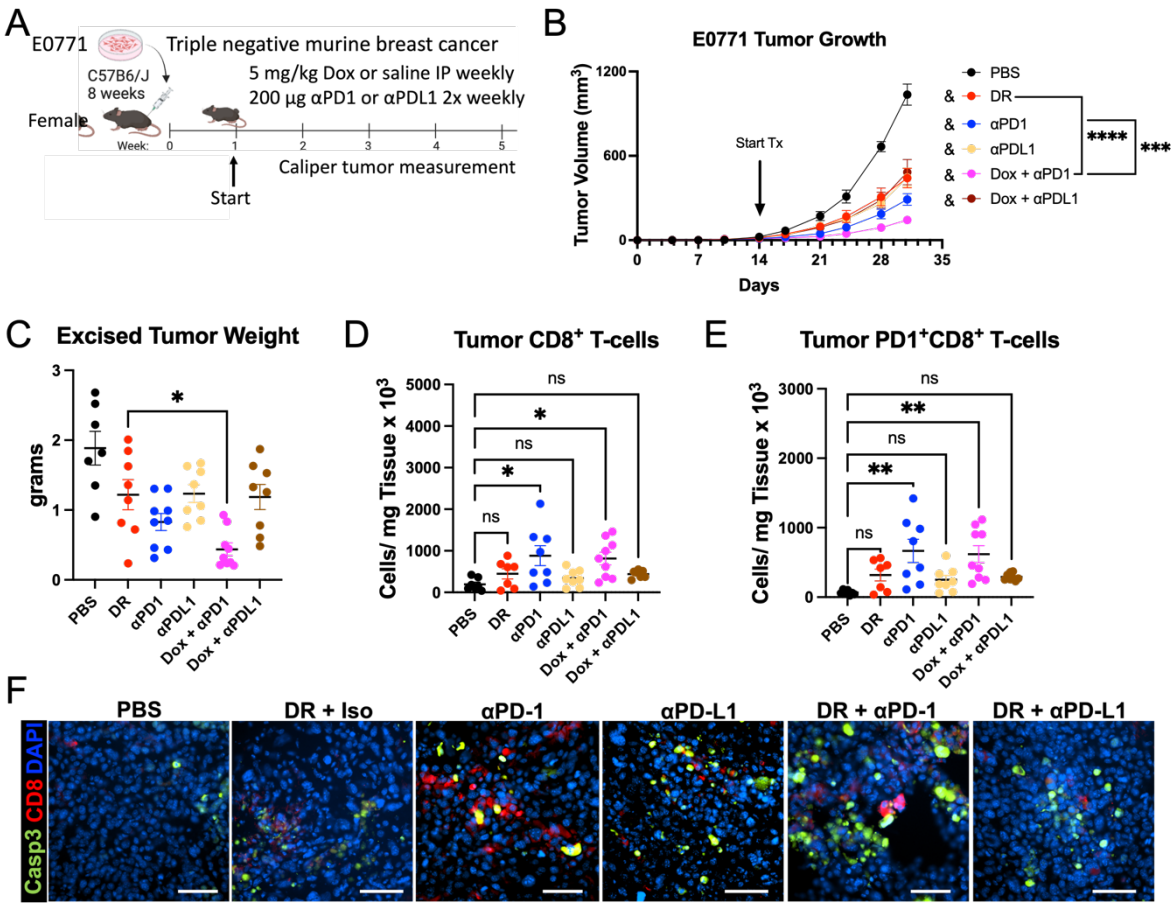


Figure 9-4 Doxorubicin Synergizes with PD-1 Inhibition for Anti-Tumor Activity

A. 200,000 E0771 cells were implanted in the 4th mammary fat pad of female WT mice, then where indicated 5 mg/kg Doxorubicin was given weekly, or 200 µg αPD-1 or αPD-L1 was given bi-weekly starting 1 week after tumor implantation when tumors were palpable. B. Tumor growth was measured with calipers. C. Excised tumor weight. D-E. Tumors were mechanically and enzymatically digested then analyzed by flow cytometry for tumor $CD8^+$ T-cells (D) or tumor $CD8^+PD1^+$ T-cells (E). F. Tumor sections were stained by immunofluorescence for cleaved caspase 3 (Casp3) and CD8, shown are representative images (scale bars = 50 µm. Statistical analysis by 2-way ANOVA with repeated measures (B) or 1-way ANOVA Tukey's multiple comparison's test (C-E). ns = no significance, & = $p < 0.05$ compared to PBS injected mice, * = $p < 0.05$, ** = $p < 0.01$, *** = $p < 0.001$, **** = $p < 0.0001$.

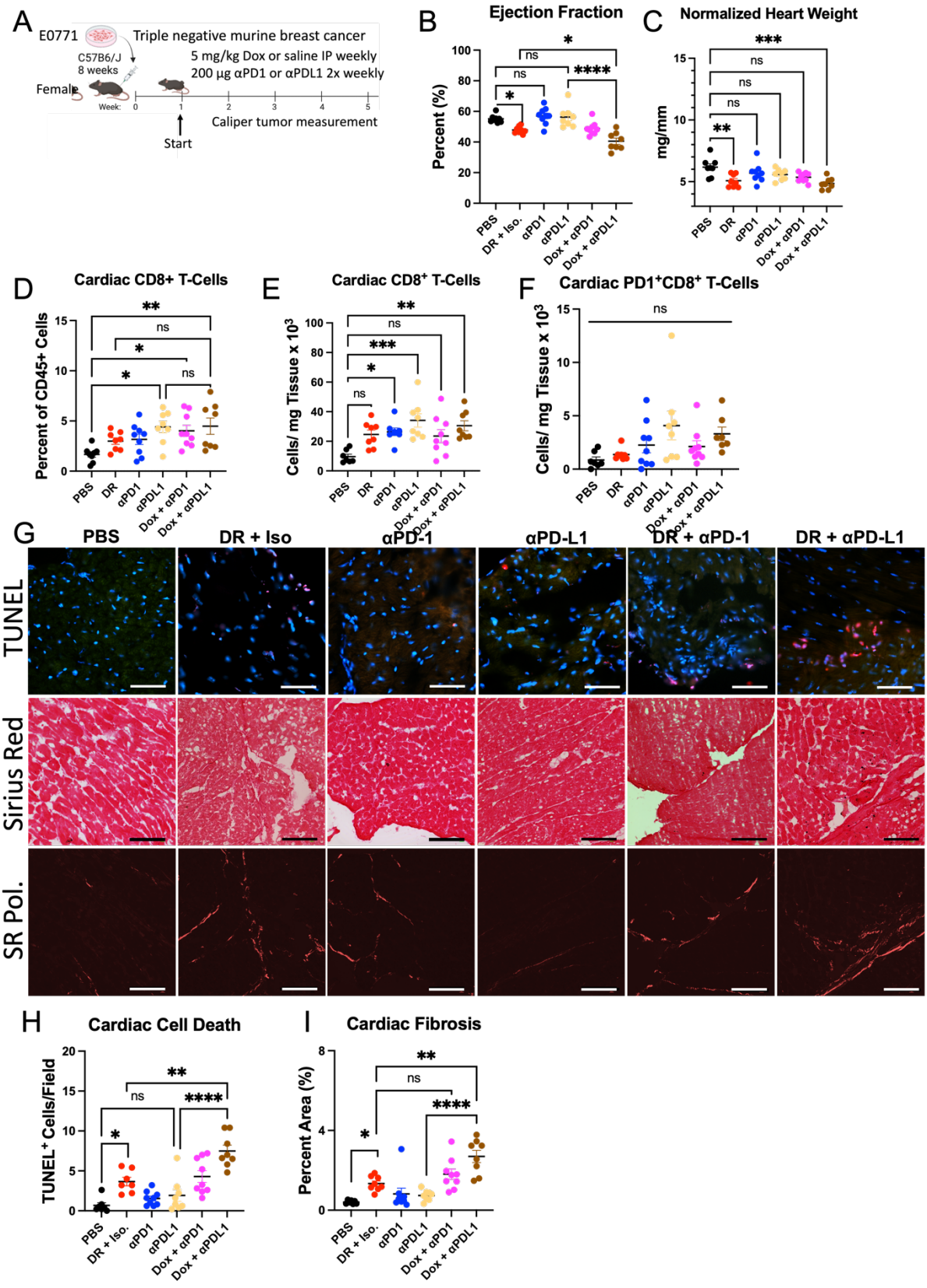

A
E0771
Triple negative murine breast cancer
C57B6/J
8 weeks
5 mg/kg Dox or saline IP weekly
200 µg αPD1 or αPDL1 2x weekly
Female
Week: 0 1 2 3 4 5
Caliper tumor measurement
Start
B
Ejection Fraction
Percent (%)
C
Normalized Heart Weight
mg/mm
D
Cardiac CD8+ T-Cells
Percent of CD45+ Cells
E
Cardiac CD8+ T-Cells
Cells/ mg Tissue x 10^3
F
Cardiac PD1+CD8+ T-Cells
Cells/ mg Tissue x 10^3
PBS
DR
DR + Iso.
αPD1
αPDL1
Dox + αPD1
Dox + αPDL1
ns
G
PBS
DR + Iso
αPD-1
αPD-L1
DR + αPD-1
DR + αPD-L1
TUNEL
Sirius Red
SR Pol.
H
Cardiac Cell Death
TUNEL+ Cells/Field
I
Cardiac Fibrosis
Percent Area (%)

Figure 9-5 Doxorubicin Synergizes with PD-L1 Inhibition for Cardiotoxicity
A. 200,000 E0771 cells were implanted in the 4th mammary fat pad of female WT mice, then where indicated 5 mg/kg Doxorubicin was given weekly, or 200 µg αPD-1 or αPD-L1 was given bi-weekly starting 1 week after tumor implantation when tumors were palpable. B. Echocardiography was used to evaluate ejection fraction. C. Heart weight normalized to tibia length. D-F. Hearts were mechanically and enzymatically digested then analyzed by flow cytometry for cardiac $CD8^+$ T-cells (E – frequency of CD45+ cells, F – total cell number) or cardiac $CD8^+PD1^+$ T-cells (F). G. Cardiac sections were stained with TUNEL or picrosirius red (SR), representative images shown (scale bars = 50 um). H. ImageJ was used to quantify TUNEL+ cardiac cells. I. ImageJ was used to quantify picrosirius red positive area under polarized light (SR Pol.) Statistical analysis by 1-way ANOVA Tukey's multiple comparison's test. ns = no significance, * = $p < 0.05$, ** = $p < 0.01$, *** = $p < 0.001$, **** = $p < 0.0001$.

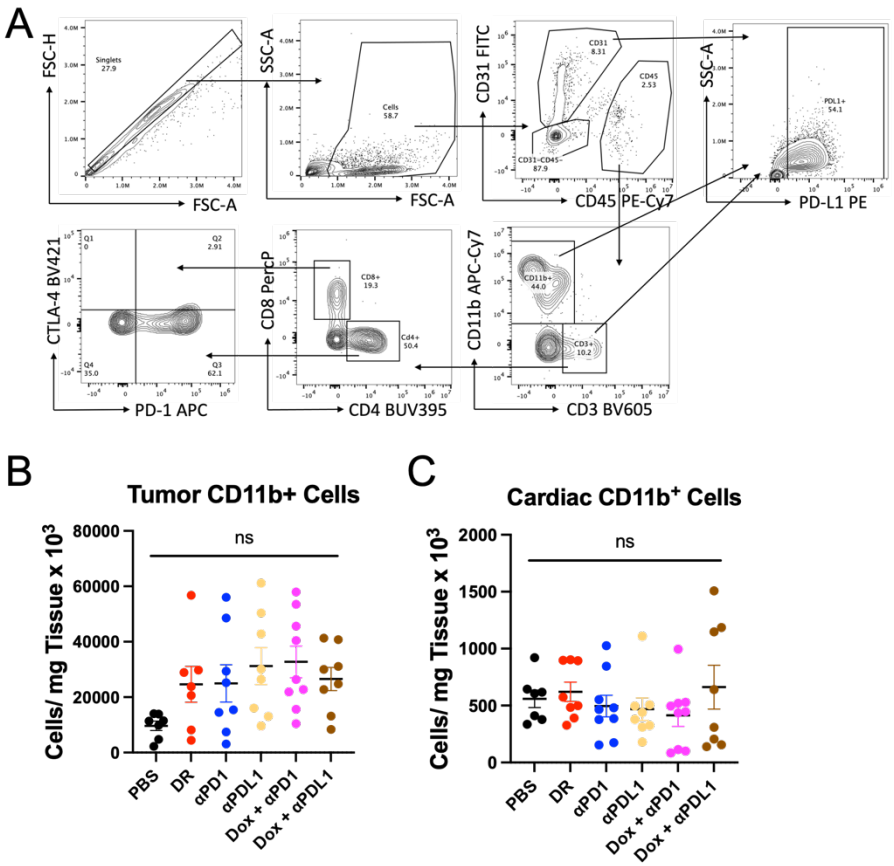


Figure 9-6 Gating Strategies for Heart and Tumor, and Myeloid Cell Quantification
A. Gating strategies used for heart and tumor flow cytometry in Figures 1-3. B. Tumor CD11b+ cells quantified from Figure 2. C. Cardiac CD11b+ cells quantified from Figure 3. Statistical analysis by 1-way ANOVA with Tukey's multiple comparison test, ns = no significance across all comparison's made.

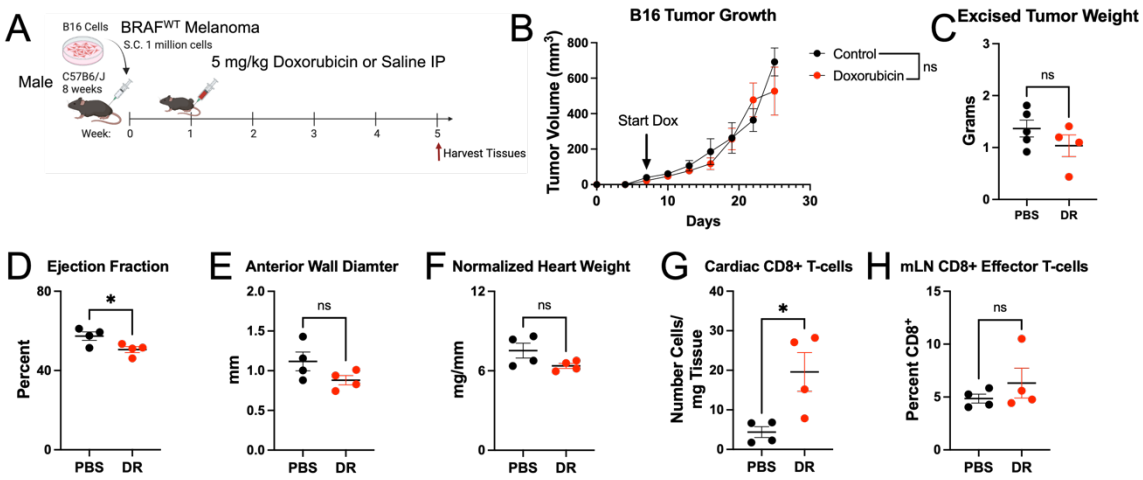


Figure 9-7 Doxorubicin Causes Cardiotoxicity and Cardiac Inflammation in Melanoma Bearing Mice
A. Wildtype mice were implanted with 1 million B16 cells in their left flanks, then 5 mg/kg Doxorubicin was given weekly starting 1 week after tumor implantation when tumors were palpable. B. Tumor growth was measured with calipers. C. Excised tumor weight. D. Echocardiography was used to evaluate cardiac function, with quantification for ejection fraction (D) or anterior wall diameter (E). F. Heart weight normalized to tibia length. G. Hearts were mechanically and enzymatically digested then analyzed by flow cytometry for cardiac $CD8^+$ T-cells H. Mediastinal lymph nodes were digested and analyzed by flow cytometry for effector T-cells. Statistical analysis by 2-way ANOVA with repeated measures (B) or T-tests (C-H), ns = no significance, * = $p < 0.05$, ** = $p < 0.01$, *** = $p < 0.001$, **** = $p < 0.0001$.

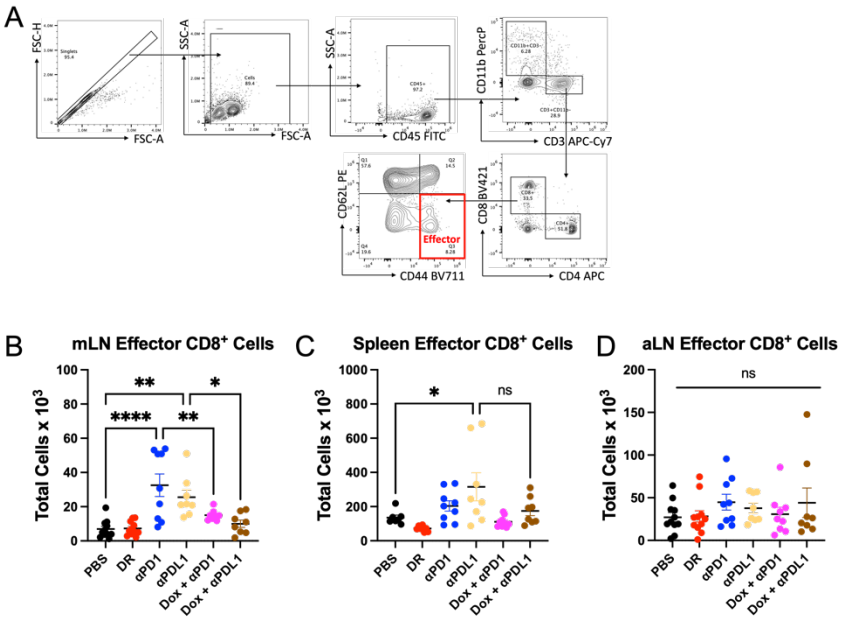


Figure 9-8 Gating Strategy for Lymphoid Tissues and Effector T-cell Quantification
A. Gating strategies used for spleen and lymph node effector T-cells. Effector CD8+ T-cells quantified from mediastinal lymph nodes (mLN – B), spleens (C), or axillary lymph nodes (aLN – D). Statistical analysis by 1-way ANOVA with Tukey's multiple comparison test, ns = no significance, * = $p < 0.05$, ** = $p < 0.01$, *** = $p < 0.001$, **** = $p < 0.0001$.

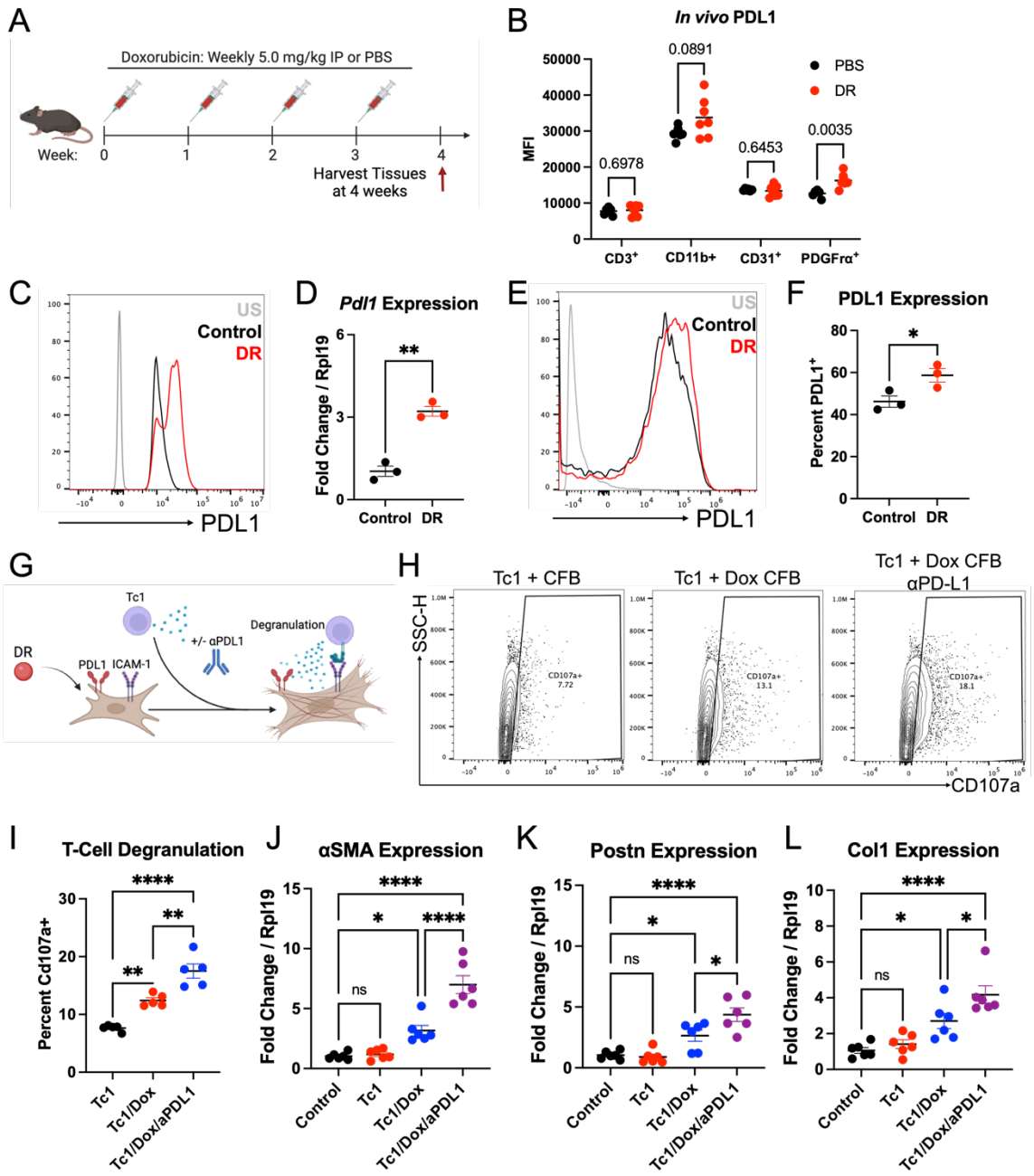


Figure 9-9 Doxorubicin Induced Cardiac Fibroblast PD-L1 Limits T-cell Degranulation and Fibroblast Transformation

A. Healthy WT mice were given 5.0 mg/kg Doxorubicin or saline weekly than euthanized after 4 weeks. B. Hearts were digested enzymatically and mechanically then analyzed by flow cytometry for PD-L1 expression on CD3+ T-cells, CD11b+ myeloid cells, CD31+ endothelial cells, or PDGFrα+ fibroblasts. C. Representative histograms for fibroblast PD-L1 expression compared to unstained (US). D-F. WT fibroblasts were treated *in vitro* with 1.0 μg/mL doxorubicin (DR) for 24 hours, then RT-qPCR was used to measure *Pdl1* expression (D) or flow cytometry was used to measure PD-L1 expression, with representative histograms shown in E, quantified in F. G. Fibroblasts were treated *in vitro* with 1.0 μg/mL doxorubicin for 24 hours, fresh media was added, then activated WT Tc1 cells were added at a ratio of 1:5 CFB:Tc1 cells in the presence or absence of 256 μg/mL αPD-L1 for 24 hours. H. T-cell CD107a expression was monitored by flow cytometry, repseentative plots shown in H. quantified in I. J-L. RT-qPCR was used to measure gene expression of aSMA (J), Postn (K) or Collagen 1 (L). Statistical analysis by T-test (B-F) or 1-way ANOVA with Tukey's multiple comparison's test (I-L). ns = no significance, * = $p < 0.05$, ** = $p < 0.01$, *** = $p < 0.001$, **** = $p < 0.0001$.

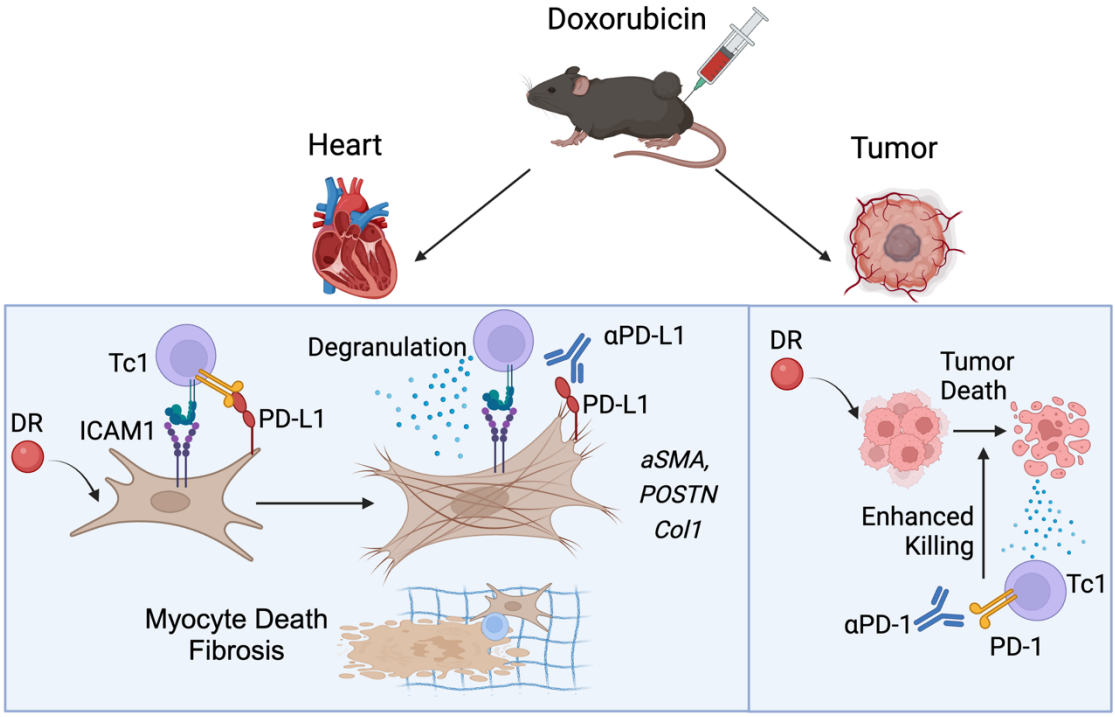


Figure 9-10 Graphical Abstract of Doxorubicin and Immune Checkpoint Inhibitor Effects

9.3 T-cell MyD88 Modulates Doxorubicin Cardiotoxicity

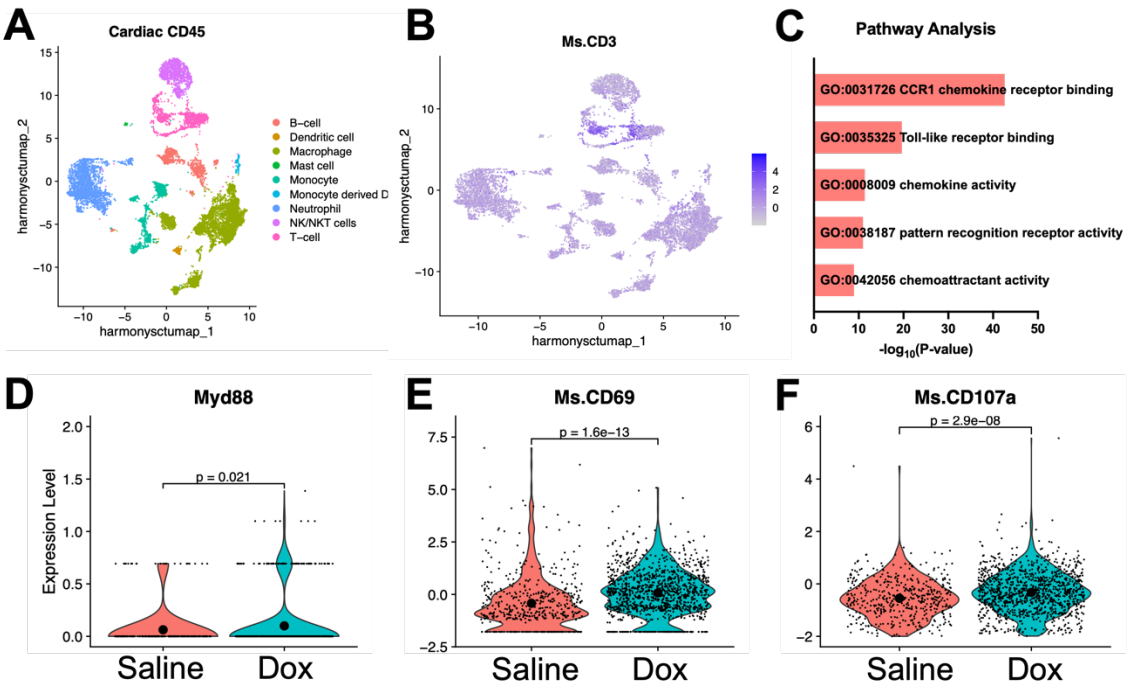


Figure 9-11 Cardiac T-cells Increase MyD88 Signaling Alongside T-cell Activation Markers in the Doxorubicin Treated Heart

A. WT mice treated with Saline or Doxorubicin (3 mg/kg, n=6 / group) every other day for 14 days, then hearts were digested to a single cell suspension, CD45 cells were isolated by magnetic selection, then analyzed by CITE-seq, shown is a UMAP display of all cardiac CD45$^+$ cells. B. Surface CD3 expression shown, highlighting clusters 3 and 7 as T-cells. C. Pathway analysis of differentially expressed genes from cardiac T-cells between saline and Doxorubicin treated mice. D. Violin plot showing T-cell expression of *Myd88* transcript in cardiac T-cells. E. Violin plot showing surface CD69 expression in cardiac T-cells. F. Violin plot showing surface CD107a expression in cardiac T-cells. Statistical analysis by T-test, p-values shown.

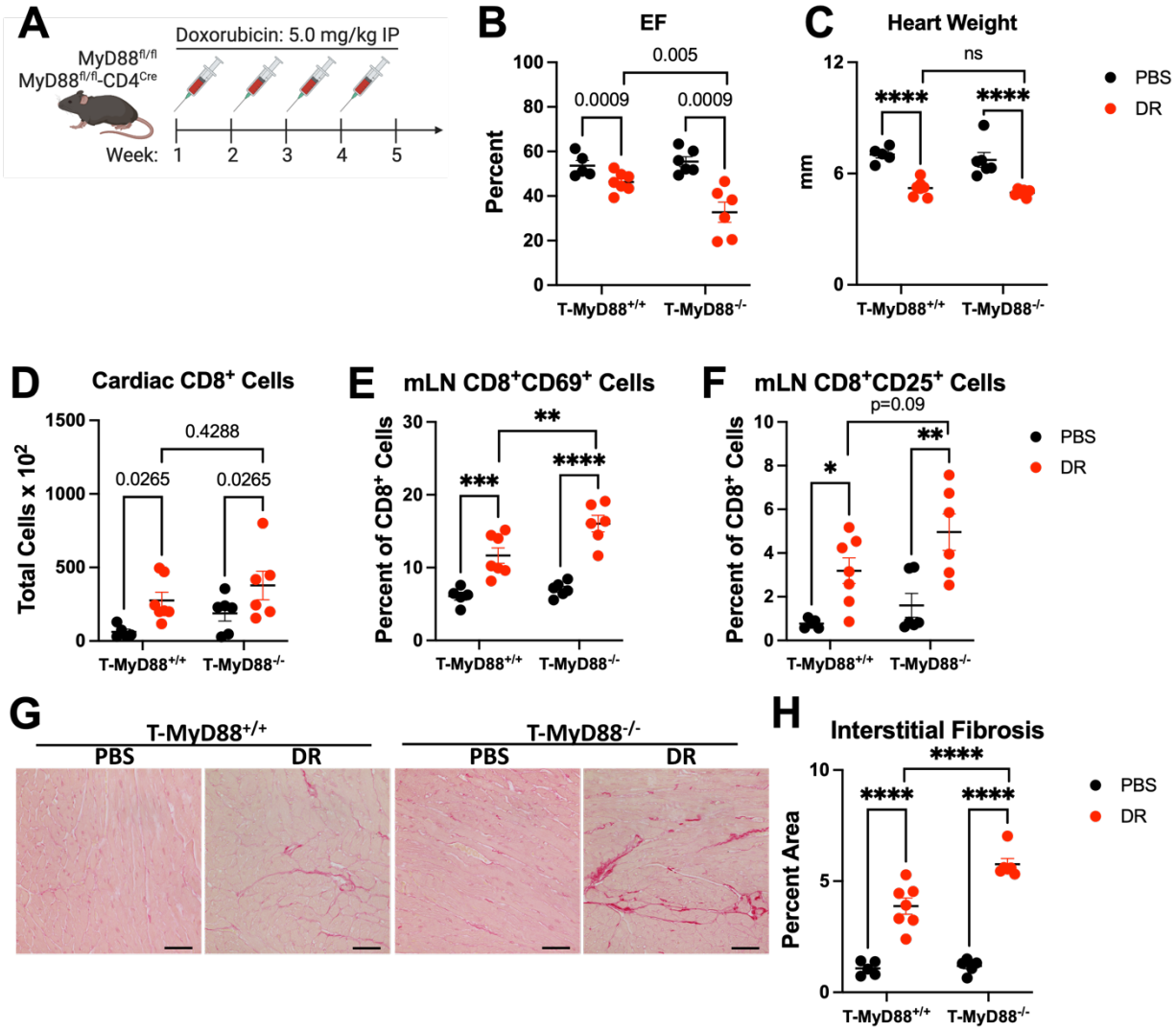


Figure 9-12 T-cell Deletion of MyD88 Worsens Doxorubicin Cardiotoxicity

A. 8-10 week old male MyD88$^{fl/fl}$ or MyD88$^{fl/fl}$CD4^{Cre} mice (n=5-7/group) were given 5mg/kg Doxorubicin or saline weekly, then euthanized after 4 weeks. B. Ejection fraction was determined by echocardiography. C. Whole heart weight was normalized to tibia length. D. Hearts were mechanically and enzymatically digested, then analyzed by flow cytometry for CD3^{+}CD8^{+} T-cells. E-F. Mediastinal lymph nodes were digested and analyzed by flow cytometry. Shown is CD69 expression in CD3^{+}CD8^{+} (E) or CD25 expression in CD3^{+}CD8^{+} (F). G-H. Heart sections were stained with Picrosirius red, shown are representative images (scale bars = 50 um) quantified in H. Statistical analysis by 2-way ANOVA with Sidak's multiple comparison's test, ns = no significance, * = $p < 0.05$, ** = $p < 0.01$, *** = $p < 0.001$, **** = $p < 0.0001$.

9.4 Mechanisms of Doxorubicin and CD8$^+$ T-cell Induced Fibroblast Transformation

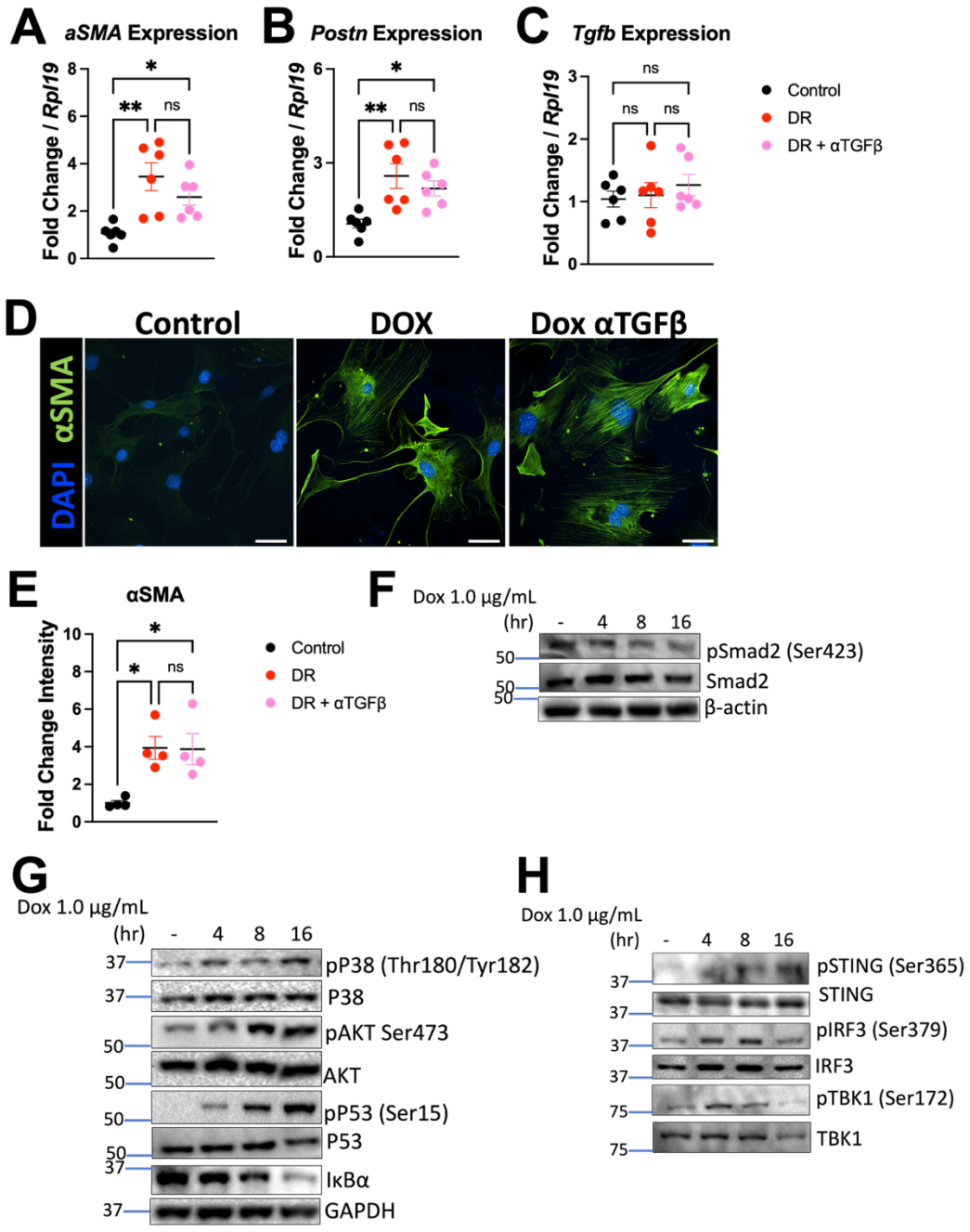


Figure 9-13 Doxorubicin Induces TGFβ Independent Myofibroblast Transformation and Activates Several Signaling Pathways

Primary WT cardiac fibroblasts were treated with 1.0 µg/mL Doxorubicin in the presence or absence of 5µm αTGFβ1/2/3 for 24 hours. RNA was isolated and RT-qPCR was used to measure aSMA (A), Postn (B) or Tgfb (C). D. αSMA was visualized by immunofluorescence, representative images shown with quantification using ImageJ shown in E for n=4 independent experiments (scale bars = 50 µm). F-H. WT cardiac fibroblasts were treated with 1.0 µg/mL Doxorubicin for the indicated time, then western blot was used to analyze the indicated targets. Statistical analysis by 1-way ANOVA with Tukey's multiple comparison test . ns = no significance, * = $p < 0.05$, ** = $p < 0.01$.

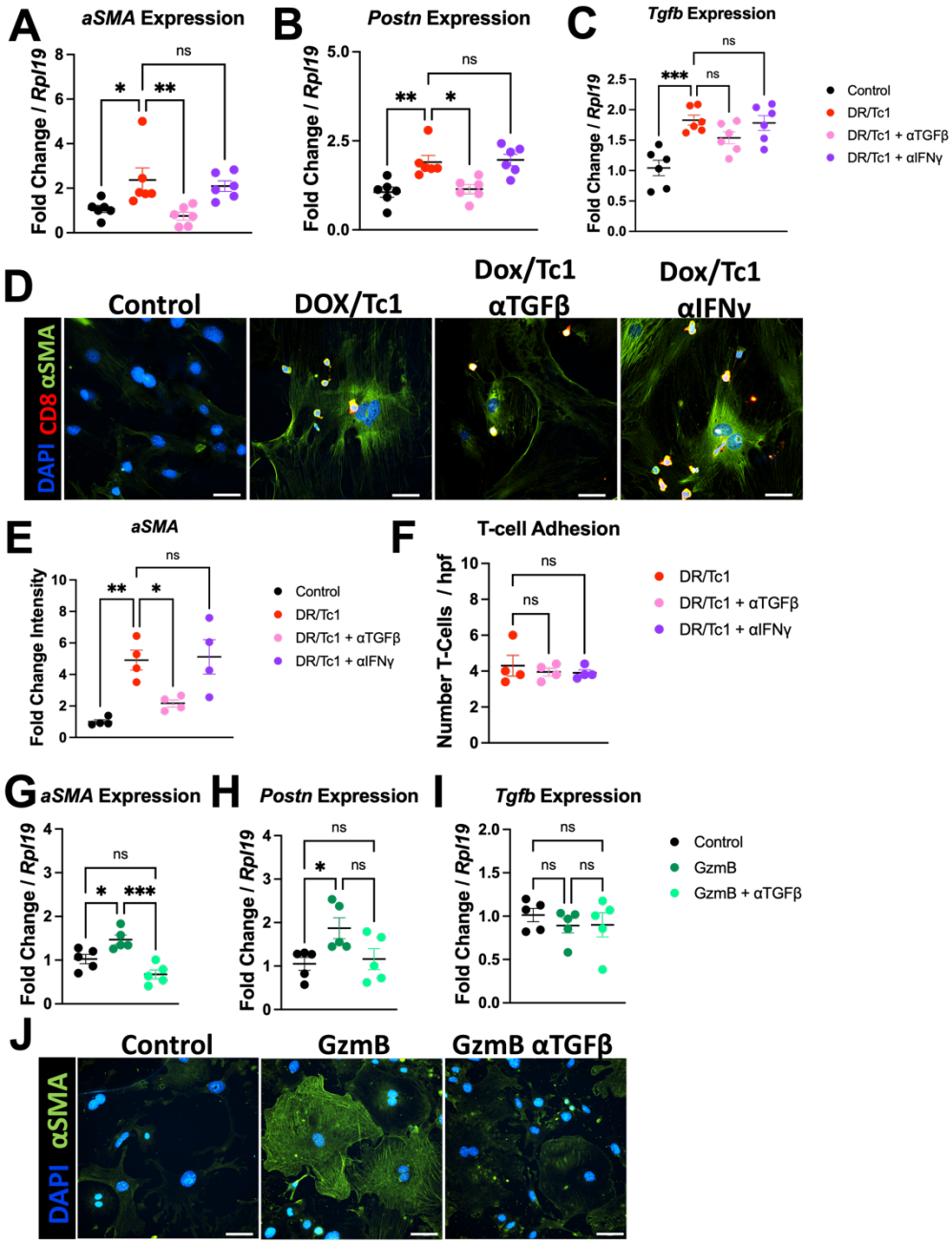


Figure 9-14 Tc1 cells Induce TGFβ Dependent But IFNγ Independent Myofibroblast Transformation of Doxorubicin Primed Fibroblasts

.WT primary cardiac fibroblasts were treated with 1.0 µg/mL Doxorubicin for 24 hours where indicated, media was changed, then primary WT Tc1 cells were added at a ratio of 1:5 CFB:Tc1 for 24 hours more in the presence or absence of 5 µm αTGFβ or αIFNγ where indicated. T-cells were detached with 5mM EDTA then RT-qPCR was used to measure aSMA (A), Postn (B) or Tgfb (C). D. T-cells were not detached, and immunofluorescence was used to visualize $CD8^{+}$ (red) and αSMA (green), representative images shown (scale bars are 50 µm) then ImageJ was used for quantification (E) and T-cells were counted manually (F). G-J WT fibroblasts were treated with 100 nm recombinant Granzyme B in the presence or absence of 5 µm αTGFβ for 24 hours. RT-qPCR was used to measure aSMA (G), Postn (H) or Tgfb (I). J. Immunofluorescence was used to visualize αSMA, representative images shown (scale bars are 50 µm). Statistical analysis by 1-way ANOVA with Tukey's multiple comparison test . ns = no significance, * = $p < 0.05$, ** = $p < 0.01$, *** = $p < 0.001$.

9.5 T-cell Deficient Mice Protected from PE/ANGII Induced Diastolic Dysfunction

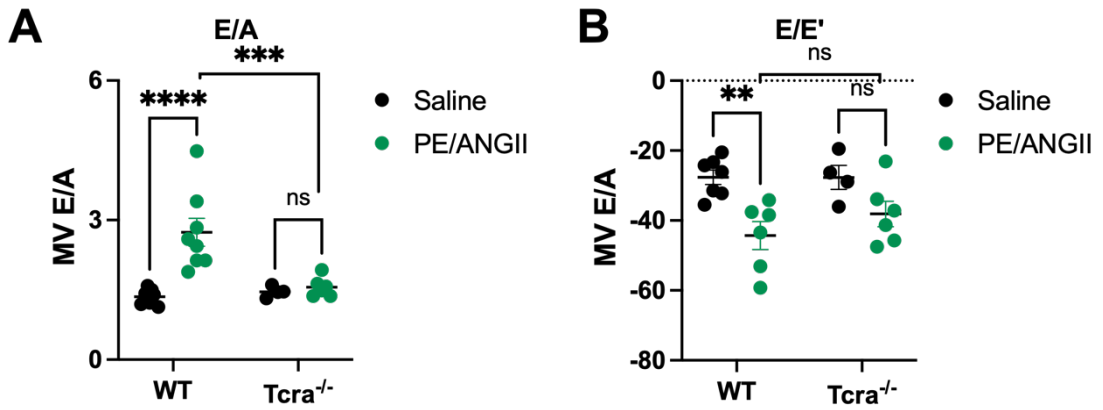


Figure 9-15 T-cell Deficient Mice are Protected from PE/ANGII Induced Diastolic Dysfunction
WT mice or Tcra$^{-/-}$ mice aged 8-10 weeks (n=10-12 / group) were implanted with osmotic minipumps secreting 50 mg/kg/day phenylephrine and 1.5 mg/kg/day angiotensin II or saline, then euthanized after 4 weeks. Doppler echocardiography was used to measure E/A ratio (A) or E/E' (B) for diastolic dysfunction. Statistical analysis by 2-way ANOVA with Sidak's multiple comparison's test, ns = no significance, * = $p < 0.05$, ** = $p < 0.01$, *** = $p < 0.001$, **** = $p < 0.0001$.

9.6 Anthracycline Treatment Causes Induces a Pro-Fibrotic State in CD8⁺ T-cells

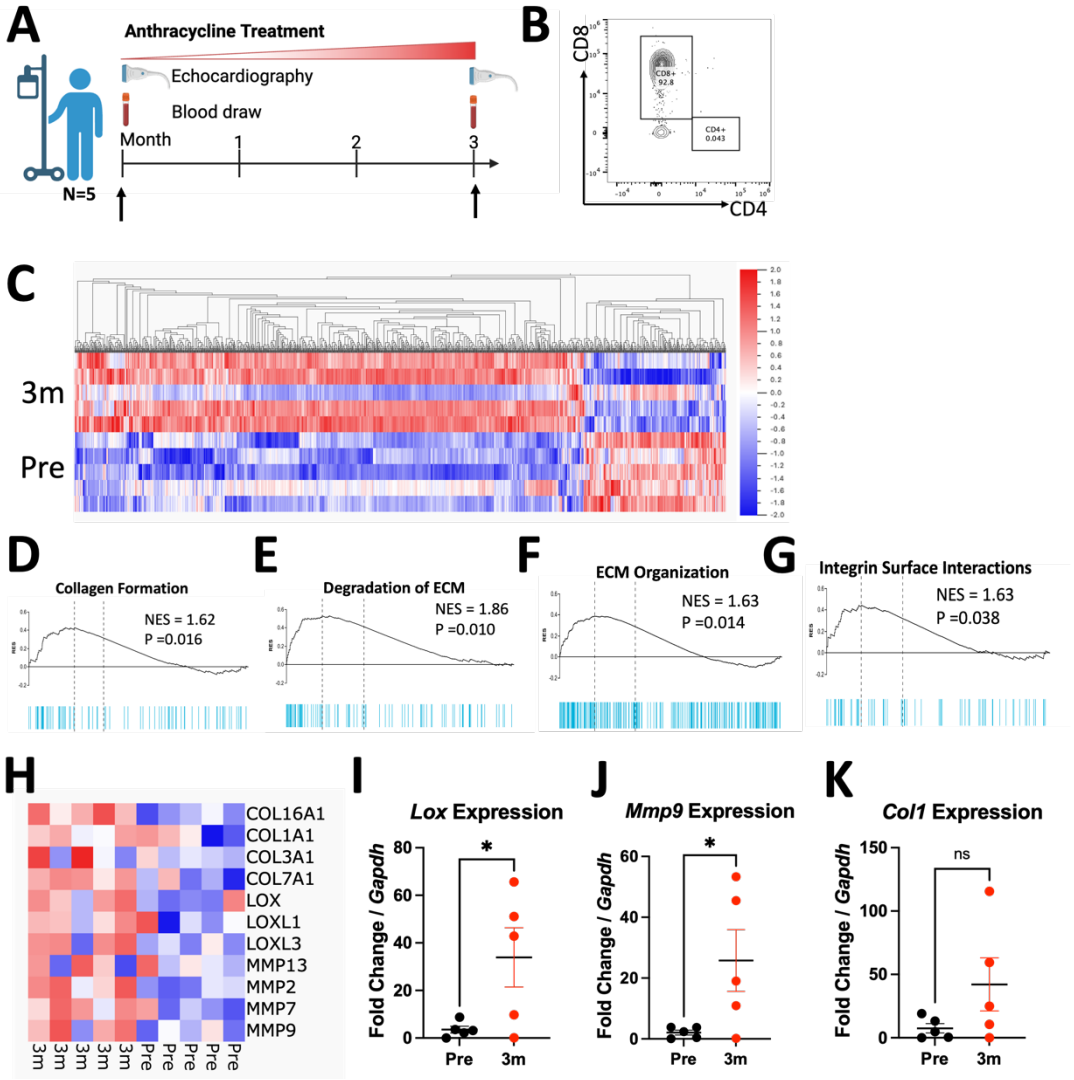


Figure 9-16 Patient Derived Cytotoxic T-cells Express a Pro-Fibrotic Transcriptome After Anthracycline Treatment

A. Schematic of patient sample collection, $CD8^+$ cells were isolated from the blood of 5 patients with hematologic malignancy before and after initiation of anthracycline-containing chemotherapy. B. Flow cytometry plot showing purity of $CD8^+$ T-cells, gated on $CD3^+$ cells. C. Bulk sequencing was performed on isolated $CD8^+$ T-cells, heat map showing DEGs with a cut-off of $p < 0.05$. D-G. Gene set enrichment analysis reveals enriched genes for collagen formation (D) degradation of extracellular matrix (E) ECM organization (F) and integrin binding (G). H. Heat map showing expression of selected fibrotic and collagen modifying genes. I-K. RT-qPCR was used to validate the expression of transcripts in original patient cDNA. Statistical analysis by T-tests, ns = no significance, * = $p < 0.05$

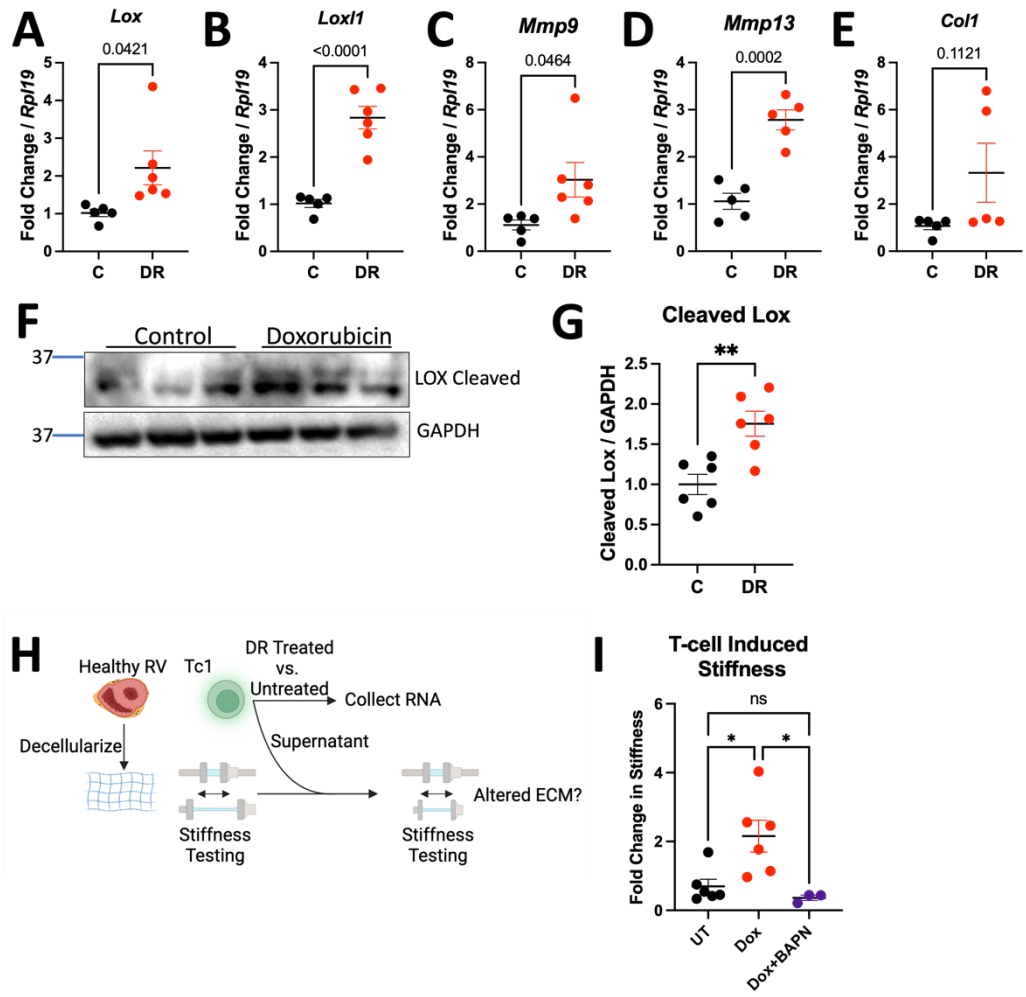


Figure 9-17 Treatment of Mouse CD8⁺ T-cells with Doxorubicin Induces Profibrotic Gene Expression and LOX-Dependent Matrix Stiffening Ability

Mouse CD8⁺ T-cells were activated with αCD3/αCD28 in the presence of IL-12 and αIL-4 (Tc1 cells), then treated for 24 hours with 0.1 μg/mL DR. A-E. RT-qPCR was used to measure transcription of selected pro-fibrotic and collagen modifying genes from n=6 independent experiments. F. Western blot was used detect cleaved (active) LOX, shown is representative from n=3, quantified in G. for n=6 independent experiments. H. Schematic of strategy to determine matrix stiffening ability. Decellularized RV ECM was subjected to unilateral tensile stretching with force measurement to determine stiffness, then incubated for 16 hours with conditioned media from untreated (UT), Doxorubicin treated (Dox) or Doxorubicin with BAPN (pan-LOX inhibitor), then stiffness was determined again. I. Fold change in stiffness to stretching. Statistical analysis by T-tests (A-G) or 1-way ANOVA (I). p-values shown, ns = no significance, * = $p < 0.05$, ** = $p < 0.01$

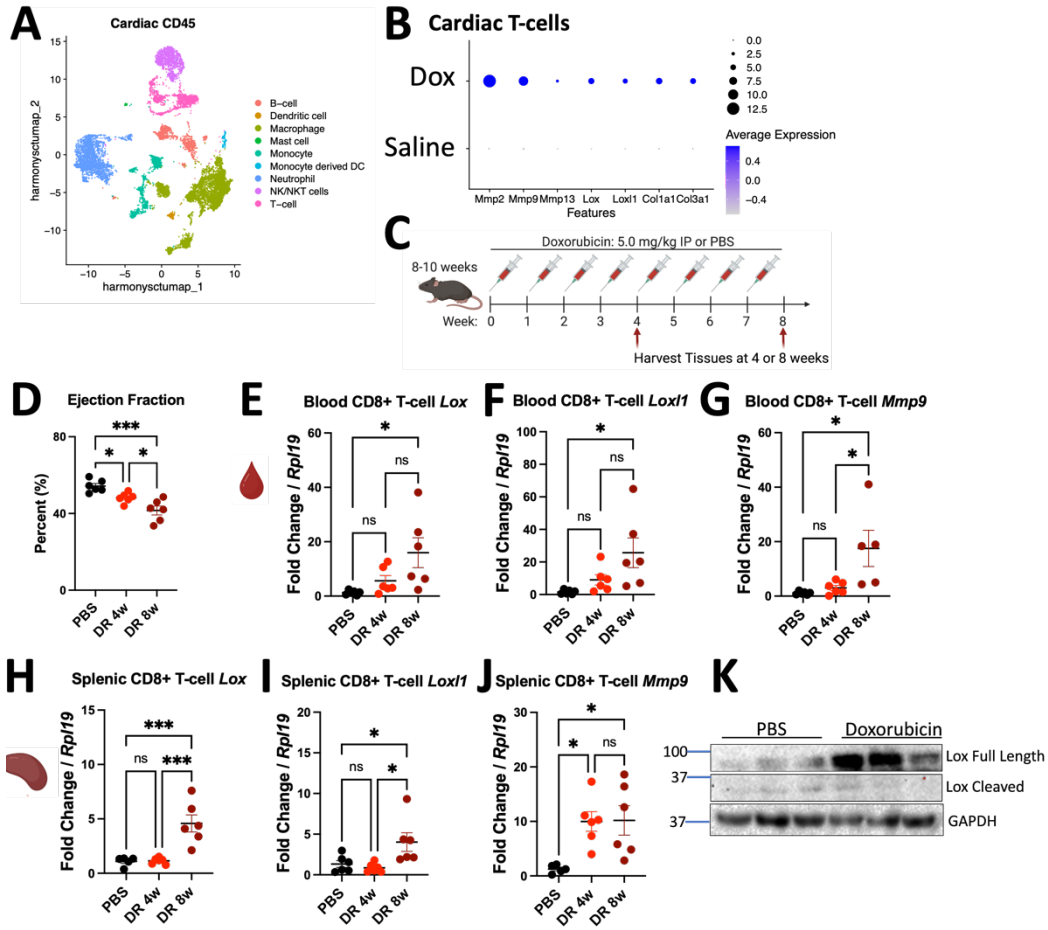


Figure 9-18 Mice Treated with Doxorubicin Increase CD8⁺ T-cell LOX Expression In Vivo
A. Cardiac CD45⁺ cells were isolated from saline or Doxorubicin (Dox) treated mice, then analyzed by CITE-seq. Shown is dimensional reduction analysis by harmony single-cell transform in UMAP plot. B. Cardiac T-cells were identified by CD3⁺ surface expression and RNA, then selected gene expression analysis shown in dot plots between Dox and Saline treated mice. C. Mice were treated with PBS or Doxorubicin (DR) for 4 or 8 weeks before harvesting tissues. D. Echocardiography was used to measure ejection fraction. E-G. CD8⁺ T-cells were isolated from blood and RT-qPCR was used to measure expression of selected ECM modifying enzymes. H-J. CD8⁺ T-cells were isolated from the spleen and RT-qPCR was used to measure expression of selected ECM modifying enzymes. K. Splenic T-cells from PBS or 8 week DR treated mice were analyzed by western blot for LOX expression. Statistical analysis by 1-way ANOVA, ns = no significance, * = $p < 0.05$, ** = $p < 0.01$, *** = $p < 0.001$.

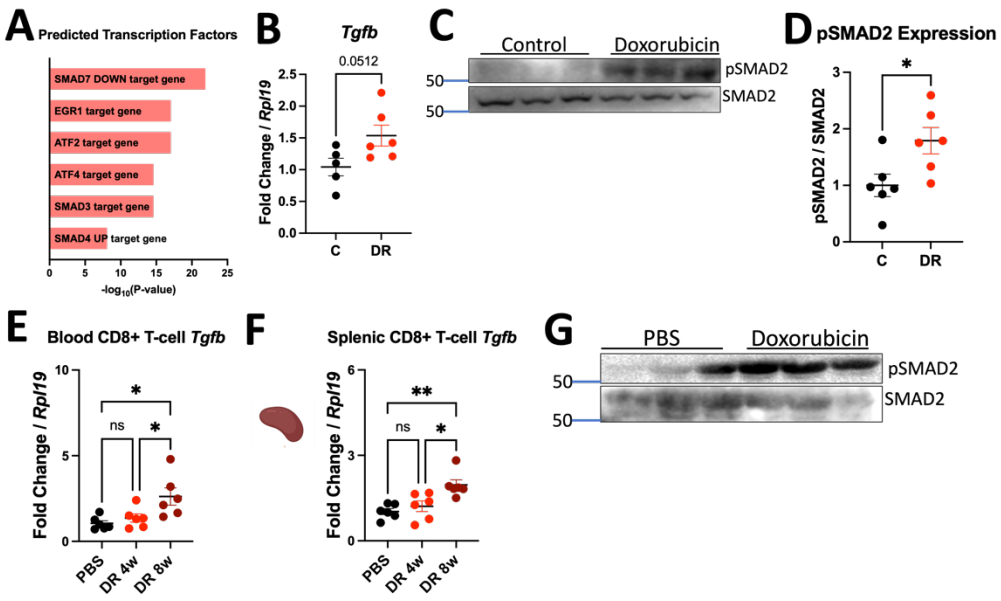


Figure 9-19 Doxorubicin Treatment of CD8⁺ T-cells Induces TGFβ Signaling
A. GO Enrichment analysis using ShinyGO 0.82 predicted transcription factors in human patient bulk-RNA sequencing. B. Mouse Tc1 cells were treated for 24 hours with 0.1 μg/mL DR, then RT-qPCR was used to measure *Tgfb* expression. C. Western blot was used to measure pSMAD2 phosphorylation in untreated or Doxorubicin treated Tc1 cells, quantified in D. for n=6 independent experiments. E-F. RT-qPCR was used on $CD8^+$ T-cells from blood (E) or spleens (F) of mice treated with Doxorubicin (DR) to measure *Tgfb* expression. G. Western blot was used to measure pSMAD2 phosphorylation in $CD8^+$ T-cells from PBS or 8 week DR treated mice. Statistical analysis by T-test (B,D), or 1-way ANOVA (E,F). p values listed, or ns = no significance, * = $p < 0.05$, ** = $p < 0.01$

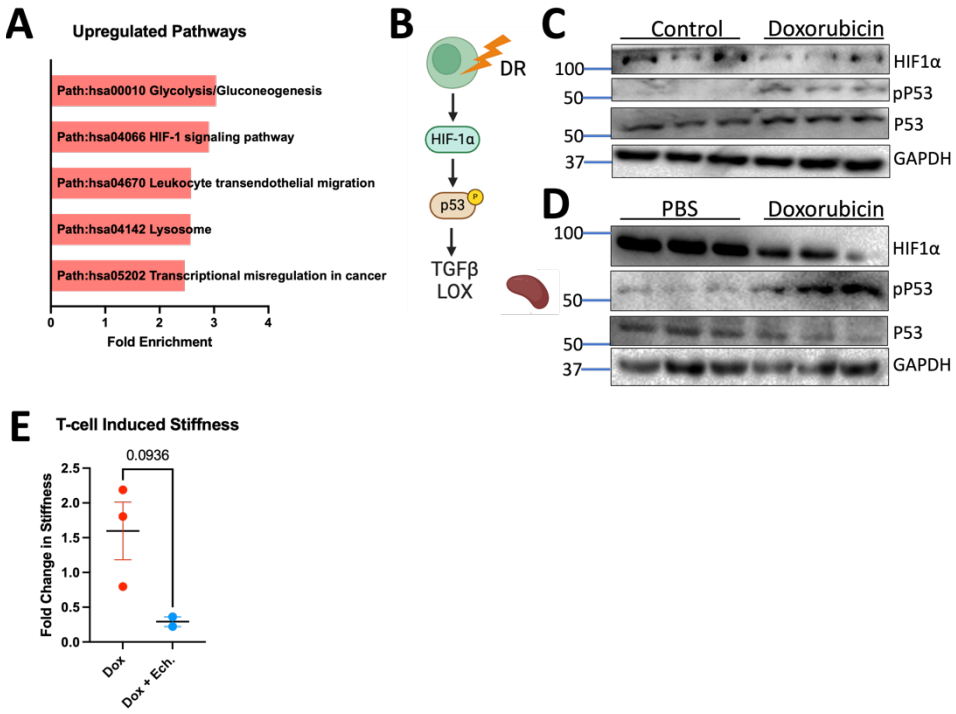


Figure 9-20 Doxorubicin Treatment Induces HIF1α-p53 Signaling That Contributes to Matrix Stiffening

A. GO Enrichment analysis using ShinyGO 0.82 for upregulated pathways in human patient bulk-RNA sequencing. B. Schematic of potential signaling downstream of DR treatment in T-cells that leads to TGFβ expression. C. Mouse Tc1 cells were treated for 24 hours with 0.1 μg/mL DR, then western blot was used to measure HIF1α levels and p53 phosphorylation from n=3 independent experiments. D. Western blot was used to measure HIF1α levels and p53 phosphorylation in splenic $CD8^+$ T-cells from mice treated with PBS or 8 weeks of DR. E. Stiffness was measured from decellularized RVs before and after treatment with DR conditioned media in the presence or absence of Echinomycin (Ech. = HIF1α inhibitor). Statistical analysis by T-test, p-value shown.

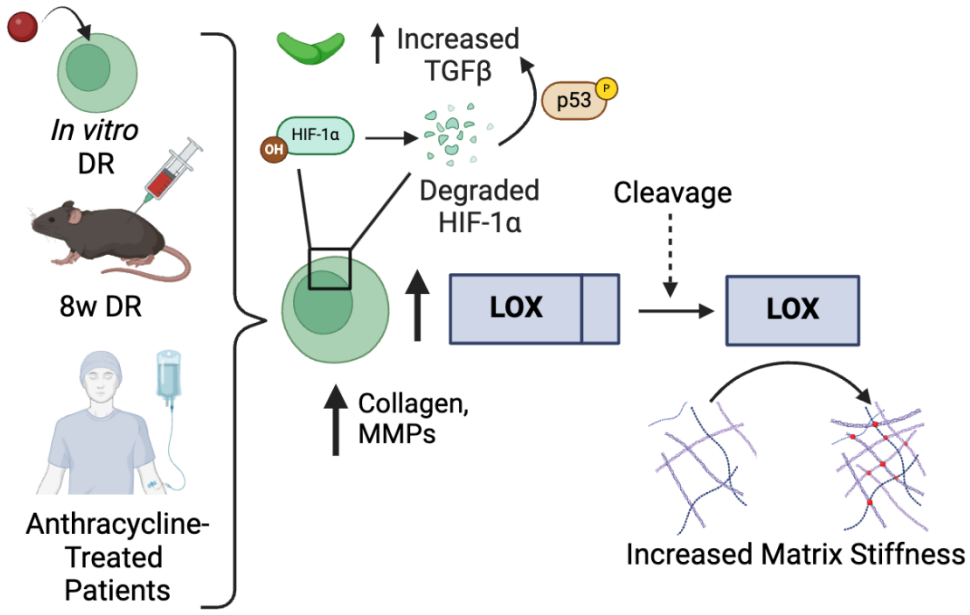


Figure 9-21 Schematic of Mechanism for DR-Induction of $CD8^+$ T-cell Matrix Stiffening

9.7 Deletion of T-cell TLR4 Does Not Alter Pressure Overload Induced Heart Failure in Mice

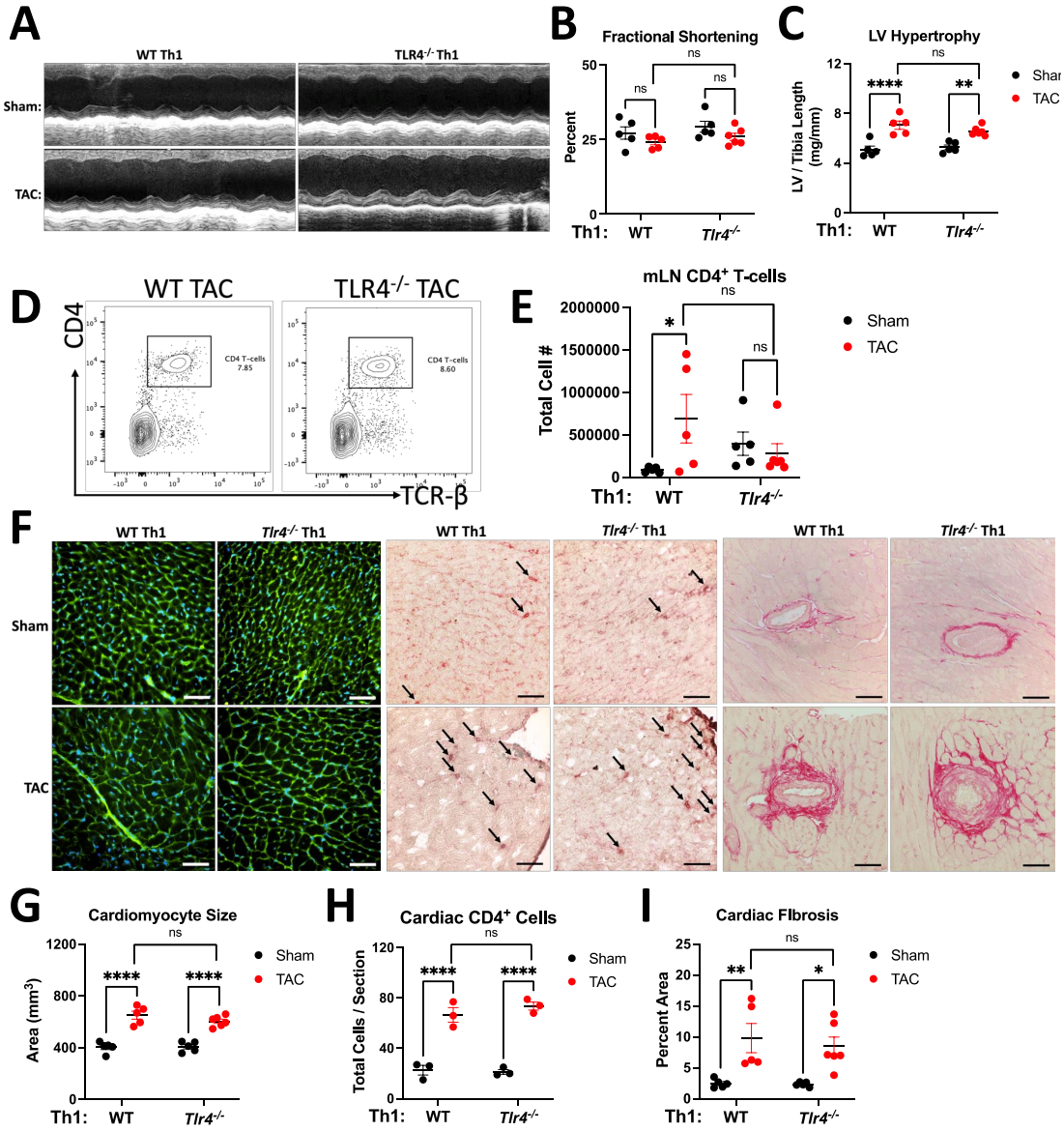


Figure 9-22 Adoptive Transfer of TLR4$^{-/-}$ Th1 Cells in the Onset of TAC Results in Similar Pathology As Transfer of WT Cells

8-10 week old male *Tcra*$^{-/-}$ mice underwent 25G TAC or Sham surgery then were reconstituted with 10 million WT or *Tlr4*$^{-/-}$ Th1 cells 2 days, then 2 weeks post surgery, and tissues were harvested after 4 weeks. A. Representative M-mode echocardiographs after 4 weeks. B. Fractional shortening as measured by echocardiography after 4 weeks. C. Measured weight of excised left ventricles normalized to tibia length. D-E. Mediastinal lymph nodes were digested to a single cell suspension, then analyzed by flow cytometry. Representative flow cytometry plots for TAC mice (D) gated on CD45^{+} cells, quantified in E. for CD4^{+}TCRβ^{+} T-cells. F. Representative images of LV of WGA (left), CD4^{+} T-cells by IHC (middle), and picrosirius red (right), Scale bars are 50 μM (left/middle) or 100 μM (right). G. Average cardiomyocyte size quantified using ImageJ on WGA stained sections. H. CD4 infiltration was counted manually after IHC stain for CD4. I. Left ventricular perivascular fibrosis quantified with ImageJ from Picrosirius red stained sections. Each data point is an individual mouse. Statistical analysis by 2-way ANOVA with Sidák's multiple comparison test, ns = no significance, * = $p < 0.05$, ** = $p < 0.01$, *** = $p < 0.001$, **** = $p < 0.0001$.

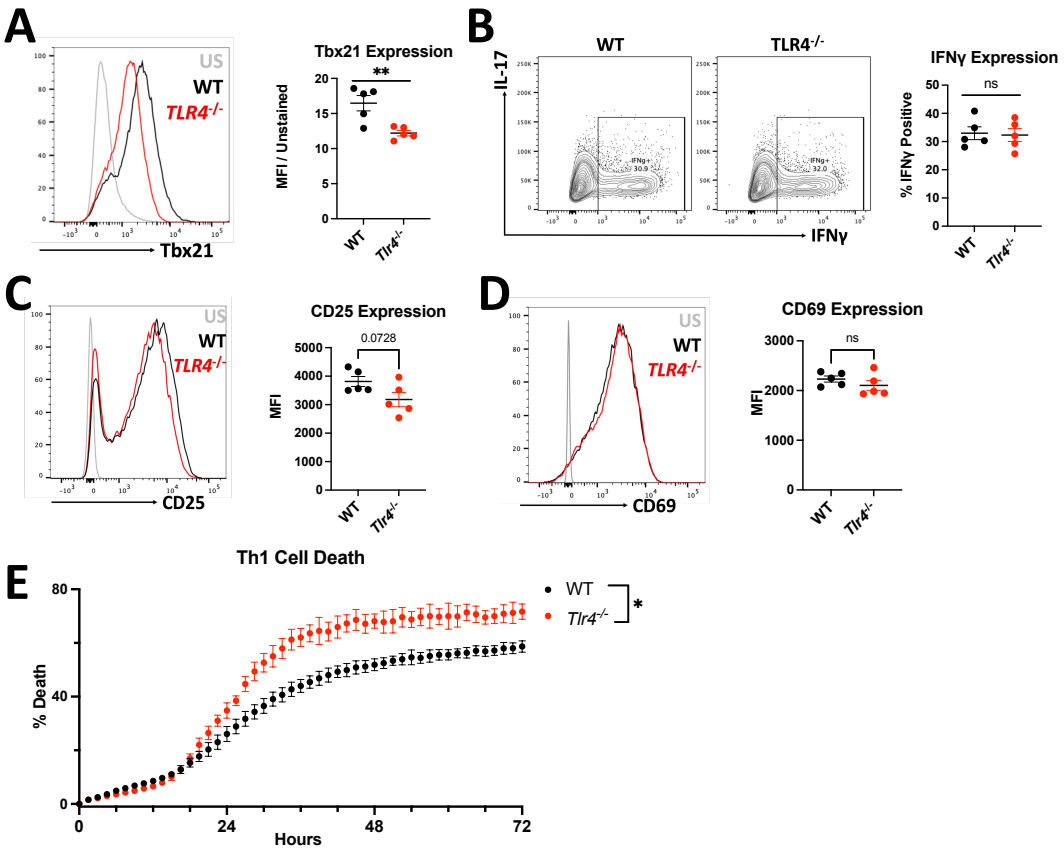


Figure 9-23 TLR4$^{-/-}$ Th1 cells Show Minor Changes in Differentiation and Worse Survival In vitro

WT or *Tlr4*$^{-/-}$ Th1 cells were differentiated *in vitro.* **A.** Cells were stained for Tbx21 using intracellular cytokine staining, representative flow cytometry plots shown in gated on CD4^{+} cells with quantification in from n=5 independent experiments**. B.** Cells were stained for IFNγ using intracellular cytokine staining, representative flow cytometry plots shown gated on CD4^{+} cells with quantification in from n=5 independent experiments**. C-D.** Cells were stained for CD25 (**C**) or CD69 (**D)** representative flow cytometry plots shown gated on CD4^{+} cells with quantification in from n=5 independent experiments. **E.** WT or *Tlr4*$^{-/-}$ Th1 cells were cultured on αCD43 coated plates (10 µg/mL) in the presence of 10 µg/mL PI in media with or without 10% FBS. PI incorporation was monitored for 72 hours, baseline subtracted, and normalized to a 100% death Triton-X treated control. Statistical analysis by T-test (A-D) or 2-way ANOVA with repeated measures, ns = no significance, * = $p < 0.05$, ** = $p < 0.01$.

9.8 DAMP Treatment of T-cells and Cardiac Fibroblasts

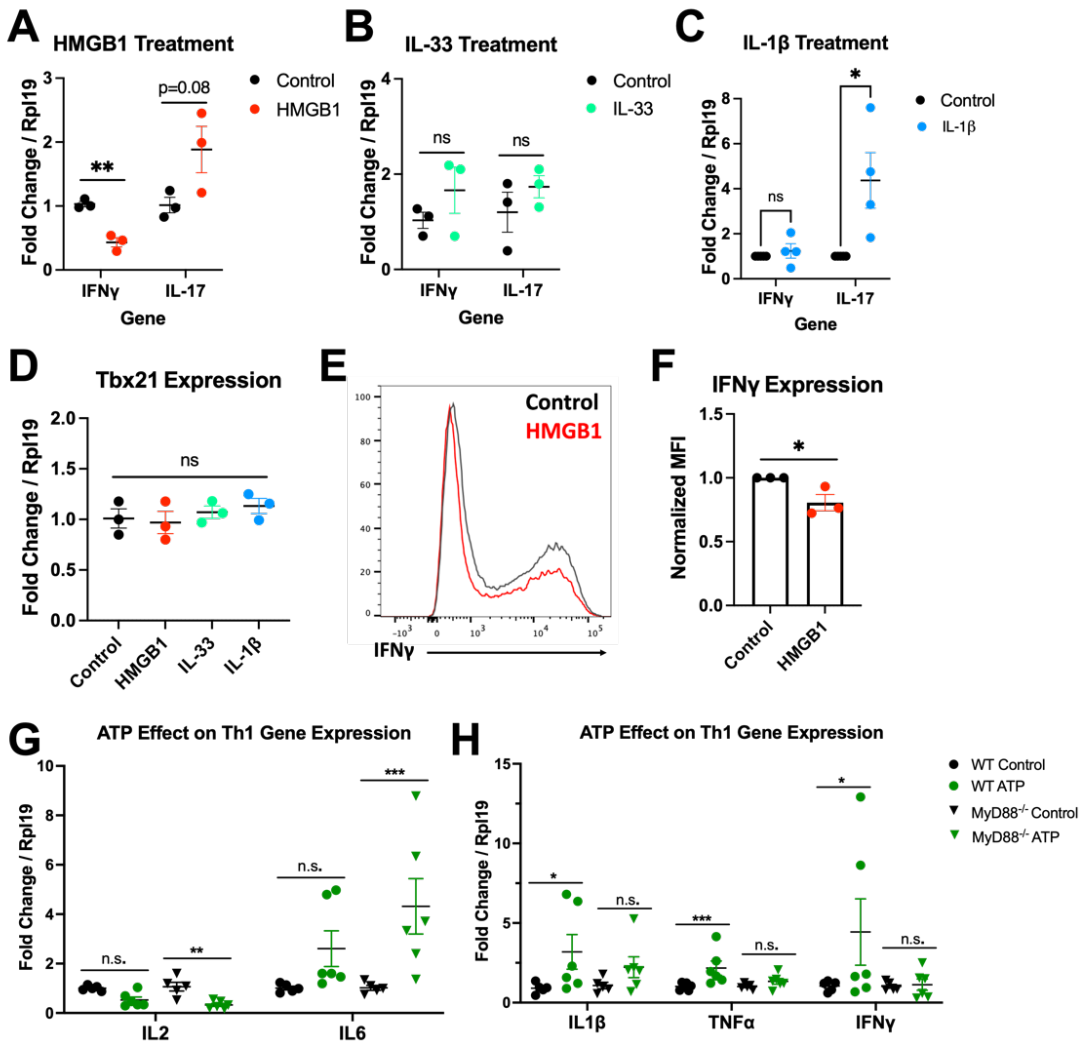


Figure 9-24 DAMP Treatment of T-cells Can Alter Cytokine Expression
WT or MyD88$^{-/-}$ activated Th1 cells were treated with 5 μg/mL HMGB1, 5 μg/mL IL-1β, 5 μg/mL IL-33 2.5 μg/mL LPS, or 200 μm ATP where indicated. All HMGB1 treatments were done in T-cell media lacking β-ME for oxidizing conditions. A-D. RNA was isolated from T-cells and RT-qPCR was used to measure IFNγ, IL-17, or Tbx21 expression. E-F. Cells were stimulated with PMA/Ionomycin in the presence of Brefeldin A and Monensin for 4 hours, then intracellular cytokine staining was used to measure IFNγ, shown are representative flow cytometry plots with normalized MFI shown in F. G-H. RNA was isolated from T-cells and RT-qPCR was used to measure IL-2, IL-6, IL-1β, TNFα, or IFNγ. Statistical analysis by T-tests, ns = no significance, * = $p < 0.05$, ** = $p < 0.01$, *** = $p < 0.001$, **** = $p < 0.0001$.

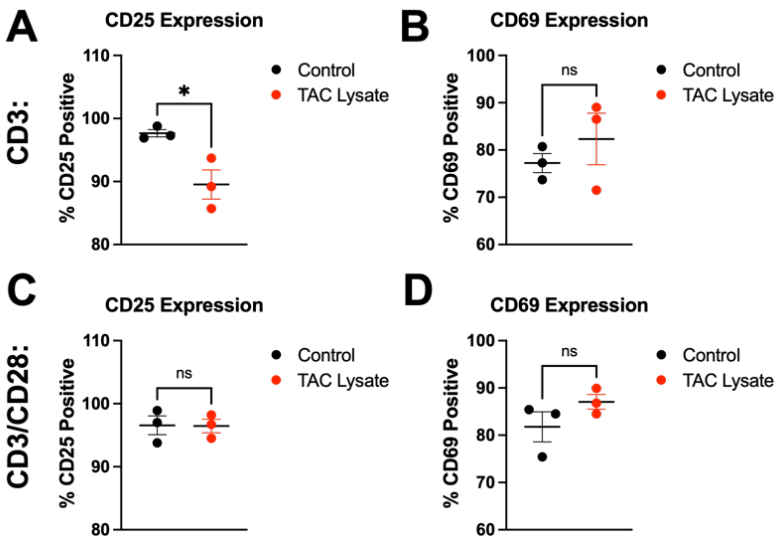


Figure 9-25 DAMPs in TAC Lysate Decrease CD25 in the Absence of Co-stimulation
WT Th1 cells were activated with 2.5 µg/mL αCD3 alone (A-B) or αCD3 and 1.0 µg/mL αCD28 (C-D) for 3 days, before treatment with 10 µg/mL LV TAC lysate. Flow cytometry was used to measure CD25 expression (A, C) or CD69 expression (B, D). Statistical analysis by T-test, ns = no significance, * = $p < 0.05$.

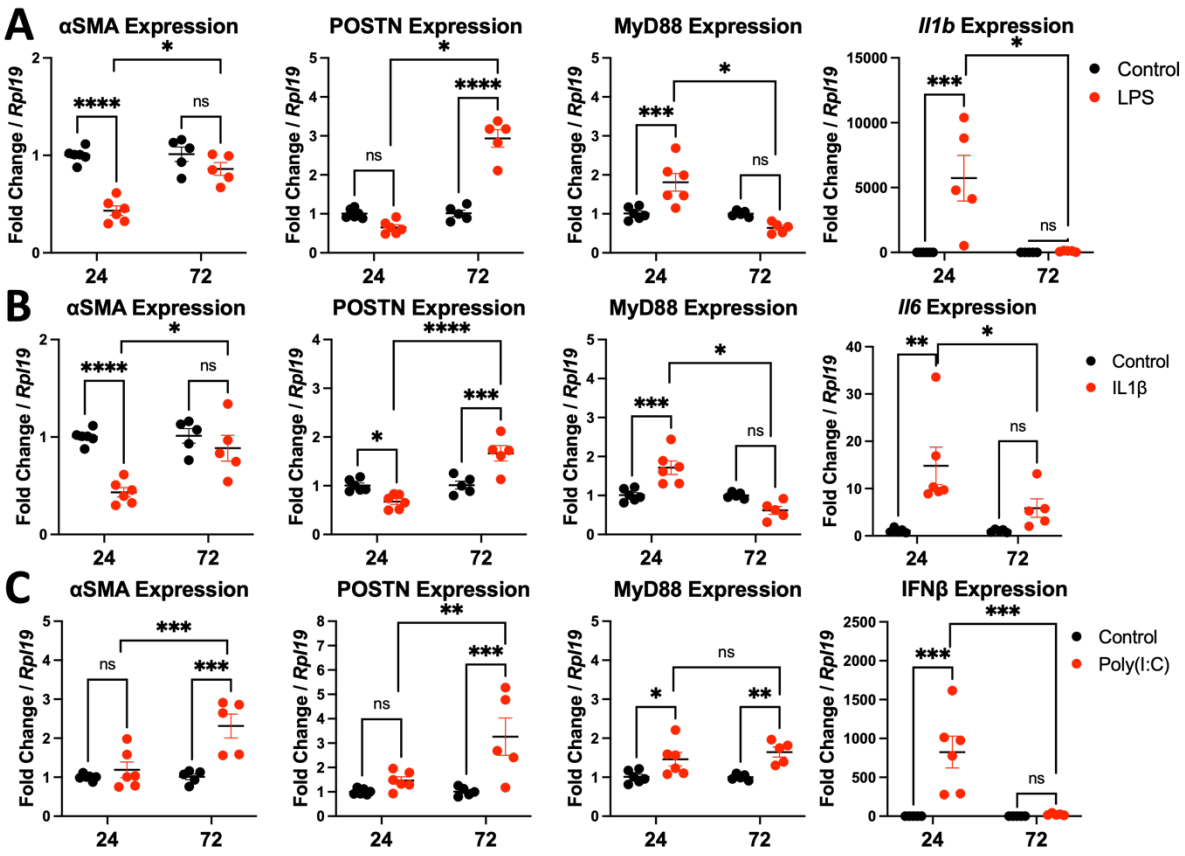


Figure 9-26 MyD88 Stimulation Regulates Fibroblast Transformation and Cytokine Expression in a Temporal Manner

WT mouse fibroblasts were treated with 2.5 μg/mL LPS (A), 100 ng/mL IL-1β (B), or transfected with 1 μg/mL low MW poly(I:C) (C) for 24 or 72 hours where indicated. RNA was isolated and RT-qPCR was used to measure aSMA, Postn, MyD88, or IFNβ expression. ns = no significance, * = $p < 0.05$, ** = $p < 0.01$, *** = $p < 0.001$, **** = $p < 0.0001$.

9.9 Additional Characterization of Systemic T-cell Inflammation in Doxorubicin Treated Mice

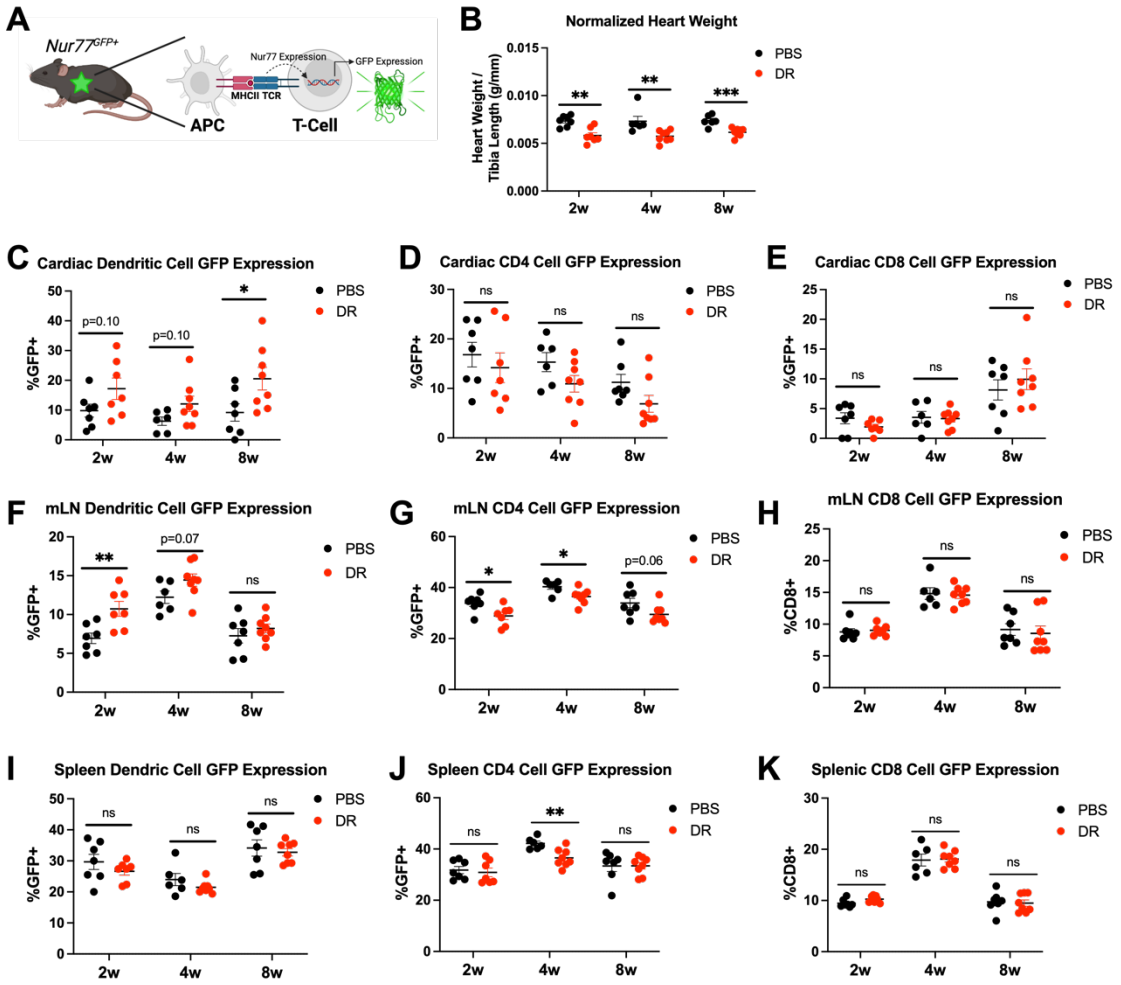


Figure 9-27 Doxorubicin Treatment of Nur77-GFP Mice

A. Nur77-GFP mice were treated with Doxorubicin 5.0 mg/kg IP or saline for 2, 4, or 8 weeks before euthanasia. B. Normalized heart weight over tibia length. C-E. Hearts were digested enzymatically and mechanically then analyzed by flow cytometry for GFP expression in dendritic cells (C – CD11b+CD11c+MHCII+), $CD4^+$ T-cells (D – CD11b-CD4+) or $CD8^+$ T-cells (E – CD11b-$CD8^+$). F-H. mLN were digested mechanically then analyzed by flow cytometry for GFP expression in dendritic cells (F) $CD4^+$ T-cells (G) or $CD8^+$ T-cells (H). I-K. Spleens were digested mechanically then analyzed by flow cytometry for GFP expression in dendritic cells (I) $CD4^+$ T-cells (J) or $CD8^+$ T-cells (K). Statistical analysis by 2-way ANOVA with Sidak's multiple comparison test. ns = no significance, * = $p < 0.05$, ** = $p < 0.01$, *** = $p < 0.001$, **** = $p < 0.0001$.

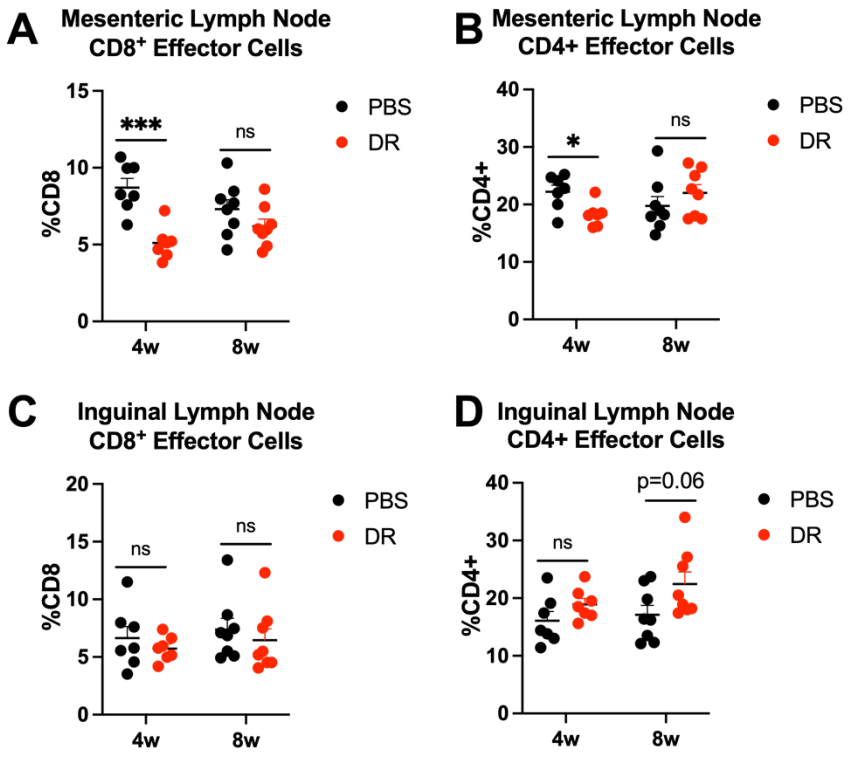


Figure 9-28 Systemic Effector T-cells in Doxorubicin Treated Mice
A. WT mice were treated with Doxorubicin 5.0 mg/kg IP or saline for 4, or 8 weeks before euthanasia. A-B. Mesenteric lymph nodes were digested mechanically, then analyzed by flow cytometry for effector T-cells ($CD44^{hi}CD62L^{lo}$ – see chapter 6 for gating strategy) of $CD8^+$ T-cells (A) or $CD4^+$ T-cells (B). C-D. Inguinal lymph nodes were digested mechanically, then analyzed by flow cytometry for effector T-cells of $CD8^+$ T-cells (C) or $CD4^+$ T-cells (D). Statistical analysis by 2-way ANOVA with Sidak's multiple comparison test. ns = no significance, * = $p < 0.05$, ** = $p < 0.01$, *** = $p < 0.001$, **** = $p < 0.0001$.

9.10 Primers and siRNAs Used

qPCR - Mouse		
Target	**Forward**	**Reverse**
α-MHC	CCTAGCCAACTCCCCGTTCT	GCCAATGAGTACCGCGTGA
β-MHC	TGAGCCTTGGATTCTCAAACGT	AGGTGGCTCCGAGAAAGGAA
ANP	GAGAGACGGCAGTGCTTCTAGGC	CGTGACACACCACAAGGGCTTAGG
BNP	CACCGCTGGGAGGTCACT	GTGAGGCCTTGGTCCTTCAA
αSMA	GTCCCAGACATCAGGGAGTAA	TCGGATACTTCAGCGTCAGGA
Col1a1	GTATGCTTGATCTGTATCTG	CGATCCTACATCTTCTG
Col3	CCTGGTCAGTCCTATGAG	CAGGAGCAGGTGTAGAAG
Cxcl9	CTTGAGCCTAGTCGTGATAAC	CCAGCTTGGTGAGGTCTATC
Cxcl10	ATGACGGGCCAGTGAGAATG	ATTCTTTTTCATCGTGGCAATGA
Fibronectin	ATGTGGACCCCTCCTGATAGT	GCCCAGTGATTTCAGCAAAGG
Granzyme B	CCACTCTCGACCCTACATGG	GGCCCCCAAAGTGACATTTATT
Icam1	GTGATGCTCAGGTATCCATCCA	CACAGTTCTCAAAGCACAGCG
Ifnα	TCTGATGCAGCAGGTGGG	AGGGCTCTCCAGACTTCTGCTCTG
Ifnβ	CGTGGGAGATGTCCTCAACT	AGATCTCTGCTCGGACCACC
Ifnar	AGCCACGGAGAGTCAATGG	GCTCTGACACGAAACTGTGTTTT
IFNγ	CGGCACAGTCATTGAAAGCCTA	GTTGCTGATGGCCTGATTGTC
IL-1β	GAAATGCCACCTTTTGACAGTG	TGGATGCTCTCATCAGGACAG
IL-6	TGATGGATGCTACCAAACTGG	TTCATGTACTCCAGGTAGCTATGG
Irf9	GCCGAGTGGTGGGTAAGAC	GCAAAGGCGCTGAACAAAGAG
Lox	TCTTCTGCTGCGTGACAACC	GAGAAACCAGCTTGGAACCAG
Loxl1	GAGTGCTATTGCGCTTCCC	GGTTGCCGAAGTCACAGGT
Mmp9	GCAGAGGCATACTTGTACCG	TGATGTTATGATGGTCCCACTTG

Mmp13	GGGCTCTGAATGGTTATGACATTC	AGCGCTCAGTCTCTTCACCTCTT
MyD88	CTAGGACAAACGCCGGAACT	ATTAGCTCGCTGGCAATGGA
MyD88 codon optimized	TCGCATAGAGGAGGATTGT	GGATCATCGAGAGTGGTAATTC
Oasl2	GGATGCCTGGGAGAGAATCG	TCGCCTGCTCTTCGAAAC
Perforin 1	CAAGGTAGCCAATTTTGCAGC	GTACATGCGACACTCTACTGTG
Postn	CACGGCATGGTTATTCCTTCA	TCAGGACACGGTCAATGACAT
Rpl19	CCCGTCAGCAGATCAGGAA	GTCACAGGCTTGCGGATGA
Tbx21	AACCGCTTATATGTCCACCCA	CTTGTTGTTGGTGAGCTTTAGC
TGFβ	CCACCTGCAAGACCATCGAC	CTGGCGAGCCTTAGTTTGGAC
VCAM1	AGTTGGGGATTCGGTTGTTCT	CCCCTCATTCCTTACCACCC
qPCR - Human		
αSMA	CAAGTCCTCCAGCGTTCTGA	TAGTCCCGGGGATAGGCAAA
Col1	GAGGGCCAAGACGAAGACATC	CAGATCACGTCATCGCACAAC
CXCL9	CCAGTAGTGAGAAAGGGTCGC	AGGGCTTGGGGCAAATTGTT
CXCL10	GCCAATTTTGTCCACGTGTTG	GGCCTTCGATTCTGGATTCA
GAPDH	GGAGCGAGATCCCTCCAAAAT	GGCTGTTGTCATACTTCTCATGG
Ifnα	GCCTCGCCCTTTGCTTTACT	CTGTGGGTCTCAGGGAGATCA
Ifnβ	ATGACCAACAAGTGTCTCCTCC	GGAATCCAAGCAAGTTGTAGCTC
Lox	GCCGACCAAGATATTCCTGGG	GCAGGTCATAGTGGCTAAACTC
Mmp9	AGACCTGGGCAGATTCCAAAC	CGGCAAGTCTTCCGAGTAGT
MyD88	GAGGCTGAGAAGCCTTTACAGG	GCAGATGAAGGCATCGAAACGC
Postn	CTCATAGTCGTATCAGGGGTCG	ACACAGTCGTTTTCTGTCCAC
Genotyping		
MyD88 Exon 3	ATACCGGAAGCAGATGGATG	AGGCTGAGTGCAAACTTGGT

STING	ACACGCTCTGTTTACTATGAACCTC	GGGGGAAGGAGAGAACTGAC
siRNAs		
Scramble	Thermofisher siRNA negative control #1 (Thermofisher 4390843)	
αSmurf2-1	GCGUAUGGAAUCAUAAGAATT	
αSmurf2-2	GGAAUCAUAUAGACAGGUCTT	

Table 9-1 Primers and siRNAs Used

Complete Published List of Works by Author During Thesis:

1. **Bayer, A. L**. & Alcaide, P. MyD88: At the heart of inflammatory signaling and cardiovascular disease. *Journal of Molecular and Cellular Cardiology* **161**, 75–85 (2021).
2. Anastasiou M, Newton GA, Kaur K, Carrillo-Salinas FJ, Smolgovsky SA, **Bayer AL**, Ilyukha V, Sharma S, Poltorak A, Luscinskas FW, et al. Endothelial STING controls Tcell transmigration in an IFN-I dependent manner. *JCI Insight* **6(15),** (2021)
3. **Bayer A.L**., Pietruska, J., Farrell, J., McRee. S., Alcaide P., Hinds, P.W. AKT1 Is Required for a Complete Palbociclib-Induced Senescence Phenotype in BRAF-V600E-Driven Human Melanoma. *Cancers* **14,** 572 (2022).
4. **Bayer, A.L.** *et al.* T-Cell MyD88 Is a Novel Regulator of Cardiac Fibrosis Through Modulation of T-Cell Activation. *Circulation Research* **133**, 412–429 (2023).
5. McRee, S. K., **Bayer, A. L.**, Pietruska, J., Tsichlis, P. N. & Hinds, P. W. AKT2 Loss Impairs BRAF-Mutant Melanoma Metastasis. *Cancers* **15**, 4958 (2023).
6. Smolgovsky, S., **Bayer, A.L.,** *et al.* Impaired T cell IRE1α-XBP1 signaling directs inflammation in experimental Heart Failure with Preserved Ejection Fraction. *J Clin Invest* (2023) doi:10.1172/JCI171874.
7. Hill CJ, Datta S, McCurtin NP, Kimball HZ, Kingsley MC, **Bayer AL**, Martin AC, Peng Q, Weerapana E, Scheck RA. A Modular Turn-On Strategy to Profile E2-Specific Ubiquitination Events in Living Cells. *Angew Chem Int Ed Engl*. 22;63(13):e202319579. (2024)
8. **Bayer, A. L.,** Padilla-Rolon, D., Smolgovsky, S., Hinds, P. W. & Alcaide, P. Deletion of MyD88 in T Cells Improves Antitumor Activity in Melanoma. *The American Journal of Pathology* **194**, 1007–1019 (2024).
9. **Bayer, A. L.** *et al.* Cytotoxic T cells drive doxorubicin-induced cardiac fibrosis and systolic dysfunction. *Nat Cardiovasc Res* **3**, 970–986 (2024).

10. **Bayer, A. L.**, Magri, Z., Muendlein, H., Poltorak, A. & Alcaide, P. MyD88 Determines T-cell Fate Through BCAP-PI3K Signaling. *The Journal of Immunology. In press* (2025).
11. Huang, Y. V., Sun, Y., Chou, H., Wagner, N., Vitale, M.R., **Bayer, A.L.,** *et al.* A Novel Therapeutic Approach using CXCR3 Blockade to Treat Immune Checkpoint Inhibitor-mediated Myocarditis. *Circ Res. In press* 2025
12. Higashikuni, Y., Platt, C., . . . **Bayer, A.L.,** *et al.* Mitigation of Doxorubicin Cardiotoxicity with Synergistic miRNA Combinations Identified Using Combinatorial Genetics en Masse (CombiGEM). *JACC CardioOncology. In press* (2025).
13. **Bayer, A.L.,** Smolgovsky, S., Aronovitz, M., *et al.* Experimental Pressure Overload Induces a Cardiac Neoantigen Specific Humoral Immune Response. *Journal of Molecular and Cellular Cardiology. In press* (2025).

Chapter 10 Bibliography:

1. Martin, S. S. *et al.* 2024 Heart Disease and Stroke Statistics: A Report of US and Global Data From the American Heart Association. *Circulation* (2024) doi:10.1161/CIR.0000000000001209.
2. Siegel, R. L., Giaquinto, A. N. & Jemal, A. Cancer statistics, 2024. doi:10.3322/caac.21820.
3. The top 10 causes of death. https://www.who.int/news-room/fact-sheets/detail/the-top-10-causes-of-death.
4. Handy, C. E. *et al.* Synergistic Opportunities in the Interplay Between Cancer Screening and Cardiovascular Disease Risk Assessment. *Circulation* **138**, 727–734 (2018).
5. Bell, C. F. *et al.* Risk of Cancer After Diagnosis of Cardiovascular Disease. *JACC: CardioOncology* **5**, 431–440 (2023).
6. Battisti, N. M. L. *et al.* Prevalence of Cardiovascular Disease in Patients With Potentially Curable Malignancies: A National Registry Dataset Analysis. *JACC: CardioOncology* **4**, 238 (2022).
7. Stoltzfus, K. C. *et al.* Fatal heart disease among cancer patients. *Nature Communications* **11**, 2011 (2020).
8. Malik, A., Brito, D., Vaqar, S. & Chhabra, L. Congestive Heart Failure. in *StatPearls* (StatPearls Publishing, Treasure Island (FL), 2024).
9. Golla, M. S. G., Hajouli, S. & Ludhwani, D. Heart Failure and Ejection Fraction. in *StatPearls* (StatPearls Publishing, Treasure Island (FL), 2024).
10. null, null. Effects of Enalapril on Mortality in Severe Congestive Heart Failure. *New England Journal of Medicine* **316**, 1429–1435 (1987).
11. Caraballo, C. *et al.* Clinical Implications of the New York Heart Association Classification. *Journal of the American Heart Association* **8**, e014240 (2019).

12. Heidenreich, P. A. *et al.* 2022 AHA/ACC/HFSA Guideline for the Management of Heart Failure: A Report of the American College of Cardiology/American Heart Association Joint Committee on Clinical Practice Guidelines. *Circulation* **145**, e895–e1032 (2022).

13. Redfield, M. M. & Borlaug, B. A. Heart Failure With Preserved Ejection Fraction: A Review. *JAMA* **329**, 827–838 (2023).

14. Roger, V. L. Epidemiology of Heart Failure. *Circulation Research* **128**, 1421–1434 (2021).

15. Bloom, M. W. *et al.* Cardio-Oncology and Heart Failure: A Scientific Statement from the Heart Failure Society of America. *Journal of Cardiac Failure* (2024) doi:10.1016/j.cardfail.2024.08.045.

16. Asnani, A. *et al.* Preclinical Models of Cancer Therapy–Associated Cardiovascular Toxicity: A Scientific Statement From the American Heart Association. *Circulation Research* **129**, e21–e34 (2021).

17. Meijers, W. C. & de Boer, R. A. Common risk factors for heart failure and cancer. *Cardiovascular Research* **115**, 844–853 (2019).

18. Lawson, C. A. *et al.* Risk Factors for Heart Failure. *Circulation: Heart Failure* **13**, e006472 (2020).

19. Inamdar, A. A. & Inamdar, A. C. Heart Failure: Diagnosis, Management and Utilization. *J Clin Med* **5**, 62 (2016).

20. Arrigo, M. *et al.* Acute heart failure. *Nat Rev Dis Primers* **6**, 1–15 (2020).

21. Update | Cardiac Biomarkers and Heart Failure. *American College of Cardiology* https://www.acc.org/http%3a%2f%2fwww.acc.org%2flatest-in-cardiology%2farticles%2f2015%2f02%2f09%2f13%2f00%2fcardiac-biomarkers-and-heart-failure.

22. Alvarez, -Cardona Jose A. *et al.* Cardio-Oncology Education and Training. *Journal of the American College of Cardiology* **76**, 2267–2281 (2020).

23. Beavers, C. J. *et al.* Cardio-Oncology Drug Interactions: A Scientific Statement From the American Heart Association. *Circulation* **145**, e811–e838 (2022).

24. Herrmann, J., (Chair) *et al.* Defining cardiovascular toxicities of cancer therapies: an International Cardio-Oncology Society (IC-OS) consensus statement. *European Heart Journal* **43**, 280–299 (2022).

25. Tini, G. *et al.* Arterial hypertension in cancer: The elephant in the room. *International Journal of Cardiology* **281**, 133–139 (2019).

26. Tsilidis, K. K., Kasimis, J. C., Lopez, D. S., Ntzani, E. E. & Ioannidis, J. P. A. Type 2 diabetes and cancer: umbrella review of meta-analyses of observational studies. *BMJ* **350**, g7607 (2015).

27. Liu, J.-J. *et al.* Inhibition of Lymphoma Cell Proliferation by Peroxisomal Proliferator-Activated Receptor-γ Ligands via Wnt Signaling Pathway. *Cell Biochem Biophys* **62**, 19–27 (2012).

28. Mani, A. *et al.* LRP6 Mutation in a Family with Early Coronary Disease and Metabolic Risk Factors. *Science (New York, N.Y.)* **315**, 1278 (2007).

29. Calvillo-Argüelles, O. *et al.* Cardiovascular Disease Among Patients With AML and CHIP-Related Mutations. *JACC: CardioOncology* **4**, 38 (2022).

30. Dorsheimer, L. *et al.* Association of Mutations Contributing to Clonal Hematopoiesis With Prognosis in Chronic Ischemic Heart Failure. *JAMA Cardiology* **4**, 32 (2018).

31. Connaughton, M. & Dabagh, M. Association of Hypertension and Organ-Specific Cancer: A Meta-Analysis. *Healthcare* **10**, 1074 (2022).

32. Peng, Q., Zhu, J., Zhang, Y. & Jing, Y. Blood hypercoagulability and thrombosis mechanisms in cancer patients -A brief review. *Heliyon* **10**, e38831 (2024).

33. Qureshi, A. I. *et al.* Incident Cancer in a Cohort of 3,247 Cancer Diagnosis Free Ischemic Stroke Patients. *Cerebrovascular Diseases* **39**, 262–268 (2015).

34. Corrao, G., Scotti, L., Bagnardi, V. & Sega, R. Hypertension, Antihypertensive Therapy and Renal-Cell Cancer: A Meta-Analysis. *http://www.eurekaselect.com*.

35. Suzuki, M. *et al.* Incidence of cancers in patients with atherosclerotic cardiovascular diseases. *International Journal of Cardiology. Heart & Vasculature* **17**, 11 (2017).

36. Libby, P. & Kobold, S. Inflammation: a common contributor to cancer, aging, and cardiovascular diseases—expanding the concept of cardio-oncology. *Cardiovascular Research* **115**, 824 (2019).

37. Koelwyn, G. J., Aboumsallem, J. P., Moore, K. J. & Boer, R. A. de. Reverse cardio-oncology: Exploring the effects of cardiovascular disease on cancer pathogenesis. *Journal of Molecular and Cellular Cardiology* **0**, (2021).

38. Narayan, V. *et al.* Mechanistic Biomarkers Informative of Both Cancer and Cardiovascular Disease. *Journal of the American College of Cardiology* **75**, 2726 (2020).

39. de Wit, S. *et al.* Heart failure-induced microbial dysbiosis contributes to colonic tumour formation in mice. *Cardiovascular Research* **120**, 612–622 (2024).

40. Koelwyn, G. J. *et al.* Myocardial infarction accelerates breast cancer via innate immune reprogramming. *Nat Med* **26**, 1452–1458 (2020).

41. Caller, T. *et al.* Small Extracellular Vesicles From Infarcted and Failing Heart Accelerate Tumor Growth. *Circulation* **149**, 1729–1748 (2024).

42. Meijers, W. C. *et al.* Heart Failure Stimulates Tumor Growth by Circulating Factors. *Circulation* **138**, 678–691 (2018).

43. de Wit, S. *et al.* Pressure Overload–Induced Cardiac Hypertrophy Stimulates Tumor Growth in Tumor-Prone ApcMin Mice. *Circulation: Heart Failure* **16**, e010740 (2023).

44. Avraham, S. *et al.* Early Cardiac Remodeling Promotes Tumor Growth and Metastasis. *Circulation* **142**, 670–683 (2020).

45. Elster, S. K., Braunwald, E. & Wood, H. F. A study of C-reactive protein in the serum of patients with congestive heart failure. *American Heart Journal* **51**, 533–541 (1956).

46. Aukrust, P. *et al.* Cytokine network in congestive heart failure secondary to ischemic or idiopathic dilated cardiomyopathy. *The American Journal of Cardiology* **83**, 376–382 (1999).

47. Testa, M. *et al.* Circulating Levels of Cytokines and Their Endogenous Modulators in Patients With Mild to Severe Congestive Heart Failure Due to Coronary Artery Disease or Hypertension. *Journal of the American College of Cardiology* **28**, 964–971 (1996).

48. Torre-Amione, G. *et al.* Proinflammatory cytokine levels in patients with depressed left ventricular ejection fraction: A report from the studies of left ventricular dysfunction (SOLVD). *Journal of the American College of Cardiology* **27**, 1201–1206 (1996).

49. Aukrust, P. *et al.* Elevated Circulating Levels of C-C Chemokines in Patients With Congestive Heart Failure. *Circulation* **97**, 1136–1143 (1998).

50. Carrillo-Salinas, F. J., Ngwenyama, N., Anastasiou, M., Kaur, K. & Alcaide, P. Heart Inflammation: Immune Cell Roles and Roads to the Heart. *The American Journal of Pathology* **189**, 1482–1494 (2019).

51. Adamo, L., Rocha-Resende, C., Prabhu, S. D. & Mann, D. L. Reappraising the role of inflammation in heart failure. *Nat Rev Cardiol* **17**, 269–285 (2020).

52. Amrute, J. M. *et al.* Targeting immune–fibroblast cell communication in heart failure. *Nature* **635**, 423–433 (2024).

53. Deswal, A. *et al.* Safety and Efficacy of a Soluble P75 Tumor Necrosis Factor Receptor (Enbrel, Etanercept) in Patients With Advanced Heart Failure. *Circulation* **99**, 3224–3226 (1999).

54. Bozkurt, B. *et al.* Results of Targeted Anti–Tumor Necrosis Factor Therapy With Etanercept (ENBREL) in Patients With Advanced Heart Failure. *Circulation* **103**, 1044–1047 (2001).

55. Ridker, P. M. *et al.* Antiinflammatory Therapy with Canakinumab for Atherosclerotic Disease. *New England Journal of Medicine* **377**, 1119–1131 (2017).

56. Chung Eugene S., Packer Milton, Lo Kim Hung, Fasanmade Adedigbo A., & Willerson James T. Randomized, Double-Blind, Placebo-Controlled, Pilot Trial of Infliximab, a Chimeric Monoclonal Antibody to Tumor Necrosis Factor-α, in Patients With Moderate-to-Severe Heart Failure. *Circulation* **107**, 3133–3140 (2003).

57. Mann, D. L. *et al.* Targeted Anticytokine Therapy in Patients With Chronic Heart Failure. *Circulation* **109**, 1594–1602 (2004).

58. Abbate, A. *et al.* Interleukin-1 blockade with anakinra and heart failure following ST-segment elevation myocardial infarction: results from a pooled analysis of the VCUART clinical trials. *European Heart Journal - Cardiovascular Pharmacotherapy* **8**, 503–510 (2022).

59. Van Tassell, B. W. *et al.* IL-1 Blockade in Patients With Heart Failure With Preserved Ejection Fraction. *Circulation: Heart Failure* **11**, e005036 (2018).

60. Parrillo, J. E. *et al.* A Prospective, Randomized, Controlled Trial of Prednisone for Dilated Cardiomyopathy. *New England Journal of Medicine* **321**, 1061–1068 (1989).

61. Frustaci, A., Russo, M. A. & Chimenti, C. Randomized study on the efficacy of immunosuppressive therapy in patients with virus-negative inflammatory cardiomyopathy: the TIMIC study. *European Heart Journal* **30**, 1995–2002 (2009).

62. Torre-Amione, G. *et al.* Results of a non-specific immunomodulation therapy in chronic heart failure (ACCLAIM trial): a placebo-controlled randomised trial. *The Lancet* **371**, 228–236 (2008).

63. Wei, F. & Sasada, T. Circulating cytokine signatures as a soluble biomarker of immune checkpoint inhibitor therapy in non-small-cell lung cancer. *Genes Immun* **25**, 89–91 (2024).

64. Shi, Y. *et al.* Circulating cytokines associated with clinical outcomes in advanced non-small cell lung cancer patients who received chemoimmunotherapy. *Thorac Cancer* **13**, 219–227 (2022).

65. Paccagnella, M. *et al.* Circulating Cytokines in Metastatic Breast Cancer Patients Select Different Prognostic Groups and Patients Who Might Benefit from Treatment beyond Progression. *Vaccines (Basel)* **10**, 78 (2022).

66. Propper, D. J. & Balkwill, F. R. Harnessing cytokines and chemokines for cancer therapy. *Nat Rev Clin Oncol* **19**, 237–253 (2022).

67. Fyfe, G. *et al.* Results of treatment of 255 patients with metastatic renal cell carcinoma who received high-dose recombinant interleukin-2 therapy. *JCO* **13**, 688–696 (1995).

68. Younes, A. *et al.* Phase II Clinical Trial of Interleukin-12 in Patients with Relapsed and Refractory Non-Hodgkin's Lymphoma and Hodgkin's Disease. *Clinical Cancer Research* **10**, 5432–5438 (2004).

69. Conlon, K. C. *et al.* Redistribution, Hyperproliferation, Activation of Natural Killer Cells and CD8 T Cells, and Cytokine Production During First-in-Human Clinical Trial of Recombinant Human Interleukin-15 in Patients With Cancer. *J Clin Oncol* **33**, 74–82 (2015).

70. Mann, D. L. The Emerging Field of Cardioimmunology: Past, Present and Foreseeable Future. *Circulation Research* **134**, 1663–1680 (2024).

71. Nidorf, S. M. *et al.* Colchicine in Patients with Chronic Coronary Disease. *New England Journal of Medicine* **383**, 1838–1847 (2020).

72. Pascual-Figal, D. *et al.* Colchicine in acutely decompensated heart failure: the COLICA trial. *European Heart Journal* **45**, 4826–4836 (2024).

73. Nevers Tania *et al.* Left Ventricular T-Cell Recruitment Contributes to the Pathogenesis of Heart Failure. *Circulation: Heart Failure* **8**, 776–787 (2015).

74. Smolgovsky, S. *et al.* Impaired T cell IRE1α-XBP1 signaling directs inflammation in experimental Heart Failure with Preserved Ejection Fraction. *J Clin Invest* (2023) doi:10.1172/JCI171874.

75. Hofmann, U. *et al.* Activation of CD4+ T Lymphocytes Improves Wound Healing and Survival After Experimental Myocardial Infarction in Mice. *Circulation* **125**, 1652–1663 (2012).

76. Nindl, V. *et al.* Cooperation of Th1 and Th17 cells determines transition from autoimmune myocarditis to dilated cardiomyopathy. *European Journal of Immunology* **42**, 2311–2321 (2012).

77. Myers, J. M. *et al.* Cardiac myosin-Th17 responses promote heart failure in human myocarditis. *JCI Insight* **1**, (2016).

78. Zhang, F. *et al.* Therapeutic potential of colchicine in cardiovascular medicine: a pharmacological review. *Acta Pharmacol Sin* **43**, 2173–2190 (2022).

79. Binnewies, M. *et al.* Understanding the tumor immune microenvironment (TIME) for effective therapy. *Nat Med* **24**, 541–550 (2018).

80. Galli, F. *et al.* Relevance of immune cell and tumor microenvironment imaging in the new era of immunotherapy. *Journal of Experimental & Clinical Cancer Research* **39**, 89 (2020).

81. Waldman, A. D., Fritz, J. M. & Lenardo, M. J. A guide to cancer immunotherapy: from T cell basic science to clinical practice. *Nature Reviews Immunology* **20**, 651–668 (2020).

82. Rosenberg, S. A. & Restifo, N. P. Adoptive cell transfer as personalized immunotherapy for human cancer. *Science* **348**, 62–68 (2015).

83. Bhaskar, S. T., Dholaria, B., Savani, B. N., Sengsayadeth, S. & Oluwole, O. Overview of approved CAR-T products and utility in clinical practice. *Clinical Hematology International* **6**, 89–95 (2024).

84. Maude, S. L. *et al.* Tisagenlecleucel in Children and Young Adults with B-Cell Lymphoblastic Leukemia. *N Engl J Med* **378**, 439–448 (2018).

85. Sarnaik, A. A. *et al.* Lifileucel, a Tumor-Infiltrating Lymphocyte Therapy, in Metastatic Melanoma. *JCO* **39**, 2656–2666 (2021).

86. Hodi, F. S. *et al.* Improved Survival with Ipilimumab in Patients with Metastatic Melanoma. *New England Journal of Medicine* **363**, 711–723 (2010).

87. Tawbi, H. A. *et al.* Relatlimab and Nivolumab versus Nivolumab in Untreated Advanced Melanoma. *New England Journal of Medicine* **386**, 24–34 (2022).

88. Wolchok, J. D. *et al.* Final, 10-Year Outcomes with Nivolumab plus Ipilimumab in Advanced Melanoma. *New England Journal of Medicine* **392**, 11–22 (2025).

89. Mogensen, T. H. Pathogen Recognition and Inflammatory Signaling in Innate Immune Defenses. *Clinical Microbiology Reviews* **22**, 240–273 (2009).

90. Mann, D. L. Innate Immunity and the Failing Heart. *Circulation Research* **116**, 1254–1268 (2015).

91. Bonilla, F. A. & Oettgen, H. C. Adaptive immunity. *Journal of Allergy and Clinical Immunology* **125**, S33–S40 (2010).

92. Carpenter, S. & O'Neill, L. A. J. From periphery to center stage: 50 years of advancements in innate immunity. *Cell* **187**, 2030–2051 (2024).

93. Pishesha, N., Harmand, T. J. & Ploegh, H. L. A guide to antigen processing and presentation. *Nat Rev Immunol* **22**, 751–764 (2022).

94. Sun, L., Su, Y., Jiao, A., Wang, X. & Zhang, B. T cells in health and disease. *Sig Transduct Target Ther* **8**, 1–50 (2023).

95. Akkaya, M., Kwak, K. & Pierce, S. K. B cell memory: building two walls of protection against pathogens. *Nat Rev Immunol* **20**, 229–238 (2020).

96. Yang, D., Han, Z. & Oppenheim, J. J. ALARMINS AND IMMUNITY. *Immunol Rev* **280**, 41–56 (2017).

97. Li, D. & Wu, M. Pattern recognition receptors in health and diseases. *Sig Transduct Target Ther* **6**, 1–24 (2021).

98. Cohen, P. The TLR and IL-1 signalling network at a glance. *J Cell Sci* **127**, 2383–2390 (2014).

99. Deguine, J. & Barton, G. M. MyD88: a central player in innate immune signaling. *F1000Prime Rep* **6**, (2014).

100. Kawai, T. & Akira, S. The role of pattern-recognition receptors in innate immunity: update on Toll-like receptors. *Nature Immunology* **11**, 373–384 (2010).

101. Balka, K. R. & De Nardo, D. Understanding early TLR signaling through the Myddosome. *Journal of Leukocyte Biology* **105**, 339–351 (2019).

102. Yang, D., Han, Z. & Oppenheim, J. J. ALARMINS AND IMMUNITY. *Immunol Rev* **280**, 41–56 (2017).

103. Pellegrini, L. *et al.* HMGB1 and repair: focus on the heart. *Pharmacology & Therapeutics* **196**, 160–182 (2019).

104. von Bernuth, H. *et al.* Pyogenic Bacterial Infections in Humans with MyD88 Deficiency. *Science* **321**, 691–696 (2008).

105. Iwasaki, A. & Medzhitov, R. Toll-like receptor control of the adaptive immune responses. *Nature Immunology* **5**, 987–995 (2004).

106. Chaplin, D. D. Overview of the Immune Response. *J Allergy Clin Immunol* **125**, S3-23 (2010).

107. Reynolds, J. M. & Dong, C. Toll-like receptor regulation of effector T lymphocyte function. *Trends in Immunology* **34**, 511–519 (2013).

108. Pasare, C. & Medzhitov, R. Control of B-cell responses by Toll-like receptors. *Nature* **438**, 364–368 (2005).

109. Marty René R. *et al.* MyD88 Signaling Controls Autoimmune Myocarditis Induction. *Circulation* **113**, 258–265 (2006).

110. Kiripolsky, J., McCabe, L. G., Gaile, D. P. & Kramer, J. M. Myd88 is required for disease development in a primary Sjögren's syndrome mouse model. *Journal of Leukocyte Biology* **102**, 1411–1420 (2017).

111. Androulidaki, A., Wachsmuth, L., Polykratis, A. & Pasparakis, M. Differential role of MyD88 and TRIF signaling in myeloid cells in the pathogenesis of autoimmune diabetes. *PLOS ONE* **13**, e0194048 (2018).

112. Hardiman, G. *et al.* Genetic Structure and Chromosomal Mapping of MyD88. *Genomics* **45**, 332–339 (1997).

113. G, H., Fl, R., S, B., Ra, K. & Jf, B. Molecular Characterization and Modular Analysis of Human MyD88. *Oncogene* https://pubmed.ncbi.nlm.nih.gov/8957090/ (1996).

114. Nishimura, M. & Naito, S. Tissue-Specific mRNA Expression Profiles of Human Toll-Like Receptors and Related Genes. *Biological and Pharmaceutical Bulletin* **28**, 886–892 (2005).

115. Kohtz, P. D. *et al.* Toll-Like Receptor-4 Is a Mediator of Proliferation in Esophageal Adenocarcinoma. *Ann. Thorac. Surg.* **107**, 233–241 (2019).

116. Holtorf, A., Conrad, A., Holzmann, B. & Janssen, K.-P. Cell-type specific MyD88 signaling is required for intestinal tumor initiation and progression to malignancy. *Oncoimmunology* **7**, (2018).

117. d'Adhemar, C. J. *et al.* The MyD88+ Phenotype Is an Adverse Prognostic Factor in Epithelial Ovarian Cancer. *PLoS One* **9**, (2014).

118. Cataisson, C. *et al.* T-Cell Deletion of MyD88 Connects IL17 and IκBζ to RAS Oncogenesis. *Mol Cancer Res* **17**, 1759–1773 (2019).

119. Huang, R. & Zhou, P.-K. DNA damage repair: historical perspectives, mechanistic pathways and clinical translation for targeted cancer therapy. *Sig Transduct Target Ther* **6**, 1–35 (2021).

120. Paludan, S. R. & Bowie, A. G. Immune sensing of DNA. *Immunity* **38**, 870 (2013).

121. Dong, M. & Fitzgerald, K. A. DNA-sensing pathways in health, autoinflammatory and autoimmune diseases. *Nat Immunol* **25**, 2001–2014 (2024).

122. Dai, Z. *et al.* Myocardial DNA Damage Predicts Heart Failure Outcome in Various Underlying Diseases. *JACC: Heart Failure* **12**, 648–661 (2024).

123. de Boer, M. *et al.* DNA repair in cardiomyocytes is critical for maintaining cardiac function in mice. *Aging Cell* **22**, e13768 (2023).

124. Higo, T. *et al.* DNA single-strand break-induced DNA damage response causes heart failure. *Nat Commun* **8**, 15104 (2017).

125. Decout, A., Katz, J. D., Venkatraman, S. & Ablasser, A. The cGAS–STING pathway as a therapeutic target in inflammatory diseases. *Nat Rev Immunol* **21**, 548–569 (2021).

126. Ishikawa, H. & Barber, G. N. STING is an endoplasmic reticulum adaptor that facilitates innate immune signalling. *Nature* **455**, 674–678 (2008).

127. Ablasser, A. *et al.* cGAS produces a 2'-5'-linked cyclic dinucleotide second messenger that activates STING. *Nature* **498**, 380–384 (2013).

128. Dunphy, G. *et al.* Non-canonical Activation of the DNA Sensing Adaptor STING by ATM and IFI16 Mediates NF-κB Signaling after Nuclear DNA Damage. *Molecular Cell* **71**, 745-760.e5 (2018).

129. Liu, Y.-P. *et al.* Endoplasmic Reticulum Stress Regulates the Innate Immunity Critical Transcription Factor IRF3. *The Journal of Immunology* **189**, 4630–4639 (2012).

130. Cao, D. J. *et al.* Cytosolic DNA Sensing Promotes Macrophage Transformation and Governs Myocardial Ischemic Injury. *Circulation* **137**, 2613–2634 (2018).

131. Hu, D. *et al.* Cytosolic DNA sensor cGAS plays an essential pathogenetic role in pressure overload-induced heart failure. *American Journal of Physiology-Heart and Circulatory Physiology* **318**, H1525–H1537 (2020).

132. Xiong, R. *et al.* STING protects against cardiac dysfunction and remodelling by blocking autophagy. *Cell Communication and Signaling* **19**, 109 (2021).

133. Luo, W. *et al.* Critical Role of the cGAS-STING Pathway in Doxorubicin-Induced Cardiotoxicity. *Circulation Research* **132**, e223–e242 (2023).

134. Yan, M. *et al.* Mitochondrial damage and activation of the cytosolic DNA sensor cGAS–STING pathway lead to cardiac pyroptosis and hypertrophy in diabetic cardiomyopathy mice. *Cell Death Discov.* **8**, 1–12 (2022).

135. Sokolowska, O. & Nowis, D. STING Signaling in Cancer Cells: Important or Not? *Arch Immunol Ther Exp (Warsz)* **66**, 125–132 (2018).

136. Li, G. *et al.* cGAS-STING pathway mediates activation of dendritic cell sensing of immunogenic tumors. *Cell. Mol. Life Sci.* **81**, 149 (2024).

137. Falahat, R. *et al.* Epigenetic state determines the in vivo efficacy of STING agonist therapy. *Nat Commun* **14**, 1573 (2023).

138. Wu, Y. *et al.* Tumor-targeted delivery of a STING agonist improves cancer immunotherapy. *Proceedings of the National Academy of Sciences* **119**, e2214278119 (2022).

139. Liu, J. *et al.* STING inhibitors sensitize platinum chemotherapy in ovarian cancer by inhibiting the CGAS-STING pathway in cancer-associated fibroblasts (CAFs). *Cancer Letters* **588**, 216700 (2024).

140. Hwang, J.-R., Byeon, Y., Kim, D. & Park, S.-G. Recent insights of T cell receptor-mediated signaling pathways for T cell activation and development. *Exp Mol Med* **52**, 750–761 (2020).

141. Courtney, A. H., Lo, W.-L. & Weiss, A. TCR Signaling: Mechanisms of Initiation and Propagation. *Trends in Biochemical Sciences* **43**, 108–123 (2018).

142. Shah, K., Al-Haidari, A., Sun, J. & Kazi, J. U. T cell receptor (TCR) signaling in health and disease. *Sig Transduct Target Ther* **6**, 1–26 (2021).

143. Poloni, C. *et al.* T-cell activation–induced marker assays in health and disease. *Immunol Cell Biol* **101**, 491–503 (2023).

144. Pérez-Ruiz, E. *et al.* Cancer immunotherapy resistance based on immune checkpoints inhibitors: Targets, biomarkers, and remedies. *Drug Resistance Updates* **53**, 100718 (2020).

145. Yousif, L. I., Tanja, A. A., de Boer, R. A., Teske, A. J. & Meijers, W. C. The role of immune checkpoints in cardiovascular disease. *Frontiers in Pharmacology* **13**, (2022).

146. Robert, C. A decade of immune-checkpoint inhibitors in cancer therapy. *Nat Commun* **11**, 3801 (2020).

147. Zhu, J. & Paul, W. E. CD4 T cells: fates, functions, and faults. *Blood* **112**, 1557–1569 (2008).

148. Jin, B., Sun, T., Yu, X.-H., Yang, Y.-X. & Yeo, A. E. T. The Effects of TLR Activation on T-Cell Development and Differentiation. *Clinical and Developmental Immunology* https://www.hindawi.com/journals/jir/2012/836485/ (2012) doi:https://doi.org/10.1155/2012/836485.

149. Rahman, A. H., Taylor, D. K. & Turka, L. A. The contribution of direct TLR signaling to T cell responses. *Immunol Res* **45**, 25–36 (2009).

150. Zhu, X. & Zhu, J. CD4 T Helper Cell Subsets and Related Human Immunological Disorders. *Int J Mol Sci* **21**, 8011 (2020).

151. Luckheeram, R. V., Zhou, R., Verma, A. D. & Xia, B. CD4+T Cells: Differentiation and Functions. *Journal of Immunology Research* **2012**, 925135 (2012).

152. Dikiy, S. & Rudensky, A. Y. Principles of regulatory T cell function. *Immunity* **56**, 240–255 (2023).

153. Koh, C.-H., Lee, S., Kwak, M., Kim, B.-S. & Chung, Y. CD8 T-cell subsets: heterogeneity, functions, and therapeutic potential. *Exp Mol Med* **55**, 2287–2299 (2023).

154. Lanitis, E., Dangaj, D., Irving, M. & Coukos, G. Mechanisms regulating T-cell infiltration and activity in solid tumors. *Annals of Oncology* **28**, xii18–xii32 (2017).

155. Borges, C. M. *et al.* T Regulatory Cell Expressed Myd88 Is Critical For Prolongation Of Allograft Survival. *Transpl Int* **29**, 930–940 (2016).

156. Togashi, Y., Shitara, K. & Nishikawa, H. Regulatory T cells in cancer immunosuppression — implications for anticancer therapy. *Nat Rev Clin Oncol* **16**, 356–371 (2019).

157. Xia, N. *et al.* A Unique Population of Regulatory T Cells in Heart Potentiates Cardiac Protection From Myocardial Infarction. *Circulation* **142**, 1956–1973 (2020).

158. Murphy, K. M. & Stockinger, B. Effector T cell plasticity: flexibility in the face of changing circumstances. *Nat Immunol* **11**, 674–680 (2010).

159. Sanders, E. & Alcaide, P. Red light-green light: T-cell trafficking in cardiac and vascular inflammation. *Am J Physiol Cell Physiol* **324**, C58–C66 (2023).

160. Amersfoort, J., Eelen, G. & Carmeliet, P. Immunomodulation by endothelial cells — partnering up with the immune system? *Nat Rev Immunol* **22**, 576–588 (2022).

161. Märkl, F., Huynh, D., Endres, S. & Kobold, S. Utilizing chemokines in cancer immunotherapy. *Trends in Cancer* **8**, 670–682 (2022).

162. Nourshargh, S. & Alon, R. Leukocyte Migration into Inflamed Tissues. *Immunity* **41**, 694–707 (2014).

163. Ngwenyama, N. *et al.* CXCR3 regulates CD4+ T cell cardiotropism in pressure overload–induced cardiac dysfunction. *JCI Insight* **4**,.

164. Patel, B. *et al.* CCR2+ Monocyte-Derived Infiltrating Macrophages Are Required for Adverse Cardiac Remodeling During Pressure Overload. *JACC: Basic to Translational Science* **3**, 230–244 (2018).

165. Abdul-Rahman, T. *et al.* The paradoxical role of cytokines and chemokines at the tumor microenvironment: a comprehensive review. *European Journal of Medical Research* **29**, 124 (2024).

166. Lesch, S. *et al.* T cells armed with C-X-C chemokine receptor type 6 enhance adoptive cell therapy for pancreatic tumours. *Nat Biomed Eng* 1–15 (2021) doi:10.1038/s41551-021-00737-6.

167. Spetz, J., Presser, A. & Sarosiek, K. A. T Cells and Regulated Cell Death: Kill or Be Killed. *Int Rev Cell Mol Biol* **342**, 27–71 (2019).

168. Krammer, P. H., Arnold, R. & Lavrik, I. N. Life and death in peripheral T cells. *Nat Rev Immunol* **7**, 532–542 (2007).

169. Bhattacharyya, N. D. & Feng, C. G. Regulation of T Helper Cell Fate by TCR Signal Strength. *Front. Immunol.* **11**, (2020).

170. Xu, G. & Shi, Y. Apoptosis signaling pathways and lymphocyte homeostasis. *Cell Res* **17**, 759–771 (2007).

171. Green, D. R., Droin, N. & Pinkoski, M. Activation-induced cell death in T cells. *Immunological Reviews* **193**, 70–81 (2003).

172. Zhang, N., Hartig, H., Dzhagalov, I., Draper, D. & He, Y. W. The role of apoptosis in the development and function of T lymphocytes. *Cell Res* **15**, 749–769 (2005).

173. Ch'en, I. L., Tsau, J. S., Molkentin, J. D., Komatsu, M. & Hedrick, S. M. Mechanisms of necroptosis in T cells. *J Exp Med* **208**, 633–641 (2011).

174. Yu, P. *et al.* Pyroptosis: mechanisms and diseases. *Sig Transduct Target Ther* **6**, 1–21 (2021).

175. Doitsh, G. *et al.* Pyroptosis drives CD4 T-cell depletion in HIV-1 infection. *Nature* **505**, 509–514 (2014).

176. Komori, S. *et al.* CD47 promotes peripheral T cell survival by preventing dendritic cell–mediated T cell necroptosis. *Proceedings of the National Academy of Sciences* **120**, e2304943120 (2023).

177. Whiteman, S. *et al.* Anatomy of the cardiac chambers: A review of the left ventricle. *Translational Research in Anatomy* **23**, 100095 (2021).

178. Trifunović-Zamaklar, D. *et al.* The basic heart anatomy and physiology from the cardiologist's perspective: Toward a better understanding of left ventricular mechanics, systolic, and diastolic function. *Journal of Clinical Ultrasound* **50**, 1026–1040 (2022).

179. Veeraraghavan, R., Gourdie, R. G. & Poelzing, S. Mechanisms of cardiac conduction: a history of revisions. *Am J Physiol Heart Circ Physiol* **306**, H619–H627 (2014).

180. Woodcock, E. A. & Matkovich, S. J. Cardiomyocytes structure, function and associated pathologies. *The International Journal of Biochemistry & Cell Biology* **37**, 1746–1751 (2005).

181. Guo, Y. & Pu, W. T. Cardiomyocyte Maturation. *Circulation Research* **126**, 1086–1106 (2020).

182. Kadow, Z. A. & Martin, J. F. Distinguishing Cardiomyocyte Division From Binucleation. *Circulation Research* **123**, 1012–1014 (2018).

183. Litviňuková, M. *et al.* Cells of the adult human heart. *Nature* **588**, 466–472 (2020).

184. Cohen, C. D. *et al.* Myocardial Immune Cells: The Basis of Cardiac Immunology. *The Journal of Immunology* **210**, 1198–1207 (2023).

185. Hulsmans, M. *et al.* Macrophages Facilitate Electrical Conduction in the Heart. *Cell* **169**, 510-522.e20 (2017).

186. Zhou, Y., Huang, C., Hu, Y., Xu, Q. & Hu, X. Lymphatics in Cardiovascular Disease. *Arteriosclerosis, Thrombosis, and Vascular Biology* **40**, e275–e283 (2020).

187. Nakamura, M. & Sadoshima, J. Mechanisms of physiological and pathological cardiac hypertrophy. *Nat Rev Cardiol* **15**, 387–407 (2018).

188. Caturano, A. *et al.* Cardiac Hypertrophy: From Pathophysiological Mechanisms to Heart Failure Development. *Rev Cardiovasc Med* **23**, 165 (2022).

189. Xue, J., Ye, B. & Sun, M. Possible pathogenic mechanisms for doxorubicin-induced splenic atrophy in a human breast cancer xenograft mouse model. *Journal of Applied Toxicology* **n/a**,.

190. Harvey, P. A. & Leinwand, L. A. Chapter 3 - Cardiac Atrophy and Remodeling. in *Cellular and Molecular Pathobiology of Cardiovascular Disease* (eds. Willis, M. S., Homeister, J. W. & Stone, J. R.) 37–50 (Academic Press, San Diego, 2014). doi:10.1016/B978-0-12-405206-2.00003-X.

191. Frangogiannis, N. G. Cardiac fibrosis. *Cardiovascular Research* **117**, 1450–1488 (2021).

192. Li, L., Zhao, Q. & Kong, W. Extracellular matrix remodeling and cardiac fibrosis. *Matrix Biology* **68–69**, 490–506 (2018).

193. López, B., Querejeta, R., González, A., Larman, M. & Díez, J. Collagen Cross-Linking But Not Collagen Amount Associates With Elevated Filling Pressures in Hypertensive Patients With Stage C Heart Failure. *Hypertension* **60**, 677–683 (2012).

194. Smolgovsky, S., Theall, B., Wagner, N. & Alcaide, P. Fibroblasts and immune cells: at the crossroad of organ inflammation and fibrosis. *American Journal of Physiology-Heart and Circulatory Physiology* **326**, H303–H316 (2024).

195. Fischer, D. *et al.* Endothelial dysfunction in patients with chronic heart failure is independently associated with increased incidence of hospitalization, cardiac transplantation, or death. *European Heart Journal* **26**, 65–69 (2005).

196. Wadowski, P. P. *et al.* Functional capillary impairment in patients with ventricular assist devices. *Sci Rep* **9**, 5909 (2019).

197. Zuchi, C. *et al.* Role of endothelial dysfunction in heart failure. *Heart Fail Rev* **25**, 21–30 (2020).

198. Swirski, F. K. & Nahrendorf, M. Cardioimmunology: the immune system in cardiac homeostasis and disease. *Nat Rev Immunol* **18**, 733–744 (2018).

199. Hofmann Ulrich & Frantz Stefan. Role of Lymphocytes in Myocardial Injury, Healing, and Remodeling After Myocardial Infarction. *Circulation Research* **116**, 354–367 (2015).

200. Kain, V., Prabhu, S. D. & Halade, G. V. Inflammation revisited: inflammation versus resolution of inflammation following myocardial infarction. *Basic Res Cardiol* **109**, 444 (2014).

201. Blanton, R. M., Carrillo-Salinas, F. J. & Alcaide, P. T-cell recruitment to the heart: friendly guests or unwelcome visitors? *American Journal of Physiology-Heart and Circulatory Physiology* **317**, H124–H140 (2019).

202. Smolgovsky, S., Ibeh, U., Tamayo, T. P. & Alcaide, P. Adding Insult to Injury - Inflammation at the Heart of Cardiac Fibrosis. *Cell Signal* **77**, 109828 (2021).

203. Brenes-Castro, D., Castillo, E. C., Vázquez-Garza, E., Torre-Amione, G. & García-Rivas, G. Temporal Frame of Immune Cell Infiltration during Heart Failure Establishment: Lessons from Animal Models. *Int J Mol Sci* **19**, 3719 (2018).

204. Richards, D. A. *et al.* Distinct Phenotypes Induced by Three Degrees of Transverse Aortic Constriction in Mice. *Sci Rep* **9**, 5844 (2019).

205. Matsiukevich, D. *et al.* Characterization of a robust mouse model of heart failure with preserved ejection fraction. *American Journal of Physiology-Heart and Circulatory Physiology* **325**, H203–H231 (2023).

206. Podyacheva, E. Y., Kushnareva, E. A., Karpov, A. A. & Toropova, Y. G. Analysis of Models of Doxorubicin-Induced Cardiomyopathy in Rats and Mice. A Modern View From the Perspective of the Pathophysiologist and the Clinician. *Front. Pharmacol.* **12**, (2021).

207. Buehning, F. *et al.* Preclinical models of cardiotoxicity from immune checkpoint inhibitor therapy. *Basic Res Cardiol* (2024) doi:10.1007/s00395-024-01070-0.

208. Axelrod, M. L. *et al.* T cells specific for α-myosin drive immunotherapy-related myocarditis. *Nature* **611**, 818–826 (2022).

209. Frantz, S. *et al.* Toll4 (TLR4) expression in cardiac myocytes in normal and failing myocardium. *J Clin Invest* **104**, 271–280 (1999).

210. Li, N. *et al.* The Th17/Treg imbalance exists in patients with heart failure with normal ejection fraction and heart failure with reduced ejection fraction. *Clinica Chimica Acta* **411**, 1963–1968 (2010).

211. Curran, F. M. *et al.* Neutrophil-to-lymphocyte ratio and outcomes in patients with new-onset or worsening heart failure with reduced and preserved ejection fraction. *ESC Heart Failure* **8**, 3168–3179 (2021).

212. Alexanian, M. *et al.* Chromatin remodelling drives immune cell–fibroblast communication in heart failure. *Nature* **635**, 434–443 (2024).

213. Baba, A., Yoshikawa, T. & Ogawa, S. Autoantibodies produced against sarcolemmal Na-K-ATPase: possible upstream targets of arrhythmias and sudden death in patients with dilated cardiomyopathy. *Journal of the American College of Cardiology* **40**, 1153–1159 (2002).

214. Baba, A. *et al.* Autoantibodies against M2-muscarinic acetylcholine receptors: new upstream targets in atrial fibrillation in patients with dilated cardiomyopathy. *European Heart Journal* **25**, 1108–1115 (2004).

215. Furusawa, S. *et al.* Cardiac Autoantibodies Against Cardiac Troponin I in Post-Myocardial Infarction Heart Failure: Evaluation in a Novel Murine Model and Applications in Therapeutics. *Circ Heart Fail* **16**, e010347 (2023).

216. Jahns, R. *et al.* Autoantibodies Activating Human β1-Adrenergic Receptors Are Associated With Reduced Cardiac Function in Chronic Heart Failure. *Circulation* **99**, 649–654 (1999).

217. Chen, W.-Y., Hong, J., Gannon, J., Kakkar, R. & Lee, R. T. Myocardial pressure overload induces systemic inflammation through endothelial cell IL-33. *Proc Natl Acad Sci U S A* **112**, 7249–7254 (2015).

218. Lin, H. *et al.* HMGB1-RAGE Axis Makes No Contribution to Cardiac Remodeling Induced by Pressure-Overload. *PLOS ONE* **11**, e0158514 (2016).

219. Kleiner, J. L. *et al.* Characterization of Transverse Aortic Constriction in Mice Based on the Specific Recruitment of Leukocytes to the Hypertrophic Myocardium and the Aorta Ascendens. *Mediators Inflamm* **2021**, 1376859 (2021).

220. Bayer, A. L. *et al.* T-Cell MyD88 Is a Novel Regulator of Cardiac Fibrosis Through Modulation of T-Cell Activation. *Circulation Research* **133**, 412–429 (2023).

221. Abe, H. *et al.* NF-κB activation in cardiac fibroblasts results in the recruitment of inflammatory Ly6Chi monocytes in pressure-overloaded hearts. *Sci Signal* **14**, eabe4932 (2021).

222. Revelo, X. S. *et al.* Cardiac Resident Macrophages Prevent Fibrosis and Stimulate Angiogenesis. *Circulation Research* **129**, 1086–1101 (2021).

223. Patel, B., Ismahil, M. A., Hamid, T., Bansal, S. S. & Prabhu, S. D. Mononuclear Phagocytes Are Dispensable for Cardiac Remodeling in Established Pressure-Overload Heart Failure. *PLoS One* **12**, e0170781 (2017).

224. Wang, Y. *et al.* Wnt5a-mediated neutrophil recruitment has an obligatory role in pressure overload-induced cardiac dysfunction. *Circulation* **140**, 487–499 (2019).

225. He, X. *et al.* Inhibition of NK1.1 signaling attenuates pressure overload-induced heart failure, and consequent pulmonary inflammation and remodeling. *Front Immunol* **14**, 1215855 (2023).

226. Ngwenyama Njabulo *et al.* Isolevuglandin-Modified Cardiac Proteins Drive CD4+ T Cell Activation in the Heart and Promote Cardiac Dysfunction. *Circulation* **0**,.

227. Laroumanie Fanny *et al.* CD4+ T Cells Promote the Transition From Hypertrophy to Heart Failure During Chronic Pressure Overload. *Circulation* **129**, 2111–2124 (2014).

228. Gröschel, C. *et al.* CD8+-T Cells With Specificity for a Model Antigen in Cardiomyocytes Can Become Activated After Transverse Aortic Constriction but Do Not Accelerate Progression to Heart Failure. *Front Immunol* **9**, 2665 (2018).

229. Nevers, T. *et al.* Th1 effector T cells selectively orchestrate cardiac fibrosis in nonischemic heart failure. *J Exp Med* **214**, 3311–3329 (2017).

230. Salvador Ane M. *et al.* Intercellular Adhesion Molecule 1 Regulates Left Ventricular Leukocyte Infiltration, Cardiac Remodeling, and Function in Pressure Overload–Induced Heart Failure. *Journal of the American Heart Association* **5**, e003126.

231. Ngwenyama, N. *et al.* Antigen presentation by cardiac fibroblasts promotes cardiac dysfunction. *Nat Cardiovasc Res* **1**, 761–774 (2022).

232. Guzik, T. J. *et al.* Role of the T cell in the genesis of angiotensin II–induced hypertension and vascular dysfunction. *Journal of Experimental Medicine* **204**, 2449–2460 (2007).

233. Hoch, N. E. *et al.* Regulation of T-cell function by endogenously produced angiotensin II. *American Journal of Physiology - Regulatory, Integrative and Comparative Physiology* **296**, R208 (2008).

234. Trott, D. W. *et al.* OLIGOCLONAL CD8+ T CELLS PLAY A CRITICAL ROLE IN THE DEVELOPMENT OF HYPERTENSION. *Hypertension* **64**, 1108 (2014).

235. Smith, H. L., Goodlett, B. L., Navaneethabalakrishnan, S. & Mitchell, B. M. Elevated Salt or Angiotensin II Levels Induce CD38+ Innate Immune Cells in the Presence of Granulocyte-Macrophage Colony Stimulating Factor. *Cells* **13**, 1302 (2024).

236. Caillon, A. *et al.* γδ T Cells Mediate Angiotensin II-Induced Hypertension and Vascular Injury. *Circulation* **135**, 2155–2162 (2017).

237. Carter, K., Shah, E., Waite, J., Rana, D. & Zhao, Z.-Q. Pathophysiology of Angiotensin II-Mediated Hypertension, Cardiac Hypertrophy, and Failure: A Perspective from Macrophages. *Cells* **13**, 2001 (2024).

238. Tallquist, M. D. & Molkentin, J. D. Redefining the identity of cardiac fibroblasts. *Nat Rev Cardiol* **14**, 484–491 (2017).

239. Banerjee, I., Fuseler, J. W., Price, R. L., Borg, T. K. & Baudino, T. A. Determination of cell types and numbers during cardiac development in the neonatal and adult rat and mouse. *American Journal of Physiology-Heart and Circulatory Physiology* **293**, H1883–H1891 (2007).

240. Fan, D., Takawale, A., Lee, J. & Kassiri, Z. Cardiac fibroblasts, fibrosis and extracellular matrix remodeling in heart disease. *Fibrogenesis & Tissue Repair* **5**, 15 (2012).

241. Gaudesius, G., Miragoli, M., Thomas, S. P. & Rohr, S. Coupling of Cardiac Electrical Activity Over Extended Distances by Fibroblasts of Cardiac Origin. *Circulation Research* **93**, 421–428 (2003).

242. Camelliti, P., Green, C. R., LeGrice, I. & Kohl, P. Fibroblast Network in Rabbit Sinoatrial Node. *Circulation Research* **94**, 828–835 (2004).

243. Smolgovsky, S., Ibeh, U., Tamayo, T. P. & Alcaide, P. Adding Insult to Injury - Inflammation at the Heart of Cardiac Fibrosis. *Cell Signal* **77**, 109828 (2021).

244. Nevers, T. *et al.* Th1 effector T cells selectively orchestrate cardiac fibrosis in nonischemic heart failure. *J Exp Med* **214**, 3311–3329 (2017).

245. Bretherton, R., Bugg, D., Olsewski, E. & Davis, J. Regulators of Cardiac Fibroblast Cell State. *Matrix Biol* **91–92**, 117–135 (2020).

246. Torimoto, K., Elliott, K., Nakayama, Y., Yanagisawa, H. & Eguchi, S. Cardiac and perivascular myofibroblasts, matrifibrocytes, and immune fibrocytes in hypertension; commonalities and differences with other cardiovascular diseases. *Cardiovascular Research* **120**, 567–580 (2024).

247. Karsdal, M. A. Introduction. in *Biochemistry of Collagens, Laminins and Elastin (Third Edition)* (ed. Karsdal, M. A.) xxvii–liv (Academic Press, 2024). doi:10.1016/B978-0-443-15617-5.02001-1.

248. Fu, X. *et al.* Specialized fibroblast differentiated states underlie scar formation in the infarcted mouse heart. *J Clin Invest* **128**, 2127–2143 (2018).

249. Mouton, A. J. *et al.* Fibroblast polarization over the myocardial infarction time continuum shifts roles from inflammation to angiogenesis. *Basic Res Cardiol* **114**, 6 (2019).

250. Tille, J.-C. & Pepper, M. S. Mesenchymal Cells Potentiate Vascular Endothelial Growth Factor-Induced Angiogenesis *in Vitro*. *Experimental Cell Research* **280**, 179–191 (2002).

251. Tuleta, I. *et al.* Fibroblast-specific TGF-β signaling mediates cardiac dysfunction, fibrosis, and hypertrophy in obese diabetic mice. *Cardiovascular Research* **120**, 2047–2063 (2024).

252. Fujiu, K. & Nagai, R. Fibroblast-mediated pathways in cardiac hypertrophy. *Journal of Molecular and Cellular Cardiology* **70**, 64–73 (2014).

253. Lighthouse, J. K. & Small, E. M. Transcriptional control of cardiac fibroblast plasticity. *J Mol Cell Cardiol* **91**, 52–60 (2016).

254. Deng, Z. *et al.* TGF-β signaling in health, disease and therapeutics. *Sig Transduct Target Ther* **9**, 1–40 (2024).

255. Massagué, J. & Sheppard, D. TGF-β Signaling in Health and Disease. *Cell* **186**, 4007–4037 (2023).

256. Humeres, C., Venugopal, H. & Frangogiannis, N. G. Smad-dependent pathways in the infarcted and failing heart. *Current Opinion in Pharmacology* **64**, 102207 (2022).

257. Molkentin, J. D. *et al.* Fibroblast-specific genetic manipulation of p38 MAPK in vivo reveals its central regulatory role in fibrosis. *Circulation* **136**, 549–561 (2017).

258. Bugg, D. *et al.* Infarct Collagen Topography Regulates Fibroblast Fate Via p38-Yap-TEAD Signals. *Circ Res* **127**, 1306–1322 (2020).

259. Hanna, A. & Frangogiannis, N. G. The Role of the TGF-β Superfamily in Myocardial Infarction. *Front. Cardiovasc. Med.* **6**, (2019).

260. Khalil, H. *et al.* Fibroblast-specific TGF-β–Smad2/3 signaling underlies cardiac fibrosis. *J Clin Invest* **127**, 3770–3783.

261. Salvarani, N. *et al.* TGF-β1 (Transforming Growth Factor-β1) Plays a Pivotal Role in Cardiac Myofibroblast Arrhythmogenicity. *Circulation: Arrhythmia and Electrophysiology* **10**, e004567 (2017).

262. Ehanire, T. *et al.* Angiotensin II Stimulates Canonical TGFβ Signaling Pathway through Angiotensin Type 1 Receptor to Induce Granulation Tissue Contraction. *J Mol Med (Berl)* **93**, 289–302 (2015).

263. Kuwahara, F. *et al.* Transforming Growth Factor-β Function Blocking Prevents Myocardial Fibrosis and Diastolic Dysfunction in Pressure-Overloaded Rats. *Circulation* **106**, 130–135 (2002).

264. Engebretsen, K. V. T. *et al.* Attenuated development of cardiac fibrosis in left ventricular pressure overload by SM16, an orally active inhibitor of ALK5. *Journal of Molecular and Cellular Cardiology* **76**, 148–157 (2014).

265. Lucas, J. A. *et al.* Inhibition of transforming growth factor-β signaling induces left ventricular dilation and dysfunction in the pressure-overloaded heart. *American Journal of Physiology-Heart and Circulatory Physiology* **298**, H424–H432 (2010).

266. King, T. E. *et al.* A Phase 3 Trial of Pirfenidone in Patients with Idiopathic Pulmonary Fibrosis. *New England Journal of Medicine* **370**, 2083–2092 (2014).

267. AlAnsari, S. *et al.* Responses to Pirfenidone Treatment in Patients with Idiopathic Pulmonary Fibrosis is Not Associated with Changes in Echocardiographic Parameters of Left Ventricular Structure and Function. *Journal of Cardiac Failure* **25**, S27 (2019).

268. AlAnsari, S., Southern, B. D., Sharma, V., Mahalwar, G. & Tang, W. W. Pirfenidone is Associated with Decreased Indexed End Diastolic and Systolic Volumes in Patients with HFpEF and a Known History of Idiopathic Pulmonary Fibrosis. *Journal of Cardiac Failure* **26**, S25 (2020).

269. Lewis, G. A. *et al.* Pirfenidone in heart failure with preserved ejection fraction: a randomized phase 2 trial. *Nat Med* **27**, 1477–1482 (2021).

270. Zhang, W. *et al.* Necrotic Myocardial Cells Release Damage-Associated Molecular Patterns That Provoke Fibroblast Activation In Vitro and Trigger Myocardial Inflammation and Fibrosis In Vivo. *J Am Heart Assoc* **4**, e001993 (2015).

271. Lugrin, J. *et al.* Interleukin-1 alpha is a crucial danger signal triggering acute myocardial inflammation during myocardial infarction. *J Immunol* **194**, 499–503 (2015).

272. Ceccato, T. L. *et al.* Defining the Cardiac Fibroblast Secretome in a Fibrotic Microenvironment. *Journal of the American Heart Association* **9**, e017025 (2020).

273. Shinde, A. V. & Frangogiannis, N. G. Fibroblasts in myocardial infarction: a role in inflammation and repair. *J Mol Cell Cardiol* **0**, 74–82 (2014).

274. Kawaguchi, M. *et al.* Inflammasome Activation of Cardiac Fibroblasts Is Essential for Myocardial Ischemia/Reperfusion Injury. *Circulation* **123**, 594–604 (2011).

275. Fan, J., Ren, M., Adhikari, B. K., Wang, H. & He, Y. The NLRP3 Inflammasome as a Novel Therapeutic Target for Cardiac Fibrosis. *J Inflamm Res* **15**, 3847–3858 (2022).

276. Sandstedt, J. *et al.* Human cardiac fibroblasts isolated from patients with severe heart failure are immune-competent cells mediating an inflammatory response. *Cytokine* **113**, 319–325 (2019).

277. Pappritz, K. *et al.* Cardiac (myo)fibroblasts modulate the migration of monocyte subsets. *Sci Rep* **8**, 5575 (2018).

278. Wang, L. *et al.* Single-cell reconstruction of the adult human heart during heart failure and recovery reveals the cellular landscape underlying cardiac function. *Nat Cell Biol* **22**, 108–119 (2020).

279. Zhao, H. *et al.* Inflammation and tumor progression: signaling pathways and targeted intervention. *Sig Transduct Target Ther* **6**, 1–46 (2021).

280. Antohe, M. *et al.* Tumor infiltrating lymphocytes: The regulator of melanoma evolution (Review). *Oncology Letters* **17**, 4155–4161 (2019).

281. Zhang, L. *et al.* Intratumoral T Cells, Recurrence, and Survival in Epithelial Ovarian Cancer. *New England Journal of Medicine* **348**, 203–213 (2003).

282. Yang, Y. *et al.* High intratumoral CD8+ T-cell infiltration is associated with improved survival in prostate cancer patients undergoing radical prostatectomy. *Prostate* **81**, 20–28 (2021).

283. Tong, G. *et al.* Intratumoral CD8+ T cells as a potential positive predictor of chemoimmunotherapy response in PD-L1-negative advanced gastric cancer patients: a retrospective cohort study. *Journal of Gastrointestinal Oncology* **13**, (2022).

284. Oh, D. Y. & Fong, L. Cytotoxic CD4+ T cells in cancer: Expanding the immune effector toolbox. *Immunity* **54**, 2701–2711 (2021).

285. Speiser, D. E., Chijioke, O., Schaeuble, K. & Münz, C. CD4+ T cells in cancer. *Nat Cancer* **4**, 317–329 (2023).

286. Del Prete, A. *et al.* Dendritic cell subsets in cancer immunity and tumor antigen sensing. *Cell Mol Immunol* **20**, 432–447 (2023).

287. Wolf, N. K., Kissiov, D. U. & Raulet, D. H. Roles of natural killer cells in immunity to cancer, and applications to immunotherapy. *Nat Rev Immunol* **23**, 90–105 (2023).

288. Cui, C. *et al.* Neutrophil elastase selectively kills cancer cells and attenuates tumorigenesis. *Cell* (2021) doi:10.1016/j.cell.2021.04.016.

289. Singhal, S. *et al.* Origin and Role of a Subset of Tumor-Associated Neutrophils with Antigen Presenting Cell Features (Hybrid TANs) in Early-Stage Human Lung Cancer. *Cancer Cell* **30**, 120–135 (2016).

290. Felix, K. & Gaida, M. M. Neutrophil-Derived Proteases in the Microenvironment of Pancreatic Cancer -Active Players in Tumor Progression. *Int J Biol Sci* **12**, 302–313 (2016).

291. Wang, Z. *et al.* Tumor-derived HMGB1 induces CD62Ldim neutrophil polarization and promotes lung metastasis in triple-negative breast cancer. *Oncogenesis* **9**, 1–17 (2020).

292. Veglia, F., Sanseviero, E. & Gabrilovich, D. I. Myeloid-derived suppressor cells in the era of increasing myeloid cell diversity. *Nat Rev Immunol* **21**, 485–498 (2021).

293. Thommen, D. S. & Schumacher, T. N. T Cell Dysfunction in Cancer. *Cancer Cell* **33**, 547–562 (2018).

294. Wherry, E. J. & Kurachi, M. Molecular and cellular insights into T cell exhaustion. *Nat Rev Immunol* **15**, 486–499 (2015).

295. Galassi, C., Chan, T. A., Vitale, I. & Galluzzi, L. The hallmarks of cancer immune evasion. *Cancer Cell* **42**, 1825–1863 (2024).

296. Wu, B., Zhang, B., Li, B., Wu, H. & Jiang, M. Cold and hot tumors: from molecular mechanisms to targeted therapy. *Sig Transduct Target Ther* **9**, 1–65 (2024).

297. Wang, L. *et al.* Hot and cold tumors: Immunological features and the therapeutic strategies. *MedComm (2020)* **4**, e343 (2023).

298. Gray-Schopfer, V., Wellbrock, C. & Marais, R. Melanoma biology and new targeted therapy. *Nature* **445**, 851–857 (2007).

299. Maleki Vareki, S. High and low mutational burden tumors versus immunologically hot and cold tumors and response to immune checkpoint inhibitors. *Journal for ImmunoTherapy of Cancer* **6**, 157 (2018).

300. Falcone, I. *et al.* Tumor Microenvironment: Implications in Melanoma Resistance to Targeted Therapy and Immunotherapy. *Cancers (Basel)* **12**, 2870 (2020).

301. Yuan, Y. *et al.* Development and Validation of a CD8+ T Cell Infiltration-Related Signature for Melanoma Patients. *Front Immunol* **12**, 659444 (2021).

302. Larkin, J. *et al.* Five-Year Survival with Combined Nivolumab and Ipilimumab in Advanced Melanoma. *New England Journal of Medicine* **381**, 1535–1546 (2019).

303. Lu, Y. *et al.* Evaluating the immunologically “cold” tumor microenvironment after treatment with immune checkpoint inhibitors utilizing PET imaging of CD4 + and CD8 + T cells in breast cancer mouse models. *Breast Cancer Research* **26**, 104 (2024).

304. Onkar, S. S. *et al.* The Great Immune Escape: Understanding the Divergent Immune Response in Breast Cancer Subtypes. *Cancer Discov* **13**, 23–40 (2023).

305. Zhao, H. *et al.* Identifying tumour microenvironment-related signature that correlates with prognosis and immunotherapy response in breast cancer. *Sci Data* **10**, 119 (2023).

306. Schmid Peter *et al.* Event-free Survival with Pembrolizumab in Early Triple-Negative Breast Cancer. *New England Journal of Medicine* **386**, 556–567 (2022).

307. Loibl, S. *et al.* Durvalumab improves long-term outcome in TNBC: results from the phase II randomized GeparNUEVO study investigating neodjuvant durvalumab in addition to an anthracycline/taxane based neoadjuvant chemotherapy in early triple-negative breast cancer (TNBC). *JCO* **39**, 506–506 (2021).

308. Marra, A., Viale, G. & Curigliano, G. Recent advances in triple negative breast cancer: the immunotherapy era. *BMC Med* **17**, 90 (2019).

309. Henriksen, P. A. Anthracycline cardiotoxicity: an update on mechanisms, monitoring and prevention. *Heart* **104**, 971–977 (2018).

310. Sritharan, S. & Sivalingam, N. A comprehensive review on time-tested anticancer drug doxorubicin. *Life Sciences* **278**, 119527 (2021).

311. Chatterjee, K., Zhang, J., Honbo, N. & Karliner, J. S. Doxorubicin Cardiomyopathy. *Cardiology* **115**, 155–162 (2010).

312. Nebigil, C. G. & Désaubry, L. Updates in Anthracycline-Mediated Cardiotoxicity. *Front. Pharmacol.* **9**, (2018).

313. Linders, A. N. *et al.* A review of the pathophysiological mechanisms of doxorubicin-induced cardiotoxicity and aging. *npj Aging* **10**, 1–9 (2024).

314. Cardinale, D. *et al.* Prevention of High-Dose Chemotherapy–Induced Cardiotoxicity in High-Risk Patients by Angiotensin-Converting Enzyme Inhibition. *Circulation* **114**, 2474–2481 (2006).

315. Gulati, G. *et al.* Prevention of cardiac dysfunction during adjuvant breast cancer therapy (PRADA): a 2 × 2 factorial, randomized, placebo-controlled, double-blind clinical trial of candesartan and metoprolol. *European Heart Journal* **37**, 1671–1680 (2016).

316. Boekhout, A. H. *et al.* Angiotensin II–Receptor Inhibition With Candesartan to Prevent Trastuzumab-Related Cardiotoxic Effects in Patients With Early Breast Cancer: A Randomized Clinical Trial. *JAMA Oncology* **2**, 1030–1037 (2016).

317. Ma, Y. *et al.* Beta-blockers for the primary prevention of anthracycline-induced cardiotoxicity: a meta-analysis of randomized controlled trials. *BMC Pharmacol Toxicol* **20**, 18 (2019).

318. Macedo, A. V. S. *et al.* Efficacy of Dexrazoxane in Preventing Anthracycline Cardiotoxicity in Breast Cancer. *JACC CardioOncol* **1**, 68–79 (2019).

319. Shaikh, F. *et al.* Cardioprotection and Second Malignant Neoplasms Associated With Dexrazoxane in Children Receiving Anthracycline Chemotherapy: A Systematic Review and Meta-Analysis. *JNCI: Journal of the National Cancer Institute* **108**, djv357 (2016).

320. Gulati, G. *et al.* Neurohormonal Blockade and Circulating Cardiovascular Biomarkers During Anthracycline Therapy in Breast Cancer Patients: Results From the PRADA (Prevention of Cardiac Dysfunction During Adjuvant Breast Cancer Therapy) Study. *Journal of the American Heart Association* **6**, e006513 (2017).

321. Yu, L.-R. *et al.* Immune response proteins as predictive biomarkers of doxorubicin-induced cardiotoxicity in breast cancer patients. *Exp Biol Med (Maywood)* **243**, 248–255 (2018).

322. Alves, M. T. *et al.* Interleukin-10 Levels are Associated with Doxorubicin-Related Cardiotoxicity in Breast Cancer Patients in a One-Year Follow-Up Study. *Immunological Investigations* **51**, 883–898 (2022).

323. Mercuro, G. *et al.* Early epirubicin-induced myocardial dysfunction revealed by serial tissue Doppler echocardiography: correlation with inflammatory and oxidative stress markers. *Oncologist* **12**, 1124–1133 (2007).

324. Liang, S. *et al.* TLR2 and TLR3 expression as a biomarker for the risk of doxorubicin-induced heart failure. *Toxicology Letters* **295**, 205–211 (2018).

325. Tanaka, R. *et al.* Reactive fibrosis precedes doxorubicin-induced heart failure through sterile inflammation. *ESC Heart Fail* **7**, 588–603 (2020).

326. Guo, L. *et al.* Irigenin treatment alleviates doxorubicin (DOX)-induced cardiotoxicity by suppressing apoptosis, inflammation and oxidative stress via the increase of miR-425. *Biomedicine & Pharmacotherapy* **125**, 109784 (2020).

327. Wang, Z. *et al.* Inhibition of TRPA1 Attenuates Doxorubicin-Induced Acute Cardiotoxicity by Suppressing Oxidative Stress, the Inflammatory Response, and Endoplasmic Reticulum Stress. *Oxidative Medicine and Cellular Longevity* **2018**, e5179468 (2018).

328. Lan, Y., Wang, Y., Huang, K. & Zeng, Q. Heat Shock Protein 22 Attenuates Doxorubicin-Induced Cardiotoxicity via Regulating Inflammation and Apoptosis. *Front. Pharmacol.* **11**, (2020).

329. Ye, S. *et al.* LCZ696 Attenuated Doxorubicin-Induced Chronic Cardiomyopathy Through the TLR2-MyD88 Complex Formation. *Front. Cell Dev. Biol.* **9**, (2021).

330. Wang, L. *et al.* Doxorubicin-Induced Systemic Inflammation Is Driven by Upregulation of Toll-Like Receptor TLR4 and Endotoxin Leakage. *Cancer Res* **76**, 6631–6642 (2016).

331. Muendlein, H. I. *et al.* ZBP1 promotes LPS-induced cell death and IL-1β release via RHIM-mediated interactions with RIPK1. *Nat Commun* **12**, 86 (2021).

332. Shamseddine, A. *et al.* Innate immune signaling drives late cardiac toxicity following DNA-damaging cancer therapies. *Journal of Experimental Medicine* **220**, e20220809 (2022).

333. Zhang, H. *et al.* Self-Maintenance of Cardiac Resident Reparative Macrophages Attenuates Doxorubicin-Induced Cardiomyopathy Through the SR-A1-c-Myc Axis. *Circulation Research* **127**, 610–627 (2020).

334. Gambardella, J. *et al.* Infiltrating macrophages amplify doxorubicin-induced cardiac damage: role of catecholamines. *Cell Mol Life Sci* **80**, 323 (2023).

335. Jadapalli, J. K. *et al.* Doxorubicin triggers splenic contraction and irreversible dysregulation of COX and LOX that alters the inflammation-resolution program in the myocardium. *Am J Physiol Heart Circ Physiol* **315**, H1091–H1100 (2018).

336. Bhagat, A. *et al.* Doxorubicin-induced cardiotoxicity is mediated by neutrophils through release of neutrophil elastase. *Front Oncol* **12**, 947604 (2022).

337. Sano, S. *et al.* TP53-mediated therapy-related clonal hematopoiesis contributes to doxorubicin-induced cardiomyopathy by augmenting a neutrophil-mediated cytotoxic response. *JCI Insight* **6**, e146076.

338. Wang, J. *et al.* Exercise Inhibits Doxorubicin-Induced Cardiotoxicity via Regulating B Cells. *Circulation Research* **134**, 550–568 (2024).

339. Zhang, P., Zhang, G. & Wan, X. Challenges and new technologies in adoptive cell therapy. *Journal of Hematology & Oncology* **16**, 97 (2023).

340. Rosenberg, S. A., Restifo, N. P., Yang, J. C., Morgan, R. A. & Dudley, M. E. Adoptive cell transfer: a clinical path to effective cancer immunotherapy. *Nat Rev Cancer* **8**, 299–308 (2008).

341. Dudley, M. E. *et al.* Cancer Regression and Autoimmunity in Patients After Clonal Repopulation with Antitumor Lymphocytes. *Science* **298**, 850–854 (2002).

342. Rosenberg, S. A. & Dudley, M. E. Adoptive cell therapy for the treatment of patients with metastatic melanoma. *Current Opinion in Immunology* **21**, 233–240 (2009).

343. Morotti, M. *et al.* Promises and challenges of adoptive T-cell therapies for solid tumours. *Br J Cancer* **124**, 1759–1776 (2021).

344. Chamberlain, C. A. *et al.* Highly efficient PD-1-targeted CRISPR-Cas9 for tumor-infiltrating lymphocyte-based adoptive T cell therapy. *Mol Ther Oncolytics* **24**, 417–428 (2022).

345. Sterner, R. C. & Sterner, R. M. CAR-T cell therapy: current limitations and potential strategies. *Blood Cancer J.* **11**, 1–11 (2021).

346. Goldman, A. *et al.* Adverse Cardiovascular and Pulmonary Events Associated With Chimeric Antigen Receptor T-Cell Therapy. *Journal of the American College of Cardiology* **78**, 1800–1813 (2021).

347. Ghosh, A. K. *et al.* CAR T Cell Therapy–Related Cardiovascular Outcomes and Management: Systemic Disease or Direct Cardiotoxicity? *JACC: CardioOncology* **2**, 97–109 (2020).

348. Koeckerling, D. *et al.* Cardiovascular Events After Chimeric Antigen Receptor T-Cell Therapy for Advanced Hematologic Malignant Neoplasms: A Meta-Analysis. *JAMA Network Open* **7**, e2437222 (2024).

349. Hinrichs, C. S. & Restifo, N. P. Reassessing target antigens for adoptive T-cell therapy. *Nat Biotechnol* **31**, 999–1008 (2013).

350. Johnson, L. A. *et al.* Gene therapy with human and mouse T-cell receptors mediates cancer regression and targets normal tissues expressing cognate antigen. *Blood* **114**, 535–546 (2009).

351. Parkhurst, M. R. *et al.* T Cells Targeting Carcinoembryonic Antigen Can Mediate Regression of Metastatic Colorectal Cancer but Induce Severe Transient Colitis. *Mol Ther* **19**, 620–626 (2011).

352. Wei, S. C., Duffy, C. R. & Allison, J. P. Fundamental Mechanisms of Immune Checkpoint Blockade Therapy. *Cancer Discov* **8**, 1069–1086 (2018).

353. Robert, C. *et al.* Pembrolizumab versus Ipilimumab in Advanced Melanoma. *New England Journal of Medicine* **372**, 2521–2532 (2015).

354. Alturki, N. A. Review of the Immune Checkpoint Inhibitors in the Context of Cancer Treatment. *J Clin Med* **12**, 4301 (2023).

355. Prasad, V., Haslam, A. & Olivier, T. Updated estimates of eligibility and response: Immune checkpoint inhibitors. *JCO* **42**, e14613–e14613 (2024).

356. Lee, D. J., Lee, H. J., Farmer, J. R. & Reynolds, K. L. Mechanisms Driving Immune-Related Adverse Events in Cancer Patients Treated with Immune Checkpoint Inhibitors. *Curr Cardiol Rep* **23**, 98 (2021).

357. Conroy, M. & Naidoo, J. Immune-related adverse events and the balancing act of immunotherapy. *Nat Commun* **13**, 392 (2022).

358. Raschi, E. *et al.* Cardiovascular Toxicity of Immune Checkpoint Inhibitors: A Guide for Clinicians. *Drug Saf* **46**, 819–833 (2023).

359. Sharma, A. *et al.* Immune Checkpoint Inhibitors and Cardiotoxicity: A Comparative Meta-Analysis of Observational Studies and Randomized Controlled Trials. *Journal of the American Heart Association* **13**, e032620 (2024).

360. Moslehi, J. & Salem, J.-E. Immune Checkpoint Inhibitor Myocarditis Treatment Strategies and Future Directions. *JACC: CardioOncology* **4**, 704–707 (2022).

361. Zhu, H. *et al.* Identification of Pathogenic Immune Cell Subsets Associated With Checkpoint Inhibitor–Induced Myocarditis. *Circulation* **146**, 316–335 (2022).

362. Zhang, L. *et al.* Extracellular high-mobility group box 1 mediates pressure overload-induced cardiac hypertrophy and heart failure. *J Cell Mol Med* **20**, 459–470 (2016).

363. Suetomi, T. *et al.* Inflammation and NLRP3 inflammasome activation initiated in response to pressure overload by CaMKIIδ signaling in cardiomyocytes are essential for adverse cardiac remodeling. *Circulation* **138**, 2530–2544 (2018).

364. Ha, T. *et al.* Blockade of MyD88 attenuates cardiac hypertrophy and decreases cardiac myocyte apoptosis in pressure overload-induced cardiac hypertrophy in vivo. *American Journal of Physiology-Heart and Circulatory Physiology* **290**, H985–H994 (2006).

365. Bayer, A. L. & Alcaide, P. MyD88: At the heart of inflammatory signaling and cardiovascular disease. *Journal of Molecular and Cellular Cardiology* **161**, 75–85 (2021).

366. Mardiney, M. & Malech, H. L. Enhanced Engraftment of Hematopoietic Progenitor Cells in Mice Treated With Granulocyte Colony-Stimulating Factor Before Low-Dose Irradiation: Implications for Gene Therapy. *Blood* **87**, 4049–4056 (1996).

367. Mombaerts, P. *et al.* Mutations in T-cell antigen receptor genes α and β block thymocyte development at different stages. *Nature* **360**, 225–231 (1992).

368. Adachi, O. *et al.* Targeted Disruption of the MyD88 Gene Results in Loss of IL-1- and IL-18-Mediated Function. *Immunity* **9**, 143–150 (1998).

369. Hou, B., Reizis, B. & DeFranco, A. L. Toll-like receptor-mediated dendritic cell-dependent and -independent stimulation of innate and adaptive immunity. *Immunity* **29**, 272–282 (2008).

370. Lee, P. P. *et al.* A Critical Role for Dnmt1 and DNA Methylation in T Cell Development, Function, and Survival. *Immunity* **15**, 763–774 (2001).

371. Carrillo-Salinas, F. J. *et al.* Gut dysbiosis induced by cardiac pressure overload enhances adverse cardiac remodeling in a T cell-dependent manner. *Gut Microbes* **12**, 1823801 (2020).

372. Kaur, K. *et al.* Sialomucin CD43 Plays a Deleterious Role in the Development of Experimental Heart Failure Induced by Pressure Overload by Modulating Cardiac Inflammation and Fibrosis. *Frontiers in Physiology* **12**, (2021).

373. Hao, Y. *et al.* Integrated analysis of multimodal single-cell data. *Cell* **184**, 3573-3587.e29 (2021).

374. Amrute, J. M. *et al.* Targeting the Immune-Fibrosis Axis in Myocardial Infarction and Heart Failure. 2022.10.17.512579 Preprint at https://doi.org/10.1101/2022.10.17.512579 (2022).

375. Anastasiou, M. *et al.* Endothelial STING controls Tcell transmigration in an IFN-I dependent manner. *JCI Insight* (2021) doi:10.1172/jci.insight.149346.

376. Martini, E. *et al.* Single-Cell Sequencing of Mouse Heart Immune Infiltrate in Pressure Overload–Driven Heart Failure Reveals Extent of Immune Activation. *Circulation* **140**, 2089–2107 (2019).

377. Piali, L. *et al.* The chemokine receptor CXCR3 mediates rapid and shear-resistant adhesion-induction of effector T lymphocytes by the chemokines IP10 and Mig. *European Journal of Immunology* **28**, 961–972 (1998).

378. Yi, J., Balagopalan, L., Nguyen, T., McIntire, K. M. & Samelson, L. E. TCR microclusters form spatially segregated domains and sequentially assemble in calcium-dependent kinetic steps. *Nat Commun* **10**, 277 (2019).

379. Schenten, D. *et al.* Signaling through the Adaptor Molecule MyD88 in CD4+ T Cells Is Required to Overcome Suppression by Regulatory T Cells. *Immunity* **40**, 78–90 (2014).

380. Johansen, K. H., Golec, D. P., Thomsen, J. H., Schwartzberg, P. L. & Okkenhaug, K. PI3K in T Cell Adhesion and Trafficking. *Frontiers in Immunology* **12**, (2021).

381. Groom, J. R. & Luster, A. D. CXCR3 in T cell function. *Exp Cell Res* **317**, 620–631 (2011).

382. Wojno, E. D. T., Hunter, C. A. & Stumhofer, J. S. The Immunobiology of the Interleukin-12 Family: Room for Discovery. *Immunity* **50**, 851–870 (2019).

383. Funayama, A. *et al.* Cardiac nuclear high mobility group box 1 prevents the development of cardiac hypertrophy and heart failure. *Cardiovasc Res* **99**, 657–664 (2013).

384. Turner, N. A. Inflammatory and fibrotic responses of cardiac fibroblasts to myocardial damage associated molecular patterns (DAMPs). *Journal of Molecular and Cellular Cardiology* **94**, 189–200 (2016).

385. Theall, B. & Alcaide, P. The heart under pressure: immune cells in fibrotic remodeling. *Current Opinion in Physiology* **25**, 100484 (2022).

386. Kanisicak, O. *et al.* Genetic lineage tracing defines myofibroblast origin and function in the injured heart. *Nat Commun* **7**, 12260 (2016).

387. Reichardt, I. M., Robeson, K. Z., Regnier, M. & Davis, J. Controlling Cardiac Fibrosis Through Fibroblast State Space Modulation. *Cell Signal* **79**, 109888 (2021).

388. Ivey, M. J. *et al.* Resident fibroblast expansion during cardiac growth and remodeling. *Journal of Molecular and Cellular Cardiology* **114**, 161–174 (2018).

389. Farhood, B., Najafi, M. & Mortezaee, K. CD8+ cytotoxic T lymphocytes in cancer immunotherapy: A review. *Journal of Cellular Physiology* **234**, 8509–8521 (2019).

390. Abbate, A. *et al.* Interleukin-1 Blockade With Anakinra to Prevent Adverse Cardiac Remodeling After Acute Myocardial Infarction (Virginia Commonwealth University Anakinra Remodeling Trial [VCU-ART] Pilot Study). *The American Journal of Cardiology* **105**, 1371-1377.e1 (2010).

391. Theall, B. & Alcaide, P. The heart under pressure: immune cells in fibrotic remodeling. *Current Opinion in Physiology* **25**, 100484 (2022).

392. te Riet, L., van Esch, J. H. M., Roks, A. J. M., van den Meiracker, A. H. & Danser, A. H. J. Hypertension. *Circulation Research* **116**, 960–975 (2015).

393. Kawano, H. *et al.* Angiotensin II Has Multiple Profibrotic Effects in Human Cardiac Fibroblasts. *Circulation* **101**, 1130–1137 (2000).

394. Chen, K., Chen, J., Li, D., Zhang, X. & Mehta, J. L. Angiotensin II Regulation of Collagen Type I Expression in Cardiac Fibroblasts. *Hypertension* **44**, 655–661 (2004).

395. Lu, W., Meng, Z., Hernandez, R. & Zhou, C. Fibroblast-specific IKK-**β** deficiency ameliorates angiotensin II–induced adverse cardiac remodeling in mice. *JCI Insight* **6**, (2021).

396. Teixeira, A. F., ten Dijke, P. & Zhu, H.-J. On-Target Anti-TGF-β Therapies Are Not Succeeding in Clinical Cancer Treatments: What Are Remaining Challenges? *Front. Cell Dev. Biol.* **8**, (2020).

397. Bayer, A. L. & Alcaide, P. MyD88: At the heart of inflammatory signaling and cardiovascular disease. *Journal of Molecular and Cellular Cardiology* **161**, 75–85 (2021).

398. Bayer, A. L. *et al.* T-Cell MyD88 Is a Novel Regulator of Cardiac Fibrosis Through Modulation of T-Cell Activation. *Circulation Research* (2023) doi:10.1161/CIRCRESAHA.123.323030.

399. Ohm, I. K. *et al.* Toll-Like Receptor 9 Mediated Responses in Cardiac Fibroblasts. *PLOS ONE* **9**, e104398 (2014).

400. Bayer, A. L., Padilla-Rolon, D., Smolgovsky, S., Hinds, P. W. & Alcaide, P. Deletion of MyD88 in T Cells Improves Antitumor Activity in Melanoma. *The American Journal of Pathology* **194**, 1007–1019 (2024).

401. Lee, Y. S. *et al.* Smad6-specific recruitment of Smurf E3 ligases mediates TGF-β1-induced degradation of MyD88 in TLR4 signalling. *Nat Commun* **2**, 460 (2011).

402. Samba-Mondonga, M., Calvé, A., Mallette, F. A. & Santos, M. M. MyD88 Regulates the Expression of SMAD4 and the Iron Regulatory Hormone Hepcidin. *Frontiers in Cell and Developmental Biology* **6**, 105 (2018).

403. Ren, Z. *et al.* Single-Cell Reconstruction of Progression Trajectory Reveals Intervention Principles in Pathological Cardiac Hypertrophy. *Circulation* **141**, 1704–1719 (2020).

404. Nevers Tania *et al.* Left Ventricular T-Cell Recruitment Contributes to the Pathogenesis of Heart Failure. *Circulation: Heart Failure* **8**, 776–787 (2015).

405. Itani, H. A. *et al.* Activation of Human T Cells in Hypertension. *Hypertension* **68**, 123–132 (2016).

406. Lugowska, I., Teterycz, P. & Rutkowski, P. Immunotherapy of melanoma. *Contemp Oncol (Pozn)* **22**, 61–67 (2018).

407. Page, D. B., Postow, M. A., Callahan, M. K., Allison, J. P. & Wolchok, J. D. Immune Modulation in Cancer with Antibodies. *Annual Review of Medicine* **65**, 185–202 (2014).

408. Haist, M. *et al.* Combination of immune-checkpoint inhibitors and targeted therapies for melanoma therapy: The more, the better? *Cancer Metastasis Rev* (2023) doi:10.1007/s10555-023-10097-z.

409. Lucas, M. W., Versluis, J. M., Rozeman, E. A. & Blank, C. U. Personalizing neoadjuvant immune-checkpoint inhibition in patients with melanoma. *Nat Rev Clin Oncol* **20**, 408–422 (2023).

410. Deguine, J. & Barton, G. M. MyD88: a central player in innate immune signaling. *F1000Prime Rep* **6**, (2014).

411. Woo, S.-R., Corrales, L. & Gajewski, T. F. Innate Immune Recognition of Cancer. *Annual Review of Immunology* **33**, 445–474 (2015).

412. Schenten, D. *et al.* Signaling through the Adaptor Molecule MyD88 in CD4+ T Cells Is Required to Overcome Suppression by Regulatory T Cells. *Immunity* **40**, 78–90 (2014).

413. Hogquist, K. A. *et al.* T cell receptor antagonist peptides induce positive selection. *Cell* **76**, 17–27 (1994).

414. McRee, S. K., Bayer, A. L., Pietruska, J., Tsichlis, P. N. & Hinds, P. W. AKT2 Loss Impairs BRAF-Mutant Melanoma Metastasis. *Cancers* **15**, 4958 (2023).

415. Cerezo-Wallis, D. *et al.* Midkine rewires the melanoma microenvironment toward a tolerogenic and immune-resistant state. *Nat Med* **26**, 1865–1877 (2020).

416. Aktas, E., Kucuksezer, U. C., Bilgic, S., Erten, G. & Deniz, G. Relationship between CD107a expression and cytotoxic activity. *Cellular Immunology* **254**, 149–154 (2009).

417. Kapnick, S. M., Stinchcombe, J. C., Griffiths, G. M. & Schwartzberg, P. L. Inducible T cell kinase regulates the acquisition of cytolytic capacity and degranulation in CD8+ cytotoxic T lymphocytes. *J Immunol* **198**, 2699–2711 (2017).

418. Bustos-Morán, E. *et al.* Aurora A controls CD8+ T cell cytotoxic activity and antiviral response. *Sci Rep* **9**, 2211 (2019).

419. Yu, X. *et al.* MYD88 L265P Mutation in Lymphoid Malignancies. *Cancer Res* **78**, 2457–2462 (2018).

420. Wang, L., Yu, K., Zhang, X. & Yu, S. Dual functional roles of the MyD88 signaling in colorectal cancer development. *Biomedicine & Pharmacotherapy* **107**, 177–184 (2018).

421. Wu, K. *et al.* TLR4/MyD88 signaling determines the metastatic potential of breast cancer cells. *Molecular Medicine Reports* **18**, 3411–3420 (2018).

422. Zhu, G. *et al.* MyD88 mediates colorectal cancer cell proliferation, migration and invasion via NF-κB/AP-1 signaling pathway. *Int J Mol Med* **45**, 131–140 (2020).

423. Collinson-Pautz, M. R. *et al.* Constitutively active MyD88/CD40 costimulation enhances expansion and efficacy of chimeric antigen receptor T cells targeting hematological malignancies. *Leukemia* **33**, 2195–2207 (2019).

424. Olson, D. J. & Odunsi, K. Adoptive Cell Therapy for Nonhematologic Solid Tumors. *JCO* **41**, 3397–3407 (2023).

425. Stribbling, S. M. & Ryan, A. J. The cell-line-derived subcutaneous tumor model in preclinical cancer research. *Nat Protoc* **17**, 2108–2128 (2022).

426. Śledzińska, A., Fairbairn, L. & Buch, T. Manipulation of T Cell Function and Conditional Gene Targeting in T Cells. in *T-Helper Cells: Methods and Protocols* (eds. Waisman, A. & Becher, B.) 153–169 (Springer, New York, NY, 2014). doi:10.1007/978-1-4939-1212-4_15.

427. Abdullah, L., Hills, L. B., Winter, E. B. & Huang, Y. H. Diverse Roles of Akt in T cells. *Immunometabolism* **3**, e210007 (2021).

428. Luff, D. H. *et al.* PI3Kδ Forms Distinct Multiprotein Complexes at the TCR Signalosome in Naïve and Differentiated CD4+ T Cells. *Frontiers in Immunology* **12**, (2021).

429. Iwasaki, A. & Medzhitov, R. Toll-like receptor control of the adaptive immune responses. *Nature Immunology* **5**, 987–995 (2004).

430. Pasare, C. & Medzhitov, R. Control of B-cell responses by Toll-like receptors. *Nature* **438**, 364–368 (2005).

431. Reynolds, J. M., Martinez, G. J., Chung, Y. & Dong, C. Toll-like receptor 4 signaling in T cells promotes autoimmune inflammation. *Proceedings of the National Academy of Sciences* **109**, 13064–13069 (2012).

432. Reynolds, J. M. & Dong, C. Toll-like receptor regulation of effector T lymphocyte function. *Trends in Immunology* **34**, 511–519 (2013).

433. Rahman, A. H., Taylor, D. K. & Turka, L. A. The contribution of direct TLR signaling to T cell responses. *Immunol Res* **45**, 25–36 (2009).

434. Liu, X. *et al.* SMAD4, activated by the TCR-triggered MEK/ERK signaling pathway, critically regulates CD8+ T cell cytotoxic function. *Science Advances* **8**, eabo4577 (2022).

435. Miao, Y. *et al.* BCAP Regulates Dendritic Cell Maturation Through the Dual-Regulation of NF-κB and PI3K/AKT Signaling During Infection. *Front Immunol* **11**, 250 (2020).

436. Okada, T., Maeda, A., Iwamatsu, A., Gotoh, K. & Kurosaki, T. BCAP: The Tyrosine Kinase Substrate that Connects B Cell Receptor to Phosphoinositide 3-Kinase Activation. *Immunity* **13**, 817–827 (2000).

437. Kelly, E., Won, A., Refaeli, Y. & Van Parijs, L. IL-2 and Related Cytokines Can Promote T Cell Survival by Activating AKT1. *The Journal of Immunology* **168**, 597–603 (2002).

438. Singh, M. D., Ni, M., Sullivan, J. M., Hamerman, J. A. & Campbell, D. J. B cell adaptor for PI3-kinase (BCAP) modulates CD8+ effector and memory T cell differentiation. *J Exp Med* **215**, 2429–2443 (2018).

439. Harberts, E., Fishelevich, R., Liu, J., Atamas, S. P. & Gaspari, A. A. MyD88 mediates the decision to die by apoptosis or necroptosis after UV irradiation. *Innate Immun* **20**, 529–539 (2014).

440. Pugazhenthi, S. *et al.* Akt/Protein Kinase B Up-regulates Bcl-2 Expression through cAMP-response Element-binding Protein*. *Journal of Biological Chemistry* **275**, 10761–10766 (2000).

441. Liu, R. *et al.* PI3K/AKT pathway as a key link modulates the multidrug resistance of cancers. *Cell Death Dis* **11**, 1–12 (2020).

442. Caron, G. *et al.* Direct Stimulation of Human T Cells via TLR5 and TLR7/8: Flagellin and R-848 Up-Regulate Proliferation and IFN-γ Production by Memory CD4+ T Cells1. *The Journal of Immunology* **175**, 1551–1557 (2005).

443. Komai-Koma, M., Jones, L., Ogg, G. S., Xu, D. & Liew, F. Y. TLR2 is expressed on activated T cells as a costimulatory receptor. *Proceedings of the National Academy of Sciences* **101**, 3029–3034 (2004).

444. Xu, J., Guo, R., Jia, J., He, Y. & He, S. Activation of Toll-like receptor 2 enhances peripheral and tumor-infiltrating CD8+ T cell cytotoxicity in patients with gastric cancer. *BMC Immunology* **22**, 67 (2021).

445. Li, Q. *et al.* Toll-Like Receptor 7 Activation Enhances CD8+ T Cell Effector Functions by Promoting Cellular Glycolysis. *Frontiers in Immunology* **10**, (2019).

446. Troutman, T. D. *et al.* Role for B-cell adapter for PI3K (BCAP) as a signaling adapter linking Toll-like receptors (TLRs) to serine/threonine kinases PI3K/Akt. *Proceedings of the National Academy of Sciences* **109**, 273–278 (2012).

447. Bennett, P., Williamson, P. & Taylor, R. Review of Canine Lymphoma Treated with Chemotherapy—Outcomes and Prognostic Factors. *Vet Sci* **10**, 342 (2023).

448. Brown, S., Okwuosa, T. M., Barac, A. & Volgman, A. S. The Role of Angiotensin-Converting Enzyme Inhibitors and β-Blockers in Primary Prevention of Cardiac Dysfunction in Breast Cancer Patients. *Journal of the American Heart Association* **9**, e015327 (2020).

449. Deswal Anita *et al.* Cytokines and Cytokine Receptors in Advanced Heart Failure. *Circulation* **103**, 2055–2059 (2001).

450. Ngwenyama Njabulo *et al.* Isolevuglandin-Modified Cardiac Proteins Drive CD4+ T Cell Activation in the Heart and Promote Cardiac Dysfunction. *Circulation* **0**,.

451. Brassington, K. *et al.* Crosstalk between cytotoxic CD8+ T cells and stressed cardiomyocytes triggers development of interstitial cardiac fibrosis in hypertensive mouse hearts. *Frontiers in Immunology* **13**, (2022).

452. Zarak-Crnkovic, M. *et al.* Heart non-specific effector CD4+ T cells protect from postinflammatory fibrosis and cardiac dysfunction in experimental autoimmune myocarditis. *Basic Res Cardiol* **115**, 6 (2019).

453. Axelrod, M. L. *et al.* T cells specific for α-myosin drive immunotherapy-related myocarditis. *Nature* **611**, 818–826 (2022).

454. Forte, E. *et al.* Cross-Priming Dendritic Cells Exacerbate Immunopathology After Ischemic Tissue Damage in the Heart. *Circulation* **143**, 821–836 (2021).

455. Fanti, S. *et al.* Circulating c-Met–Expressing Memory T Cells Define Cardiac Autoimmunity. *Circulation* **146**, 1930–1945 (2022).

456. Bhagat, A., Shrestha, P. & Kleinerman, E. S. The Innate Immune System in Cardiovascular Diseases and Its Role in Doxorubicin-Induced Cardiotoxicity. *International Journal of Molecular Sciences* **23**, 14649 (2022).

457. Clarke, S. Rm. *et al.* Characterization of the ovalbumin-specific TCR transgenic line OT-I: MHC elements for positive and negative selection. *Immunology & Cell Biology* **78**, 110–117 (2000).

458. Warden, C. *et al.* Direct Detection of Isolevuglandins in Tissues Using a D11 scFv-Alkaline Phosphatase Fusion Protein and Immunofluorescence. *JoVE (Journal of Visualized Experiments)* e62603 (2021) doi:10.3791/62603.

459. Dittrich, K. *et al.* Baseline tumor gene expression signatures correlate with chemoimmunotherapy treatment responsiveness in canine B cell lymphoma. *PLOS ONE* **18**, e0290428 (2023).

460. McLinden, G. P. *et al.* Safety and biologic activity of a canine anti-CD20 monoclonal antibody in dogs with diffuse large B-cell lymphoma. *J Vet Intern Med* **38**, 1666–1674 (2024).

461. Rue, S. M. *et al.* Identification of a candidate therapeutic antibody for treatment of canine B-cell lymphoma. *Veterinary Immunology and Immunopathology* **164**, 148–159 (2015).

462. Seelig, D. M. *et al.* Canine T-Zone Lymphoma: Unique Immunophenotypic Features, Outcome, and Population Characteristics. *J Vet Intern Med* **28**, 878–886 (2014).

463. Liu, J. *et al.* Circulating hemopexin modulates anthracycline cardiac toxicity in patients and in mice. *Science Advances* **8**, eadc9245 (2022).

464. Kirabo, A. *et al.* DC isoketal-modified proteins activate T cells and promote hypertension. *J Clin Invest* **124**, 4642–4656 (2014).

465. Valentini, N., Requejo Cier, C. J. & Lamarche, C. Regulatory T-cell dysfunction and its implication for cell therapy. *Clinical and Experimental Immunology* **213**, 40–49 (2023).

466. Learmonth, M., Corker, A., Dasgupta, S. & DeLeon-Pennell, K. Y. Regulation of cardiac fibroblasts by lymphocytes after a myocardial infarction: playing in the major league. *American Journal of Physiology-Heart and Circulatory Physiology* **325**, H553–H561 (2023).

467. Shen, Y. *et al.* Granzyme B Deficiency Protects against Angiotensin II–Induced Cardiac Fibrosis. *The American Journal of Pathology* **186**, 87–100 (2016).

468. Santos-Zas, I. *et al.* Cytotoxic CD8+ T cells promote granzyme B-dependent adverse post-ischemic cardiac remodeling. *Nat Commun* **12**, 1483 (2021).

469. Schips, T. G. *et al.* FoxO3 induces reversible cardiac atrophy and autophagy in a transgenic mouse model. *Cardiovascular Research* **91**, 587–597 (2011).

470. Pandya, K., Kim, H.-S. & Smithies, O. Fibrosis, not cell size, delineates β-myosin heavy chain reexpression during cardiac hypertrophy and normal aging in vivo. *Proceedings of the National Academy of Sciences* **103**, 16864–16869 (2006).

471. Huber, S. A. Doxorubicin-induced alterations in cultured myocardial cells stimulate cytolytic T lymphocyte responses. *Am J Pathol* **137**, 449–456 (1990).

472. Ngwenyama, N. *et al.* CXCR3 regulates CD4+ T cell cardiotropism in pressure overload–induced cardiac dysfunction. *JCI Insight* **4**,.

473. Farhood, B., Najafi, M. & Mortezaee, K. CD8+ cytotoxic T lymphocytes in cancer immunotherapy: A review. *Journal of Cellular Physiology* **234**, 8509–8521 (2019).

474. Ali, H. R. *et al.* Association between CD8+ T-cell infiltration and breast cancer survival in 12 439 patients. *Annals of Oncology* **25**, 1536–1543 (2014).

475. Mattarollo, S. R. *et al.* Pivotal Role of Innate and Adaptive Immunity in Anthracycline Chemotherapy of Established Tumors. *Cancer Research* **71**, 4809–4820 (2011).

476. Ni, C. *et al.* Doxorubicin-induced cardiotoxicity involves IFNγ-mediated metabolic reprogramming in cardiomyocytes. *The Journal of Pathology* **247**, 320–332 (2019).

477. Ma, P. *et al.* Temporary blockade of interferon-γ ameliorates doxorubicin-induced cardiotoxicity without influencing the anti-tumor effect. *Biomedicine & Pharmacotherapy* **130**, 110587 (2020).

478. Yang, D., Liu, J., Qian, H. & Zhuang, Q. Cancer-associated fibroblasts: from basic science to anticancer therapy. *Exp Mol Med* **55**, 1322–1332 (2023).

479. Chandler, C., Liu, T., Buckanovich, R. & Coffman, L. The double edge sword of fibrosis in cancer. *Transl Res* **209**, 55–67 (2019).

480. Ba, Y. *et al.* Current management of chemotherapy-induced neutropenia in adults: key points and new challenges. *Cancer Biol Med* **17**, 896–909 (2020).

481. Nitiss, J. L. Targeting DNA topoisomerase II in cancer chemotherapy. *Nat Rev Cancer* **9**, 338–350 (2009).

482. Kim, S.-Y. *et al.* Doxorubicin-induced reactive oxygen species generation and intracellular Ca2+ increase are reciprocally modulated in rat cardiomyocytes. *Exp Mol Med* **38**, 535–545 (2006).

483. Christidi, E. & Brunham, L. R. Regulated cell death pathways in doxorubicin-induced cardiotoxicity. *Cell Death Dis* **12**, 1–15 (2021).

484. Upshaw, J. N. *et al.* Dexrazoxane to Prevent Cardiotoxicity in Adults Treated with Anthracyclines. *JACC CardioOncol* **6**, 322–324 (2024).

485. Bayer, A. L. *et al.* Cytotoxic T cells drive doxorubicin-induced cardiac fibrosis and systolic dysfunction. *Nat Cardiovasc Res* **3**, 970–986 (2024).

486. Huang, Y. V. *et al.* A Novel Therapeutic Approach using CXCR3 Blockade to Treat Immune Checkpoint Inhibitor-mediated Myocarditis. 2024.01.30.576279 Preprint at https://doi.org/10.1101/2024.01.30.576279 (2024).

487. Anastasiou, M. *et al.* Endothelial STING controls Tcell transmigration in an IFN-I dependent manner. *JCI Insight* (2021) doi:10.1172/jci.insight.149346.

488. Lei, Y. *et al.* Cooperative sensing of mitochondrial DNA by ZBP1 and cGAS promotes cardiotoxicity. *Cell* **186**, 3013-3032.e22 (2023).

489. Jin, L. *et al.* MPYS is required for IRF3 activation and type I IFN production in the response of cultured phagocytes to bacterial second messengers c-di-AMP and c-di-GMP. *J Immunol* **187**, 2595–2601 (2011).

490. Luscinskas, F. W., Brock, A. F., Arnaout, M. A. & Gimbrone, M. A. Endothelial-leukocyte adhesion molecule-1-dependent and leukocyte (CD11/CD18)-dependent mechanisms contribute to polymorphonuclear leukocyte adhesion to cytokine-activated human vascular endothelium. *J Immunol* **142**, 2257–2263 (1989).

491. Larkin, B. *et al.* Cutting Edge: Activation of STING in T Cells Induces Type I IFN Responses and Cell Death. *The Journal of Immunology* **199**, 397–402 (2017).

492. Corbera-Bellalta, M. *et al.* Blocking interferon γ reduces expression of chemokines CXCL9, CXCL10 and CXCL11 and decreases macrophage infiltration in ex vivo cultured arteries from patients with giant cell arteritis. *Annals of the Rheumatic Diseases* **75**, 1177–1186 (2016).

493. Boivin, W. A., Cooper, D. M., Hiebert, P. R. & Granville, D. J. Intracellular versus extracellular granzyme B in immunity and disease: challenging the dogma. *Lab Invest* **89**, 1195–1220 (2009).

494. de Graaf, K. L. *et al.* NI-0801, an anti-chemokine (C-X-C motif) ligand 10 antibody, in patients with primary biliary cholangitis and an incomplete response to ursodeoxycholic acid. *Hepatol Commun* **2**, 492–503 (2018).

495. A phase II, randomized, double-blind, placebo-controlled study evaluating the efficacy and safety of MDX-1100, a fully human anti-CXCL10 monoclonal antibody, in combination with methotrexate in patients with rheumatoid arthritis. doi:10.1002/art.34330.

496. Christen, U. *et al.* Combination treatment of a novel CXCR3 antagonist ACT-777991 with an anti-CD3 antibody synergistically increases persistent remission in experimental models of type 1 diabetes. *Clinical and Experimental Immunology* **214**, 131–143 (2023).

497. Shengchao, M. *et al.* Long-term CXCR3 antagonist AMG487 mitigated acute graft-versus-host disease by inhibiting T cell activation in a murine model. *Transplant Immunology* **87**, 102128 (2024).

498. Medzhitov, R. *et al.* MyD88 Is an Adaptor Protein in the hToll/IL-1 Receptor Family Signaling Pathways. *Molecular Cell* **2**, 253–258 (1998).

499. Wesche, H., Henzel, W. J., Shillinglaw, W., Li, S. & Cao, Z. Pillars Article: MyD88: An Adapter That Recruits IRAK to the IL-1 Receptor Complex. Immunity. 1997. 7: 837–847. *The Journal of Immunology* **190**, 5–15 (2013).

500. Kawai, T., Adachi, O., Ogawa, T., Takeda, K. & Akira, S. Unresponsiveness of MyD88-Deficient Mice to Endotoxin. *Immunity* **11**, 115–122 (1999).

501. Villano, J. S., Rong, F. & Cooper, T. K. Bacterial Infections in Myd88-Deficient Mice. *Comp Med* **64**, 110–114 (2014).

502. Scanga, C. A. *et al.* MyD88-Deficient Mice Display a Profound Loss in Resistance to Mycobacterium tuberculosis Associated with Partially Impaired Th1 Cytokine and Nitric Oxide Synthase 2 Expression. *Infect Immun* **72**, 2400–2404 (2004).

503. Ma, M., Jiang, W. & Zhou, R. DAMPs and DAMP-sensing receptors in inflammation and diseases. *Immunity* **57**, 752–771 (2024).

504. Gong, T., Liu, L., Jiang, W. & Zhou, R. DAMP-sensing receptors in sterile inflammation and inflammatory diseases. *Nat Rev Immunol* **20**, 95–112 (2020).

505. Pandolfi, F., Altamura, S., Frosali, S. & Conti, P. Key Role of DAMP in Inflammation, Cancer, and Tissue Repair. *Clinical Therapeutics* **38**, 1017–1028 (2016).

506. Oliveira, A.-C. *et al.* Crucial role for T cell-intrinsic IL-18R-MyD88 signaling in cognate immune response to intracellular parasite infection. *eLife* **6**, e30883 (2017).

507. Rahman, A. H. *et al.* Antiviral memory CD8 T-cell differentiation, maintenance, and secondary expansion occur independently of MyD88. *Blood* **117**, 3123–3130 (2011).

508. Rahman, A. H. *et al.* MyD88 Plays a Critical T Cell-Intrinsic Role in Supporting CD8 T Cell Expansion during Acute Lymphocytic Choriomeningitis Virus Infection. *J Immunol* **181**, 3804–3810 (2008).

509. LaRosa, D. F. *et al.* T cell expression of MyD88 is required for resistance to Toxoplasma gondii. *Proceedings of the National Academy of Sciences* **105**, 3855–3860 (2008).

510. Bayer, A. L., Magri, Z., Muendlein, H. I., Poltorak, A. & Alcaide, P. MyD88 Determines T-cell Fate Through BCAP-PI3K Signaling. *The Journal of Immunology* (2025).

511. Fukata, M. *et al.* The myeloid differentiation factor 88 (MyD88) is required for CD4+ T cell effector function in a murine model of inflammatory bowel disease. *J Immunol* **180**, 1886–1894 (2008).

512. Imanishi, T. *et al.* Cutting Edge: TLR2 Directly Triggers Th1 Effector Functions1. *The Journal of Immunology* **178**, 6715–6719 (2007).

513. González-Navajas, J. M. *et al.* TLR4 signaling in effector $CD4^+$ T cells regulates TCR activation and experimental colitis in mice. *J Clin Invest* **120**, 570–581 (2010).

514. Gelman, A. E. *et al.* The Adaptor Molecule MyD88 Activates PI-3 Kinase Signaling in CD4+ T Cells and Enables CpG Oligodeoxynucleotide-Mediated Costimulation. *Immunity* **25**, 783–793 (2006).

515. Marsland, B. J. *et al.* TLR Ligands Act Directly upon T Cells to Restore Proliferation in the Absence of Protein Kinase C-θ Signaling and Promote Autoimmune Myocarditis1. *The Journal of Immunology* **178**, 3466–3473 (2007).

516. Petersen, C. *et al.* T cell–mediated regulation of the microbiota protects against obesity. *Science* **365**, (2019).

517. Kubinak, J. L. *et al.* MyD88 Signaling in T Cells Directs IgA-Mediated Control of the Microbiota to Promote Health. *Cell Host & Microbe* **17**, 153–163 (2015).

518. Mandraju, R. *et al.* MyD88 Signaling in T Cells Is Critical for Effector CD4 T Cell Differentiation following a Transitional T Follicular Helper Cell Stage. *Infect Immun* **86**, (2018).

519. Lee, M. S. J. *et al.* B cell-intrinsic MyD88 signaling controls IFN-γ-mediated early IgG2c class switching in mice in response to a particulate adjuvant. *European Journal of Immunology* **49**, 1433–1440 (2019).

520. Tilstra, J. S. *et al.* B cell–intrinsic Myd88 regulates disease progression in murine lupus. *J Exp Med* **220**, e20230263 (2023).

521. Hosseini, H. *et al.* Toll-Like Receptor (TLR)4 and MyD88 are Essential for Atheroprotection by Peritoneal B1a B Cells. *J Am Heart Assoc* **5**, (2016).

522. Tian, M. *et al.* B Cell–Intrinsic MyD88 Signaling Promotes Initial Cell Proliferation and Differentiation To Enhance the Germinal Center Response to a Virus-like Particle. *The Journal of Immunology* **200**, 937–948 (2018).

523. Theobald, D., Nair, A. R., Sriramula, S. & Francis, J. Cardiomyocyte-specific deletion of TLR4 attenuates angiotensin II-induced hypertension and cardiac remodeling. *Front Cardiovasc Med* **10**, 1074700 (2023).

524. Luo, W. *et al.* Blockage of MyD88 in cardiomyocytes alleviates cardiac inflammation and cardiomyopathy in experimental diabetic mice. *Biochemical Pharmacology* **206**, 115292 (2022).

525. Gao, W. *et al.* Retinol-Binding Protein 4 Induces Cardiomyocyte Hypertrophy by Activating TLR4/MyD88 Pathway. *Endocrinology* **157**, 2282–2293 (2016).

526. Chen, W., Huang, Z., Jiang, X., Li, C. & Gao, X. Overexpression of myeloid differentiation protein 88 in mice induces mild cardiac dysfunction, but no deficit in heart morphology. *Braz J Med Biol Res* **49**, (2015).

527. Chen, W. *et al.* Overexpressing dominant negative MyD88 induces cardiac dysfunction in transgenic mice. *Chin. Sci. Bull.* **55**, 3569–3575 (2010).

528. Yu, M. *et al.* MyD88-dependent interplay between myeloid and endothelial cells in the initiation and progression of obesity-associated inflammatory diseases. *J Exp Med* **211**, 887–907 (2014).

529. Raschi, E. *et al.* Role of the MyD88 transduction signaling pathway in endothelial activation by antiphospholipid antibodies. *Blood* **101**, 3495–3500 (2003).

530. Boettcher, S., Gerosa, R., Radpour, R. & Manz, M. G. Endothelial Cells Are Essential to Sense Lipopolysaccharide in a MYD88-Dependent Manner and to Subsequently Induce Emergency Myelopoiesis. *Blood* **120**, 641 (2012).

531. Harari, O. A., Alcaide, P., Ahl, D., Luscinskas, F. W. & Liao, J. K. Absence of TRAM Restricts Toll-Like Receptor 4 Signaling in Vascular Endothelial Cells to the MyD88 Pathway. *Circ Res* **98**, 1134–1140 (2006).

532. Lee, G.-L. *et al.* TLR4-Activated MAPK-IL-6 Axis Regulates Vascular Smooth Muscle Cell Function. *Int J Mol Sci* **17**, (2016).

533. Song, Y. *et al.* Aging enhances the basal production of IL-6 and CCL2 in vascular smooth muscle cells. *Arterioscler Thromb Vasc Biol* **32**, 103–109 (2012).

534. Hernanz, R. *et al.* Toll-like receptor 4 contributes to vascular remodelling and endothelial dysfunction in angiotensin II-induced hypertension. *Br J Pharmacol* **172**, 3159–3176 (2015).

535. Goumenaki, P. *et al.* The innate immune regulator MyD88 dampens fibrosis during zebrafish heart regeneration. *Nat Cardiovasc Res* **3**, 1158–1176 (2024).

536. Yuan, Q. *et al.* MyD88 in myofibroblasts regulates aerobic glycolysis-driven hepatocarcinogenesis via ERK-dependent PKM2 nuclear relocalization and activation. *The Journal of Pathology* **n/a**, (2022).

537. Liu, Y. *et al.* MyD88 in myofibroblasts enhances nonalcoholic fatty liver disease-related hepatocarcinogenesis via promoting macrophage M2 polarization. *Cell Communication and Signaling* **22**, 86 (2024).

538. Yuan, Q. *et al.* MyD88 in myofibroblasts enhances colitis-associated tumorigenesis via promoting macrophage M2 polarization. *Cell Reports* **34**, (2021).

539. Ikebe, M. *et al.* Lipopolysaccharide (LPS) increases the invasive ability of pancreatic cancer cells through the TLR4/MyD88 signaling pathway. *J Surg Oncol* **100**, 725–731 (2009).

540. Koliaraki, V. *et al.* Innate Sensing through Mesenchymal TLR4/MyD88 Signals Promotes Spontaneous Intestinal Tumorigenesis. *Cell Reports* **26**, 536-545.e4 (2019).

541. Salcedo, R. *et al.* MyD88-mediated signaling prevents development of adenocarcinomas of the colon: role of interleukin 18. *Journal of Experimental Medicine* **207**, 1625–1636 (2010).

542. Zarember, K. A. & Godowski, P. J. Tissue Expression of Human Toll-Like Receptors and Differential Regulation of Toll-Like Receptor mRNAs in Leukocytes in Response to Microbes, Their Products, and Cytokines. *The Journal of Immunology* **168**, 554–561 (2002).

543. Rosenberger, K. *et al.* The impact of single and pairwise Toll-like receptor activation on neuroinflammation and neurodegeneration. *Journal of Neuroinflammation* **11**, 166 (2014).

544. Benjelloun, F. *et al.* Activation of Toll-Like Receptors Differentially Modulates Inflammation in the Human Reproductive Tract: Preliminary Findings. *Front. Immunol.* **11**, (2020).

545. Bender, A. T. *et al.* TLR7 and TLR8 Differentially Activate the IRF and NF-κB Pathways in Specific Cell Types to Promote Inflammation. *ImmunoHorizons* **4**, 93–107 (2020).

546. Boyd, J. H., Mathur, S., Wang, Y., Bateman, R. M. & Walley, K. R. Toll-like receptor stimulation in cardiomyoctes decreases contractility and initiates an NF-κB dependent inflammatory response. *Cardiovascular Research* **72**, 384–393 (2006).

547. Fisch, D. *et al.* Molecular definition of the endogenous Toll-like receptor signalling pathways. *Nature* 1–10 (2024) doi:10.1038/s41586-024-07614-7.

548. Dossang, A. C. G. *et al.* The N-terminal loop of IRAK-4 death domain regulates ordered assembly of the Myddosome signalling scaffold. *Sci Rep* **6**, 37267 (2016).

549. George, J. *et al.* Two Human MYD88 Variants, S34Y and R98C, Interfere with MyD88-IRAK4-Myddosome Assembly. *J Biol Chem* **286**, 1341–1353 (2011).

550. Yamamoto, M. *et al.* Essential role for TIRAP in activation of the signalling cascade shared by TLR2 and TLR4. *Nature* **420**, 324–329 (2002).

551. Dai, P. *et al.* Modulation of TLR Signaling by Multiple MyD88-Interacting Partners Including Leucine-Rich Repeat Fli-I-Interacting Proteins1. *The Journal of Immunology* **182**, 3450–3460 (2009).

552. Honda, K. *et al.* Role of a transductional-transcriptional processor complex involving MyD88 and IRF-7 in Toll-like receptor signaling. *Proceedings of the National Academy of Sciences* **101**, 15416–15421 (2004).

553. Lauenstein, J. U. *et al.* Negative Regulation of TLR Signaling by BCAP Requires Dimerization of Its DBB Domain. *J Immunol* **204**, 2269–2276 (2020).

554. Chaudhary, A. *et al.* The *Brucella* TIR-like protein TcpB interacts with the death domain of MyD88. *Biochemical and Biophysical Research Communications* **417**, 299–304 (2012).

555. Hussain, B. *et al.* Activation of STING Based on Its Structural Features. *Front. Immunol.* **13**, (2022).

556. Shi, C.-S. & Kehrl, J. H. MyD88 and Trif Target Beclin 1 to Trigger Autophagy in Macrophages*. *Journal of Biological Chemistry* **283**, 33175–33182 (2008).

557. Yang, G. *et al.* A mutation in MYD88 (L265P) supports the survival of lymphoplasmacytic cells by activation of Bruton tyrosine kinase in Waldenström macroglobulinemia. *Blood* **122**, 1222–1232 (2013).

558. Janssens, S., Burns, K., Tschopp, J. & Beyaert, R. Regulation of Interleukin-1- and Lipopolysaccharide-Induced NF-κB Activation by Alternative Splicing of MyD88. *Current Biology* **12**, 467–471 (2002).

559. Lee, F. F. Y., Harris, C. & Alper, S. RNA Binding Proteins that Mediate LPS-induced Alternative Splicing of the MyD88 Innate Immune Regulator. *Journal of Molecular Biology* **436**, 168497 (2024).

560. Burns, K. *et al.* Inhibition of Interleukin 1 Receptor/Toll-like Receptor Signaling through the Alternatively Spliced, Short Form of MyD88 Is Due to Its Failure to Recruit IRAK-4. *Journal of Experimental Medicine* **197**, 263–268 (2003).

561. Janssens, S., Burns, K., Vercammen, E., Tschopp, J. & Beyaert, R. MyD88S, a splice variant of MyD88, differentially modulates NF-κB- and AP-1-dependent gene expression. *FEBS Letters* **548**, 103–107 (2003).

562. Pustelny, K. *et al.* Mechanism of MyD88S mediated signal termination. *Cell Commun Signal* **20**, 10 (2022).

563. Vickers, T. A. *et al.* Modification of MyD88 mRNA Splicing and Inhibition of IL-1β Signaling in Cell Culture and in Mice with a 2'-O-Methoxyethyl-Modified Oligonucleotide. *The Journal of Immunology* **176**, 3652–3661 (2006).

564. Kim, Y.-C. *et al.* Toll-like receptor mediated inflammation requires FASN-dependent MYD88 palmitoylation. *Nat Chem Biol* **15**, 907–916 (2019).

565. Yi, Y.-S. *et al.* Syk-MyD88 Axis Is a Critical Determinant of Inflammatory-Response in Activated Macrophages. *Front. Immunol.* **12**, (2021).

566. Gurung, P. *et al.* SYK licenses MyD88 to instigate IL-1α-mediated inflammatory disease. *Immunity* **46**, 635–648 (2017).

567. Xie, L. *et al.* Protein Phosphatase 2A Catalytic Subunit α (PP2Ac) Plays a MyD88-dependent, Central Role in the Gene-Specific Regulation of Endotoxin Tolerance (ET). *Cell Rep* **3**, 678–688 (2013).

568. Loiarro, M. *et al.* Mutational Analysis Identifies Residues Crucial for Homodimerization of Myeloid Differentiation Factor 88 (MyD88) and for Its Function in Immune Cells. *J Biol Chem* **288**, 30210–30222 (2013).

569. Minderman, M. *et al.* The oncogenic human B-cell lymphoma MYD88 L265P mutation genocopies activation by phosphorylation at the Toll/interleukin-1 receptor (TIR) domain. *Blood Cancer J.* **13**, 1–10 (2023).

570. Murphy Schafer, A. R., Smith, J. L., Pryke, K. M., DeFilippis, V. R. & Hirsch, A. J. The E3 Ubiquitin Ligase SIAH1 Targets MyD88 for Proteasomal Degradation During Dengue Virus Infection. *Front. Microbiol.* **11**, (2020).

571. Wang, C. *et al.* The E3 ubiquitin ligase Nrdp1 'preferentially' promotes TLR-mediated production of type I interferon. *Nat Immunol* **10**, 744–752 (2009).

572. Jin, X. *et al.* CRL3–SPOP ubiquitin ligase complex suppresses the growth of diffuse large B-cell lymphoma by negatively regulating the MyD88/NF-κB signaling. *Leukemia* **34**, 1305–1314 (2020).

573. Yu, X. *et al.* MYD88 L265P elicits mutation-specific ubiquitination to drive NF-κB activation and lymphomagenesis. *Blood* **137**, 1615–1627 (2021).

574. Zhao, Y. *et al.* OTUD4 is a phospho-activated K63 deubiquitinase that regulates MyD88-dependent signaling. *Mol Cell* **69**, 505-516.e5 (2018).

575. Yan, F., Guan, J., Peng, Y. & Zheng, X. MyD88 NEDDylation negatively regulates MyD88-dependent NF-κB signaling through antagonizing its ubiquitination. *Biochemical and Biophysical Research Communications* **482**, 632–637 (2017).

576. Menden, H. *et al.* Histone deacetylase 6 regulates endothelial MyD88-dependent canonical TLR signaling, lung inflammation, and alveolar remodeling in the developing lung. *American Journal of Physiology-Lung Cellular and Molecular Physiology* **317**, L332–L346 (2019).

577. Prinzing, B. *et al.* MyD88/CD40 signaling retains CAR T cells in a less differentiated state. *JCI Insight* **5**, (2020).

578. Mata, M. *et al.* Inducible Activation of MyD88 and CD40 in CAR T Cells Results in Controllable and Potent Antitumor Activity in Preclinical Solid Tumor Models. *Cancer Discovery* **7**, 1306–1319 (2017).

579. Geng, D. *et al.* Amplifying TLR-MyD88 signals within tumor-specific T-cells enhances antitumor activity to suboptimal levels of weakly-immunogenic tumor-antigens. *Cancer Res* **70**, 7442–7454 (2010).

580. Alcaide, P., Kallikourdis, M., Emig, R. & Prabhu, S. D. Myocardial Inflammation in Heart Failure With Reduced and Preserved Ejection Fraction. *Circulation Research* **134**, 1752–1766 (2024).

581. Bui, T. M., Wiesolek, H. L. & Sumagin, R. ICAM-1: A master regulator of cellular responses in inflammation, injury resolution, and tumorigenesis. *J Leukoc Biol* **108**, 787–799 (2020).

582. Kong, D.-H., Kim, Y. K., Kim, M. R., Jang, J. H. & Lee, S. Emerging Roles of Vascular Cell Adhesion Molecule-1 (VCAM-1) in Immunological Disorders and Cancer. *International Journal of Molecular Sciences* **19**, 1057 (2018).

583. Lakins, M. A., Ghorani, E., Munir, H., Martins, C. P. & Shields, J. D. Cancer-associated fibroblasts induce antigen-specific deletion of CD8 + T Cells to protect tumour cells. *Nat Commun* **9**, 948 (2018).

584. Hall, C. *et al.* Chronic activation of human cardiac fibroblasts in vitro attenuates the reversibility of the myofibroblast phenotype. *Sci Rep* **13**, 12137 (2023).

585. Singh, M. V. *et al.* MyD88 mediated inflammatory signaling leads to CaMKII oxidation, cardiac hypertrophy and death after myocardial infarction. *J Mol Cell Cardiol* **52**, 1135–1144 (2012).

586. Sun, D. & Ding, A. MyD88-mediated stabilization of interferon-γ-induced cytokine and chemokine mRNA. *Nat Immunol* **7**, 375–381 (2006).

587. Morandini, A. C., Chaves Souza, P. P., Ramos-Junior, E. S., Souza Costa, C. A. & Santos, C. F. MyD88 or TRAM Knockdown Regulates Interleukin (IL)-6, IL-8, and CXCL12 mRNA Expression in Human Gingival and Periodontal Ligament Fibroblasts. *Journal of Periodontology* **84**, 1353–1360 (2013).

588. Zhang, J. *et al.* MyD88 in hepatic stellate cells enhances liver fibrosis via promoting macrophage M1 polarization. *Cell Death Dis* **13**, 1–14 (2022).

589. Monteran, L. & Erez, N. The Dark Side of Fibroblasts: Cancer-Associated Fibroblasts as Mediators of Immunosuppression in the Tumor Microenvironment. *Front. Immunol.* **0**, (2019).

590. Won, T. *et al.* Cardiac myosin-specific autoimmune T cells contribute to immune-checkpoint-inhibitor-associated myocarditis. *Cell Reports* **41**, (2022).

591. Rieckmann, M. *et al.* Myocardial infarction triggers cardioprotective antigen-specific T helper cell responses. *J Clin Invest* **129**, 4922–4936.

592. Basavalingappa, R. H. *et al.* Identification of an Epitope from Adenine Nucleotide Translocator 1 That Induces Inflammation in Heart in A/J Mice. *The American Journal of Pathology* **186**, 3160 (2016).

593. Hapke, N. *et al.* Identification of a novel cardiac epitope triggering T-cell responses in patients with myocardial infarction. *Journal of Molecular and Cellular Cardiology* **173**, 25–29 (2022).

594. Aminkeng, F. *et al.* Recommendations for genetic testing to reduce the incidence of anthracycline-induced cardiotoxicity. *Br J Clin Pharmacol* **82**, 683–695 (2016).

595. Al-Otaibi, T. K., Weitzman, B., Tahir, U. A. & Asnani, A. Genetics of Anthracycline-Associated Cardiotoxicity. *Front. Cardiovasc. Med.* **9**, (2022).

596. Butcher, M. J. *et al.* Atherosclerosis-Driven Treg Plasticity Results in Formation of a Dysfunctional Subset of Plastic IFNγ+ Th1/Tregs. *Circulation Research* **119**, 1190–1203 (2016).

597. Bansal, S. S. *et al.* Dysfunctional and Proinflammatory Regulatory T-Lymphocytes Are Essential for Adverse Cardiac Remodeling in Ischemic Cardiomyopathy. *Circulation* **139**, 206–221 (2019).

598. Vénéreau, E., Ceriotti, C. & Bianchi, M. E. DAMPs from Cell Death to New Life. *Front. Immunol.* **6**, (2015).

599. Park, J. Y. *et al.* Doxorubicin enhances CD4+ T-cell immune responses by inducing expression of CD40 ligand and 4-1BB. *International Immunopharmacology* **9**, 1530–1539 (2009).

600. Sánchez-Margalet, V. *et al.* Circulating regulatory T cells from breast cancer patients in response to neoadjuvant chemotherapy. *Translational Cancer Research* **8**, (2019).

601. Van der Borght, K. *et al.* Myocardial Infarction Primes Autoreactive T Cells through Activation of Dendritic Cells. *Cell Reports* **18**, 3005–3017 (2017).

602. Diffuse Large B-Cell Lymphoma (Non-Hodgkin Lymphoma) Treatment Protocols: Treatment Protocols. (2024).

603. Larsen, C. M. *et al.* Association of Anthracycline With Heart Failure in Patients Treated for Breast Cancer or Lymphoma, 1985-2010. *JAMA Network Open* **6**, e2254669 (2023).

604. Kremer, L. C. M. & Caron, H. N. Anthracycline Cardiotoxicity in Children. *New England Journal of Medicine* **351**, 120–121 (2004).

605. Nathan, P., Kulkarni, K. & MacDonald, T. Incidence and risk factors of anthracycline-induced cardiotoxicity in long-term survivors of pediatric cancer: A population based cohort study. *Pediatric Hematology Oncology Journal* **7**, 136–141 (2022).

606. Shinzawa, M. *et al.* Reversal of the T cell immune system reveals the molecular basis for T cell lineage fate determination in the thymus. *Nat Immunol* 1–12 (2022) doi:10.1038/s41590-022-01187-1.

607. Mittelbrunn, M. & Kroemer, G. Hallmarks of T cell aging. *Nat Immunol* **22**, 687–698 (2021).

608. Han, S., Georgiev, P., Ringel, A. E., Sharpe, A. H. & Haigis, M. Age-associated remodeling of T cell immunity and metabolism. *Cell Metab* **35**, 36–55 (2023).

609. Weigelin, B. & Friedl, P. T cell-mediated additive cytotoxicity – death by multiple bullets. *Trends in Cancer* **8**, 980–987 (2022).

610. Chiong, M. *et al.* Cardiomyocyte death: mechanisms and translational implications. *Cell Death Dis* **2**, e244–e244 (2011).

611. Chen, D.-S., Yan, J. & Yang, P.-Z. Cardiomyocyte Atrophy, an Underestimated Contributor in Doxorubicin-Induced Cardiotoxicity. *Front Cardiovasc Med* **9**, 812578 (2022).

612. Kamalov, G. *et al.* ATROPHIC CARDIOMYOCYTE SIGNALING IN HYPERTENSIVE HEART DISEASE. *J Cardiovasc Pharmacol* **62**, 10.1097/FJC.0000000000000011 (2013).

613. Meehan, S., Wu, A. J., Kang, E. C., Sakai, T. & Ambudkar, I. S. Interferon-γ induces a decrease in the intracellular calcium pump in a human salivary gland cell line. *American Journal of Physiology-Cell Physiology* **273**, C2030–C2036 (1997).

614. Cosper, P. F., Harvey, P. A. & Leinwand, L. A. Interferon-γ Causes Cardiac Myocyte Atrophy via Selective Degradation of Myosin Heavy Chain in a Model of Chronic Myocarditis. *Am J Pathol* **181**, 2038–2046 (2012).

615. Mirzaei, S. *et al.* The involvement of epithelial-to-mesenchymal transition in doxorubicin resistance: Possible molecular targets. *European Journal of Pharmacology* **908**, 174344 (2021).

616. Schäfer, S. *et al.* CD8+ T Cells Drive Plaque Smooth Muscle Cell Dedifferentiation in Experimental Atherosclerosis. *Arteriosclerosis, Thrombosis, and Vascular Biology* **44**, 1852–1872 (2024).

617. Lei, Y. *et al.* Cooperative sensing of mitochondrial DNA by ZBP1 and cGAS promotes cardiotoxicity. *Cell* **186**, 3013-3032.e22 (2023).

618. Caiazza, C. *et al.* The Lack of STING Impairs the MHC-I Dependent Antigen Presentation and JAK/STAT Signaling in Murine Macrophages. *Int J Mol Sci* **23**, 14232 (2022).

619. Fan, X. *et al.* cGAS-STING signaling in cancer: Regulation and therapeutic targeting. *MedComm – Oncology* **2**, e49 (2023).

620. Pérez-Guijarro, E., Day, C.-P., Merlino, G. & Zaidi, M. R. Genetically Engineered Mouse Models of Melanoma. *Cancer* **123**, 2089–2103 (2017).

621. Schratz, K. E. *et al.* T cell immune deficiency rather than chromosome instability predisposes patients with short telomere syndromes to squamous cancers. *Cancer Cell* **41**, 807-817.e6 (2023).

622. Buchanich, J. M. *et al.* Use of immunosuppression and subsequent cancer incidence: cohort study. *bmjonc* **2**, (2023).

623. Penn, I. & Starzl, T. E. The Effect of Immunosuppression on Cancer. *Proc Natl Cancer Conf* **7**, 425–436 (1972).

624. Blum, S. M. *et al.* Immune responses in checkpoint myocarditis across heart, blood and tumour. *Nature* **636**, 215–223 (2024).

625. Kciuk, M. *et al.* Doxorubicin—An Agent with Multiple Mechanisms of Anticancer Activity. *Cells* **12**, 659 (2023).

626. Sawasdee, N. *et al.* Doxorubicin sensitizes breast cancer cells to natural killer cells in connection with increased Fas receptors. *International Journal of Molecular Medicine* **49**, 1–12 (2022).

627. Wennerberg, E. *et al.* Doxorubicin sensitizes human tumor cells to NK and T cell-mediated killing by augmented TRAIL-receptor signaling. *Int J Cancer* **133**, 1643–1652 (2013).

628. Alizadeh, D. *et al.* Doxorubicin Eliminates Myeloid-Derived Suppressor Cells and Enhances the Efficacy of Adoptive T-Cell Transfer in Breast Cancer. *Cancer Research* **74**, 104–118 (2014).

629. Zirakzadeh, A. A. *et al.* Doxorubicin enhances the capacity of B cells to activate T cells in urothelial urinary bladder cancer. *Clinical Immunology* **176**, 63–70 (2017).

630. Zhu, S., Waguespack, M., Barker, S. A. & Li, S. Doxorubicin Directs the Accumulation of Interleukin-12–Induced IFNγ into Tumors for Enhancing STAT1–Dependent Antitumor Effect. *Clinical Cancer Research* **13**, 4252–4260 (2007).

631. Hussner, J. *et al.* Regulation of Interferon-Inducible Proteins by Doxorubicin via Interferon γ-Janus Tyrosine Kinase-Signal Transducer and Activator of Transcription Signaling in Tumor Cells. *Molecular Pharmacology* **81**, 679–688 (2012).

632. Jenh, C.-H. *et al.* A selective and potent CXCR3 antagonist SCH 546738 attenuates the development of autoimmune diseases and delays graft rejection. *BMC Immunology* **13**, 2 (2012).

633. O'Boyle, G. *et al.* Chemokine receptor CXCR3 agonist prevents human T-cell migration in a humanized model of arthritic inflammation. *Proc Natl Acad Sci U S A* **109**, 4598–4603 (2012).

634. Yellin, M. *et al.* A phase II, randomized, double-blind, placebo-controlled study evaluating the efficacy and safety of MDX-1100, a fully human anti-CXCL10 monoclonal antibody, in combination with methotrexate in patients with rheumatoid arthritis. *Arthritis & Rheumatism* **64**, 1730–1739 (2012).

635. Wang, X. *et al.* The role of CXCR3 and its ligands in cancer. *Front Oncol* **12**, 1022688 (2022).

636. Russo, E., Santoni, A. & Bernardini, G. Tumor inhibition or tumor promotion? The duplicity of CXCR3 in cancer. *Journal of Leukocyte Biology* **108**, 673–685 (2020).

637. Choe, J. H. *et al.* SynNotch-CAR T cells overcome challenges of specificity, heterogeneity, and persistence in treating glioblastoma. *Science Translational Medicine* **13**, (2021).

638. Schmid, P. *et al.* Overall Survival with Pembrolizumab in Early-Stage Triple-Negative Breast Cancer. *New England Journal of Medicine* **391**, 1981–1991 (2024).

639. Lee, E. K. *et al.* Combined pembrolizumab and pegylated liposomal doxorubicin in platinum resistant ovarian cancer: A phase 2 clinical trial. *Gynecologic Oncology* **159**, 72–78 (2020).

640. Wilky, B. A. *et al.* A single-arm, open-label phase 2 trial of doxorubicin plus zalifrelimab, a CTLA-4 inhibitor, with balstilimab, a PD-1 inhibitor, in patients with advanced/metastatic soft tissue sarcomas. *JCO* **41**, 11501–11501 (2023).

641. Lee, S.-H. *et al.* Cancer Therapy-Related Cardiac Dysfunction in Patients Treated with a Combination of an Immune Checkpoint Inhibitor and Doxorubicin. *Cancers (Basel)* **14**, 2320 (2022).

642. Yati, S. *et al.* Extracellular Vesicle-Mediated IL-1 Signaling in Response to Doxorubicin Activates PD-L1 Expression in Osteosarcoma Models. *Cells* **11**, 1042 (2022).

643. Abiko, K. *et al.* IFN-γ from lymphocytes induces PD-L1 expression and promotes progression of ovarian cancer. *Br J Cancer* **112**, 1501–1509 (2015).

644. Wang, J. *et al.* Sorafenib inhibits doxorubicin-induced PD-L1 upregulation to improve immunosuppressive microenvironment in Osteosarcoma. *J Cancer Res Clin Oncol* (2022) doi:10.1007/s00432-022-04458-4.

645. Solinas, C. *et al.* Programmed cell death-ligand 2: A neglected but important target in the immune response to cancer? *Translational Oncology* **13**, 100811 (2020).

646. Garcia-Diaz, A. *et al.* Interferon Receptor Signaling Pathways Regulating PD-L1 and PD-L2 Expression. *Cell Rep* **19**, 1189–1201 (2017).